Advances in Electrochemical Science and Engineering, Volume 8. Edited by Richard C. Alkire

ISBNs: 3-527-30211-5 (Hardback); 3-527-60078-7 (Electronic)

Advances in Electrochemical Science and Engineering

Volume 8

Advances in Electrochemical Science and Engineering, Volume 8. Edited by Richard C. Alkire

ISBNs: 3-527-30211-5 (Hardback); 3-527-60078-7 (Electronic)

Advances in Electrochemical Science and Engineering

In collaboration with the International
Society of Electrochemistry

Advances in Electrochemical Science and Engineering, Volume 8. Edited by Richard C. Alkire

ISBNs: 3-527-30211-5 (Hardback); 3-527-60078-7 (Electronic)

Advances in Electrochemical Science and Engineering

Volume 8

Edited by Richard C. Alkire
and Dieter M. Kolb

Contributions from

J. Fleig, Stuttgart
K. Krischer, Berlin
Y. V. Pleskov, Moskow
H.-H. Strehblow, Düsseldorf

WILEY-VCH

Advances in Electrochemical Science and Engineering, Volume 8. Edited by Richard C. Alkire

ISBNs: 3-527-30211-5 (Hardback); 3-527-60078-7 (Electronic)

Editors:
Prof. Richard C. Alkire
University of Illinois
600 South Mathews Avenue
Urbana, IL 61801
USA

Prof. Dieter M. Kolb
University of Ulm
Department of Electrochemistry
Albert-Einstein-Allee 47
89081 Ulm
Germany

Library of Congress Card No.: applied for

A catalogue record for this book is available from the British Library.

Bibliographic information published by Die Deutsche Bibliothek
Die Deutsche Bibliothek lists this publication in the Deutsche Nationalbibliografie; detailed bibliographic data is available in the Internet at http://dnb.ddb.de

ISBN 3-527-30211-5

Composition: Asco Typesetters, Hong Kong.
Printing: betz-druck gmbh, Darmstadt.
Bookbinding: J. Schäffer GmbH & Co. KG, Grünstadt.
Printed in the Federal Republic of Germany.

Advances in Electrochemical Science and Engineering, Volume 8. Edited by Richard C. Alkire

ISBNs: 3-527-30211-5 (Hardback); 3-527-60078-7 (Electronic)

Introduction

This eighth volume continues the series established by the late Heinz Gerischer and Charles W. Tobias. The favourable reception of the first seven volumes and the steady increase of interest in electrochemical science and technology provide good reasons for the continuation of this series with the same high standards. The purpose of the series is to provide high quality advanced reviews of topics of both fundamental and practical importance for the experienced reader.

Richard C. Alkire
Dieter M. Kolb

Advances in Electrochemical Science and Engineering, Volume 8. Edited by Richard C. Alkire

ISBNs: 3-527-30211-5 (Hardback); 3-527-60078-7 (Electronic)

Preface

Fleig reviews fundamental aspects of solid state ionics, and illustrates many similarities between the field of solid state electrochemistry and liquid electrochemistry. These include the consideration of mass and charge transport, electrochemical reactions at electrode/solid interfaces, and impedance spectroscopy. Recent advances in microelectrodes based on solid state ionics are reviewed, along with their application to measuring inhomogeneous bulk conductivities, grain boundary properties, and electrode kinetics of reactions on anion conductors.

Krischer describes in detail the use of nonlinear dynamics in simulating the behavior of systems that can spontaneously form patterns in time and/or space. The discussion illustrates the underlying principles of how such patterns emerge owing to the interplay of homogeneous dynamics and coupling with electrode kinetics, migration, conductivity, cell geometry, and the external circuit. The wide variety of electrochemical systems that give patterns has led to their wide use as convenient "model systems" for exploring fundamentals of nonlinear phenomena. Such knowledge may eventually lead to applications that depend upon controlled instability for useful purposes such as (temporal) catalyst regeneration or (spatial) self-assembly and pattern formation.

The overview by Pleskov covers the literature on electrochemical behavior of synthetic diamond films, as well as the use of electrochemical methods in their characterization. The rapid advancement of the field of diamond electrochemistry was triggered by progress in the technology of deposition of polycrystalline diamond thin films on diamond and other substrates. Advances around the world have by now led to formation of a self-consistent, but as yet incomplete, view of electrochemical behavior of diamond. While discrepancies and scatter between data from different research groups still exist, the rapid advance in film quality and in reliable methods of evaluation point to a promising future.

In the last chapter, Strehblow provides a review of experimental methodology and theoretical concepts of passivation and passivity of metals. The topics of emphasis include growth and composition of passive layers, their structure and electronic properties, and their breakdown. Current accomplishments are discussed in detail for a selected number of key metal and alloy systems. Summarized in some detail are the most important analytical methods for elucidation of chemical composition, electronic properties and structure of passive layers. It is shown for many systems that the application of multiple combinations of electrochemical and spectroscopic methods provide many insights and confidence in the interpretation of the passive behavior of metals.

Advances in Electrochemical Science and Engineering, Volume 8. Edited by Richard C. Alkire

ISBNs: 3-527-30211-5 (Hardback); 3-527-60078-7 (Electronic)

Contents

Advances in Electrochemical Science and Engineering, Volume 8. Edited by Richard C. Alkire

ISBNs: 3-527-30211-5 (Hardback); 3-527-60078-7 (Electronic)

List of Contributors

Jürgen Fleig
Max-Planck-Institute for Solid State Research
Heisenbergstr. 1
D-70569 Stuttgart
Germany
juergen.fleig@mpg.de

Katharina Krischer
Fritz-Haber-Institut der Max-Planck-Gesellschaft
Faradayweg 4–6
D-14195 Berlin
Germany
krischer@ph.tum.de

Yuri V. Pleskov
A. N. Frumkin Institute of Electrochemistry
Russian Academy of Sciences
Leninsky Prospekt 31
117071 Moscow
Russia
Pleskov@electrochem.msk.ru

Hans-Henning Strehblow
Institut für Physikalische Chemie und Elektrochemie
Heinrich-Heine-Universität
Universitätsstr. 1
D-40225 Düsseldorf
Germany
Henning@uni-düsseldorf.de

Advances in Electrochemical Science and Engineering, Volume 8. Edited by Richard C. Alkire

ISBNs: 3-527-30211-5 (Hardback); 3-527-60078-7 (Electronic)

Index

Advances in Electrochemical Science and Engineering, Volume 8. Edited by Richard C. Alkire

ISBNs: 3-527-30211-5 (Hardback); 3-527-60078-7 (Electronic)

Microelectrodes in Solid State Ionics

Jürgen Fleig

Max–Planck–Institute for Solid State Research, Heisenbergstr. 1, D-70569 Stuttgart, Germany

Contents

List of Symbols

A	area
A_{gb}	grain boundary area
A_{in}	area of the electrochemically inactive (inner) part of a microelectrode
A_{ring}	area of the electrochemically active ring at the three-phase boundary of a microelectrode
b_{ring}	width of the electrochemically active zone at a three-phase boundary
c	concentration
c_{def}	defect concentration
c_{dop}	dopant concentration
c_e	electron concentration
c_h	hole concentration
c_V	vacancy concentration
C	capacitance
C_{bulk}	bulk capacitance
C_{el}	electrode capacitance
C_{gb}	grain boundary capacitance
$\tilde{C}_{in}$	area-related (specific) capacitance of the electrochemically inactive (inner) part of a microelectrode
C_{in}	nominal capacitance of the electrochemically inactive (inner) part of a microelectrode ($\tilde{C}_{in}A_{in}$)
$\tilde{C}_{ring}$	area-related (specific) capacitance of the electrochemically active ring at the three-phase boundary of a microelectrode
C_{ring}	nominal capacitance of the electrochemically active ring at the three-phase boundary of a microelectrode ($\tilde{C}_{ring}A_{ring}$)
C_{spr}	spreading capacitance
C_{stray}	stray capacitance
$\tilde{D}$	chemical diffusion coefficient
d_{me}	microelectrode diameter
e	elementary charge
E	electrical field
Δg	free formation enthalpy of a defect pair
Δh	formation enthalpy of a defect pair
h_R	resistance correction factor
h_C	capacitance correction factor
I	current
$\mathbf{J}$	particle flux
$\mathbf{j}$	current density
k	Boltzmann constant

K	thermodynamic equilibrium constant
L	length (thickness) of a sample
L_g	grain size
LSM	Sr-doped lanthanum manganite
$p(O_2)$	oxygen partial pressure
r	radius
R	resistance
R_{bulk}	bulk resistance
R_{el}	electrode resistance
$\tilde{R}_{el}$	area-related (specific) electrode resistance
$\tilde{R}_{el}^{eff}$	effective area-related (specific) electrode resistance ($R_{el}^{eff} A_{el}$)
R_{el}^{eff}	effective (i.e. measured or simulated) electrode resistance
R_{gb}	grain boundary resistance
$R_{gb,c}$	grain boundary resistance between two large contact electrodes
$R_{gb,me}$	grain boundary resistance between two microelectrodes
R_{spr}	spreading resistance
$R_{\Delta cc}$	additional bulk resistance due to current constriction close to the three-phase boundary
R_{ongb}	resistance measured with a microelectrode on a grain boundary
$R_{ongrain}$	resistance measured with a microelectrode on a grain
$\tilde{R}_{ring}$	area-related (specific) resistance of the electrochemically active ring at the three-phase boundary of a microelectrode
Δs	local formation entropy of a defect pair
t	time
t_{me}	microelectrode thickness
T	temperature
u	electrical mobility
U	voltage
U_{bias}	dc bias voltage
w	thickness
w_{gb}	grain boundary thickness
$\Delta\tilde{Y}_{gb}$	area-related excess grain boundary conductance
$\tilde{Y}_{gb}$	area-related grain boundary conductance
YSZ	yttria-stabilized zirconia
z	charge number
z_{def}	charge number of the defect
z_{dop}	charge number of the dopant
Z	impedance
3PB	three-phase boundary
ε	permittivity
ε_{bulk}	bulk permittivity
ε_{gb}	grain boundary permittivity
ε_{sc}	space charge permittivity
λ_D	Debye length
μ	chemical potential
$\tilde{\mu}$	electrochemical potential
ρ_{bulk}	bulk resistivity
ρ_{gb}	grain boundary resistivity
σ	conductivity
σ_{bulk}	bulk conductivity
σ_{gb}	grain boundary conductivity
φ	electrical potential
$\Delta\varphi$	space charge potential
ω	angular frequency
ω_r	angular relaxation frequency

Subscripts

bulk	bulk of the material, grain interior
ce	counter electrode
def	defect
dop	dopant
e	electron
eff	effective
el	electrode
eon	electronic charge carrier
gb	grain boundary
h	hole
im	imaginary part
ion	ionic charge carrier
me	microelectrode
RC	resistor in parallel with a capacitor
re	real part
ring	electrochemically active region at the three-phase boundary of a microelectrode
spr	spreading
tot	total
V	vacancy
W	Warburg

1 Introduction

The interdisciplinary field of solid state ionics deals with properties that are related to ionic charge carriers and ionic transport phenomena in solids. It incorporates therefore aspects of solid state chemistry, physical chemistry, solid state physics and materials science. The materials that are investigated in solid state ionics are predominantly ceramics, to be specific inorganic ionic compounds such as crystalline AgCl, NaCl, LaF_3, ZrO_2, SnO_2, $SrTiO_3$, $LaMnO_3$, $LiCoO_2$, Li_4SiO_4, $BaCeO_3$, CuBr or Nasicon ($Na_{1+x}Zr_2P_{3-x}Si_xO_{12}$), and amorphous $(Li_2O)_x(Na_2O)_y(B_2O_3)_{1-x-y}$, or $(AgPO_3)_{1-x}(AgI)_x$ [1–5]. Important phenomena and properties that receive attention are i) ionic conductivity and diffusion in solids; ii) chemical and electrochemical reactions on or in ionic compounds (e.g. oxidation, intercalation, sintering, corrosion); and iii) physics and chemistry of defects in ionic solids. Solid state ionics is thus concerned with the basics of many technologically relevant processes, such as the fabrication and degradation of ceramic materials. However, it is the use of ionic solids in several key technologies, for example in fuel cells, sensors and batteries, which explains the considerable interest in this field during the last ten or twenty years:

i) Fuel cells are considered to play an important role in future electrical-power generation for stationary power supply, vehicles, and portable electrical appliances [6–13]. There are several fuel cell concepts using different electrolytes, of which solid oxide fuel cells (SOFCs) are certainly one of the most promising,

particularly for stationary power supply. SOFCs are based on an ion-conducting oxide (e.g. Y-doped ZrO_2), and research directed towards new solid electrolytes, advanced electrode materials, or improved electrochemical performance of the cells yields important contributions to the field of solid state ionics.

ii) Numerous current research activities in solid state ionics are concerned with investigating sensors for gases such as O_2, CO_2, SO_2, NO_x, H_2 or Cl_2 [14–20]. Sensors based on zirconia ceramics are, for example, employed by the automotive industry to control the combustion process.

iii) Li batteries exhibit the highest energy density of all existing batteries and constitute a market of several hundred million dollars [21–26]. Cathodes of rechargeable Li batteries (e.g. $LiCoO_2$) are ionic intercalation compounds into which Li can be incorporated. The investigation of new cathode materials, and an understanding of intercalation mechanisms, are but two topics in battery research related to solid state ionics.

These examples and the general subjects mentioned above illustrate that ion conduction and the electrochemical properties of solids are particularly relevant in solid state ionics. Hence, the scope of this area considerably overlaps with the field of solid state electrochemistry, and the themes treated, for example, in textbooks on solid state electrochemistry [27–31] and books or journals on solid state ionics [1, 32] are very similar indeed. Regrettably, for many years solid state electrochemistry/solid state ionics on the one hand, and liquid electrochemistry on the other, developed separately. Although developments in the area of polymer electrolytes or the use of experimental techniques such as impedance spectroscopy have provided links between the two fields, researchers in both solid and liquid electrochemistry are frequently not acquainted with the research activities of the sister discipline. Similarities and differences between (inorganic) solid state electrochemistry and liquid electrochemistry are therefore emphasized in this review. In Sec. 2, for example, several aspects (non-stoichiometry, mixed ionic and electronic conduction, internal interfaces) are discussed that lead to an extraordinary complexity of electrolytes in solid state electrochemistry.

The main purpose of this contribution, however, is to review recent advances in solid state ionics achieved by means of microelectrodes, i.e. electrodes whose size is in the micrometer range (typically 1–250 μm). In liquid electrolytes (ultra)-microelectrodes are rather common and applied for several reasons: they exhibit a very fast response in voltametric studies, facilitate the investigation of fast charge transfer reactions and strongly reduce the importance of ohmic drops in the electrolyte, thus allowing e.g. measurements in low-conductive electrolytes [33, 34]. Microelectrodes are also employed to localize reactions on electrodes and to scan electrochemical properties of electrode surfaces (scanning electrochemical microscope [35, 36]); further developments refer to arrays of microelectrodes, e.g. for (partly spatially resolved) electroanalysis [37–39], applications in bioelectrochemistry and medicine [40, 41] or spatially resolved pH measurements [42]. Reviews on these and other applications of microelectrodes are, for example, given in Ref. [33, 34, 43–47].

In solid state ionics, on the other hand, microelectrodes are far less commonly used and only recently has the number of studies using microelectrodes increased

noticeably. This might be surprising, since – particularly because of the complexity of the solid electrolytes – there are many different problems in solid state electrochemistry to which microelectrodes could be applied. They are, for example, destined to quantify inhomogeneous bulk conductivities, to detect highly conductive grain boundaries, or to investigate the distribution of the properties of highly resistive grain boundaries. This is detailed in Sec. 3. Interpreting the results of microelectrode measurements on solid electrolytes is by no means straightforward, however. The equations for the local determination of bulk conductivities are well known [48–50]. On the other hand, the theoretical basis for a quantitative analysis of experiments on grain boundaries, and of impedance studies involving electrodes with electrochemically active three-phase boundaries, have been developed only recently [51–54]; these theoretical considerations are discussed in detail in Sec. 4. From an experimental point of view, microelectrode experiments in solid state ionics can be demanding as well: they often yield very high resistances, since many ceramics exhibit rather low conductivities. Furthermore, even very small stray capacitances can generate considerable measurement artefact. In Sec. 5, some experimental aspects of microelectrode experiments on ionic solids are reviewed. Lastly, Sec. 6 is devoted to examples of microelectrode measurements on ionic compounds. An overview is presented which touches upon most of the recent microelectrode literature in solid state ionics. (Measurements with miniaturized electrodes whose size is of the order of millimeters, and scanning-probe microscopy studies using nanometer-sized electrodes, are not considered.) Four experiments are discussed in more detail: i) a study of inhomogenous bulk conductivities due to non-stoichiometry effects in an oxide ($SrTiO_3$); ii) microelectrode experiments in order to determine the distribution of grain boundary properties in an oxide ($SrTiO_3$); iii) measurements for the detection and quantification of highly conductive grain boundaries in a silver ion conductor (AgCl); and iv) an electrode kinetic study of the oxygen reduction reaction on an anion conductor (ZrO_2). These examples are chosen with the aim of giving at least an idea of the variety of scientific problems (bulk, grain boundary and electrode phenomena) treated in solid state ionics. Furthermore, these experiments provide evidence that microelectrodes are very useful tools in tackling solid state electrochemical problems.

2 Charge Transport and Electrochemistry in Ionic Solids

2.1 Defects in Ionic Crystals

2.1.1 Defects and their Notation

Many important phenomena in solid state ionics, such as ionic conduction, gas permeation through dense solids, solid state reactions, high temperature corrosion, or sintering of polycrystals, involve mobile ionic charge carriers. In most crystalline

lattices, however, only point defects such as vacancies (unoccupied lattice sites) or interstitials (ions on non-regular lattice sites) facilitate the transport of ions. In a certain sense, ionic solids are therefore similar to pure water, wherein "defects" (i.e. H_3O^+ and OH^-) are also necessary for an ionic current [55]. Thus, in most cases defects, rather than regular constituents, are the particles relevant in electrical and electrochemical phenomena in ceramics.

For reasons of clarity, a standard notation for defects in ionic solids has been developed (Kröger–Vink notation [56, 57]). The main symbol of the notation indicates whether the defect is a vacancy "V" or an ion, such as "Ag" in AgCl: a subscript denotes the site that the defect occupies, either the regular lattice site (eg. "Ag" in AgCl) or an interstitial site "*i*", and a superscript identifies the relative charges with respect to the perfect lattice. Dots ($^\bullet$) represent positive charges, dashes ($^\prime$) are used for negative charges, and *x* denotes electroneutrality with respect to the perfect lattice. Hence, a silver vacancy and a silver interstitial in AgCl are $V_{Ag}^{\prime}$ and $Ag_i^{\bullet}$ respectively, whereas $V_O^{\bullet\bullet}$ denotes an oxygen vacancy in an oxide. In the following sections, the mechanisms that determine the concentration of point defects in ionic solids are discussed, emphasizing the similarities and differences between solid and liquid electrochemistry.

2.1.2 Intrinsic Disorder

Let us first consider a pure ionic solid with negligible impurity concentration. The two most common types of point defects in such solids are vacancies and interstitials. These defects are usually charged relative to the perfect lattice, and in the bulk oppositely charged defects co-exist in order to balance the charge. Two defect combinations mainly occur in ionic lattices: i) Frenkel disorder (Fig. 1a) with vacancies and interstitials of the same ion being the dominating defects (e.g. in AgCl, AgBr, BaF_2, CaF_2; in the case of anionic defects (BaF_2, CaF_2) the term Anti-Frenkel disorder is often used); ii) Schottky disorder with anion and cation vacancies as the predominant defects (e.g. in NaCl, $SrTiO_3$, MgO).

The formation of defects involves the breaking of bonds; in thermodynamic equilibrium, defects can therefore only exist if the endothermic formation enthalpy is counterbalanced by entropic effects. The predominant contribution to this entropy comes from the increasing number of configurations in which the particles can be arranged in a lattice if defects are present. With analytical expressions for this configuration entropy, the mass action law

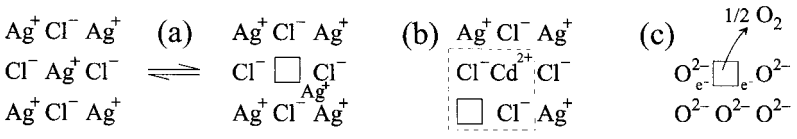

Fig. 1. Defect chemical phenomena: (a) formation of a silver vacancy and an interstitial silver ion in AgCl; (b) formation of a silver vacancy in AgCl by doping with $CdCl_2$; (c) non-stoichiometry in an oxide caused by the excorporation of oxygen.

$$c_A c_B = n_A n_B e^{-\Delta g/kT} = n_A n_B e^{-\Delta h/kT} e^{\Delta s/k} \tag{1}$$

can be deduced for two oppositely charged defects of dilute concentration c_A, c_B [58–60]. In Eq. (1) n_A, n_B are the concentrations of sites available for the defects A, B and Δg, Δh, Δs denote the free formation enthalpy, the formation enthalpy and the local formation entropy of a defect pair.

The situation is equivalent to the formation of H_3O^+ (''proton interstitial'') and OH^- (''proton vacancy'') in water where the endothermic formation enthalpy of the water dissociation reaction is also compensated by the gain of configuration entropy [61]. In both cases, defect chemical reactions can be formulated: the dissociation reaction in water

$$H_2O + H_2O \rightleftharpoons H_3O^+ + OH^- \tag{2}$$

corresponds to the Frenkel pair formation reaction

$$Ag_{Ag}^{x} + V_i^{x} \rightleftharpoons Ag_i^{\bullet} + V_{Ag}^{|}. \tag{3}$$

The defect concentration is exponentially related to $\Delta h/T$ (Eq. (1)) and intrinsic defect concentrations can therefore differ greatly. The materials parameter Δh varies between several tens of kJ/mol and some hundred kJ/mol [62–64], and intrinsic defect concentrations at room temperature can be higher than in pure water (e.g in AgBr), but also much lower than one defect per cm^3 (estimated for MgO). Increasing the temperature strongly enhances the defect concentrations and defect mole fractions in the range of a few percent can be reached, e.g. in AgBr near the melting point, or in β-PbF_2 and β-AgI near the transition temperature to the superionic phase (i.e. to a phase with a highly disordered sublattice of mobile ions) [65–68].

2.1.3 Extrinsic Disorder

The defect concentrations in ionic solids can be enhanced by doping with aliovalent ions: if, for example, Cd^{2+} ions replace Ag^+ ions in AgCl, additional positive charges are introduced that are compensated by negative silver vacancies (Fig. 1b). In terms of a defect chemical reaction the doping can be written as:

$$CdCl_2 \rightarrow 2Cl_{Cl}^{x} + Cd_{Ag}^{\bullet} + V_{Ag}^{|}. \tag{4}$$

The doping of a solid is similar to the enhancement of the H_3O^+ or OH^- concentration in water by adding a strong acid or base. However, while in water mobilities of ''dopant'' ions are frequently similar to those of the native defects H_3O^+ and OH^- [69, 70], dopant ions in solids (e.g. $Cd_{Ag}^{\bullet}$ in AgCl) are almost immobile. This is also why supporting electrolytes (i.e. electrolytes with dissolved ''dopants'' that enhance the ionic conductivity, but do not influence electrochemical electrode reactions [71, 72], are unknown in solid state electrochemistry.

If the intrinsic defect concentration is much lower than the dopant (or impurity) concentration c_{dop}, electroneutrality requires a defect concentration c_{def} according to

$$c_{def} = c_{dop}\left|\frac{z_{dop}}{z_{def}}\right| \tag{5}$$

with z_{dop} and z_{def} being the charge numbers of dopant and compensating defect respectively. Such extrinsic disorder occurs particularly at lower temperatures, where the intrinsic concentrations are rather low. In the case of large defect formation enthalpies (e.g. in oxides), the extrinsic disorder prevails even at high temperatures. However, it should be remembered that – as in water – the mass action law of the defect equilibrium (Eq. (1)) is valid even in the extrinsic regime.

2.1.4 Non-Stoichiometry of Solids

Ionic solids can always exhibit certain deviations from their stoichiometric composition. In thermodynamic equilibrium, tin dioxide ($SnO_{2-\delta}$) is oxygen-deficient, whereas cobalt oxide ($Co_{1-\delta}O$) is a metal-deficient compound. In both cases the δ-value depends on the oxygen partial pressure. On an atomistic scale, deviations from the stoichiometric composition again lead to defects: the oxygen deficiency of a binary oxide $MO_{1-\delta}$, for example, may either be due to metal interstital ions ($M_i^{\bullet\bullet}$) or oxygen vacancies ($V_O^{\bullet\bullet}$). The decreased number of oxide ions, however, needs less positive charge to preserve electroneutrality, and hence the cations are partly reduced in such a case. From a charge carrier point of view, this reduction of cations corresponds to the formation of mobile electrons in the band scheme of the solid. In other words, non-stoichiometry not only introduces ionic defects, but also electronic charge carriers (Fig. 1c). This non-stoichiometry has no direct counterpart in water and leads to a manifold of phenomena such as diffusion of (formally neutral) oxygen in an oxide, mixed ionic and electronic conductivity and reduced electromotive forces that distinguish solid state from liquid electrochemistry [30, 73–75].

With respect to the electronic charge carriers in ionic solids, it should be mentioned that semiconductor-like band structures with relatively wide band gaps (for example ca. 3.1 eV in $SrTiO_3$, 7.3 eV in NaCl and 3.2 eV in AgCl [76–78]) can often be found. In these solids, electrons in the conduction band (CB), and holes in the valence band (VB), can be regarded as electronic defects in equilibrium via the reaction

$$e'_{VB} + h^{\bullet}_{CB} \rightleftharpoons e'_{CB} + h^{\bullet}_{VB}. \tag{6}$$

Similar to a Frenkel disorder, or to the dissociation equilibrium in water, a mass action law according to

$$c_e c_h = K_e \tag{7}$$

can be formulated for the electron concentrations in the conduction band c_e and the hole concentration in the valence band c_h [73, 79].

The extent of non-stoichiometry, i.e. the extent to which a compound can partly be reduced or oxidized, strongly depends on the kind of cation. In $Co_{1-\delta}O$ or $SnO_{2-\delta}$, δ can be of the order of one percent and in several oxides such as $CeO_{2-\delta}$ and $Mn_{1-\delta}O$ even several percent are possible; in Al_2O_3 or MgO, on the other hand, the degree of non-stoichiometry is extremely small [78, 80–82]. Nevertheless, even very small δ-values can determine the charge carrier concentration in a solid, and thus effects such as the kinetics of solid state reactions.

Let us further consider an oxygen-deficient oxide $MO_{1-\delta}$. The equilibrium with the surrounding gas, which determines the stoichiometry, can be written as

$$O_O^x \rightleftharpoons \tfrac{1}{2}O_2 + V_O^{\bullet\bullet} + 2e' \tag{8}$$

and leads to the mass action law

$$c_e^2 c_V \sqrt{(p(O_2)} = K_\delta \tag{9}$$

with c_V and $p(O_2)$ denoting the oxygen vacancy concentration and the oxygen partial pressure. If the defect concentration is solely determined by the non-stoichiometry, Eq. (9) can be used to calculate the partial pressure dependence of c_e and c_V. Owing to the electroneutrality equation, $2c_V$ equals c_e and

$$c_V = \tfrac{1}{2}c_e = \sqrt[3]{K_\delta/4}(p(O_2))^{-1/6} \tag{10}$$

results. Such a $-1/6$ relationship is frequently found in experiments (e.g. in $BaTiO_3$ [83], $SrTiO_3$ [77, 84], SnO_2 [85, 86] or CeO_2 [87, 88]).

2.1.5 Brouwer Diagrams and Frozen-In Profiles

In many ceramics, intrinsic and extrinsic disorder, as well as the disorder due to non-stoichiometry, have to be considered. Independent of the dopant level, the mass action laws of intrinsic disorder, of the e-h equilibrium and of the reaction with the surrounding phase are valid in thermodynamic equilibrium. Together with the electroneutrality equation

$$\left(z_{dop}c_{dop} + \sum_i z_{def,i}c_{def,i}\right) = 0, \tag{11}$$

a system of four equations results. These equations unambiguously define the four defect concentrations c_{V_O}, c_{V_M}, c_e, and c_h in a binary oxide with Schottky disorder ($V_O^{\bullet\bullet}$ and $V_M^{\|}$) and given dopant level c_{dop}.

For broad partial pressure regimes, however, only two mobile defects, or one mobile defect and the dopant, play a role in the electroneutrality equation (Eq. (11)). In theses cases simple partial pressure dependences, namely power laws with concentrations being proportional to $p(O_2)^n$, can be calculated (see e.g. Refs. [57, 80, 89, 90]). One example of such a simplified situation has been examined above (Eq. (10)).

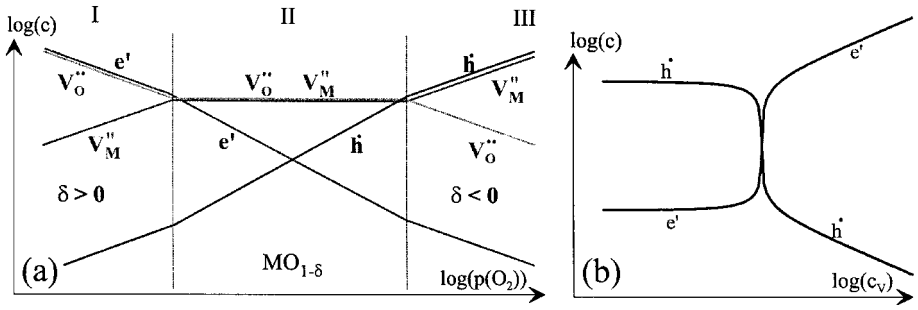

Fig. 2. (a) Sketch of the relations between defect concentrations and partial pressure (Brouwer diagram) of a pure oxide $MO_{1-\delta}$. In regime II the intrinsic Schottky disorder determines the concentration, whereas in I and III non-stoichiometry prevails. (b) Dependence of the hole and electron concentration on the frozen-in oxygen vacancy concentration in a negatively (acceptor) doped oxide.

Considering different pairs of majority defects, all relationships between defect concentrations and partial pressure can be constructed from simplified situations, and this leads to so-called Brouwer diagrams. Figs. 2a and 3a show such Brouwer diagrams for a pure oxide $MO_{1-\delta}$ with Schottky disorder, and for a Schottky-disordered oxide with a negative dopant. (Please notice that the exact curves calculated from the complete electroneutrality equation (Eq. (11)) exhibit smooth transitions rather than sharp bends.)

In the case of a pure oxide (Fig. 2a), three partial pressure regimes are found: the intrinsic regime for medium $p(O_2)$ and two regimes with defect concentrations being dominated by non-stoichiometry. In the case of a doped oxide (Fig. 3a), two different extrinsic regimes have to be distinguished: at low $p(O_2)$ a regime with vacancy-compensated dopant charge (II) and at higher oxygen partial pressure a regime with holes compensating the dopant charge (III).

However, the partial pressures at which the predominant defect(s) change and the width of the different $p(O_2)$ regimes strongly depend on the material under consideration. Frequently, only one or two regimes can be detected in the partial pressure range that is typically used (ca. 10^{-20} bar to 1 bar). In the case of highly doped ZrO_2, which is the electrolyte usually employed in solid oxide fuel cells (SOFCs), only the vacancy-compensated extrinsic regime (II in Fig. 3a) is found [91, 92]; highly doped $LaCrO_3$ (interconnect material in SOFCs) displays the transition from extrinsic vacancy to extrinsic hole compensation (II and III in Fig. 3a) [93, 94]; in nominally pure $CeO_{2-\delta}$ only regimes I and II (Fig. 2a) are observed [87]; and $Fe_{1-\delta}O$ is in its entire stability range metal-deficient ($\delta < 0$) [78]. Defect interactions, however, can lead to deviations from the simple power-laws of Figs. 2 and 3.

It should be emphasized that the kinetics of the equilibration process after a change of the surrounding phase (e.g. a $p(O_2)$ change) requires the movement of defects and can be rather sluggish, particularly at lower temperatures. Therefore, non-equilibrated ionic solids with composition gradients can easily occur, and often the preparation conditions rather than the actual surroundings determine the defect concentrations (frozen-in compositions). On the other hand, internal defect reactions

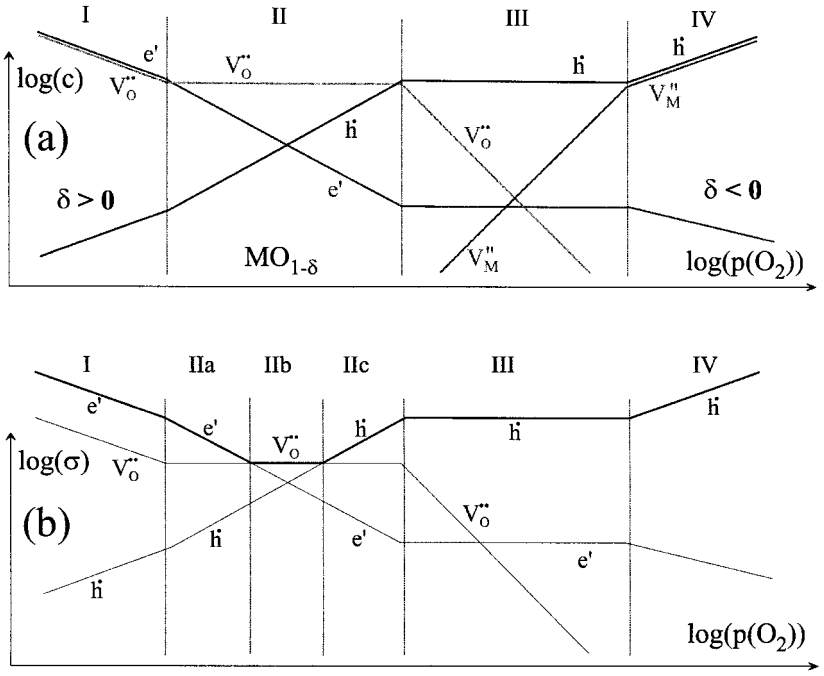

Fig. 3. (a) Sketch of the relations between defect concentrations and partial pressure (Brouwer diagram) of a negatively (acceptor) doped oxide $MO_{1-\delta}$ exhibiting Schottky disorder. Two extrinsic regimes (II and III) and two regimes with prevailing non-stoichiometry (I and IV) are visible. (b) Sketch of the corresponding partial conductivities and the total conductivity (bold line) for $u_e = u_n \gg u_{\text{ion}}$. Oxygen vacancies are assumed to be the only mobile ionic defects. The regime with predominant vacancy concentration is divided into three sub-regimes with electron, vacancy, and hole conduction (IIa, IIb, and IIc).

can be in local equilibrium even if the exchange reaction with the surrounding atmosphere is frozen-in. In particular, the mass action laws of the e-h-equilibrium, and of the Frenkel disorder, can usually be assumed to hold even at low temperatures. In other words, the defect concentrations of, for example, electrons and holes will adjust according to the concentrations of the frozen-in defects.

The dependence of the electronic charge carriers on a frozen-in oxygen vacancy concentration is shown in Fig. 2b. According to this relation, considerable electron and hole concentration gradients can be expected if a vacancy concentration gradient is frozen-in, e.g. due to quenching of the sample during its equilibration process at high temperatures. Oxygen vacancy concentration gradients, and thus c_e and c_h gradients, can also appear if a voltage is applied to ceramics: in an oxide that cannot equilibrate with its surroundings, the oxygen vacancies move in the electrical field, but cannot leave or enter the sample. Consequently, $V_O^{\bullet\bullet}$ accumulate in the vicinity of the cathode, deplete at the anode, and the resulting oxygen vacancy gradient can lead to strong electronic conductivity gradients. This phenomenon plays an important role in the degradation of electroceramic components and spatially resolved mea-

surements of the corresponding conductivity gradients by means of microelectrodes are presented in Sec. 6.2.

2.2 Mass and Charge Transport in Ionic Crystals

In thermodynamic equilibrium, the electrochemical potential of a particle k ($\tilde{\mu}_k = \mu_k + z_k e\varphi$, $\mu_k =$ chemical potential, $\varphi =$ electrical potential, $z_k =$ charge number of the particle, $e =$ elementary charge) is constant. Gradients in $\tilde{\mu}_k$ lead to a particle flux $\mathbf{J_k}$ and from linear irreversible thermodynamics [95] the fundamental transport equation

$$\mathbf{J_k} = -\frac{\sigma_k}{z_k^2 e^2} \nabla \tilde{\mu}_k \tag{12}$$

can be derived. The electrical conductivity σ_k is proportional to mobility u_k and concentration c_k of the mobile charge carrier and is given by:

$$\sigma_k = |z_k| e u_k c_k. \tag{13}$$

A sub-case of Eq. (12) – valid if the chemical potential is constant ($\nabla\mu = 0$) – is Ohm's law, which relates the current density $\mathbf{j_k} = z_k e \mathbf{J_k}$ and $\nabla\varphi$ via

$$\mathbf{j_k} = -\sigma_k \nabla \varphi. \tag{14}$$

Eqs. (12–14) are valid for ionic (vacancies, interstitials), as well as for electronic (electrons, holes), defects. The total conductivity σ_{tot} of an ionic solid is then the sum of ionic and electronic contributions, and both consist of conductivities of different ionic (k,ion) and electronic (m,eon) defects leading to

$$\sigma_{\text{tot}} = \sum_k |z_{k,\text{ion}}| e u_{k,\text{ion}} c_{k,\text{ion}} + \sum_m |z_{m,\text{eon}}| e u_{m,\text{eon}} c_{m,\text{eon}}. \tag{15}$$

Since σ_k is proportional to c_k, the relation between σ_{tot} and the oygen partial pressure can easily be constructed from the Brouwer diagrams with $|z_k| u_k$ as weighting factors. In Fig. 3b, the conductivities of a doped binary oxide (cf. Fig. 3a) are sketched. The much higher mobility of electronic charge carriers frequently leads to partial pressure regimes (IIa, IIc) in which the total conductivity is dominated by electronic species, although the dopant is mainly compensated by ionic defects. Such regimes are characterized by $\sigma \propto p(O_2)^{\pm 1/4}$ and are often experimentally observed (e.g. in doped or impurity-dominated $SrTiO_3$ [77, 84, 96], CeO_2 [97, 98], $LaCrO_3$ [93], SnO_2 [86], or $BaTiO_3$ [99]). It is a typical, though not trivial, task in solid state ionics to reconstruct the defect chemistry from $p(O_2)$-, temperature-, and dopant-dependent conductivity measurements. The great number of ceramic materials, the complication of defect concentrations being partial-pressure-dependent, and the occurrence of mixed ionic and electronic conductivity, are probably why in solid

state electrochemistry bulk (i.e. electrolyte) properties are often the focus of interest; investigations in liquid electrochemistry frequently deal with electrochemical processes at electrodes (“ionics” vs. “electrodics” [100]).

The movement of ionic defects is a thermally activated hopping process and typical activation energies are, for example, 0.03–0.05 eV for $Ag_i^{\cdot}$ in AgCl [101, 102] or $\geq$0.65 eV for $V_O^{\bullet\bullet}$ in various oxides [91, 98, 103–105]. Besides temperature-dependent defect concentrations in the intrinsic regime, this activated hopping process is the main reason for the strong temperature dependence of the conductivity in most ceramic materials (e.g. $\sigma \approx 10^{-1}$ S cm^{-1} in 8–10 mole % Y_2O_3-doped ZrO_2 at 1000 °C, but $\sigma \approx 5 \cdot 10^{-6}$ S cm^{-1} at 300 °C [91, 106, 107]).

2.3 Charge Transport Along and Across Grain Boundaries

Ceramic materials are frequently polycrystalline and their electrical properties are not only determined by the bulk conductivity, but also by the charge transport along and across grain boundaries. From a structural point of view, the grain boundary is a thin region (ca. 0.5–2 nm thick) exhibiting crystallographic and often also chemical differences from the bulk, such as modified lattice distances, enhanced disorder, amorphous regions, segregated impurities or even thin films of a second phase [108, 109]. This structurally modified region is often referred to as the core of a grain boundary [108, 110]. The defect concentration in the core, and thus its electrical properties, can strongly differ from that of the bulk. In ZrO_2 or CeO_2, for example, high grain boundary resistivities are often attributed to siliceous phases at the grain boundaries [111–114]. On the other hand, fast grain boundary diffusion has also been observed in ionic materials [115–117]; this indicates that highly resistive, as well as highly conductive, core regions are possible.

From an electrical point of view, the grain boundary consists not only of its core zone, but also of space charge layers in the adjacent bulk regions with defect concentrations differing from that of the bulk. In order to understand the occurrence of such space charge layers, let us consider a ceramic in the extrinsic regime (negative dopant) with one predominant defect (e.g. oxygen vacancies). In a *Gedankenexperiment*, we introduce a grain boundary into a grain. Owing to the different surroundings, the chemical potential of the mobile charge carrier in the bulk and in the grain boundary core can be expected to be different. Thus, charge carriers begin to move to the region with lower chemical potential. This charge exchange yields net charges in the core and in the adjacent bulk regions (Fig. 4a), and thus an electrical field. Charges move until, in equilibrium, the electrical potential difference balances the chemical potential difference and $\tilde{\mu}$ is constant. The exact charge distribution in the bulk regions follows Poisson’s equation $\mathrm{div}(\mathrm{grad}(\varphi) = -\theta/\varepsilon_{sc}$ (θ = charge density; ε_{sc} = permittivity in the space charge region); the charge is distributed over a zone of typically several nm in thickness, the so-called space charge layer.

With respect to charge transport in space charge layers, two main cases have to be distinguished: decreased charge carrier concentrations, and thus highly resistive space charge layers, and accumulation of charge carriers, i.e. highly conductive space charges. Let us first consider the depletion case. For a spatially constant dopant

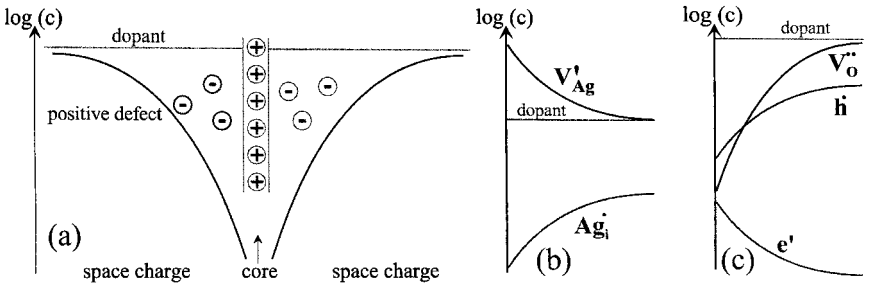

Fig. 4. (a) Model of a grain boundary with a positively charged core region and negative space charges. In the space charge mobile positive defects are depleted. (b) Sketched concentration profiles in a space charge of an extrinsic (positively doped) silver halide. (c) Sketched concentration profiles of majority charge carriers (singly-charged dopant and oxygen vacancies) and minority charge carriers (electrons and holes) in a space charge layer of a negatively (acceptor) doped, mixed conducting oxide.

concentration c_{dop}, the defect concentration in the space charge can easily be calculated from an approximate solution of Poisson's equation leading to the parabolic shape of $\log(c_{\mathrm{def}})$ sketched in Fig. 4a [118]. Concerning the resistance perpendicular to such space charge layers, two limiting cases can be distinguished [118, 119]:

i) If the mean free path of the charge carrier is much smaller than the space charge thickness, the transport through the layer is again governed by the transport equation Eq. (12) [118]. This so-called "drift-diffusion model" applies for ionic defects and is sometimes also discussed for electronic charge carriers, for example for small electron polarons. The approximate small signal ac resistance

$$R_{\mathrm{gb}} = \frac{2\exp(z_{\mathrm{def}} e\Delta\varphi/kT)}{\sigma_{\mathrm{bulk}} A_{\mathrm{gb}}} \sqrt{\frac{\varepsilon_{\mathrm{sc}} k^2 T^2}{2 z_{\mathrm{def}}^2 e^3 c_{\mathrm{dop}} |z_{\mathrm{dop}} \Delta\varphi|}} \tag{16}$$

and capacitance

$$C_{\mathrm{gb}} = \frac{A_{\mathrm{gb}}}{2} \sqrt{\frac{|z_{\mathrm{dop}}| \varepsilon_{\mathrm{sc}} e c_{\mathrm{dop}}}{2|\Delta\varphi|}} \tag{17}$$

as well as the corresponding effective thickness

$$w_{\mathrm{gb}} = 2\sqrt{\frac{2\varepsilon_{\mathrm{sc}}|\Delta\varphi|}{|z_{\mathrm{dop}}| e c_{\mathrm{dop}}}} \tag{18}$$

of such a double space charge layer at a grain boundary can be calculated in straightforward manner [51, 118]. Here the symbol $\Delta\varphi$ denotes the electrical potential difference between the grain boundary core and the bulk interior; A_{gb} is the grain boundary area, and σ_{bulk} represents the conductivity of the grain interior (bulk of the material). In many cases $\varepsilon_{\mathrm{sc}}$ can be approximated by the bulk permittivity $\varepsilon_{\mathrm{bulk}}$.

ii) In the case of electronic charge carriers, the mean free path can be much larger than the space charge thickness and a transfer across the space charge takes place in one step; the charge carriers ''feel'' the energy barrier ($z_{\mathrm{def}} e\Delta\varphi$) rather than the local conductivity [118]. The corresponding ''thermionic emission model'' is often assumed in semiconductors with band conduction such as Si or ZnO [119–121]. Eqs. (17) and (18) are again valid, but the small signal ac resistance follows a modified equation [118]. However, since the drift-diffusion and the thermionic emission model lead to similar I-V and C-V characteristics [118, 119], it can be difficult to decide which of the models should be applied to interpret the experimental results.

The current-voltage (I-V) and capacitance-voltage (C-V) relationships of grain boundaries, however, are rather complicated, since under bias an asymmetric charge redistribution between the core and the two space charge layers takes place. This redistribution depends on the (usually unknown) density and energy of the levels (states) in the core of the grain boundary and complex I-V and C-V characteristics result [121–123]. Ohmic, sub-ohmic ($\mathrm{dlog(I/A)/dlog(U/A)} = \alpha < 1$) and super-ohmic ($\alpha > 1$) regimes can, for example, be observed in a single I-V curve.

In the case of an enhanced charge carrier concentration in the space charge (cf. Fig. 4b), mainly the current parallel to the grain boundary plane is important. The corresponding parallel excess grain boundary conductance

$$\Delta \tilde{Y}_{\mathrm{gb}} \approx 4\lambda_D \sigma_{\mathrm{bulk}} \exp(e\Delta\varphi/2kT) \tag{19}$$

has been deduced in Ref. [124] for $|z_{\mathrm{dop}}| = |z_{\mathrm{def}}| = 1$, with the Debye length λ_D being defined as $\sqrt{(\varepsilon_{\mathrm{sc}} kT)/2e^2 c_{\mathrm{def,\,bulk}}}$. In the case of transport along the grain boundary, the mean free path of the charge carrier plays often no role and Eq. (19) is valid for both ionic and electronic defects. Accumulation space charge layers play an important role in heterogeneous doping of solid ionic conductors (i.e. the addition of a non-soluble insulating compound, e.g. Al_2O_3 in AgCl) [125–127].

The majority charge carrier determines the electrical potential profile in a space charge layer, but the minority charge carriers are also in thermodynamic equilibrium, and thus their concentrations adapt to the given electrical potential. Consequently, in an oxide with a negative dopant and oxygen vacancy depletion, holes are depleted as well, whereas the electron concentration is enhanced in the space charge (Fig. 4c). It is also worth mentioning that, although dopants exhibit a very low mobility and do not contribute to the ionic current, they can equilibrate at high temperatures and frequently display concentration profiles in space charge layers [128]. If the majority charge carrier is depleted, then the dopant concentration is enhanced in the space charge region; this is often referred to as ''segregation of the dopant''.

2.4 Electrical Transport and Electrochemical Reactions at Electrode/Solid Interfaces

In the case of electrical transport across and along space charge layers at grain boundaries, there is usually no fundamental difference between electronic and ionic charge carriers. At electrodes, however, electrons and ions behave completely differ-

ent: the electron transfer into the electrode is again mostly determined by space charge layers (Schottky barriers) [118, 119] and considerations similar to those mentioned in the previous section apply. I-V characteristics and C-V relations can be derived analytically (a diode-like I-V curve and a linear relationship between $1/C^2$ and the voltage V); for more detailed information, consult the extensive literature on Schottky contacts. Let here suffice a remark with respect to the terminology used later on: If the space charge layer at an electrode represents negligible impediment to carrier flow, then the corresponding electrode is termed "ohmic".

In the case of ions, space charges at electrodes might again play a role; however, at an electrode the ionic current has primarily to be transferred into an electronic current, and hence electrochemical reactions are always involved. It is these electrochemical redox reactions that are frequently of prime interest in liquid electrochemistry. In contrast, in solid state electrochemistry fewer investigations have dealt with such electrode reactions. One reason is the complexity of the bulk itself (see above). Moreover, oxidation and reduction reactions of "dopants" at electrodes, i.e. of ions and molecules being dissolved in the liquid electrolyte (e.g. Fe^{3+}/Fe^{2+}) have no counterpart in ionic solids, since the dopants are mostly immobile. Hence, only electrochemical reactions involving the mobile cation or anion of a solid electrolyte are usually investigated. Several papers have discussed the deposition or dissolution of metals on cation conducting solid electrolytes and the double layer of the corresponding electrolyte/metal interface [129–144]. In such investigations, the morphology and contact geometry of electrode/electrolyte interfaces irreversibly changes during the deposition or dissolution of metal, thus complicating mechanistic electrode kinetic studies on cation conductors considerably. The largest number of electrode kinetic studies in solid state ionics, however, deals with the electrochemical reactions taking place in solid oxide fuel cells (SOFCs), namely the reduction of oxygen and the oxidation of fuel (H_2, CO, CH_4) on oxide ion conductors (Fig. 5a). Nevertheless, there are still many open questions concerning the reaction mechanisms of these reactions.

In the rest of this section some aspects of the oxygen reduction reaction

$$\tfrac{1}{2}O_2(\text{gas}) + 2e^-(\text{cathode}) \rightleftharpoons O^{2-}(\text{electrolyte}) \tag{20}$$

are discussed. The electrochemical mechanism of this cathodic reaction has been investigated on perovskite electrodes [145–173], platinum electrodes [174–182], gold electrodes [182, 183] and silver electrodes [184, 185]. Since the gas cannot be supplied via the electrolyte, mostly porous cathodes are used in such studies and frequently the experimental results are discussed in terms of the following two reaction paths (e.g. Refs. [148, 150, 154, 155, 158, 165, 169, 184–188]):

i) The *surface path* includes adsorption of oxygen on the electrode surface, diffusion of a (possibly dissociated and partly ionized) oxygen species along the surface towards the three-phase boundary (3PB), complete ionization, and an ionic transfer step into the electrolyte (Fig. 5b). The incorporation into the electrolyte does not necessarily occur directly at the 3PB; surface or interface diffusion of the ionized species could lead to a certain broadening of the incorporation zone. Modifications of this path include direct adsorption of oxygen at the 3PB (without surface diffusion

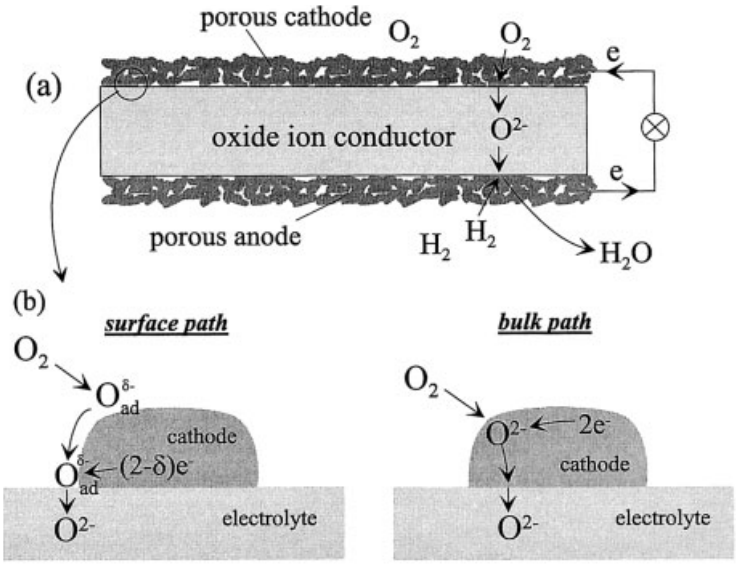

Fig. 5. (a) Working principle of a solid oxide fuel cell. (b) Sketch of possible reaction paths of the oxygen reduction reaction, taking place on a particle of a solid oxide fuel cell cathode.

on the cathode surface), or adsorption on the electrolyte plus surface diffusion to the 3PB. I-V characteristics and partial pressure dependencies of some possible rate determining steps have been discussed e.g. in Refs. [164, 175, 180, 187].

ii) The *bulk path* consists of oxygen dissolution in the electrode, oxygen transport through the electrode, ionization step(s), and the transfer of the ion into the electrolyte. In metal electrodes with sufficient oxygen solubility, diffusion of neutral oxygen species is possible. In the case of oxide cathodes (often perovskites) the oxygen incorporation into the electrode material (Fig. 5b) includes the ionization of oxygen, and hence oxygen transport in the bulk comprises the conduction of ions.

A third path, namely the ionization of the oxygen on the electrolyte surface followed by a direct incorporation into the electrolyte, can also not be excluded. In this case the electronic charge carriers, which are required in the oxygen reduction reaction, have to be supplied from the electrolyte. In solid electrolytes with very low electronic conductivity (e.g. zirconia), it can therefore be expected that the active zone is restricted to a region very close to the three-phase boundary. Hence, this path is, from a geometrical point of view, similar to the surface path discussed above.

The surface path is regarded as predominant for Pt and Au electrodes [174–183]. In doped $LaMnO_3$, which is the most widely used SOFC cathode material, the ionic conductivity is rather low and it is often also assumed that the reaction via the surface path determines the current, although for certain electrode geometries, or under high overvoltages, significant oxide ion transport through doped $LaMnO_3$ can not be excluded [148, 150, 155, 165]. In mixed ionic and electronic conductors with considerable ionic conductivity (e.g. doped $LaCoO_3$ or $LaFeO_3$), on the other hand,

the bulk path can be expected to be "open", thus lowering the polarization resistance [158, 171, 189, 190]. Owing to the relative high solubility of oxygen and the non-negligible oxygen diffusion coefficient in Ag, it is assumed that also in the case of silver electrodes the bulk path may dominate the reaction rate [184, 185, 191–193].

Different partial pressure dependences, current voltage characteristics and activation energies have been reported for the same electrode material, the absolute values of the polarization resistances considerably vary from investigation to investigation and even nominally identical preparation procedures can lead to distinctly different results [194–196]. These inconsistencies, which often hinder generally accepted mechanistic interpretations, can partly be explained by the fact that the porous cathodes are often morphologically and chemically ill-defined, considerably depend on the preparation procedure, and can change during the measurements [194–196]. Plenty of research is still required to solve this complex problem; new results obtained by means of defined microelectrodes are discussed in Sec. 6.5.

Finally, two remarks regarding terminology. If an electrochemical reaction displays a negligible resistance, the corresponding electrode is called a "reversible electrode". Reversible electrodes are known for cation conductors, but have not been reported for oxide ion conductors. The term "electrode resistance" denotes the electrical resistance due to the electrochemical reaction, or to the transfer through the space charge, rather than the resistance of the electrode material itself.

2.5 Impedance Spectroscopy in Solid State Ionics

Conventional two-electrode dc measurements on ceramics only yield conductivities that are averaged over contributions of bulk, grain boundaries and electrodes. Experimental techniques are therefore required to split the total sample resistance R_{tot} into its individual contributions. Four-point dc measurements using different electrodes for current supply and voltage measurement can, for example, be applied to avoid the influence of electrode resistances. In 1969 Bauerle [197] showed that impedance spectroscopy (i.e. frequency-dependent ac resistance measurements) facilitates a differentiation between bulk, grain boundary and electrode resistances in doped ZrO_2 samples. Since that time, this technique has become common in the field of solid state ionics and today it is probably the most important tool for investigating electrical transport in and electrochemical properties of ionic solids. Impedance spectroscopy is also widely used in liquid electrochemistry and reviews on this technique be found in Refs. [198–201]. In this section, just some basic aspects of impedance spectroscopic studies in solid state ionics are discussed.

Different kinds of plots based on impedance Z, admittance Z^{-1}, modulus $i\omega Z$, or complex capacitance $(i\omega Z)^{-1}$ can be used to display impedance data. In solid state ionics, particularly plots in the complex impedance plane (real versus imaginary part of Z) and impedance Bode-plots ($\log(Z) - \log(\omega)$) are common. A RC element (resistor in parallel with a capacitor) has, for example, an impedance according to

$$Z_{\mathrm{RC}} = \left(\frac{1}{R} + i\omega C\right)^{-1} = \frac{R}{1 + i\omega RC} \tag{21}$$

(ω = angular frequency) and yields one semicircle in the complex impedance plane (Z-plane) with R being the diameter of the semicircle (Fig. 6a). In the log(Z)-log(ω) plot, a maximum in the negative imaginary part of Z results for the same element (Fig. 6a).

The frequency at which the currents via the resistor and the capacitor are equal and the imaginary part of the impedance reaches its maximum is the characteristic frequency ω_r (relaxation frequency) of a RC element. It is given by

$$\omega_r = \frac{1}{RC}. \tag{22}$$

Two serial RC elements with distinctly different relaxation frequencies lead to well-separated dispersion signals in impedance spectra. Depending on the absolute values of the resistances and capacitances, certain representations of the impedance data provide information of this dispersion; in many cases, two different relaxation frequencies yield two semicircles in the complex Z-plane and each arc can be related to one RC element (Fig. 6b). In order to intuitively understand this relaxation behavior, let us consider a circuit with R_A similar to R_B, but $C_B \gg C_A$. In the dc case, the current has to pass both resistances, and $R_A + R_B$ results. Increasing the frequency leads to a dielectric "opening" of the large capacitance, that means C_B short-circuits R_B, the impedance decreases and describes – because of the phase shift between the current and the applied voltage – an arc in the Z-plane. At medium frequencies, the impedance of RC-element B is negligible compared with that of A, and the impedance is just given by R_A. A further frequency increase, finally, opens the capacitance C_A and causes the high-frequency arc. Hence, the impedances of the two RC-elements can easily be separated in such a case.

It is especially this feature to separate electrical and electrochemical processes with different relaxation frequencies that makes impedance spectroscopy so attractive in solid state ionics. This is specified for an ionic solid consisting of homogeneous grains and highly resistive grain boundaries. For the sake of simplicity, let us assume a so-called brick layer model [124, 202, 203], i.e. a polycrystal consisting of cubic grains, laterally homogeneous grain boundaries and identical, homogeneous electrodes (Fig. 7a). Since the charge transport along the highly resistive grain boundaries is negligible, the sample reduces to a quasi-one-dimensional series of bulk layers, grain boundary planes and electrodes (Fig. 7b).

The ac current in a bulk layer consists of the faradaic current resulting from mobile charge carriers (Eq. (12)) and the dielectric displacement current. For frequency-independent conductivities and permittivities, the one-dimensional current flow in such a homogeneous bulk layer can be expressed by a RC-element with the resistor representing the faradaic current and the capacitor describing the displacement current. Processes causing highly resistive grain boundaries (space charge layers or second phases) can frequently be represented by a RC element as well. The same holds good for space charge depletion layers at electrodes [204]. Lastly, the equivalent circuit of an electrochemical electrode reaction strongly depends on its rate-determining step: an oxygen reduction reaction (Fig. 5b) with adsorption of oxygen on the electrode surface being rate-limiting also leads to a RC element [205]. If, on the other

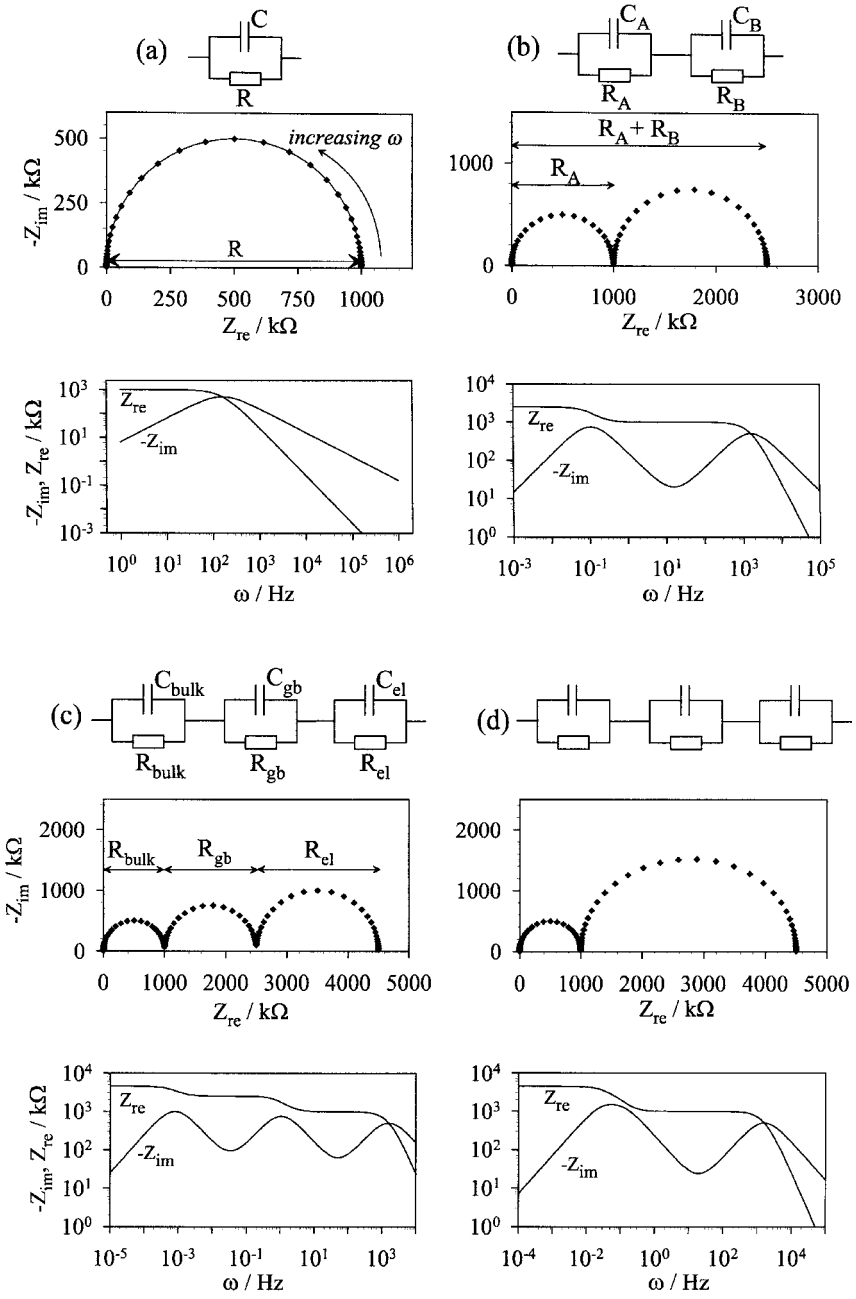

Fig. 6. Impedance spectra in the Z plane and in the Bode plot ($\log(Z)$ vs. $\log(\omega)$) for (a) one RC element; (b) two RC elements; (c) three RC elements representing the situation of a polycrystal with non-ohmic electrodes and highly resistive grain boundaries; and (d) three RC elements with two similar relaxation frequencies ($\omega_{r2} = 3\omega_{r3}$) leading to overlapping semicircles.

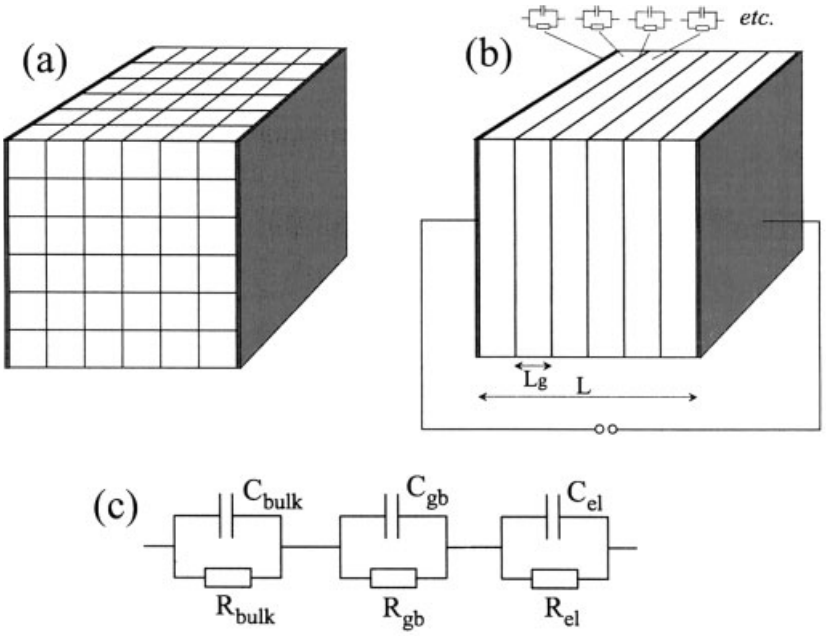

Fig. 7. (a) Polycrystal consisting of cubic grains, identical and laterally homogeneous highly- resistive grain boundaries, and laterally homogeneous electrodes (brick layer model); (b) Polycrystal after removing the grain boundary planes, which are negligible for the current flow. Electrodes, grain boundary planes, and bulk layers can be described by *RC* elements. (c) Resulting overall equivalent circuit.

hand, the transport of oxide ions through a mixed conducting electrode is rate-determining, a finite Warburg impedance, $Z_w = R_{\mathrm{el}}(T_W i\omega)^{-1/2}\tanh((T_W i\omega)^{1/2})$, in parallel with a capacitance, can be expected [206, 207] (R_{el} = electrode resistance, T_W = fit parameter related to the diffusion coefficient; cf. Sec. 6.5). For the sake of simplicity, let us assume a *RC*-like electrode impedance.

Hence, in simple cases each bulk layer, each grain boundary plane, and both electrodes of the brick layer model sample, can be represented by separate *RC* elements (Fig. 7b). The *RC* elements of the n bulk layers can be combined to a single *RC* element with the n-fold resistance and the $1/n$-fold capacitance of a single layer. The $n-1$ grain boundary impedances can also be summed, as can the two electrode impedances, and hence the model sample corresponds to a series connection of three RC elements (Fig. 7c) with

$$R_{\mathrm{bulk}} = \frac{L}{\sigma_{\mathrm{bulk}} A} \tag{23}$$

$$C_{\mathrm{bulk}} = \frac{\varepsilon_{\mathrm{bulk}} A}{L} \tag{24}$$

$$R_{\mathrm{gb}} = \frac{w_{\mathrm{gb}}}{\sigma_{\mathrm{gb}} A}(L/L_g - 1) \tag{25}$$

$$C_{\mathrm{gb}} = \frac{\varepsilon_{\mathrm{gb}} A}{w_{\mathrm{gb}}} \frac{1}{(L/L_g - 1)} \tag{26}$$

$$R_{\mathrm{el}} = \frac{2w_{\mathrm{el}}}{\sigma_{\mathrm{el}} A} \tag{27}$$

$$C_{\mathrm{el}} = \frac{\varepsilon_{\mathrm{el}} A}{2w_{\mathrm{el}}}. \tag{28}$$

Subscripts bulk, gb, and el denote grain interior, grain boundaries and electrode parameters, symbol w represents thicknesses, A and L are the sample area and length, respectively, and L_{g} is the grain size. For space charges causing electrode or grain boundary impedances, w_{gb} and w_{el} are the thicknesses of the corresponding space charge layers (cf. Eq. (18)) and σ_{gb}, σ_{el} are effective conductivity values of the space charge zones. If electrochemical reactions lead to the electrode impedance w_{el}, σ_{el}, and $\varepsilon_{\mathrm{el}}$ have often no physical meaning and area-related resistances and capacitances can be considered. According to Eqs. (23–28) the relaxation frequencies $\omega_{r,i}$ of bulk, grain boundaries, and electrodes read

$$\omega_{r,i} = \frac{\sigma_i}{\varepsilon_i} \tag{29}$$

and are thus geometry-independent parameters.

In polycrystalline ceramics with the relaxation frequencies of bulk, grain boundaries, and electrodes being sufficiently different (e.g. in doped, polycrystalline ZrO_2 [208–210]) three semicircles result in the Z-plane (Fig. 6c) and each arc can be related to one electrical or electrochemical process. Conductivities (or area-related resistances) of bulk, grain boundaries and electrodes may be calculated from the resistances according to Eqs. (23), (25) and (27) (if the geometrical parameters are known), or from the corresponding relaxation frequencies (if sensible permittivity values can be assumed in Eq. (29)). The bulk capacitance C_{bulk} yields the bulk permittivity and Eqs. (26) and (28) allow the determination of thicknesses from the grain boundary and electrode capacitances if reasonable permittivities (usually the bulk value) are used. For space charges, thicknesses of the order of a few nm to 100 nm can typically be expected, while electrochemical electrode processes usually lead to apparent values below 1 nm.

In experimental impedance spectroscopic studies, however, several factors may complicate the interpretation of the spectra and a few of these complications will briefly be touched upon: i) If high conductivities are considered ($\sigma > 10^{-3}$ S cm^{-1}), then the corresponding relaxation frequencies are well above the measurement range of a conventional impedance set-up (frequencies up to ca. 10 MHz). Hence, processes with high conductivites cannot be separated by conventional impedance spectroscopy. ii) The assumption of a quasi-one-dimensional current flow, which is the basis of the above presented brick layer model, is often violated [203, 211–214]. Some complications due to multi-dimensional potential distributions will be discussed in Sec. 3.2.1. iii) Highly conductive regions perpendicular to the electrodes (e.g. highly

conductive grain boundaries) yield additional parallel current paths, and thus cause parallel instead of serial RC elements. These parallel RC elements cannot be separated by impedance spectroscopy (cf. Sec. 3.2.2). iv) Relaxation frequencies of electrochemical processes on electrodes are often sufficiently low to separate grain boundary and electrode effects; however, such a separation is difficult if space charges determine electrode as well as grain boundary resistances. Similar relaxation frequencies may result, and hence the corresponding semicircles strongly overlap, as sketched in Fig. 6d. In the case of ideal RC elements, a non-linear least-square fit [215] would still allow an exact determination of all R- and C-values. In reality, however, ideal RC elements are rather rare, and it is often difficult to decide whether e.g. a non-ideal semicircle is due to different transport mechanisms involved, spatially varying relaxation frequencies of one and the same process, or other non-idealities, such as frequency-dependent current lines [212, 214, 216] or frequency-dependent conductivities [217–220]. If only two semicircles are measured, and it is not obvious whether the second arc is due to electrodes or grain boundaries, the corresponding capacitance value gives at least a hint: since in polycrystalline samples usually numerous grain boundary planes are in series while only two electrodes are present, C_{el} can be expected to be much larger than C_{gb}. The electrode capacitance C_{el} is typically of the order of $\mu F\ cm^{-2}$ and, in the case of electrochemical electrode reactions, even values greater than $1 mF\ cm^{-2}$ are possible; C_{gb} on the other hand is often less than $100\ nF\ cm^{-2}$. Further possibilities to identify the origin of a second arc are measurements with different electrode materials, sample-thickness-dependent measurements, or (rather difficult [221]) four-point impedance measurements.

3 Indications for Microelectrode Experiments

3.1 Transport Properties of the Bulk

3.1.1 Inhomogeneous Bulk Conductivities

Owing to several reasons, bulk conductivities in ceramics are frequently inhomogeneous:

i) If the surrounding or the temperature of an equilibrated ionic solid is changed, diffusion processes are required to adjust to the new conditions. Since the diffusion coefficients in ionic solids can be rather low, non-equilibrium situations – that means stoichiometry gradients – are often met, particularly at lower temperatures. The conductivity is closely related to the exact composition and such stoichiometry gradients are therefore often accompanied by conductivity gradients (cf. also Sec. 2.1.5).

ii) Dopants are added to ionic solids in order to achieve certain properties as e.g. high conductivities. However, mobilities of dopants are frequently very low and during the preparation of the solid, dopant profiles (and thus conductivity variations) can easily occur. If a homogeneous solid solution $(A_xB_{1-x})O$ is exposed to an oxygen

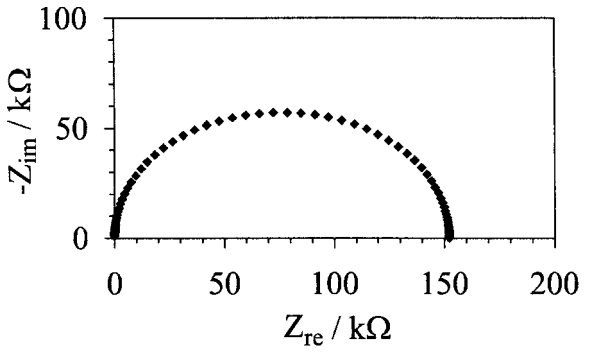

Fig. 8. Impedance spectrum calculated for a cubic sample (size $L = 1$ cm) with a linear, one-dimensional conductivity gradient $\sigma_{bulk} = 10^{-6}\,S\,cm^{-1} + (1 - x/L) \cdot 2 \cdot 10^{-5}\,S\,cm^{-1}$. Ohmic/reversible electrodes are assumed.

partial pressure gradient, the different mobilities of the cations initiate a kinetic demixing and an inhomogeneous composition again results [222–224]. This phenomenon may also lead to dopant concentration gradients in initially homogeneous oxides [224].

iii) Inhomogeneous bulk properties also arise if different phases are present, i.e. if a composite material is investigated. Composites can unintentionally form if metastable materials such as tetragonal partially stabilized zirconia [225–227] are under investigation. On the other hand, composites are often deliberately produced, since they can yield overall materials properties being superior to those of the individual phases. Fiber- and whisker-reinforced ceramics for the purpose of increased fracture toughness [228], thick-film resistors consisting of RuO_2 and lead borosilicate glass [229, 230], or heterogeneously doped solid electrolytes such as LiI/Al_2O_3 and AgI/Al_2O_3 [125, 231–233] might serve as examples of ceramic composites. In these multiphase samples considerable conductivity variations can be expected.

Impedance spectroscopy is sensitive to different dielectric relaxation frequencies $\omega_r = \sigma/\varepsilon$ (Sec. 2.5) and hence should reveal conductivity gradients in solids. Figure 8 presents the impedance spectrum calculated for a linear, one-dimensional conductivity profile. Obviously a depressed semicircle results and this "deformation" reflects the distribution of relaxation frequencies. However, the calculation of the conductivity profile from a measured impedance spectrum is only possible in one-dimensional cases with conductivities being continuously decreasing or increasing [234], and even in such cases the recalculation is numerically challenging and requires very accurate experimental data. Moreover, other phenomena, such as frequency-dependent current lines [212, 214, 216] (see also below) or frequency-dependent conductivities [217–220] also yield depressed semicircles and an unambiguous relation of the frequency dispersion to conductivity gradients is often not possible. Hence, there is definitely a demand for spatially resolved conductivity measurements, particularly if there are any hints at inhomogeneous conductivities (e.g. depressed bulk impedance arcs). Microelectrodes facilitate such local investigations of conductivity profiles and can therefore be a very useful tool in solid state ionics. This is demonstrated in Sec. 6.2 for the probably most typical inhomogeneity effect in this field, namely a spatially varying stoichiometry in an oxide.

3.1.2 Mixed Ionic and Electronic Conductivity

The total bulk conductivity of an ionic solid can frequently be obtained from the high-frequency semicircle of an impedance spectrum; the determination of the partial ionic and electronic conductivities, however, requires further efforts. In the most common approach, a cell is used in which either the ionic or the electronic charge carriers are blocked at an electrode (Hebb–Wagner experiment) [73, 235–237]. The ionic current in AgCl can, for example, be blocked by Pt electrodes; for an inhibition of the electronic current, an ion conductor with extremely low electronic conductivity (e.g. Y-doped ZrO_2) is used in series with the solid under investigation (e.g. $LaCoO_3$). Immediately after applying a dc voltage, all mobile charge carriers move in the electrical field. However, the blocked charge carriers accumulate or deplete at the blocking interface(s) and a concentration gradient, i.e. a stoichiometry gradient is built up. This concentration gradient gives rise to a backward driving force and after some time a steady state situation results in which the concentration gradient of the blocked particle and the electrical potential gradient counterbalance each other; the flux of the corresponding charge carrier vanishes. The steady state current is thus solely carried by the non-blocked charge carriers and yields their partial conductivity. The relaxation time to reach this steady state depends on the electrode configuration and in the case of conventional macroscopic electrodes, hours, weeks or even years may be required to perform such experiments. Microelectrodes shorten the relaxation times by orders of magnitude and thus extend the application of Hebb–Wagner experiments considerably [238, 239] (see also Sec. 4.1). This effect of miniaturization has a counterpart in liquid electrochemistry where the steady state of diffusion is also reached much faster if microelectrodes are used [33, 34, 45, 46].

3.2 Electrical Properties of Grain Boundaries

3.2.1 Spatially Varying Properties of Highly Resistive Grain Boundaries

The brick layer model (Sec. 2.5) allows a quantitative analysis of the grain boundary impedance caused by highly resistive grain boundaries. However, one-dimensionality has to be assumed in such an analysis, and it is an important question in how far the model is applicable to real ceramic materials. In Refs. [214, 240, 241] it has been shown that the assumption of cubic-shaped grains of equal grain size (brick layer model) is frequently a satisfactory approximation: although inhomogeneous current densities result for more complicated microstructures the corresponding effective resistances and capacitances are close to those expected for the simple brick layer case. Only relatively extreme grain size distributions (e.g. some large and many small grains) yield significant deviations [214].

Serious problems with respect to a quantitative analysis can occur if the assumption of identical grain boundaries is violated. In sintering processes, inhomogeneities are the rule rather than the exception and grain boundary cores in one and the same polycrystal can easily differ in terms of structure and chemistry [109, 120, 242–246]. Hence, core as well as space charge conductivities might also vary from boundary to

boundary. Different space charge potentials and thus very different grain boundary conductivities have e.g. been observed for Σ3, Σ5, and Σ13 grain boundaries in $SrTiO_3$ bicrystals [246, 247, 248]. In Refs. [214, 249] it has been discussed how such varying grain boundary properties influence the effective grain boundary impedance. It was shown that the current makes detours around highly resistive grain boundaries, but flows through the less resistive ones. The current distribution is thus no longer one-dimensional. Owing to this multidimensionality of the potential distribution, it is not possible to separate the different grain boundary relaxation frequencies by means of a one-dimensional equivalent circuit consisting of serial RC elements.

As long as the distribution of grain boundary properties is relatively narrow, at least the mean grain boundary conductivity can approximately be determined by a brick layer analysis [214]. If, however, grain boundary properties in a polycrystal vary by orders of magnitude a quantitative analysis of conventionally obtained grain boundary impedances is no longer conceivable. Even a qualitative misinterpretation of the grain boundary arc in the complex impedance plane is possible: Let us, for example, consider a polycrystal with approximately 1/3 of the grain boundaries being completely insulating while the other grain boundaries exhibit bulk conductivity. The resulting inhomogeneous dc potential distribution (Fig. 9a) shows that the current makes detours and goes around the insulating grain boundaries; the dc resistance is a pure bulk resistance which is influenced by the detours. An increasing frequency leads to a capacitive ''opening'' of the insulating grain boundaries, current can pass these boundaries and the current lines change. At high frequencies, the insulating grain boundaries are dielectrically highly conductive and a homogeneous potential distribution results (Fig. 9b); the corresponding bulk resistance is therefore that of a single crystal. This frequency dependence of the current lines yields an additional arc in the complex impedance plane (Fig. 9c) but the resistance of this arc reflects the difference between the dc bulk resistance (including detours) and the high-frequency bulk resistance (without detours) rather than grain boundary properties.

In such cases the term ''grain boundary resistance'' is only meaningful in the sense that the corresponding resistance is *caused by the grain boundaries* and would not exist in a single crystal. However, the apparent grain boundary resistances do usually not exhibit the temperature dependence of the grain boundary resistivity, but are influenced or even determined by the temperature dependence of the bulk conductivity [214]. This clearly shows that conventional impedance spectroscopy can be very misleading if varying grain boundary properties and thus multidimensional, frequency-dependent current lines are involved. A tool for investigating the homogeneity of grain boundary properties of ceramics would therefore often be very helpful. Localized measurements using microelectrodes can provide such additional information (Sec. 4.2), and an experimental study on the homogeneity of grain boundaries in $SrTiO_3$ is presented in Sec. 6.3.

3.2.2 Highly Conductive Grain Boundaries

A quantitative interpretation of grain boundary contributions to the overall impedance of polycrystals with highly resistive grain boundaries can be problematic (see

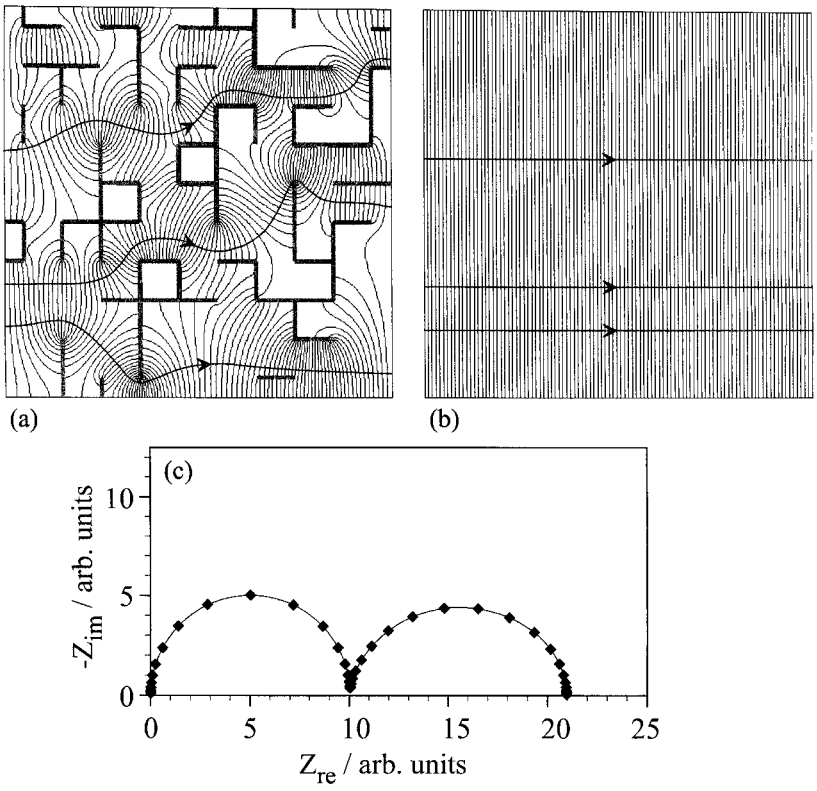

Fig. 9. (a) dc potential distribution (calculated by the finite element method) in a square polycrystal consisting of 10×10 grains. One-third of all grain boundaries are completely insulating (grey), while all other grain boundaries (not shown) exhibit bulk conductivity, and hence are negligible. The voltage drop between two neighboring equipotential lines is U/100 with U being the applied voltage; the three sketched current lines indicate the current detours that increase the bulk resistance. (b) Homogeneous potential distribution at high frequencies ($> \sigma_{bulk}/\varepsilon_{bulk}$); (c) corresponding impedance spectrum.

above), but impedance spectroscopy at least facilitates a separation of bulk effects and contributions *caused* by highly resistive grain boundaries. In the case of highly conductive grain boundaries, however, the situation is even worse. In a simplified brick layer model, highly conductive grain boundaries parallel to the electrodes do not represent a significant resistance and can therefore be neglected as long as their volume fraction is small. The "fast" grain boundaries perpendicular to the electrodes, on the other hand, substantially contribute to the current flow and have to be considered (Fig. 10). The grain boundary planes as well as the grain layers can be represented by RC elements and since these are in parallel a single effective RC element is sufficient to describe the polycrystal. Hence, only one relaxation, i.e. one semicircle, is visible in the impedance spectrum (Fig. 10c) and impedance spectroscopy can not be used to distinguish between grain boundary and bulk effects. A quantitative analysis of the resulting total resistance has been performed in Refs. [124, 250] and an effective conductivity σ_{eff} according to

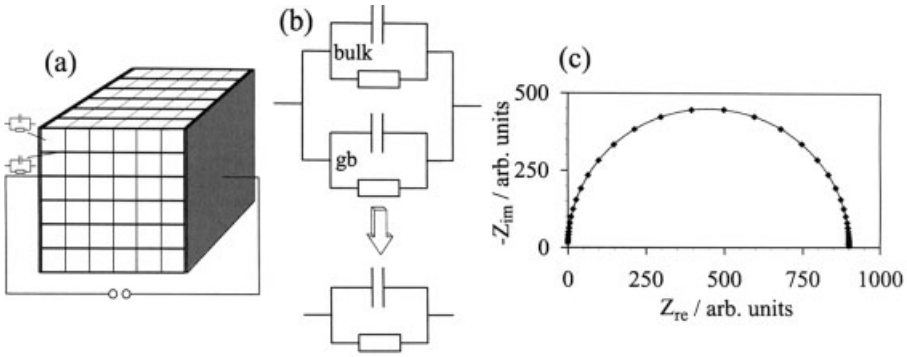

Fig. 10. (a) Sketch of the grain boundaries which have to be considered in a brick layer model of a polycrystal with highly conductive grain boundaries (bold lines) and equivalent circuits of grain boundary (gb) planes and bulk layers. (b) Resulting equivalent circuit: bulk and highly conductive grain boundaries are in parallel, and hence only one *RC* element results leading to a single semicircle in the complex impedance plane (c).

$$\sigma_{\text{eff}} = \sigma_{\text{bulk}} + 2\sigma_{\text{gb}} \frac{w_{\text{gb}}}{L_g} \tag{30}$$

was derived for samples being much larger than the grain size (L_g) and $w_{\text{gb}} \ll L_g$. Therefore, neither bulk nor grain boundary properties can be deduced from the impedance spectrum.

In order to check whether highly conductive grain boundaries exist, one might compare measurements obtained on a single crystal and on a polycrystal, respectively. However, different preparation procedures (e.g. different impurity levels) can cause differences even without any highly conductive boundaries. One might also compare samples with different grain sizes, since they should lead to different effective conductivities if grain boundaries are highly conductive (Eq. (30)). However, grain size variations are usually achieved by different preparation conditions, and hence also other factors such as impurity segregation [128] or density can vary and impede a quantitative analysis. A very powerful technique to detect and to quantitatively characterize solids with highly conductive grain boundaries makes use of microelectrodes and is introduced in Sec. 4.3. The method was applied to investigate polycrystalline AgCl and the corresponding experiments are exemplarily discussed in Sec. 6.4.

3.3 Electrochemical Processes at Electrodes

3.3.1 Reference Electrodes

Impedance spectroscopy is predestined to separate the contributions of bulk and electrodes to the overall electrical properties of a solid and can thus be employed to investigate the kinetics of electrochemical reactions. However, the relaxation fre-

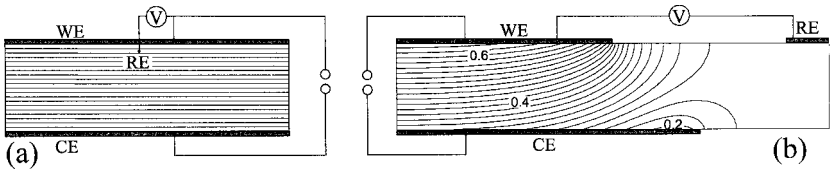

Fig. 11. (a) Potential distribution in a sample with a quasi-one-dimensional three-electrode configuration (WE = working electrode, CE = counter-electrode, RE = reference electrode). (b) Calculated potential distribution for an electrode configuration, which is typical in solid state electrochemistry: the reference electrode is on the sample surface. For both working and counter-electrodes specific (area-related) resistances of L/σ_{bulk} (L = sample thickness) are assumed. The voltage drop between two neighboring equipotential lines is U/50, with U being the applied voltage. The numbers indicate the potential in fractions of U. Owing to the different sizes of working and counter-electrode, an unsymmetrical potential distribution results and the voltage between reference electrode (on potential 0.247 U) and working electrode reflects a part of the overvoltage of the counter-electrode.

quencies of the processes occurring at the two electrodes are often similar and a separation of the corresponding electrode impedances is therefore difficult. In principle, reference electrodes can solve this problem: the voltage is measured between the working and the reference electrode while the current flows from the working to the counter-electrode. (In the following we only consider the additional voltage caused by the current flow and neglect any contribution due to an equilibrium cell voltage.) In a one-dimensional case (Fig. 11a) the measured voltage is solely determined by the properties of the working electrode and a residual bulk resistance; impedance spectroscopy could therefore be used to separate these two contributions.

In solids, however, reference electrodes are frequently located on the same surface as working or counter-electrode and multidimensional potential distributions result (Fig. 11b). These can lead to considerable problems since the voltage between reference electrode and working electrode might also be influenced by the polarization of the counter-electrode (Fig. 11b). In other words, the reference electrode "sees" a part of the voltage drop at the counter-electrode and this hinders a proper determination of the working electrode properties. A detailed analysis of such geometrical effects has been performed by Reinhardt and Göpel [251]. Further investigations discussing this phenomenon and/or possible locations and shapes of the electrodes, can be found in Refs. [252–255]. It should be noted that these problems are caused by the voltage drop in the bulk and vanish for $\sigma_{\text{bulk}} \rightarrow \infty$. In liquid electrochemistry, supported electrolytes can therefore be used to avoid such complications, but in the case of solid electrolytes sufficiently high ionic conductivities are often difficult to be achieved. It is also worth mentioning that, owing to the large variety of "solvents" (i.e. materials), standard reference electrodes such as the calomel electrode in aqueous solutions are unknown in solid state electrochemistry. Often identical reference and working electrodes are used.

Miniaturized working electrodes offer a possibility to cope with these difficulties: Owing to their much larger electrochemically active areas, macroscopic counter-electrodes lead to voltage drops which are often negligible compared to the overpotential of a microelectrode. A reference electrode is therefore not necessary to get rid of the influence of the counter-electrode. As an example of an electrochemical

study without reference electrode, $LaMnO_3$ microelectrodes have been utilized to investigate the technologically eminently important oxygen reduction reaction on ZrO_2 solid electrolytes (Sec. 6.4).

It can be a further advantage of microelectrodes that they often increase the electrode resistance to bulk resistance ratio R_{el}/R_{bulk}. This is so because R_{el} frequently scales with the inverse area of the electrode, whereas the bulk resistance between a circular microelectrode and a counter-electrode is proportional to the inverse microelectrode diameter d_{me} (see Sec. 4.1). Hence $R_{el}/R_{bulk} \propto d_{me}^{-1}$ results and the importance of the bulk resistance decreases with decreasing microelectrode diameter. This is particularly helpful in order to investigate electrode polarization phenomena below the detection limit in experiments using macroscopic electrodes. (The reduced importance of the electrolyte resistance is also one of the reasons for ultramicroelectrodes to be applied in liquid electrochemistry [33, 34].)

3.3.2 Porous Gas Electrodes

Electrochemical reduction and oxidation reactions of gases (e.g. O_2, H_2) on oxide ion conductors are in the focus of many electrode kinetic studies in solid state electrochemistry. Since gaseous species have to be supplied to the electrochemically active sites, mostly porous electrodes are investigated in this context. (It is worth mentioning that porous electrodes in liquid [256] and solid state electrochemistry usually behave in a different manner, since in liquids pores are filled with electrolyte while on a solid the pores are mostly gas-filled [257].) In order to quantitatively compare experimental results obtained on different porous electrodes, knowledge of geometrical parameters such as contact area, surface area and three-phase boundary length is required. Relations between electrochemical performance and geometrical parameters can also yield important mechanistic information with respect to the reaction under investigation [160, 161, 185]. The determination of the relevant geometrical parameters, however, is rather difficult for porous electrodes and it is even more difficult to vary them in a defined manner. Dense, macroscopic electrode films exhibit a defined geometry, but they prevent electrochemical reactions at three-phase boundaries and are often no alternative to porous electrodes. Dense microelectrodes combine both aspects: They allow significant reaction rates at three-phase boundaries and therefore correspond, in a certain sense, to single particles of porous electrodes. On the other hand, a controlled variation and determination of geometrical parameters is much easier than in the case of porous electrodes.

For this reason, dense microelectrodes can be very useful to perform geometry-dependent electrode kinetic studies. If, for example, mainly the surface path introduced in Sec. 2.4 contributes to the oxygen reduction reaction on an oxide ion conducting electrolyte and a charge transfer reaction close to the three-phase boundary (3PB) is the rate determining step, an electrode resistance proportional to the inverse 3PB length of the microelectrode should result. If, on the other hand, the bulk path dominates the oxygen incorporation into the electrolyte and the transport of oxide ions through the cathode is rate determining, $R_{el} \propto t_{me}/{d_{me}}^2$ should be obtained for thin circular microelectrodes of thickness t_{me} and diameter d_{me}. The mi-

croelectrode experiments presented in Sec. 6.5 demonstrate that geometry-dependent measurements can really yield valuable mechanistic information with respect to the oxygen reduction reaction on $LaMnO_3$/YSZ interfaces.

4 Theoretical Aspects of Microelectrode Experiments in Solid State Ionics

4.1 Investigation of Local Bulk Properties

Electrical bulk properties of ionic solids can be rather inhomogeneous (Sec. 3.1). In the following it is shown that microelectrodes are a very useful tool to gain spatially resolved information on the conductivity of such inhomogeneous solids. Let us first consider the case of a spherical microelectrode (radius r_{me}) atop a sample with homogeneous bulk conductivity σ_{bulk}. The bulk resistance R between the microelectrode and a hemispherical counter-electrode of radius r_{ce} (Fig. 12a) can be calculated by integrating the infinitesimal resistances of hemispherical shells according to

$$R = \int_{r_{me}}^{r_{ce}} \frac{1}{\sigma_{bulk}} \frac{1}{A(r)} dr \tag{31}$$

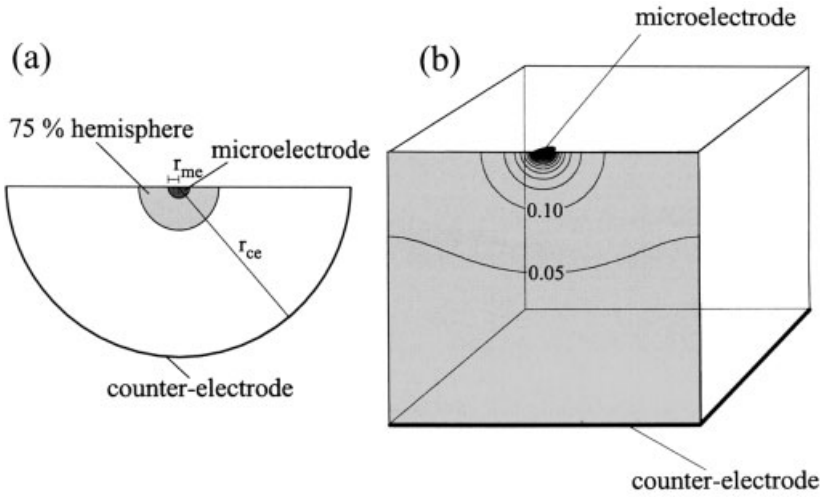

Fig. 12. (a) Sketch of a cross-section through a sample with a hemispherical microelectrode and a hemispherical counter-electrode. The 75% hemisphere indicates the region in which 75% of the total voltage drops if a homogeneous conductivity is assumed. (b) Calculated potential distribution in a cross-section of a homogeneous crystal with a circular microelectrode and a flat counter-electrode. The cross-section exactly bisects the microelectrode. The voltage drop between two neighboring equipotential lines is U/20, with U being the applied voltage. The numbers indicate the potential in fractions of U. Sample size: $17.5d_{me} \times 20d_{me} \times 25d_{me}$.

with $A(r) = 2\pi r^2$ being the surface area of a hemisphere with radius r. Hence

$$R = \frac{1}{2\pi r_{\mathrm{me}}\sigma_{\mathrm{bulk}}}\left(1 - \frac{r_{\mathrm{me}}}{r_{\mathrm{ce}}}\right) \tag{32}$$

results and in the limit of a half-infinite sample ($r_{\mathrm{ce}} \to \infty$) the resistance is given by

$$R = \frac{1}{\pi d_{\mathrm{me}}\sigma_{\mathrm{bulk}}} \tag{33}$$

with $d_{\mathrm{me}} = 2r_{\mathrm{me}}$. Eq. (33) is also a rather good approximation for a non-hemispherical counter-electrode as long as it is much larger than the microelectrode and sufficiently far away. In the case of a disc-like sample (thickness $L \gg d_{\mathrm{me}}$) with an extended electrode on its back, Eq. (33) can therefore be used as well and the bulk resistance of such a microcontact experiment is independent of the sample thickness.

For a circular microelectrode the calculation of the resistance between the microelectrode and the counter-electrode is more complicated [48–50], but again a very simple relation, namely

$$R_{\mathrm{spr}} = \frac{1}{2d_{\mathrm{me}}\sigma_{\mathrm{bulk}}} \tag{34}$$

can be deduced for the half-infinite case. Eq. (34) is also valid if a macroscopic counter-electrode in a large distance to the microelectrode is employed. For both circular and hemispherical microelectrodes the current is strongly constricted in the zone close to the microelectrode and the corresponding bulk resistance is therefore often called constriction or spreading resistance. In the following, the term spreading resistance (R_{spr}) is used for the bulk resistance between a circular microelectrode and a large counter-electrode (Eq. (34)). The extreme current constriction is reflected in a strong potential drop in the vicinity of the microelectrode (Fig. 12b) and this is also why location and shape of the counter-electrode essentially play no role.

From Eqs. (31) and (32) it can be calculated that 75% of the total resistance between a hemispherical microelectrode and a counter-electrode comes from a hemisphere with a radius of only $2d_{\mathrm{me}}$ and a semi-ellipsoid of a similar size can be defined for a circular microelectrode [49]. For that reason, the measured resistance reflects the electrical properties of a very small sample region. Microelectrodes can therefore serve as local conductivity probes on inhomogeneous solids: as long as conductivity gradients occur on a much larger length scale than d_{me} ($\nabla\sigma/\sigma \ll d_{\mathrm{me}}^{-1}$), the conductivity in the "75% hemisphere" is almost constant and the local conductivity obtained with circular microelectrodes reads

$$\sigma_{\mathrm{bulk}} = \frac{1}{2d_{\mathrm{me}}R_{\mathrm{spr}}}. \tag{35}$$

The repetition of microelectrode measurements on many different locations yields conductivity maps of the surface-near regions of inhomogeneous solids. Measure-

ments along bevels can be performed in order to get depth information and are, for example, rather common to determine dopant profiles in semiconductor devices [258–262]. With respect to typical problems in the field of solid state ionics the following aspects should be considered:

i) If the local conductivity gradient is large, the conductivity varies within the "75% hemisphere". Hence, again mean conductivity values are obtained, although averaged over much smaller space regions than in conventional experiments using macroscopic electrodes. Only in some special cases as e.g. for one-dimensional conductivity gradients, the local values can be recalculated from a measured spreading resistance profile [258, 260–262].

ii) The assumption that most of the applied potential drops very close to the microelectrode is not valid if any (hidden) highly resistive regions significantly block the current on its way to the counter-electrode. It is therefore useful to measure the resistance versus two different counter-electrodes. If identical values are obtained, it is rather unlikely that hidden highly resistive regions affect the result. It is also possible to measure between two neighboring microelectrodes to avoid such resistive regions. If the distance between the two microelectrodes is sufficiently large ($>5d_{\mathrm{me}}$), the total resistance is almost twice the spreading resistance, i.e.

$$R \approx \frac{1}{d_{\mathrm{me}}\sigma_{\mathrm{bulk}}}. \tag{36}$$

Hence, again local conductivity measurements are possible though with somewhat less spatial resolution. However, this electrode configuration can cause considerable artefacts in impedance spectroscopic studies: an "inductive" loop, i.e. a loop in the positive plane of the imaginary part of the impedance is often observed. This loop stems from a capacitive coupling between the sample and conductive parts of the experimental set-up such as sample holder, heating table or shielding box. A thorough discussion of this phenomenon has been performed in Ref. [263]. An increased distance between sample and conductive surrounding decreases the coupling capacitance and hence reduces this artefact.

iii) If a highly conductive surface layer exists, equipotential planes strongly flatten [264], and the spreading resistance formula Eq. (34) is no longer valid. Microelectrodes of different diameters can be employed in order to test the validity of $R \propto 1/d_{\mathrm{me}}$ and thus to check whether highly conductive layers exist. If the bulk conductivity is known, microelectrode measurements also facilitate a quantitative determination of the electrical properties of a highly conductive surface layer [264].

iv) Pronounced conductivity variations also occur in composites. Microelectrodes can serve as a tool to measure the conductivity of individual particles in such composites and thus to determine the electrical properties of the constituents. If the phases exhibit very different conductivities, two microelectrodes atop highly conductive particles might be required in order to avoid an influence of the low conductive phase.

v) Microelectrodes can also be favorable to investigate small samples with complicated shapes since the geometrical factor which is required to deduce the conductivity from the measured resistance is very simple ($1/d_{\mathrm{me}}$ for two microelectrodes).

vi) Microelectrode impedance measurements facilitate a spatially resolved analysis of the bulk permittivity $\varepsilon_{\text{bulk}}$. Analogous to the derivation of Eq. (33), the capacitance between a hemispherical microelectrode and a hemispherical counter-electrode can be regarded to be a series connection of thin capacitors with area $A(r) = 2\pi r^2$ and the total capacitance C is given by

$$C^{-1} = \int_{r_{\text{me}}}^{r_{\text{ce}}} \frac{1}{\varepsilon_{\text{bulk}}} \frac{1}{A(r)} dr. \tag{37}$$

For an extended counter-electrode which is far off the hemispherical microelectrode

$$C = \pi d_{\text{me}} \varepsilon_{\text{bulk}} \tag{38}$$

results, whereas a circular microelectrode leads to

$$C_{\text{spr}} = 2 d_{\text{me}} \varepsilon_{\text{bulk}}. \tag{39}$$

Hence the relaxation frequency of the bulk semicircle ($R_{\text{spr}}{}^{-1} C_{\text{spr}}{}^{-1}$) equals $\sigma_{\text{bulk}}/\varepsilon_{\text{bulk}}$ and is again geometry-independent. However, stray capacitances can impede the quantitative determination of local permeabilities, and therefore also of bulk relaxation frequencies (Sec. 5).

The extreme current constriction in the vicinity of miniaturized electrodes is also advantageous for the investigation of partial ionic and electronic conductivities in mixed conducting ceramics. If selectively blocking microelectrodes are employed to suppress the dc current flow of one charge carrier (Sec. 3.1.2), the resulting concentration and potential gradients are restricted to the region close to the contact, and the time to achieve the steady state is orders of magnitude smaller than in conventional measurements [238, 239]. In such Hebb–Wagner experiments with microelectrodes, the relation between the differential dc resistance in the steady state and the partial conductivity of the non-blocked charge carrier is again given by Eq. (33) (or Eq. (34)) [238, 239] provided the microelectrode is ohmic (reversible) for the non-blocked particles. With respect to the time-dependent microelectrode resistance $R(t)$, Wiemhöfer and Rickert derived for hemispherical microelectrodes the relation [238]

$$R(t) - R(t=0) = (R(t=\infty)) - R(t=0)) \exp\left(-d_{\text{me}}/\sqrt{\pi \tilde{D} t}\right) \tag{40}$$

for $t > d_{\text{me}}^2/\tilde{D}$. Time-dependent microelectrode measurements thus also allow a rapid determination of the chemical diffusion coefficient $\tilde{D}$ of the mobile component (for examples O in oxides and Ag in silver halides).

4.2 Investigation of "Individual" Highly Resistive Grain Boundaries

4.2.1 Relations Between Impedance Data and Local Properties

The quantitative analysis of conventionally obtained grain boundary impedance data is problematic if grain boundary properties strongly vary from boundary to bound-

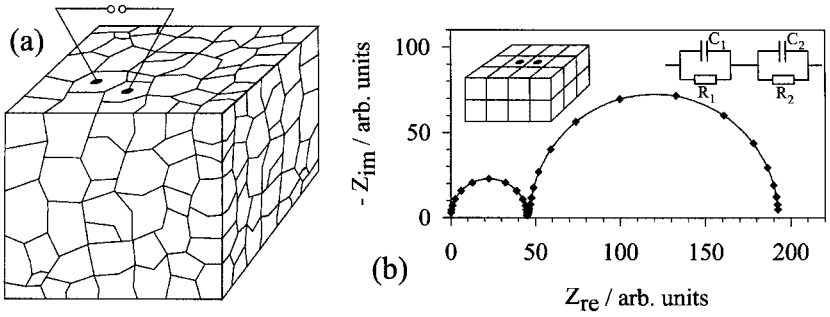

Fig. 13. (a) Sketch of the microelectrode configuration used to investigate the distribution of grain boundary properties. (b) Typical impedance spectrum calculated for a model sample (inset) consisting of 24 cubic grains and two microelectrodes on adjacent grains. An equivalent circuit consisting of two serial *RC*-elements (inset) can be used to fit the spectrum.

ary (Sec. 3.2.1). However, from an impedance spectrum alone it cannot be judged how much grain boundary properties vary within the corresponding polycrystal. In this section, it is demonstrated that electrical measurements between microelectrodes on adjacent grains (Fig. 13a) can yield information about the distribution of grain boundary properties. Finite element calculations have been performed to simulate the impedance of experiments with ohmic (reversible) microelectrodes on adjacent grains [51, 265]. The corresponding model sample is sketched in Fig. 13b. These calculations revealed that again two semicircles occur in the complex impedance plane which can, to a first approximation, be described by two serial RC-elements (Fig. 13b). At a first glance one might believe that the low-frequency arc facilitates a quantification of the electrical properties of the grain boundary between the microelectrodes. However, even though such local measurements yield valuable information, their quantitative interpretation is more intricate.

Since resistive grain boundaries are dielectrically short-circuited at high frequencies, the high-frequency arc reflects the situation without grain boundaries: R_1 is twice the spreading resistance if the distance between the microelectrodes is larger than $5d_{me}$ and C_1 approximately corresponds to $\varepsilon_{bulk}d_{me}$, at least for negligible stray capacitances. The calculations for a hypothetical bigrain experiment (Fig. 14a) showed that the resistance (R_2) and the capacitance (C_2) of the low-frequency semicircle are given by

$$R_2 \approx \frac{\rho_{gb} w_{gb}}{A_{gb}}, \tag{41}$$

with $\rho_{gb} = {\sigma_{gb}}^{-1}$ being the grain boundary resistivity and

$$C_2 \approx \frac{\varepsilon_{gb} A_{gb}}{w_{gb}}. \tag{42}$$

Hence, values as in a quasi one-dimensional case (electrodes on two sides, Fig. 14b)

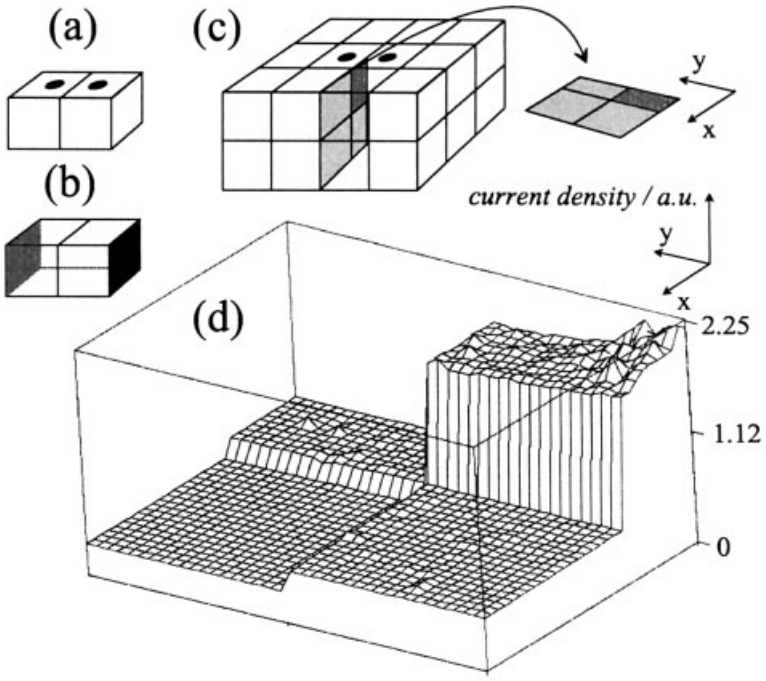

Fig. 14. Hypothetical bi-grain with microelectrodes (a), and square electrodes on the sides (b). (d) Current density distribution in the grain boundary plane of the 24-grain model sample, and sketch of the grain boundaries for which the current density distribution is plotted (c). Parameters used in the finite element calculations: $d_{\mathrm{me}} = 1/5\ L_g$, $w_{\mathrm{gb}} = 10^{-3}\ L_g$, and $\rho_{\mathrm{gb}} = 10^5\ \rho_{\mathrm{bulk}}$ for all grain boundaries. The spikes are due to numerical errors. Owing to computational reasons, the considered plane is not the grain boundary plane itself, but a plane in a distance of $0.05L_g$ to the grain boundaries.

are obtained. Considering the current density distribution in the grain boundary, this can be understood: in order to achieve a low grain boundary resistance, the current uses the entire grain boundary area equally; therefore a homogeneous current density distribution as for the electrode configuration in Fig. 14b results even for two microelectrodes. As long as comparably resistive grain boundaries are concerned, R_2 and C_2 are even almost independent of the size and location of the microelectrodes (also see below).

If, however, a sample consists of more than two grains (Fig. 14c), additional current paths are opened. Fig. 14d shows the resulting current density distribution in the marked grain boundary plane if identical properties of all grain boundaries are assumed. The current density across the grain boundary under investigation is highest by far. However, the current across all other grain boundaries in the plane sums to approximately the same value as for the investigated grain boundary. In other words, a correction factor h_R has to be included into Eq. (41), which takes account of the current across neighboring grain boundaries and

$$R_2 = h_R \frac{\rho_{\mathrm{gb}} w_{\mathrm{gb}}}{A_{\mathrm{gb}}} \tag{43}$$

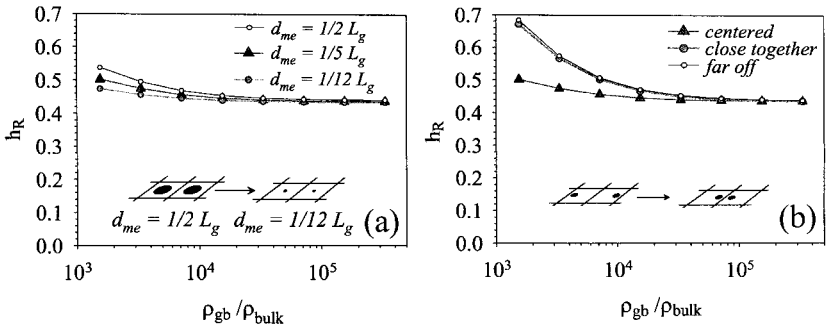

Fig. 15. (a) The factor h_R versus ρ_{gb}/ρ_{bulk} for different diameters of the microcontacts indicating the minor influence of the electrode size. (b) Factor h_R for different locations of the microcontacts.

results. The numerical calculations revealed that h_R can indeed be interpreted as the current fraction passing the grain boundary under investigation: a factor $h_R = \frac{1}{2}$ means that approximately one half of the total current flows across the grain boundary between the two contacted grains [51, 265].

For pronounced grain boundary effects ($(\rho_{gb} w_{gb})/(\rho_{bulk} L_g) > \approx 10$) h_R is quite independent of the electrode size and location (Fig. 15) and amounts to about 0.435 for the 24-grain sample under investigation. In this sample, an entire grain shell around the two considered grains is taken into account. It can therefore be expected that the h_R-value is not much enhanced for larger polycrystals and a value of about 0.4 might serve as a reasonable estimate of h_R for highly resistive grain boundaries in samples with cubic-shaped grains and identical grain boundary properties. The changes of h_R for less resistive grain boundaries (Fig. 15) are due to the widening of the current lines in order to obtain a homogeneous current density across the grain boundary [51]. This widening yields a resistance increase which influences h_R. However, compared with the true grain boundary resistance, this effect becomes negligible for large ρ_{gb}-values.

Similar considerations are valid with respect to the grain boundary capacitance. Again, a correction factor h_C takes account of displacement currents across neighboring grain boundaries and

$$C_2 = h_C \frac{\varepsilon_{gb} A_{gb}}{w_{gb}} \tag{44}$$

results. The finite element calculations revealed that h_C and $1/h_R$ are almost identical as long as uniform grain boundary properties are assumed and $h_C \approx 2.5$ is a reasonable estimate for a polycrystal with cubic-shaped grains.

The situation complicates, if arbitrarily shaped grains of different grain size are considered. A grain boundary between two large grains (compared with all others) carries much more than 50% of the total current and $h_R > 0.5$ results [51]. The opposite is valid if small grains are investigated. Owing to this uncertainty and the unknown grain boundary area, rather large $\rho_{gb} w_{gb}$ and ε_{gb}/w_{gb} fluctuations could be

expected if Eqs. (43, 44) and constant h_R, h_C-values are used to quantitatively analyze the experiments. Therefore, it is sensible to determine a third parameter, namely the relaxation frequency $\omega_2 = (R_2 C_2)^{-1}$ of the grain boundary semicircle. If uniform grain boundary properties are assumed, ${h_R}^{-1} \approx h_C$ holds, and according to Eqs. (43, 44) all unknown factors cancel in the product $R_2 C_2$. Hence, the relaxation frequency ω_2 reads

$$\omega_2 \approx \frac{1}{\varepsilon_{\mathrm{gb}} \rho_{\mathrm{gb}}} \tag{45}$$

and represents a very important parameter with respect to local grain boundary investigations.

So far only identical grain boundaries have been considered. The usual purpose of such localized measurements, however, is the investigation of variations of the grain boundary properties. Numerical calculations showed how the fraction of current passing the grain boundary under investigation changes if the corresponding resistivity differs from that of the neighboring grain boundaries. For the case that all surrounding grain boundaries exhibit resistivity ρ_{gb2}, the current fraction flowing across the grain boundary under investigation (resistivity ρ_{gb1}) is displayed in Fig. 16. The current fraction decreases from one for only slightly blocking boundaries to

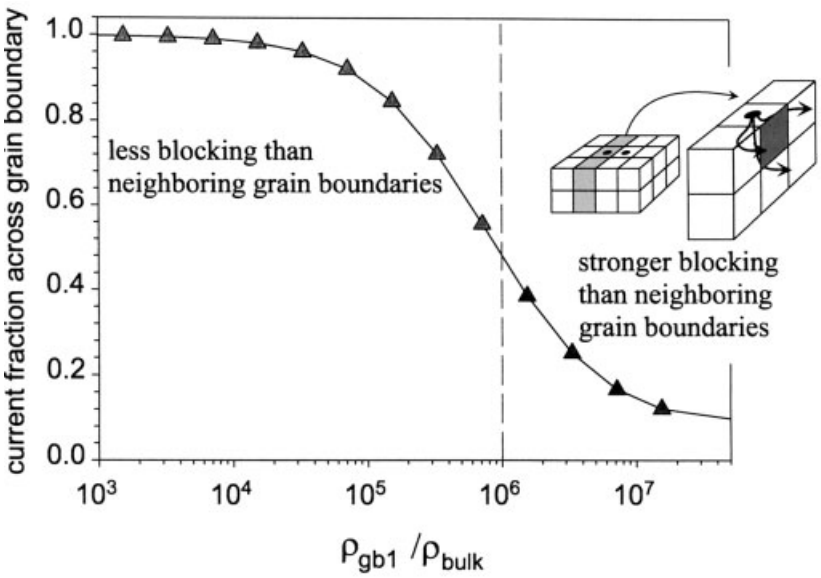

Fig. 16. Current fraction passing the grain boundary under investigation versus normalized resistivity ρ_{gb1} of the considered grain boundary. Other parameters: $d_{\mathrm{me}} = 1/5\ L_g$, $\rho_{\mathrm{gb2}} = 10^6\ \rho_{\mathrm{bulk}}$, $w_{\mathrm{gb}} = 10^{-3}\ L_g$. The vertical line indicates the case of uniform grain boundaries, i.e. $\rho_{\mathrm{gb1}} = \rho_{\mathrm{gb2}} = 10^6\ \rho_{\mathrm{bulk}}$. The diagram demonstrates that strongly blocking grain boundaries are by-passed as sketched in the inset. Owing to computational reasons, the considered plane is not the grain boundary plane itself, but a plane in a distance of $0.05 L_g$ to the grain boundaries. Because of this, the current fraction does not converge to zero.

almost zero for very blocking boundaries. This reveals a general restriction of "individual" grain boundary measurements in a polycrystal: Boundaries which are much less blocking than the average lead to rather small low-frequency semicircles and can therefore be identified. Grain boundaries that are much stronger blocking than the average, however, are bypassed (Fig.16) and do *not* lead to correspondingly large resistances. Hence, measurements of individual grain boundaries by microelectrodes "see" variations in the direction of less resistive boundaries but are "blind" with respect to very resistive boundaries.

The capacitance C_2, and hence h_C, are almost independent of the distribution of grain boundary resistivities. This can be understood by taking into account that capacitive displacement currents do not depend on ρ_{gb}, but on the permittivity of the grain boundaries, which is still assumed to be homogeneous. In the case of spatially varying grain boundary properties, ${h_R}^{-1}$ and h_C are therefore unequal and the relaxation frequency $\omega_2 = (R_2 C_2)^{-1}$ reads $(\varepsilon_{gb}\rho_{gb} h_R h_C)^{-1}$. However, compared with R_2 the relaxation frequency ω_2 is less sensitive to varying shapes and sizes, and for this reason the distribution of ρ_{gb} is better characterized by ω_2 than by R_2. Further details on these calculations are discussed in Ref. [51].

4.2.2 The Interpretation of "Individual" Grain Boundary Measurements

These considerations show that a quantitative determination of individual grain boundary properties from a single microelectrode measurement is only possible if all additional pathways are excluded, for example by separating two grains from the matrix [266]. In a common polycrystal it would be necessary to know the data of all surrounding grain boundaries in order to correctly determine the parameters of an individual boundary. Only in few cases such data can be obtained and therefore the following analysis is proposed: The peak frequency distribution can be used to check the uniformity of the grain boundary resistivity. If there are only small variations of ω_2 (say up to about half an order of magnitude), it can be concluded that many grain boundaries exhibit similar properties and that weakly blocking grain boundaries are not present. From Eq. (45) an average grain boundary resistivity can be estimated. A brick layer analysis of a conventional experiment should be reasonable in such cases, and the locally obtained mean resistivity and the macroscopically determined ρ_{gb} should therefore differ by less than a factor of 2 or 3. However, it cannot be ruled out that very blocking grain boundaries exist. A broad distribution of ω_2, on the other hand, indicates strongly varying grain boundary resistivities, and hence a brick layer analysis of a conventional impedance spectrum is not appropriate. A direct relation of the resistance to a certain grain boundary and thus a quantitative determination of the resistivity of an individual grain boundary is possible for peak frequencies much larger than the average: the corresponding grain boundaries are weakly blocking compared to all others and h_R in Eq. (43) becomes ≈ 1 (cf. Fig. 16) [51].

In order to determine the grain boundary thickness, C_2-values have to be analyzed according to Eq. (44). As for R_2, the specific geometry of the investigated grain boundary and its surroundings affects the analysis since only estimates of the grain boundary area and the f_C-factor are available. Hence, a relatively broad distribution

of evaluated apparent w_{gb}-values is to be expected even for a constant grain boundary thickness and only rough estimates of w_{gb} are possible.

The calculations presented above have also consequences for the analysis of nonlinear current-voltage characteristics of "individual" grain boundaries in varistors. Varistors (variable resistors) are usually based on ZnO and exhibit a rather extreme current-voltage curve with very large grain boundary resistances at low voltages and a sharp drop of the resistance at a certain threshold voltage [120, 267]. The low-voltage data obtained across one grain boundary can be expected to be considerably influenced by neighboring grain boundaries. For high voltages, however, the situation changes considerably: once the resistance of the investigated grain boundary breaks down at the critical voltage, the current mainly flows across this boundary provided no surrounding grain boundary resistances break down as well. Consequently, the measured breakdown voltage reflects the true breakdown voltage of the grain boundary under investigation (if electrode and bulk contributions are negligible). Thus, situations are probable in which the low-voltage I–V characteristics is determined by neighboring grain boundaries, whereas for high voltages the influence of the grain boundary under investigation dominates the results.

4.3 Polycrystals with Highly Conductive Grain Boundaries

Conventional impedance spectroscopy does not allow a separation of grain boundary and bulk contributions in samples with highly conductive grain boundaries (cf. Sec. 3.2). The two microelectrode configurations sketched in Fig. 17a, however, can be applied i) to easily check whether highly conductive grain boundaries exist; and ii) to quantitatively determine the bulk conductivity σ_{bulk} and the grain boundary conduc-

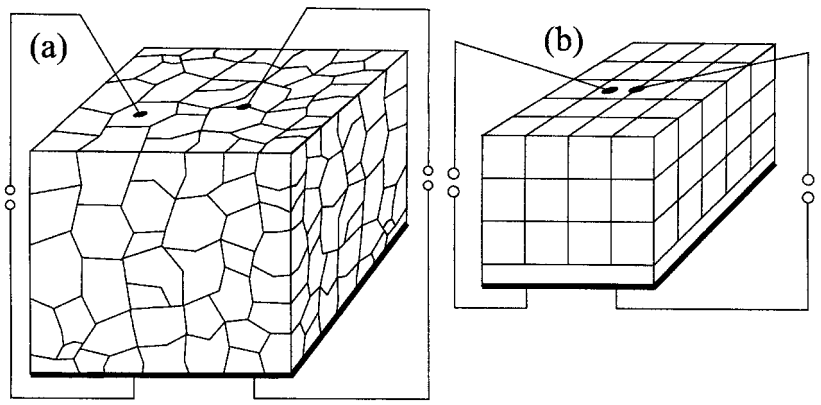

Fig. 17. (a) Measurement principle to investigate the bulk conductivity and the grain boundary conductance of samples with highly conductive grain boundaries. (b) Corresponding model system used for the numerical finite element calculations. Owing to computational reasons, a highly conductive layer is included between counter-electrode and the sample. However, the calculations are not influenced by its conductivity as long as there is no significant potential drop within this region.

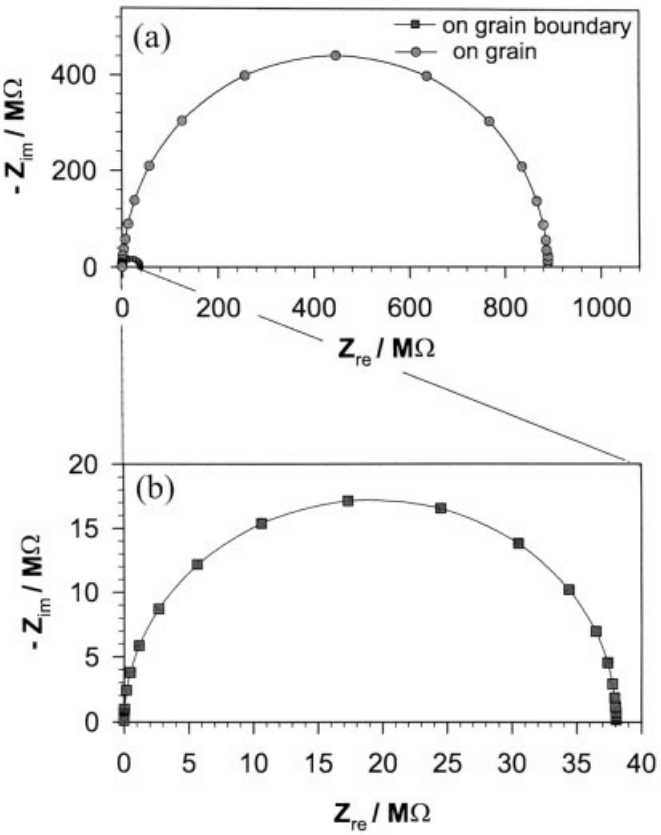

Fig. 18. (a) Calculated impedance spectra for microelectrodes on a grain, and on a grain boundary. Parameters: $d_{me} = 5$ μm, $L_g = 25$ μm, $\sigma_{gb} = 10^{-2}$ Ω^{-1} cm^{-1}, $\sigma_{bulk} = 10^{-6}$ Ω^{-1} cm^{-1}, $w_{gb} = 25$ nm. (b) Magnification of the spectrum calculated for a microelectrode on a grain boundary. Ohmic/reversible electrodes are assumed.

tance $\tilde{Y}_{gb}$ $(= \sigma_{gb} w_{gb})$ in a polycrystal with highly conductive grain boundaries. In the following, the basic principles of such investigations are discussed from numerical calculations on a 60-grain model sample (Fig. 17b).

As shown in Fig. 18, both microelectrode locations (on a grain and on a grain boundary) lead to one semicircle if ohmic (reversible) electrodes are assumed. However, if the grain boundary is highly conductive, the resistance obtained by a microelectrode on a grain boundary is considerably smaller than that measured with a microelectrode on a grain. This is because a highly conductive grain boundary short-circuits the grain bulk and leads to an enhanced current. Hence, such a comparison can easily prove the existence of highly conductive grain boundaries.

In the quantitative interpretation, the resistance obtained with a microelectrode atop a grain shall be considered first. Fig. 19a displays a cross section of the potential distribution obtained for the 60-grain model sample. As in the case of a homogeneous material without grain boundaries, most of the voltage drops in a very small

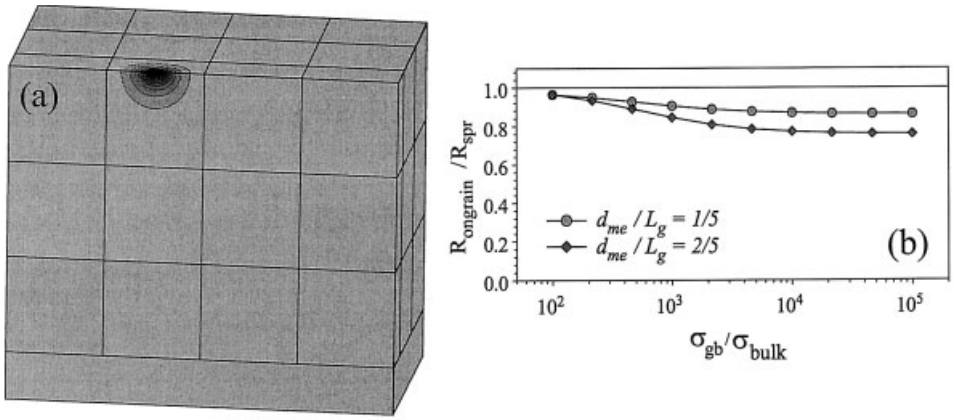

Fig. 19. (a) Calculated potential distributions in one half of the model sample with highly conductive grain boundaries for a microelectrode located on a grain. The lines and color jumps indicate equipotential lines, the voltage drop between two neighboring lines is U/12, with U being the applied voltage. Other parameters: $\sigma_{gb} = 10^5\ \sigma_{bulk}$, $w_{gb} = 10^{-3}\ L_g$. (b) Resistance (normalized with respect to the spreading resistance) for a microelectrode on a grain indicating that – despite highly conductive grain boundaries – the resistance is close to the spreading resistance value.

region beneath the microelectrode. Only the outer equipotential lines differ significantly from those in a single crystal, indicating that the resistance is mainly determined by the bulk conductivity close to the microelectrode. Therefore the spreading resistance formula Eq. (34) is a rather good approximation in order to quantify the resistance measured on a grain. According to Fig. 19b, the deviation from R_{spr} is always less than about 15% if the grain size (L_g) is five times larger than the contact diameter (d_{me}). Even for $d_{me} = 0.4\ L_g$ an estimate of the bulk conductivity is possible with an error of at most 25%. Hence, although some further deviations can be expected if the electrode is off-center and if grains are not cube shaped, the method allows a satisfactory calculation of the true bulk conductivity of a grain.

The quantitative analysis of the data obtained on a grain boundary is more complicated. As shown in Fig. 20a "heart-shaped" equipotential lines result indicating that within grains current lines are bent in direction of the highly conductive paths. Since microelectrode diameters (a few μm) are usually considerably larger than grain boundary thicknesses (typically 1–2 nm core and several nm space charge thickness) the resistance is not only determined by the grain boundary, but also by the bulk. Hence, a simple evaluation of the grain boundary conductivity according to the spreading resistance formula is definitely not sensible. Fig. 20b gives the numerically calculated relationship between the ratio R_{spr}/R_{ongb} on the one hand (R_{ongb} = resistance measured with a microelectrode on a grain boundary) and the normalized grain boundary conductance $\tilde{Y}_{gb}/{R_{spr}}^{-1}$ on the other hand. The spreading resistance can satisfactorily be approximated by the resistance measured with a microcontact on a grain $R_{ongrain}$. Thus, for a given L_g/d_{me} ratio the measured resistance ratio $R_{ongrain}/R_{ongb}$ ($\approx R_{spr}/R_{ongb}$) can be unambiguously related to $\tilde{Y}_{gb}/{R_{spr}}^{-1}$ and the

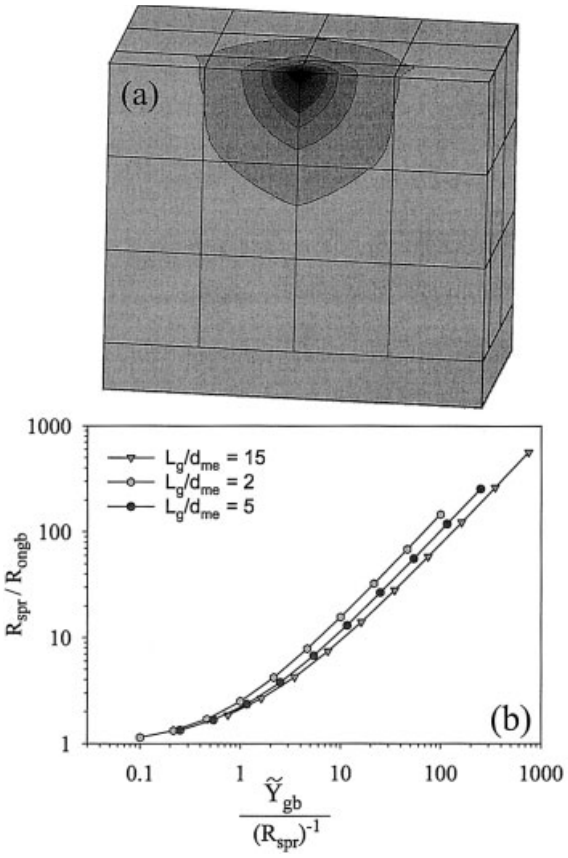

Fig. 20. (a) Potential distribution in one half of a model sample for a microelectrode located on a highly conductive grain boundary. The lines and color jumps indicate equipotential lines, the voltage drop between two neighboring lines is U/12, with U being the applied voltage. Other parameters: $\sigma_{gb} = 10^5\ \sigma_{bulk}$, $w_{gb} = 10^3\ L_g$. (b) Ratio of the ideal spreading resistance to the resistance measured on a grain boundary versus the normalized grain boundary conductance for different ratios of grain size to microelectrode diameter. The graph allows the determination of the grain boundary conductance from the experimentally available resistance ratio.

grain boundary conductance $\tilde{Y}_{gb}$ can therefore be determined from two microcontact experiments.

According to Fig. 20b the grain size is of minor importance with respect to the evaluation of $\tilde{Y}_{gb}$. An increase of the grain size L_g by e.g. a factor of 7.5 changes R_{spr}/R_{ongb} by less than a factor of two in the entire parameter range considered here. This can be understood from the potential distribution: Although the shapes of the equipotential lines in a single crystal and for a microcontact on a grain boundary of a polycrystal differ considerably, the density of potential lines is only slightly affected. This means that, for an electrode positioned on a grain boundary, again most of the potential drops within a very small region beneath the contact: For $d_{me} = L_g/5$ about 90% of the resistance drops along the grain boundary in question.

Owing to this sharp potential drop, the resistances obtained on "short" and "long" grain boundaries are very similar. Consequently, the influence of the detailed geometry/microstructure on the quantitative analysis is much less pronounced than one might have expected at a first glance. Hence, an approximate analysis according to Fig. 20b is also possible for realistic polycrystals. The error owing to different grain sizes and grain shapes can be expected to be less than about a factor of 2 for

microcontacts in the range of $L_g/3 \ldots L_g/20$. Further details with respect to these calculations are given in Ref. [52].

These considerations showed that the evaluated conductance $\tilde{Y}_{gb}$ is mainly determined by the grain boundary under investigation. Hence, a one-to-one relation between the locally obtained R_{ongb} and $\tilde{Y}_{gb}$ of the grain boundary under investigation is possible, and the spatial distribution of grain boundary properties can be studied. Adjacent grain boundaries play an important role only if most of them are much less conductive than the investigated one and thus interrupt the highly conductive current path. In order to check in how far the fast grain boundaries percolate, two microelectrodes on one and the same grain boundary can be used. Since both microelectrodes cause a current constriction, approximately twice the resistance of a measurement with one microelectrode and an extended counter-electrode can be expected for percolating grain boundary paths. If the resistance between two microelectrodes is not higher but lower than that of a measurement using one microelectrode, the grain boundary paths are probably non-percolating. In experiments, further non-idealities have to be considered such as non-ideal positioning of the microelectrode on the grain boundary or sloping grain boundaries, but an approximate analysis according to Fig. 20b is usually expected to be still possible.

Two other applications of this technique should be mentioned: i) In composites enhanced conductivities along interfaces between different constituents can be investigated. Such effects play an important role, for example, in heterogeneously doped solid electrolytes [125, 126]. ii) Microelectrodes can be used to investigate strongly anisotropic grain boundaries, i.e. grain boundaries which are laterally highly conductive (e.g. due to a highly conductive core), but blocking in perpendicular direction (e.g. due to a depletion space charge layer) [124] or vice versa. Two microelectrodes along a single grain boundary can detect the highly conductive parts while two electrodes on neighboring grains can be utilized to measure the blocking characteristics.

4.4 Investigation of Electrochemical Processes at Electrodes

Dense, geometrically well-defined microelectrodes facilitate quantitative geometry-dependent electrode polarization experiments without a reference electrode (cf. Sec. 3.4). Here two important aspects are discussed that should be taken into account in the interpretation of impedance measurements using such microelectrodes. Let us first consider a laterally homogeneous, dense, circular microelectrode. Its local electrochemical properties shall be described by a space-independent, area-related (specific) resistance $\tilde{R}_{el}$ (in Ω cm^2). Such a situation can, for example, be assumed if the electrode resistance is caused by a space charge layer or an ion transfer across the entire electrolyte/electrode interface. Using impedance spectroscopy, one can separate the effective (i.e. the measured or simulated) dc electrode resistance R_{el}^{eff} from the spreading resistance of the bulk R_{spr} and an effective area-related resistance R_{el}^{eff} according to

$$\tilde{R}_{el}^{eff} = R_{el}^{eff} A_{el} \tag{46}$$

can be calculated.

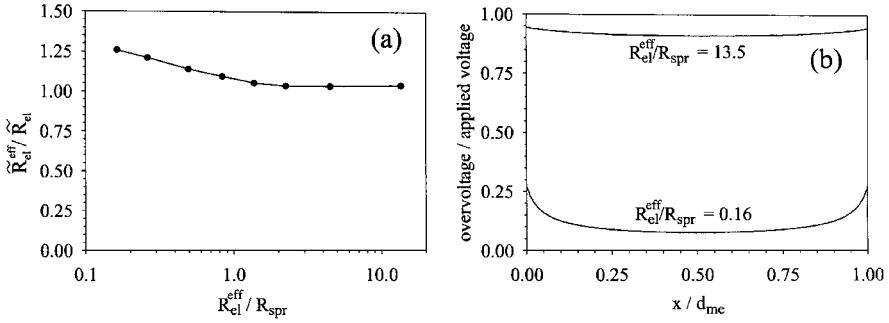

Fig. 21. (a) Calculated ratio between the effective and true area-related electrode resistance of a microelectrode for different normalized effective electrode resistances. For small electrode resistances, the effective and the true values differ significantly. (b) Local variation of the overvoltage along a microelectrode for pronounced and small electrode resistances. For pronounced electrode effects, most of the applied voltage drops at the electrode and a rather homogeneous overvoltage results.

Numerical simulations reveal that this effective value $\tilde{R}_{el}^{eff}$ differs form $\tilde{R}_{el}$ if the measured (simulated) R_{el}^{eff} is smaller than R_{spr} (Fig. 21a). These deviations are connected with the inhomogeneous potential distribution in the vicinity of a microelectrode yielding laterally varying electrode overvoltages for small electrode resistances (Fig. 21b). In microelectrode experiments, however, the ratio R_{el}^{eff}/R_{spr} is often large (cf. Sec. 3.4) and hence $\tilde{R}_{el} \approx \tilde{R}_{el}^{eff}$ is usually a reasonable approximation. In liquid electrochemistry, similar effects are discussed in the context of primary ($\tilde{R}_{el} = 0$) and secondary ($\tilde{R}_{el} > 0$) current distributions [268, 269].

On the other hand, even dense, well-defined microelectrodes can exhibit laterally varying properties since an electrochemical reaction involving a gaseous species is frequently restricted to a narrow, ring-like region close to the three-phase boundary (3PB) (cf. surface path of the oxygen reduction reaction in Sec. 2.4). This can yield serious complications with respect to a quantitative analysis of impedance measurements. Here the considerations are restricted to the simplified case that a ring at the rim of a circular microelectrode exhibits constant electrochemical properties for the oxygen reduction reaction, while the inner part of the microelectrode is electrochemically inactive (Fig. 22a). The reaction in this ring is locally taken into account by a specific (local) impedance $1/(\tilde{R}_{ring}^{-1} + i\omega\tilde{C}_{ing})$ with $\tilde{R}_{ring}$ (in Ω cm^2) and $\tilde{C}_{ring}$ (in F cm^{-2}) being the area-related resistance and capacitance respectively. The large inner part of the electrode/electrolyte interface is locally described by a specific capacitance $\tilde{C}_{in}$ meaning that this region is blocking for faradic current but permeable for dielectric displacement currents.

In the dc case, the current has to flow to the electrochemically active sites close to the 3PB and a considerable current constriction results (Fig. 22b). Hence, the dc resistance consists of the resistance due to the electrochemical reaction and the bulk resistance, which includes the current constriction in the vicinity of the active ring. At higher frequencies, the inner part of the microelectrode becomes dielectrically permeable and the current flows to the entire microelectrode area (Fig. 22c). In other words, the current lines in the bulk, and thus the bulk resistance, are frequency-

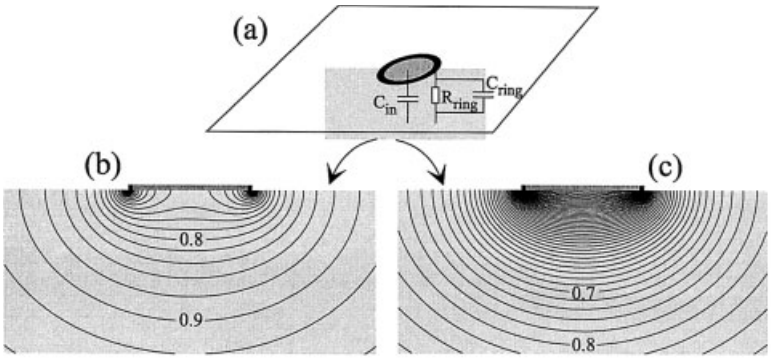

Fig. 22. (a) Sketch of a microelectrode with laterally inhomogeneous electrochemical activity (e.g. oxygen reduction at the three-phase boundary). The black ring indicates the electrochemically active area and can be represented by a resistive and a capacitive element, whereas the inner part of the electrode behaves purely capacitive. (In the calculations, local, i.e. specific, parameters rather than R_{ring}, C_{ring} and C_{in} are used.) (b) Calculated dc potential distribution in the grey plane of the sketch (a). The voltage drop between two neighboring equipotential lines is U/50, with U being the applied voltage. The numbers indicate the potential in fractions of U. Parameters: $\tilde{R}_{ring} = 10^{-4}$ Ω cm^2, $\sigma_{bulk} = 10^{-2}$ S cm^{-1}, $d_{me} = 20$ μm, $b_{ring} = 20$ nm. A significant part of the potential drops in the vicinity of the ring and leads to an additional resistance $R_{\Delta cc}$. (c) Potential distribution at high frequencies: owing to the capacitive current across the inner part of the microelectrode, the potential distribution corresponds to the conventional spreading resistance case.

dependent. At high frequencies, the bulk resistance is just the spreading resistance of the microelectrode, while in the dc case the bulk resistance is increased by an additional current constriction term $R_{\Delta cc}$.

Numerically calculated impedance spectra (Fig. 23a) reveal that, depending on the ratio of the nominal capacitances C_{ring} ($=\tilde{C}_{ring}A_{ring}$) and C_{in} ($=\tilde{C}_{in}A_{in}$), two or three semicircles are visible in the complex Z-plane (A_{ring} and A_{in} are the areas of the electrochemically active ring and of the inactive inner disc of diameter d_{me} respectively). The possibility of three arcs might be surprising, since only two resistive mechanisms are involved, namely the transport in the bulk and the electrochemical reaction. An intuitively constructed equivalent circuit can help to understand this behavior: The additional bulk resistance due to the low-frequency current constriction near the ring ($R_{\Delta cc}$), as well as the resistance caused by the electrochemical reaction R_{ring} can be short-circuited by the capacitance of the electrode/electrolyte interface C_{in}. This interface capacitance is therefore in parallel to a series connection of $R_{\Delta cc}$ and the impedance due to the electrode reaction given by R_{ring}, C_{ring} (Fig. 23b). The bulk spreading resistance and spreading capacitance determine the high-frequency behavior and are in series to these elements. Similar to three serial RC elements, such a circuit leads to three arcs in the complex impedance plane if $C_{in} \ll C_{ring}$ [54], even though only two transport mechanisms are included.

Numerical calculations of several impedance spectra confirmed that a fit to the intuitive circuit (Fig. 23b) really yields sensible approximations to the expected parameters (cf. Ref. [53]). The circuit can therefore be applied to analyze such microelectrode experiments and particularly to separate the true electrochemical im-

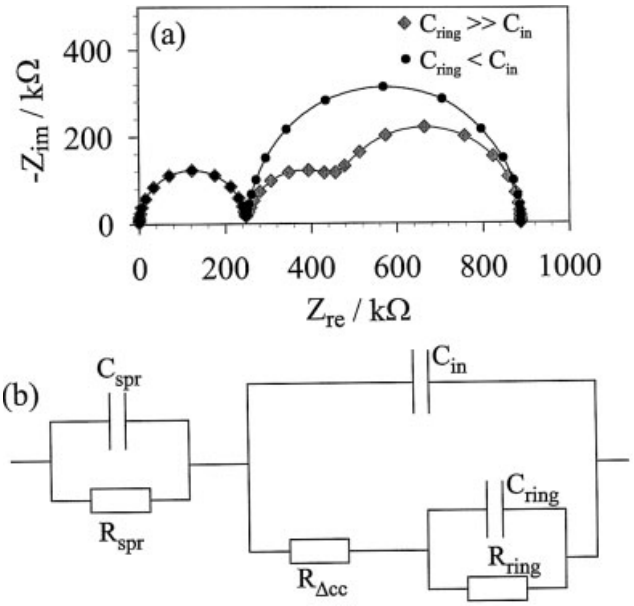

Fig. 23. (a) Impedance spectra calculated for the microelectrode sketched in Fig. 22. Parameters: $d_{me} = 20$ μm, $b_{ring} = 20$ nm, $\sigma_{bulk} = 10^{-3}$ S cm^{-1}, $\tilde{R}_{ring} = 5 \cdot 10^{-3}$ Ω cm^2, $\tilde{C}_{ring} = 5000\ \tilde{C}_{in}$ (i.e. $C_{ring} \gg C_{in}$) or $\tilde{C}_{ring} = 50\ \tilde{C}_{in}$ (i.e. $C_{ring} < C_{in}$). (b) Intuitive equivalent circuit deduced for the inhomogeneous microelectrode of Fig. 22.

pedance and the additional bulk resistance $R_{\Delta cc}$. An analysis in terms of three serial RC elements, on the other hand, does not lead to fit results that have simple meanings and should therefore be avoided in this case [54]. As predicted by the intuitive circuit, $C_{in} > C_{ring}$ yields spectra with only two semicircles (Fig. 23a) and the low-frequency arc then not only includes the electrode polarization resistance, but also the additional current constriction resistance $R_{\Delta cc}$. This is rather problematic, since the resistance of the low-frequency arc could easily be interpreted in terms of one polarization process, although it includes two contributions. Only further partial pressure, temperature or voltage-dependent measurements together with an appropriate model might allow a separation into the two parts.

It is also important to discuss the magnitude of $R_{\Delta cc}$ compared to R_{spr}. In Fig. 24, the ratio $R_{\Delta cc}/R_{spr}$ is shown for some ring widths b_{ring}; in the case of a 20 μm microelectrode with an active ring of 10 nm, for example, $R_{\Delta cc}$ and R_{spr} are almost identical. The occurrence of $R_{\Delta cc}$, however, is not necessarily disadvantageous. Its value could also be used to experimentally determine the effective width of the electrochemically active ring from Fig. 24: if $R_{\Delta cc}$ and R_{spr} are obtained from a fit of the experimental data to the equivalent circuit in Fig. 23b, the ring width can be calculated unambiguously. Such an analysis could be extremely valuable, since it allows a reasonable estimate of the extension of the so-called 3PB region of gas electrodes, which has been under discussion for many years [148, 158, 163, 185, 270]. Unfortunately, a successful analysis of impedance spectra in terms of this width has not been reported yet.

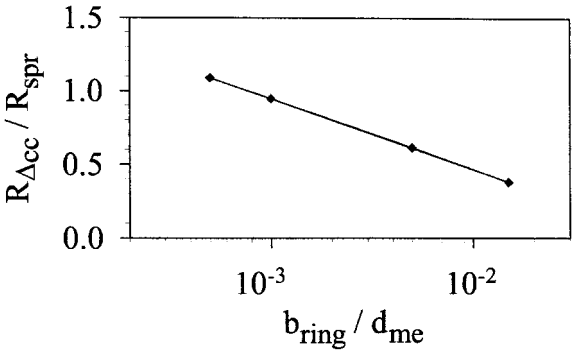

Fig. 24. Ratio of the additional current constriction resistance to the conventional spreading resistance for different ring widths (b_{ring}) normalized to the diameter of the electrochemically inactive inner part (d_{me}), indicating that for small active rings the additional resistance becomes rather important.

5 Experimental Realization of Microelectrode Measurements

Mainly, two kinds of microelectrodes are used in order to realize local electrical measurements on ceramics:

i) Lithographic patterning of thin films, which is common to semiconductor technology, can also be applied to produce microelectrodes on ionic solids. Fig. 25 displays two patterns of microelectrodes established by means of lithographic masks. Such microelectrodes can, for example, be contacted under the microscope by (commercially available) contact needles having typically a tip radius of 0.5 to 5 μm. To give some examples of electrode materials used so far in solid state ionics: Au and $YBa_2Cu_3O_{6+\delta}$ on $SrTiO_3$; Au and Al on ZnO; $LaMnO_3$ and Ag on yttria-stabilized zirconia; Al on $BaTiO_3$; and Ag on AgCl [160, 161, 264, 266, 271–277].

ii) A relatively sharp needle mechanically pressed onto the sample can also be used as a microelectrode [52, 97, 148, 154, 156, 165, 238, 239, 264, 278–311]. However, since the actual contact geometry depends on plastic and elastic deformations of the tip as well as of the sample, an appropriate choice of the tip material and a "calibration" of the deformations are necessary. Tungsten tips of ca. 5 μm tip radius are, for example, suitable to make reproducible microcontact imprints on AgCl (Fig. 26). A disadvantage of microelectrodes realized by mechanical pressure is their ill-defined local contact geometry. Even if the diameter of the imprint is known, the contact probably consists of a number of "nano-contacts", which is particularly disadvantageous if electrochemical processes at three-phase boundaries of gas electrode are investigated (cf. Sec. 4.4). Bulk conductivity measurements might also be distorted, since the measured resistance includes current constriction effects close to these established nano-contacts. Hence, it is important to perform calibration experiments on samples with known conductivity in order to check whether correct spreading resistance values can be obtained.

Two further techniques to realize microelectrodes should be mentioned. Thin metal wires have been embedded into relatively soft ionic crystals such as AgCl and

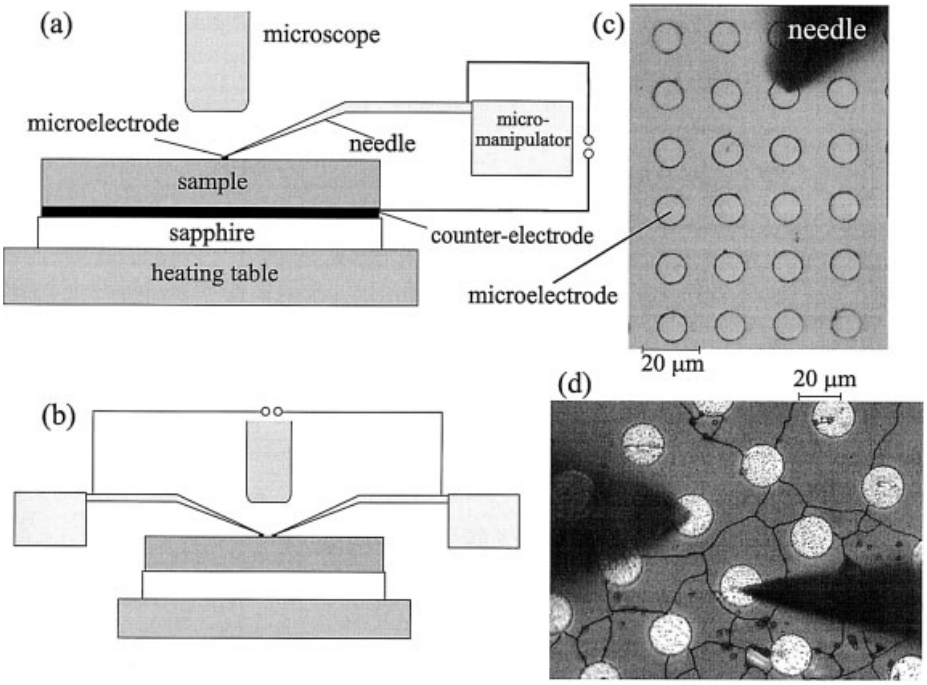

Fig. 25. (a) Sketch of a possible set-up to perform microcontact measurements using one microelectrode and an extended counter-electrode. The microelectrode is contacted under the microscope by a sharp needle. (b) Set-up for two microelectrodes. (c) Evaporated Au microelectrodes on $SrTiO_3$ and the needle-like tungsten tip to contact the electrodes. Such a configuration is used to perform spatially resolved bulk conductivity measurements (Sec. 6.2). (d) Ag-coated $YBa_2Cu_3O_{6+\delta}$-microelectrodes on a $SrTiO_3$ polycrystal contacted by two tungsten tips. The corresponding local grain boundary measurements are discussed in Sec. 6.3.

AgBr by the aid of thermal treatment [312, 313]. These wires can, for example, be used as local potential probes. Moreover, very fine metal wires have been welded on oxide surface [314, 315].

In several studies, large contact electrodes at the periphery of a sample have been used to feed the current. As sketched in Fig. 27, a connection line is deposited in order to connect microelectrodes and contact electrodes; in some cases the ends of such thin connection lines are regarded as the microelectrodes. However, such a set-up can be very problematic since experimental results are, in many cases, determined by the current between the two large contact electrodes rather than by the current between the microelectrodes.

This can be understood from the electrode configuration shown in Fig. 27b: extended electrodes on two sides of a square sample are used as current feed electrodes and very thin, highly conductive lines connect these contacts and circular microelectrodes on top of the sample. In the case of a single crystal, the resistance between two circular microelectrodes R_{me} is given by $(\sigma_{bulk} d_{me})^{-1}$, whereas the resistance between the two contact electrodes reads $(\sigma_{bulk} h)^{-1}$ with h being the sample height. The

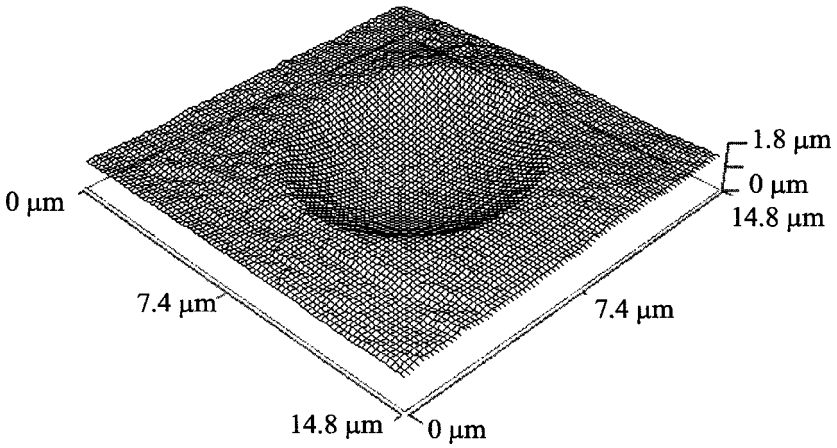

Fig. 26. AFM picture of the imprint of a tungsten needle (7-μm tip radius) into a silver chloride single crystal. The z-axis is over-elevated.

resistance between the microelectrodes therefore typically exceeds the resistance between the current feed electrodes by one to three orders of magnitude. Since the total resistance is to a good approximation given by a parallel connection of both contributions, a total bulk resistance R according to

$$R = \frac{1}{\sigma_{\text{bulk}}(d_{\text{me}} + h)} \tag{47}$$

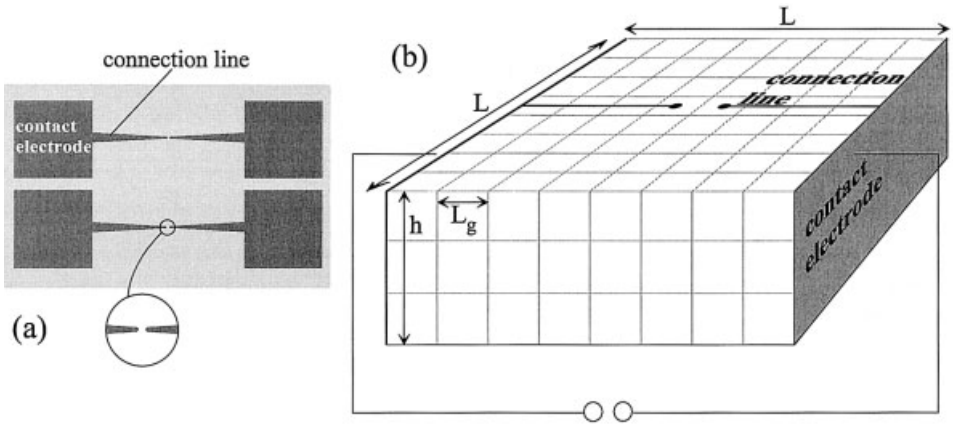

Fig. 27. (a) Electrode configuration frequently used to perform microelectrode measurements. The end of the connection line represents the microelectrode. However, if the sample surface and the contact electrodes for current feed are not separated by an insulator, such a set-up often measures the overall properties between the contact electrodes rather than the local properties. (b) Sketch of a model sample with extended contact electrodes, very thin highly conductive connection lines, and circular microelectrodes.

results, which is almost identical to the bulk resistance between the large electrodes. Thus, most of the current flows between the contact electrodes and local conductivities cannot be deduced from such measurements.

For a polycrystalline sample with highly resistive, identical grain boundaries the situation is very similar. The grain boundary resistance between the two microelectrodes on adjacent grains $R_{\mathrm{gb,me}}$ is – for identical grain boundaries – approximately given by

$$R_{\mathrm{gb,me}} \approx \frac{0.4 w_{\mathrm{gb}}}{\sigma_{\mathrm{gb}} L_g^2} \tag{48}$$

(cf. Sec. 4.2), whereas the grain boundary resistance between the two contacts $R_{\mathrm{gb,c}}$ reads

$$R_{\mathrm{gb,c}} \approx \frac{w_{\mathrm{gb}}}{\sigma_{\mathrm{gb}} L_g h}. \tag{49}$$

Thus, a resistance ratio $R_{\mathrm{gb,me}}/R_{\mathrm{gb,c}} \approx 0.4h/L_g$ results, and the measured grain boundary resistance is usually again determined by the grain boundary resistance between the two large contacts. (For the sake of clarity, the grains in Fig. 27b are unrealistically large.) Measurements using electrode configurations similar to that sketched in Fig. 27 are thus mostly macroscopic and lead to resistance and capacitance values typical for conventional impedance experiments; true microelectrode measurements yield much higher resistances and much lower capacitances.

If, however, the grain boundary between the microelectrodes is considerably less resistive than all others, correct results may be obtained even for electrode configurations similar to those in Fig. 27. For example, this can be the case if a voltage above the threshold voltage of a ZnO varistor grain boundary is applied. The resistance of the grain boundary between the microelectrodes then breaks down, while all other grain boundaries remain highly resistive.

Contact electrodes insulated from the sample prevent a dc current between the current feed electrodes and therefore also facilitate reasonable dc microelectrode measurements. However, in this case, impedance measurements can be impeded by capacitive currents across the insulation layer between the large contacts and the sample.

An experimental problem may arise with respect to the absolute value of impedances/resistances to be measured in microelectrode studies. Bulk conductivities $<10^{-4}$ S cm^{-1} are often met in experiments on ionic solids. In conventional measurements using macroscopic electrodes, this leads to bulk resistances of the order of kΩ-MΩ. For microelectrodes, however, resistances are orders of magnitude higher. According to the spreading resistance formula Eq. (34), a bulk conductivity of 10^{-6} S cm^{-1}, measured by a 5-μm microelectrode, already yields 1000 MΩ. Therefore, high impedance converters are often required to conduct microelectrode impedance experiments.

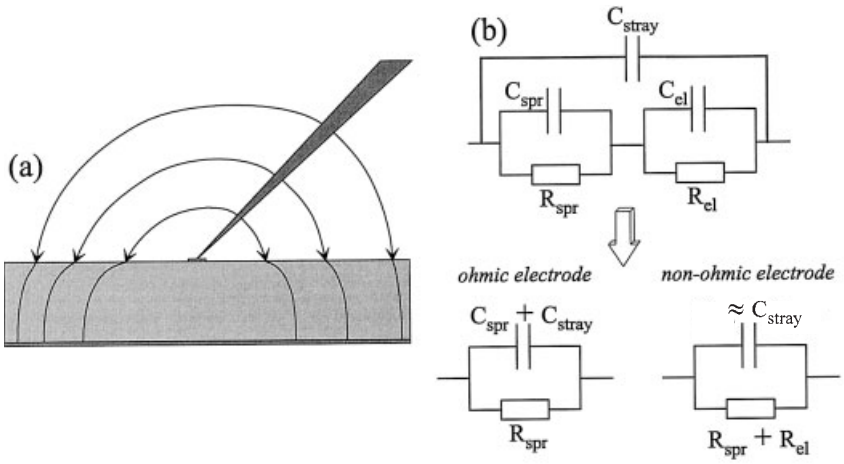

Fig. 28. (a) Sketch of current lines of the dielectric displacement current between a contact needle and a counter-electrode indicating the influence of the stray capacitance. (b) Equivalent circuit (including the stray capacitance) representing microelectrode measurements on single crystals and the two simplified subcases for ohmic and non-ohmic microelectrodes.

Lastly, a remark concerning the lower limit of microelectrode diameters. By means of lithographic techniques it is certainly possible to prepare microelectrodes with diameters below 1–2 μm. The contacting procedure might be difficult under an optical microscope, but could work in atomic-force or scanning-tunneling microscopes (AFM/STM). However, dielectric displacement currents between unshielded parts of the contact needle and the counter electrode (Fig. 28a), or between two unshielded contact tips, can hinder reasonable impedance measurements with submicron microelectrodes: the corresponding stray capacitance is in parallel to the impedance of the sample, and for a single crystal the circuit sketched in Fig. 28b results. For the sake of simplicity, the microelectrode impedance is represented by an ideal RC element. If ohmic/reversible microelectrodes are used, the circuit reduces to a single RC element with C being mainly determined by the stray capacitance, since typical spreading capacitances for $d_{me} < 1$ μm amount to less than one fF, whereas typical stray capacitances are of the order of several 10 fF. The resistance still represents the correct bulk spreading resistance and at least correct bulk conductivities can be obtained from such measurements. However, if non-ohmic electrodes are used and $C_{stray} \gg C_{el}$, the equivalent circuit reduces to one RC element with R being $R_{bulk} + R_{el}$ and hence a separation into bulk and electrode properties by impedance spectroscopy fails. Even if a very accurate open-circuit calibration ($\pm$ few fF) of the stray capacitance is performed, microelectrodes >100 nm are required to separate the impedance of the bulk and of typical electrode capacitances (C_{el}/A of a few μF cm^{-2}). In other words, the use of nanoelectrodes to quantitatively investigate local conductivities in ionic solids is restricted to cases for which reversible/ohmic nanoelectrodes can be found.

6 Examples of Microelectrode Measurements in Solid State Ionics

6.1 Overview

i) *Spatially resolved measurements of bulk properties*. Two microelectrode studies in solid state ionics deal with spatially resolved bulk conductivity measurements: firstly, the inhomogeneous conductivity caused by a dopant (Cd^{2+}) profile was measured in AgCl and yielded the diffusion coefficient of Cd^{2+} [278]; secondly, local microelectrode measurements were conducted on $SrTiO_3$ to investigate stoichiometry polarization phenomena under high-field stress [273]. The latter experiments are discussed in more detail in Sec. 6.2. In several further studies, microelectrodes served as potential probes to determine the spatial distribution of the electrochemical potential of electrons and ions in ionic solids [308, 309, 311–313, 316]. Thin Pt wires embedded in the sample were, for example, used to investigate the local chemical potential of silver in silver halides during Hebb–Wagner experiments [311, 313, 316]; from the measured profile the relationship between the electronic conductivity and the silver activity was calculated. Ag wires embedded in silver halide crystals allowed the determination of local electrochemical potentials of Ag^+ ions [312, 313]. Ionically conducting microelectrodes consisting of AgBr [309] or AgI [308] were employed to examine the local electrochemical potential of Ag^+ in Ag_2S samples exposed to a temperature gradient [308] and to a dc voltage [309]. Furthermore, Pt microelectrodes revealed the spatial distribution of the electrochemical potential of electrons in Ag_2S under the Soret stationary conditions [308].

ii) *Highly resistive grain boundaries*. Several experiments were performed in order to understand the conduction mechanism in ZnO-based varistors. In particular the breakdown voltages of grain boundaries were investigated by means of microelectrodes on adjacent grains. These studies showed that the varistor effect is a grain boundary effect and that the breakdown voltage of single grain boundaries is usually between 3 and 4 V [244, 266, 267, 274, 276, 314, 317]. By examining an ultrasonically isolated bigrain, even the influence of neighboring grain boundaries could be excluded [266]. It has been reported that some grain boundaries do not exhibit a varistor-like behavior and that the varying grain boundary properties can be correlated to the bismuth content in the core [244, 276, 281, 314, 317, 318]. Microelectrode measurements on $BaTiO_3$ showed that the PTC (positive temperature coefficient) effect mainly originates from the grain boundary [275, 315], though bulk properties possibly also contribute to the global PTC behavior [277]. Tungsten microelectrodes that were mechanically pressed into the sample could be used as potential probes in four-point measurements on Mn–Zn ferrites [310]. These revealed the potential drops across grain boundaries. Impedance spectroscopy was applied to investigate the distribution of grain boundary properties in Fe-doped $SrTiO_3$ [51, 271]; it was demonstrated that a brick layer analysis is reasonable in this material. These measurements are presented in Sec. 6.3. In most of the abovementioned experiments, evaporated microelectrodes were used. Several studies on the properties of highly resistive grain

boundaries suffer from the fact that large current feed electrodes were used; these can strongly influence the experimental results (cf. Sec. 5).

iii) *Highly conductive interfaces*. Microelectrodes were also applied to study highly conductive grain boundaries in polycrystalline silver halides [52, 265, 279, 280]. In Ref. [52] the basic principles of such measurements have been developed and the applicability of the method has been demonstrated for the case of polycrystalline AgCl. Temperature-dependent measurements on AgCl and AgBr [279, 280] yielded further information on the grain boundary properties and showed that a brick layer model for highly conductive grain boundaries correctly predicts the overall conductivity of silver halide polycrystals. Highly conductive surface layers were also studied by means of microelectrodes: In Ref. [264] it is shown how microelectrodes with different diameters can be used to determine the thickness and the conductivity of a highly conductive surface layer on polished AgCl single crystals. Moreover, the enormous sensitivity of microelectrodes with respect to highly conductive surface layers was used to investigate the gas-solid interaction of NH_3 and AgCl: an enhanced surface conductance could be observed on AgCl exposed to ammonia [319]. In these studies, microelectrodes were mostly realized by silver-coated tungsten needles that were mechanically pressed onto the sample's surface.

iv) *Electrochemical processes at electrodes*. Several publications deal with the electrode kinetics on miniaturized gas electrodes [148, 154, 156, 160, 161, 185, 282–296]. Owing to its relevance in solid-oxide fuel cells, the oxygen reduction reaction on yttria-doped zirconia has been investigated in particular [148, 154, 156, 160, 161, 165, 185, 282–285, 288, 290]. In most cases, pointed ceramic crystals (doped $LaMnO_3$, $LaCrO_3$ and $LaFeO_3$) or metal wires (Pt, Ag, Au) were pressed onto the zirconia sample. In Ref. [284] a systematic comparison of several microelectrode materials is shown: Ag electrodes turned out to exhibit the lowest electrode geometry-related resistance. The microelectrode diameter was determined from the known ionic conductivity of zirconia and the measured bulk resistance (Eq. (34)). From partial pressure, bias, and geometry-dependent experiments on $LaMnO_3$ microelectrodes it has been concluded that probably both the bulk and the surface path can play a role for the oxygen reduction reaction on $LaMnO_3$ cathodes [148, 165]. An activation of $LaMnO_3$ electrodes by cathodic and anodic polarization has been reported in Ref. [156]. Experiments on Pt-microelectrodes revealed current-induced changes in the surface structure of the Pt/ZrO_2 interface [288]; this changing morphology can also affect the corresponding electrochemical properties [290]. Similar effects might influence the performance of a Ni/H_2 microelectrode on doped zirconia [287]. Electrode kinetic studies on the anodic H_2 oxidation on proton conducting oxides (doped $SrCeO_3$ and $SrZrO_3$) can be found in Refs. [286, 289, 292–294]; in these measurements again pointed metal electrodes (Ni, Ag, Au, Pt) served as microelectrodes. The advantage of such pressed microcontacts is certainly their relatively simple experimental realization, the possibility of measurements without reference electrodes, and the chance to subsequently perform several measurements on one and the same sample. However, owing to nanopores and nanocontacts along the electrode/electrolyte interface, an exact determination of the established contact area, as well as of the three-phase boundary length, is problematic. In very few studies, geometrically well-defined microelectrodes were therefore employed: droplets of Ag

solidified on a zirconia surface exhibited a rather defined contact geometry and were utilized to determine the geometry dependence of the electrode resistance of silver electrodes [185]; moreover, electrochemical investigations on dense, circular $LaMnO_3$ microelectrodes of 20–200 μm diameter have been discussed in Refs. [160, 161]. The latter experiments are presented in Sec. 6.4 in more detail.

v) *Partial conductivities and diffusion coefficients in mixed ionic and electronic conducting ceramics*. The chemical diffusion coefficient of Cu was detected in Cu_2S and Cu_2Se by means of Pt microelectrodes [238, 300, 307]. Similar investigations on $CuInS_2$ and $CuInSe_2$ using Pt or Au microelectrodes yielded diffusion coefficients of Cu, as well as information on a change from p- to n-type conduction with increasing Cu concentration [302, 303, 320]. Ion-blocking Pt microelectrodes were also applied in order to investigate the ionic conductivity and the stability behavior of Ag_2S and Cu_2S [238, 239, 299]. Moreover, encapsulated Pt-microelectrodes enabled the determination of the electronic conductivity of doped CeO_2 [97, 306]. Ion-conducting microelectrodes consisting of Y-doped zirconia were employed to block the electronic conduction (as well as the proton conduction); the oxide-ion conductivity of several ceramics (doped $LaCoO_3$, $BaCeO_3$, $YBa_2Cu_3O_{6+\delta}$) could thus be obtained as a function of the oxygen activity [297, 298, 301, 304, 305, 320]. In these studies, microelectrodes were mechanically pressed onto the sample and the diameter of the micro-contact was determined either by measuring the size of the imprint or from Eq. (33), if the bulk conductivity could be obtained from a separate experiment.

A few further applications of microelectrodes in solid state ionics are worthy of mention: Microelectrodes are used to investigate the deposition process of silver on mechanically pre-structured (i.e. scratched) AgCl surfaces [321]. The silver deposits turned out to grow preferentially in or along such prestructured tracks. This aligned deposition could be used to electromechanically write miniaturized silver structures on crystalline electrolytes. M-β''-Al_2O_3 microelectrodes have been employed to locally dope ionic solids by means of charge transport in an electrical field [322]; and a Pt-tip microelectrode has been used to investigate the Li-ion extraction and insertion behavior of a micrometer-sized $LiMn_2O_4$ single crystal [323].

In the following, four examples of quantitative microelectrode measurements are discussed in more detail. Each reflects a typical field of solid state ionics (non-stoichiometry, highly resistive grain boundaries, highly conductive interface, electrode reactions) and thus provides evidence for the vast potential of microelectrodes in solid state electrochemistry.

6.2 Stoichiometry Profiles in $SrTiO_3$ after High DC Field Stress

6.2.1 Definition of the Problem

Perovskite-type titanates (e.g. $SrTiO_3$, $BaTiO_3$) constitute an important class of electroceramic materials and are, for example, used in PTC (positive temperature coefficient) resistors, capacitors, varistors or sensors [324–326]. A degradation process that

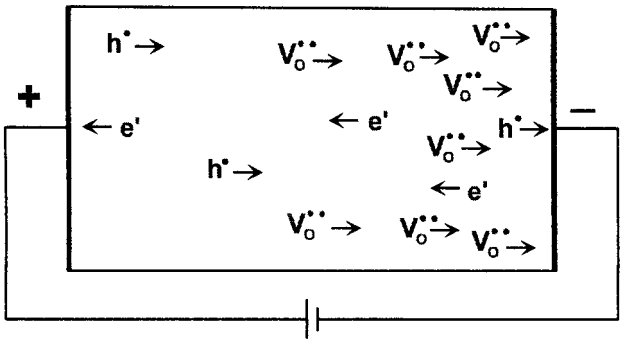

Fig. 29. Sketch to illustrate the defect motion in acceptor-doped $SrTiO_3$ during high field stress. The oxygen vacancies are blocked at the electrodes and therefore accumulate at the cathode, but deplete at the anode. Electrons and holes can pass the electrodes.

occurs particularly in dielectric applications of such titanates is so-called resistance degradation, which is characterized by a slow increase in the leakage current under dc field stress [327–335]. It is also referred to frequently as electrocoloration, as it can be accompanied by the movement of a dark color front from the anode and a light colored front from the cathode into the sample. In Refs. [328–330] it has been demonstrated that a model based on the assumption of field-induced stoichiometry gradients can explain all the experimental observations with respect to the time, field and temperature dependences of the leakage current: In acceptor-doped $SrTiO_3$, for example, oxygen vacancies, electrons and holes are mobile charge carriers. The model only assumes that oxygen vacancies are blocked at the $SrTiO_3$/electrode interface while the additional resistance due to the transfer of electrons and holes across this interface is low. After applying an electrical field, all mobile charge carriers begin to move. Owing to the blocked oxygen exchange reaction at the electrodes, oxygen vacancies accumulate at the cathode and deplete at the anode (Fig. 29) leading to a pronounced vacancy concentration profile (stoichiometry polarization, Hebb–Wagner experiment; cf. Sec. 3.1.2). The spatially varying vacancy concentration also causes variations of the electron and hole concentrations in the entire sample (cf. Fig. 2b). The resulting space- and time-dependent conductivity variations, finally, lead to an increase of the leakage current, and thus to the observed resistance degradation.

When the electrical field is switched off, the composition gradient relaxes due to diffusion processes. However, low diffusion coefficients can lead to a very slow equilibration, and hence distinct conductivity variations can be expected in $SrTiO_3$ or $BaTiO_3$, not only during but also after high field stress. A detection of these conductivity profiles would directly confirm the assumed stoichiometry polarization. In the following, spatially resolved microelectrode measurements are presented that allow such a test of the theory of resistance degradation on Fe-doped $SrTiO_3$ single crystals and polycrystals.

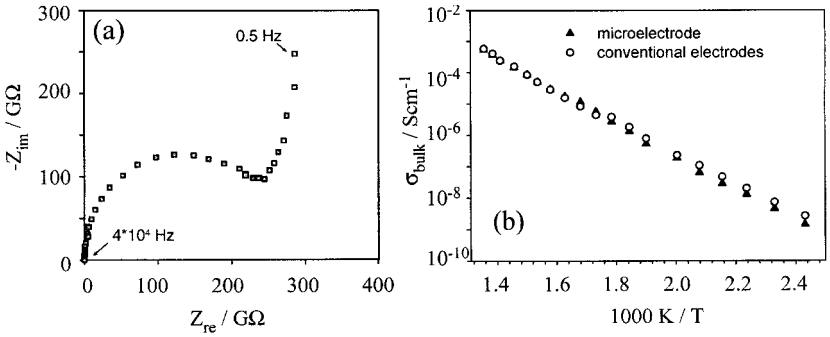

Fig. 30. (a) Impedance spectrum measured with a Au microelectrode ($d_{me} = 20$ μm) on a Fe-doped $SrTiO_3$ single crystal. The arc represents the bulk properties. The rather high impedances are measured by means of a home-made impedance converter. (b) The applicability of microcontact impedance spectroscopy on $SrTiO_3$ is evidenced by the agreement of the bulk conductivity σ_{bulk} obtained by measurements with macroscopic electrodes and microelectrodes on a homogeneous crystal.

6.2.2 Bulk Conductivities in $SrTiO_3$ Measured by Means of Microelectrodes

Firstly, it has to be excluded that highly conductive surface layers influence the results. Conductivities obtained by microelectrodes and by conventional macroscopic electrodes have therefore been compared for a nominally homogeneous Fe-doped $SrTiO_3$ single crystal. A lithographic lift-off process was used to prepare circular microelectrodes (ca. 15 ... 220 μm in diameter) from an evaporated 20 nm Cr/200 nm Au film. Impedance spectra were measured between microelectrodes and an extended Au counter-electrode (Fig. 30a) and between two macroscopic electrodes. Both the microscopic and the macroscopic bulk resistances are gained from the corresponding high-frequency semicircle of the impedance spectra and temperature-dependent bulk conductivities have been calculated (Fig. 30b). In the entire temperature range, the agreement between the two values is satisfactory. Moreover, within the accuracy of the microelectrode measurement (resistance variation for different contacts of identical size is about 15%), the bulk resistance is inversely proportional to d_{me} (Fig. 31a) as predicted by Eq. (34). This proves that enhanced surface conductivities do not distort the results and that microcontact impedance spectroscopy can be applied to $SrTiO_3$ in order to obtain local conductivity data. The linear relation between d_{me} and the measured capacitance could also be confirmed with a capacitance offset of ca. 250 fF for $d_{me} \rightarrow 0$ due to stray capacitances (Fig. 31b).

6.2.3 Conductivity Profiles in $SrTiO_3$ Single Crystals after High Field Stress

The electrocoloration (high-field stress) experiments were performed on Fe-doped $SrTiO_3$ single crystals (0.22 mol % Fe). Circular microelectrodes (10 μm in diameter and 20 or 30 μm in distance) were again prepared by a lithographic lift-off process from an evaporated 20 nm Cr/200 nm Au film. Two further Cr/Au electrode stripes were used to achieve the resistance degradation (see Fig. 32a). At 493 K, an electrical

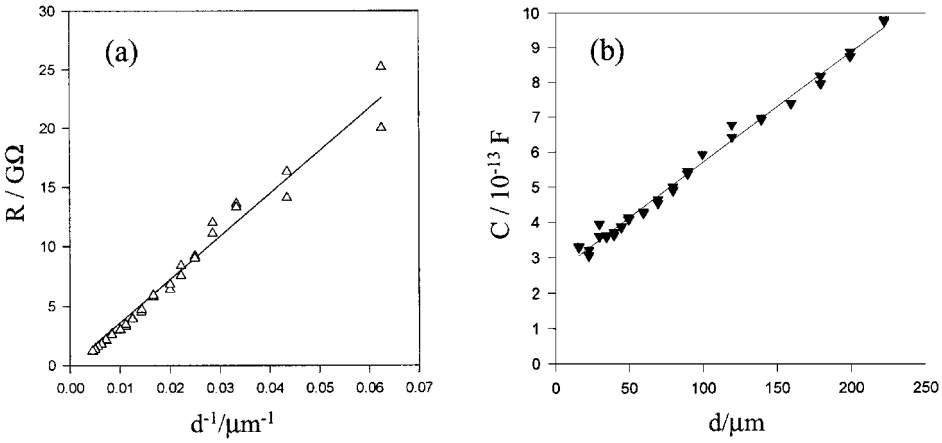

Fig. 31. (a) Resistance and (b) capacitance of the high frequency semicircle measured on $SrTiO_3$ with microelectrodes of different diameter ($T = 473$ K).

field was applied between the two stripe electrodes, which leads to a significant movement of a dark color front from the anode and a light color front from the cathode into the sample. After disconnecting the stripe electrodes, the conductivity distribution was determined at ca. 415 K or 473 K by subsequently contacting all microelectrodes in a line with a tungsten tip and measuring the impedance spectra between the microelectrode and a counter-electrode (Fig. 32b). As a counter-electrode, a Cr/Au electrode on the backside, or one of the stripe electrodes, was used. The local conductivities measured were independent of the location of the counter-electrode.

Before a large dc field was applied to a single crystal, a homogeneous conductivity could be detected [273]. After a high field stress (10^3 V cm^{-1} for 90 minutes), however, a distinct conductivity profile has developed in the sample (Fig. 33a). It consists of four characteristic regions: i) an enhanced conductivity region at the anode with a relatively smooth drop towards the center of the sample; ii) a sharp

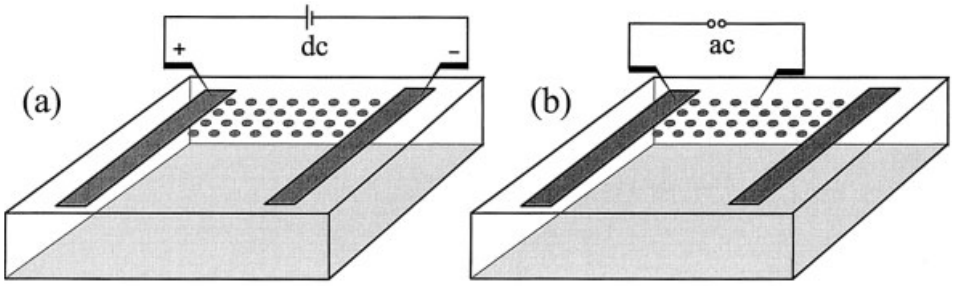

Fig. 32. Sketches of the electrode geometries used (a) for the electrocoloration of the $SrTiO_3$ sample and (b) for the microcontact impedance measurements to determine the local conductivity distribution. The sketch does not give the true scale; the number of microelectrodes is much larger than shown.

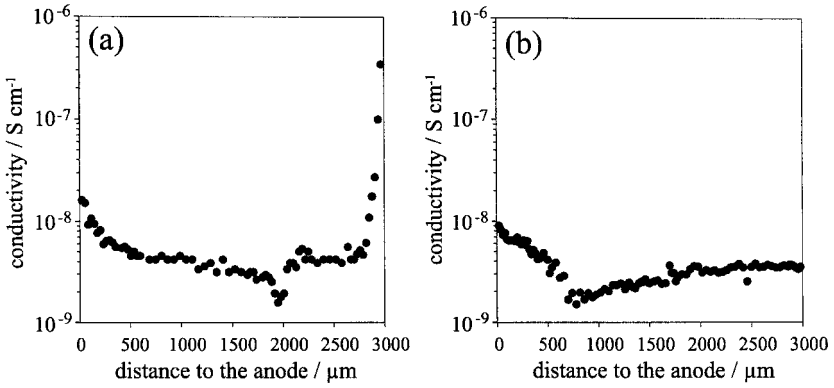

Fig. 33. (a) Conductivity profile in a Fe-doped $SrTiO_3$ single crystal obtained at 417 K after electrocoloration with Au electrodes ($E = 10^3$ V cm^{-1} at 493 K for 90 min). (b) Profile after subsequent annealing at about 613 K for two hours; profiling temperature: 417 K.

conductivity minimum; iii) a plateau exhibiting the conductivity of the sample before the high field stress; and iv) a sharp conductivity increase close to the cathode. This profile corresponds to a situation in which the leakage current is already enhanced, though the steady state has not been reached yet. Temperature-dependent measurements of the conductivity distribution demonstrate that the conductivity minimum is much less pronounced for higher temperatures. The profiles did not significantly change during their measurement. However, a conductivity measurement after annealing the sample at higher temperatures (two hours at $\approx$613 K) and subsequent cooling to the profiling temperature revealed a relaxation of the profile (Fig. 33b): the cathodic conductivity enhancement vanished, the anodic enhancement decreased and the minimum moved towards the anode by ca. 1 mm.

6.2.4 Comparison with Theory

The conductivity variations due to resistance degradation were numerically simulated in order to check whether the main qualities of the experimentally observed profiles correspond to the theoretically predicted ones. A more detailed description of the calculation procedure is given in Refs. [273, 330, 336, 337]. The calculated concentration distribution of oxygen vacancies for the experimental parameters used in the measurements is shown in Fig. 34a. Obviously, a strong depletion of oxygen vacancies, and thus an enhanced hole concentration in the anodic region (partial oxidation of the sample), can be expected (cf. Fig. 2b). At the cathode the oxygen vacancy concentration is enhanced (partial reduction of the sample), which leads to an enhanced electron concentration. These concentration distributions of electrons, holes and vacancies yield a very characteristic total conductivity distribution, which is shown in Fig. 34b. Again, four different regimes occur: i) a conductivity enhancement at the anode; ii) a sharp minimum; iii) a plateau; and iv) a conductivity enhancement at the cathode. It is worth stressing that different parts of the sample even

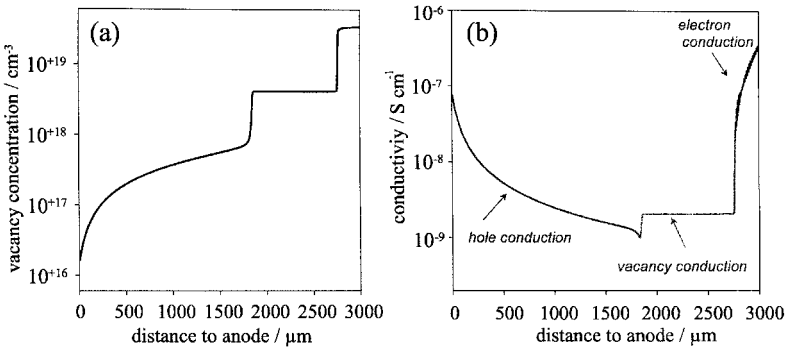

Fig. 34. (a) Calculated vacancy concentration at 417 K after high field stress ($E = 10^3$ V cm^{-1} at 493 K for 90 min) of a Fe-doped $SrTiO_3$ single crystal. (b) Corresponding calculated conductivity profile at 417 K. The regions of predominant hole, vacancy, and electron conduction are indicated.

exhibit different conduction mechanisms: in the anodic region holes dominate the conduction, the mechanism changes at the minimum to ionic oxygen vacancy conduction, and the cathodic conductivity enhancement is due to electron conduction. The calculated depth of the conductivity minimum is temperature-dependent and decreases with increasing temperature.

There is a striking similarity between the experimentally observed and the theoretically calculated profiles, and all four characteristic features occur in both. The calculated location of the minimum, which mainly depends on the vacancy mobility, is close to the location observed in the experiment. The computed temperature dependence of the depth of the minimum corresponds with the results of the measurement. Obviously, the stoichiometry polarization model of resistance degradation correctly predicts the conductivity variations. In particular the almost quantitative agreement of the very characteristic shape of the conductivity distribution proves the validity of the existing model described above. It should be noted that in the calculations only the hole mobility is chosen such that the theoretically and the experimentally observed depth of the minimum is similar, but all other parameters used in the simulation are taken from literature [77, 336, 338].

The profiles can be regarded as frozen-in at the profiling temperatures, since the diffusion length of oxygen during the conductivity measurements is less than 20 µm [339]. However, the oxygen vacancy profile in an electrocolored sample should equilibrate at higher temperatures [328], leading to a shift of the sharp oxygen vacancy front. Assuming the oxygen vacancy front diffuses with the chemical diffusion coefficient of oxygen $\tilde{D}$, a movement of this front by 0.5 mm can be estimated via $2\sqrt{\tilde{D}t}$ ($\tilde{D} \approx 10^{-7}$ cm^{2}s^{-1} at 613 K [339] and $t = 120$ minutes). Hence, after the annealing the conductivity minimum should have moved by about 0.5 mm. This differs only by a factor of about 2 from the experimentally obtained distance. Taking into account the error bar of the literature value of $\tilde{D}$, and that diffusion processes during heating to the annealing temperature also play a role, this is again a satisfactory agreement. In summary, all measurements confirm the stoichiometry polarization

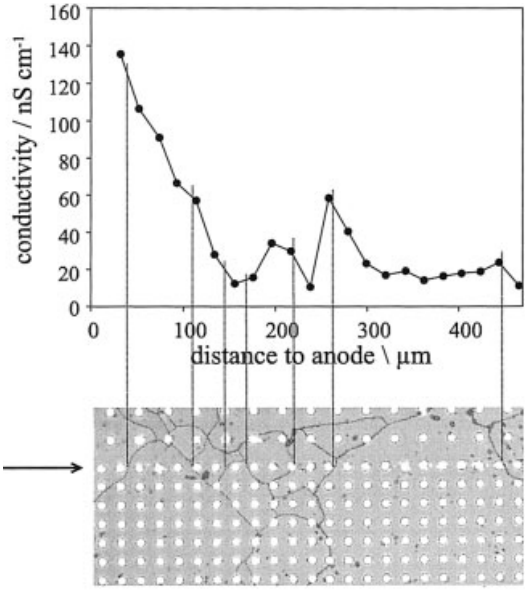

Fig. 35. Detail of the conductivity profile measured close to the anode of an electrocolored Fe-doped $SrTiO_3$ polycrystal ($E = 10^3$ V cm^{-1}, electrocoloration with Au electrodes at about 493 K for 60 min). The corresponding area of the sample with evaporated microelectrodes ($d_{me} = 10$ µm) is depicted below the diagram. The dotted lines indicate grain boundaries; the arrow, the investigated electrode line. The profile was measured at 473 K.

model of dc electrical degradation (electrocoloration) of electroceramics. A more detailed discussion of these experiments is given in Refs. [273, 337].

6.2.5 Conductivity Profiles in Polycrystals

Conductivity distributions obtained after electrocoloration of polycrystalline $SrTiO_3$ samples (0.2 mol % Fe-doped) exhibit a larger scatter compared to profiles in single crystals, but again a cathodic and an anodic conductivity increase can be measured [273]. Experiments with a higher spatial resolution revealed that there is not only an overall profile in the entire sample but also frequently conductivity peaks close to grain boundaries (Fig. 35). Particularly in large grains pronounced subprofiles with an enhanced conductivity close to the grain boundaries were observed.

In this case, a quantitative discussion of the measured conductivity distribution is complicated. It is known that grain boundaries in Fe-doped $SrTiO_3$ exhibit space charge layers with decreased oxygen vacancy concentration [246, 247, 340, 341], which hinders the transport of oxygen vacancies through the boundary. Simplified calculations using a fixed transfer factor for ionic defects at grain boundaries [330] revealed that in polycrystalline samples the overall profile should be modified such that close to grain boundaries the conductivity exhibits maxima (a saw tooth profile). This is again in accordance with the experimentally observed conductivity distributions and therefore supports the assumption that grain boundaries hinder the oxygen vacancy transport and slow down the electrocoloration process. In other words, the profiles measured in single grains reflect the pile-up of vacancies on one side of a grain, and their depletion on the other. However, since considerable conductivity

gradients can be expected within single grains, the conductivity values shown in Fig. 35 definitely suffer from averaging effects.

6.2.6 Effect of the Electrode Material

Electrocoloration in $SrTiO_3$ and $BaTiO_3$ has been observed for different electrode materials (Al [331], Ag [329, 334], Au [273, 328] and Pt [329]); hence, all these metals have been assumed to be almost completely inactive with respect to the oxygen exchange at the oxide/electrode interface. On the other hand, on ZrO_2 or CeO_2 silver electrodes turned out to be much less blocking with respect to the electrochemical oxygen reduction reaction than gold electrodes [183, 184, 284]. Hence, one may expect that the shape of the stoichiometry and conductivity profiles inside the samples also depends on the kind of electrodes used. In order to investigate the effect of the electrode material on the electrocoloration process, conductivity profiles have also been studied for electrocoloration electrodes consisting of a 150 nm silver layer (with a 15 nm adhesion layer of Cr) [342].

Fig. 36 shows the corresponding conductivity profile in a Fe-doped $SrTiO_3$ single crystal obtained after electrocoloration with a silver electrode (10^3 V cm^{-1} for 90 min. at 493K). In contrast to gold electrodes, an enhanced conductivity could only be measured close to the electrocoloration anode. Finite difference calculations revealed that for partially permeable electrodes the cathodic conductivity enhancement can almost vanish, whereas the anodic enhancement only slightly decreases [342]. This corresponds to the measured data and supports the assumption that Ag/Cr electrodes, though leading to an electrocoloration and a conductivity enhancement at the anode, are far from being completely ionically blocking. This interpretation is supported by additional SIMS experiments performed after electrocoloration in an $^{18}O_2$ atmosphere, which also yielded an enhanced oxygen incorporation rate at the Ag/Cr electrodes on $SrTiO_3$ [342].

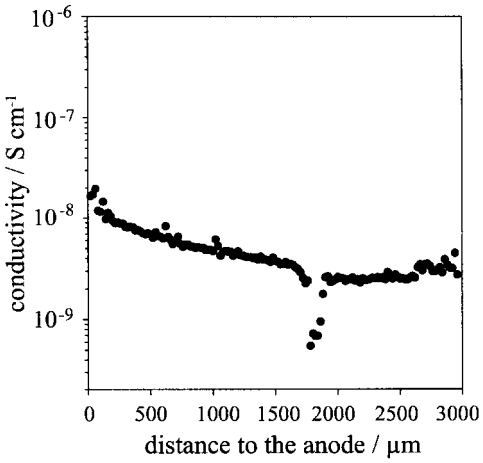

Fig. 36. Conductivity profile in a Fe-doped $SrTiO_3$ single crystal obtained at 417 K after electrocoloration with Ag electrodes ($E = 10^3$ V cm^{-1} at 493 K for 90 min).

In summary, all these local measurements demonstrate the power of microelectrodes i) to determine local bulk conductivities in ionic solids; and ii) to study an important phenomenon in solid state ionics, namely the occurrence of non-stoichiometry profiles in mixed conducting solids.

6.3 Highly Resistive Grain Boundaries in $SrTiO_3$

6.3.1 Definition of the Problem and Experimental Details

A quantitative analysis of grain boundary impedances measured with macroscopic electrodes can be rather problematic if grain boundary properties vary from boundary to boundary (cf. Sec. 3.2). Hence, additional information on the distribution of grain boundary resistivities is often desired. Microelectrode measurements can yield such additional information (Sec. 4.2) and below a microcontact impedance spectroscopic study of grain boundaries in a polycrystal is exemplarily presented. The material of choice is again $SrTiO_3$ (0.2 mol % Fe-doped), which represents a model material for the technologically highly important class of perovskite-type titanates (see also above).

The microelectrodes applied in this study ($d_{me} = 20$ μm) consisted of $YBa_2Cu_3O_{6+\delta}$ (150 nm) covered with a thin Ag layer (50 nm). The electrodes were contacted by two tungsten tips (1 μm tip radius) positioned by micromanipulators (Fig. 25b and d). The $YBa_2Cu_3O_{6+\delta}$ electrodes turned out to be ohmic [343], i.e. a measurement with two electrodes in one grain yields only one, namely the bulk semicircle in the complex impedance plane (Fig. 37a). A measurement across a grain boundary, on the other hand, results in two arcs (Fig. 37b). The high-frequency arc of such a spectrum reflects the bulk properties according to Eq. (36), whereas the second arc (characterized by R_2 and C_2) is due to the grain boundaries. The relaxation frequency of the grain boundary arc ω_2 was obtained from R_2 and C_2 via $\omega_2 = (R_2C_2)^{-1}$. Further details on the determination of R_2 and C_2 are given in Ref. [271].

It is worth mentioning that the spectra measured with two microelectrodes on adjacent grains can exhibit artefacts that deserve attention (Fig. 37c, d): i) Most high-frequency arcs are not ideal semicircles, but exhibit a kind of a loop. The size of the loop, and hence the deviation from an ideal bulk semicircle, depends on the size of the metallic heating table and on the distance between sample and heating table. Such loops have already been mentioned in Sec. 4.1 and are connected with the capacitive coupling of contact tips and electrodes to the ground, i.e. to the heating table in this case [263, 271]. ii) A more or less pronounced shoulder can appear at the high-frequency side of the grain boundary arc. This shoulder is caused by a widening of the current lines in the grain in order to achieve a homogeneous current density across the entire grain boundary area. This phenomenon has been discussed in more detail in Ref. [271]. Since the shoulder reflects a current detour in the bulk rather than grain boundary properties, all grain boundary arcs exhibiting such a feature were fitted with two serial RC elements, but only the always much larger low-frequency part is discussed in terms of grain boundary properties.

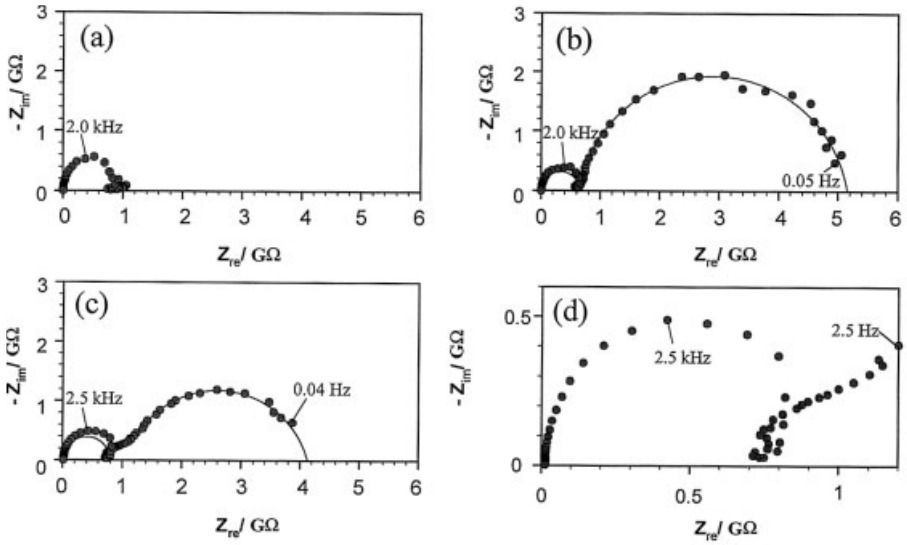

Fig. 37. Impedance spectra obtained by means of microelectrodes on a Fe-doped $SrTiO_3$ polycrystal at 585 K. (a) Spectrum measured with microelectrodes on one and the same grain demonstrating that only a bulk semicircle occurs. (b) Spectrum measured across a grain boundary. (c) Spectrum measured across another grain boundary; there is a pronounced shoulder at the high frequency part of the grain boundary arc. (d) Bulk arc of spectrum (c) indicating the loop due to capacitive coupling to the ground.

6.3.2 Distribution of Grain Boundary Properties

About 30 "individual" grain boundaries, i.e. 30 different electrode configurations were investigated by microcontact impedance spectroscopy. The resulting histograms of the resistance, capacitance and relaxation frequency obtained from an equivalent circuit fit of the low-frequency arc are shown in Fig. 38. For comparison, a conventional (macroscopic) impedance measurement was performed on an identically prepared sample. The relaxation frequency of the grain boundary semicircle is indicated in Fig. 38c by a solid line.

Several conclusions can now be drawn from the experimentally observed histograms. As expected (cf. Sec. 4.2), the relaxation frequency distribution is considerably smaller than the resistance distribution and a fit to a Gauss function ($\propto \exp(-0.5(\log(\omega_2) - \log(\omega_2{}^*))^2/\gamma^2)$) leads to a logarithmic half width γ of about 0.2 and a mean value $\omega_2{}^*$ of 3.0 Hz. Hence, the half-width of the grain boundary resistivity can be estimated to be less than half an order of magnitude, provided the permittivity ε_{gb} is constant for all boundaries (cf. Eq. (45)). Taking into account that grain boundary resistivities could vary by several orders of magnitude, the resistivity distribution measured here is rather narrow. It is particularly interesting that not a single non-blocking grain boundary has been observed. However, lateral inhomogeneities along single grain boundaries, as well as the existence of some very blocking grain boundaries, cannot be excluded from these measurements.

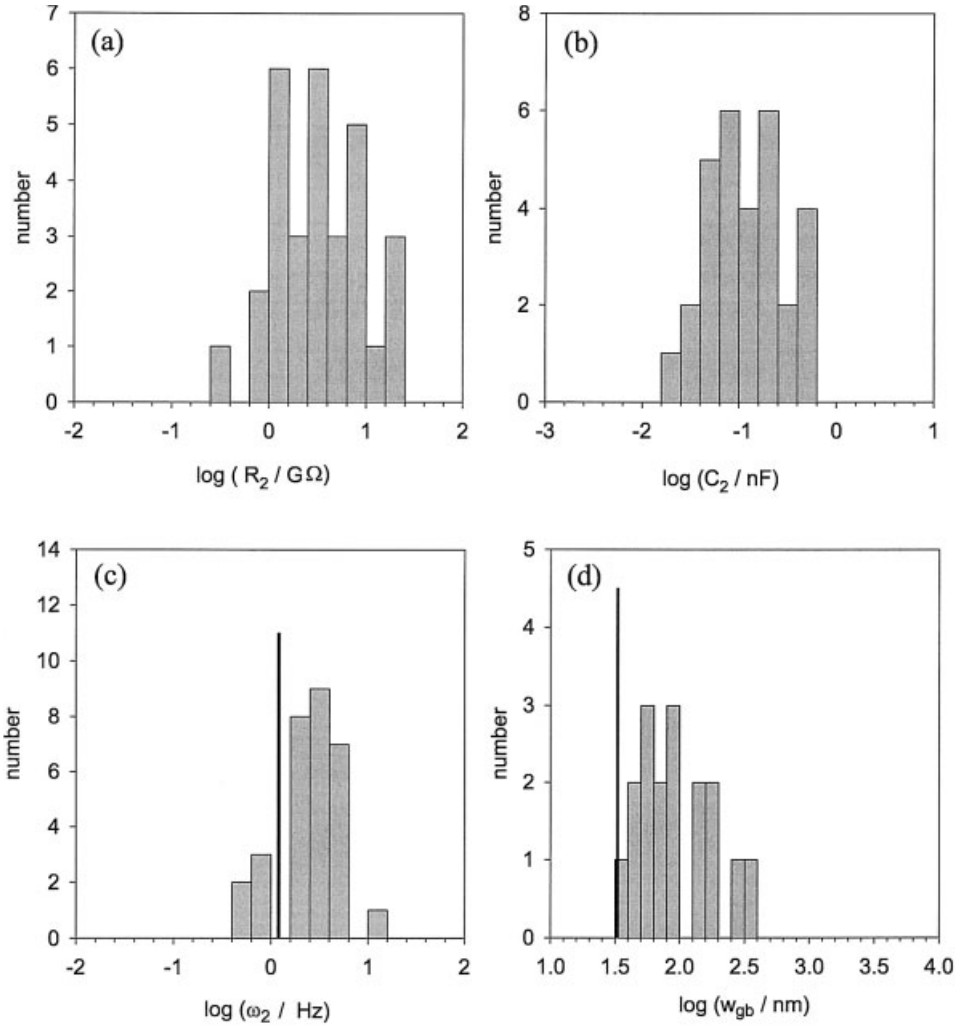

Fig. 38. (a): Resistance histogram (R_2) of microelectrode grain boundary measurements on $SrTiO_3$ obtained at 585 K; (b) capacitance histogram (C_2); (c) relaxation frequency histogram (ω_2), the solid line indicating the value obtained from a conventional impedance experiment; (d) apparent grain boundary thickness histogram determined from the measured grain boundary capacitances; the solid lines in (c) and (d) indicate the value obtained from a brick layer analysis of a conventional impedance experiment.

In accordance with literature [246, 247, 340, 341] and the mechanistic discussion given below, the grain boundary impedance is interpreted in terms of space charge layers (double Schottky barriers) characterized by a depletion of positive charge carriers (Fig. 4c). For a space charge layer, $\varepsilon_{gb} \approx \varepsilon_{bulk}$ can be assumed, and Eq. (45) allows an estimate of the mean grain boundary resistivity of $\bar{\rho}_{gb} \approx 1.6 \cdot 10^{10}\ \Omega$ cm at a temperature of 585 K from the center ($\omega_2{}^* \approx 3.0$ Hz) of the logarithmic relaxation frequency histogram. Moreover, from the ratio of bulk resistivity ρ_{bulk} (determined from the bulk semicircle) to mean grain boundary resistivity $\bar{\rho}_{gb}$, a mean space

charge potential (barrier height) $\Delta\bar{\varphi}$ of ca. 630 mV could be estimated from Eqs. (16) and (17) (drift-diffusion model) [271].

It is particularly interesting to test whether an analysis of a conventional macroscopic impedance measurement based on a brick layer model leads to the same results as obtained with microcontacts. The relaxation frequency of the grain boundary arc measured in the conventional impedance experiment (1.2 Hz) is similar to the mean value (3.0 Hz) deduced from the microelectrode experiments, although not identical. One possible reason for the moderate discrepancy is the inaccuracy with respect to the temperature measurement, which is somewhat difficult in the case of the microelectrode set-up. A temperature error of about 20 K could already explain the difference.

For several grain boundaries, the visible length was determined under the microscope and an apparent grain boundary width was deduced according to Eq. (44) [271]. The resulting distribution of the apparent grain boundary widths (Fig. 38d) is rather broad, which is, at least partly, a consequence of the considerable uncertainty in estimating the grain boundary area from the visible grain boundary length. According to the brick layer model, the grain boundary thickness can also be calculated from a conventional impedance experiment via Eq. (26). An effective grain boundary thickness of about 33 nm was deduced from the conventional measurement of the polycrystalline sample and indicated in Fig. 38d. Obviously, the macroscopically obtained value is at the lower end of the distribution. This might be connected with several shortcomings, such as the uncertainty in calculating the grain boundary area, or uncertainties with respect to the correction factor h_C in Eq. (44). However, despite these deviations the agreement of the ρ_{gb}- and w_{gb}-values obtained from microscopic and macroscopic measurements is sufficiently close to conclude that a brick layer analysis of conventional impedance measurements on Fe-doped $SrTiO_3$ leads to reasonable estimates of the grain boundary properties.

6.3.3 Voltage-dependent Measurements and Mechanistic Considerations

Additional information with respect to the mechanism of the grain boundary resistance can be obtained from temperature- and voltage-dependent impedance measurements. The grain boundary semicircle varies, for example, considerably with the applied dc bias (Fig. 39a). The current-voltage relations calculated from such bias-dependent impedance measurements are thus non-linear. In the logarithmic plot (Fig. 39b) it can be seen that the low bias regime exhibits a non-linearity factor α $(= d\log(I/A)/d\log(U/V))$ of almost one (ohmic behavior), while at a bias value of about 0.35 V this factor changes to $\alpha \approx 2$.

From conventional (macroscopic) impedance and time-dependent polarization measurements on acceptor-doped $SrTiO_3$ polycrystals [246, 247, 340, 341] it has already been concluded that the enhanced grain boundary resistivity is caused by space charge layers (double Schottky barriers, cf. Sec. 2.3): A positive core charge is compensated by the negative charge of the ionized dopant ions in the adjacent space charge layers while all positive mobile charge carriers (holes, vacancies) are depleted in this space charge region. This yields concentration profiles as sketched in 4c. (It

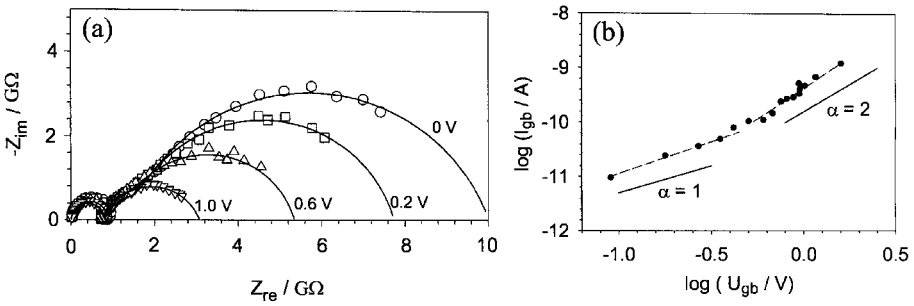

Fig. 39. (a) Influence of a dc voltage on microcontact impedance measurements on $SrTiO_3$ at 585 K. The voltage values given indicate the total voltage U_{bias} rather than the voltage drop across the grain boundaries U_{gb}; (b) log-log plot of the current-voltage characteristics of a microcontact measurement across a grain boundary.

should be remembered that although the vacancy concentration exceeds the hole concentration in the bulk, the higher mobility of the holes leads to predominant hole conduction in the temperature range considered here.) The theoretical current-voltage (I-V) characteristics of such double Schottky barriers are often rather complex (cf. Sec. 2.3) The experimentally obtained transition from an ohmic to a superohmic regime at relatively low voltages is in agreement with the I-V curves which can be expected for double Schottky barriers with few available interface states around the Fermi level [344]. Hence the measurements support the interpretation in terms of space charge layers.

The equilibrium thickness w_{gb} of a space charge layer depends on the space charge potential (cf. Eq. (18)). Using an equation which takes into account that the dopant Fe can trap holes ($Fe'_{Ti} + h^{\bullet} \leftrightarrows Fe^{x}_{Ti}$), a theoretical thickness of 40 nm can be calculated for $\Delta\varphi \approx 630$ mV [271]. The mean grain boundary thickness ($\approx 60 \ldots 70$ nm) deduced from Fig. 38d is somewhat larger, but regarding the uncertainties that influence the calculation of the w-histogram, the agreement is reasonable and the results are again consistent. It has also been shown in Ref. [271] that the temperature dependence of the resistance, as well as the temperature and voltage dependence of the capacitance, can also be understood in terms of the space charge model. Hence, all experimental results are in accordance with the model that space charge depletion layers at the grain boundaries of $SrTiO_3$ cause the grain boundary resistance and capacitance. In summary, the microelectrode measurements completed the knowledge of grain boundaries in Fe-doped $SrTiO_3$ and proved that a conventional analysis of macroscopic experiments is reasonable in this case.

6.4 Highly Conductive Grain Boundaries in AgCl

6.4.1 Definition of the Problem and Experimental Details

Solely from a conventionally measured impedance spectrum it is neither possible to draw conclusions on the existence of short-circuiting paths, nor to determine grain

boundary or bulk properties of samples with highly conductive grain boundaries (Sec. 3.2). In this section it is exemplarily shown on an AgCl polycrystal that microelectrodes can be used to quantitatively investigate highly conductive grain boundaries. The silver-ion conductor AgCl has been chosen, since earlier studies gave evidence for enhanced ionic interface conductivity in AgCl, either because of heterogeneous doping with an insulating oxide [125], or surface-gas interaction [319, 345]. Moreover, experiments are reported that point to the existence of highly conductive grain boundaries in AgCl polycrystals [124].

Silver microelectrodes on AgCl are established by carefully pressing a silver-coated tungsten needle onto the sample. Several imprints were analyzed with AFM demonstrating the quality of the contacts (Fig. 26). The width of the imprint was usually measured with an optical microscope after removing the needle (error less than 20%). In the experiments presented here, imprints with a diameter of ≈ 5 μm are used. The impedance was measured between a microelectrode on top of the sample and the extended counter-electrode (sputtered Ag) on the bottom. By repeating the contact procedure several times, a conductivity map of a polycrystal was obtained. Although the Ag electrodes were almost reversible, impedance spectroscopy rather than dc techniques was used in order to avoid time-dependent morphological changes of the electrodes, which arise in dc measurements. It has been proven on AgCl single crystals that microelectrodes yield conductivity values in accordance with the spreading resistance formula (Eq. (34)) if the sample has been etched for several minutes in $Na_2S_2O_3$ solution to remove surface layers of enhanced conductivity [264].

6.4.2 Determination of the Bulk Conductivity and the Grain Boundary Conductance

An image of a region of the AgCl surface under investigation is shown in Fig. 40. The points indicate some locations at which the impedance was measured. Two kinds of impedance spectra have been observed (Fig. 41): large semicircles for most microcontacts located on grains, and (usually) smaller semicircles for microelectrodes on grain boundaries. Corresponding inverse resistances are given in Fig. 40. It has been demonstrated in Sec. 4.3 that measurements with microelectrodes on grains can be used to determine the bulk conductivity of the grains. The values obtained for σ_{bulk} from Eq. (34) (about $5\text{–}10 \cdot 10^{-9}\ \Omega^{-1}\text{cm}^{-1}$) are similar to the conductivity known from nominally pure AgCl single crystals [102]. Conversely, the inverse resistances measured on grain boundaries R^{-1}_{ongb} (Fig. 40, bottom numbers) were up to 10 times higher than the values associated with the bulk of the grains. Hence, it can be deduced that an enhanced conductivity along grain boundaries exists in AgCl. Apparent grain resistances R_{ongrain}, which are found to be considerably smaller than the expected bulk resistance (cf. Fig. 40), are possibly connected with (hidden) grain boundaries in close proximity to the electrode.

The numerical results of Fig. 20 allow an estimate of the local grain boundary conductance at room temperature from the measured inverse resistance ratio $(R^{-1}_{\text{ongb}}/R^{-1}_{\text{ongrain}})$. For such an estimate an inverse resistance of $8 \cdot 10^{-12}\ 1/\Omega$ for the grains and of $50 \cdot 10^{-12}\ 1/\Omega$ for grain boundaries, a grain size of about 25 μm, and a

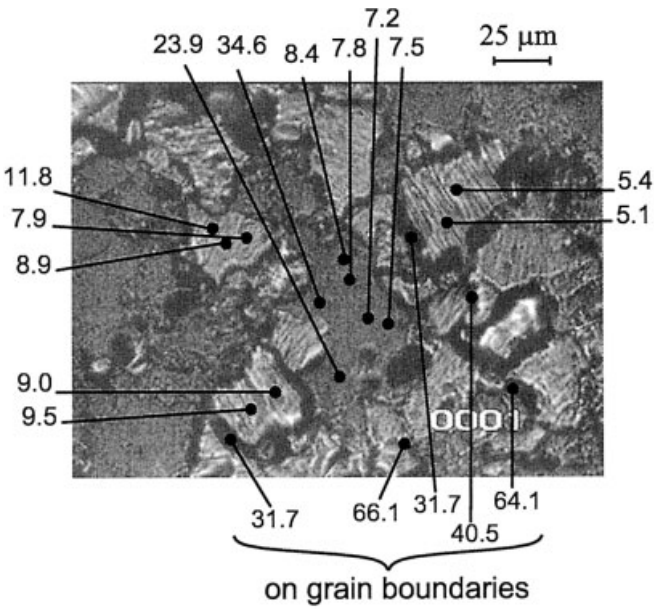

Fig. 40. Micrograph of a polycrystalline AgCl sample. Some points are indicated at which microelectrode measurements were performed at room temperature. The numbers show the measured inverse resistances in $10^{-12}\ \Omega^{-1}$.

contact diameter of 5 µm have been used. This yields a grain boundary conductance of $\tilde{Y}_{gb} = 4 \cdot 10^{-11}\ \Omega^{-1}$. The calculated value is relatively independent of the grain size chosen in this analysis: $\tilde{Y}_{gb}$ changes by less than 30% if grain sizes of 10 µm or 125 µm instead of 25 µm are assumed. That different grain sizes are involved in the measurement is therefore of minor importance.

It is worth comparing these locally obtained values with the effective conductivity σ_{eff} of the same sample measured in a conventional setup. A measurement with macrosopic electrodes yields one semicircle in the complex impedance plane and an effective conductivity of $42 \cdot 10^{-9}\ \Omega^{-1}\ cm^{-1}$. According to the brick layer model for

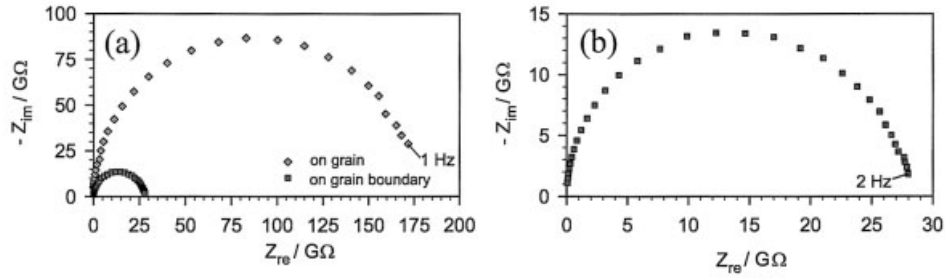

Fig. 41. (a) Measured impedance spectra with microelectrodes in a grain, and on a grain boundary of an AgCl polycrystal at room temperature, and (b) magnification of the spectrum measured on a grain boundary.

highly conductive grain boundaries, the effective conductivity is given by Eq. (30) and for a known bulk conductivity again a grain boundary conductance can be evaluated. However, in contrast to the microelectrode experiments, the bulk conductivity cannot be determined from a conventional measurement on an AgCl polycrystal. Hence σ_{bulk} gained from the microelectrode measurements has been used and a grain boundary conductance value of $\tilde{Y}_{\text{gb}} = 4.3 \cdot 10^{-11}\ \Omega^{-1}$ results. There is obviously a fairly good agreement between the locally determined grain boundary conductance and the value obtained from the conventional measurement. This similarity is a strong indication that highly conductive paths really percolate in the sample and that the measured R_{ongb}-values are mainly determined by the grain boundary under investigation (cf. Sec. 4.3). The only moderate variation of R_{ongb} therefore also points towards similar properties of all grain boundaries in the sample.

6.4.3 Mechanistic Interpretation of the Grain Boundary Conductance in AgCl

At room temperature the bulk properties of AgCl are determined by extrinsic divalent cations, and silver vacancies are the relevant mobile charge carriers in the bulk. It is known that space charges at interfaces play a significant role in AgCl: heterogeneous doping of an AgCl polycrystal with alumina increases the overall conductivity considerably, which can be explained by space charge layers at the $AgCl/Al_2O_3$ interface [125]. The highly conductive grain boundaries in extrinsic AgCl can be interpreted in a similar way: owing to the different chemical potentials of Ag^+ ions in the core of the boundary and in the grain bulk, a space charge is built-up leading to an accumulation of Ag^+ in the core and an enhanced silver vacancy concentration in the adjacent space charge layers (Fig. 4b).

In the case of a space charge, the grain boundary conductivity is not homogeneous and an excess grain boundary conductance $\Delta\tilde{Y}_{\text{gb}}$ of a single grain boundary in an infinitely extended crystal is defined more generally as the integral over the spatially varying excess conductivity:

$$\Delta\tilde{Y}_{\text{gb}} = \int_{-\infty}^{+\infty} (\sigma(x) - \sigma_{\text{bulk}})dx \approx \tilde{Y}_{\text{gb}}. \tag{50}$$

Eq. (19) gives a solution of this integral, and hence the grain boundary conductance for enhanced silver vacancy concentration reads

$$\tilde{Y}_{\text{gb}} \approx \sigma_{\text{bulk}} \exp(e\Delta\varphi/2kT)\sqrt{\varepsilon_{\text{sc}} kT/2e^2 c_{V,\text{bulk}}}, \tag{51}$$

with $c_{V,\text{bulk}}$ denoting the bulk concentration of silver vacancies.

While $\tilde{Y}_{\text{gb}}$ and σ_{bulk} are deduced from the measurements, we still need the bulk concentration of vacancies to calculate the space charge potential according to Eq. (52). Using the room-temperature mobility of vacancies obtained from literature data [102], and ε_{sc} as the bulk permittivity of AgCl, a bulk vacany concentration of $5.8 \cdot 10^{15}\ \text{cm}^{-3}$ can be evaluated from the measured bulk conductivity. This value is used to determine an effective space charge potential of about 300 mV and a grain

boundary width (4 Debye lengths [124]) of ≈150 nm. This space charge potential corresponds to a surface charge in the core of the grain boundary of $3 \cdot 10^{13} e$ cm^{-2}. Taking into account that the density of Ag^+ surface sites of a (100) surface is $6 \cdot 10^{14}$ cm^{-2}, this value can be regarded as physically reasonable and the enhanced grain boundary conductivity measured by microelectrodes can therefore consistently be explained by space charge layers at grain boundaries, although other interpretations cannot be excluded.

6.5 Investigation of the Oxygen Reduction Reaction on $LaMnO_3$ Microelectrodes

6.5.1 Definition of the Problem and Experimental Details

Most investigations of electrochemical electrode reactions involving gaseous species are performed on porous electrodes and thus have to tackle the problem of ill-defined electrode geometries. Quantitative relations between measurement parameters (e.g. electrode resistance) and geometrical parameters (e.g. contact area, three-phase boundary length) are difficult to obtain. In this section the advantages and possibilities of electrode kinetic studies by means of well-defined microelectrodes are exemplarily demonstrated for the case of the oxygen reduction reaction

$$\tfrac{1}{2}O_2(\text{gas}) + 2e^-(\text{cathode}) \rightleftharpoons O^{2-}(\text{electrolyte}) \tag{52}$$

taking place at electronically highly conductive Sr-doped $LaMnO_3$ (LSM) cathodes on Y-stabilized ZrO_2 (YSZ) solid electrolytes.

Doped $LaMnO_3$ electrodes were investigated, since they are the state-of-the-art cathodes in solid oxide fuel cells (SOFCs). However, the overpotentials due to the oxygen reduction reaction at such electrodes strongly influence the efficiency of the entire fuel cell. The mechanisms leading to the polarization of the LSM cathodes have been studied extensively in the past [145–169, 194] and the basic models to understand the kinetics of the underlying reaction have already been outlined in Sec. 2.4: the oxide-ion incorporation into the electrolyte can take place via a surface path or via a bulk path (Fig. 5), and in both cases different reaction steps can be rate-limiting. It is frequently assumed that the surface path is predominant with respect to the reaction rate on LSM cathodes, but particularly in thin electrodes and under strong cathodic bias also the bulk path has been seen to play an important role [148, 150, 155, 156, 165]. Hence, a final conclusion concerning the mechanisms has not yet been reached, and further insight could be expected from microelectrode experiments.

Pulsed Laser Deposition (PLD) was used to grow thin films of A-site deficient LSM ($(La_{0.8}Sr_{0.2})_{0.92}MnO_3$) on 9.5 mole % Y_2O_3-doped ZrO_2 (YSZ) single crystals. Investigations by different experimental techniques (SEM, AFM, SIMS, X-ray) proved the films to be dense and of the same composition as the ablation target. Circular microelectrodes with diameters ranging from ca. 20 μm to 200 μm and nominal thicknesses of 100...800 nm were patterned into the films by using photo-

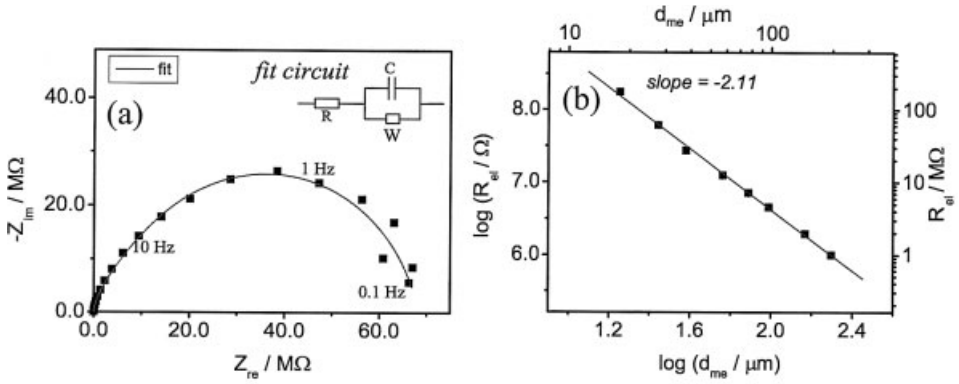

Fig. 42. (a) Impedance spectrum obtained on a 30 µm LSM microelectrode at a temperature of approx. 800 °C. The inset shows the equivalent circuit used to fit the data. (b) Electrode resistance R_{el} as a function of the microelectrode diameter at a temperature of approx. 800 °C. The solid line is a linear regression of the resistance data and shows the proportionality of R_{el} to the inverse of the square of the microelectrode diameter.

lithographic techniques and ion-beam etching. The circular microelectrodes were contacted with tungsten carbide tips and bias-dependent impedance spectra and I-V characteristics were measured between a microelectrode and an extended Pt counter-electrode on the back of the sample (Fig. 25a). More details on the fabrication of LSM microelectrodes, the microcontact impedance set-up, and the electrical measurements are given in Refs. [160, 346].

6.5.2 The Geometry Dependence of the Impedance Data

A typical impedance spectrum obtained on LSM microelectrodes is shown in Fig. 42a. The arc represents the impedance due to the electrochemical reaction at the LSM microelectrode. A small ohmic drop caused by the YSZ electrolyte (and partly by the sheet resistance due to the finite electronic conductivity of the LSM electrode) is more than three orders of magnitude smaller than the electrode resistance and not visible in the figure. The impedance spectra for nominally identical microelectrodes turned out to be reproducible with a standard deviation $<15\%$. The data of Fig. 42b display the relation between the electrode resistance R_{el} and the microelectrode diameter d_{me}: several series of experiments with different electrode thicknesses consistently revealed that the resistance R_{el} is approximately proportional to d_{me}^{-2}, and hence to the inverse electrode area.

From this observation it can be concluded that the rate-determining process directly involves the electrode area, i.e. occurs i) at the surface of the LSM; ii) in the bulk of the thin LSM electrodes; or iii) at the LSM/YSZ interface. From thickness-dependent measurements further information with respect to the rate-determining step could be expected, since a predominant bulk path with transport of oxide ions through LSM being rate-limiting should yield $R_{el} \propto t_{me}$ (t_{me} = microelectrode thickness). Hence, a sample with 60 µm microelectrodes of two different thicknesses

(100 nm and 250 nm) was examined. The data extracted from measurements on 60 microelectrodes showed that the electrode polarization resistance R_{el} scales almost linearly with the thickness [161]. This is a strong indication in favor of a bulk path determining the oxygen reduction rate with transport of oxide ions in LSM being the rate-determining step. For such a case an equivalent circuit can theoretically be deduced [206, 207], consisting of a parallel connection of the interfacial capacitance of the LSM/YSZ interface C and a finite Warburg impedance W, the impedance of which is given by

$$Z_W = R_{el}\frac{\tanh((T_W i\omega)^{1/2})}{(T_W i\omega)^{1/2}} \tag{53}$$

(Fig. 42a). In Eq. (53) R_{el} is the ionic (transport) resistance of the LSM electrode

$$R_{el} = \frac{t_{me}}{\sigma_{ion} A_{me}}, \tag{54}$$

with A_{me}, and σ_{ion} being the area and ionic conductivity of the microelectrode, whereas T_W depends on the chemical diffusion coefficient of oxygen $\tilde{D}$ and reads

$$T_W = \frac{t_{me}^2}{\tilde{D}}. \tag{55}$$

(In the fits, a free parameter β instead of $\frac{1}{2}$ has been used in Eq. (53); β-values are between 0.4 and 0.45, and thus are sufficiently close to 0.5 in order to rationalize a quantitative interpretation in terms of Eqs. (54) and (55).)

The fit parameter T_W does not depend on the microelectrode diameter, but rather increases by a factor of 3.5 if the nominal thickness is increased from 100 to 250 nm. These relationships are further indications that the ionic transport in the LSM microelectrodes considerably influences the electrode impedance. However, it is expected that, should polarization be determined solely by the ionic transport in LSM, the fit parameter T_W actually scales with the square of the thickness t_{me} (Eq. (55)) and deviations from this relation are a hint that possibly a further step, for example the oxygen incorporation into LSM or the transfer at the LSM/YSZ interface, also influences the impedance. The considerable and reproducible thickness dependence, on the other hand, suggests that the transport is predominant with respect to the polarization resistance. Hence, the ionic conductivity of LSM at ca. 800 °C (±ca. 50 °C) could at least be estimated from R_{el} and a value of $8 \cdot 10^{-8}$ S cm^{-1} follows, which is in good agreement with previously determined values [117, 150, 155]. Besides the ionic conductivity, a chemical diffusion coefficient $\tilde{D}$ of $3 \cdot 10^{-9}$ cm^2 s^{-1} can be calculated from the T_W-values. This is lower than previously measured diffusivities [347–349], but the large spread in the reported $\tilde{D}$-values, probably caused by varying sample preparations, sample densities and partial pressure regions under investigation, could explain these differences.

The capacitance C turns out to be proportional to the area and almost thickness-independent. The value of ca. 60 μF cm^{-2} is relatively large, but still reasonable for a

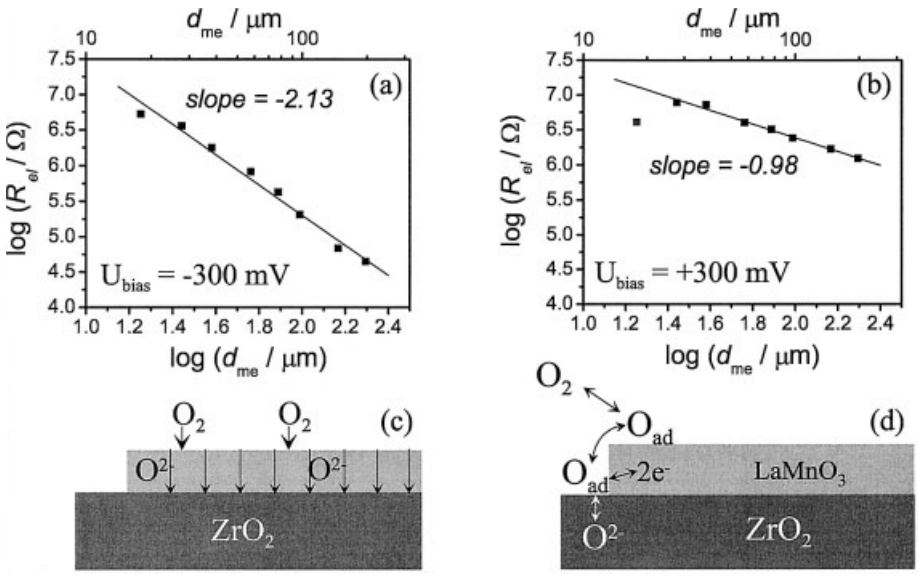

Fig. 43. Double-logarithmic plot of the electrode polarization resistance versus the microelectrode diameter measured with impedance spectroscopy (ca. 800 °C) at (a) a cathodic dc bias of −300 mV, and (b) at an anodic dc bias of +300 mV. In (b) the first data point of the 20-µm microelectrode is not included in the fit. (c) Sketch illustrating the path of the oxygen reduction reaction for cathodic bias. (d) Path of the electrochemical reaction under anodic bias; the rate-determining step occurs close to the three-phase boundary.

double-layer capacitance at the electrode/electrolyte interface, and hence also this parameter is in accordance with the interpretation of the oxygen reduction reaction in terms of a bulk path.

6.5.3 Mechanistic Variations under Bias

Bias-dependent measurements were performed in order to check to what extent the mechanism depends on the electrical operation conditions. Fig. 43 shows double-logarithmic plots of the electrode polarization resistance (determined from the arc in the impedance spectrum) versus the microelectrode diameter observed at a cathodic bias of −300 mV and at an anodic bias of +300 mV respectively. In the cathodic case the electrode polarization resistance again scales with the inverse of the electrode area, whereas in the anodic case it scales with the inverse of the microelectrode diameter. These findings are supported by I-V measurements on LSM microelectrodes with diameters ranging from 30–80 µm: the differential resistance is proportional to the inverse microelectrode area in the cathodic regime and comes close to an inverse linear relationship with the three-phase boundary (3PB) length in the anodic regime [161].

In the particular case considered here, it can therefore be deduced that in the anodic regime the surface path determines the overall current, since all steps of the

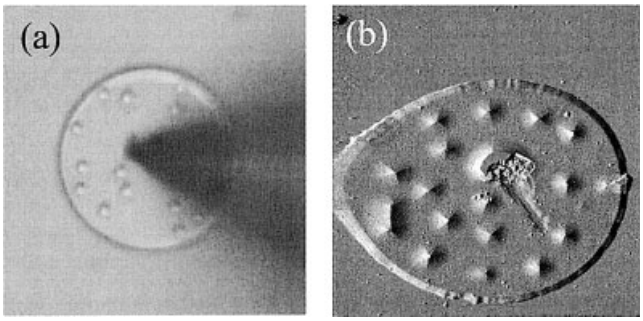

Fig. 44. (a) Optical microscope image of a 60-μm LSM microelectrode after dc polarization with a large anodic bias (0.6 V). (b) A 74 × 74 μm AFM image of a microelectrode after dc polarization with 1.25 V.

bulk path involve the area of the microelectrodes used (Fig. 43). This mechanism change can be understood from the partial pressure dependence of the defect concentrations in ionic solids (Sec. 2.1): according to Nernst's equation, an anodic bias corresponds to an enhancement of the oxygen activity at the YSZ/LSM interface and hence further decreases the already low oxygen vacancy concentration in doped $LaMnO_3$. A strong anodic bias therefore completely blocks the bulk path and only a reaction via the surface path is possible.

This interpretation is also supported by the following observation. At high anodic polarization (>500 mV) "bubbles" spontaneously form on the microelectrode surface. Fig. 44 shows pictures of 60 μm LSM microelectrodes that were subjected to such large anodic bias. Since an anodic bias corresponds to a high oxygen activity at the YSZ/LSM interface, the corresponding high driving force for oxygen excorporation leads to the formation of extrusions. In I-V measurements it is also observed that the anodic current increases by 2 to 3 orders of magnitude upon the formation of such "bubbles".

With respect to the rate-determining step of the surface path, which predominates under large anodic bias, a final conclusion cannot be drawn yet. Ionization and ion transfer as rate-limiting steps, for example, would lead to a resistance proportional to the inverse circumference (3PB length) and hence are in accordance the experimental findings. However, if the surface diffusion of oxygen on LSM is slow and only oxygen species close to the 3PB can contribute to the electrochemical reaction also a combined adsorption/desorption and diffusion limitation can lead to $R_{el}^{-1} \propto$ 3PB length. Therefore, other parameters such as oxygen partial pressure, composition or surface morphology should be varied in order to gain further mechanistic knowledge.

It is important to notice that i) both the bulk path and the surface path run in parallel; and ii) it depends on the geometrical parameters how they are weighted, i.e. how much they contribute to the overall current. Other electrode aspect ratios, for example, can lead to a shift of the voltage at which the mechanism changes from the bulk to the surface path. In the case of the thin, broad microelectrodes considered here, the current via the bulk path is predominant at $U = 0$ and in the cathodic regime. For an increasing three-phase boundary length, the weight of the surface path

increases and in porous cathodes used in fuel cells a situation might result in which the bulk path is relevant only under significant cathodic bias, whereas without bias the surface path is dominating.

7 Summary and Outlook

In most cases, point defects constitute the mobile charge carriers of solid and liquid electrolytes. Several factors make the treatment of ionic solids more complicated, however: electronic charge carriers frequently contribute to charge transport, non-stoichiometry often influences the defect concentrations, and internal interfaces such as grain boundaries or phase boundaries strongly affect the overall ionic and electronic transport properties. Moreover, each ionic solid represents a separate "solvent", whereas liquid electrochemistry predominantly deals with only one solvent, namely water. Because of these intricacies, investigations of transport phenomena in electrolytes are more important in current solid state ionics research than in modern liquid electrochemistry.

Transport studies on ionic solids are further complicated by inhomogeneities: owing to low diffusion coefficients, non-equilibrium states (non-stoichiometry profiles or dopant profiles) can easily occur and hinder accurate determination of the conductivity. Highly resistive grain boundaries are frequently investigated by means of impedance spectroscopy, but spatially varying grain boundary properties may cause quantitative as well as qualitative misinterpretation of impedance data. Highly conductive grain boundaries are even more problematic, since they do not lead to separate dispersion signals in impedance studies, and thus are easily overseen in conventional electrical experiments.

Microelectrodes provides us with a means of tackling such difficulties. For example, they facilitate local conductivity measurements and thus the study of inhomogeneous ceramics, they can be used to quantitatively investigate the electrical properties of highly conductive grain boundaries, and they enable investigations on the distribution of grain boundary properties in polycrystals with highly resistive grain boundaries. Miniaturized working electrodes are also advantageous in electrode kinetic studies as measurements without reference electrodes are possible. Moreover, well-defined microelectrodes allow geometry-dependent electrode polarization experiments on gas electrodes to be made; thus, they exhibit a considerable advantage compared with conventional porous electrodes. However, numerical calculations are often necessary in order to relate measurement data of microelectrode experiments and parameters such as the grain boundary conductance, the conductivity of grains or the effective size of electrochemically active electrode regions.

The applicability of microelectrodes in various fields of solid state ionics has been demonstrated in four examples: i) Local conductivity measurements on $SrTiO_3$ revealed pronounced conductivity profiles after high-field stress and confirmed that non-stoichiometry effects due to blocked ion exchange at the electrodes cause the phenomenon of resistance degradation in perovskite-type electroceramics. ii) Micro-

electrode experiments on polycrystalline Fe-doped $SrTiO_3$ indicated that grain boundary properties only slightly vary in this material, and that a brick layer analysis of conventional impedance measurements therefore leads to reasonable results. iii) Microelectrodes allowed the determination of bulk conductivities and grain boundary conductances of polycrystalline AgCl. The measurements showed that grain boundaries are highly conductive in this ionic conductor. iv) Well-defined $LaMnO_3$ microelectrodes on Y-doped ZrO_2 were used to investigate the mechanism of the electrochemical oxygen reduction reaction in solid-oxide fuel cells. Geometry-dependent measurements showed that – depending on the applied dc voltage – the reaction occurs via a bulk path through $LaMnO_3$, or via a surface path with a rate-determining step at the three-phase boundary.

A few other potential applications provide further evidence for the vast potential of microelectrodes in solid state ionics: the possibility of investigating inhomogeneous bulk conductivities makes microelectrodes very attractive for analyzing, for example, functionally graded materials, interdiffusion and reaction between solids, demixing and other degradation processes in electroceramics. Solid electrolytes with highly conductive interfaces are attractive for applications in electrochemical energy conversion and microcontacts are an ideal tool to characterize such materials. Microelectrodes on adjacent grains of a polycrystal could be used to observe in situ grain boundary aging phenomena, or the effect of chemical diffusion along grain boundaries. The growing interest in composites in order to achieve new or improved materials properties creates a further area of application for microelectrodes: the bulk conductivities of the constituents, as well as the interface conductivities, can be analyzed locally. In summary, one may expect that in the future the use of microelectrodes in solid state electrochemistry will become as common as it is today in liquid electrochemistry.

8 References

1. T. Kudo and K. Fueki, Solid State Ionics, VCH, Weinheim (1990).
2. A. R. West in Solid State Electrochemistry, editor P. G. Bruce, Cambridge University Press, Cambridge, p. 7 (1995).
3. C. Julien and G. A. Nazri, Solid State Batteries: Materials Design and Optimization, Kluwer Academic Publishers, Boston, (1994).
4. P. Hagenmuller and W. Van Gool (editors), Solid Electrolytes, Academic Press, New York (1978).
5. T. Kudo in The CRC Handbook of Solid State Electrochemistry, editors P. J. Gelling and H. J. M. Bouwmeester, CRC Press, Boca Raton, p. 195 (1997).
6. S. Gottesfeld in Advances in Electrochemical Science and Engineering Volume 5, editors R. C. Alkire, H. Gerischer, D. M. Kolb, and C. W. Tobias, Wiley-VCH, Weinheim, p. 195 (1997).
7. A. Hamnett, Phil. Trans. R. Soc. Lond A 354, 1653 (1996).
8. A. Appleby, Phil. Trans. R. Soc. Lond A 354, 1681 (1996).
9. A. K. Kordesch and G. Simader, Fuel Cells and Their Applications, VCH, Weinheim (1996).

10. S. C. Singhal, Solid State Ionics 315, 305 (2000).
11. T. F. Fuller, The Electrochemical Society Interface 6 (3), 26 (1997).
12. L. J. M. J. Blomen (editor) Fuel cell systems, Plenum Press, New York (1993).
13. http://216.51.18.233/index_e.html
14. P. Fabry and E. Siebert in The CRC Handbook of Solid State Electrochemistry, editors P. J. Gelling and H. J. M. Bouwmeester, CRC Press, Boca Raton, p. 329 (1997).
15. G. Vandrish, Key Eng. Mat. 122–124, 185 (1996).
16. H.-D. Wiemhöfer and K. Cammann in Sensors: A Comprehensive Survey Volume 2 editors W. Göpel, H. Hesse and J. N. Zemel, VCH, Weinheim, 159 (1991).
17. W. Göpel and H.-D. Wiemhöfer, Sensors and Actuators B 4, 365 (1991).
18. N. Yamazoe and N. Miura, J. Electroceramics 2, 243 (1998).
19. J. Janata, Principles of Chemical Sensors, Plenum Press, New York, Ch. 4. (1989).
20. W. Göpel and K.-D. Schierbaum, Sensors and Actuators B 26–27, 1 (1995).
21. B. Scrosati in Modern Batteries, 2nd edition, editors C. A. Vincent and B. Scrosati, Arnold, London, p. 198 (1997).
22. A. D. Robertson, A. R. West, and A. G. Ritchie, Solid State Ionics 104, 1 (1997).
23. P. Bruce, Phil. Trans. R. Soc. Lond A 354, 1577 (1996).
24. M. Wakihara and O. Yamamoto (editors), Lithium Ion Batteries: Fundamentals and Performance, Wiley-VCH, Weinheim (1998).
25. R. J. Brodd, The Electrochemical Society Interface 8 (3), 20 (1999).
26. C. Julien in The CRC Handbook of Solid State Electrochemistry, editors P. J. Gelling and H. J. M. Bouwmeester, CRC Press, Boca Raton, p. 371 (1997).
27. P. G. Bruce (editor), Solid State Electrochemistry, Cambridge University Press, Cambridge (1995).
28. P. J. Gelling and H. J. M. Bouwmeester (editors), The CRC Handbook of Solid State Electrochemistry, CRC Press, Boca Raton, (1997).
29. C. Deportes, M. Duclot, P. Fabry, J. Fouletier, A. Hammou, M. Kleitz, E. Siebert, and J.-L. Souquet, Electrochimie des Solides, Presses Universitaires de Grenoble (1994).
30. H. Rickert Electrochemistry of Solids, Springer-Verlag, Berlin (1982).
31. K. S. Goto, Solid State Electrochemistry and its Applications to Sensors and Electronic Devices, Mat. Sci. Monographs 45, Elsevier, Amsterdam (1988).
32. Solid State Ionics, Journal by North-Holland, Amsterdam. ▌
33. J. Heinze, Angew. Chem. Int. Ed. Engl. 32, 1268 (1993).
34. A. J. Bard and L. F. Faulkner, Electrochemical Methods, 2nd edition, John Wiley & Sons, New York, p. 216 (2001).
35. A. J. Bard, F. R. F. Fan, J. Kwak, and O. Lev, Anal. Chem. 61, 132 (1989).
36. A. J. Bard in Electroanalytical Chemistry Vol. 18, editor A. J. Bard, Marcel Dekker Inc., New York, 243 (1994).
37. J. H. Pei, M. L. Tercier-Waeber, J. Buffle, G. C. Fiaccabrino, and M. Koudelka-Hep, Anal. Chem. 73, 2273 (2001).
38. P. R. M. Silva, M. A. El Khakani, M. Chaker, A. Dufresne, and F. Courchesne, Sensors and Actuators 76, 250 (2001).
39. H. Frebel, G.-C. Chemnitius, K. Cammann, R. Kakerow, M. Rospert, and W. Mokwa, Sensors and Actuators B 43, 87 (1997).
40. E. Neher, Angew. Chem. Int. Ed. Engl. 104, 824 (1992).
41. W.-R. Schlue, W. Kilb, and D. Günzel, Electrochim. Acta 42, 3197 (1997).
42. E. Klusmann and J. W. Schulze, Electrochim. Acta 42, 3123 (1997).
43. J. W. Schulze and V. Tsakova, Electrochim. Acta 44, 3605 (1999).
44. R. M. Whightman and D. O. Wipf in Electroanalytical Chemistry Vol. 15, editor A. J. Bard, Marcel Dekker Inc., New York, 267 (1989).
45. R. M. Wightman, Science 240, 415 (1988).

46. B. R. Scharifer in Modern Aspects of Electrochemistry, Number 22, editors J. O'M. Bockris, B. E. Conway, and R. E. White, Kluwer Academic/Plenum Press, New York, p. 467 (1992).
47. M. I. Montenegro, M. A. Queiros, J. L. Daschbach (editors), Microelectrodes: Theory and Applications, NATO ASI series, Vol 197, Kluwer Academic Publishers, Dordrecht (1991).
48. F. L. Jones, The Physics of Electrical Contacts, Clarendon Press, Oxford, p. 15 (1957).
49. R. Holm, Electric Contacts Handbook, 3rd edition, Springer-Verlag, Berlin, p. 17 (1958).
50. J. Newman, J. Electrochem. Soc. 113, 501 (1966).
51. J. Fleig, S. Rodewald, and J. Maier, J. Appl. Phys. 87, 2372 (2000).
52. J. Fleig and J. Maier, Phys. Chem. Chem. Phys. 1, 3315 (1999).
53. J. Fleig and J. Maier, J. Electrochem. Soc. 144, L302 (1997).
54. J. Fleig, P. Pham, P. Sztulzaft, and J. Maier, Solid State Ionics 113–115, 739 (1998).
55. J. Maier, Angew. Chem. Int. Ed. Eng. 32, 313 (1993).
56. F. A. Kröger and H. J. Vink in Solid State Physics Volume III, editors F. Seitz, D. Turnbull, Academic Press, New York, p. 307 (1956).
57. F. A. Kröger, Chemistry of Imperfect Crystals, North-Holland, Amsterdam (1964).
58. A. B. Lidiard in Handbuch der Physik, Band XX, editor S. Flügge, Springer-Verlag, Berlin, p. 246 (1957).
59. H. Rickert, Electrochemistry of Solids, Springer-Verlag, Berlin, p. 13 (1982).
60. J. Maier, Festkörper – Fehler und Funktion, B. G. Teubner, Stuttgart, p. 110 (2000).
61. J. Maier, Chem. Eur. J. 7, 4762 (2001).
62. A. D. Franklin in Point Defects in Solids Volume 1, editors J. H. Crawford and L. M. Slifkin, Plenum Press, New York, p.1 (1972).
63. L. Smart and E. Moore, Einführung in die Festkörperchemie, Vieweg, Braunschweig, p. 150 (1997).
64. J. Corish, P. W. M. Jacobs, and S. Radhakrishna in Surface and Defect Properties of Solids Volume 6, The Chemical Society, London, p. 218 (1977).
65. F. Zimmer, P. Ballone, M. Parrinello, and J. Maier, Solid State Ionics 127, 277 (2000).
66. F. Zimmer, P. Ballone, J. Maier, and M. Parrinello, J. Chem. Phys. 112, 6416 (2000).
67. N. Hainovsky and J. Maier, Phys. Rev. B 51, 15789 (1995).
68. R. J. Friauf, J. Phys. Colloq. 41, C6–97 (1980).
69. J. O'M. Bockris and A. K. N. Reddy, Modern Electrochemistry Volume 1: Ionics 2nd edition, Plenum Press, New York, p. 442 (1998).
70. D. R. Lide (editor), The CRC Handbook of Chemistry and Physics 79th edition, CRC Press, Boca Raton, pp. 5–93 (1998).
71. A. J. Bard and L. F. Faulkner, Electrochemical Methods, 2nd edition, John Wiley & Sons, New York, p. 143 (2001).
72. J. S. Newman, Electrochemical Systems, 2nd edition, Prentice Hall, Englewood Cliffs, p. 21 (1991).
73. L. Heyne in Topics of Applied Physics, Volume 21: Solid Electrolytes, editor S. Geller, Springer-Verlag, Berlin, p. 167 (1977).
74. I. Riess in The CRC Handbook of Solid State Electrochemistry, editors P. J. Gelling and H. J. M. Bouwmeester, CRC Press, Boca Raton, p. 223 (1997).
75. J. Maier, Festkörper – Fehler und Funktion, B. G. Teubner, Stuttgart, Ch. 6 and 7 (2000).
76. T. Bieger, J. Maier, and R. Waser, Ber. Bunsenges. Phys. Chem. 97, 1098 (1993).
77. R. Moos and K. H. Härtl, J. Am. Ceram. Soc. 80, 2549 (1997).
78. Y.-M. Chiang, D. Birnie, and W. D. Kingery, Physical Ceramics, John Wiley & Sons, New York, Ch. 2.1 (1997).
79. N. W. Ashcroft and N. D. Mermin, Solid State Physics, Saunders College, Philadelphia, p. 574 (1988).

80. K. Kosuge, Chemistry of Non-Stoichiometric Compounds, Oxford University Press, Oxford, p.104 (1994).
81. H. L. Tuller and A. S. Nowick, J. Electrochem. Soc. 126, 209 (1979).
82. L. Smart and E. Moore, Einführung in die Festkörperchemie, Vieweg, Braunschweig, p. 171 (1997).
83. N.-H. Chan, E. K. Sharma, and D. M. Smyth, J. Am. Ceram. Soc. 64, 556 (1981).
84. N.-H. Chan, R. K. Sharma, and D. M. Smyth, J. Electrochem. Soc. 128, 1762 (1981).
85. J. Mizusaki, H. Koinuma, J. Shimoyama, M. Kawasaki, and K. Fueki, J. Solid State Chem. 88, 443 (1990).
86. J. Maier and W. Göpel, J. Solid State Chem. 72, 293 (1988).
87. H. L. Tuller and A. S. Nowick, J. Electrochem. Soc. 126, 209 (1979).
88. I. Kosacki, T. Suzuki, V. Petrovsky, and H. U. Anderson, Solid State Ionics 136–137, 1225 (2000).
89. J. Schoonman in The CRC Handbook of Solid State Electrochemistry, editors P. J. Gelling and H. J. M. Bouwmeester, CRC Press, Boca Raton, p. 161 (1997).
90. Y.-M. Chiang, D. Birnie, and W. D. Kingery, Physical Ceramics, John Wiley & Sons, New York, Ch. 2.2 (1997).
91. J.-H. Park and B. N. Blumenthal, J. Electrochem. Soc. 136, 2867 (1989).
92. W. Weppner, J. Solid State Chem. 20, 305 (1977).
93. I. Yasuda and M. Hishinuma, Solid State Ionics 80, 141 (1995).
94. J. Mizusaki, S. Yamauchi, K. Fueki, and A. Ishikawa, Solid State Ionics 12, 119 (1984).
95. H. Schmalzried, Chemical Kinetics of Solids, VCH, Weinheim, p. 79 (1995)
96. G.-M Choi and H. L. Tuller, J. Am. Ceram. Soc. 71, 201 (1988).
97. S. Lübke and H.-D. Wiemhöfer, Ber. Bunsenges. Phys. Chem. 102, 642 (1998).
98. H. L. Tuller and A. S. Nowick, J. Electrochem. Soc. 122, 255 (1975).
99. H.-I. Yoo and C.-R. Sang, Solid State Ionics 135, 619 (2000).
100. J. O'M. Bockris and A. K. N. Reddy, Modern Electrochemistry Volume 1: Ionics 2nd edition, Plenum Press, New York, p. 4 (1998).
101. H. C. Abbink and D. S. Martin, J. Phys. Chem. Solids 27, 205 (1966).
102. J. Corish and D. C. A. Mulcahy, J. Phys. C: Solid St. Phys. 13, 6459 (1980).
103. K. Huang, M. Feng, and J. B. Goodenough, J. Am. Ceram. Soc. 81, 357 (1998).
104. K. Huang, R. S. Tichy, and J. B. Goodenough, J. Am. Ceram. Soc. 81, 2565 (1998).
105. A. Nakamura and J. B. Wagner, J. Electrochem. Soc. 133, 1542 (1986).
106. M. J. Verkerk, B. J. Middelhuis, and A. J. Burggraaf, Solid Sate Ionics 6, 159 (1982).
107. S. P. S. Badwal, Solid State Ionics 52, 23 (1992).
108. Y.-M. Chiang, D. Birnie, and W. D. Kingery, Physical Ceramics, John Wiley & Sons, New York, p. 176 (1997).
109. M. G. Norton and C. B. Carter in Materials Interfaces, editor D. Wolf and S. Yip, Chapman & Hall, London, p. 151 (1992).
110. J. Jamnik, J. Maier, and S. Pejovnik, Solid State Ionics 75, 51 (1995).
111. N. M. Beekmans and L. Heyne, Electrochim. Acta 21, 303 (1976).
112. M. Gödickemeier, B. Michel, A. Orliukas, P. Bohac, K. Sasaki, L. Gauckler, H. Heinrich, P. Schwander, G. Kostorz, H. Hofmann, and O. Frei, J. Mater. Res. 9, 1228 (1994).
113. S. P. S. Badwal and S. Rajendran, Solid State Ionics 70–71, 83 (1994).
114. R. Gerhardt and A. S. Nowick, J. Am. Ceram. Soc. 69, 641 (1986).
115. E. G. Moya in Science of Ceramic Interfaces II, editor J. Nowotny, Elsevier Science, Amsterdam, p. 277 (1994).
116. U. Brossmann, R. Würschum, U. Södervall, and H.-E. Schaefer, J. Appl. Phys. 85, 7646 (1999).
117. R. A. De Souza and J. A. Kilner, Solid State Ionics 106, 175 (1998).
118. H. K. Henisch, Semiconductor Contacts, Clarendon Press, Oxford, p. 42, (1984).

119. S. M. Sze, Physics of Semiconductor Devices, 2nd edition, John Wiley & Sons, New York, Ch. 5 (1981).
120. F. Greuter and G. Blatter, Semicond. Sci. Tech. 5, 111 (1990).
121. G. E. Pike, Phys. Rev. B 30, 795 (1984).
122. G. Blatter and F. Greuter, Phys. Rev. B 33, 3952 (1986).
123. G. E. Pike and C. H. Seager, J. Appl. Phys. 50, 3414 (1979).
124. J. Maier, Ber. Bunsenges. Phys. Chem. 90, 26 (1986).
125. J. Maier, Prog. Solid St. Chem. 23, 171 (1995).
126. J. Maier, J. Electrochem. Soc. 134, 1524 (1987).
127. T. Jow and J. B. Wagner, J. Electrochem. Soc. 126, 1963 (1979).
128. Y.-M. Chiang, D. Birnie, and W. D. Kingery, Physical Ceramics, John Wiley & Sons, New York, p. 159 (1997).
129. D. O. Raleigh in Electroanalytical Chemistry Vol. 6, editor A. Bard, Marcel Dekker Inc., New York, p. 87 (1973).
130. R. D. Armstrong and R. Mason, Electroanal. Chem. and Interfacial Electrochem. 41, 231 (1973).
131. I. D. Remez and V. N. Chebotin, Electrochim. Acta 29, 1389 (1984).
132. D. O. Raleigh and H. R. Crowe, J. Electrochem. Soc. 118, 79 (1971).
133. J. Zhao and R. P. Buck, J. Electrochem. Soc. 136, 3342 (1989).
134. R. D. Armstrong, T. Dickonson, and P. M. Willis, Electroanal. Chem. and Interfacial Electrochem. 57, 231 (1974).
135. R. D. Armstrong, T. Dickinson, H. R. Thirsk, and R. Whitfield, J. Electroanal. Chem. 29, 301 (1971).
136. M. F. Bell and U. v. Alpen, J. Electroanal. Chem. 129, 315 (1981).
137. C. Bazan and L. E. Fasano, Electrochim. Acta 34, 309 (1989).
138. J. C. Bazan, J. A. Harrison, G. Staikov, E. Schmidt, K. Jüttner, and W. J. Lorenz, Electrochim. Acta 34, 1271 (1989).
139. H. Schmalzried and C. Wagner, Trans. AIME 227, 539 (1963).
140. J. Vedel in Electrode Processes in Solid State Ionics, editors M. Kleitz and J. Dupuy, D. Reidel Publishing Company, Dordrecht, p. 223 (1976).
141. J. Corish and C. D. O'Briain, J. Crystal Growth 13/14, 62 (1972).
142. S. Villain, J. Cabane, D. Roux, L. Roussel and P. Knauth, Solid State Ionics 76, 229 (1995).
143. J. Janek, Solid State Ionics 101–103, 721 (1997).
144. J. Janek and S. Majoni, Ber. Bunsenges. Phys. Chem. 99, 14 (1997).
145. J. Mizusaki, H. Tagawa, K. Tsuneyoshi, and A. Sawata, J. Electrochem. Soc. 138, 1867 (1991).
146. J. Van Herle, A. J. McEvoy and K. R. Thampi, Electrochim. Acta 41, 1447 (1996).
147. A. Mitterdorfer and L. J. Gauckler, Solid State Ionics 111, 185 (1998).
148. E. Siebert, A. Hammouche and M. Kleitz, Electrochim. Acta 40, 1741 (1995).
149. M. J. L. Ostergard and M. Mogensen, Electrochim. Acta 38, 2015 (1993).
150. J. Mizusaki, T. Saito and H. Tagawa, J. Electrochem. Soc. 143, 3065 (1996).
151. H. Y. Lee, W. S. Cho, S. M. Oh, H.-D. Wiemhöfer, and W. Göpel, J. Electrochem. Soc. 142, 2659 (1995).
152. H. Fukunaga, M. Ihara, K. Sakaki, and K. Yamada, Solid State Ionics 86–88, 1179 (1996).
153. H. Kamata, A. Hosaka, J. Mizusaki and H. Tagawa, Solid State Ionics 106, 237 (1998).
154. A. Hammouche, E. Siebert, A. Hammou, M. Kleitz, and A. Caneiro, J. Electrochem. Soc. 138, 1212 (1991).
155. A. Endo, M. Ihara, H. Komiyama and K. Yamada, Solid State Ionics 86–88, 1191 (1996).
156. M. Odgaard and E. Skou, Solid State Ionics 86–88, 1217 (1996).

157. F. P. F. Berkel, F. H. van Heuveln, and J. P. P. Huijsmans, Solid State Ionics 72, 240 (1994).
158. B. C. H. Steele, Solid State Ionics 86–88, 1223 (1996).
159. K. Sasaki, J.-P. Wurth, R. Gschwend, M. Gödickemeier, and L.J. Gauckler, J. Electrochem. Soc. 143, 530 (1996).
160. V. Brichzin, J. Fleig, H.-U. Habermeier, and J. Maier, Electrochem. Solid St. Let. 3, 403 (2000).
161. V. Brichzin, J. Fleig, H.-U. Habermeier, G. Cristiani, and J. Maier, Solid State Ionics, accepted.
162. S. Wang, Y. Jiang, Y. Zhang, J. Yan, and W. Li, J. Electrochem. Soc. 146, 1932 (1998).
163. F. H. van Heuveln, H. J. M. Bouwmeester, and F. P. F. van Berkel, J. Electrochem. Soc. 144, 126 (1997).
164. F. H. van Heuveln and H. J. M. Bouwmeester, J. Electrochem. Soc. 144, 134 (1997).
165. H. Lauret and A. Hammou, J. Europ. Ceram. Soc. 16, 447 (1996).
166. L. G. J. de Haart, R. A. Kuipers, K. J. de Vries, and A. J. Burggraaf, J. Electrochem. Soc. 138, 1970 (1991).
167. Y. Takeda, R. Kanno, N. Noda, Y. Tomida, and O. Yamamoto, J. Electrochem. Soc. 134, 2656 (1987).
168. T. Horita, K. Yamaji, M. Ishikawa, M. Sakai, H. Yokokawa, T. Kawada and T. Kato, J. Electrochem. Soc. 145, 3196 (1998).
169. J. Divisek, L. G. J. de Haardt, P. Holtappels, T. Lennartz, W. Mallener, U. Stimming, and K. Wippermann, J. Power Sources 49 (1994) 257.
170. G. M. Christie, F. H. van Heuveln, and F. P. F. van Berkel, Proc. 17th Riso Int. Symp. on Mat. Sci: High Temperature Electrochemistry: Ceramics and Metals, editors F. W. Poulsen, N. Bonanos, S. Linderoth, M. Mogensen, and B. Zachau-Christiansen, Riso Nat. Lab., Roskilde, Denmark, p. 205 (1996).
171. S. B. Adler, J. A. Lane, and B. C. H. Steele, J. Electrochem. Soc. 143, 3554 (1996).
172. S. B. Adler, Solid State Ionics 111, 125 (1998).
173. M. Liu, Z. Wu, Solid State Ionics 107, 105 (1998).
174. M. J. Verkerk, M. W. J. Hammink, and A. J. Burggraaf, J. Electrochem. Soc. 130, 70 (1983).
175. D. Y. Wang and A. S. Nowick, J. Electrochem. Soc. 126, 1155 (1979).
176. A. J. A. Winnubst, A. H. A. Scharenborg, and A. J. Burggraaf, Solid State Ionics 14, 319 (1984).
177. T. M. Gür, I. D. Raistrick, and R. A. Huggins, J. Electrochem. Soc. 127, 2620 (1980).
178. E. J. L. Schouler and M. Kleitz, J. Electrochem. Soc. 134, 1045 (1987).
179. D. Braunshtein, D. S. Tannhauser, and I. Riess, J. Electrochem. Soc. 128, 82 (1981).
180. J. Mizusaki, K. Amano, S. Yamauchi, and K. Fueki, Solid State Ionics 22, 313 (1987).
181. J. Poppe, A. Schaak, J. Janek, and R. Imbihl, Ber. Bunsenges. Phys. Chem. 102, 1019 (1998).
182. C. Schwandt and W. Weppner, J. Electrochem. Soc. 144, 3728 (1997).
183. B. A. van Hassel, B. A. Boukamp, and A. J. Burggraaf, Solid State Ionics 48, 155 (1991).
184. J. Van Herle and A. J. McEvoy, J. Phys. Chem. Solids 55, 339 (1994).
185. R. Jimenez, T. Kloidt, and M. Kleitz, J. Electrochem. Soc. 144, 582 (1997).
186. M. Kleitz and F. Petitbon, Solid State Ionics 92, 65 (1996).
187. A. M. Svensson, S. Sunde, and K. Nisancioglu, J. Electrochem. Soc. 144, 2719 (1997).
188. A. M. Svensson, S. Sunde, and K. Nisancioglu, J. Electrochem. Soc. 145, 1390 (1998).
189. B. C. H. Steele, Solid State Ionics 134, 3 (2000).
190. T. Kawada and H. Yokokawa, Key. Eng. Mat. 125–126, 187 (1997).
191. T. A. Ramanarayanan and R. A. Rapp, Metall. Trans. 3, 3239 (1972).
192. S. P. S. Badwal, M. Bannister, and M. Murray, J. Electroanal. Chem. 168, 363 (1984).
193. F. K. Moghadam and D. A. Stevenson, J. Electrochem. Soc. 133, 1329 (1986).

194. M. J. Jorgensen and M. Mogensen, J. Electrochem. Soc. 148, A433 (2001).
195. M. J. Jorgensen, S. Primdahl, and M. Mogensen, Electrochim. Acta 44, 4195 (1999).
196. M. J. Jorgensen, P. Holtappels, and C. C. Appel, J. Appl. Electrochem. 30, 411 (2000).
197. J. E. Bauerle, J. Phys. Chem. Solids, 30, 2657 (1969).
198. J. R. Macdonald (editor), Impedance Spectroscopy emphasizing solid materials and systems, John Wiley & Sons, New York (1987).
199. A. J. Bard and L. F. Faulkner, Electrochemical Methods, 2nd edition, John Wiley & Sons, New York, p. 368 (2001).
200. A. Lasia in Modern Aspects of Electrochemistry, Number 32, editors B. E. Conway, J O'M. Bockris and R. E. White, Kluwer Academic / Plenum Press, New York, p. 143 (1999).
201. L. M. Peter and D. Vanmaekelbergh in Advances in Electrochemical Science and Engineering, Volume 6, editors R. C. Alkire and D. M. Kolb, Wiley-VCH, Weinheim, p. 77 (1999).
202. N. Bonanos, B. C. H. Steele and E. P. Butler in Impedance Spectroscopy, editor J. R. Macdonald, John Wiley and Sons, New York, p. 191 (1987).
203. J. Fleig and J. Maier, J. Am. Ceram. Soc. 82, 3485 (1999).
204. J. Jamnik, S. Pejovnik, and J. Maier, Electrochim. Acta 38, 1975 (1993).
205. C. Deportes, M. Duclot, P. Fabry, J. Fouletier, A. Hammou, M. Kleitz, E. Siebert, and J.-L. Souquet, Electrochimie des Solides, Presses Universitaires de Grenoble, p. 271 (1994).
206. J. Jamnik, J. Maier, and S. Pejovnik, Electrochim. Acta 44, 4139 (1999).
207. J. Jamnik and J. Maier, Phys. Chem. Chem. Phys. 3, 1668 (2001).
208. E. J. L. Schouler, N. Mesbahi, and G. Vitter, Solid State Ionics 9–10, 989 (1983).
209. S. S. Liou and W. L. Worrell, Appl. Phys. A 49, 25 (1989).
210. R. K. Slotwinski, N. Bonanos, and E. P. Butler, J. Mat. Sci. Let. 4, 641 (1985).
211. J. Fleig and J. Maier, J. Electroceramics 1, 73 (1997).
212. J. Fleig, Ceram. Trans. 109, 31 (2000).
213. J. Fleig, P. Pham, P. Sztulzaft, and J. Maier, Solid State Ionics 113–115, 739 (1998).
214. J. Fleig, Solid State Ionics 131, 117 (2000).
215. B. A. Boukamp, Solid State Ionics 20, 31 (1986).
216. J. Fleig and J. Maier, Electrochim. Acta 41, 1003 (1996).
217. A. K. Jonscher, Universal relaxation law, Chelsea Dielectrics Press, London (1996).
218. K. Funke, Prog. Solid St. Chem. 22, 111 (1993).
219. K. Funke, Defect and Diffusion Forum 143–147, 1243 (1997).
220. A. K. Jonscher, Nature 267, 673 (1977).
221. G. Hsieh, S. J. Ford, T. O. Mason, and L. R. Pederson, Solid State Ionics 100, 297 (1997).
222. H. Schmalzried, W. Laqua, and P. I. Lin, Z. Naturforsch. 34A, 192 (1979).
223. O. Teller and M. Martin, Solid State Ionics 101, 475 (1997).
224. D. Monceau, M. Filal, B. Tebtoub, C. Petot, and G. Petot-Ervas, Solid State Ionics 73, 221 (1994).
225. I. Birkby and R. Stevens, Key. Eng. Mat. 122–124, 527 (1996).
226. K. Kobayashi, H. Kuwajima, and T. Masaki, Solid State Ionics 3–4, 489 (1981).
227. F. F. Lange, G. L. Dunlop, and B. I. Davis, J. Am. Ceram. Soc. 69, 237 (1986).
228. K. Komeya and M. Matsui in Materials Science and Technology Vol. 11: Structure and Properties of Ceramics, editor M. Swain, VCH, Weinheim, p. 518 (1994).
229. A. J. Moulson and J. M. Herbert, Electroceramics, Chapman & Hall, London, p. 128 (1990).
230. R. W. Vest, Am. Ceram. Soc. Bull. 65, 631–636 (1986).
231. C. C. Liang, J. Electrochem. Soc. 120, 1289 (1973).
232. K. Shahi and J. B. Wagner, J. Solid St. Chem. 42, 107 (1982).
233. J. S. Lee, S. Adams, and J. Maier, J. Electrochem. Soc. 147, 2407 (2000).

234. J. Jamnik, M. Gaberscek, and S. Pejovnik, Electrochim. Acta 35, 423 (1990).
235. M. H. Hebb, J. Chem. Phys. 20, 185 (1952).
236. C. Wagner, Z. Elektrochemie 60, 4 (1956).
237. I. Yokota, J. Phys. Soc. Jpn. 16, 2213 (1961).
238. H. Rickert and H.-D. Wiemhöfer, Solid State Ionics 11, 257 (1983).
239. H. Rickert and H.-D. Wiemhöfer, Ber. Bunsenges. Phys. Chem. 87, 236 (1986).
240. J. Fleig and J. Maier, J. Electrochem. Soc. 145, 2081 (1998).
241. J. Fleig, Solid State Ionics, 150, 181 (2002).
242. D. R. Clarke and M. L. Gee in Materials Interfaces, editors D. Wolf and S. Yip, Chapman & Hall, London, p. 255 (1992).
243. J. E. Blendell, W. C. Carter, and C. A. Handwerker, J. Am. Ceram. Soc. 82, 1889 (1999).
244. E. Olsson and G. L. Dunlop, J. Appl. Phys. 66, 3666 (1989).
245. M. A. Gülgün, V. Putlayev, and M. Rühle, J. Am. Ceram. Soc. 82, 1849 (1999).
246. I. Denk, J. Claus, and J. Maier, J. Electrochem. Soc. 144, 3526 (1997).
247. M. Leonhardt, J. Jamnik, and J. Maier, Electrochem. and Solid St. Let. 2, 333 (1999).
248. X. Guo, J. Fleig, and J. Maier, J. Electrochem. Soc. 148, J50 (2001).
249. J. Fleig and J. Maier, J. Europ. Ceram. Soc. 19, 693 (1999).
250. H. Näfe, Solid State Ionics 13, 255 (1984).
251. G. Reinhardt and W. Göpel in Proceedings of the Third International Symposium on Ionic an Mixed Conducting Ceramics, editor T. A. Ramanarayanan, The Electrochem. Soc. Proc. Vol. 97–24, p. 610 (1998).
252. S. B. Adler, B. T. Henderson, M. A. Wilson, D. M. Taylor, and R. E. Richards, Solid State Ionics 134, 35 (2000).
253. J. Winkler, P. V. Hendriksen, N. Bonanos, and M. Mogensen, J. Electrochem. Soc. 145, 1184 (1998).
254. A. I. Pham and R. S. Glass, Mat. Res. Soc. Symp. Proc. Vol. 411, 237 (1996).
255. G. Hsieh, T. O. Mason, E. J. Garboczi, and L. R. Pederson, Solid State Ionics 96, 153 (1997).
256. J. S. Newman, Electrochemical Systems, 2nd edition, Prentice Hall, Englewood Cliffs, p. 454 (1991).
257. J. Fleig and J. Maier, Solid State Ionics 94, 199 (1997).
258. W. Orton and P. Blood, The electrical characterization of semiconductors, Academic Press, London, p. 53 and p. 206 (1990).
259. R. G. Mazur and D. H. Dickey, J. Electrochem. Soc. 113, 255 (1966).
260. D. C. D'Avanzo, R. D. Rung, A. Gat, and R. W. Dutton, J. Electrochem. Soc. 125, 1170 (1978).
261. P. A. Schumann and E. E. Gardner, Sol. St. Electron. 12, 371 (1969).
262. S. C. Choo, M- S. Leong, H. L. Hong, L. Li, and L. S. Tan, Sol. St. Electron. 21, 769 (1978).
263. J. Fleig, J. Jamnik, J. Maier, and J. Ludvig, J. Electrochem. Soc. 143, 3636 (1996).
264. J. Fleig, F. Noll, and J. Maier, Ber. Bunsenges. Phys. Chem. 100, 607 (1996).
265. J. Fleig, S. Rodewald, and J. Maier, Solid State Ionics 136–137, 905 (2000).
266. R. Einzinger, Advances in Ceramics Volume 1, editor L. M. Levinson, The American Ceramic Society, Columbus, p. 359 (1981).
267. R. Einzinger, Ann. Rev. Mater. Sci. 17, 299 (1987).
268. A. J. Bard and L. F. Faulkner, Electrochemical Methods, 2nd edition, John Wiley & Sons, New York, p. 344 (2001).
269. J. S. Newman, Electrochemical Systems, 2nd edition, Prentice Hall, Englewood Cliffs, p. 379 (1991).
270. M. Kleitz, L. Dessemond, T. Kloidt, and M. C. Steil in Proceedings of the 4th International Symposium on Solid Oxide Fuel Cells, editors M. Dokiya, O. Yamamoto, H. Tagawa, and S. C. Singhal, The Electrochem. Soc. Proc. Vol. PV 95–1, p. 527 (1995).

271. S. Rodewald, J. Fleig, and J. Maier, J. Am. Ceram. Soc. 84, 521 (2001).
272. S. Rodewald, J. Fleig, and J. Maier, J. Europ. Ceram. Soc. 19, 797 (1999).
273. S. Rodewald, J. Fleig, and J. Maier, J. Am. Ceram. Soc. 83, 1969 (2000).
274. G. D. Mahan, L. M. Levinson, and H. R. Philipp, J. Appl. Phys. 50, 2799 (1979).
275. Z. Feng and C. Zechun, J. Appl. Phys. 80, 1033 (1996).
276. H.-T. Sun, L.-Y. Zhang, and X. Yao, J. Am. Ceram. Soc. 76, 1150 (1993).
277. C. Gillot and J.-P. Michenaud, J. Phys. D: Appl. Phys. 27, 2180 (1994).
278. J. Fleig and J. Maier, Solid State Ionics 85, 9 (1996).
279. A. S. Skapin, J. Jamnik, and S. Pejovnik, Solid State Ionics 133, 129 (2000).
280. A. S. Skapin, S. Pejovnik, and J. Jamnik, J. Europ. Ceram. Soc. 21, 1759 (2001).
281. S. Tanaka and K. Takahashi, Key. Eng. Mat., 157–158, 241 (1999).
282. A. Hammouche, E. Siebert, and A. Hammou, Mat. Res. Bull. 24, 367 (1989).
283. P. Fabry and M. Kleitz, Electroanal. Chem. and Interfacial Electrochem. 57, 165 (1974).
284. R. Baker, J. Guindet, and M. Kleitz, J. Electrochem. Soc. 144, 2427 (1997).
285. M. Juhl, M. Mogensen, T. Jacobsen, B. Zachau-Christiansen, N. Thorup, and E. Skou in Proceedings of the 4th International Symposium on Solid Oxide Fuel Cells, editors M. Dokiya, O. Yamamoto, H. Tagawa and S. C. Singhal, The Electrochem. Soc. Proc. Vol. PV 95–1, p. 554 (1995).
286. D. Kek, N. Bonanos, M. Mogensen, and S. Pejovnik, Solid State Ionics 131, 249 (2000).
287. R. J. Aaberg, R. Tunold, M. Mogensen, B. W. Berg, and R. Odegard, J. Electrochem. Soc. 145, 2244 (1998).
288. L. Bay and T. Jacobsen, Solid State Ionics 93, 201 (1997).
289. N. Bonanos and M. Mogensen, Solid State Ionics 97, 483 (1997).
290. T. Jacobsen, B. Zachau-Christiansen, L. Bay, and M. J. Jorgensen, Electrochim. Acta 46, 1019 (2001).
291. T. Horita, N. Sakai, H. Yokokawa, M. Dokiya, and T. Kawada, Solid State Ionics 86–88, 1259 (1996).
292. D. Kek and N. Bonanos, Solid State Ionics 125, 345 (1999).
293. B. Gharbage, F. M. B. Marques, and J. R. Frade, Solid State Ionics 136–137, 933 (2000).
294. B. Gharbage, F. M. B. Marques, and J. R. Frade, Electrochim. Acta, 43, 2687 (1998).
295. E. Maguire, B. Gharbage, F. M. B. Marques, and J. A. Labrincha, Solid State Ionics 127, 329 (2000).
296. P. Vernoux, J. Guindet, and M. Kleitz, J. Electrochem. Soc. 145, 3487 (1998).
297. G. Reinhardt, doctoral dissertation, University of Tübingen (1994).
298. T. Hauber, doctoral dissertation, University of Tübingen (1993).
299. S. Miyatani, J. Phys. Soc. Jpn. 11, 1059 (1956).
300. U. Tinter and H.-D. Wiemhöfer, Solid State Ionics 9–10, 1213 (1983).
301. W. Zipprich, S. Waschilewski, F. Rocholl, and H.-D. Wiemhöfer, Solid State Ionics 101–103, 1015 (1997).
302. M. Kleinfeld and H.-D. Wiemhöfer, Solid State Ionics 28–30, 1111 (1988).
303. M. Kleinfeld and H.-D. Wiemhöfer, Ber. Bunsenges. Phys. Chem. 90, 711 (1986).
304. W. Zipprich and H.-D. Wiemhöfer, Solid State Ionics 135, 699 (2000).
305. S. Wienströer and H.-D. Wiemhöfer, Solid State Ionics 101–103, 1113 (1997).
306. S. Lübke and H.-D. Wiemhöfer, Solid State Ionics 117, 229 (1999).
307. T. Pauporte and J. Vedel, Solid State Ionics 116, 311 (1999).
308. J.-W. Hahn, Solid State Ionics 81, 119 (1995).
309. H. Schmalzried, M. Ullrich, and H. Wysk, Solid State Ionics 51, 91 (1992).
310. J.-Y. Laval, C. Canabel, and M.-H. Berger, J. Am. Ceram. Soc. 81, 1133 (1998).
311. J. Mizusaki, K. Fueki, and T. Mukaibo, Bull. Chem. Soc. Jpn. 48, 428 (1975).
312. T. Große and H. Schmalzried, Z. Phys. Chem. 172, 197 (1991).
313. C. Rosenkranz and J. Janek, Solid State Ionics 82, 95 (1995).
314. M. Tao, Bui Ai, O. Dorlanne, and A. Loubiere, J. Appl. Phys. 61, 1562 (1987).

315. H. Nemoto and I. Oda, J. Am. Ceram. Soc. 63, 398 (1980).
316. J. Mizusaki and K. Fueki, Rev. Chim. Min. 17 (1980) 356.
317. B. A. Haskell, S. J. Souri, and M. A. Helfand, J. Am. Ceram. Soc. 82, 2106 (1999).
318. H. Wang, W. Li, and J. F. Cordaro, Jpn. J. Appl. Phys. 34, 1765 (1995).
319. M. Holzinger, J. Fleig, J. Maier, and W. Sitte, Ber. Bunsenges. Phys. Chem. 99, 1427 (1995).
320. H.-D. Wiemhöfer, Ber. Bunsenges. Phys. Chem. 97, 461 (1993).
321. A. Spangenberg, J. Fleig, and J. Maier, Adv. Mat. 13, 1466 (2001).
322. K. Kamada, S. Udo, S. Yamashita, and Y. Matsumoto, Solid State Ionics, 46, 387 (2002).
323. K. Dokko, M. Nishizawa, M. Mohamedi, M. Umeda, I. Uchida, J. Akimoto, Y. Takahashi, Y. Gotoh, and S. Mizuta, Electrochem. Solid.-St. Lett. 4, A151 (2001).
324. R. Mauczok and R. Wernicke, Philips Tech. Rev. 41, 338 (1983).
325. J. Daniels, K. H. Härdtl, and R. Wernicke, Philips Tech. Rev. 38, 73 (1979).
326. J. Gerblinger and H. Meixner, Sensors and Actuators B 4, 99 (1991).
327. A. Raith, R. Rijnen and R. Waser, Ber. Bunsenges. Phys. Chem. 92, 1516 (1988).
328. R. Waser, T. Baiatu, and K.-H. Härdtl, J. Am. Ceram. Soc. 73, 1645 (1990).
329. R. Waser, T. Baiatu, and K.-H. Härdtl, J. Am. Ceram. Soc. 73, 1654 (1990).
330. T. Baiatu, R. Waser, and K.-H. Härdtl, J. Am. Ceram. Soc. 73, 1663 (1990).
331. J. Blanc and D. L. Staebler, Phys. Rev. B 4, 3548 (1971).
332. J. Rödel and G. Tomandl, J. Mater. Sci. 19, 3515 (1984).
333. E. Loh, J. Appl. Phys. 53, 6229 (1982).
334. W. A. Schulze, L. E. Cross and W. R. Buessem, J. Am. Ceram. Soc. 63, 83 (1980).
335. J. B. McChesney, P. K. Gallagher, and F. V. DiMarcello, J. Am. Ceram. Soc. 46, 197 (1963).
336. T. Baiatu, Fortschr.-Ber. VDI Reihe 21, Nr. 34, VDI-Verlag, Düsseldorf (1988).
337. S. Rodewald, Doctoral dissertation, University of Stuttgart (1999).
338. I. Denk, W. Münch, and J. Maier, J. Am. Ceram. Soc. 78, 3265 (1995).
339. I. Denk, F. Noll, and J. Maier, J. Am. Ceram. Soc. 80, 279 (1997).
340. M. Vollmann, R. Hagenbeck, and R. Waser, J. Am. Ceram. Soc. 80, 2301 (1997).
341. M. Vollmann and R. Waser, J. Electroceramics 1, 51 (1997).
342. S. Rodewald, N. Sakai, K. Yamaji, H. Yokokawa, J. Fleig, and J. Maier, J. Electroceramics 7, 105 (2001).
343. F. Noll, W. Münch, I. Denk, and J. Maier, Solid State Ionics 86–88, 711 (1996).
344. J. Fleig, unpublished.
345. J. Maier, U. Lauer, and W. Göpel, Solid State Ionics 40, 463 (1990).
346. V. Brichzin, Doctoral dissertation, University of Stuttgart (2002).
347. I. Yasuda and M. Hishinuma, J. Solid St. Chem. 123, 382 (1996).
348. A. Belzner, T. M. Gür, and R. A. Huggins, Solid State Ionics 57, 327 (1992).
349. T. Bak, J. Nowotny, M. Rekas, C. C. Sorrell, and E. R. Vance, Solid State Ionics 135, 557 (2000).

Advances in Electrochemical Science and Engineering, Volume 8. Edited by Richard C. Alkire

ISBNs: 3-527-30211-5 (Hardback); 3-527-60078-7 (Electronic)

Nonlinear Dynamics in Electrochemical Systems

Katharina Krischer

Fritz–Haber–Institut der MPG, Faradayweg 4–6, D-14195 Berlin, Germany
e-mail: krischer@pt.tum.de

Contents

List of Abbreviations

NDR	negative differential resistance
N-NDR	"N-type" NDR
S-NDR	"S-type" NDR
HN-NDR	hidden negative differential resistance of the "N-type"
upd	under potential deposition
pzc	point of zero charge
sn	saddle node
WE	working electrode
RE	reference electrode
CE	counter electrode
NHE	normal hydrogen electrode

List of Symbols

A	Area of the WE
C	specific, differential double layer capacitance
c	concentration
c_b	bulk concentration
c_i	concentration of species i
D_i	diffusion coefficient of species i
F	Faraday's constant (96484.6 C/equiv)
I	total current through the electrochemical cell
$I_F(i_F)$	faradaic current (faradaic current density)
k_B	Boltzmann constant
L	length or circumference of the WE (used in 1d WE geometries)
n	(a) wave number; (b) number of electrons involved in a charge transfer process
n_i	charge number of species i
R_{cell}	electrolyte resistance between the WE and the CE
R_{comp}	compensated electrolyte resistance (resistance between the RE and the CE)
R_{ex}	external series resistance
R_G	"global resistance", $R_G = R_{\text{ex}} - R_{\text{comp}}$
r_i	spatial coordinates in a plane parallel to the working electrode
R_{uncomp}	uncompensated electrolyte resistance (resistance between the WE and the RE)
R_Ω	effective ohmic resistance in series to the WE: $R_\Omega = R_{\text{uncomp}} + R_{\text{ex}}$
U	potentiostatically fixed outer voltage
u_i	mobility of species i (average velocity when acted upon by a force of 1 N mol^{-1})
w	(a) distance between the WE and the CE; (b) geometry factor entering R_{cell} in a general cell geometry
x	spatial direction along the WE
z	spatial coordinate perpendicular to the WE
Z_F	general faradaic impedance
T	absolute temperature
α	(a) strength of global coupling (Eq. (1.3)); (b) geometrical factor (Eq. (4.8)); (c) transfer coefficient
β	aspect ratio $2\pi w/L$ for a 2-d, cylindrical geometry
δ	Nernst diffusion layer thickness
ε	dielectric constant
ε_0	permittivity of free space
φ	electrode potential; $\varphi = \phi_{\text{DL}} - \phi_{\text{DL, RE}}$
$\phi(\mathbf{r}, z)$	electric potential within the (electroneutral) electrolyte
ϕ_2	potential at the outer Helmholtz plane (with respect to the end of the double layer, $\phi\|_{z=\text{WE}}$)
ϕ_{DL}	potential drop across the double layer at the WE
$\phi_{\text{DL, CE(RE)}}$	potential drop across the double layer at the CE (RE)
$\phi_{\text{WE(CE)}}$	inner (Galvani) potential of the WE (CE)
γ	$R_{\text{comp}}/R_{\text{cell}}$
θ	coverage
ρ	radial coordinate
σ	conductivity

1 Introduction

Nonlinear dynamics deals with the evolution of states in systems that are governed by nonlinear evolution laws. Whenever a system's behavior is decisively influenced

by nonlinearities, it is far from thermodynamic equilibrium [1–4]. One of the great achievements of science during the last century was the recognition that systems kept far from the thermodynamic equilibrium can spontaneously form a pattern on a scale that is much larger than the atoms or molecules that are its constituents. A process that results in the spontaneous emergence of such patterns by exporting entropy out of the system is called self-organization. One objective of nonlinear dynamics is to uncover mechanisms that provide systems with the potential to organize themselves without an input from the outside. Over the last decades, theoretical progress in this field has led to the development of concepts that can be applied in practically any discipline and guide the search for the properties essential for self-organization phenomena.

Self-organization phenomena are especially widespread in electrochemical systems, which can already be anticipated from their long history. The first reports on oscillating reaction rates during metal dissolution date back to 1828 [5]; studies during the last 100 years have revealed that virtually any electrochemical reaction may exhibit dynamic instabilities in a certain range of parameters [6, 7].

Within the last ten years the application of the above-mentioned concepts and tools from dynamical systems theory to electrochemical reactions brought about major progress in the understanding of the basic principles underlying electrochemical self-organization processes [8–10]. It allowed classifying electrochemical oscillators according to their dynamic behavior [9–12], and relating the equations governing pattern formation in electrochemistry to prototypical, generic equations whose dynamic behavior has been analyzed in detail. This review article focuses on this new view of electrochemical pattern formation.

Spatiotemporal pattern formation at the electrode|electrolyte interface is described by equations that belong in a wider sense to the class of reaction-diffusion (RD) systems. In this type of coupled partial differential equations, any sustained spatial structure comes about owing to the interplay of the homogeneous dynamics or ''reaction dynamics'' and spatial transport processes. Therefore, the evolution of each variable, such as the concentration of a reacting species, can be separated into two parts: the ''reaction part'', which depends only on the values of the other variables at one particular location, and another part accounting for transport processes that are induced by spatial variations in the variables. These latter processes constitute a spatial coupling among different locations.

Let us first consider a homogeneous situation in which the transport terms become zero. Then, the temporal evolution of the system is described by a set of ordinary differential equations of the general form

$$\frac{dc_i}{dt} = f_i(c_j, \mu_k), \tag{1}$$

where c_i are the variables, μ_k symbolize parameters that affect the dynamics and can be controlled from outside, such as the externally applied voltage in a potentiostatic experiment. The nonlinear functions f_i constitute the ''reaction part''. In a real system, the number of quantities that change in time is usually large. However, in most cases the system's dynamics is captured by a few variables only. The other variables

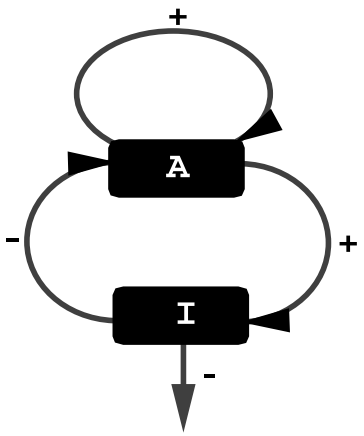

Fig. 1. Positive (autocatalytic) and negative feedback loops between the activator (A) and inhibitor (I) variable.

adjust immediately to their stationary values and thus do not represent true degrees of freedom. In a mathematical description they often can be neglected completely. In the majority of cases that are considered in this review the kinetics is captured by one or two dependent variables. One-variable systems can exhibit bistable behavior, i.e. in a range of parameters the system might be in one of two stable stationary states, for example one with a high current density the other one with a low current density. For bistability to occur the reaction kinetics must contain a self-enhancing step, i.e. a positive feedback loop.

If a second variable participates in an additional feedback loop with a negative regulation, oscillations become possible. The mutual dependencies of the two variables, which have been coined activator and inhibitor, are depicted in Fig. 1. A, the autocatalytic species is the activator: it activates the production of I, and I is the inhibitor because it slows down or inhibits the growth of A [13, 14]. Oscillations arise in activator-inhibitor systems if characteristic changes of the activator occur on a faster time-scale than the ones of the inhibitor. In other words, the inhibitor must respond to a variation of the activator variable with some delay. In fields as diverse as semiconductor physics, chemistry, biochemistry or astrophysics, and also in electrochemistry, most simple periodic oscillations can be traced back to such an activator-inhibitor scheme.

In most electrochemical systems displaying nonlinear phenomena, the electrode potential is an essential variable, that is, it participates in one of the above-mentioned feedback loops.[1] In the overwhelming number of cases it takes on the role of the activator variable, but occasionally it also acts as the negative feedback variable. Depending on the mechanistic role of the electrode potential, the instabilities that prevail the dynamic properties in these two classes of systems are fundamentally different.

[1] Thus far, there seems to be only one convincing example of a reaction mechanism's giving rise to oscillations if the electrode potential is kept fixed [15]. For further discussion of essential variables, see [16].

In a spatially extended system, fluctuations that are always present cause the variables to differ somewhat in space, inducing transport processes, the most common one being diffusion. In the case of constant diffusion coefficients D_i, the system's dynamics is then governed by reaction-diffusion equations:

$$\frac{\partial c_i}{\partial t} = f_i(c_j, \mu_k) + D_i \Delta c_i \tag{2}$$

A transport process couples different locations in space with each other. In other words, it provides the system with the ability to exchange information between different positions about their present state. The lateral "communication" through diffusion, a process that in the absence of the reaction terms inevitably leads to a flat, that is homogeneous, state, can maintain sustained patterns when acting together with nonlinear reaction terms. The characteristic length scale of the patterns is – roughly speaking – on the order of $\sqrt{D/k}$, if k is a characteristic rate constant of the homogeneous dynamics. Pattern formation in reaction-diffusion systems has been an active field of research for the last thirty years (see e.g. Ref. [17]).

Above we stated that electrochemical systems could be classified as reaction-diffusion systems in a wider sense. Now this statement can be specified: The equations governing electrochemical pattern formation can be formulated as a sum of a "reaction part" or "homogeneous dynamics" and a part that vanishes in a homogeneous situation and describes the spatial coupling, in analogy to the diffusion term in reaction-diffusion systems. However, electrochemical systems possess a number of unique properties that distinguish them from the classical reaction-diffusion systems (Eq. (2)). Nearly all these properties are associated with electrical quantities. Above we also mentioned that, in most of the electrochemical systems displaying nonlinear phenomena, the electrode potential is an essential variable. This means that if the electrode potential is strictly constant, then the system does not exhibit dynamic instabilities. From this we can already conclude that in a potentiostatic experiment self-organization requires some voltage drop through the electrolyte, since only then the electrode potential has the freedom to vary in time or space. Therefore, in the context of dynamic instabilities in electrochemical systems, one often distinguishes between *strictly potentiostatic* conditions, in which the electrode potential reduces to a parameter, and *potentiostatic* conditions, which imply that the sum of the electrode potential and the potential drop across some portion of the electrolyte is constant, but the electrode potential itself can vary.

From the facts that the electrode potential is an essential variable, and that the potential drop through the electrolyte is important for dynamical instabilities, two further important conclusions can be drawn. First, lateral variations of the potential induce migration currents, and it was shown that in electrochemical systems the dominant spatial coupling is migration coupling. As will be discussed below, migration coupling cannot be described mathematically by a diffusion term. Second, due to the participation of the bulk electrolyte in the dynamics, the geometry of the electrochemical cell, and in particular the relative position of the working (WE), counter (CE) and reference (RE) electrodes, become important for pattern formation. Changes in the geometry might affect both, the homogeneous dynamics and the

spatial coupling. This opens the peculiar possibility to influence pattern formation by tuning the spatial coupling. Moreover, the control of the experiment brings about a global coupling among different sites of the electrode. In a strict sense, a global coupling exists if a local change of a variable is felt by all the other locations with the same strength independent of their distance to the location of the local variation. In the course of a potentiostatic or a galvanostatic experiment, the electric control device will respond to a local change of the potential drop across the double layer (i.e. the electrode potential) or the current density. It does this by varying the potential of the WE (or the CE), which clearly is always uniform and thus its change affects all positions of the electrode.

Global coupling in systems of the reaction-diffusion type has been an active area of research over the last decade (see Refs. [18–22] and references therein), which helped also to elucidate the role of global coupling in electrochemical systems. The strong general interest in global coupling arose because of its frequent occurrence and its strong impact on pattern formation. In the presence of global coupling, Eq. (2) can often be written as

$$\frac{\partial c_i}{\partial t} = f_i(c_j, \mu_k, \alpha) + D_i \Delta c_i + \alpha(c_i - \langle c_i \rangle), \tag{3}$$

where the squared brackets indicate the spatial average. Note that the parameter α, which determines the strength of the global coupling in general also enters the reaction part.

Patterns at the electrode/electrolyte interface arise due to the interplay of the homogeneous dynamics, migration coupling and global coupling, which in turn depend on electrode kinetics, migration, conductivity of the electrolyte, cell geometry and the external electric circuitry. In this review emphasis is placed on establishing the influence of these individual quantities on pattern formation. In Section 2, the general equation for the spatiotemporal evolution of the electrode potential is derived starting from the fundamental conservation laws of charge and mass. The assumptions and approximations used are pointed out. The goal of this section is to elucidate the origin of the two types of spatial coupling in electrochemical systems, migration coupling and global coupling, and to demonstrate how they depend on the experimentally accessible parameters, most importantly the relative placement of the electrodes.

In Section 3 the homogeneous dynamics of the two main classes of electrochemical systems is discussed, in which the electrode potential takes the role of the activator or inhibitor variable, respectively. In the first case, wherein the electrode potential is involved in the positive feedback loop, there are not only far more examples known, but also two subclasses are distinguished with different dynamic properties. The characteristic properties common to all systems in the different categories, respectively subcategories as well as prototype models are compiled first, and then selected examples are discussed. Here emphasis is placed on elucidating the role of the individual reaction steps in the dynamic behavior, and thus forge links between the common properties and the prototype models to different reactions. The examples chosen are either ''classical oscillating reactions'', which should not be

missing in an overview on electrochemical nonlinear systems, or new results that are not included in earlier review articles [6, 7, 9, 10]. Because of the huge number of papers dealing with oscillations during electrode reactions, a comprehensive review would go beyond the scope of this article.

Section 4 investigates the interaction between the homogeneous dynamics and the spatial couplings. It is thus concerned with spatiotemporal patterns. Its structure follows naturally from the results of the two preceding sections. Subsections 4.1 and 4.2 deal with patterns that arise in systems in which the electrode potential takes the role of the positive and the negative feedback variable, respectively. The general patterns that exist in different combinations of homogeneous dynamics and types of spatial coupling are discussed from a general point of view as well as with experimental examples. Since the progress in the understanding of spatial instabilities in electrochemical systems was considerable within the last five years and allows a new access to many of the observed phenomena, and moreover most of the experimental results are also new, in this section a nearly complete survey of the literature on spatiotemporal dynamics is given (disregarding works from the first half of the twentieth century).

Section 5 contains a summary of the basic mechanisms giving rise to spatiotemporal instabilities in electrochemical systems and discusses perspectives and challenges in future research.

2 The Evolution Law of the Potential Drop Across the Double Layer and the Nature of Spatial Coupling in Electrochemical Systems

2.1 Derivation of the Evolution Law of the Potential Drop Across the Double Layer

The properties characteristic for electrochemical nonlinear phenomena are determined by the electrical properties of electrochemical systems, most importantly the potential drop across the electrochemical double layer at the working electrode (WE). Compared to the characteristic length scales of the patterns that develop, the extension of the double layer perpendicular to the electrode can be ignored.[2] The potential drop across the double layer can therefore be lumped into one variable, ϕ_{DL}, and the temporal evolution law of ϕ_{DL} at every position $\boldsymbol{r}$ along the (in general two-dimensional) electrode|electrolyte interface is the central equation of any electrochemical model describing pattern formation.[3] It results from a local charge bal-

[2] An exception hereto are patterns that form during electropolishing of Al, which have a wavelength of the order of 10—100 nm [23, 24]. They cannot be described with the model discussed in this review.

[3] In short, ϕ_{DL} is termed below also double layer potential. It is related to the electrode potential, φ, through the potential drop across the double layer at the reference electrode, $\phi_{DL,RE}$: $\varphi = \phi_{DL} - \phi_{DL,RE}$. Since $\phi_{DL,RE}$ is constant in time, $(\partial\varphi/\partial t) = (\partial\phi_{DL}/\partial t)$.

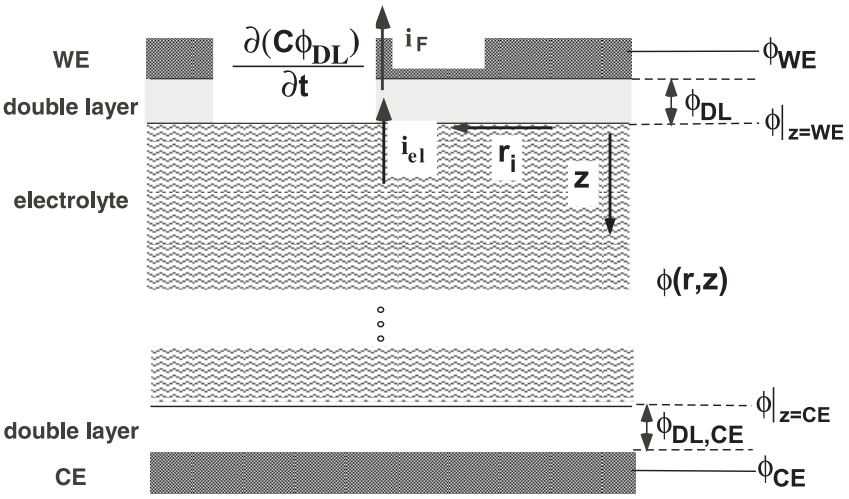

Fig. 2. Local charge balance at the electrode|electroyte interface and notation of different potentials and potential drops in the electrochemical cell.

ance at the interface (Fig. 2), and in a very general form it reads

$$\frac{\partial(C\phi_{\mathrm{DL}}(\mathbf{r},t))}{\partial t} + i_F(\mathbf{r},t) = i_{\mathrm{el},z}(\mathbf{r}, z = \mathrm{WE}, t). \tag{4}$$

Here C is the specific differential double layer capacitance. The two terms on the left side of Eq. (4) describe the capacitive and faradaic current densities at a position $\mathbf{r}$ at the electrode|electrolyte interface. The sum of these two terms is equal to the current density due to all fluxes of charged species that flow into the double layer from the electrolyte side, $i_{\mathrm{el},z}$ $(\mathbf{r}, z = \mathrm{WE})$, where z is the direction perpendicular to the electrode, and $z = \mathrm{WE}$ is at the working electrode, more precisely, at the transition from the charged double layer region to the electroneutral electrolyte. $i_{\mathrm{el},z}$ is composed of diffusion and migration fluxes, which, in the Nernst–Planck approximation, are given by

$$i_{\mathrm{el},z}|_{z=\mathrm{WE}} = -F\sum_i \left(n_i^2 F u_i c_i(z = \mathrm{WE}) \left.\frac{\partial\phi}{\partial z}\right|_{z=\mathrm{WE}} + D_i n_i \left.\frac{\partial c_i}{\partial z}\right|_{z=\mathrm{WE}} \right), \tag{5}$$

where F is Faraday's constant, u_i the mobility[4] and n_i the charge number of species i. c_i and D_i are the concentrations and diffusion coefficients of the respective ions. $\phi(\boldsymbol{r}, z)$ denotes the electric potential within the (electroneutral) electrolyte.

To solve Eq. (4) with i_{el} given by Eq. (5) the component of the electric field normal to the electrode and the differential changes of concentrations with infinitesimal changes in z have to be determined. At this point potential and concentration dis-

[4] Notice that here mobility is defined as the velocity of a particle under the influence of a unit force.

tributions of the bulk electrolyte come into play, and the rigorous treatment of the problem becomes extremely demanding. It involves the solution of Poisson's equation, which reads for a medium with uniform dielectric constant ε

$$\nabla^2\phi = \frac{F}{\varepsilon\varepsilon_0}\sum_i n_i c_i \tag{6}$$

and relates the charge density in the electrolyte to the Laplacian of the electric potential, as well as the solution of the material balance equations for every charged species. For diluted solutions and in the absence of convection, they read

$$\frac{\partial c_i}{\partial t} = -\nabla\cdot(-n_i u_i F c_i \nabla\phi - D_i \nabla c_i). \tag{7}$$

Equation (4) is thus a time-dependent boundary condition to Eqs. (6, 7), which, supplemented by the remaining boundary conditions (which also involve external constraints resulting from the operation mode of the experiment, s.b.) and possibly by the incorporation of convection, form the most basic Ansatz for modeling patterns of the reaction-transport type in electrochemical systems. However, so far, there are no studies on electrochemical pattern formation that are based on this generally applicable set of equations. Rather, one assumption was made throughout that proved to capture the essential features of pattern formation in electrochemistry and greatly simplifies the problem: it is assumed that the potential distribution in the electrolyte can be calculated by Laplace's equation, i.e. Poisson's equation (6) becomes:

$$\Delta\phi = 0. \tag{8}$$

Although this seems to be an excellent approximation, since any electrolyte solution adheres electroneutrality very closely, one should be aware that rigorously taken it is valid only if the conductivity of the electrolyte, σ, which can be expressed as

$$\sigma = F^2\sum_i n_i^2 u_i c_i, \tag{9}$$

is uniform within the entire electrolyte. This further implies that all diffusion coefficients D_i are equal and that the concentrations c_i are constant in space. For a further discussion about the problems that arise when employing Laplace's equation if these conditions are not fulfilled see, e.g. Ref. [25]. Given Eqs. (8 and 9) hold, all diffusional fluxes vanish and the mass balance equations (7) are no longer necessary. Furthermore, the contribution of the individual species to the migration current can be combined such that Eq. (5) becomes

$$i_{\mathrm{el},z}\big|_{z=\mathrm{WE}} = -\sigma\left.\frac{\partial\phi}{\partial z}\right|_{z=\mathrm{WE}}. \tag{10}$$

Assuming, in addition, that the capacitance of the electrode is independent of ϕ_{DL}, an assumption, which also has been made so far in simulations of electrochemical pattern formation, the differential charge conservation law at the interface (Eq. (4)) becomes [26]

$$C\frac{\partial \phi_{\mathrm{DL}}(\mathbf{r},t)}{\partial t} = -i_F(\mathbf{r},t) - \sigma \left.\frac{\partial \phi(\mathbf{r},t)}{\partial z}\right|_{z=\mathrm{WE}}. \tag{11}$$

This equation constitutes the central equation of state-of-the-art modeling of pattern formation in electrochemistry. Its integration requires the knowledge of the electric field component normal to the interface, which is obtained from the solution of Laplace's equation.

The necessity to solve Laplace's equation requires formulating all boundary conditions, and at this point the cell geometry becomes important. Generally, there are two types of boundary conditions that come into play. Any electrically insulating cell wall is mathematically described by zero-flux or von Neumann boundary conditions:

$$\left.\frac{\partial \phi}{\partial r_i}\right|_{(z,r_j,r_i=\text{cell wall})} = 0, \qquad \left.\frac{\partial \phi}{\partial z}\right|_{(\mathbf{r},z=\text{cell wall})} = 0, \tag{12}$$

where r_i is the spatial direction normal to the respective cell wall and r_j the second spatial direction parallel to the working electrode. At a conducting surface, i.e. the WE and the CE, the (uniform) potential in the interior of the conductor has to be specified:

$$\phi_{\mathrm{WE}} = a, \quad \phi_{\mathrm{CE}} = b, \tag{13}$$

where a and b result from the way the experiment is conducted (s.b.) and may vary in time. The respective potential drops across the double layers are then given by $\phi_{\mathrm{DL}} = \phi_{\mathrm{WE}} - \phi|_{z=\mathrm{WE}}$, and $\phi_{\mathrm{DL,CE}} = \phi_{\mathrm{CE}} - \phi|_{z=\mathrm{CE}}$ (see Figs. 2 and 7). To solve Laplace's equation, their initial profiles must be given; their temporal evolution then obeys Eq. (11), respectively a corresponding one for the CE. However, in electrochemical modeling it is generally assumed that the reactions at the CE have no decisive impact on pattern formation at the WE, and the boundary condition at the CE is considerably simplified. Birzu et al. [27–29] assume linear kinetics, neglecting the capacitive current, such that for the CE Eq. (11) becomes

$$-\sigma \left.\frac{\partial \phi}{\partial z}\right|_{z=\mathrm{CE}} = k\phi_{\mathrm{DL,CE}}, \tag{14a}$$

where k is the rate constant. Elsewhere [26, 30–39] it is assumed that the double layer potential at the CE is uniform in space throughout. Thus, also the electrolyte potential at the border between the CE double layer and the electroneutral electrolyte, $\phi|_{z=\mathrm{CE}}$, constitutes an equipotential plane, whose potential is conveniently set to zero:

$$\phi|_{z=\mathrm{CE}} = 0. \tag{14b}$$

In this case, the potential drop across the double layer at the CE does not need to be further considered. In the following considerations we shall, unless stated otherwise, refer to this boundary condition at the CE.

Thus, in practice, the potential distribution within the electrolyte is obtained by solving Laplace's equation subject to a time-dependent, Dirichlet-type boundary condition at the end of the double layer of the WE, a given value of ϕ at the end of the double layer of the CE and zero-flux or periodic boundary conditions at all other domain boundaries. Knowing the potential distribution, the electric field at the WE can be calculated, and the temporal evolution of the double layer potential is obtained by integrating Eq. (11) in time, which results in changed boundary conditions (b.c.) at the WE.

Now, we are in a position to recognize, how different parts of the interface are coupled together, which is not apparent from Eq. (11) since it does not contain a spatial operator acting in the direction parallel to the electrode: A local change of the potential at the interface of the working electrode i.e. of the b.c. affects the potential distribution in the entire electrolyte. Accordingly, also the normal derivative of the electric potential at the entire electrode|electrolyte interface is changed, i.e. the migration current densities entering the double layer. From a physical point of view, different parts of the electrode are coupled together because the electrolyte has a strong tendency to stay electroneutral so that local disturbances of ϕ_{DL} cause instantaneously a change of the migration currents at the entire interface. This spatial coupling through the electric field, also called migration coupling, corresponds to the coupling through diffusion in reaction-diffusion systems. Since the impact of a local change of ϕ_{DL} on the evolution of ϕ_{DL} at a distant position depends on the cell geometry, the cell design plays a decisive role for the spatial coupling in electrochemical systems. This is discussed in more detail in the next section.

2.2 Migration Coupling

There are two types of cell design that give rise to different coupling properties. In the first kind the WE extends from one wall of the cell to the other one, in the second class it is embedded into an insulating material. Examples of the two types that were also considered in literature are shown in Fig. 3. Among the first type of geometries are, e.g., cylindrical cells with a disk-shaped WE that covers the top of the cell or a box-like cell with a rectangular WE at one side of the box (Fig. 3a,b). Also ring electrodes whose circumference is large compared with the width of the ring fall into this category, since here pattern formation occurs only into the azimuthal direction in which no insulating boundary exists (Fig. 3c). A simplified 2-d geometry, with which most knowledge about the spatial coupling in electrochemical systems and the features, in which electrochemical models are different from reaction-diffusion models, were first obtained, is shown in Fig. 3d [26, 31, 34]. Here the electrolyte is confined to a cylindrical surface, which is bound from one side by the WE and from the other side by the CE. In another two-dimensional model, the electrolyte is a rectangle, the two electrodes being wires at two opposing sides (Fig. 3e).

Common to all these geometries is that for a homogeneous potential distribution

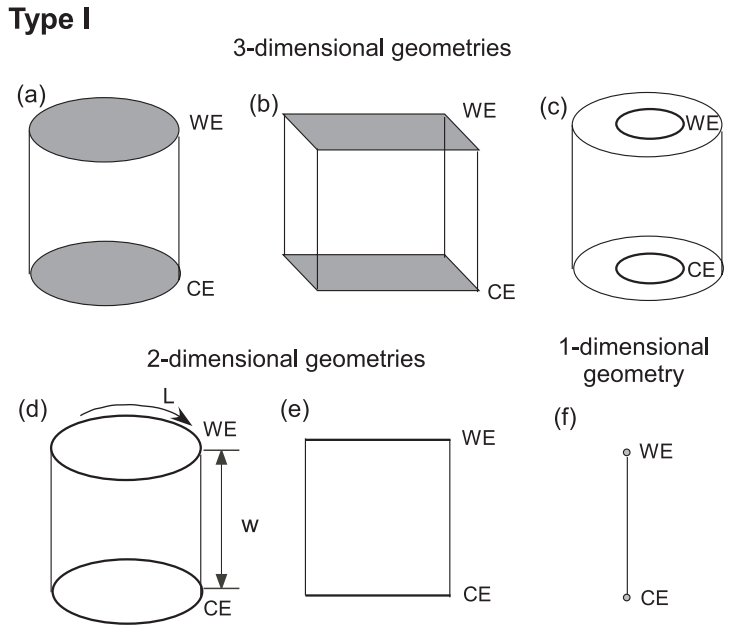

Fig. 3. Different cell geometries. Type I: For a uniform potential distribution at the electrode|electroyte interface, the current density is uniform. Type II: For a uniform potential distribution at the electrode|electroyte interface, the current density is not uniform.

at the WE and the CE there are no components of the electric field along the coordinate in which the electrode is extended. Hence, this ''homogeneous'' situation is captured by a one-dimensional, ''point-like'' arrangement of the electrodes, as depicted in Fig. 3f.

When the electrode is embedded in an insulating plane, such as in the geometries shown in Fig. 3g,h, current density and double layer potential are never uniform at the same time. This fact, first pointed out by Newman [40], considerably complicates pattern formation.

Let us first discuss the properties of migration coupling in the first type of systems. Here, the solution of Laplace's equation for any homogeneous situation yields a linear dependence of ϕ on z, i.e. with boundary condition 14b and the origin of the z-axis, $z = 0$ at the CE,

$$\phi(z) = \phi|_{z=\mathrm{WE}} z. \tag{15}$$

This means that in a homogeneous case the migration current density in Eq. (11) is given by:

$$\sigma \frac{\partial \phi}{\partial z}\bigg|_{z=\mathrm{WE}} = \frac{\sigma}{w} \phi|_{z=\mathrm{WE}}, \tag{16}$$

where w is the distance between the WE and the CE.

In an inhomogeneous case, the migration current density at the WE deviates from the one that would result from a linear potential drop between the WE and the CE. The deviation between the actual migration current density and the one that would flow if the potential dropped linearly between the WE and the CE corresponds to migration currents that flow only because of an inhomogeneous interfacial potential distribution; it constitutes thus the migration coupling, i.e. the dominant spatial coupling in electrochemical systems, $i_{\mathrm{mig,\,coupling}}$:

$$i_{\mathrm{mig,\,coupling}} = \sigma \left(\frac{\partial \phi}{\partial z} - \frac{\phi}{w} \right)\bigg|_{z=\mathrm{WE}} \tag{17}$$

Unlike a diffusional coupling in one spatial dimension, which is given by $D(\partial^2 c/\partial x^2)$ and depends only on the diffusion coefficient, the migration coupling depends on two parameters, σ and w, or, in physical terms, the conductivity of the electrolyte and the distance between the WE and the CE. The conductivity plays the role of the diffusion coefficient in diffusional coupling, i.e. it determines how fast an inhomogeneous potential distribution is evened out with time (in the absence of a reaction term) just as the diffusion coefficient determines how fast an inhomogeneous concentration distribution disappears. For a given size of the WE, w determines the *range of the coupling*, which is a measure of the characteristic distance over which a change in the state at a particular position instantaneously affects neighboring parts. The coupling range also depends on the extension of the electrode and thus a better characterization is the aspect ratio of the cell. For the two-dimensional cylindrical geometry (Fig. 3d), e.g., the aspect ratio is conveniently defined as $\beta = (2\pi w)/L$, where L is the circumference of the electrode [31].

The effect of β on the coupling range is illustrated in Fig. 4 in which the migration coupling term $i_{\mathrm{mig,\,coupling}}$ is plotted against position for a rectangular potential profile at the ring electrode. The potential distribution mimics a nonstationary situation in the bistable regime where a large part of the electrode acquires one of the two steady states and a small part the other one, both parts being connected by a sharp interface (Fig. 4 top). The three curves in Fig. 4 (bottom) correspond to three different values of β. First, we see that wherever $\phi_{\mathrm{DL}}(x)$ is lower than the average, ϕ_{DL} is

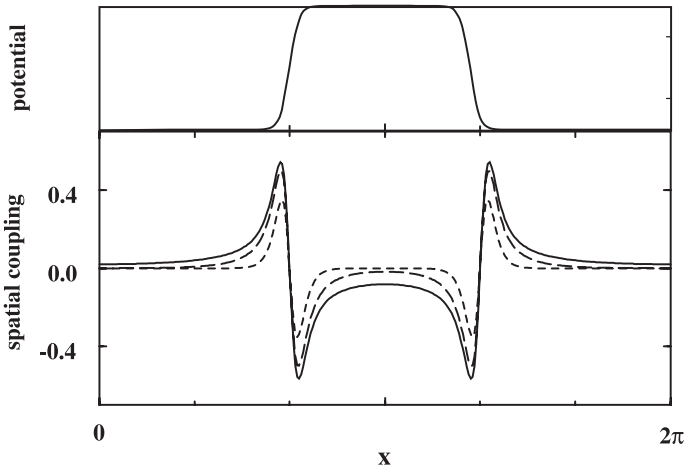

Fig. 4. Top: Potential distribution at the working electrode ($z = \mathrm{WE}$). Bottom: Corresponding spatial coupling term (Eq. 17) for the 2-d cylinder geometry (cf. Fig. 2.2d) and three different values of β: Solid line, $\beta = 4$; long-dashed line $\beta = 0.5$; dashed line $\beta = 0.1$.

increased by the migration coupling, and vice versa, wherever $\phi_{\mathrm{DL}}(x)$ is larger than the average, it is decreased. Thus, the migration coupling is a synchronizing coupling; it smoothes out any potential gradients tangential to the WE, just as diffusion homogenizes a concentration profile.

Furthermore, the solid curve, obtained for the largest value of β, does not fall off to 0, even for positions farthest from the interface. This means that the migration coupling leads to a recharging of the entire interface, though the recharging is the stronger the closer positions are to positions where ϕ_{DL} changes strongly. This is characteristic for any nonlocal coupling. For smaller values of β, the impact of the migration coupling on positions far from the potential front is less pronounced and thus the coupling range decreases, leading in the limit of vanishing β to local or diffusive coupling (the short- and long-dashed curves in Fig. 4). Since β is an experimentally accessible parameter, the coupling range can be deliberately tuned; this is a singular property of electrochemical systems.

For the case of the two-dimensional cylindrical geometry, Laplace's equation can be solved analytically yielding also an analytical expression for the migration current density at the working electrode, which allows investigating the coupling range as a function of β in quantitative terms. As shown in [26, 31] for this geometry the migration current density can be expressed by the infinite series:

$$\tilde{\sigma}\frac{\partial\tilde{\phi}}{\partial\tilde{z}}\bigg|_{\tilde{z}=-1} = \tilde{\sigma}\sum_{n=1}^{\infty}[A_n(\tilde{t})\cos(n\tilde{x}) + B_n(\tilde{t})\sin(n\tilde{x})]n\beta\cosh(n\beta) + A_0(\tilde{t}) \tag{18}$$

where β is the aspect ratio of the cell as defined above, n are wave numbers, A_n, B_n the corresponding time-dependent Fourier coefficient, and $\sim$ indicates that di-

mensionless quantities are used; for its transformation to the corresponding physical quantities, see the original literature [10, 31]. Writing ϕ_{DL} as a Fourier series,

$$\tilde{\phi}_{\mathrm{DL}}(\tilde{x},\tilde{t}) = \sum_{n=1}^{\infty}[a_n(\tilde{t})\cdot\cos(n\tilde{x}) + b_n(\tilde{t})\cdot\sin(n\tilde{x})] + a_0(\tilde{t}) \tag{19}$$

we can express the evolution equation of ϕ_{DL}, Eq. (11), as an infinite number of coupled ordinary differential equations for the temporal evolution of a_n and b_n once the boundary condition that relates $\tilde{\phi}_{\mathrm{DL}}$ and $\tilde{\phi}|_{\tilde{z}=-1}$ is known. For potentiostatic control (s.b., U is the applied voltage), A_n (B_n) and a_n (b_n) are linked according to

$$a_0 = U + A_0 \quad \text{and} \quad a_n = A_n\sinh(n\beta), b_n = B_n\sinh(n\beta) \tag{20}$$

and the evolution equations for the coefficients a_n become

$$\frac{da_0}{d\tilde{t}} = -f_0(a_i,b_i) - \frac{\tilde{\sigma}}{\beta}a_0 =: g_0(a_i,b_i) \tag{21a}$$

and

$$\begin{aligned}\frac{da_n}{d\tilde{t}} &= -f_n(a_i,b_i) - \tilde{\sigma}\cdot n\cdot\coth\cdot(n\beta)a_n \\ &=: g_n(a_i,b_i) - \tilde{\sigma}\left(n\cdot\coth(n\beta) - \frac{1}{\beta}\right)a_n\end{aligned} \tag{21b}$$

The terms $f_n(a_i,b_i)(n,\ i=0,1,\ldots,\infty)$ are the Fourier components of the reaction current density, $\tilde{i}_F$. Owing to the symmetry of the problem, the equations for the coefficients of the sine modes, b_n, are analogous to those of the cosine modes, a_n. The ''reaction part'' (the dynamics of the homogeneous system) was lumped into the function g. In this way, the term defining the spatial coupling (Eq. (17)) is easily discernible. In accordance with our general considerations about the characteristics of the migration coupling, it is apparent from Eqs. (21a,b) that σ only influences the relative time scales of spatial coupling and homogeneous kinetics and thus defines the coupling strength. On the other hand, β influences the ratio of damping terms of the different modes. Thus, varying β changes the range of the coupling.

Equations (21a,b) allow quantifying the two limiting cases of maximum and minimum coupling range, $\beta\to 0$ and $\beta\to\infty$, respectively. For arguments $< \pi$, the coth in Eq. (21b) can be expanded, leading to the following expression

$$\lim_{\beta\to 0}[-\tilde{\sigma}(n\coth(n\beta) - \beta^{-1})] = -\frac{1}{3}\tilde{\sigma}\beta n^2 + O(\beta^3 n^4). \tag{22}$$

The first term on the right formally represents a contribution of a second spatial derivative and can thus be formally considered as originating from a diffusional pro-

cess. Consequently, in the limit of very small aspect ratios the spatial coupling converges to a local, diffusional coupling with a formal diffusion coefficient $(\tilde{\sigma}\beta)/3$.

If, on the other hand, the aspect ratio is very large, the spatial coupling converges toward a characteristic function with a maximum range

$$\lim_{\beta\to\infty}(-\tilde{\sigma}(n\coth(n\beta)-\beta^{-1}))=-\tilde{\sigma}n. \tag{23}$$

The right side of Eq. (23) is already a good approximation from $\beta\sim 3$ on, i.e. if the length of the WE is about twice the distance between the WE and the CE.

Recently, Christoph et al. [35–37] introduced a mathematically different formulation of the coupling term that employs an approach that was shown to be helpful when dealing with long-range effects, since it allows an intuitive representation of the nonlocality of the spatial coupling [14]. In a first step, the potential distribution in the electrolyte is expressed in terms of the boundary conditions at the electrode with help of a Green's function. Inverting the Green's function results in the coupling function H such that the spatial coupling can be represented by an integral formalism. In this case, the migration coupling is expressed as

$$i_{\text{mig, coupling}}=\sigma\int_{x'=0}^{2\pi}H(|x-x'|)(\phi_{\text{DL}}(x',t)-\phi_{\text{DL}}(x,t))\,dx', \tag{24}$$

where again for simplicity the cylindrical 2-d geometry is considered, but the formalism can be applied independent of the geometry. In this formulation it can be seen immediately that the coupling term vanishes in a homogeneous situation, i.e. if $\phi_{\text{DL}}(x)=\phi_{\text{DL}}(x')$ for every x'. For an inhomogeneous situation the coupling function $H(x-x')$ quantifies the effect any location x' has on the dynamics at the position x. It depends on the aspect ratio β. The change of the range of the coupling with β is obvious from a comparison of the two coupling functions shown in Fig. 5, which correspond to a small (dashed line) and large (solid line) distance, respectively. The fact that for a large value of β the coupling function is considerably different from zero everywhere is a manifestation of the nonlocality of the coupling. For vanishing β, H is practically 0 everywhere, except for locations in the immediate neighborhood of the reference point x, a situation that characterizes a local coupling.

Although the quantitative considerations above concerned the simplified two-dimensional geometry, qualitatively the results hold for all the geometries without insulating boundaries in the plane of the WE: the migration coupling is in general long-range and the range depends on the aspect ratio of the cell. If the electrode is embedded in an insulating plane, such as in the geometries shown in Fig. 3(g,h), additional features complicate the migration coupling. They arise due to two reasons: the local effective resistance depends on position, which means that there is a variation of a parameter of the local dynamics with space, and thus different positions of the electrode might be in different dynamic regimes; and the strength with which two points are coupled together through migration coupling does not decay monotonically from a reference position, but increases again towards the edge of the electrode where it diverges. This important result was recently obtained by Christoph [37]. It

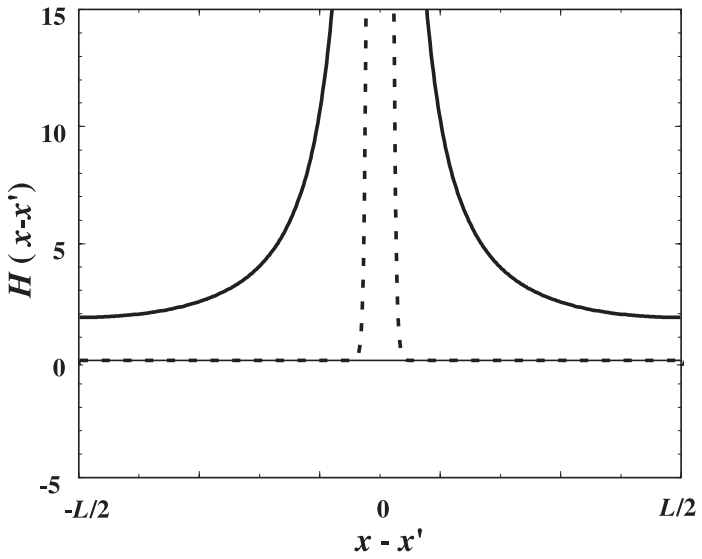

Fig. 5. Coupling functions H in Eq. (24) for ring working electrodes with circumference L for two different values of β. Solid line: large aspect ratio β resulting in nonlocal spatial coupling. Dashed line: very small aspect ratio β resulting in local (diffusive) spatial coupling. (Courtesy of J. Christoph.)

implies that every point at the electrode is coupled more closely to points at the edge of the electrode than to neighboring positions. Hence, in addition to the nonlocal coupling discussed above, there is a remote coupling to the edges of the electrode.

Let us consider the potential distribution for one such mixed boundary value problem in more detail. If a disk electrode of radius ρ_0 embedded in an infinite insulating plane and with the counter electrode far away has a uniform double layer potential, ϕ_{DL}, then the current distribution at the electrode normalized to the average current density, i_{avg}, is given by [40]

$$\frac{i_{\mathrm{mig}}(\rho)|_{z=\mathrm{WE}}}{i_{\mathrm{avg}}} = \frac{0.5}{\sqrt{1-\rho^2/\rho_0^2}}. \tag{25}$$

The corresponding equipotential and current lines within the electrolyte are shown in Fig. 6 [25]. The equipotential lines are close together at the edge of the electrode, and, as immediately apparent from Eq. (25), the current density is infinite at $\rho = \rho_0$, i.e. at the edge. Thus, at the edge, the effective resistance of the electrolyte vanishes, and it increases when approaching the center of the disk. The higher current density at the rim of the electrode is to be attributed to the current flow through the solution beyond the electrode.

Although the detailed dependence of the current density from the distance of the edge is different for every electrode geometry, the qualitative behavior is identical for all the systems in which the electrode is embedded in an insulator. The current density is always largest at the electrode edge and it decreases toward the middle of the

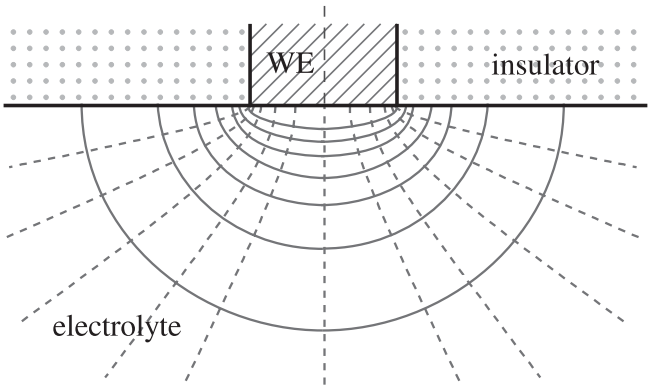

Fig. 6. Equipotential and current lines (solid and dashed lines, respectively) for a disk electrode embedded in an insulator.

electrode. Thus, also the dynamic effects due to these properties will be qualitatively similar.

The repercussion of the insulator embedding the WE on the dynamics becomes most apparent when reformulating the migration current density in the following way

$$\sigma \frac{\partial \phi}{\partial z}\bigg|_{z=\mathrm{WE}} = \frac{\sigma}{w(\rho)}\phi|_{z=\mathrm{WE}} + \sigma\left(\frac{\partial \phi}{\partial z} - \frac{1}{w(\rho)}\phi\right)\bigg|_{z=\mathrm{WE}} \tag{26}$$

where the first term is the local migration current density that would exist in a point-like system with a resistance $w(\rho)/\sigma$, whereby $w(\rho)$ is a geometric parameter which depends on space. The second term determines the spatial or migration coupling. Since the resistance differs with position, all electrochemical models for electrodes embedded in insulators are models with a distributed parameter.

Obviously, also migration coupling depends on the position-dependent effective resistance, w/σ, which leads to the already mentioned strong coupling of every position to edge-near positions of the electrode and thus to non-monotonic coupling functions [37]. Theoretical investigations of this complicated and unusual coupling behavior can thus far only be found in [37]. Since the results are fairly new, and experimental confirmations of the additional effects originating from the remote migration coupling have not yet been obtained, we refrain from discussing this coupling in more detail.

2.3 Global Coupling

As follows from Eq. (13), our equations are only fully specified if the potential of the WE, ϕ_{WE}, is known, which relates the potential drop across the double layer and the

electrolyte potential at $z = \mathrm{WE}$ according to

$$\phi_{\mathrm{DL}}(\mathbf{r}, t) = \phi_{\mathrm{WE}}(t) - \phi(\mathbf{r}, t)|_{z=\mathrm{WE}}. \tag{27}$$

Usually, that is except under open circuit conditions, the working electrode is embedded in an electric circuit, which imposes a constraint on $\phi_{\mathrm{WE}}(t)$ and thus defines its value with respect to some potential scale (in our case Eq. (14b)). Moreover, ϕ_{WE} will in general evolve in time and thus the external constraint directly influences the dynamics of the system. The two most important operation modes of electrochemical systems are the potentiostatic and the galvanostatic operation.

Under potentiostatic conditions, the voltage between the WE and the RE is kept constant. Since the potential drop across the interface of the reference electrode is constant, the potentiostatic control can be formulated in terms of the voltage difference between the location in the electrolyte at which the reference electrode is positioned $(z_{\mathrm{RE}}, \mathbf{r}_{\mathrm{RE}})$ and the working electrode[5]

$$U = \phi_{\mathrm{DL}}(\mathbf{r}) + (\phi(\mathbf{r})|_{z=\mathrm{WE}} - \phi|_{z=\mathrm{RE}, r=\mathrm{RE}}), \tag{28}$$

where U is the externally applied voltage.

The galvanostatic operation mode gives rise to the following integral constraint for the total current

$$I_{\mathrm{tot}} = \int_{\mathrm{WE}} \sigma \frac{\partial \phi}{\partial z}\bigg|_{z=\mathrm{WE}} dA \tag{29}$$

where I_{tot} is the preset current density.

In general, both the galvanostatic and the potentiostatic operation mode lead to a change of the potential of the working electrode, ϕ_{WE}, with time, which causes a further spatial coupling among different sites of the electrode.[6] Consider first the galvanostatic case. If the faradaic current at a particular position at the electrode changes (e.g. due to a local fluctuation), the total current changes accordingly, and the galvanostat provides the difference current between the actual and the set current by changing the potential of the WE. Since the feedback depends only on the total current density, and hence the *average* double layer potential, we are dealing here with a *global* coupling or feedback.

In the potentiostatic case the feedback arises because a local change of ϕ_{DL} induces a redistribution of the potential everywhere in the electrolyte, and, hence, also at the position of the reference electrode if the reference electrode is placed some-

[5] If a Luggin–Haber capillary is used, $(z_{\mathrm{RE}}, \mathbf{r}_{\mathrm{RE}})$ would be at the end of the capillary; if the reference electrode is in a separate compartment, it is at the connection between the main and the reference electrode compartment.

[6] In some experiments the WE is grounded and the potential of the CE is controlled such that the potentiostatic or the galvanostatic constraint is fulfilled. This problem is completely equivalent, and thus everything we discuss here about the global coupling under potentiostatic or galvanostatic conditions holds also in that case.

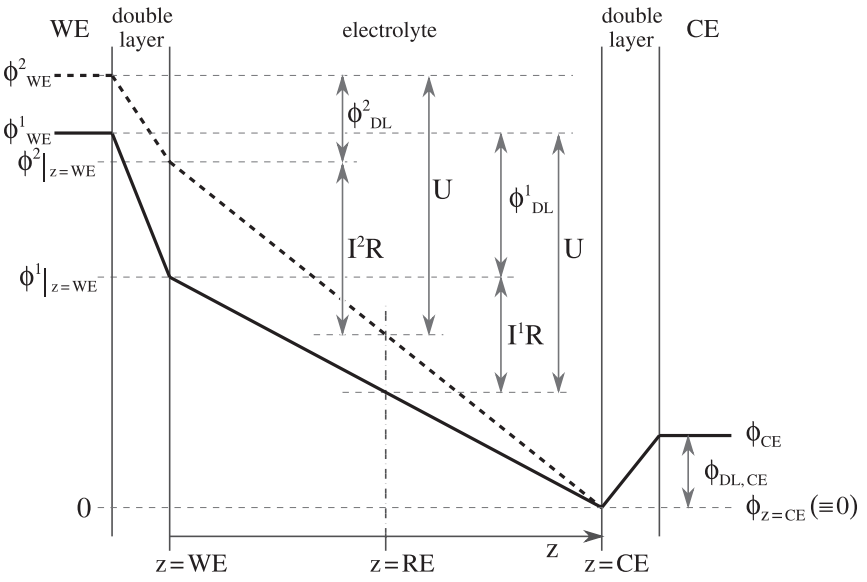

Fig. 7. Potential profiles perpendicular to the WE with corresponding potential drops for two different current densities (I^1 and I^2) at the same value of the applied voltage U, demonstrating the origin of the global coupling. (The potential parallel to the cell is assumed to be uniform.)

where between the WE and the CE. However, as soon as $\phi|_{(z_{RE},\mathbf{r}_{RE})}$ changes, the potentiostat changes the potential of the WE accordingly such that Eq. (28) is always fulfilled (Fig. 7). If the potential at $(z_{RE},\mathbf{r}_{RE})$ is influenced by every position on the WE in the same manner, it again depends on the average double layer potential and the feedback is global. Such a situation exists only for thin ring electrodes if the RE (or the tip of a Luggin–Haber capillary) is placed on the axis of the ring. Most of the experiments, in which the impact of the position of the ring electrode on pattern formation was investigated, have been carried out with such a symmetric set-up. For all other electrode geometries and arrangements, in particular for all two-dimensional WEs, $\phi|_{(z_{RE},\mathbf{r}_{RE})}$ is a function of a weighted average of ϕ_{DL}. Positions at the WE that are closer to the RE have a larger influence on $\phi|_{(z_{RE},\mathbf{r}_{RE})}$ than those that are further away. In these asymmetric situations, the impact of the global feedback on pattern formation is superimposed by an additional "asymmetry effect". In the remaining of this section we concentrate on the much better investigated and simpler symmetric case.

Despite the similar origin of the global coupling in the potentiostatic and the galvanostatic cases, there is an important difference between the two types of global coupling. Let us first investigate the global coupling under potentiostatic conditions in more detail. Let us denote the "uncompensated" resistance between the WE and the RE by R_{uncomp}, the "compensated" resistance between the RE and the CE by R_{comp} and the one between the WE and the CE by $R_{cell} = w/(A\sigma) = R_{uncomp} + R_{comp}$, where A is the area of the working electrode and w is a geometry factor de-

pending on the particular cell geometry. The migration coupling density can then be expressed as the sum of three terms (as shown in [41] this follows from Eq. (4b) in Ref. [42][7] and was also derived employing the above-mentioned integral formulation [35–37]):

$$-\sigma\left.\frac{\partial\phi}{\partial z}\right|_{z=\mathrm{WE}} = \frac{1}{AR_{\mathrm{uncomp}}}\phi|_{z=\mathrm{WE}} - \frac{1}{AR_{\mathrm{cell}}}\frac{R_{\mathrm{comp}}/R_{\mathrm{cell}}}{(1-R_{\mathrm{comp}}/R_{\mathrm{cell}})}(\langle\phi_{\mathrm{DL}}\rangle - \phi_{\mathrm{DL}}) - \sigma\left.\left(\frac{\partial\phi}{\partial z}-\frac{\phi}{w}\right)\right|_{z=\mathrm{WE}} \tag{30}$$

With the first and the last terms we are already familiar. They describe the local migration current density that would also flow in a homogeneous situation (or in the respective point-like system) and the migration coupling, respectively. The second term arises due to the global feedback. It obviously depends on the difference between the local value of ϕ_{DL} and the average double layer potential, $\langle\phi_{\mathrm{DL}}\rangle$, and thus vanishes in a homogenous situation. The coefficient in front of this term is a measure of the strength of the global coupling. It becomes zero if $R_{\mathrm{comp}} = 0$, which is the case when the RE is on the height of or behind the CE. In this situation, the potential of the working electrode, ϕ^{WE}, is fixed by the potentiostatic constraint, and consequently also the global feedback is absent. In other words, the potential at the RE is not influenced by any change of ϕ_{DL}. The larger R_{comp}, that is the closer the RE is to the WE, the stronger is the coupling. Whether global or migration coupling dominates pattern formation depends on conductivity, cell resistance and compensated resistance in a nontrivial manner.

Note that the local term depends through $R_{\mathrm{uncomp}} = R_{\mathrm{cell}} - R_{\mathrm{comp}}$ on the compensated and the cell resistance. Therefore, it is not possible to change the strength of the global coupling without also changing the local dynamics.

Next, let us turn to the galvanostatic case. In the mathematical formulation the global coupling due to the constant current constraint becomes especially transparent when formulating the problem for the potentiostatic case with an external resistor in series to the working electrode, as was done in Ref. [32]. The limit of infinite external resistance and infinite voltage corresponds to the galvanostatic control mode, whereby the finite ratio between the two quantities defines the preset current density. The externally imposed voltage, U, is now composed of the potential drop across the external resistor, the uncompensated resistance and the double layer. Assume that the RE is far away from the WE, and thus the above-discussed global coupling is absent. Then one can again write the migration current density in terms of a local contribution and two contributions due to the spatial coupling, originating from the global coupling owing to the external resistance, R_{ex}, and the migration coupling, respectively [10–32, 37]:

[7] Note that Eq. 4b in Ref. [42] is identical to Eq. 4a and thus it is correct. However, the term that is claimed to describe the migration coupling does not vanish in a homogeneous situation and its interpretation is thus erroneous.

$$-\sigma\frac{\partial\phi}{\partial z}\bigg|_{z=\mathrm{WE}} = \frac{1}{A(R_{\mathrm{ext}}+R_{\mathrm{cell}})}\phi|_{z=\mathrm{WE}} + \frac{1}{AR_{\mathrm{cell}}}\frac{R_{\mathrm{ex}}/R_{\mathrm{cell}}}{(1+R_{\mathrm{ex}}/R_{\mathrm{cell}})}(\langle\phi_{\mathrm{DL}}\rangle - \phi_{\mathrm{DL}}) - \sigma\left(\frac{\partial\phi}{\partial z}-\frac{\phi}{w}\right)\bigg|_{z=\mathrm{WE}} \tag{31}$$

When varying the external resistance between 0 and infinity, that is when going from the potentiostatic control (with the RE far away from the WE) to the galvanostatic limit, the strength of the global coupling varies between 0 and $(1/AR_{\mathrm{cell}}) = \sigma/w$. Hence, it is most pronounced for high electrolyte conductivity or a close distance between the working and the counter electrodes. Since the strength of the migration coupling is also proportional to the electrolyte conductivity, the global coupling will dominate pattern formation the more the closer the WE and the CE are. Again we see that because global coupling and migration coupling depend both on the cell geometry in a functionally different manner, their relative contribution has to be carefully determined for each electrochemical cell. Pattern formation might differ from cell to cell even if the WE and the composition of the electrolyte are the same.

When comparing the two global coupling terms in Eqs. (30) and (31), it is apparent that they are transformed into each other when setting $R_{\mathrm{ex}} = -R_{\mathrm{comp}}$. This means that the compensated part of the electrolyte resistance acts exactly like an external ohmic resistor with a negative resistance of the same magnitude would do. Furthermore, the negative sign of the resistance in the latter case changes the sign of the global coupling term, which leads to exactly the opposite repercussion on pattern formation. For a positive global resistance, R_{ex}, and thus also under galvanostatic control, the global coupling acts in a synchronizing manner, as also migration coupling does: differences between the local value of the double layer potential and the average value are damped by the coupling. In contrast, when the global resistance is negative, any difference between the local values of ϕ_{DL} and $\langle\phi_{\mathrm{DL}}\rangle$ become enhanced. Thus, the global coupling acts toward a destabilization of homogeneous states. It is thus desynchronizing and strongly promotes pattern formation. Thus synchronizing and desynchronizing global coupling, which are also termed positive and negative global coupling, respectively, have a complementary impact on pattern formation. We will demonstrate this below with many experimental examples.

When defining a global resistance R_G, with $R_G = R_{\mathrm{ex}} - R_{\mathrm{comp}}$, we arrive at a more general formulation that incorporates both a close reference electrode and an additional external resistance. In this case the global coupling term becomes

$$\frac{1}{AR_{\mathrm{cell}}}\frac{R_G/R_{\mathrm{cell}}}{(1+R_G/R_{\mathrm{cell}})}(\langle\phi_{\mathrm{DL}}\rangle - \phi_{\mathrm{DL}}). \tag{32}$$

3 Homogeneous Dynamics

In the preceding section we discussed the spatial coupling in electrochemical systems, which possesses several peculiar features. Its interplay with the homogeneous dy-

namics manifests itself in distinct and unusual patterns. Thus, before reviewing these patterns, it is useful to examine the characteristics of the homogeneous systems, which is the subject of this section.

In all the electrochemical oscillators we consider here, the electrode potential is an essential variable. Hence, also the nonlinear phenomena of the homogeneous systems are decisively determined by the evolution equation for ϕ_{DL}, which in turn depends on a delicate interplay of the interfacial kinetics and properties of the external electrical circuit. The interfacial kinetics of all electrochemical systems that exhibit nonlinear phenomena possesses one common property, namely a negative differential resistance (NDR) in the current-potential characteristic. The most frequent type of NDR is the so-called N-NDR, which is associated with an N-shaped current-potential curve. The other type of NDR systems possesses an S-shaped I/ϕ_{DL} characteristic and for this reason has been abbreviated S-NDR system. As will be discussed below, in N-NDR systems the double layer potential takes the role of the activator, i.e. the corresponding evolution equation possesses an enhancing, positive feedback. In contrast, in S-NDR systems ϕ_{DL} is the negative feedback variable, i.e. the inhibitor. Thus, in these two classes of electrochemical systems the mechanistic role of the variable on which migration and global coupling act is different, giving rise to contrasting spatiotemporal behaviors.

In the following the dynamic properties of N-NDR and S-NDR systems are compiled. We start out by reviewing causes for the occurrence of an N-shaped current-potential curve. Subsequently, the conditions for bistability in one-variable N-NDR systems are discussed. Then, two classes of N-NDR oscillators with dynamically different behaviors are introduced and finally the properties of S-NDR systems are summarized. For both types of NDRs, the most important representatives of the classes are reviewed, whereby the very recent examples that are not discussed in earlier review-type articles as well as those systems with which most of the spatial measurements were done are in the foreground.

3.1 N-NDR Systems: The Electrode Potential as Autocatalytic Variable

3.1.1 Causes for the Occurrence of a Negative Differential Resistance (NDR)

By far most electrochemical instabilities are associated with an N-shaped dependence of the current on the electrode potential. In fact, an N-type NDR forms very easily, and its abundant occurrence is also the reason why oscillations are so frequently encountered in electrochemical systems. The possible origins for an N-NDR were discussed in a concise way by Koper and we follow essentially the argumentation from Ref. [8]. Starting from a general expression for the reaction current

$$I_{reac}(\phi_{DL}) = nFA(\phi_{DL})c(\phi_{DL})k(\phi_{DL}) \tag{33}$$

where n is the number of electrons involved in the charge-transfer process, F Faraday's constant, A the available electrode area, k the rate constant, and c the

concentration of the reacting species at the electrode (i.e. at the location of the reaction), the faradaic impedance Z_F is given by

$$Z_F{}^{-1} = \frac{dI_{\mathrm{reac}}(\phi_{\mathrm{DL}})}{d\phi_{\mathrm{DL}}} = nF\left(ck\frac{dA}{d\phi_{\mathrm{DL}}} + Ac\frac{dk}{d\phi_{\mathrm{DL}}} + Ak\frac{dc}{d\phi_{\mathrm{DC}}}\right). \tag{34}$$

From Eq. (34) it follows that there are three possible origins for a negative impedance: (1) $dA/d\phi_{\mathrm{DL}} < 0$, (2) $dk/d\phi_{\mathrm{DL}} < 0$, and (3) $dc/d\phi_{\mathrm{DL}} < 0$. For all three cases there are numerous experimental examples.

(1) The available electrode area decreases with increasing polarization if a potential dependent adsorption of a species occurs that completely inhibits the reaction and the extent of the adsorption increases with increasing overpotential for the reaction. The most prominent example of such an "electrode poisoning" is the formation of oxide layers in many metal dissolution reactions [43]. But also the adsorption of anions or cations (which might be discharged upon adsorption) can completely inhibit a reaction. One recent example involves the inhibition of H_2O_2 reduction by upd hydrogen adsorption on Pt [44–46].

(2) The decrease of the electron transfer rate with increasing polarization can have two different origins: It can be caused by adsorbates that do not totally inhibit a reaction (in which case (1) would apply), but increase the activation energy for the reaction. Extensively studied examples are the reduction of metal ions in the presence of organic agents [47–49]. Furthermore, the negative sign of the potential dependence of the rate constant can also be the result of the potential-dependent desorption of a catalyst. The most famous and by now classical examples falling into this category are irreversible reduction reactions at Hg that are made reversible in the presence of halides or halide-like anions such as thiocyanate reduction [47–52]. More recently, it was discovered that during H_2O_2 reduction on Ag and Pt adsorbed OH, which is a reaction intermediate, has a catalytic effect for H_2O_2 reduction [45, 53–57]. Since the OH coverage of the electrode decreases with increasing overpotential, this autocatalytic rate enhancement gives rise to an N-NDR in the polarization curve.

(3) The decrease of the concentration of the electroactive species with increasing potential has to be attributed to double layer effects. As first pointed out by Frumkin [58], in dilute solutions the electron transfer rate is affected by variations of the potential in the double layer in two ways. The potential in the outer Helmholtz plane, ϕ_2, is due to the extension of the double layer not identical to the potential in the solution (at the end of the double layer), so that the effective driving force of the reaction is $\phi_{\mathrm{DL}} - \phi_2$. Furthermore, the concentration of ionic reactants in the reaction plane, c, is influenced by electrostatic effects and differs from the concentration just outside the double layer, c_0, by a Boltzmann term:

$$c = c_0 \exp(-nF\phi_2/RT) \tag{35}$$

where n is the (signed) charge number of the electroactive species. Hence, $dc/d\phi_{\mathrm{DL}}$ can become negative if cations (positive n) are oxidized positive to the

point of zero charge (pzc) or anions are reduced negative to the pzc at low ionic strength. (For high ionic strength, ϕ_2 becomes negligible.) There are numerous examples of an N-NDR during anion reduction and cation oxidation in the literature; many of them are compiled in Ref. [59]. The best known of these reactions is perhaps the reduction of peroxodisulfate, studied thoroughly by Frumkin and his school [60, 61] and later with the aim of formulating quantitative conditions for the occurrence of nonlinear phenomena by Wolf et al. [62].

3.1.2 Bistability

The simplest nonlinear phenomenon is bistability of stationary states. It arises already in one-variable systems. In N-NDR systems this variable is the double layer potential, ϕ_{DL}, and bistability is encountered under galvanostatic control and under potentiostatic control if the electrolyte resistance exceeds a critical value.

Bistability arises in N-NDR systems because the middle branch of an N-shaped polarization curve, i.e. the "NDR-branch", gives rise to a positive feedback under current control or under potential control provided R_Ω exceeds a critical value. This can be seen easily. Suppose one can prepare the system in a state on the middle branch of the I/ϕ_{DL} curve. Then, a small fluctuation of ϕ_{DL} to larger values causes a decrease of the current. In a galvanostatic experiment, this prompts a further increase in ϕ_{DL} that initially leads to yet a smaller current. Thus, the fluctuation is enhanced, growing "autocatalytically" until the system reaches a state on the outer branch of the N, which possesses a positive slope. In very much the same way a fluctuation to lower potentials is enhanced until the system reaches the other outer branch. This simple consideration already reveals that the NDR-branch is always unstable, and thus not accessible, in a galvanostatic experiment. Rather, depending on the sign of the fluctuations (or on the initial conditions) the system acquires either a state on the positively sloped branch at low double layer potential or a state on the corresponding branch at high double layer potential. Hence, the system is bistable.

Consider the situation under potentiostatic conditions. Here, the potential control takes care that the sum of the potential drop across the double layer, ϕ_{DL}, and through the electrolyte up to the position of the RE (and possibly additional external series resistances) is constant, i.e. that $U = \phi_{\mathrm{DL}} + I^* R_\Omega$ or $I = (U - \phi_{\mathrm{DL}})/R_\Omega$. R_Ω is the sum of the uncompensated cell resistance and possible external resistances and I the total current through the cell. Hence, a perturbation of a state on the NDR branch towards larger values of ϕ_{DL} causes, on the one hand, a decrease of the faradaic current I_F, and, on the other hand, a decrease of the current through the electrolyte, I. The charge balance through the cell, which can be readily obtained from the general equivalent circuit of an electrochemical cell (Fig. 8), tells us whether the fluctuation is enhanced or decays:

$$CA\frac{d\phi_{\mathrm{DL}}}{dt} = -I_F(\phi_{\mathrm{DL}}) + I = -I_F(\phi_{\mathrm{DL}}) + \frac{U - \phi_{\mathrm{DL}}}{R_\Omega}. \tag{36}$$

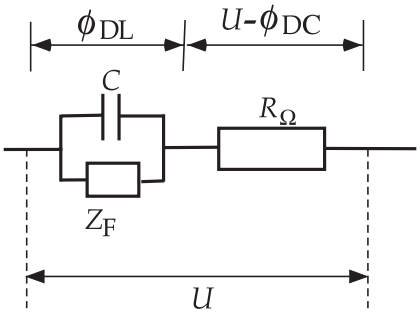

Fig. 8. General equivalent circuit of an electrochemical cell. C: double layer capacitance; ϕ_{DL}: potential drop across the double layer; Z_F: faradaic impedance; R_Ω: series resistance (comprising the uncompensated ohmic cell resistance and all external resistances). U is a potentiostatically fixed voltage drop. (It differs from the potentiostatically applied voltage by the constant potential drop across the RE; see footnote 3).

If the decrease of the faradaic current exceeds the decrease of the total current, ϕ_{DL} is driven towards larger values and the fluctuation is enhanced, otherwise it decays. Thus, whether the state is stable or not depends on the value of the ohmic resistance. For a sufficiently large resistance, states on the NDR branch are unstable and the system is again bistable. For vanishing resistance states on the NDR branch are stable and the system possesses a unique steady state. Recalling that the galvanostatic control mode is the limiting case of the potentiostatic control mode for $(R_\Omega, U) \to \infty$ with the preset current I given by the finite ratio of U and R_Ω, it is clear that when starting with the galvanostatic case and lowering R_Ω there will be a transition between a bistable and a monostable U/I curve.

If a qualitative change in the dynamic behavior is encountered when varying one parameter, a bifurcation occurs. The border between monostable and bistable behavior is formed by saddle-node (sn) bifurcations. At an sn bifurcation, two stationary states merge at the bifurcation point, disappearing when the parameter is changed in one direction and separating when it is changed in the other direction. In Fig. 9a, an sn bifurcation corresponds to the degenerate case where the load line, defined by $I = (U - \phi_{DL})/R_\Omega$, and the current-potential characteristic coincide in *two* points. From a linear stability analysis of Eq. (36) it can be readily shown that at a saddle node bifurcation [8]

$$|Z_F| = R_\Omega \quad \text{and} \quad Z_F < 0, \text{with } {Z_F}^{-1} = \left.\frac{\partial I_F}{\partial \phi_{DL}}\right|_{\phi_{DL}^{ss}}, \tag{37}$$

where Z_F denotes the (zero frequency) faradaic impedance. Within the bistable region, for a stationary state on the NDR branch, ϕ_{DL}^{ss}, Z_F is smaller than the ohmic resistance: $|Z_F(\phi_{DL}^{ss})| < R_\Omega$. Figure 9(b) illustrates how a current-voltage curve looks like for a system with an I/ϕ_{DL} characteristic as shown in Fig. 9a and an overcritical ohmic resistance. At the saddle node bifurcation, the system jumps from one outer branch to the other; the middle branch is not accessible.

For a given N-shaped I/ϕ_{DL} curve, there are two parameters that determine the bistable region, R_Ω and U. In the U/R_Ω parameter diagram, this region becomes broader while shifting toward larger values of U for increasing R_Ω, irrespective of the electrochemical reaction (Fig. 9c).

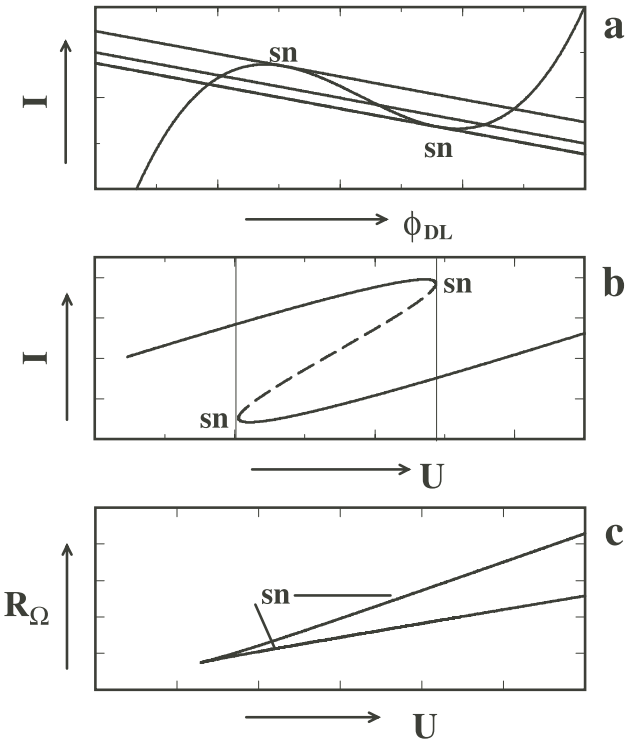

Fig. 9. (a) N-shaped current-potential curve and load lines (resulting from the external circuit) for three different values of the external voltage, U. The intersection of both curves are steady states. The two outer load lines mark the border of the bistable regime. (b) Bistable region in a current vs. external voltage plot referring to the situation shown in (a). (c) Location of the saddle-node bifurcation separating monostable and bistable regions in the U/R_Ω parameter plane. (sn = saddle-node bifurcation).

3.1.3 N-NDR Oscillators

Whenever there is at least one additional slow process that introduces a negative feedback loop into a system that possesses also an N-NDR, i.e. a fast-destabilizing feedback loop with ϕ_{DL} being a member of this loop, there is a parameter range for which the system exhibits sustained oscillations. According to the mechanistic features of the negative feedback, two types of oscillators are distinguished, which are termed N-NDR and HN-NDR oscillators [63, 64], or according to earlier notations NDR and HNDR oscillators [10, 12], class 2 and class 3 oscillators [11], as well as class 3 and class 4 oscillators [12], respectively. We use here the terminology N-NDR and HN-NDR systems exclusively, since, as will become obvious below, it is the most intuitive one. An apparent difference between the two system types is that HN-NDR systems oscillate under voltage and current control, whereas N-NDR oscillators oscillate only for a fixed outer voltage. In this subsection we discuss the characteristic properties of N-NDR oscillators, and in the next subsection those of HN-NDR oscillators.

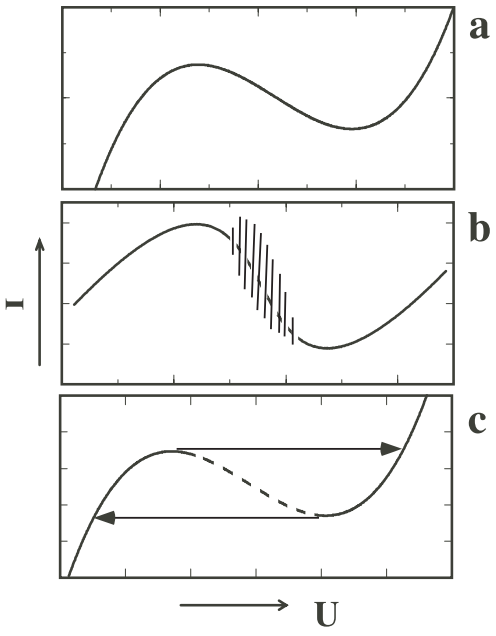

Fig. 10. Current-potential curves of an N-NDR oscillator (a) under strictly potentiostatic conditions; (b) under potentiostatic control with a finite electrolyte resistance; (c) under current control.

Let us start by summarizing the principle characteristics of N-NDR systems. N-NDR systems possess:

(a) an N-shaped current-potential curve for vanishing ohmic resistance R_Ω (Fig. 10a);
(b) oscillations around a branch of negative slope for intermediate values of R_Ω (Fig. 10b); and
(c) bistable behavior under current control and for large values of the electrolyte resistance (Fig. 10c).

Mass-transport Limited Negative Feedback

The perhaps simplest mechanism that complies with these features invokes a change transfer reaction possessing an N-shaped current-potential characteristics and transport limitation of the reactive species. The negative feedback loop results from the dependence of the current density on the concentration and the potentiostatic operation mode: consider again a stationary state on the NDR branch. A fluctuation of ϕ_{DL} to larger values causes a decrease of the faradaic current, such that the replenishment of the concentration of the reactive species in front of the electrode due to mass transport (for example diffusion) is larger than its consumption by the reaction. A larger concentration, however, leads to a larger faradaic current such that under potentiostatic conditions, where $U = \phi_{\mathrm{DL}} + IR_\Omega$, ϕ_{DL} is lowered again; its further growth is inhibited by the induced variations of c.

A general mathematical formulation and a detailed analysis of the dynamic behavior of this mass-transport induced N-NDR oscillations were given by Koper and Sluyters [8, 65]. The concentration of the electroactive species at the electrode decreases owing to the electron-transfer reaction and increases due to diffusion. For the mathematical description of diffusion, Koper and Sluyters [65] invoke a linear diffusion layer approximation, that is, it is assumed that there is a diffusion layer of constant thickness, and the concentration profile across the diffusion layer adjusts instantaneously to a linear profile. Thus, they arrive at the following dimensionless set of equations for the double layer potential, ϕ_{DL}, and the concentration at the electrode, c

$$\varepsilon \frac{d\tilde{\phi}_{\mathrm{DL}}}{d\tilde{t}} = -\tilde{c}\tilde{k}'(\tilde{\phi}_{\mathrm{DL}}) + \frac{\tilde{U} - \tilde{\phi}_{\mathrm{DL}}}{\tilde{R}_{\Omega}} \tag{38a}$$

$$\frac{d\tilde{c}}{d\tilde{t}} = -\tilde{c}\tilde{k}'(\tilde{\phi}_{\mathrm{DL}}) + 1 - \tilde{c}, \tag{38b}$$

where the tilde denotes again that the corresponding quantities are dimensionless. For their scaling, see [8].

The dynamic behavior of this system was examined using linear stability analysis [8] and is thoroughly discussed in the review articles [9, 10]. The results can be best summarized in a so-called two-parameter bifurcation diagram, in which, similar to phase diagrams, regions with qualitatively different behavior (states) are indicated. The dominant regimes of the N-NDR oscillator (Eqs. (38a,b)) are depicted in Fig. 11

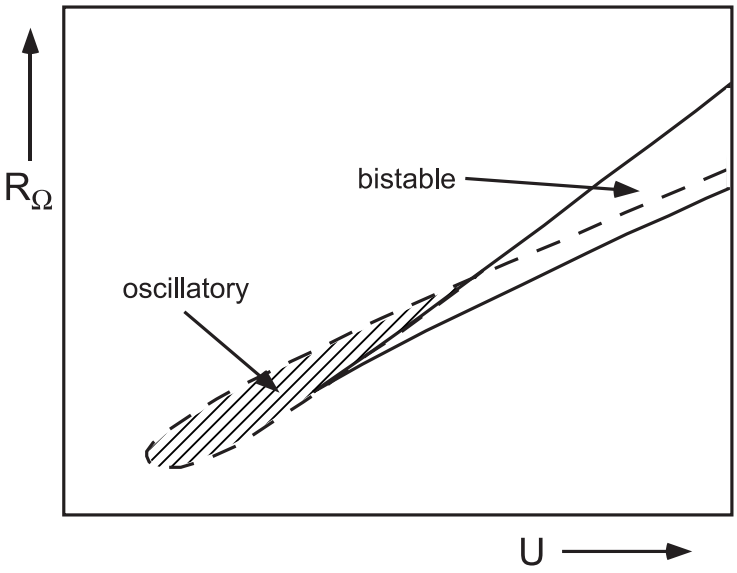

Fig. 11. Two-parameter skeleton bifurcation diagram of the N-NDR oscillator model (Eqs. 38a,b) in the U/R_Ω parameter plane. Solid line: location of saddle node bifurcations; dashed line: location of Hopf bifurcations.

in the U/R_Ω parameter plane. Bistable behavior is found in a V-shaped region, which lies diagonally in the voltage/resistance plane and opens toward large values of R_Ω and U. Oscillations are mainly found at smaller values of U and R_Ω in a region that loops around the tip of the V. Qualitative changes in the dynamics are called bifurcations and the parameter points at which they occur are bifurcation points. The line separating monostable and bistable behavior (solid line in Fig. 11) marks saddle-node bifurcation points (see also Section 3.1.1). The boundary to the oscillatory region is formed by Hopf bifurcations (dashed line). At a Hopf bifurcation the stability of a stationary state changes and a periodic orbit or limit cycle is born. A limit cycle is a closed loop in phase space toward which neighboring phase space points are attracted or from which they are repelled. If all neighboring points are attracted to the limit cycle, it is stable; otherwise, it is unstable (see Ref. [3]). The periodic orbit emerging from a Hopf bifurcation can be stable or unstable. In the N-NDR oscillator, for most parameter values for which the Hopf bifurcation loops around the tip of the bistable region, stable limit cycles emerge in the Hopf bifurcation. For a given N-shaped $\tilde{k}'(\phi_{\mathrm{DL}})$, Eqs. (38a,b) depend not only on R_Ω and U but also on ε, which describes the ratio of the times scales of potential and concentration changes. As already mentioned above, it is well known from the theory of activator-inhibitor systems that oscillations occur only if the characteristic time of the activator variable is shorter than the one of the inhibitor, i.e. the activator has to be the fast variable. Hence, to observe oscillations, ε should be sufficiently small, which is usually fulfilled in N-NDR systems.

The qualitative locations of Hopf and sn bifurcations are universal for all N-NDR systems, and the three main features of these systems, which were summarized above, can be directly read from the diagram (Fig. 11): For vanishing resistance, i.e. $R_\Omega \to 0$, the system is monostable and the current-voltage curve looks like the one in Fig. 10a. For an intermediate external resistance, we cross the Hopf bifurcation twice when varying U. A steady state that is destabilized in a Hopf bifurcation lies always on the NDR branch, resulting in a cyclic voltammogram as shown in Fig. 10b. And finally, at very large values of R_Ω, the two saddle-node bifurcations that encompass the ends of the hysteresis in a stationary current-voltage measurement, lie very far apart, ensuring an increasingly broader hysteresis in the cyclic voltammogram for an increasing R_Ω. Since the line of Hopf bifurcations ends at some intermediate values of R_Ω (one end meets the sn at the left side of the V; the other, outside the parameter range shown), oscillations do not exist under galvanostatic conditions under which the system always exhibits bistability (Fig. 10c).

Bifurcation Analysis Employing Impedance Spectroscopy

Experimentally, a corresponding bifurcation diagram can be constructed by measuring cyclic voltammograms at a very slow scan rate for various values of the R_Ω (most conveniently by employing an external resistor) and plotting the voltage values of the beginning and the end of the oscillatory region and the bistable behavior in a U/R-diagram. However, as Koper pointed out [9, 11] there is a more elegant way to experimentally determine the location of saddle-node and Hopf bifurcations employing

impedance spectroscopy. A system's frequency response over a sufficiently broad frequency range contains all the linear information about the system, and thus also about the (linear) stability of its steady states, the quantitative relation between the stability of the systems and the frequency response going back to Nyquist [66]. At a local bifurcation, small perturbations are neither enhanced nor damped (in the linear approximation). Hence, when driving the system externally with its eigenfrequency the system has zero real and imaginary impedance, and the intersection of the impedance spectrum with the origin of the complex plane indicates a bifurcation. If the intersection occurs at a finite perturbation frequency ω, the system exhibits a Hopf bifurcation; if the impedance spectrum ends in the origin for zero perturbation frequency, the system exhibits a saddle-node bifurcation [9, 11]. Under galvanostatic control, a more convenient way to formulate the criteria for the detection of bifurcations employs the admittance $Y(\omega) = dI/d\phi_{\mathrm{DL}}$, which becomes zero at a bifurcation. Hence, in summary [11]: "Under potentiostatic control

– a saddle-node bifurcation occurs if $Z(\omega) = 0$ for $\omega = 0$; and
– a Hopf bifurcation if $Z(\omega) = 0$ for $\omega = \omega_H \neq 0$.

Under galvanostatic control, an electrochemical system exhibits a

– a saddle-node bifurcation if $Y(\omega) = 0$ for $\omega = 0$; and
– a Hopf bifurcation if $Y(\omega) = 0$ for $\omega = \omega_H \neq 0$."

There is one further important practical aspect that has to be considered when taking this approach to performing an experimental bifurcation analysis: impedance measurements can only be carried out with stable stationary states; it is not feasible to measure unstable stationary states, or states close to a bifurcation. However, as we discussed above, N-NDR and HN-NDR systems become unstable due to ohmic losses in the circuit, whereas they are always stable for vanishing R_Ω. Being aware that an ohmic series resistor causes only a horizontal shift of the impedance spectrum in the complex plane, it is apparent that it is possible to infer about the existence of bifurcations from impedance measurements at sufficiently low solution resistance (or when invoking an *IR*-compensation, an option many potentiostats provide). This is illustrated with the schematic impedance spectrum shown in Fig. 12, which depicts a typical impedance spectrum of an N-NDR system. The spectrum possesses two

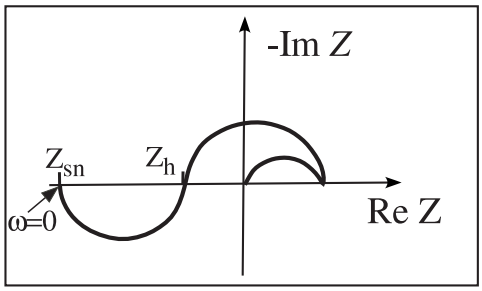

Fig. 12. Schematic impedance behavior of an N-NDR system for a (stable) steady state on the NDR branch.

intersections with the negative real impedance axis, one at a finite and one at zero excitation frequency. For this particular situation, the system exhibits a Hopf bifurcation for a resistance $R_\Omega = Z_h(\omega_h)$, whereby the oscillations emerge with the perturbation frequency ω_h. The resistance Z_{sn} is exactly equal to the inverse slope of steady-state polarization curve (see Eq. (37)). Moreover, upon insertion of an ohmic resistance R_{sn}, the impedance spectrum terminates in the origin of the complex plane and thus, at this particular combination of external voltage and cell resistance, the system undergoes a saddle-node bifurcation. Since the relation between impedance spectra and local bifurcations has been established, the power of impedance analysis for investigating local bifurcations has been exploited frequently, and quantitative relations between the width of the oscillatory region and the series resistance were established and helped clarifying apparent discrepancies between results obtained in different laboratories [67].

Experimental Examples for Mass-Transfer Limited Oscillations

For the oscillations we have discussed so far, the only requirement on the interfacial kinetics of the system is that it possess an N-NDR. Oscillations come into play as a result of the interplay of the interfacial kinetics with ohmic losses and transport limitations. Hence, for nearly every electron-transfer system that possesses an N-NDR, conditions can be set up under which stable limit cycles exist, and many experimentally observed oscillations could be traced back to this mechanism. Overviews of these experimental systems can be found in Refs. [9, 10, 68]. Here we compile only a few examples. Figure 13 shows experimental cyclic voltammograms of the reduction

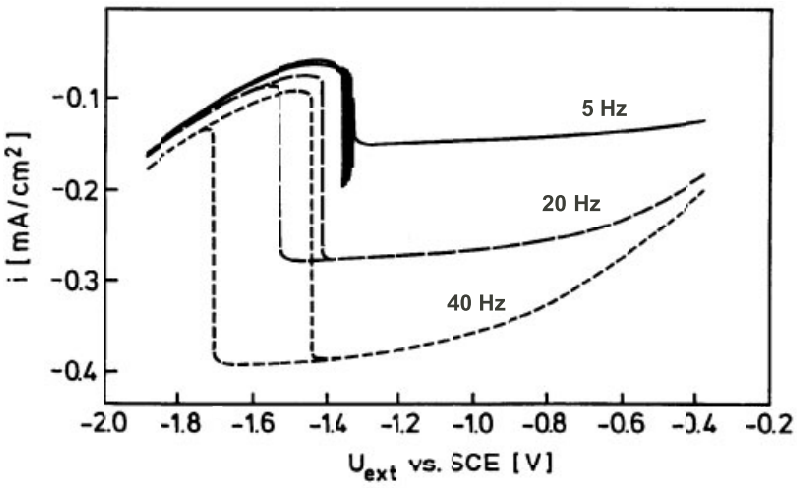

Fig. 13. Current-voltage curves of a rotating Ag electrode in a solution containing 1 mM $Na_2S_2O_8$ and 0.5 mM Na_2SO_4 (pH5) at three different rotation rates, f, of the electrode: solid line, f = 5Hz; long-dashed line, f = 20Hz; short dashed line, f = 40Hz [166].

of $S_2O_8{}^{2-}$ at a rotating Ag electrode for three different rotation rates. For high rotation rates, and thus an effective mass transport, the system exhibits bistable behavior. The width of the bistable region becomes smaller and shifts towards more positive voltage for decreasing rotation rates. Finally, for the slowest mass transport, the system exhibits oscillations around the branch that has a negative polarization slope. These dynamic features are in agreement with the simple N-NDR oscillator model based on transport limitation, suggesting strongly that they are indeed the result of the interaction of the N-shaped current-potential curve (arising due to double layer effects), the external electric circuitry and slow transport [62].

Other quite recent examples stem from the reduction of H_2O_2 on Ag and Pt electrodes. On Ag [53, 54] as well as on atomically flat Pt(111) electrodes [56, 69] adsorbed OH_{ad} was proved to act as a catalyst for H_2O_2 reduction. In the course of the normal reduction of H_2O_2, the unstable species OH_{ad} is produced as an intermediate:

$$H_2O_2 + H^+ + * + e^- \xrightarrow{k_1} OH_{ad} + H_2O \tag{R3.1}$$

$$OH_{ad} + H^+ + e^- \xrightarrow{k_2} * + H_2O \tag{R3.2}$$

In a parallel reaction the adsorbate, OH_{ad}, acts as a catalyst for the H_2O_2 reduction and is thus an autocatalytic species:

$$H_2O_2 + H^+ + OH_{ad} + * + e^- \xrightarrow{k_a} 2OH_{ad} + H_2O. \tag{R3.3}$$

Since OH_{ad} desorbs with increasing overpotential (i.e. increasing negative charge on the electrode), the reaction rate shows a maximum at some intermediate value of the overpotential manifesting itself in an N-NDR in the current potential curve. A cyclic voltammogram of the reduction of H_2O_2 on a rotating Ag electrode is reproduced in Fig. 14a. It exhibits a pronounced N-NDR around which the system oscillates.

The impedance spectrum shown in Fig. 14b has exactly the characteristics typical for N-NDR oscillators. It intersects the real axis at negative values at finite perturbation frequency; the form of the impedance curve at low frequency suggests that it also terminates on the negative real impedance axis at larger absolute impedance values indicating that the system is bistable at higher electrolyte resistance. Current-voltage plots and impedance measurements could be well reproduced with a model based on the mechanisms (R3.1–3.3) and taking into account the diffusion of H_2O_2 [53, 54].

During H_2O_2 reduction on Pt in acidic solutions Nakato and colleagues observed an extremely rich dynamic behavior [44–46, 55–57, 69–73]. In part this can be traced back to the existence of two distinct NDR regions, which can be seen in the cyclic voltammogram obtained on atomically flat Pt(111) for a low concentration of H_2O_2 (Fig. 15). The N-NDR at more negative values of the potential (between 0.1 and 0 V vs. NHE) is caused by the inhibition of H_2O_2 reduction due to underpotentially deposited hydrogen. The second N-NDR region around 0.25V vs. NHE is due to the above-discussed autocatalytic effect. On Pt, however, the autocatalytic effect is only pronounced on atomically flat (111) surfaces. It disappears when a Pt(111) electrode

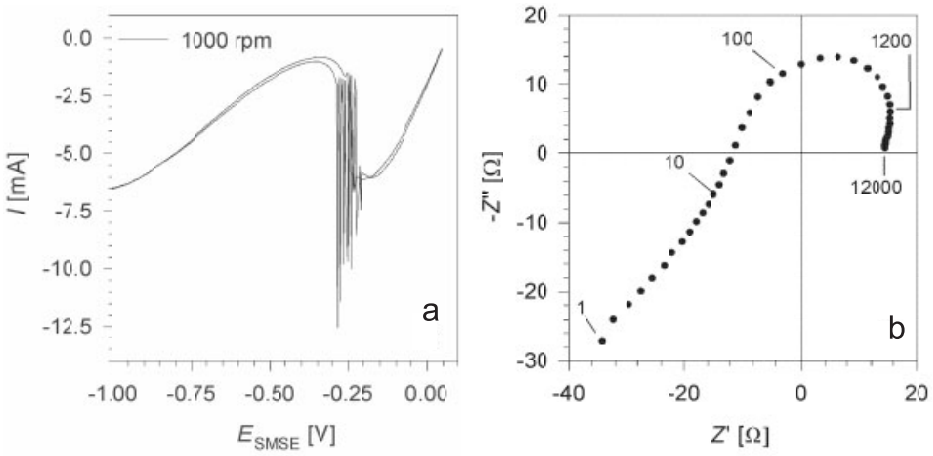

Fig. 14. (a) Cyclic voltammogram of the reduction of 0.02 M H_2O_2 on a rotating Ag(pc) in 0.1 M $HClO_4$; scan rate 50 mV s^{-1}. (b) Impedance spectrum in the complex impedance plane of Ag(pc) in the same electrolyte measured at $E_{SMSE} = -0.20$ V and a rotation speed lower than in (a) where the NDR branch is stable. Numbers indicate the frequency ν. (Reproduced from C. Eickes, K. G. Weil and K. Doblhofer, PCCP 2 (2000), 5691–5697 by permission of The Royal Society of Chemistry on behalf of the PCCP Owner Societies.)

is roughened by oxidation-reduction cycles and is absent on the other low-indexed single crystal faces and on polycrystalline Pt. Nakanishi et al. [69] attribute the autocatalytic effect of OH^- to the fact that, once OH_{ad} is formed, it polarizes the neighboring Pt atoms positively. This promotes the O–O bond cleavage at these

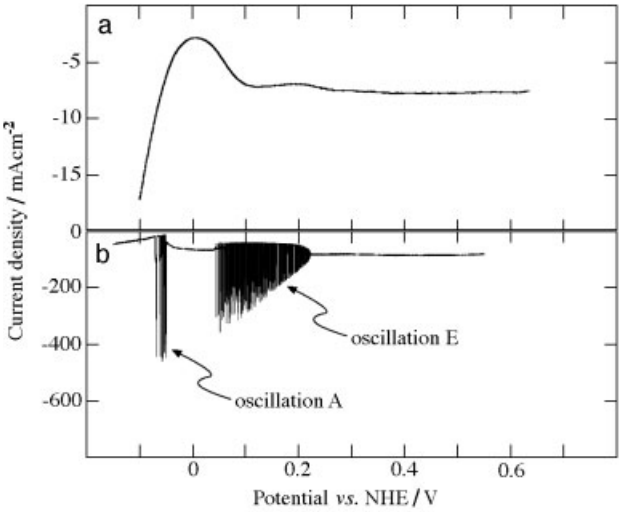

Fig. 15. Current density vs voltage curves for an atomically flat Pt(111) electrode. (a) 0.2 M $H_2O_2 + 0.3$ M H_2SO_4; scan rate: 10 mV s^{-1}. (b) 1 M $H_2O_2 + 0.3$ M H_2SO_4; scan rate: 5 mV s^{-1}. (Reproduced with permission from S. Nakanishi, Y. Mukouyama, K. Karasumi, A. Imanishi, N. Furuya, Y. Nakato, J. Phys. Chem. B 104 2000, 4181–4188, © (2000) American Chemistry Society.)

positively polarized sites (given that H_2O_2 adsorbs with the oxygen atoms directed toward the Pt surface.) The authors explain the missing catalytic effect on the other Pt surfaces with the smaller number of "pairs of Pt atoms" adjacent to an adsorbed OH species. It is interesting to note that the NDR is strongly enhanced when adding small amounts of iodide to the electrolyte showing an extension of its region toward positive potential, and giving also rise to a considerable NDR (and also oscillations) on Pt(100). The explanation is again through the polarization of Pt atoms in the next neighborhood to adsorbed iodine.

When increasing the H_2O_2 concentration around both NDR branches, stable oscillations occur (Fig. 15b), in accordance with the properties of model Eq. (38a,b). The authors termed the limit cycles around the more negative N-NDR oscillations A, the ones around the positive N-NDR oscillations E. Both oscillatory regions were also obtained in a model based on the mechanistic steps discussed above as well as further reaction steps that improve the quantitative agreement between experiments and simulations [69] but do not introduce qualitatively new features compared to our model. Below we discuss other results by Nakato and colleagues that exemplify the type of mechanistic ingredients necessary to turn an N-NDR into an HN-NDR, and thus to qualitatively change the dynamics of the electrochemical system.

Restrictions of the Two-Variable Model

Despite of the great success of the linear diffusion layer model in predicting simple periodic oscillations nearly quantitatively in many systems, one should be aware that it is a simplification that in some parameter ranges fails to reproduce even qualitatively the dynamics which is obtained when the original diffusion equation is taken into account. Instead of an instant approach of the linear steady-state concentration profile, curved profiles will establish due to a delayed response of the diffusion layer to concentration changes at the electrode. As Koper and Gaspard [50] showed, this delayed response manifests itself in an additional degree of freedom in the dynamics and more complex oscillation, such as chaotic or mixed-mode oscillations, may arise where simple oscillations are obtained with the original model [50, 51, 74, 75]. Qualitatively, the intricate sequences of complex oscillations, which characteristically occur close to the onset of oscillations and cover only a small fraction of the total oscillatory region, are already captured when introducing a second diffusion layer. Thus, all the oscillators considered so far will show complex motions in some parameter ranges that are caused by the slow transport; further interfacial processes are not involved. (Of course, such processes that bring about additional complex oscillations might also exist.)

Restrictions of Alternative General Definitions of N-NDR Oscillators

N-NDR oscillations can also arise due to mechanistic steps other than transport limited diffusion. Strasser et al. [12] make an attempt to formulate "necessary and sufficient mechanistic ingredients of N-NDR oscillators". According to their definition, the common features of these mechanisms are that

(a) the slow species, such as the concentration of a reactive species in the reaction plane or the coverage of an adsorbate, is consumed by *all principal charge transfer processes* and it is replenished by *potential-independent* processes [in the above model, this step is diffusion]; and
(b) at least one of the charge transfer processes exhibits an N-shaped I/ϕ_{DL} profile.

However, these criteria are not as general as claimed by the authors. As is demonstrated in the next section, metal dissolution reactions that oscillate at the active passive transition possess all the characteristics of N-NDR oscillators, but do not comply with Strasser et al.'s mechanistic ingredients. Hence, the above conditions (a) and (b) are sufficient, but not necessary.

Oscillations at the Active|Passive Transition in Metal Electrodissolution

The perhaps best-known electrochemical oscillations at all are those occurring at the active/passive transition of metals. Intense investigations of their dynamic behavior were initiated by Ostwald at the beginning of the twentieth century [76–78] and put forth by Bonhoeffer [79–81] and Franck [82–86] with remarkable success, given that at that time the modern concepts of nonlinear dynamics were not yet developed. Franck, in collaboration with FitzHugh [86], also formulated the first mathematical description of an electrochemical oscillating reaction, namely the oscillating iron dissolution in sulfuric acid. Although Franck and FitzHugh were mistaken in some features of the model, most importantly the positive feedback mechanisms [87], which is in the original model of chemical nature, but was shown to be due to ohmic losses in connection with an N-shaped polarization curve [88], their most important idea concerns the origin of the negative feedback loop, which is still believed to be correct. It involves the shift of the Flade potential, i.e. the equilibrium potential of the oxide formation, due to changes in the surface pH.

A useful starting point of a discussion of the fundamental mechanism that is believed to produce oscillations at the active/passive transition of many metal dissolution systems, among them iron dissolution in H_2SO_4, Co dissolution in H_3PO_4 [89, 90], or Zn dissolution in NaOH [91] is the cyclic voltammogram shown in Fig. 16. It was obtained during the anodic polarization of Fe in sulfuric acid. At low overpotentials the electrooxidation of the electrode follows Tafel's law with an exponential relationship between current and electrode potential. Positive to the Tafel region, a mass-transfer limited region follows in which the current is independent of the applied voltage. The transport limitation is caused by the precipitation of a $FeSO_4$ film, which keeps the Fe^{2+} ion concentration in front of the electrode below a threshold. When the potential exceeds a critical value, the formation of iron oxide sets in, which causes a transition from the active dissolution state to a passive state in which the electrode is covered by a nearly perfectly insulating oxide film. Russel and Newman [88] presented experimental evidence that when correcting for the IR-drop in the electrolyte, the steady-state polarization curve is single-valued, possessing a region with a steep NDR. Owing to the steepness of the NDR, which is a caused by the high reaction rates, the NDR region is destabilized already in concentrated acidic sol-

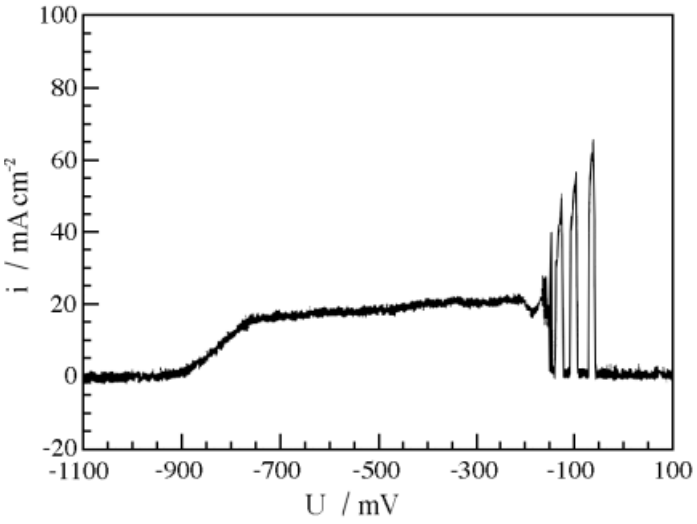

Fig. 16. Cyclic voltammogram of Fe in 2N H_2SO_4; scan rate 0.5mV s^{-1}. (Courtesy of J. L. Hudson.)

utions. According to the ideas of Franck and FitzHugh, the high reaction rate in the active state causes protons to migrate from the surface to such a degree that the pH at the surface becomes considerably higher than in the bulk solution. When the active electrode experiences a transition into the passive state, the proton concentration will attain its bulk value again by back-diffusion of H^+. The potential at which the oxide film forms depends on the electrode surface pH according to the reaction

$$\mathrm{Me} + n\mathrm{H_2O} \underset{k_r}{\overset{k_o}{\leftrightarrow}} [\mathrm{MeO}_n]_{\mathrm{ads}} + 2n\mathrm{H}^+ + 2n\mathrm{e}^-, \tag{R3.4}$$

where Me stands for "metal", and $[MeO_n]$ is the passivating oxide layer. Thus, at a low pH (and hence in the passive state) the equilibrium potential of reaction (R 3.4), which is also known as the Flade potential, U_F, is more anodic than at high pH, that is in the active state. In this mechanism, the proton concentration in the reaction plane provides the negative feedback that, together with the autocatalysis caused by the N-NDR, gives rise to oscillations.

The simplest model describing the active/passive oscillations is used by Birzu et al. [27–29] to model spatiotemporal patterns during metal dissolution (see Sec. 4.1). The homogeneous dynamics of the model reads:

$$CA\frac{d\phi_{\mathrm{DL}}}{dt} = -nFk(\phi_{\mathrm{DL}}, c) + \frac{(U - \phi_{\mathrm{DL}})}{R_\Omega}, \tag{39a}$$

$$\frac{dc}{dt} = \frac{2D}{\delta^2}(c - c_b) + \frac{2Fu_{\mathrm{H}}c}{\delta}\,\frac{U - \phi_{\mathrm{DL}}}{w}. \tag{39b}$$

Here, c is the surface concentration of protons, δ the Nernst diffusion layer thickness,

u_H the mobility of protons and w the distance between the working and the reference electrodes. The other symbols have the same meaning as above. Obviously, this model is based on many simplifications, the most important ones being: a) a steady-state approximation of the oxide coverage can be made such that $k(\phi_{\mathrm{DL}})$ exhibits a steep decrease at some value of ϕ_{DL}; b) the influence of the salt film [different from giving rise to a mass-transport limited plateau which is included in the functional dependence of $k(\phi_{\mathrm{DL}})$] on the reaction current can be neglected. This includes the neglect of any ohmic resistance of the salt film; c) the metal ion concentration in front of the electrode can be neglected; and d) the system is strictly electroneutral, which also implies that the conductivity is uniform within the electrolyte. Because of the large current densities, this seems to be the most questionable simplification. However, the good agreement between the qualitative dynamic behavior of experiments and calculations on the one hand, and the much larger complexity a more realistic and quantitative model would require, seem to justify this approach.

A refined model that takes into account a simple kinetics for the formation of the salt layer, leading to a refined description of the dissolution rate, as well as the change of the surface metal ion concentration with time due to salt layer formation, its dissolution and migration of the metal ions, was proposed by Koper and Sluyters [87]. It improves the quantitative description and removes some of the critical (since not strictly physical) assumptions from above. However, the positive and the basic negative feedback loop[8], and thus the heart of the model, are identical to the ones in the simplified model. For this reason we refrain from discussing the model in more detail. However, notice that the objections against model II in [87] do not apply to Eq. (39). In model II it was assumed that the protons carry all the current, which caused negative surface proton concentrations in certain phases of the oscillations, a clearly unphysical solution. In Eq. (39) the migration current is formulated through the mobility and the concentration of protons, which excludes negative surface concentrations *a priori*.

3.1.4 HN-NDR Oscillators

The second class of systems, in which the positive feedback arises due to an N-shaped current-potential curve, is called hidden N-NDR (HN-NDR) class, for reasons that become clear soon. Let us again start our discussion of their dynamic behavior by compiling the crucial properties of HN-NDR system:

(a) In HN-NDR systems the branch of interest of the *stationary* I/ϕ_{DL} curve possesses a positive slope[9], i.e. for vanishing ohmic series resistance, all states on this branch are unconditionally stable (Fig. 17a) and the zero frequency impedance, $Z(\omega = 0)$ is strictly positive (Fig. 17d);

[8] This three variable model contains a second feedback loop, which manifests itself in the occurrence of mode oscillations.

[9] This branch is often adjacent to an N-NDR branch, which is, however, not necessary for the dynamic behavior of HN-NDR systems.

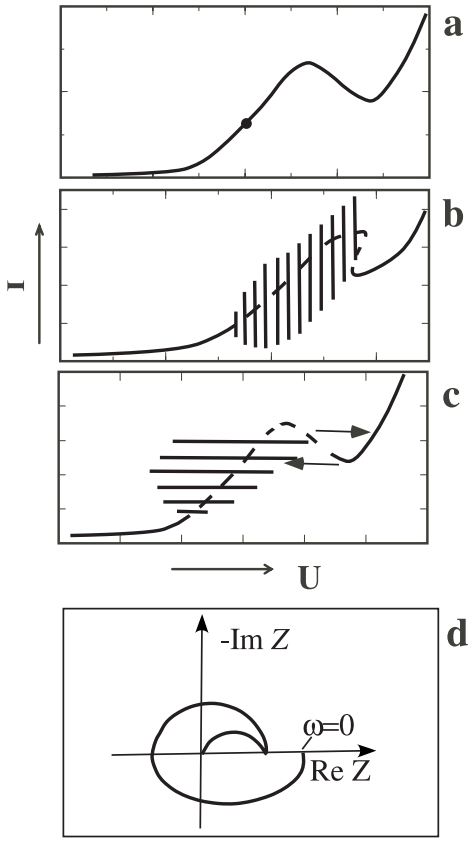

Fig. 17. Characteristic I-U curves of HN-NDR systems (a) under potential control for vanishing ohmic series resistance, R_Ω; (b) under potential control for intermediate values of R_Ω; and (c) under current control. (d) Typical impedance spectrum of an HN-NDR system in the complex impedance plane at the point indicated in (a).

(b) Current oscillations occur around a branch of positive slope if the ohmic series resistance, R_Ω, exceeds a critical value, $R_{\Omega,\mathrm{crit}}$ (Fig. 17b). The oscillations are the manifestation of a negative real faradaic impedance, $\mathrm{Re}(Z(\omega)) < 0$, for a finite excitation frequency ω (Fig. 17d); and
(c) HN-NDR systems oscillate under galvanostatic control (Fig. 17c).

Thus, the fundamental difference between N-NDR and HN-NDR systems is that the former's stationary polarization curve exhibits a range of negative real impedance, whereas for the latter the zero-frequency impedance is strictly positive in the potential region of interest. From this observation one might get the impression that the mechanisms of electrode reactions are fundamentally different for systems in the two groups. But in fact it is only a small step, or more precisely, one additional potential-dependent process, that transforms an N-NDR system into an HN-NDR system. Formally, any HN-NDR system is composed of a subsystem with an N-shaped stationary polarization curve whose NDR is hidden by at least one further *slow and potential-dependent* step of the interfacial kinetics of the total system. This step dominates the faradaic impedance at low perturbation frequencies, whereas at higher

excitation frequencies the negative faradaic impedance of the fast subsystem dominates the system's behavior. In particular its interaction with the ohmic drop forms a positive feedback loop. The destabilizing elements are thus in N-NDR and HN-NDR systems identical, the autocatalytic (activator) variable is the double layer potential, ϕ_{DL}, the difference stemming from properties of the slow, negative feedback.

Prototype Model

The by far most widespread mechanism by which an N-NDR is hidden is the adsorption of a species that inhibits the main electron-transfer process. The species might be dissolved in the electrolyte, e.g., it might be the anion of the supporting electrolyte, or it is formed in a side reaction path, as it is the case in nearly all oxidation reactions of small organic molecules. Before we introduce specific examples of this type of HN-NDR oscillators, it is useful to study the dynamics of a prototype model. This will then help us to identify the essential mechanistic steps in real systems whose quantitative description requires more variables such that the basic feedback loops are not as obvious.

Consider an electrolyte that contains an electroactive species E, which is either oxidized or reduced, and a species P with a potential-dependent adsorption isotherm. In the absence of species P the I/ϕ_{DL} curve be N-shaped (Fig. 18a, dashed line). Furthermore, the isotherm of P be such that its coverage decreases with increasing overpotential for the conversion of E somewhere in the N-NDR range of $k\ (\phi_{\mathrm{DL}})$ (Fig. 18a, solid line). In addition, adsorbed P inhibits the electrochemical conversion of E (Fig. 18b). The following set of equations represents the simplest formulation of the mechanism:

$$CA\frac{d\phi_{\mathrm{DL}}}{dt} = -nFk'(\phi_{\mathrm{DL}})(1-\theta) + \frac{U-\phi_{\mathrm{DL}}}{R_{\Omega}} \tag{40a}$$

$$\frac{d\theta}{dt} = k_P[\theta_0(\phi_{\mathrm{DL}}) - \theta], \tag{40b}$$

where θ denotes the coverage of species P and $\theta_0(\phi_{\mathrm{DL}})$ the potential-dependent equilibrium value of θ. Thus, the term $[\theta_0(\phi_{\mathrm{DL}}) - \theta]$ represents the deviation of the actual coverage from its equilibrium value, and the rate constant k_p determines how fast the coverage relaxes to its equilibrium value.

The second equation introduces the negative feedback necessary for oscillations to occur: Suppose the system attains a state on the I/ϕ_{DL} curve where the steady state coverage is between 0 and 1. Then a fluctuation of ϕ_{DL}, let's say to *larger* values, leads at first to a *smaller* current, since we are at potentials where $k\ (\phi_{\mathrm{DL}})$ has a negative slope and the coverage reacts much slower on a change of ϕ_{DL} than the electron-transfer reaction. Together with the potentiostatic or galvanostatic external constraints, this initiates the "usual" N-NDR induced, positive feedback, i.e. an increasing ϕ_{DL} and, hence, a further decrease of I. With a delayed response, however, also θ will adjust to the new values of ϕ_{DL}; its desorption causes an increase in the

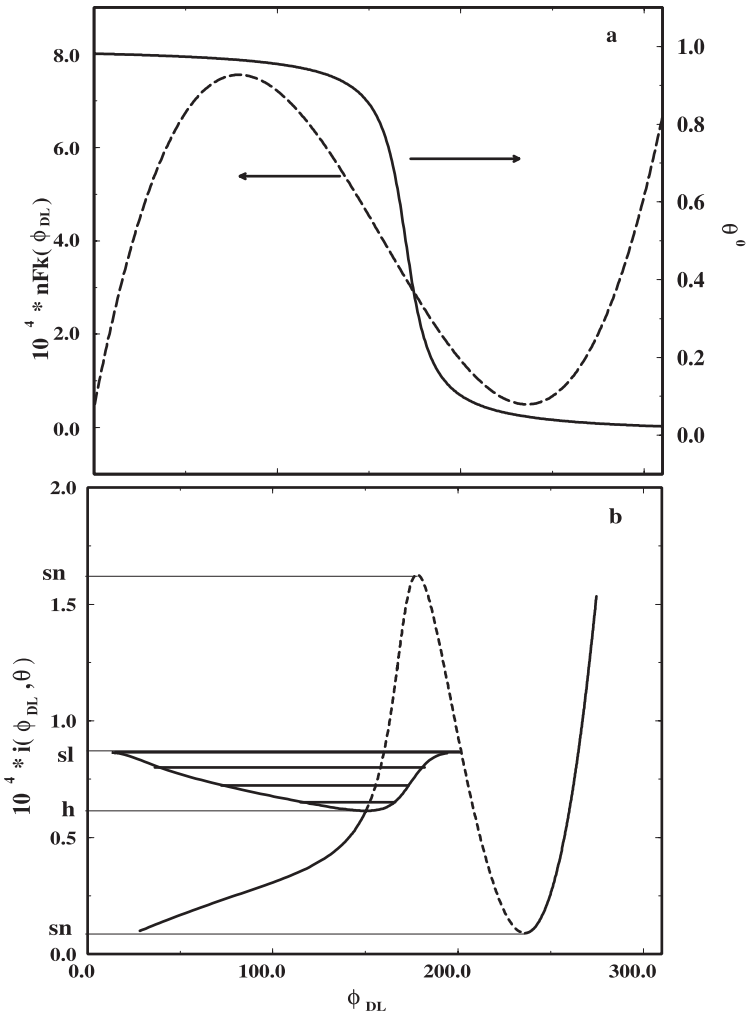

Fig. 18. (a) Example of a combination of a reaction current $nFk(\phi_{DL})$ (dashed curve) in the absence of an inhibiting species P [Eq. (40a), $\theta = 0$] and an equilibrium coverage of the species P (solid curve) that admits a Hopf bifurcation. (b) Stationary polarization curve in the presence of E and P for overcritical resistance. The dashed line indicates where the stationary state is unstable under galvanostatic conditions. The horizontal bars display the amplitudes of the oscillations. sn: saddle-node bifurcation; sl: saddle-loop bifurcation; h: Hopf bifurcation.

current density, and thus counteracts a further growth of ϕ_{DL}, which introduces a negative feedback loop into the system. As was emphasized already, the presence of a positive and negative feedback loop in general gives rise to oscillatory behavior in some region of the parameter space.

The crucial difference between the prototype HN-NDR model (Eq. (40)) and N-NDR model (Eqs. (38 a,b)) is that the potential-dependent terms of θ do not

coincide with those determining the reaction current. This gives the system the necessary "freedom" to oscillate also under galvanostatic conditions [92].

The main results of the theoretical analysis of HN-NDR models of the "reaction-inhibition" type are contained in the one- and two-parameter bifurcation diagrams reproduced in Figs. 18(b) and 19, respectively. Fig. 18b shows the stationary current-potential curve of the model system (Eqs. (40a,b)). The dashed line denotes steady states that are unstable under galvanostatic control; the solid line, those that are stable. Obviously, the steady-state branch with a *positive* slope becomes unstable (owing to the hidden N-NDR of k (ϕ_{DL})) and oscillations are born in a Hopf bifurcation. The oscillations, indicated by the horizontal bars in Fig. 18b, exist in a certain current interval until their amplitude becomes so large that the limit cycle collides with the saddle point through which it is destroyed. This type of bifurcation is called saddle-loop bifurcation. Obviously, the saddle point lies on a branch of the I/ϕ_{DL} curve with a negative slope. A comparison with Fig. 18a shows that the NDR part arises because the inhibitor P has become desorbed completely at potentials at which k (ϕ_{DL}) still exhibits a negative slope such that in this potential range the I/ϕ_{DL} characteristics of the full system is practically identical to the one of the fast subsystem. According to the explanations above, under galvanostatic control, the NDR-branch is always unstable.

From Fig. 18b it is clear that under galvanostatic conditions the limit cycle coexists with a stationary state at high overpotentials. The latter is the only attractor at large current densities. Hence, when the current density is increased above the value of the saddle-loop bifurcation, the potential jumps to a steady state far in the anodic region. Once the system has acquired the anodic steady state, it will stay on this branch as the current density is lowered until the stationary state disappears in a saddle-node bifurcation.

The qualitative location of the oscillation region in the U/R_{Ω} parameter plane is shown in the two-parameter bifurcation diagram reproduced in Fig. 19. The most

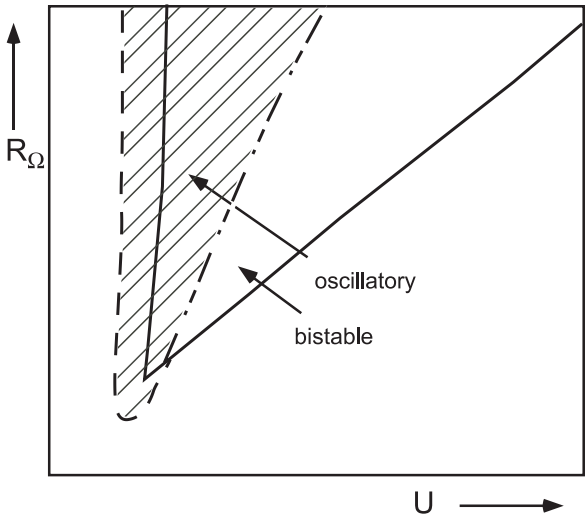

Fig. 19. Skeleton bifurcation diagram in the U/R_{Ω} parameter plane of an HN-NDR system of the "reaction-inhibition" class (such as the prototype model Eqs. (40a,b)). The solid, dashed and dotted-dashed lines denote the location of saddle-node, Hopf and saddle-loop bifurcations, respectively.

important difference to the corresponding bifurcation diagram of N-NDR oscillators is that the oscillatory region is not limited towards large values of the ohmic series resistance, and oscillations exist also under galvanostatic conditions (infinite R_Ω).

Besides the potential-dependent adsorption of a poison, i.e. a species that is different from the electroactive species or current carrier, other mechanisms are discussed that may hide a region of negative differential resistance and thus give rise to oscillations on a branch of the I-U curve with positive slope. According to specific mechanistic features, a subdivision of HN-NDR oscillators was proposed into originally three subclasses [12].

The first model in which a hidden NDR was identified as the source of instability was based on a hypothetic mechanism that involves the potential-dependent adsorption of the electroactive species and the electron-transfer reaction from the adsorbed state [92]:

$$E + * \longleftrightarrow E_{\text{ads}}$$

$$E_{\text{ads}} + e^- \rightarrow P + *$$

The bifurcation diagram in the U/I parameter plane of this ''adsorption/reaction'' mechanism, which was designated subclass 1, is the same as the one of the above discussed ''reaction-poison'' mechanism that forms subclass 2.

Starting again from our prototype N-NDR oscillator (Eqs. (38a,b)), subclass 3 arises when an additional faradaic reaction takes place at potentials in or close to the range in which the ''original'' faradaic process [12, 93]. Thereby, this additional reaction should be an oxidation (reduction) current if the original process is an oxidation (reduction) reaction. Clearly, when the increase in the current density of the additional process is larger than the decrease in the NDR branch of the original process, the NDR is hidden. Model calculations confirm that such a superposition of faradaic currents in addition with the slow recovery of the electroactive species that is associated with the NDR gives rise to galvanostatic oscillations. The succession of bifurcations when increasing the external voltage, however, is different compared to the other two subcategories, thus yielding also a qualitatively different bifurcation diagram in the U/R_Ω parameter plane.

This mechanism was originally derived by Strasser et al. [93] to model oscillations during the galvanostatic reduction of iodate where, according to the authors, the NDR is due to Frumkin repulsion and the second faradaic reaction is hydrogen evolution. The simulations compare favorable with the experiments. The authors conjecture that also the galvanostatic potential oscillations observed during the electrooxidation of $Fe(CN)_6^{4-}$ concomitant to O_2 evolution on a Pt electrode, and during the reduction of $Fe(CN)_6^{3-}$ concomitant to H_2 evolution arise due to the same mechanism [94]. However, Li et al. [95] presented experimental evidence that for the latter system there is no oscillatory instability when replacing the gas evolution reactions by another faradaic process that does not involve the formation of gas bubbles. As discussed in Ref. [95] this strongly points to the essential role convection may play in the oscillation mechanism of all the mentioned oscillators. The authors suppose that the oscillations arise because of a ''depletion-convection'' mechanism: At low overpotentials, the concentration of the electroactive ion at the electrode

surface depletes due to reaction, which leads to a shift of the potential towards larger overpotentials at which the second reaction, and thus gas-bubble formation sets in. The arising convection causes an enhanced mass transport and thus the replenishment of the ion concentration at the electrode surface resulting in an increased current and thus a backward shift of the reaction. As plausible as this mechanism might be at first sight, it lacks an autocatalytic process and will therefore not lead to oscillations, as also pointed out in Ref. [96]. Hence, the origin of the potential oscillations during iodate reduction or $Fe(CN)_6^{4-}$ oxidation remains obscure.

So far, there are no unambiguous experimental examples for subcategories 1 or 3. More recently, an HN-NDR-type oscillation was observed during H_2O_2 reduction on Pt whose mechanism did not fall into any of the three subdivisions, and thus the classification scheme was enlarged [57]. The features of this subclass will be discussed below in connection with oscillations during H_2O_2 reduction. The discovery of further basic mechanisms is to be expected. As their number increases, other criteria that are common to a few of such subclasses might turn out to constitute a superior basis for subdivision. One such criterion might be the two-parameter bifurcation diagram in the plane spanned by the "electrical parameters" U and R, which are identical in two of the three originally proposed subcategories.

In the following, experimental examples of HN-NDR oscillators will be discussed in which the essential elementary steps of the oscillation mechanism appear to be unequivocally uncovered.

H_2 Oxidation in the Presence of Poisons

The oxidation of hydrogen on Pt in the presence of electrosorbing cations, such as Cu^{2+}, Ag^+, Cd^{2+}, or Bi^{3+} and strongly adsorbing anions, examples are Cl^- and Br^-, constitutes the first experimental example for which the importance of the hidden negative differential resistance for oscillatory behavior was recognized [97, 98]. Furthermore, the individual steps of the oscillation mechanism can easily be studied separately, allowing easy assignment of the essential features of the mechanism. Therefore, this system represents an ideal experimental model for illustrating the properties of HN-NDR oscillators. However, its importance goes far beyond historical and didactical aspects. A completely analogous mechanism seems to be operative when the H_2 gas, which is bubble through the cell, is contaminated with traces of CO. Since in H_2/O_2 low-temperature fuel cells CO impurities in the H_2 feed are the main source of voltage losses at the anode, an understanding of the dynamic behavior of $H_2|CO$ mixtures is also of considerable practical importance.

The oxidation of H_2 in the presence of electrosorbing cations and anions was first studied by Horányi and Visy [99] with the goal to demonstrate that oscillations during hydrogen oxidation must not necessarily be accompanied by oxide formation. This system was subsequently investigated by Kodera et al. [100–102] and by Wolf, Krischer et al. [97, 98, 103–106]. Most of the experiments were carried out in solutions containing Cu^{2+} as the electrosorbing species as well as a small amount of Cl^-. Thus, parallel to the following reaction steps, responsible for the oxidation of H_2,

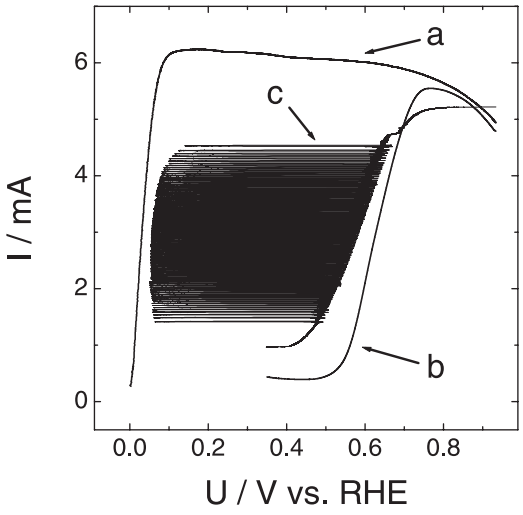

Fig. 20. Experimental I/U curve obtained during the H_2 electrooxidation on Pt in H_2-saturated 0.1 M H_2SO_4 electrolyte solution in the presence of 10^{-3} M HCl (curve a) and after addition of 10^{-4} M $CuSO_4$ (curves b and c). The Pt ring-electrode (area 0.911 cm^2) was rotated (rotation rate 20Hz). Curves a and b were obtained during a potential sweep (sweep rate 10mV s^{-1}), curve c during a current scan with 7 μA s^{-1}.

$$H_2^{bulk} \rightarrow H_2^{surface} \tag{R3.5}$$

$$2Pt + H_2^{surface} \rightarrow 2Pt - H \tag{R3.6}$$

$$Pt - H + H_2O \rightarrow H_3O^+ + e + Pt \tag{R3.7}$$

i.e. the diffusion of H_2 from the bulk electrolyte to the electrode surface (reaction R3.5), the dissociative adsorption of surface H_2 onto bare Pt sites (R3.6), and the electrochemical oxidation of adsorbed hydrogen atoms accompanied by hydration (R3.7), the reversible adsorption of Cu^{2+} and Cl^- affects the overall behavior, as clearly seen in the current-voltage plots in Fig. 20:

$$X^- + * \longleftrightarrow X_{ads}^{\delta-1} + \delta e^- \tag{R3.8}$$

$$Cu^{2+} + 2e^- + * \longleftrightarrow Cu \tag{R3.9}$$

Curve a in Figure 20 represents the H_2 oxidation current in 0.1 M H_2SO_4 after addition of 10^{-3} M HCl. At potentials more positive than about 100mV vs. SHE, the I/ϕ_{DL} curve exhibits a region of negative differential resistance that is caused by the adsorption of Cl^-. The addition of Cu^{2+} to the Cl^--containing sulfuric acid (curve b in Fig. 20) inhibits H_2 oxidation at potentials negative to about 550 mV almost completely, owing to under potential deposition (upd) of 1 monolayer Cu (and at the very negative potentials also bulk deposition). Hence, in the presence of Cu^{2+} ions the NDR caused by Cl^- adsorption is hidden up to about 750 mV, and Cu^{2+} plays exactly the role of species P. Concurrent with the beginning desorption of the upd monolayer at $U \geq 550$ mV, hydrogen oxidation sets in, and once the entire Cu is stripped from the electrode, the oxidation current reaches the level of the one in the Cu^{2+} free, Cl^--containing electrolyte. Above we discussed that an HN-NDR leads to oscillatory behavior if the process that causes the NDR is faster than the one that

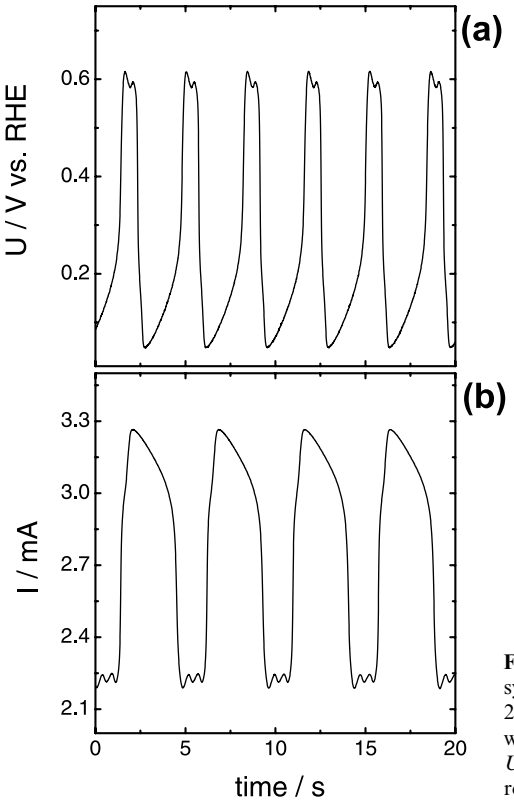

Fig. 21. Oscillations in the $H_2|Cl^-,H_2SO_4,Cu^{2+}|Pt$ system. (a) Under galvanostatic control ($I = 2.5$ mA) and (b) under potentiostatic control with an external series resistor, $R_{ext} = 500\ \Omega$, $U = 1.69$ V vs RHE. Electrolyte solution and rotation rate as in Fig. 20.

hides it. In the $H_2 \mid Cl^-,H_2SO_4,Cu^{2+} \mid Pt$ system, this is the very case. The adsorption/desorption equilibrium of Cl^- adjusts much faster than the one of Cu^{2+}, as proved by cyclic voltammetry with different scan rates [97] and by impedance spectroscopy [106]. Curve c in Figure 20 displays the I/U characteristics obtained when scanning the applied current. Potential oscillations arise when the potential adjusts to the value at which Cu desorption sets in. Observe that the potential is oscillating between curves a and b. Examples of oscillations obtained for a constant value of the applied current (a) and a fixed value of the external voltage (b) are displayed in Fig. 21. The oscillations are not simple periodic, but composed of alternating small and large amplitude oscillations. Such mixed-mode oscillations (MMOs) are typical for oscillations during hydrogen oxidation [105]. Their occurrence requires at least three degrees of freedom, i.e. three bound variables (provided the MMOs do not arise due to spatial instabilities). In contrast to the fundamental mechanism giving rise to simple periodic oscillations, the origin of the MMOs is not yet understood.

As already mentioned, oscillations are also observed if a small amount of CO (typically less than 1%) is contained in the H_2 fuel gas [107, 108]. The oscillations were studied in concentrated sulfuric acid electrolytes (0.5 or 2 M) under galvanostatic conditions. Yamazaki and Kodera [108] propose a model to describe the galvanostatic oscillations that assumes strong attractive interactions between the CO

molecules, which gives rise to an S-shaped current potential curve. This assumption is not supported by experiments, and although CO bulk oxidation was recently shown to exhibit an S-shaped current potential curve under certain conditions (see below), a mechanism equivalent to the one above is considered much more likely, where CO takes the role of Cu. It adsorbs and inhibits hydrogen oxidation at low potentials and becomes oxidized in the NDR region when OH adsorption sets in (at about 800 mV SHE). At this point it is important to note that with CO as poison Cl^- is not essential for the oscillations to occur. H_2 oxidation is negligible on Pt oxides. Thus, the oxidation of the Pt surface

$$Pt + H_2O \rightarrow Pt - OH + H^+ + e^- \tag{R3.10}$$

$$Pt - OH \rightarrow Pt - O + H^+ + e^- \tag{R3.11}$$

also gives rise to an N-NDR, but at more positive potentials than Cl^-. Since also CO desorbs more positive than Cu (namely through the reaction with adsorbed OH), negative and positive feedback loop can interact and may lead to an oscillatory instability. Thus, there is a nearly 1:1 correspondence between the mechanisms causing the oscillations in the two systems; we only need to replace Cl^- with OH and Cu^{2+} with CO. In fact, the I/U characteristic shown in Fig. 20 (curve b) is similar to those observed during H_2 electrooxidation in the presence of 2% CO as studied by Markovic and colleagues [109].

H_2O_2 Reduction on Pt

As already mentioned above, Nakato and colleagues [45, 46, 55–57, 69–73, 96, 110, 111] reported exceedingly rich nonlinear behaviors during H_2O_2 reduction on Pt in acidic media. They identified two potential regions in which the reaction exhibits a negative faradaic impedance. One N-NDR arises from the suppression of the H_2O_2 reduction by formation of upd hydrogen in a potential region just before hydrogen evolution sets in, and the other from a decrease in the coverage of adsorbed OH, which catalyses H_2O_2 reduction. In "pure" aqueous H_2SO_4, N-NDR-type oscillations are observed in accordance with the mass-transport limited N-NDR oscillator model (see Section 3.1.3).

When adding a small amount of halide ions, both NDRs are hidden in the stationary polarization curve. Impedance spectra taken at identical values of the potential and in electrolyte solutions that differ only by the presence of absence or 1.0×10^{-4} M KBr provide clear-cut evidence of this transformation [57] (Fig. 22). Both spectra exhibit real negative faradaic impedance for a finite excitation frequency ω_h, indicating the occurrence of a Hopf bifurcation at higher ohmic resistance. In the absence of Br^-, the real part of the impedance stays negative for perturbation frequencies $\omega < \omega_h$, suggesting strongly that the zero-frequency impedance is negative: $Z(\omega = 0) < 0$. In contrast, in the presence of Br^-, the impedance curve turns around in the positive direction of $\mathrm{Re}(Z)$ such that the zero-frequency impedance is positive again: $Z(\omega = 0) > 0$, and thus the N-NDR is hidden in the station-

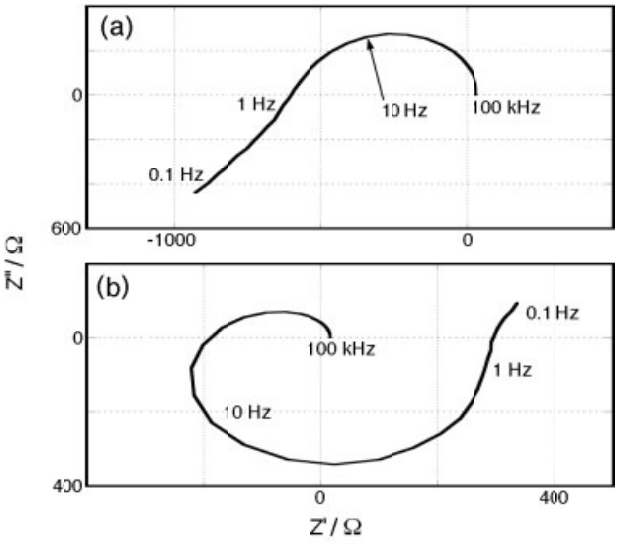

Fig. 22. Impedance diagrams for poly-Pt at −0.15 V vs. SCE in (a) 0.3 M $H_2SO_4 + 0.3$ M H_2O_2 and (b) 0.3 M $H_2SO_4 + 0.3$ M $H_2O_2 + 1.0 \times 10^{-4}$ M KBr. (Reproduced with permission from Y. Mukouyama, S. Nakanishi, T. Chiba, K. Murakoshi, and Y. Nakato, J. Phys. Chem. B 105 (2001) 7246–7253, © American Chemical Society (2000)).

ary polarization curve. Similar spectra are obtained in the potential region of the second N-NDR.

Mechanistically, the transformation of the N-NDR into an HN-NDR can be explained by the fact that adsorbed halides inhibit the dissociative adsorption of H_2O_2. The decrease in the reaction current due to the loss of PtOH or the formation of upd-H upon a negative voltage shift is overcompensated by the increase in current density due to the desorption of halide ions. Sustained periodic oscillations appear under potentiostatic as well as galvanostatic conditions in the presence of halides [57] (Fig. 23). The oscillations that are associated with the NDR in the upd-H region were termed oscillations D, those connected to the autocatalytic adsorption of H_2O_2 oscillations C.

When Nakato et al. incorporated adsorption and desorption of halides into their mathematical description, the new type of oscillations could be reproduced in simulations [57]. Furthermore, the calculations revealed that oscillations D required, besides the poisoning of the electrode by halide adsorption, the transient current due to the upd-H formation. Hence, the oscillations necessitate two N-NDR hiding factors: the adsorption of a poison and an additional current (stemming from a transient process and not a independent current carrier as in Strasser's type HN-NDR subcategory 3). This led the authors to introduce a new HN-NDR subcategory 4.

Although apparently not linked to the presence of an HN-NDR, two further dynamic properties of the Pt|H_2SO_4,H_2O_2 system are noteworthy. First, besides oscillations A, C, D and E discussed above, Nakato's group reported a fifth type of oscillation, oscillations B (see Fig. 23) [96]. These oscillations appear in the most negative potential region, and only for rough surfaces. Moreover, although the

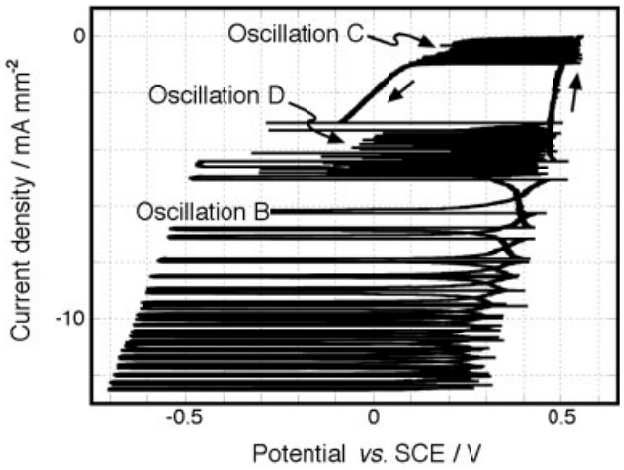

Fig. 23. Type B, C and D oscillations observed for an atomically flat Pt(111) electrode during a potentiodynamic scan. Electrolyte: 1 M H_2O_2 and 0.3 M H_2SO_4; scan rate: 5 mV s^{-1}. (Reproduced from Y. Mukouyama, S. Nakanishi, H. Konishi, and Y. Nakato, J. Electroanal. Chem. 473 (1999) 156–165, with permission from Elsevier Science.)

oscillations are found under galvanostatic conditions, an HN-NDR was not detected in impedance measurements, a clear hint that the oscillations do not fall into one of the two oscillator classes considered in this chapter. Furthermore, during the oscillations the electrode potential reaches values at which hydrogen evolution occurs, and gas bubbles are observed concomitant to the current or potential oscillations. In Ref. [96] it is proposed that the rough electrodes are composed of "active" and "non-active" parts, whereby on the active (rough) areas, H_2O_2 reduction is not inhibited by a full coverage of under-potential deposited hydrogen, contrary to the "normal", nonactive areas, occupying the major part of the electrode. The oscillations arise because of the electric coupling between active and non-active areas in connection with effective solution stirring through gas evolution reactions. The positive feedback loop is still due to an NDR, namely the one that arises on the *non-active* areas due to upd of hydrogen and causes oscillations A for different values of the external parameters (e.g. external potential). In accordance with these ideas, in mathematical simulations oscillations were only observed when taking into account: (i) the coupling between active and non-active surfaces; and (ii) strong stirring of the electrolyte by H_2 evolution. Mukouyama et al. propose for this new-type of electrochemical oscillation mechanism the name C-NDR (coupled NDR).

The second remarkable nonlinear behavior to be mentioned here which is not connected to an HN-NDR is the bistability between a high-current state and the low-current behavior, which was considered above in connection with oscillations A-E (Fig. 24). The high current state involves a strongly enhanced transport of H_2O_2 to the electrode by solution stirring through catalytic oxygen-gas evolution on Pt, as well as a large increase in the rate of dissociative adsorption of H_2O_2 due to the autocatalytic effect of adsorbed OH. Since the autocatalytic effect is most pronounced on flat Pt surfaces, the high-current states tend to appear more readily on flat surfaces.

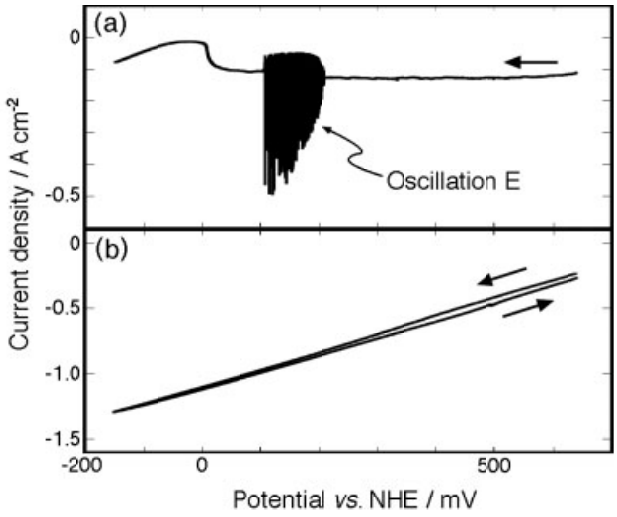

Fig. 24. Coexisting cyclic voltammograms exhibiting low (a) and high (b) current states for an atomically flat Pt(111) electrode. Electrolyte: 1 M H_2O_2 and 0.3 M H_2SO_4 (scan rate: 10 mV s^{-1}). (Reproduced from Y. Mukouyama, S. Nakanishi, H. Konishi, K. Karazumi, and Y. Nakato, Phys. Chem. Chem. Phys. 3 (2001) 3284–3289, by permission of The Royal Society of Chemistry on behalf of the PCCP Owner Societies.)

The discussed nonlinear phenomena during H_2O_2 reduction on Pt in acidic media constitute impressive examples of how small differences in the interfacial kinetics owing to structural effects, for example, or to minor changes in the composition of the electrolyte, can affect the dynamic response in a qualitative manner.

Electrooxidation of Formic Acid and Other Small Organic Molecules

Many oxidation reactions of small organic molecules possess two common features that make these reactions especially susceptible to dynamic instabilities. Firstly, the reactions proceed through a dual-path mechanism [112–114]: the educt is either "directly" oxidized to CO_2 without the formation of any long-living surface intermediate, or the electrode catalyzes the heterogeneous dissociation of the educt (or an intermediate of the reaction) into at least one stable adsorbate, which requires a higher overvoltage to be oxidized. This adsorbate acts as a poison for the direct path, leading to a considerable decrease of the current density with time at low overpotentials. Secondly, there is a competition for free adsorption sites between the organic molecule and water, the bond strength between metal and water becoming stronger with increasing potential [115, 116]. Neglecting the indirect path, the second property gives rise to an N-NDR, since the available surface sites for the direct path, and thus the oxidation current, become fewer with increasing overpotential due to OH adsorption. The indirect path, on the other hand, suppresses the direct oxidation at low overvoltage, giving way to free surface sites only when it is oxidized by strongly bonded water or surface bonded hydroxyl radicals well in the NDR region.

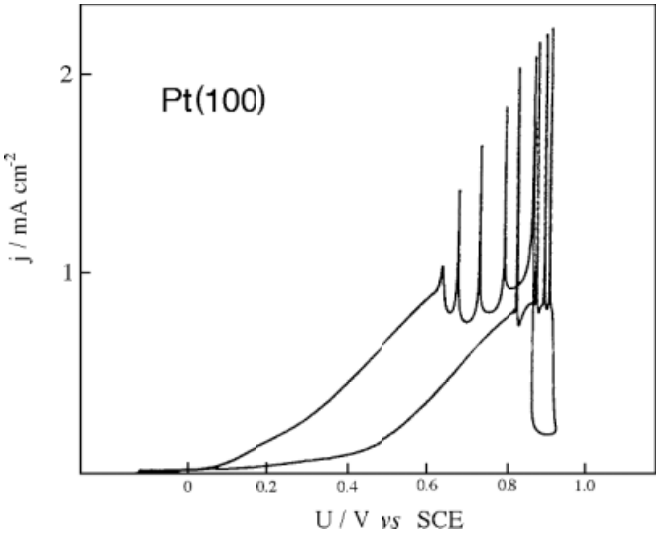

Fig. 25. Cyclic voltammogram of formic acid oxidation on Pt(100) in a 0.05 M HCOOH, 10^{-3} M $HClO_4$ electrolyte solution. In this experiment, an external resistance ($R_{ex} = 600\ \Omega$) was used; scan rate: 5 mV s^{-1}. (Reproduced from P. Strasser, M. Lübke, F. Raspel, M. Eiswirth and G. Ertl, J. Chem. Phys. 107 (1997) 979–990, by permission of the American Institute of Physics.)

Hence, the indirect path hides the NDR partly. These considerations strongly suggest that many of the electrooxidation reactions of organic molecules will fall into the class of HN-NDR systems, irrespectively of the detailed reaction mechanism. This presumption is supported by the fact that most of the reactions oscillate under galvanostatic control.

With regard to the dynamic behavior, formic acid oxidation is the best-studied oxidation reaction of small organic molecules. In many early studies it was suggested that the oscillation mechanism be of purely chemical nature, and thus an NDR is not involved in the essential steps [117–125]. However, in more recent studies clear-cut experimental evidence is presented that – at least under many experimental conditions – formic acid oxidation belongs to the class of HN-NDR systems. A cyclic voltammogram of formic acid oxidation on Pt(100) is shown in Fig. 25. It possesses the characteristic attributes of self-poisoning oxidation reactions of small organic molecules. The most important features are a slowly increasing current for $U > 0.5$ V, owing to the reactive removal of the poisoning CO in parallel to the onset of OH adsorption at about 0.5 V, and the occurrence of a kinetic hysteresis in the negative potential region owing to the small rate of the poisoning reaction. Furthermore, the I/U curve exhibits the typical features of HN-NDR systems under potentiostatic conditions: oscillations around a branch with positive slope in the polarization curve close to the maximum of the curve, a steep decrease in current density for potentials positive to the oscillatory region and a hysteresis on the backward voltage sweep. When increasing the conductivity no oscillations were observed anymore.

In fact, formic acid oxidation is a transparent example in which the features that lead to sustained oscillations in oxidation reactions of organic molecules and are described above in general terms can be deduced from the reaction mechanism in a straightforward manner. It is widely accepted that formic acid is oxidized in two parallel pathways,

$$\mathrm{HCOOH} + * \longleftrightarrow \mathrm{HCOOH_{ad}} \begin{cases} \rightarrow \cdot\mathrm{COOH_{ad}} + \mathrm{H^+} + \mathrm{e^-} \xrightarrow{\text{fast}} \mathrm{CO_2} + * + 2\mathrm{H^+} + 2\mathrm{e^-} & \text{(R3.12)} \\ \rightarrow \mathrm{CO_{ad}} + \mathrm{H_2O} & \text{(R3.13)} \end{cases}$$

where $*$ denotes a free adsorption site. The first path (R3.12) represents the direct oxidation of formic acid where adsorbed HCOOH is oxidized to a reactive intermediate, most likely $\cdot\mathrm{COOH_{ad}}$, which is immediately further oxidized to the final product, CO_2. The indirect path is associated with the heterogeneously catalyzed dissociation of formic acid to water and adsorbed CO, which blocks the surface sites for further adsorption of HCOOH. The removal of the poison CO proceeds via an electrochemical reaction with surface bonded H_2O, as it is assumed in [125], or adsorbed hydroxide, which is formed at about 0.5 V by water dissociation [115] according to the following steps:

$$\mathrm{H_2O} + * \longleftrightarrow \mathrm{OH_{ad}} + \mathrm{H^+} + \mathrm{e^-} \quad \text{(R3.14)}$$

$$\mathrm{CO_{ads}} + \mathrm{OH_{ad}} \rightarrow \mathrm{CO_2} + \mathrm{H^+} + \mathrm{e^-} + 2* \quad \text{(R3.15)}$$

OH_{ad} (or surface bonded water) block surface sites for HCOOH oxidation.

Let us elucidate the role of the individual steps for the dynamic behavior. The direct reaction path (R3.12) accounts for most of the oxidation current. It is inhibited by the adsorption of OH (R3.14), which is a fast process. Thus, reactions (R3.12) and (R3.14) give rise to a current-potential characteristic with a negative slope in the potential region where OH adsorption occurs. They form an N-NDR subsystem, just as H_2 oxidation (R3.5)–(R3.7) and Cl^- adsorption (R3.8) do in the $H_2|Cl^-,Cu^{2+},H_2SO_4|Pt$ system. For potentials negative to OH adsorption, CO slowly poisons the surface according to (R3.13) and it is removed in reaction (R3.15). Hence, it suppresses the direct oxidation of formic acid for potentials negative to the onset of OH adsorption, giving way to free surface sites and thus an appreciable oxidation current only when CO is removed. Therefore, reaction (R3.13) and (R3.15) take the role of Cu adsorption and desorption in the $H_2|Cl^-,Cu^{2+},H_2SO_4|Pt$ system. Furthermore, these steps are identical to the ones hiding the NDR in the $H_2,CO|H_2SO_4|Pt$ system. Strasser et al. [126] translated the chemical reaction scheme (R3.12–R3.15) into a mathematical model that was summarized in a previous review article [10].

Several groups report that the dynamic behavior of formic acid oxidation on low-index single crystal planes exhibits structural effects [119, 120, 124, 127]. According to these studies, current oscillations were easily observed on Pt(100), seemed to exist in only a small parameter interval on Pt(110), and proved to be even more difficult

to detect on Pt(111). Furthermore, on Pt(100) current spikes appeared in the cyclic voltammogram, predominantly on the cathodic scan. In contrast, on Pt(110) they showed up mainly on the anodic scan, and were often absent on Pt(111), although oscillations emerged under stationary conditions. These differences are reproduced with the mathematical model when employing different rate constants for the poisoning reaction (R3.13), in accordance with experimental findings [126, 128].

In two recent papers Naito et al. [129, 130] discuss a slightly modified model that differs in some details of the chemical reaction steps, but apparently not in the origin of the positive and negative feedback loops. One important conclusion from their studies is that the electrode potential can be eliminated adiabatically. As far as the differences in the mechanistic steps of the two models are concerned, without further studies it does not seem possible to decide which one describes the system better.

A shortcoming of both models is that they do not capture the occurrence of complex periodic or aperiodic potential oscillations under current control, which were observed in many different electrolytes. Impressive studies of such complicated temporal motions during formic acid oxidation can e.g. be found in Refs. [118, 121]. Schmidt et al. [131] suggest that the adsorption of anions, which leads to a competition for free surface sites not only between two species, formic acid and water, but between three species, formic acid, water and anions, can induce complex nonlinear dynamics. This conjecture is derived from differences in the oscillatory behavior found in perchloric and sulfuric acid for otherwise similar conditions. Complex motions were only observed in the presence of sulfuric acid.

Schell et al. present evidence that the role of anions in the electrocatalyzed oxidations of formic acid in current-control experiments can be even more than simply blocking reactive surface sites [132–135]. They conjecture that the adsorbed anions affect the nature and reactivity of surface water and OH, and thus their reaction with surface CO. Most remarkable results were obtained when perturbing an aqueous solution containing 0.1 M HCOOH and 0.5M $HClO_4$ by a small amount of HBF_4 [133]. The addition of BF_4^- anions caused more than a 60% increase in the value of the applied current for which low-valued stationary potentials remain stable. The current increases by more than 50% at relevant potential values in potential-control experiments. Together with the overall reaction rates the nonlinear behavior exhibited by formic acid oxidation changed drastically in the presence of a small amount of BF_4^-.

Also the presence of certain cations was shown to change the nonlinear behavior of formic acid oxidation qualitatively. Examples include Cu^{2+} ions, whose addition induced complex oscillation patterns as well increased frequency oscillations [136], and Bi^{3+} ions, that were found to significantly enhance the current density as well as the existence range of oscillations and spatiotemporal self-organization (see Section 4.2) [137].

This list of examples in which small perturbations of the chemical composition of the electrolyte qualitatively changed the nonlinear dynamics demonstrates how intricate the repercussion of interfacial reaction steps on temporal motions can be. It is likely that in all of the mentioned systems the basic instability is the same and can be understood in terms of the interaction of (a) surface poisoning by the indirect path; (b) replenishing of the surface by the reaction between CO and surface bonded

water or surface OH; and (c) the feedback between the total coverage of the electrode on the electrode potential. Still, a realistic description of the oscillations and an understanding of the occurrence of complex oscillations require the incorporation of chemical steps that are specific to the individual systems. It is a challenge for future research to refine the models discussed above and to uncover the additional feedback loops in the individual systems that cause the complex oscillations.

As already mentioned, also for the other oxygenated C1 compounds, i.e. formaldehyde [118, 138–147] and methanol [148–154], as well as for larger organic molecules, dynamic instabilities are reported. Many of them are compiled in Ref. [154], for formaldehyde oxidation on Rh and Pt [147] and methanol oxidation on Pt [155] the oscillations could be clearly identified as HN-NDR type oscillations. However, in view of the number of reaction steps involved in these oxidation reactions and of the possible complexity of the interaction of the supporting electrolyte with the dynamics even in the much simpler formic acid oxidation, it is not astonishing that any quantitative considerations should still be missing. There are some attempts to qualitatively explain the observed phenomena with reaction mechanisms that go beyond the simple dual-path model described above. However, at the time being, they are quite speculative. Therefore I shall not discuss them in more detail in this article. A summary of these works can be found in [156].

3.2 S-NDR Systems: The Electrode Potential as the Negative Feedback Variable

Electrochemical systems belonging to the class of S-NDR systems are complementary in most dynamic properties to N-NDR systems. They are characterized by:

(a) A stationary S-shaped polarization curve for vanishing ohmic series resistance. In other words, S-NDR systems possess a bistable I/ϕ_{DL} curve (Fig. 26a). The differential resistance of the middle, sandwiched branch is clearly negative (that's why these systems are called S-NDR); this branch is unstable and cannot be detected in a potentiostatic experiment with IR_Ω compensation (or sufficiently small R_Ω).
(b) The I/U characteristic becomes single-valued if the ohmic series resistance, R_Ω, exceeds a critical value, $R_{\Omega,\mathrm{crit}}$ (Fig. 26b); around steady states with intermediate current values that correspond to values on the NDR branch for vanishing R_Ω, oscillations might exist, but they are by far less likely than in (H)N-NDR systems. However, an instability with respect to spatial perturbations can be expected (see Sec. 4.2.1).
(c) S-NDR systems might oscillate under galvanostatic control, when the preset current corresponds to current values of the NDR branch; however, as under potentiostatic conditions, corresponding parameter values are rather improbable. And again, also under fixed current conditions S-NDR systems are very likely to experience a spatial instability such that the homogeneous NDR branch is also not accessible under galvanostatic control (see Section 4.2.2), and a stationary I/ϕ_{DL} measurement exhibits a hysteresis (Fig. 26c).

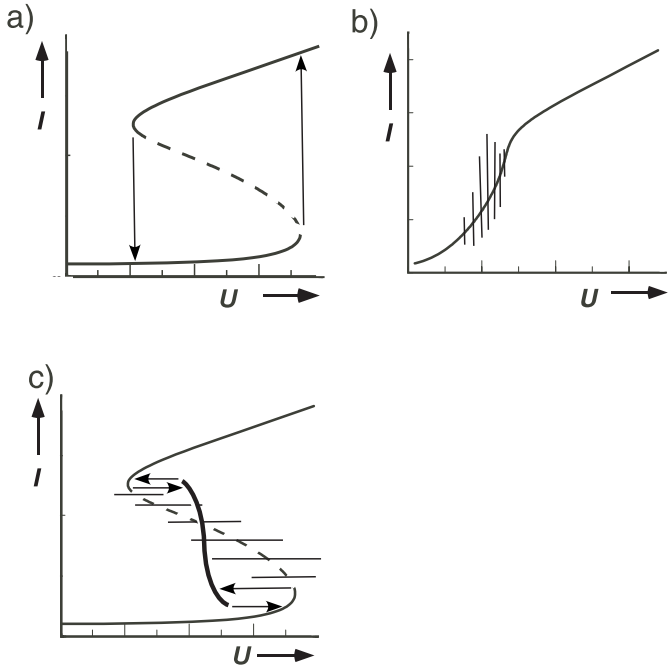

Fig. 26. Characteristic I-U curves of S-NDR systems (a) under potential control for vanishing ohmic series resistance, R_Ω; (b) under potential control for intermediate values of R_Ω. The dashed vertical lines indicate that S-NDR systems might oscillate in an intermediate interval of U, but corresponding parameter values are very unlikely such that in general an experimental cyclic voltammogram will look like the solid curve (c) under current control, where the sandwiched branch is unstable with respect to spatial variations and an I/U measurement exhibits a hysteresis, as indicated by the arrows. The middle, thick curve corresponds to a spatially structured state (see Section 4.2.2).

3.2.1 General Properties

The existence of bistability in the I/ϕ_{DL} characteristic, i.e. under conditions under which ϕ_{DL} reduces to a parameter, implies that a chemical variable, on which the current depends, exhibits bistability as a function of ϕ_{DL}. Thus, in S-NDR systems we have to require that the dynamic equations contain a *chemical* autocatalysis. As set forth below, ϕ_{DL} takes the role of the negative feedback variable. The positive feedback might be due to chemical autocatalytic reaction steps as is the case in Zn deposition [157, 158] or CO bulk oxidation on Pt [159]. S-shaped current-potential characteristics may also arise in systems with potential-dependent surface phase transitions between a disordered (dilute) and an ordered (condensed) adsorption state due to attractive interactions among the adsorbed molecules.

Writing the evolution law of the autocatalytic (chemical) species, c, as

$$\frac{dc}{dt} = f(c, \phi_{\mathrm{DL}}), \tag{41}$$

whereby $f(c, \phi_{DL})$ is a function that is bistable in ϕ_{DL} (e.g. the coverage of an adsorbate with attractive interactions), then, depending on how the faradaic current depends on c, the resulting current-potential characteristic exhibits the form of a Z or an S (cf. Fig. 29). The temporal evolution of the double layer potential is again given by the equation

$$C\frac{d\phi_{DL}}{dt} = -i_{reac}(c, \phi_{DL}) + \frac{U - \phi_{DL}}{R_\Omega}. \tag{42}$$

Eq. (42) gives rise to a negative feedback loop if the current potential curve is S-shaped, but not for Z-shaped characteristics. Thus, in S-NDR systems ϕ_{DL} may stabilize the middle branch of the S, or it may induce oscillations. This is not possible in Z-shaped systems, where an incorporation of ϕ_{DL} in the dynamic description only increases the width of the bistable region but never results in *qualitatively* different behavior. For this reason, ϕ_{DL} is not an essential variable in the latter type of systems. Thus, they have to be classified as systems with chemical instabilities only and will not be further treated here.

The relative locations of saddle node and Hopf bifurcations in the U/R_Ω parameter plane are universal for all S-NDR systems, as it was the case for the other classes we discussed (Fig. 27). Again, the bistable region has the form of a V, however, this time its broadest extension is for zero ohmic resistance, and it closes towards larger values of R_Ω and U. Oscillatory behavior might exist in a region opposite to the bistable region, i.e. at large values of R_Ω and U. However, the requirement that the destabilizing process has to be faster than the stabilizing process for oscillations to occur makes oscillations in S-NDR systems the exception. It means that the typical time scale on which the autocatalytic species changes is shorter than the double layer charging. Clearly, this prerequisite is fulfilled only for extremely fast reactions or adsorption steps, or unusually large values of the double layer capacitance. Up to now, there is no convincing experimental example of an oscillatory S-NDR system. However, one should have in mind that for typical parameter ranges S-NDR systems underlie spatial instabilities, resulting in stationary potential and adsorbate or con-

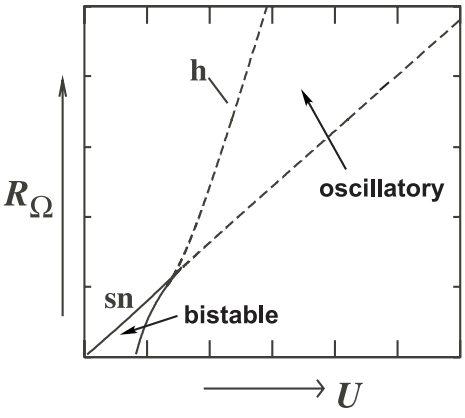

Fig. 27. Qualitative locations of saddle-node (sn) and Hopf (h) bifurcations in the external voltage (U)/ series resistance (R_Ω) parameter plane.

centration patterns (see Section 4.2). In the following we discuss two experimental S-NDR systems in more detail, one in which a surface phase transition of organic adsorbates is involved and bulk CO oxidation.

3.2.2 S-NDR Systems Involving a Surface Phase Transition of Organic Adsorbates

S-shaped current potential curves emerge when a surface phase transition of an organic adsorbate is coupled with a faradaic reaction of some electroactive species. As a representative of such a system, the periodate reduction on Au(111) single crystal electrodes in the presence of camphor was studied [160]. Camphor adsorbed on Au(111) electrodes exhibits two first-order phase transitions upon variation of the electrode potential [161]. In a cyclic voltammogram, the phase transition manifests itself in a pair of needle-like peaks (Fig. 28 (A)). Between the peak pairs, a condensed, well-ordered camphor film exists. At more negative potentials, the camphor coverage is low, while the state of the adsorbate at positive potentials beyond the second phase transition is not yet known. The small hystereses between the respective anodic and cathodic peaks are caused by the finite nucleation rate of the respective thermodynamically stable phase.

Periodate in a camphor-free electrolyte is reduced on Au(111) in the potential range that we consider here, as reflected by the CV of Fig. 28b. In the presence of camphor, however, IO_4^- reduction is inhibited when the condensed camphor film

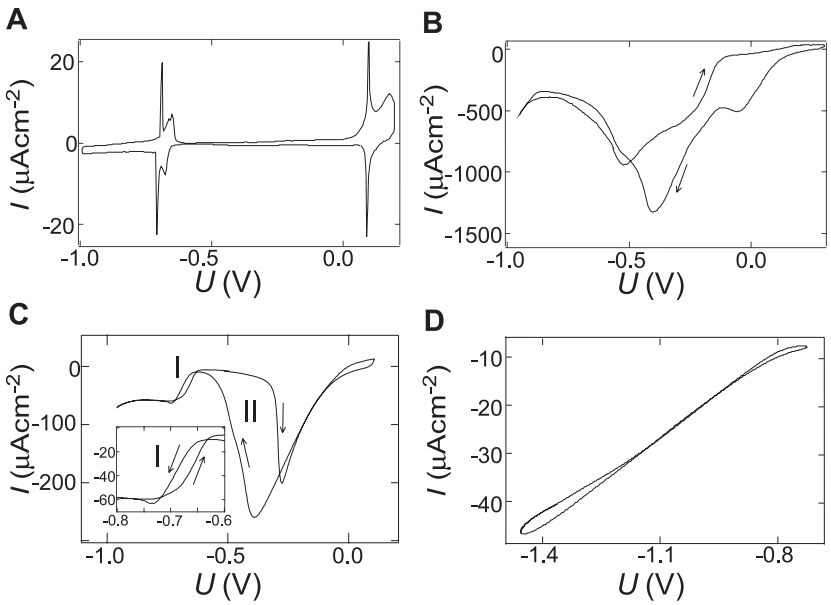

Fig. 28. Cyclic voltammograms of an Au electrode in contact with different electrolytes [160]: (A) 5 mM camphor and 50 mM $NaClO_4$; (B) 5 mM $NaIO_4$ and 100 mM $NaClO_4$; (C) 5mM camphor, 32 mM $NaClO_4$ and 5mM $NaIO_4$; and (D) 5mM camphor, 0.5 mM $NaClO_4$ and 0.5 mM $NaIO_4$. Scan rate: 50 mV s^{-1}.

covers the electrode, i.e. between about −300 and −700 mV (Fig. 28c). The phase transitions accompanying the formation or dissolution of the condensed camphor film, respectively, cause the hystereses in the CV, which also persist under stationary conditions. The bistability I in the more negative potential range exhibits the shape of an S, whereas the other bistability II in the more positive range is of the Z type. When lowering the conductivity, the S-type bistability disappears and the current-voltage curve becomes single-valued (Fig. 28d), in agreement with the general two-parameter bifurcation diagram of S-NDR systems (Fig. 27). Notice that in the camphor/periodate system the characteristic rates of adsorption and desorption of camphor are obviously not fast enough to support an oscillatory instability. However, in Section 4.2.1 it will be emphasized that the system exhibits a spontaneous emergence of stationary patterns for low electrolyte concentrations, such as those underlying Fig. 28d.

With this concrete system, we can also demonstrate the origin of the autocatalysis and negative feedback loop that comes about when the ohmic series resistance is not negligible. (This critical resistance depends on the width of the bistable region in the I/ϕ_{DL} curve; it might be as small as a few 10 Ω.) The positive feedback is due to the attractive interactions between the camphor molecules, which cause an avalanche-like (i.e. autocatalytic) building of the condensed phase when the coverage exceeds a critical value. Now suppose that the system is in a state at a potential negative to the one where the complete condensed phase exists. Then a fluctuation in ϕ_{DL} towards more positive values causes an increase of the equilibrium concentration of adsorbed camphor (and for suitable parameter values the autocatalytic building of the condensed film). Since camphor inhibits the reduction of IO_4^-, the current density I decreases. Under potentiostatic conditions, however, a decrease in I prompts a shift of ϕ_{DL} toward more negative values. Hence, the fluctuation is damped.

The homogeneous dynamics of the system could be reproduced qualitatively describing the time evolution of the camphor coverage, θ, in the Bragg–Williams approximation [33], following earlier suggestions by Frumkin [162]:

$$\frac{d\theta}{dt} = k_{\mathrm{ad}}(1-\theta)\mathrm{e}^{w(\phi_{\mathrm{DL}})}\mathrm{e}^{-g\theta/2RT} - k_d\theta\mathrm{e}^{-w(\phi_{\mathrm{DL}})}\mathrm{e}^{g\theta/2RT} \tag{43}$$

with

$$w(\phi_{\mathrm{DL}}) = \left(-\frac{1}{2}(C_0 - C_1)\phi_{\mathrm{DL}}^2 + C_1\phi_{\mathrm{DL}}\phi_{\mathrm{sh}}\right)\frac{1}{N_{\max}k_BT}, \tag{44}$$

where $N_{\max}$ denotes the maximum number of molecules that can adsorb on a unit area and k_B Boltzmann's constant. The two terms in $w(\phi_{\mathrm{DL}})$ account for the work expended in the adsorption process due to a decrease in the dielectric constant and to an increase in the double layer thickness upon adsorption, on the one hand, and the energy associated with the dipole moment of the molecules adsorbed, on the other hand. (ϕ_{DL} is measured versus the pzc at $\theta = 0$, ϕ_{sh} is the shift in pzc during the transition from $\theta = 0$ to $\theta = 1$.) The specific capacities of the bare and the adsorbate-covered electrode are denoted by C_0 and C_1, respectively. g represents the interaction

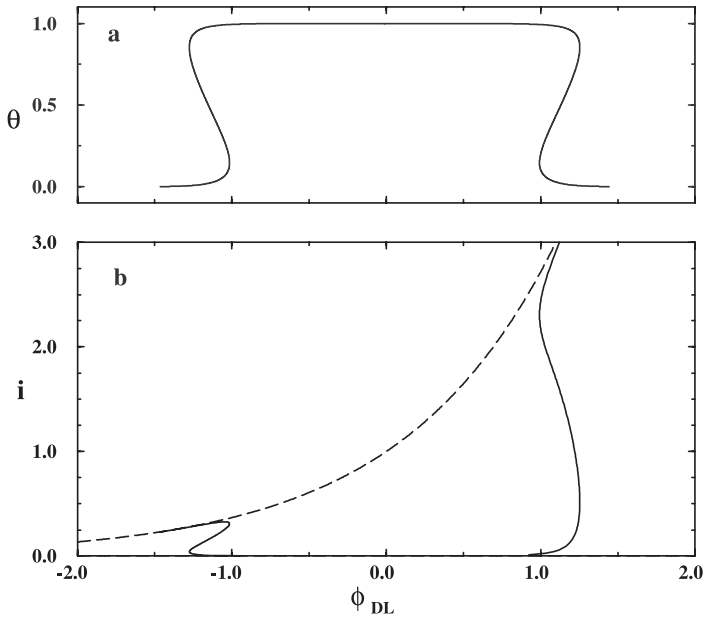

Fig. 29. (a) Coverage of a neutral species, θ, as a function of the electrode potential as described by Eqs. (43, 44). (b) Current-potential characteristic in the absence (dashed line) and in the presence (solid line) of the adsorbate according to Eq. (45). For parameter values, see Ref. [33].

energy between the molecules. For $g < -4$, Eq. (43) describes an isotherm with a high coverage, corresponding to the condensed phase, in a potential interval around the pzc and two multivalued regions arising from the phase transition to a dilute phase (Fig. 29a).

If the adsorbate itself does not react electrochemically, but inhibits the electron transfer of a faradaic reaction that proceeds via Butler–Volmer kinetics on the free surface, the temporal evolution of ϕ_{DL} reads

$$C_0 \frac{d\phi_{\mathrm{DL}}}{dt} = -(1-\theta) n F c_r k_r \mathrm{e}^{\delta(\phi_{\mathrm{DL}} - V)} + \frac{U - \phi_{\mathrm{DL}}}{R_\Omega} \quad \text{with} \quad \delta = \frac{\alpha n F}{RT}, \tag{45}$$

where the coverage dependence of the double layer capacitance C was neglected and a sufficient overvoltage for the faradaic reaction was assumed such that the backward reaction can be neglected too. c_r stands for the bulk concentration of the electroactive species, k_r for the rate constant, and V for the equilibrium potential of the reaction. α denotes the transfer coefficient. In the two regions in which the isotherm is multivalued, the stationary current-potential curve possesses the form of an S or Z, respectively. Focusing on the S-region, Eqs. (43–45) capture the transition from the bistable to the monostable region (cf. Figs. 27 and 28) for realistic values of the parameters whereas an oscillatory instability is absent, in agreement with the experi-

ments. With this model also the first theoretical studies on spatially extended S-NDR systems were carried out, predicting the existence of stationary patterns in large parameter regions. Thus, we shall encounter it again in Section 4.2.1.

3.2.3 CO Bulk Oxidation

Studies on electrochemical CO oxidation by either stripping voltammetry of a preadsorbed (sub-) monolayer of CO or by the continuous oxidation of CO on rotating disk electrodes revealed that CO oxidation proceeds through a Langmuir–Hinshelwood mechanism [109, 163, 164]. The latter implies that both reacting species, CO and OH, adsorb at the electrode prior to their reaction to CO_2. In the context of dynamic instabilities this result is of utmost importance since the Langmuir–Hinshelwood mechanism leads to an instability in the current-voltage characteristic if the adsorption rate of one of the educts comes into the transport limited region [16].

Indeed, the occurrence of an S-shaped current potential curve during the continuous electrochemical oxidation of CO on rotating Pt single-crystal electrodes was reported recently [159]. Cyclic voltammograms obtained during CO oxidation on a rotating Pt(110) electrode in perchloric acid for different scan rates and disk rotation rates are reproduced in Fig. 30a. Besides the sharp "ignition peak" in the anodic scan, the I/U curves exhibit a coexistence region between a low current state and a reactive state. The bistable region becomes narrower for slower scan rates, but remains finite at the lowest rates used, indicating that the system is in fact bistable under stationary conditions.

Further evidence for the existence of an S-shaped I/ϕ_{DL} curve was obtained from current-controlled measurements. The galvanodynamic curves possess the form of an S at high sweep rates and decreasing current densities (Figure 30b). However, at low scan rates the obtained curves were rather irregular, the potential fluctuating around a value that is nearly independent of the imposed current.

It should be mentioned that the behavior discussed so far was typical for the three low-indexed Pt single crystal electrodes and for a polycrystalline Pt disk in perchloric and sulfuric acid, with one exception, Pt(111) in H_2SO_4 [159]. Here, the potential oscillates regularly under galvanostatic control when imposing a current density that corresponds to a state on the NDR branch. So far, there is not yet a mechanistic explanation of the oscillations. However, because of the relatively small rate of CO adsorption, it seems to be unlikely that ϕ_{DL} would be responsible for the negative feedback. Under potentiostatic control, the current density of the active, high-current branch decreases when increasing the applied voltage, which is interpreted as a blockage of the surface by sulfate adsorption. Koper et al. speculate that the oscillations might be related to this negative differential resistance, but they also emphasize that further experimental evidence is necessary for a real understanding of this oscillatory instability.

Azevedo et al. observed oscillations during CO electrooxidation also on rotating polycrystalline Pt disc electrodes under potentiostatic conditions [165]. The oscillations arose only in a small window of the external potential and required the rotation of the electrode. Since the conditions were such that the IR_Ω drop was negligible, it is

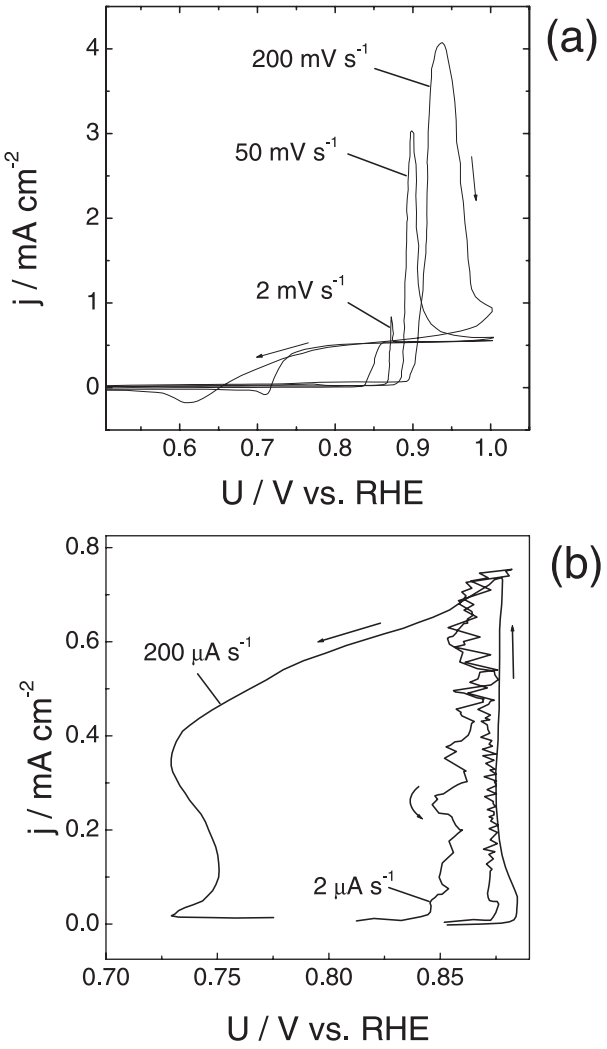

Fig. 30. I/U plots obtained during CO oxidation on a rotating Pt (110) electrode in 0.1 M $HClO_4$ electrolyte solution (CO saturated) for different scan rates (a) during potential sweep experiments ($\omega = 100$rpm); and (b) during current scans. (Reproduced with permission from M. T. M. Koper, T. J. Schmidt, N. M. Markovik, and P. N. Ross, J. Phys. Chem. B 105 (2001) 8381, © (2001) American Chemical Society.)

likely that the source of the instability is of chemical nature. But again, at the present stage, this should be seen as a working hypothesis.

Koper et al. [159] also discuss a simple model for the continuous electrochemical CO oxidation that can reproduce their main observations. The following steps are taken into account:

(a) a finite mass transport rate of CO from the bulk to the surface,

$$CO_{bulk} \longleftrightarrow CO_r; \tag{R3.16}$$

(b) the competitive adsorption of CO and OH,

$$CO_r + * \rightarrow CO_{ads} \tag{R3.17}$$

$$H_2O + * \longleftrightarrow OH_{ads} + H^+ + e^-; \tag{R3.18}$$

and (c) the reaction between the adsorbed species,

$$CO_{ads} + OH_{ads} \rightarrow CO_2 + H^+ + e^- + 2 * . \tag{R3.15}$$

Formulating appropriate rate laws for CO adsorption, OH adsorption and the reaction between these two surface species, a set of four coupled ordinary differential equations is obtained, whereby the dependent variables are the average coverages of CO and OH, the concentration of CO in the reaction plane and the electrode potential. In accordance with the experiments, the model describes the S-shaped I/U curve and thus also bistability under potentiostatic control. However, neither oscillatory behavior is found for realistic parameter values (see the discussion above) nor can the nearly current-independent, fluctuating potential be reproduced, which is observed for slow galvanodynamic sweeps (c.f. Fig. 30b). As we shall discuss in Section 4.2.2, this feature might again be the result of a spatial instability.

4 Spatiotemporal Patterns

From an electrochemical point of view, all the spatiotemporal patterns interesting in our context are the result of the interaction of interfacial kinetics, migration currents, and global feedbacks that arise from the control of the experiment. In the terminology of nonlinear dynamics, the same fact would be phrased somewhat differently, namely that electrochemical patterns originate from the interplay of the homogeneous or local dynamics, and spatial coupling. In an attempt to bridge both viewpoints, in Section 2 it was shown that migration currents and global constraints couple the individual sites of the electrode among each other, and thus contribute to the spatial coupling in electrochemical systems. Neglecting any spatial inhomogeneities, Section 3 dealt with the conditions under which the homogeneous system exhibits dynamic instabilities. This approach enables us to shed light on the way in which the interaction of the interfacial kinetics, migration currents and operation mode gives rise to spatial instabilities, which is the topic of this section.

The spatial coupling in electrochemical systems is manifold and crucially depends on the cell geometry. The electric field distribution in the entire electrolyte determines the so-called migration coupling; the position of the reference electrode regulates the strength of a superimposed negative (desynchronizing) global coupling; and there is an additional positive global coupling if the experiment is carried out under current control.

As for instabilities in homogeneous electrochemical systems, we distinguish between two main classes, N-NDR systems, which are connected with an N-shaped current-potential curve and S-NDR systems, in which the current-potential curve

traces the form of an S. From a dynamic point of view, the decisive difference between N-NDR and S-NDR systems is that in the former the double layer potential is the autocatalytic variable, i.e. the activator, whereas in the latter, it is the negative feedback variable, or the inhibitor. Migration coupling and global constraints have a repercussion on the electrode potential, and thus these modes of spatial coupling act on the activator variable in N-NDR systems and on the inhibitor variable in S-NDR systems, giving rise to fundamentally different spatial instabilities in the two types of systems. For this reason, we again divide this section into two main subsections that are devoted to patterns in N-NDR and S-NDR systems, respectively. In each subsection we investigate first the impact of migration coupling on pattern formation under conditions under which both types of global coupling can be ignored, then the effect of either an additional negative or an additional positive global coupling is considered.

4.1 N-NDR Systems: The Electrode Potential as Autocatalytic Variable

4.1.1 Nonlocal Migration Coupling

As discussed in Section 2, any global coupling stemming from the operation mode of the cell is absent under potential control if the RE is far away from the WE, i.e. on the height of or further away than the CE. Then, all the "communication" among different positions occurs exclusively through the electric field within the electrolyte, i.e. through migration coupling. In this subsection we shall exclusively refer to such a situation.

We also showed in Section 2 that the migration coupling differs qualitatively in systems, in which the WE is surrounded by an insulating plane, such as a disk electrode embedded in a Teflon cylinder, from those in which there is no conductor/insulator transition in the plane of the WE along the pattern forming spatial direction (cf. Fig. 3). An example of the second type of electrodes would be a thin-ring electrode. The latter geometries give rise to a simpler spatial coupling, and we will refer to it as the "base geometry".

Let us first consider pattern formation in systems with base geometry. Furthermore, let us assume that the CE is placed in a plane parallel to the WE and has about the same geometry as the WE. Then, there exist states with uniform potential and current distribution, i.e. homogeneous states, and we can investigate the response of a system to local perturbations or spatial fluctuations.

The simplest situation arises for bistable systems in which the basic pattern is a front, i.e. an interfacial region that connects the two locally stable stationary states and propagates in space.[10] Thereby one of the two states expands on the expense of the other one. Two experimental examples of potential fronts propagating along the

[10] In the strict, mathematical sense, fronts (or traveling waves) exist only in an infinite domain. In a finite domain, the moving interfaces are transient phenomena. However, for practical purposes, we can still identify moving interfaces as fronts as long as the domain is much larger than the width of the interface.

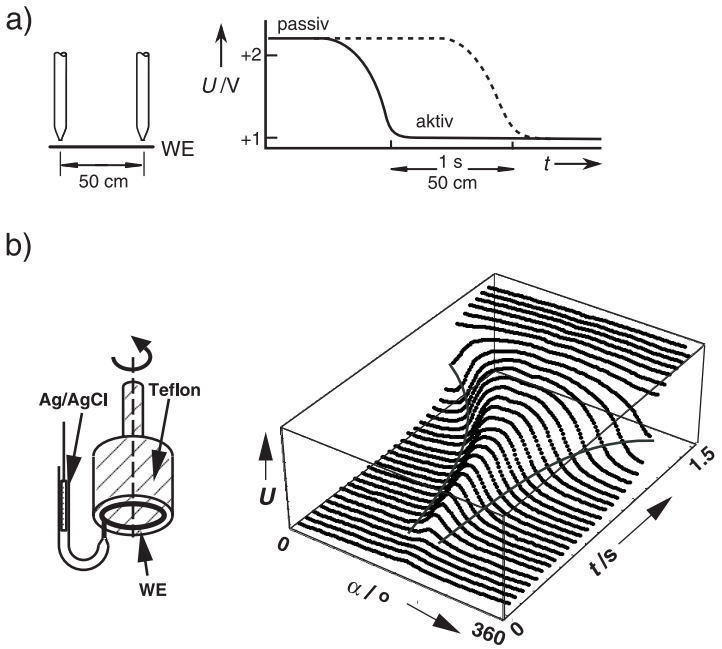

Fig. 31. Experimental potential fronts (a) during the corrosion of gold in a concentrated HCl/NaCl solution (after Ref. [85]); (b) during the potentiostatic reduction of $S_2O_8^{2-}$ on a silver ring electrode in dilute electrolyte [166]. On the left are the corresponding set-ups.

electrode/electrolyte interface are depicted in Fig. 31. Figure 31a shows plots of potential versus time for the electrodissolution of gold at two positions of a wire 50 cm apart [85]. The large drop in the electrode potential by more than 1 V is the result of a passing passive front. This front passes the second potential probe one second later. Both curves are of an identical shape, which implies that both, front profile and front velocity are constant.

In contrast, front profile and velocity vary in the example shown in Fig. 31b. These potential profiles were recorded in front of a ring electrode during the reduction of peroxodisulfate [166]. The spatial resolution was obtained with a single measuring probe over which the ring electrode was rotated. The rotation of the ring thus served two purposes: to obtain information about the double layer potential as a function of space, and to ensure a defined mass transport. Notice that it does not affect pattern formation. In this example we see the whole transition from an initially homogeneous passive (low-current) state to an active (high-current) state. The front emerged through a local fluctuation at about 180°, and then the active state expanded with increasing velocity. In other words, the fronts accelerate with time. Accelerating potential fronts have since been found for several electrochemical systems, such as for cobalt [167] and iron dissolution [168, 169].

Before the origin of the acceleration as well as the different behaviors observed in the two systems is explained, it is useful to briefly review how the interaction of the

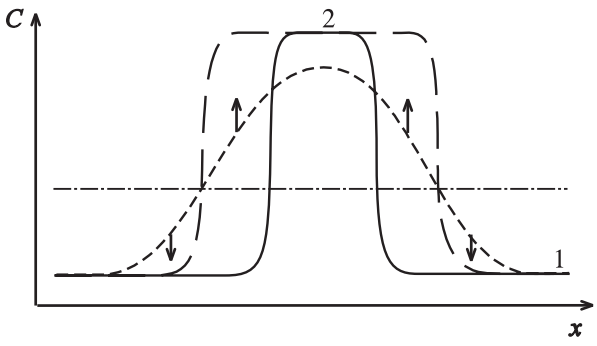

Fig. 32. Illustration of front motion in a bistable system due to the interplay of homogeneous dynamics and migration coupling (see text).

homogeneous dynamics and migration coupling generates a front. Imagine a situation corresponding to the initial state of the transition shown in Fig. 31b, i.e. that a bistable system is in one of the two stable states (state 1) and a fluctuation drives it at some position in the other one (state 2) (Fig. 32, solid line). The arising inhomogeneous potential profile at the electrode leads instantaneously to a reconfiguration of the potential distribution within the entire electrolyte, thereby also changing the electric field, and thus the migration currents, at the electrode/electrolyte interface. These changes, which actually constitute the migration coupling, cause a recharging of the double layer in such a way that the profile becomes broadened (Fig. 32 short dashed line). In the absence of the reaction, the profile would continue to lose structure because of the migration coupling and eventually the electrode would be again in a homogeneous state. However, the homogeneous dynamics tries to drive the system back to the steady states. All positions in which the electrode potential is above the unstable steady state (the horizontal dot-dashed line in Fig. 32) tend to evolve towards the upper steady state and all states below this separatrix to the lower one, as indicated by the arrows. Hence, the overall effect caused by the combined action of transport process and reaction is the motion of the two interfaces, and the more stable of the two stationary states (state 2 in Fig. 32) expands on the expense of the other (metastable) one (Fig. 32 long dashed profile).

The manner in which it expands depends on the range of the spatial coupling. In Section 2 it was derived that in electrochemical systems with base geometry the coupling range depends on the ratio between the extension of the WE in the pattern forming region (e.g. the circumference of a ring electrode) and the distance between the WE and the CE. If this aspect ratio is much smaller than 1, or, in other words, if the CE is close to the WE, the migration coupling is local: a change of the electrode potential at a particular position leads instantaneously only to a measurable recharging of the double layer at positions very close to the perturbation (Fig. 33b). In bistable systems with local coupling fronts move with constant speed and shape [2, 14]. The most important coupling mechanism leading to local coupling is diffusion [14]. Hence, in the classical reaction-diffusion systems (Eq. (2)), fronts move always with constant speed.

If the distance between the WE and the CE is equal or larger than the length of the WE in the pattern forming direction, then the migration coupling is long-range or

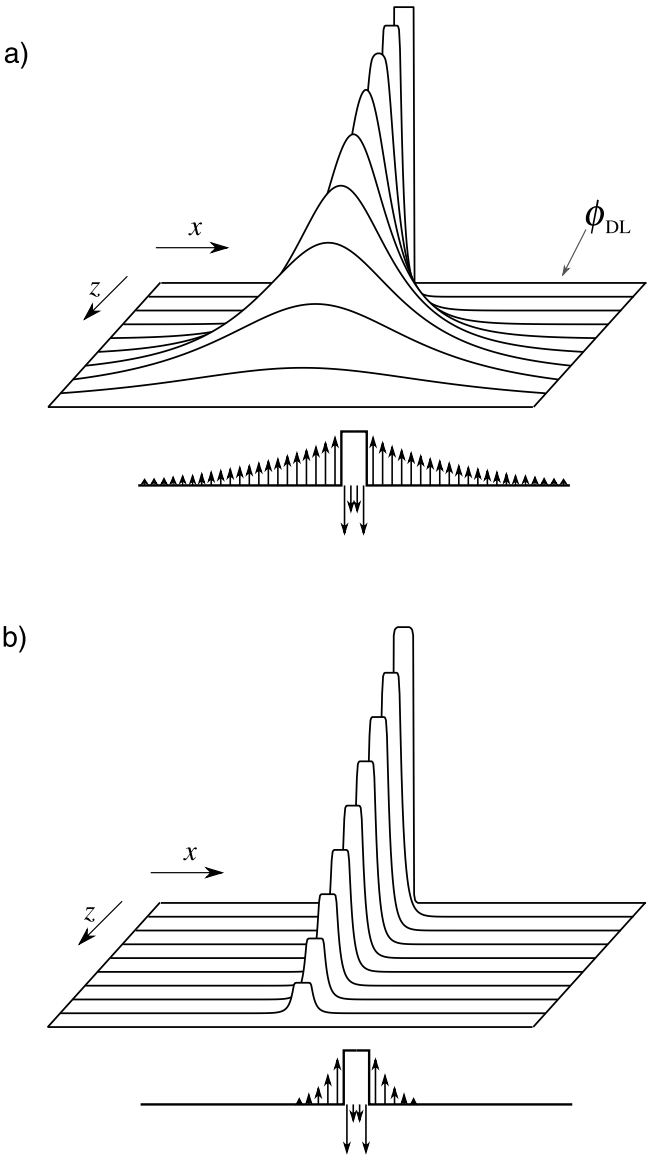

Fig. 33. Schematic representation of the potential distribution in the electrolyte as a result of an inhomogeneous distribution of the electrode potential, ϕ_{DL}, and the effect of migration currents induced by the inhomogeneous potential distribution on the local temporal evolution of the potential (a) for the case that the length of the WE is much smaller than the distance between the WE and the CE; and (b) for the case that the length of the WE is much larger than the distance between the WE and the CE. The length of the arrows in the representations below the potential distributions indicate how the contribution of the migration couplings to the temporal evolution of ϕ_{DL} changes as a function of distance from the disturbance. (x, z: spatial coordinates parallel and perpendicular to the WE, respectively. The electrode is assumed to be one-dimensional and the electrolyte two-dimensional.)

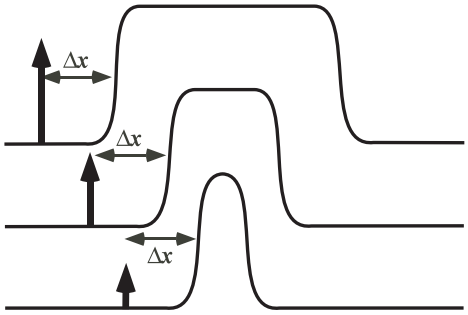

Fig. 34. Illustration showing why nonlocal coupling leads to accelerated front motion. The arrows indicate the contribution of the migration coupling on the temporal evolution of the double layer at a certain distance from the interface (e.g. the inflection point) for different potential distributions.

nonlocal (Fig. 33a): A perturbation of the state of the electrode at a certain location x_0 instantaneously causes a change of states at locations far away from the disturbance. The closer a given location is to x_0, the larger the change at this location. Thus, for aspect ratios > 1, a local perturbation causes the recharging of the double layer along the entire interface, though to a decreasing amount with increasing distance from the interface (see also Section 2.2). The same fact can be also expressed differently: The contribution of the migration coupling to the temporal evolution of ϕ_{DL} at a particular position depends on the value of double layer potential at all the other positions.

With this in mind, it can be illustrated why nonlocal spatial coupling causes the acceleration of waves. In general, the front velocity depends on the characteristic rates of homogeneous dynamics and transport processes. The larger both rates, the faster the front velocity. The vital effect of the nonlocal coupling on the front speed is that it leads to an increase of the characteristic rate of the transport term with time. Consider a position at a certain distance from the moving interface, as indicated in Fig. 34. Depicted again is a situation during a transition in the bistable regime. The spatial coupling causes the potential profile to smear out. For the situation of Fig. 34, this means there is a positive contribution from the spatial coupling term to the temporal evolution at our reference distance from the interface (arrows). Because every point along the interface that is in a state different from the reference state contributes to the spatial coupling, the magnitude of the coupling term becomes the larger the more points are in a state with a double layer potential more positive than our reference state. In other words, the strength of the coupling that the reference state experiences increases with the portion of the electrode that is already in the other state. Clearly, this portion increases during the transition, and for this reason also the front velocity increases.

Hence, the different front behavior depicted in Fig. 31 is most likely due to a difference in the coupling range. In the experimental set-up with which the data of Fig. 31b were measured, the electrode geometry was clearly such that the coupling was long-range. At the time the measurements shown in Fig. 31a were carried out, the connection between cell geometry and propagation behavior of fronts was not yet known, and the relative location of the electrodes can unfortunately no longer be reconstructed. However, since a wire of more than 50 cm in length was used as a

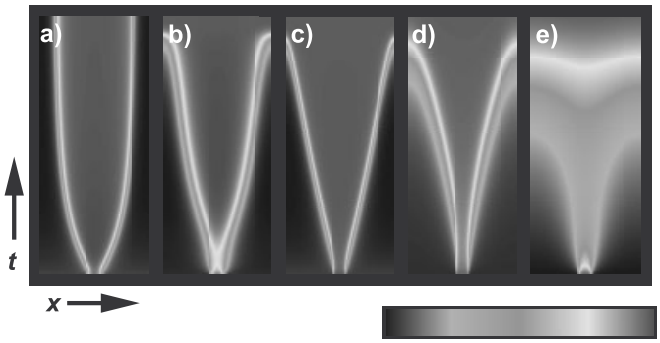

Fig. 35. Simulations showing the influence of electrode geometry on front behavior (one-variable system): (a) short distance between the WE and the RE (strong negative global coupling); (b) intermediate distance between the RE and the WE, the CE far away from the WE (undercritical negative global coupling); (c) close distance between the WE and the CE (approximate local migration coupling, no global coupling); (d) large distance between the CE and the WE, RE placed behind the CE (nonlocal migration coupling, no global coupling); (e) under galvanostatic conditions (positive global coupling). The simulations were carried out for a ring-electrode; the x-scale runs between 0 and 2π.

working electrode, it is likely that the ratio of the distance between the working and the counter electrode relative to the length of the electrode was $\ll 1$. Thus, conditions probably existed in which the migration coupling can be approached by a diffusion coupling. This variation of the front behavior with the aspect ratio of the cell is also reproduced in simulations, with the base geometry and the one-variable systems (Eq. (11)), whereby $k(\phi_{\mathrm{DL}})$ was modeled by a polynomial of third degree. Fig. 35c depicts a simulation in which the distance between the WE and the CE was small, the fronts move with constant velocity. The accelerated fronts shown in Fig. 35d were obtained with a large aspect ratio of electrode length to distance between the WE and the CE.

The nonlocal coupling manifests itself also in other dynamic regimes. Baba et al. investigated the spatiotemporal behavior of a 3 cm long iron wire during oscillations at the active/passive transitions in sulfuric acid (Fig. 36A). They monitored the local current density with 16 one-bit logical analyzers. In general, they found that the increase of the current density was accompanied by a potential front that traveled across the wire with increasing velocity, whereby the front speed depended strongly on the applied voltage (Fig. 36B). The repassivation occurred much slower and apparently without the formation of a front. A similar behavior was reported by Jaeger and coworkers, who investigated waves during oscillations at the active-passive transition during electrodissolution of a thin cobalt ribbon electrode [170]. In this case, two active areas emerged simultaneously at the edges of the thin ribbon electrode and propagated toward the center with increasing velocity.

Although neither a wire nor a thin ribbon is a strict example of a WE supporting base geometry, we can expect that for both cases, i.e. essentially one-dimensional electrodes in a three-dimensional electrolyte, edge effects are much less pronounced than in the case of two-dimensional electrodes surrounded by an insulating plane. Hence, we can tentatively interpret the observations by assuming that the accelerated

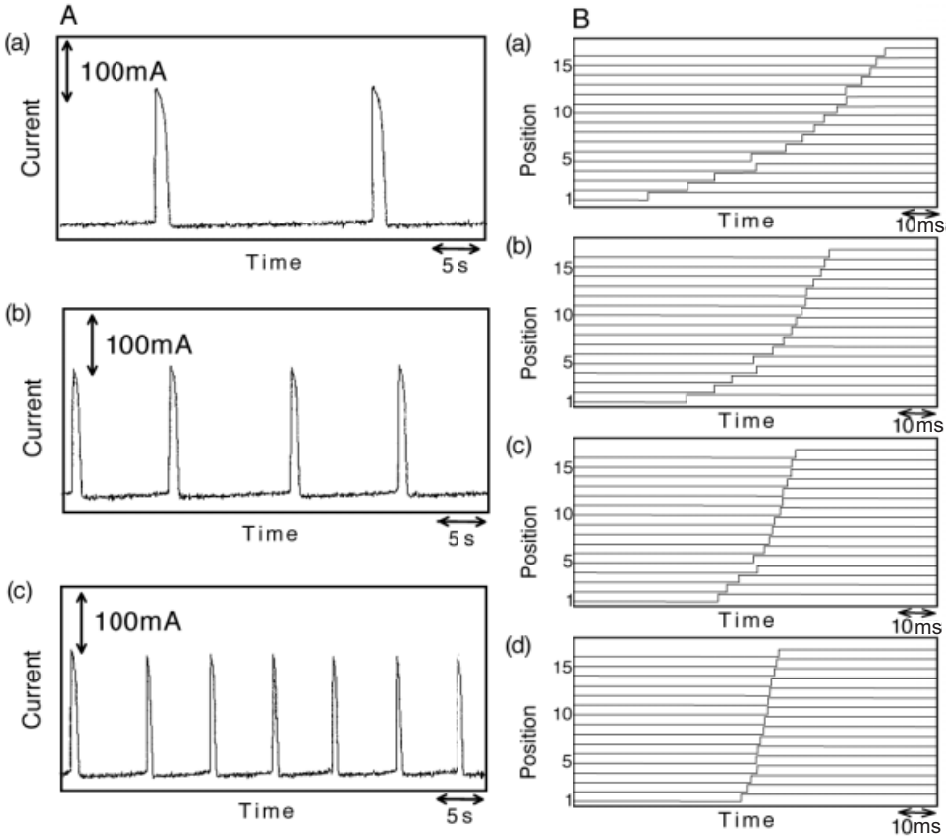

Fig. 36. (A) Self-sustained oscillations during the dissolution of a 3 cm long iron wire in 1 M sulfuric acid at different electrode potentials (a) 0.290 V, (b) 0.285 V, and (c) 0.280 V vs. SCE. (B) Position of the activation front (i.e. during the rising part of the oscillations) versus time. Electrode potentials (a) 0.38 V, (b) 0.34 V, (c) 0.30 V, (d) 0.28 V vs. SCE. (Reproduced from R. Baba, Y. Shiomi, S. Nakabayashi, Chem. Eng. Science 55 (2000) 217 – 222 with permission from Elsevier Science, © 2000).

activation fronts are induced by the nonlocal migration coupling in very much the same way as in the bistable region.

In fact, simulations with the prototype N-NDR oscillator (i.e. the homogeneous system given by Eqs. (38a,b) and the spatial coupling[11] by Eq. (17)) in a parameter region in which the oscillations are relaxation-like, show a very similar picture (Fig. 37) [34]. The increase in current density is accompanied by the accelerated propagation of a sharp potential interface across the surface. During the remaining part of an oscillation the potential becomes increasingly homogeneous. Thus, the spatiotemporal picture during an oscillation can be described as a kind of ''source point'' which sends out a fast and accelerating activation wave that propagates across the

[11] Diffusion of the inhibitor parallel to the electrode is much smaller than the characteristic rate of spatial coupling of the activator (migration), and can therefore be ignored [26].

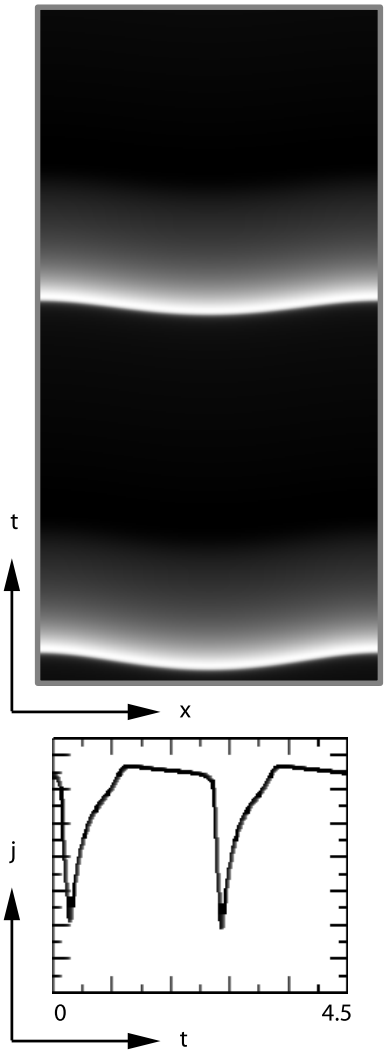

Fig. 37. Gray-scale representation of a calculated spatio-temporal evolution of the potential at a ring electrode (top) and time series of the global current (bottom) in the oscillatory regime of the N-NDR oscillator. (The calculation was done for reduction currents; hence, the largest current is in the peak of the oscillation.)

whole surface and leaves behind a nearly uniform and reactive electrode. For the rest of the cycle the electrode slowly passivates again in an almost homogeneous manner.

The origin of the instability in the simulations, and most likely also in the Fe and Co dissolution experiments, can perhaps be best understood in the picture of the mode equations (Eqs. (21a,b)). The homogeneous modes undergo an oscillatory instability according to the mechanisms discussed in Section 3.1.3. The arising homogeneous limit cycle may excite also higher modes due to the nonlinearity of the reaction terms. However, the growth of the modes is damped by the migration coupling (proportional to $-\sigma n \coth(n\beta)$). Whether the homogeneous oscillation is stable thus depends on whether the damping of the modes by the migration coupling is stronger

than their excitation due to the nonlinearity of the reaction term. During the fast increase in current density, the nonlinear coupling of the modes is especially effective, and a potential wave emerges that is damped again when the temporal changes are slower. In the terminology of nonlinear dynamics, this is a Benjamin–Feir unstable limit cycle [2, 171].

The N-NDR prototype model possesses also a small parameter regime close to the Hopf bifurcation in which the spatiotemporal picture becomes much richer. Depending on the conductivity of the electrolyte and the size of the electrodes either comparatively regular wave patterns with a low wave number or turbulent looking patterns with much higher wave number establish [34, 172].

An experimental confirmation of such patterns in systems whose dynamics seem to be well described by the prototype N-NDR model (i.e. where the negative feedback arises from a delayed transport of the electroactive species) is still missing. This is not really astonishing because the predicted parameter region for ''complex'' patterns is quite small in the model [31, 34]. It also depends on the parameters entering the reaction term such that probably not all N-NDR oscillators exhibit these wave phenomena. Hence, the requirements for spatial instabilities of limit cycles are much more restrictive than for temporal oscillations where any system with an N-NDR (independent of the detailed kinetic) possesses also an experimentally accessible parameter range that exhibits oscillations.

There is, however, an experimental HN-NDR system that possesses an impressively rich variety of spatiotemporal behaviors, the oxidation of H_2 on a Pt ring electrode in the presence of Cu^{2+} and Cl^-. In the entire parameter region investigated so far, all temporal oscillations of current or potential were found to be accompanied by spatial structures [173, 174]. In wide parameter ranges, the temporal oscillations are simple periodic, the patterns possessing predominantly wave number 1. However, for relatively low Cu concentrations, transitions from this regular behavior with a simple spatial structure to more complex irregular patterns were observed for increasing values of the external voltage (Fig. 38) [175]. The larger the external voltage, the higher the wave numbers that are excited such that the characteristic length of the patterns decreases. The corresponding time series of the global current (not shown) exhibit aperiodic oscillations with increasingly smaller amplitude. These observations point to the fact that this is an experimental example for a transition from periodic spatiotemporal structures to spatiotemporal turbulence, to

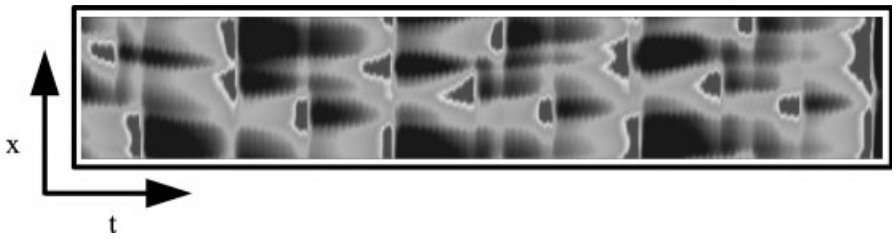

Fig. 38. Irregular spatiotemporal behavior during H_2 oxidation on a Pt ring at a fixed external potential. Electrolyte: 0.5 mM H_2SO_4, 10^{-5} M Cu^{2+}, 0.1 mM Cl^-. (For clarity, the homogeneously oscillating part of the data has been subtracted.)

the best of my knowledge the first ever in a chemical system. From a theoretical point of view, there are many interesting open questions. The first question concerns the "basic instability" of the homogeneous oscillation, which appears in a parameter range that is much larger than in the N-NDR oscillators. This could be characteristic for HN-NDR oscillators, but specific features of the reaction mechanism of this particular system could also cause it. Other questions are which bifurcations are involved in the transition and again, what the essential features for the occurrence of the spatiotemporal complexity are.

Otterstedt et al. carried out a series of experiments on spatiotemporal pattern formation during cobalt electrodissolution in phosphate solutions [170, 176]. Some of these experiments were done with a "quasi one-dimensional" ribbon WE, where edge effects are not pronounced. The arrangement of the remaining electrodes was such that the negative global coupling is minimized. Hence, we can assume that also here the patterns arise owing to the interplay of reaction dynamics and migration coupling only. Above, we already mentioned that simple periodic oscillations were characteristically accompanied by accelerating activation fronts. If the parameters are varied (such as the phosphate concentration), the activation phase becomes longer and the current time trace is superimposed by small oscillations (Fig. 39a). These small oscillations arise from oscillations in the width of the active range: the motion of the leading front is an accelerating motion (Fig. 39b); the back front displays a pulsating behavior in the passive range, however [170]. Similar phenomena are also observed for the dissolution of cobalt in the excitable range of the reaction,

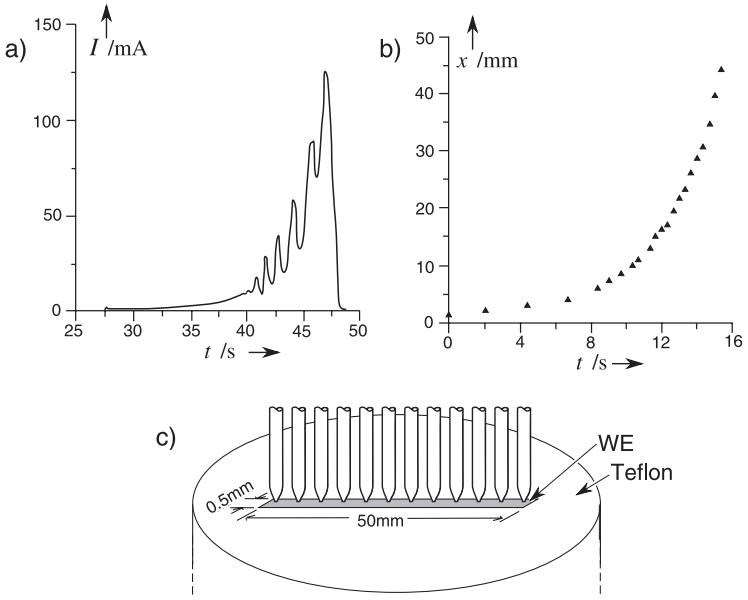

Fig. 39. (a) Total current; (b) position of the leading front as a function of time for a single, autonomous oscillation during dissolution of a cobalt ribbon electrode; and (c) experimental set-up. (Reproduced with permission from R. D. Otterstedt, P. J. Plath, N. I. Jaeger and J. L. Hudson, Phys. Rev. E 54 (1996) 3744, © (1996) by the American Physical Society.)

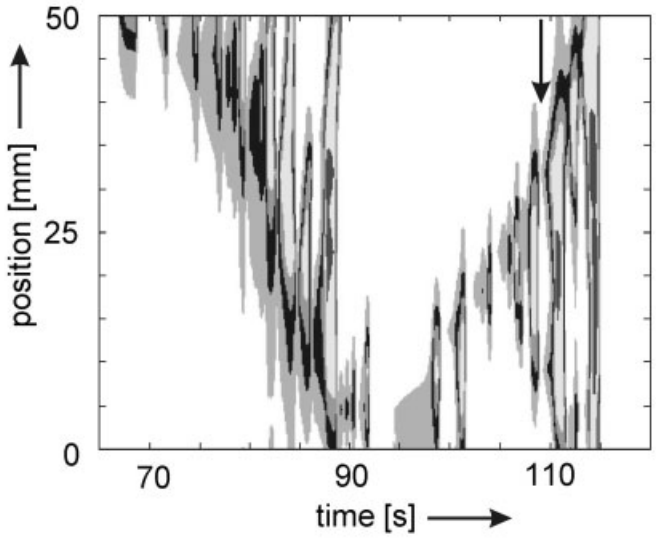

Fig. 40. Activation of a ribbon electrode with modulation and reflection at the end of the ribbon during Co dissolution in buffered phosphoric acid. The patterns were measured with 16 potential probes. White denotes total passivity; black, highest activity. (Reproduced with permission from R. D. Otterstedt, N. I. Jaeger, P. J. Plath and J. L. Hudson, Phys. Rev. E 58 (1998) 6810, © (1998) by the American Physical Society).

where a local excitation at one end of the ribbon caused the formation of an active pulse that changed its width while propagating across the electrode [176]. For larger phosphate concentration, bringing about a faster repassivation, the motion of the pulse became even more complex. Wave splitting events as well as the reflection of the pulse at the end of the ribbon occurred (Fig. 40). The authors discuss how the interaction of the kinetics of the repassivation of the electrode and long-range migration coupling could give rise to the complex motions. It is a challenge for future work to convert these ideas into a mathematical model.

So far, all examples discussed, theoretical as well as experimental ones, involved quasi one-dimensional electrodes. Concerning studies with two-dimensional electrodes and base symmetry, there is only one theoretical approach. Karantonis and Nakabayashi investigated pattern formation on a disk electrode in a set-up with base geometry, i.e. the disk forms the top of a hollow cylinder (cf. Fig. 3a) [39]. As a first step they only considered pattern formation in the radial direction, while assuming the azimuthal direction to be uniform. This allowed the solution of Laplace's equation by an infinite series of Bessel functions. In Fig. 41 snapshots of the electrode potential distribution at different phases of an oscillation are reproduced, showing clearly the participation of a low eigenmode in the oscillation. The model underlying these calculations is an electrodissolution model that follows the dissolution-participation model introduced in Ref. [87]. We should note that the model is less realistic than the original model since it does not incorporate changes of the surface pH for all long-term solution (thus the negative feedback is not due to a shift in the Flade potential but due to the salt film dynamics). Hence, this study aims at con-

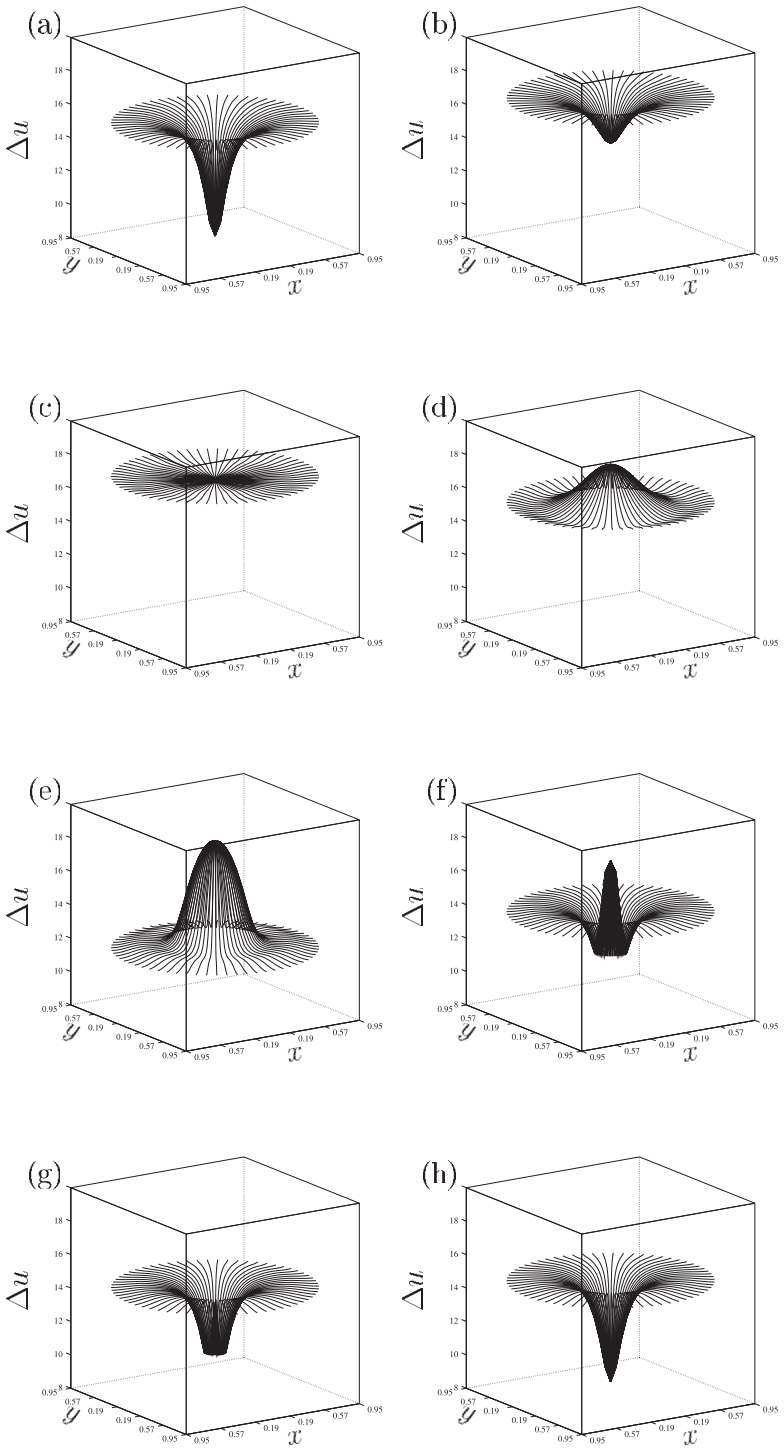

Fig. 41. Calculated spatial variation of the double layer potential of a disk-shaped electrode in a hollow cylinder (cf. Fig. 3a) at different phases of an oscillation. (Reproduced from A. Karantonis and S. Nakabayashi, Electrochimica Acta 46 (2000) 745–757 with permission from Elsevier Science.)

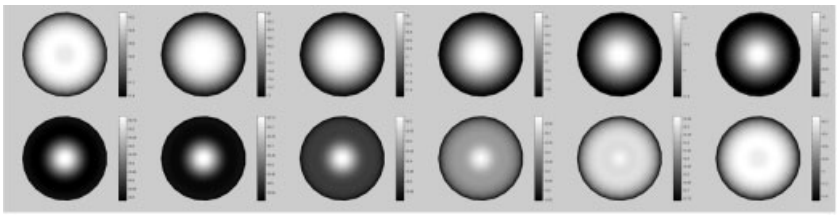

Fig. 42. Calculated potential distribution at a disk electrode embedded in an insulator at different instants in time during one oscillation of the global current. Black denotes the most passive state of the electrode surface; white, the most active one. (Reprinted from A. Birzu, B. J. Green, R. D. Otterstedt, J. L. Hudson, N. I. Jaeger, Z. Phys. Chem. 216, 459 (2002) with permission from Oldenbourg Wissenschaftsverlag.)

tributing an answer to the question of what type of patterns might emerge in oscillating systems with a certain type of geometry, rather than giving a realistic description of a specific metal dissolution reaction.

The first truly two-dimensional patterns were calculated by Birzu et al. for a disk electrode embedded in an insulating surface [28]. This is a typical example of a geometry with edge effects where the change of the *effective* electrolyte resistance along the radial direction strongly influences, if not dominates, pattern formation. For the simulations, the two-variable model for oscillations at the active/passive transition of metal dissolution reactions was employed.[12] The dominant pattern obtained when placing the RE on the axis of the disk and close to the CE, i.e. without an additional negative global coupling, is reproduced in Fig. 42. It is clearly axially symmetric, and it appears as if the rim of the electrode sends out a passivation wave, whereas the reactivation of the electrode starts in the center of the disk and moves outward. Also in the few experimental studies of patterns on disk electrodes reported so far, radially symmetric waves emerging from the rim of the electrode constituted a dominant pattern [177–180].

Note that these ''primary'', radially symmetric waves on disk electrodes are, from a dynamic point of view, fundamentally different from all the waves discussed above. The latter ones emerge due to a spatial instability of a homogeneous state, whereas for disc electrodes such a homogeneous state does not exist. In Section 2.2 it was shown that for electrodes embedded in an insulator, the effective resistance changes with the radius. Neglecting the spatial coupling through the electrolyte, the differential equation for the double layer potential depends on the radial position ρ according to

$$C\frac{d\phi_{\mathrm{DL}}}{dt} = -i_F(\phi_{\mathrm{DL}}) + \frac{U - \phi_{\mathrm{DL}}}{AR_\Omega(\rho)}. \tag{46}$$

Since at the edge of the electrode $R_\Omega(\rho_{\mathrm{edge}}) = 0$, $\phi_{\mathrm{DL}}(\rho_{\mathrm{edge}})$ is always identical to the

[12] In a rigorous sense, the incorporation of changes of the proton concentration due to migration is problematic when Laplace's equation is used to determine the potential distribution [25]. On the other hand, it seems to be highly unlikely that, when determining the true potential distribution, the patterns would be affected by more than a minor correction. This justifies the approach chosen by Birzu et al.

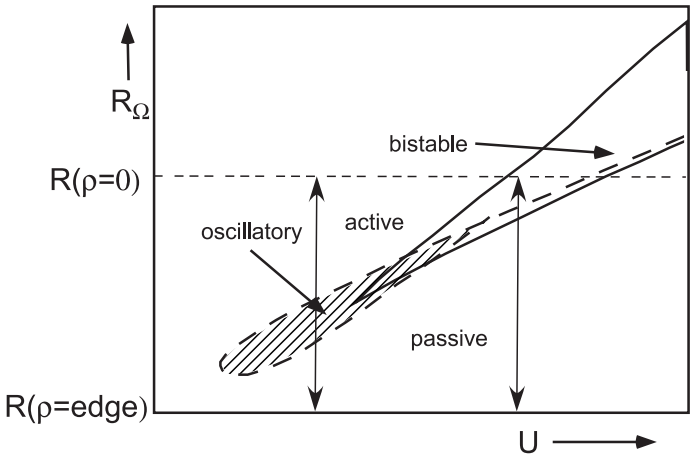

Fig. 43. Skeleton bifurcation diagram of an N-NDR oscillator. $R(\rho = 0)$: effective resistance at the center of a disk electrode; $R(\rho = \text{edge}) = 0$: effective resistance at the edge of the disk electrode.

externally applied voltage U, and the disk is in the most passive state, whereas the center acquires the most active state. The states involved and their corresponding dynamics can be read off from a skeleton bifurcation diagram of the homogeneous system as sketched in Fig. 43: Depending on U and the effective resistance in the center of the disk ($\rho = 0$), there are situations where – without migration coupling – the rim would be in a passive state, the center in an active state, and in an intermediate range the dynamics would be oscillatory; or, for higher electrolyte conductivity, the central region would be oscillatory and an outer circle in the passive state and so on. Thus, even without any migration coupling the potential distribution varies radially. The migration coupling tends to adjust the potentials such that the differences will be smoothened. Moreover, an oscillating region can enforce oscillations in a region that would be otherwise stationary. Hence, on any disk electrode, an oscillation is accompanied by radially symmetric waves even if the interplay of reaction dynamics and migration coupling would not result in a spatial instability in a system with base geometry (i.e. without edge effects). Of course, spatial instabilities will often occur in addition, manifesting itself e.g. in a broken symmetry along the azimuthal direction, or a more complex behavior in the radial direction.

The spatial "unfolding" of the potential-dependent bifurcation structure can also be achieved by employing an asymmetric placement of the WE and the CE electrodes, as demonstrated by Steinbock and coworkers [181]. An asymmetric arrangement leads inevitably to an asymmetric distribution of the electric field, excluding the possibility of truly homogeneous states. An extreme case is the set-up shown in Fig. 44a: The cathode, a steel wire, and the anode, a Pt electrode, are placed along one line. Hence, the effective resistance between a point on the cathode and the anode changes monotonically along the steel wire. As can be seen in Fig. 44b, going from the region closest to the anode to larger distances, the iron wire is first in a stationary state; adjacent to this is an oscillatory region that exists only in a comparatively small interval. It sends out pulses to its right, which fail to propagate at a certain position

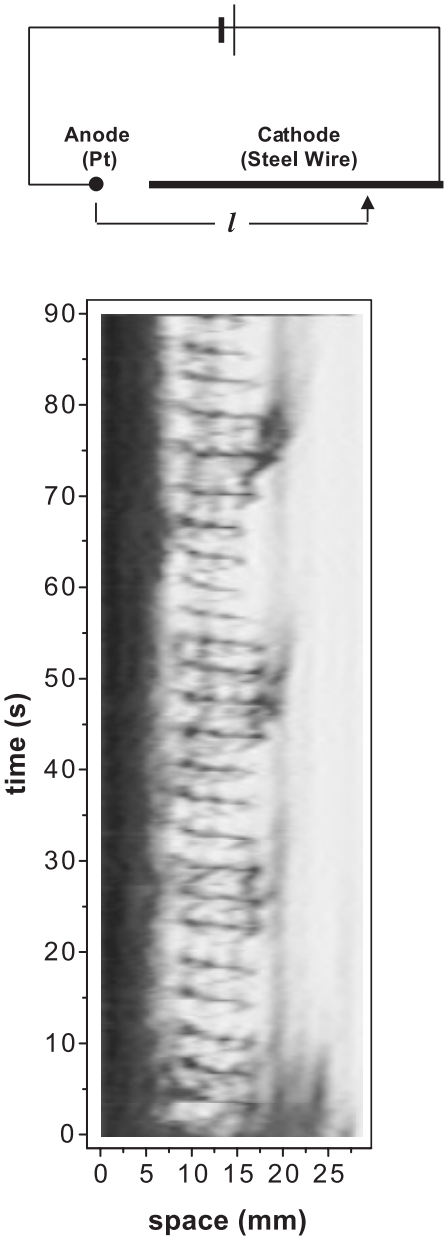

Fig. 44. (a) Scheme of the electrochemical cell. (b) Time-space plots of the electrodissolution of steel in 12.2 M HNO_3. (Reproduced from K. Agladze, S. Thouvenel-Romans, and Oliver Steinbock, Phys. Chem. Chem. Phys. 3 (2001) 1326 by permission of the Royal Society of Chemistry on behalf of the PCCP Owner Societies.)

behind which the system is again in a stationary state, which is however different from the first one[13].

[13] The authors identify the region closest to the anode with the active region, and the one at the other end of the wire with the passive one. If the certainly simplified consideration is correct that the origin of the different states is the increasing effective electrolyte resistance with increasing distance from the anode, then this assignment should be just the other way around (cf. Fig. 43).

4.1.2 Negative Global Coupling: Close Distance Between the WE and the RE

In many experiments the RE probes the electrolyte potential not at the height of or behind the CE, but somewhere between the CE and the WE. As shown in Section 2.3, this introduces a global, negative feedback into the system, i.e. a local change of the double layer potential is fed back (through the potentiostat) to all the positions of the WE in such a way that differences in ϕ_{DL} are enhanced. In general, a negative global feedback strongly promotes the development of patterns [2, 18, 19]. Also in electrochemical systems a close RE proved to give rise to a rich abundance of patterns. Since the use of a Luggin–Haber capillary is a standard method in electrochemistry to minimize the voltage drop through the electrolyte, an understanding of the impact of the placement of the RE on the stability of homogeneous states is of particular importance.

Electrochemical pattern formation that is dominated by a negative global coupling is discussed in this subsection. The basic destabilization mechanism is easiest explained with one-variable systems whose dynamics can be captured by considering the double layer potential only which will be discussed first. Then we deal with pattern formation in oscillatory systems. Since again the complete geometry of the electrode arrangement determines the patterns, in each case first systems with base symmetry and than those with edge effects are discussed. Furthermore, as soon as the RE is placed between the WE and the CE, the lateral position of the RE becomes important, too. Hence, for both the one-variable and the two-variable systems we start with the simplest geometry, which is always the most symmetric one, and then demonstrate the effect of a ''perturbation'' of the cell symmetry.

Stationary Domains in One-Variable Systems

Homogeneous one-variable N-NDR systems might be monostable or bistable, depending on the resistance, R_Ω, between the WE and the RE. A negative global coupling can destabilize the homogeneous steady state on the NDR branch that exists for low values of the resistance in a parameter range that is similar to the range of resistances in which oscillations are found in two-variable N-NDR systems (cf. Fig. 11). Furthermore, within the bistable parameter range it supports the emergence of stationary domains with greatly different ϕ_{DL} that coexist with the two homogeneous stationary states.

The simplest geometry with which these effects can be proven is a ring WE with the RE on the axis of the ring, as was the case in the experiments reproduced in Figs. 45 and 46. Fig. 45 shows stationary potential domains that were measured during the reduction of $S_2O_8^{2-}$ on an Ag ring electrode [42]. When placing the RE close to the WE, the cyclic voltammogram exhibited an N-NDR region (Fig. 45a). Note that, due to the small value of the uncompensated resistance, the cyclic voltammogram does not exhibit a bistable region, and does not contain any sign of a dynamic instability. However, when the outer voltage was fixed in the NDR range, the electrode slipped into a patterned state consisting of two domains with different double layer

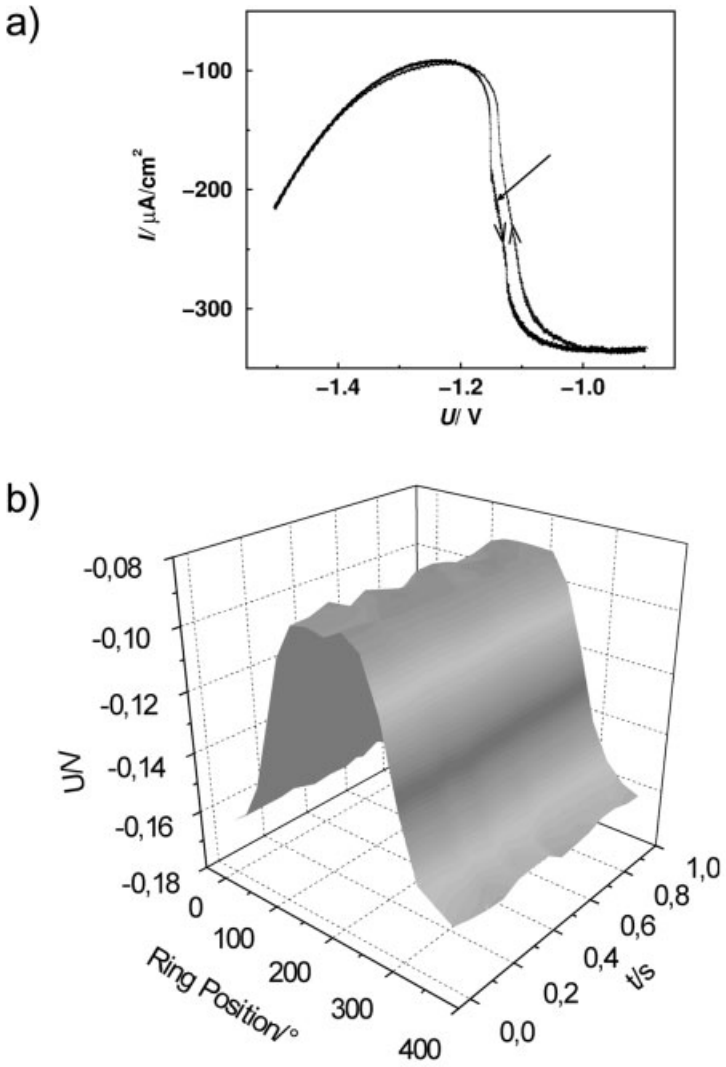

Fig. 45. (a) Cyclic voltammogram and (b) stationary potential domains during the reduction of $S_2O_8^{2-}$ on a Ag ring electrode at fixed outer potential ($U = -1.13$V) [42]. The end of a Haber–Luggin capillary was positioned on the axis of the ring and close to the WE.

potentials and different reaction rates. These states were stationary in time (Fig. 45b).

Grauel and Krischer also detected similar stationary domains during the oxidation of H_2 on a Pt ring electrode in sulfuric acid [182]. As can be seen in the cyclic voltammogram in Fig. 46a, in this case the homogeneous active branch coexisted with the oxide covered passive branch, and thus the homogeneous dynamics were bistable. The stationary structure displayed in Fig. 46b spontaneously formed when a

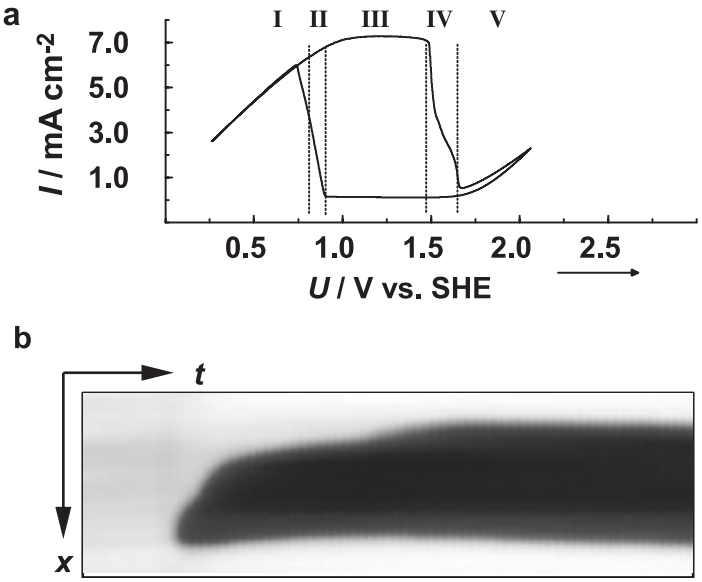

Fig. 46. (a) Cyclic voltammogram and (b) position-time plot of the local double layer potential during the oxidation of H_2 on a Pt ring electrode in 1mM H_2SO_4. (ϕ_{DL} is coded in gray scale; the largest potential value is shown in black, the smallest one in white). x runs between 0° and 360°, the time axis covers an interval of about 75 s. The roman numerals in (a) denote different dynamical regimes: (I) monostable (homogenous active state); (II) bistable (coexistence of stationary domains and the homogeneous active state); (III) tristable (coexistence of stationary domains and the homogeneous active and passive state); (IV) bistable (coexistence of stationary domains and the homogeneous passive state); and (V) monostable (homogenous passive state).

constant potential was adjusted on the active branch close to its positive end. When sweeping the voltage slowly once the system had attained the domain state, it could be shown that the domains existed in a large region of the externally applied voltage that reached at both ends beyond the saddle-node bifurcations of the homogeneous system. When changing the voltage, the relative size of the two domains changed continuously, whereby the active domain was the larger the smaller the voltage was and, correspondingly, the passive domain grew when increasing the voltage. When increasing the distance between the WE and the RE, the stationary domains eventually ceased to exist and front transitions were observed [182].

The stationary, self-organized domains could be reproduced in calculations based on the model introduced in Section 2, whereby the equation for the double layer potential is conveniently formulated as [27, 29, 37, 64]

$$C\frac{\partial \phi_{DL}}{\partial t} = g(\phi_{DL}) - \frac{\sigma}{w}\frac{\gamma}{1-\gamma}(\langle \phi_{DL}\rangle - \phi_{DL}) - \sigma\left(\frac{\partial \phi}{\partial z} - \frac{\phi}{w}\right)\Bigg|_{z=WE} \tag{47}$$

where the homogeneous dynamics has been lumped into the function g, the second and third term describe the global coupling and the migration coupling, respectively.

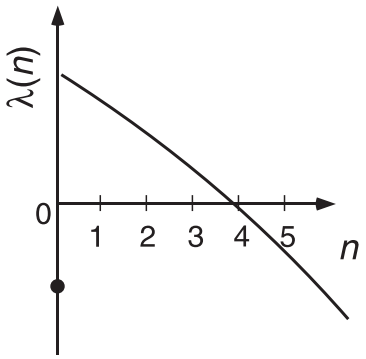

Fig. 47. Schematic of the growth rate $\lambda(n)$ (as defined in Eqs. (48) and (49)) of a perturbation of the homogeneous steady state versus the wave number of the perturbation in the case of negative global coupling.

$\gamma = R_{\text{comp}}/R_{\text{cell}}$ is defined as the ratio between the compensated part of the cell resistance, R_{comp}, and the total cell resistance $R_{\text{cell}} = \sigma/w$, (i.e. the resistance between WE and CE, where σ is the conductivity of the electrolyte and w results from the cell geometry). A calculation carried out with the two-dimensional cylinder geometry of the cell (cf. Fig. 3d), an N-shaped current-potential dependence and a value of $R_{\text{uncomp}} = 0.1 * R_{\text{cell}}$ is reproduced in Fig. 35a. Also when the electrolyte was modeled as a three-dimensional medium, stationary domains were stable solutions of the model if the RE was positioned sufficiently close to the WE [29].

Performing a linear stability analysis, it can be readily shown under what conditions the global coupling destabilizes the homogeneous steady state [37]. Therefore, we consider again the two-dimensional cylinder geometry (Fig. 3d), and perturb the homogeneous steady state $\phi_{\text{DL}}^{\text{ss}}$ with Fourier modes of small amplitude: $\delta\phi_{\text{DL}}(n) - \phi_{\text{DL}}^{\text{ss}} = \delta a_n(t)\cos(nx)$. Then, in linear approximation, a homogeneous perturbation ($n = 0$) will develop according to

$$\frac{d\delta a_0}{dt} = \left.\frac{dg(\phi_{\text{DL}})}{d\phi_{\text{DL}}}\right|_{\phi_{\text{DL}}^{\text{ss}}} \delta a_0 =: \lambda_0 \delta a_0 \tag{48}$$

and a perturbation with wave number n according to

$$\frac{d\delta a_n}{dt} = \left[\left.\frac{dg(\phi_{\text{DL}})}{d\phi_{\text{DL}}}\right|_{\phi_{\text{DL}}^{\text{ss}}} + \frac{\sigma}{w}\left(\frac{\gamma}{1-\gamma}\right) - \sigma(n\coth(n\beta) - w^{-1})\right]\delta a_n =: \lambda_n \delta a_n. \tag{49}$$

whereby the second term in Eq. (49) arises from the global coupling. From its positive sign, it follows that it destabilizes all inhomogeneous modes, or, equivalently, the homogeneous mode is stabilized. The last term stems from the synchronizing migration coupling and was derived in Section 2 (cf. Eq. (21)).

Clearly, a perturbation with a wave number n will decay, if the growth rate λ_n is negative and for positive growth rates, the perturbations will grow. The qualitative dependence of the growth rate as a function of n is plotted in Fig. 47. It has a monotonically decreasing characteristic for $n > 0$, but exhibits a jump toward smaller

values for $n = 0$. Since the contribution of the migration coupling approaches 0 as n approaches zero, this jump is due to the negative global coupling. If a system's parameter is varied, such as the externally applied voltage, then the whole curve, including the value for $n = 0$, is shifted along the ordinate.[14] Starting with a stable homogeneous stationary state, i.e. all $\lambda(n) < 0$, for a shift in the positive direction, the growth rate becomes positive, first for a range of wave numbers $0 < n \leq n_{\max}$, and then for the homogeneous mode ($n = 0$). For sufficiently large systems, $n_{\max} > 1$, and the first physical meaningful mode that becomes unstable is the mode corresponding to $n = 1$. The situation $\lambda_1 = 0$ thus signifies a bifurcation at which the homogeneous stationary state becomes unstable and a stable pattern with $n = 1$ branches off the homogeneous steady state: the stationary domains are born. Notice that the monotonic decay of the growth rate with increasing wave number excludes the possibility of the emergence of a pattern with a defined wavelength, that is, a wavelength that is independent of the size of the electrode.

Christoph [37] showed that the domain bifurcation can only occur if the zero-frequency impedance Z_F is negative. This can be easily seen with a few algebraic transformations. Realizing that

$$\left.\frac{\partial g(\phi_{\mathrm{DL}})}{\partial \phi_{\mathrm{DL}}}\right|_{\phi_{\mathrm{DL}}^{\mathrm{ss}}} = -\left.\frac{\partial i_F}{\partial \phi_{\mathrm{DL}}}\right|_{\phi_{\mathrm{DL}}^{\mathrm{ss}}} - \frac{1}{R_{\mathrm{uncomp}}} = -{Z_F}^{-1}|_{\phi_{\mathrm{DL}}^{\mathrm{ss}}} - \frac{1}{R_{\mathrm{uncomp}}} \tag{50}$$

and

$$\frac{\sigma}{\omega}\left(\frac{\gamma}{1-\gamma}\right) = \frac{1}{R_{\mathrm{uncomp}}} - \frac{\sigma}{\omega}, \tag{51}$$

the linearized evolution equations of the homogeneous mode (Eq. (48)) and the first inhomogeneous mode (Eq. (49) with $n = 1$) become

$$\frac{d\delta a_0}{dt} = \left[{Z_F}^{-1}|_{\phi_{\mathrm{DL}}^{\mathrm{ss}}} - \frac{1}{R_{\mathrm{uncomp}}}\right]\delta a_0 \quad \text{and} \quad \frac{d\delta a_1}{dt} = [{Z_F}^{-1}|_{\phi_{\mathrm{DL}}^{\mathrm{ss}}} - \sigma \coth(\beta)]\delta a_1, \tag{52}$$

respectively. Since the coth with a positive argument is always positive, the growth rate λ_n can become only positive if the stationary state is on the negative differential branch. Furthermore, $\lambda_1 > 0$ and $\lambda_0 < 0$ can only be satisfied simultaneously if

$$\frac{1}{R_{\mathrm{uncomp}}} = \frac{\sigma}{\alpha} < \sigma \coth(\beta), \tag{53}$$

where the uncompensated part of the cell resistance is expressed through the conductivity and a geometric factor α. Since β depends on the relative placement of the

[14] Because σ and β not only enter the local dynamics, but determine also the migration coupling, a variation of these two parameters leads to a shift of the curve along the ordinate, as well as to a change in the form of the curve.

WE and the CE and α on the relative placement of the WE and the RE, whether stationary domains might occur or not depends on the relative positions of all three electrodes in a nontrivial manner.

This was illustrated by Jaeger and coworkers with model calculations employing a three-dimensional geometry, in which the ring-shaped WE and the ring-shaped CE were concentrically placed in one plane, the CE surrounding the WE. The RE was positioned on the axis of the rings close to the plane in which the WE and the CE lay (Fig. 48a). Choosing two different radii of the CE and otherwise identical parameters, stationary domains were found for a small radius of the CE, but not for a large radius (Fig. 48b,c). This is a manifestation of the fact that the strength of the global coupling depends in a complex manner on both, the total cell resistance and the uncompensated cell resistance.

Another peculiar effect originating from the interplay of negative global coupling and migration coupling is the possibility to remotely trigger waves in the bistable region of a (H)N-NDR system [36]. The experiment by Eiswirth and coworkers depicted in Fig. 49a shows data obtained during the oxidation of formic acid oxidation on a stationary Pt ring electrode using a close RE. The local potential was measured with the help of 11 stationary potential probes. These probes were placed, together with a trigger electrode at position 12 over the ring electrode (Fig. 49b). The double layer potential was pushed further into the passive range at the location marked by the arrows (the ring position $12 = 0$) by a pulse produced with the trigger electrode at time 0. This caused a transition to the active state at the 180° position, that is, exactly opposite the disturbance. This phenomenon, termed "remote triggering", shows that the farther away the positions are from the reference position, the more pronounced is the antiphase behavior induced by the negative coupling; at these positions the migration coupling, which opposes the negative coupling, is the smallest.

So far, all the discussed experiments and simulations were carried out with ring electrodes whereby the RE was located on the axis of the ring. Only in this case is the potential at the position of the RE equally affected by all locations of the WE, and only then constitutes the feedback induced by the position of the RE a purely global coupling, that is, it depends on the *average* double layer potential. For any asymmetric condition, the potential at the position of the RE is a function of a weighted average of ϕ_{DL}, $g(\phi_{\mathrm{DL}}) = \int_x w(x)\phi_{\mathrm{DL}}(x)dx$, positions at the WE that are closer to the RE having a larger weight $w(x)$. For one-variable systems and ring electrodes, Birzu et al. [27] investigated the effect of an asymmetrically placed RE on the dynamic behavior in the bistable state. Depending on the angular distance between the RE and the location of the disturbance, the system may remain in the same state, undergo a transition to the other homogeneous state or acquire a stationary domain state.

The only two-dimensional electrode geometry for which the influence of a close RE on the dynamic behavior in a one-variable N-NDR system has been investigated is a disk electrode embedded in an insulator. Here, a close reference electrode located on the axis of the ring induces a symmetry breaking of the azimuthal direction. The resulting pattern consists of two regions, one that has the form of a crescent moon, the other one occupying the remaining oval-shaped part of the disk (Fig. 50).

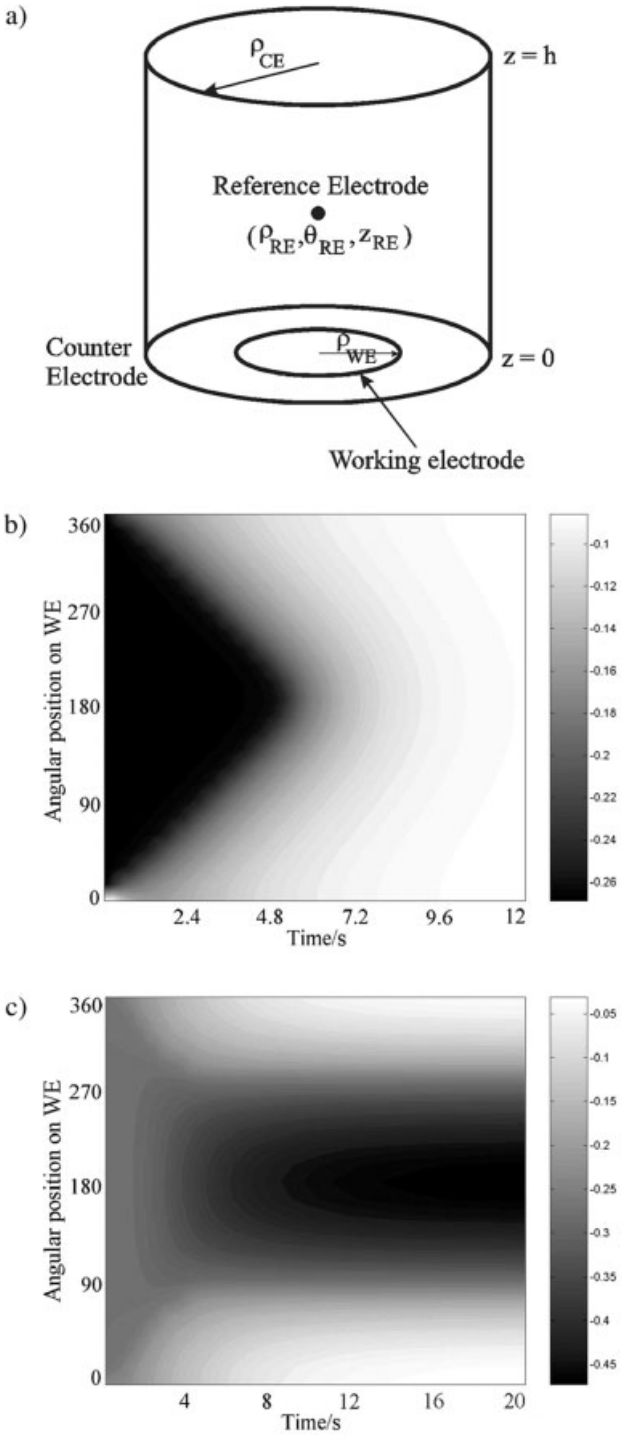

Fig. 48. (a) Three-dimensional geometry used in the calculations. (b) and (c) Calculated space-time plots of the double layer potential in a gray scale representation where all model parameters were identical but the circumference of the CE, r_{CE}; (b) $r_{CE} = 11.7$ cm.; (c) $r_{CE} = 5.0$ cm. (Reproduced from A. Birzu, B. J. Green, N. I. Jaeger, J. L. Hudson, J. Electroanal. Chem. 504 (2001) 126, © (2001), with permission from Elsevier Science.)

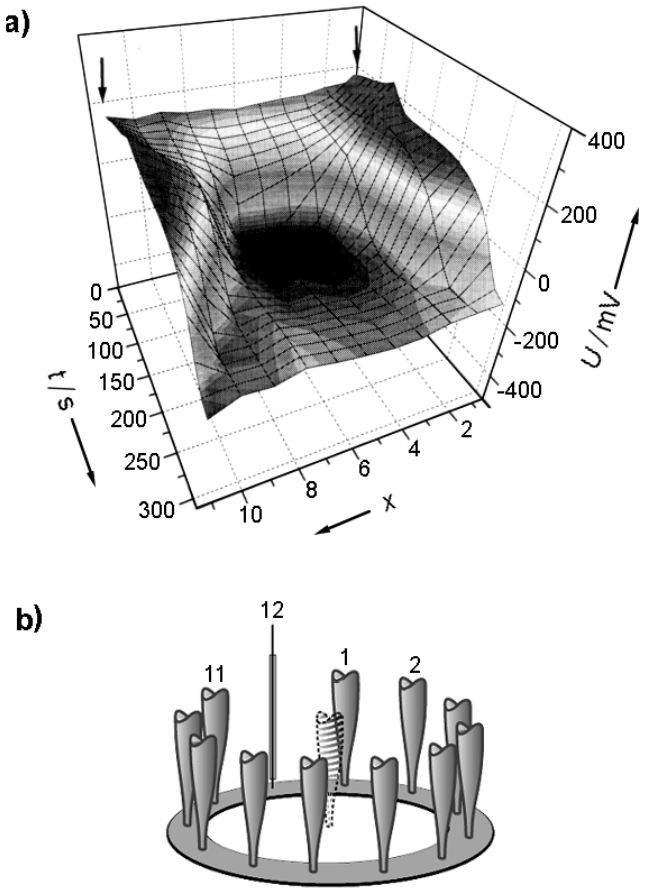

Fig. 49. (a) Local potential drop across the double layer as a function of position and time during a remotely induced transition in the bistable regime of the oxidation of formic acid on a Pt ring electrode. The RE was positioned close to the WE. At the position marked by the arrows the potential was disturbed locally toward positive values. The ring position gives the electrode number of (b). (b) Set-up for measurements used to obtain the data of (a). The outside potential probes serve to measure the local potential; the central one serves as the reference electrode. At position 12 is a trigger electrode. (This figure was provided by courtesy of P. Strasser and M. Eiswirth; see also Ref. [36].)

Waves and Pulses in Two-Variable Systems

The largest variety of patterns in electrochemical systems was found in the oscillatory region of an electrode reaction in the presence of a negative global coupling. The pioneering experiments on pattern formation with a close RE go back to Otterstedt et al. [183], who studied the electrodissolution of Co disk and ring electrodes at a time where the influence of the RE on pattern formation was yet unknown. The experimental set-up (Fig. 51A) was chosen such that the surface of the WE was facing upward. Since active and passive ranges of the electrode have a visible contrast, the

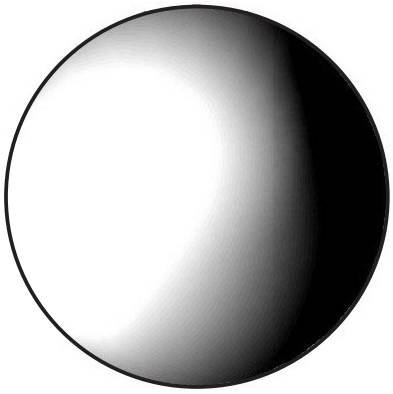

Fig. 50. Calculated stationary potential pattern that forms on a disk electrode embedded in an insulator when the RE is on the axis of the disk and close to the WE. Reprinted from A. Birzu, B. J. Green, R. D. Otterstedt, J. L. Hudson, N. I. Jaeger, Z. Phys. Chem. 216, 459 (2002) with permission from Oldenbourg Wissenschaftsverlag.)

spatiotemporal dynamics could be followed with a video camera. On both, ring and disk electrodes narrow, traveling domains of high activity, that is, a high rate of dissolution, emerged on an otherwise passive electrode. An example of such a pulse rotating around the center of a disk electrode is depicted in Fig. 51B.

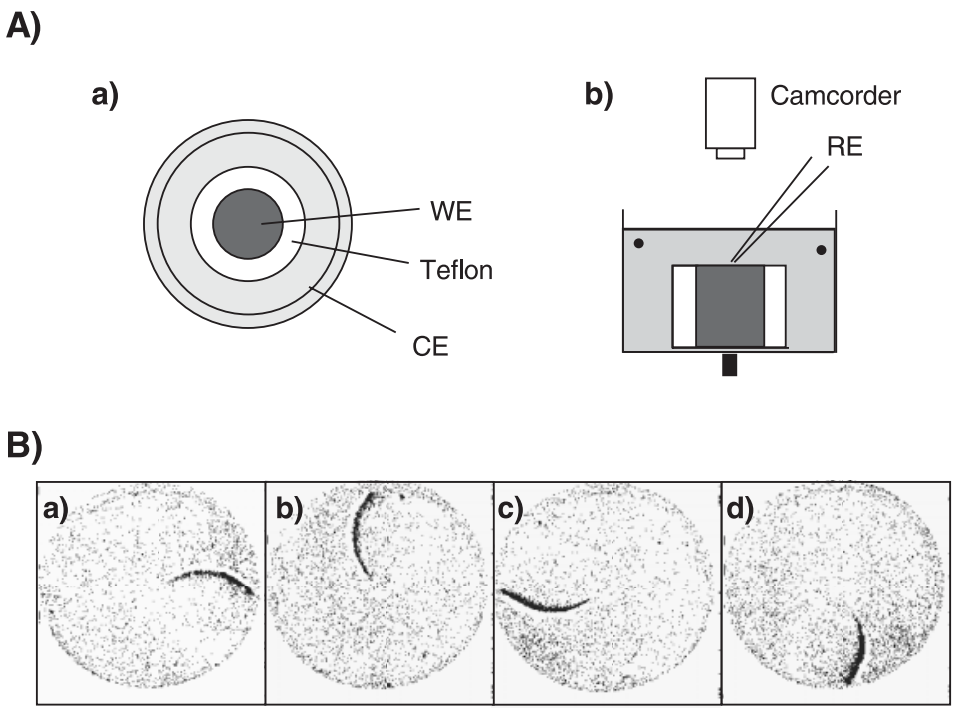

Fig. 51. (A) (a) Top view and (b) side view of the experimental set-up. (B) Rotating active region during the oxidation of a Co disk-electrode with a close RE. (Courtesy of R. D. Otterstedt and N. I. Jaeger; for experimental details see Ref. [183].)

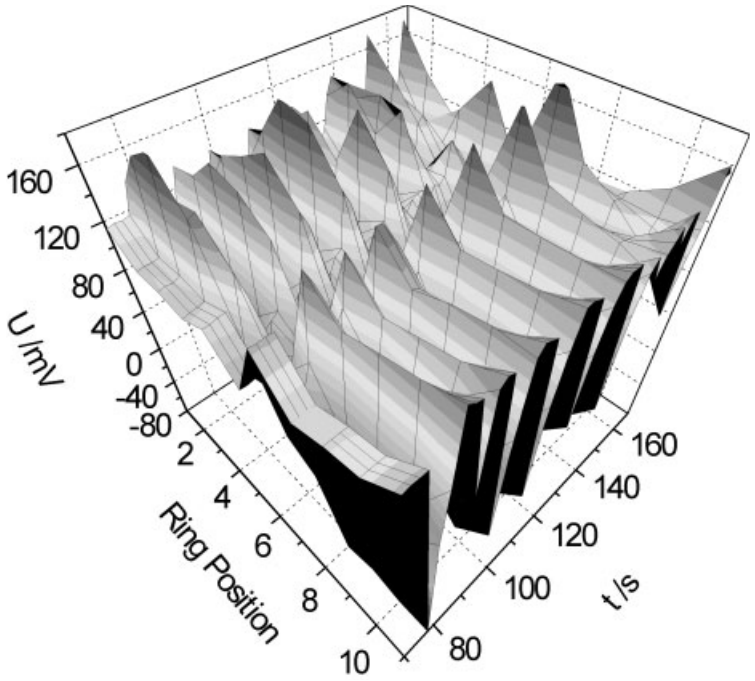

Fig. 52. Standing wave observed during the potentiostatic oxidation of formic acid on a Pt ring electrode. The RE was located on the axis of and close to the WE. See Fig. 51(B) for the experimental set-up. (Courtesy of P. Strasser and M. Eiswirth, for details see [184].)

These experiments triggered theoretical investigations as well as further experiments with a close reference electrode. In studies of the oscillatory oxidation of formic acid on a Pt ring electrode, standing waves developed whenever the RE was brought close enough to the WE (Fig. 52) [184]. When employing Bi-modified Pt electrodes, transitions from standing waves to pulses were observed as a function of the applied voltage (Fig. 53) [137].

Standing waves and pulses constitute the base patterns existing in the oscillatory region of an electrochemical reaction for a strong negative global coupling. Pulses were also found during H_2 oxidation on Pt ring electrodes [173], standing waves during periodate reduction on a rectangular Au electrode in a geometry that is an approximation to the one shown in Fig. 3b, i.e. edge effects were marginal [41]. In the latter experiments, the lateral resolution of the double layer potential and of possibly adsorbed species was studied by means of surface plasmon imaging (Fig. 54) [185]. There were two peculiarities in these studies. First, the RE was located close to one short side of the 30×8 mm^2 large electrode and about half way between the WE and the CE, and thus in an asymmetric position. Second, an electronic device was inserted between the WE and the CE which acted like an external *negative ohmic resistor*. Hence, there were two sources of negative (destabilizing) feedback. Potential profiles along the horizontal direction of the electrode as a function of time are re-

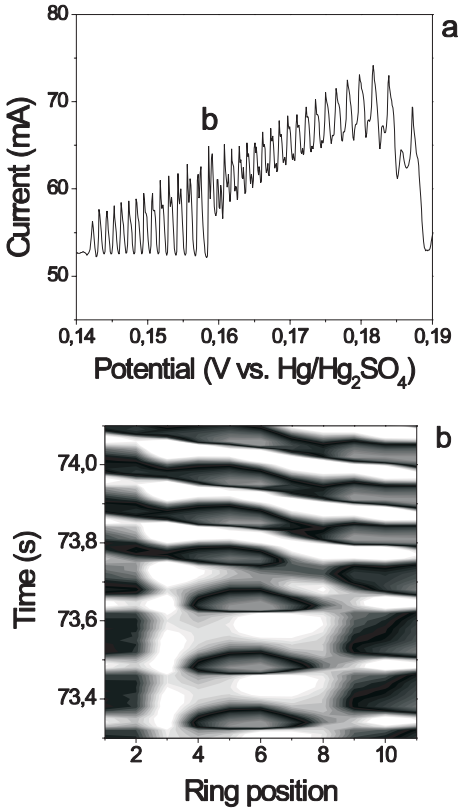

Fig. 53. (a) Cyclic voltammogram during the formic acid oxidation on a Bi-modified Pt ring electrode; scan rate: 5mV s^{-1}. The change in the oscillation form close to $t = 73.7$ s (i.e. U = 0.16 V) indicates a qualitative change in the dynamics. (b) Spatio-temporal profile of the interfacial potential in the transition region of the oscillation form in (a). For the experimental set-up, see Fig. 49b. (Reproduced from J. Lee, J. Christoph, P. Strasser, M. Eiswrith and G. Ertl, J. Chem. Phys. (2001) 115, 1485 by permission of the American Institute of Physics.)

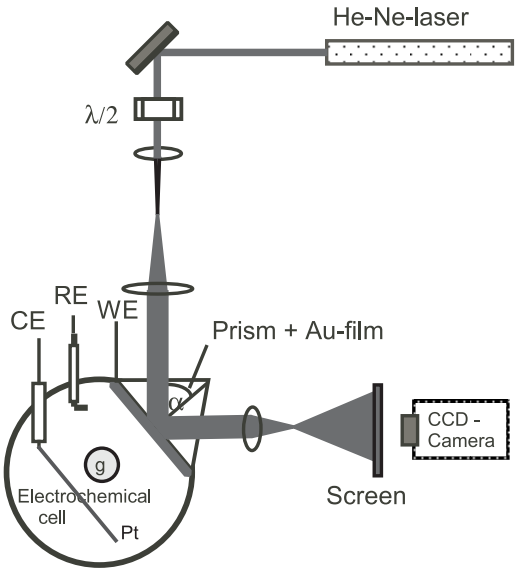

Fig. 54. Experimental set-up for recording patterns at the electrode/electrolyte interface by means of surface plasmon imaging (top view; g: gas inlet).

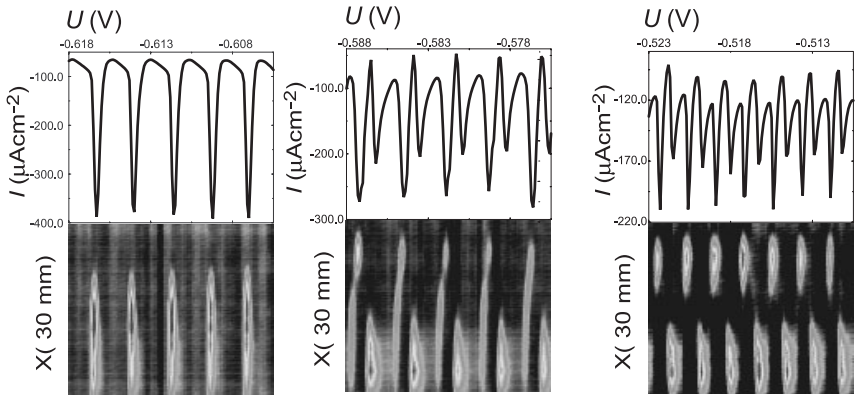

Fig. 55. Time series and potential profiles of the double layer potential along the horizontal direction of the 30×8 mm^2 large electrode as a function of time during a slow potential scan (1 mV s^{-1}) in three different regions of the external potential. The RE was located in an asymmetric position between the CE and the WE. The negative coupling was enhanced by inserting an electronic device between the WE and the potentiostat that behaves like a negative ohmic resistor (see also Ref. [41]).

produced in Fig. 55. At the positive end of the oscillatory region, standing waves existed over a large voltage interval (right image). At the negative end, about two-thirds of the electrode oscillated in a nearly homogeneous manner, whereas the remaining part stayed nearly stationary (left image). Between these two regions, there existed a small voltage interval with quite unexpected behavior: pulses were periodically sent from one end of the electrode to the other one, and in between two such events, an oscillation occurred only on the side of the electrode that sent out the pulses (middle image).

During the oscillatory oxidation of H_2 on Pt ring electrodes in the presence of Cl^- and Cu^{2+} ions, pattern formation was studied as a function of the distance between the symmetrically placed RE and the WE [173]. While propagating pulses were the only stable patterns when the RE was put closest to the plane of the working electrode, for intermediate distances, and thus also intermediate strengths of the global coupling a diversity of spatiotemporal motions was observed as a function of the applied voltage (Fig. 56). In Fig. 56b and c examples of so-called one-dimensional asymmetric and symmetric target patterns are shown. In the case of a symmetric target pattern, at a certain position, a ''wave source'' emits two pulses in opposite directions that propagate around the ring and annihilate each other when they collide. For the asymmetric target pattern, only one pulse is emitted, which, however, does not continuously travel around the ring – as for ''normal'' pulses – but is extinguished as soon as it comes close to the wave source. In Fig. 56d target patterns and asymmetric target patterns transform continuously into each other. In the most complex case, seen in Fig. 56a, four types of behavior take turns: slightly imperfect target patterns are followed firstly by asymmetric target patterns, then by pulses, and lastly by the expansion of the less-reactive portion of the pulse over the entire electrode before the scenario starts again.

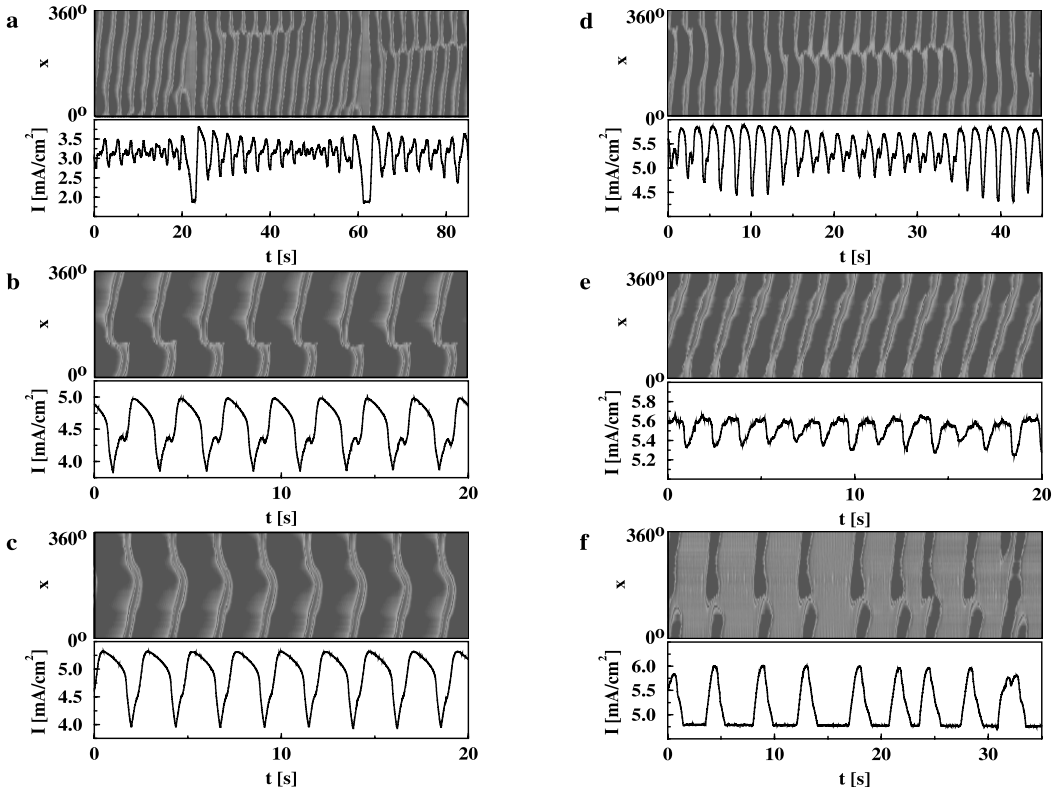

Fig. 56. Position-time plots of the local double layer potential and corresponding time series of the global current during the oxidation of H_2 on a Pt ring electrode for 6 different values of the external potential [173]. The RE was on the axis of the ring in an intermediate distance between the WE and the RE. (Electrolyte: 0.5 mM H_2SO_4, 0.1 mM HCl, and 0.025 mM $CuSO_4$ saturated with H_2.)

Most of the patterns discussed so far seem to be much akin to each other, and are connected to bifurcations of the homogeneous stationary state. Hence, before reviewing a different type of spatiotemporal motion induced by the negative global coupling, the theoretical background to the presented experiments will be given, as far as it is known. Again, we shall consider first the simplified two-dimensional geometry for ring electrodes. Combining all terms that contribute to the dynamics of a homogeneous situation in the functions $g_1(\phi_{\mathrm{DL}}, c)$ and $g_2(\phi_{\mathrm{DL}}, c)$, the temporal evolution equations for the double layer potential, ϕ_{DL}, and the slow, chemical variable, c, read:

$$\frac{\partial \phi_{\mathrm{DL}}}{\partial t} = g_1(\phi_{\mathrm{DL}}, c) - \frac{\sigma}{w}\frac{\gamma}{1-\gamma}(\langle \phi_{\mathrm{DL}} \rangle - \phi_{\mathrm{DL}}) - \sigma\left(\frac{\partial \phi}{\partial z} - \frac{\phi}{w}\right)\Big|_{z=\mathrm{WE}} \tag{54a}$$

$$\frac{\partial c}{\partial t} = g_2(\phi_{\mathrm{DL}}, c). \tag{54b}$$

Again, a lateral transport process of c is neglected because the corresponding term in Eq. (54b) would be by far smaller than the migration term in Eq. (54a) and thus is insignificant for spatiotemporal solutions [14].

We are interested under which conditions the homogeneous steady state undergoes an oscillatory (Hopf) bifurcation. In general, a Hopf bifurcation occurs when the trace of the Jacobian matrix of the linearized evolution equations, $\boldsymbol{J}$, transverses zero as a parameter is varied, and the determinant of the Jacobian matrix is positive, i.e. if

$$\operatorname{Tr}\boldsymbol{J} = 0, \quad \text{and} \quad \operatorname{Det}\boldsymbol{J} > 0. \tag{55}$$

In other words, at a Hopf bifurcation the eigenvalues $\lambda_{n_{1,2}}$ of the Jacobian matrix are complex and the real part of the eigenvalues passes through zero. Denoting the Jacobian matrix of the homogenous system by

$$\boldsymbol{J}_{\text{hom}} = \begin{pmatrix} j_{11} & j_{12} \\ j_{21} & j_{22} \end{pmatrix} = \begin{pmatrix} \partial g_1(\phi_{\text{DL}}, c)/\partial\phi_{\text{DL}} & \partial g_1(\phi_{\text{DL}}, c)/\partial c \\ \partial g_2(\phi_{\text{DL}}, c)/\partial\phi_{\text{DL}} & \partial g_2(\phi_{\text{DL}}, c)/\partial c \end{pmatrix}, \tag{56}$$

small homogeneous perturbations $\delta\phi_{\text{DL}}(n=0) - \phi_{\text{DL}}^{\text{ss}} = \delta a_0(t)$, $\delta c(n=0) - c^{\text{ss}} = \delta b_0(t)$, of the homogeneous steady state, $(\phi_{\text{DL}}^{\text{ss}}, c^{\text{ss}})$, evolve according to

$$\begin{pmatrix} \dfrac{d\delta a_0}{dt} \\ \dfrac{d\delta b_0}{dt} \end{pmatrix} = \begin{pmatrix} j_{11} & j_{12} \\ j_{21} & j_{22} \end{pmatrix}\Bigg|_{(\phi_{\text{DL}}^{\text{ss}}, c^{\text{ss}})} \begin{pmatrix} \delta a_0 \\ \delta b_0 \end{pmatrix}. \tag{57}$$

For small perturbations with the wave number n, $\delta\phi_{\text{DL}}(n) - \phi_{\text{DL}}^{\text{ss}} = \delta a_n(t)\cos(nx)$, $\delta c(n) - c^{\text{ss}} = \delta b_n(t)\cos(nx)$, the linearized evolution equations read (cf. Eq. (21))

$$\begin{pmatrix} \dfrac{d\delta a_n}{dt} \\ \dfrac{d\delta b_n}{dt} \end{pmatrix} = \begin{pmatrix} j_{11} + \dfrac{\sigma}{w}\dfrac{\gamma}{1-\gamma} - \sigma(n\coth(n\beta) - w^{-1}) & j_{12} \\ j_{21} & j_{22} \end{pmatrix}\Bigg|_{(\phi_{\text{DL}}^{\text{ss}}, c^{\text{ss}})} \begin{pmatrix} \delta a_n \\ \delta b_n \end{pmatrix}. \tag{58}$$

A plot of the real part of the eigenvalues, $\operatorname{Re}(\lambda_n)$, exhibits necessarily the same form as the growth rate λ_n in the one-variable system (cf. Fig. 47), that is, for $n > 0$ a plot of $\operatorname{Re}(\lambda_n)$ versus n decays monotonically, and $\operatorname{Re}(\lambda(n=0)) < \operatorname{Re}(\lambda(n \to +0))$. Hence, if the destabilizing effect of the global coupling is larger than the damping of the migration coupling, i.e. if

$$\frac{\sigma}{w}\frac{\gamma}{1-\gamma} > \sigma(\coth(\beta) - w^{-1}), \tag{59}$$

an oscillatory instability will develop first for $n = 1$. Only when the homogenous steady state is already unstable with respect to perturbations of wave number one

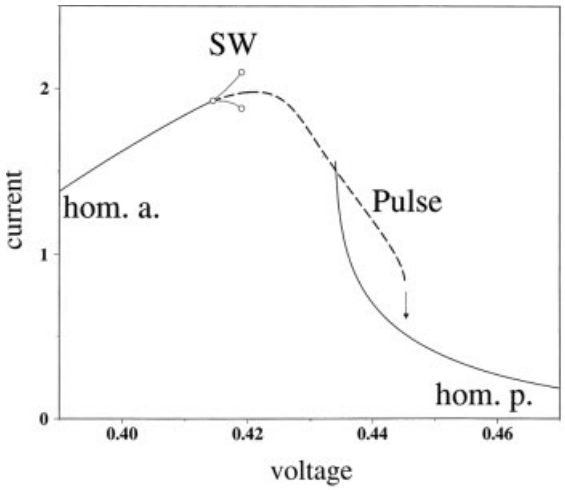

Fig. 57. Numerical, one-parameter bifurcation diagram displaying the global current of stable solutions as a function of the applied potential. In the case of the standing waves (SW), the global current is oscillatory and the open circles denote maximum and minimum of the oscillations. (hom.a. = homogeneous active stationary state; hom.p. = homogeneous passive stationary state.) (Reproduced from J. Lee, J. Christoph, P. Strasser, M. Eiswirth and G. Ertl, J. Chem. Phys. 115 (2001), 1485 by permission of the American Institute of Physics.)

will it become unstable with respect to homogeneous perturbations. Thus, it is this nontrivial Hopf bifurcation through which the two basic patterns, standing waves with $n = 1$ and pulses, arise: since the eigenfunctions of our rotationally invariant system are Fourier modes, sine and cosine modes are degenerate and become unstable simultaneously. The final attractor might be a standing wave (in which one of the two modes participates) or a pulse (where sine and cosine mode are excited and have a phase shift of approx. 90°). Both solutions can also coexist.

Model calculations with generic N-NDR [37] and HN-NDR [137] models revealed that the standing wave solution becomes unstable at higher values of the applied potential, the system exhibiting a transition to traveling pulses (Fig. 57), as was observed during formic acid oxidation (cf. Fig. 53). Furthermore, the standing wave solution was found to always coexist with the pulse, whereby the pulse is the more stable attractor, i.e. possesses the larger basin of attraction. Lee et al. attribute the occurrence of stationary waves in their experiments to intrinsic inhomogeneities of the catalytic electrode surface that stabilize the standing wave close to the bifurcation point.

In an N-NDR model Christoph et al. [35, 37] found stable target patterns coexisting with the pulse solution for values of the external voltage for which the stationary state is also unstable with respect to homogeneous perturbations. In contrast, the asymmetric target patterns and the more complex motions observed during H_2 oxidation on Pt ring electrodes (cf. Fig. 56) have not yet been reproduced in simulations.

In a series of papers Jaeger, Hudson and coworkers investigated how the spatiotemporal behavior is affected by different model parameters, such as reaction rate, electrode capacitance, the geometry of the WE and the relative positions of all three electrodes, WE, CE and RE in the simplified N-NDR model for electrodissolution reactions [27–29]. Below, we discuss a few examples taken from these works. For a geometry similar to the one discussed above, i.e. with ring-shaped working and

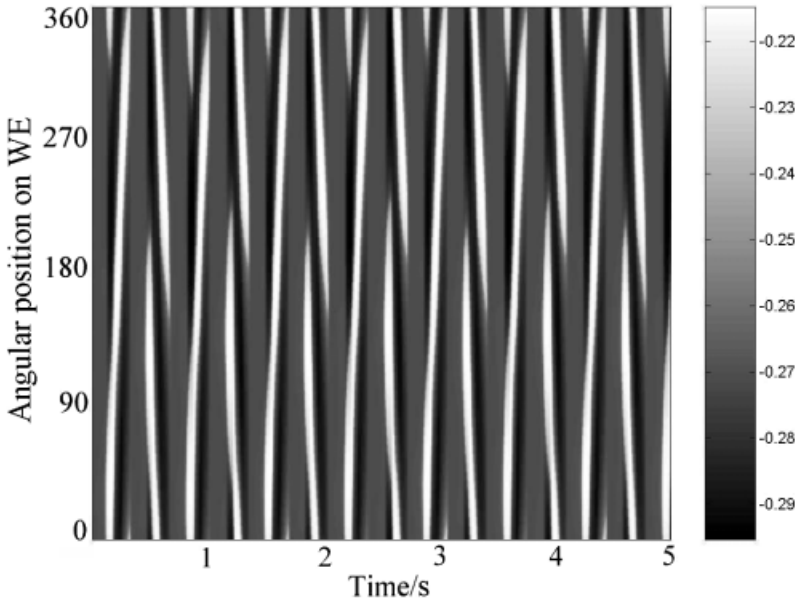

Fig. 58. Calculated plot of the double layer potential as a function of position and time for a low value of the double layer capacitance. Model geometry: ring-shaped WE and CE, symmetric RE close to the CE (weak negative global coupling). (Reproduced form A. Birzu, B. J. Green, N. I. Jaeger, J. L. Hudson, J. Electroanal. Chem. 504 (2001) 126, with permission of Elsevier Science.)

counter electrodes and the RE positioned on the common axis of the WE and the CE, the pattern reproduced in Fig. 58 was obtained for values of the double layer capacitance much lower than the one for which rotating pulses existed. The RE was comparatively close to the CE on the axis of the two rings such that the negative global coupling was weak. Thus, at these parameter values there is still a tendency to form a pulse; however, at a given point the pulse vanishes and the whole electrode approaches a passive state. Phenomenologically, this spatiotemporal motion resembles the one shown in Fig. 56f, which was observed during the oxidation of H_2 for a specific set of parameters.

A study of the influence of the horizontal position of the reference electrode close to a ribbon electrode in a two-dimensional geometry is reproduced in Fig. 59 [27]. It is remarkable that an asymmetrically placed RE gave rise to a patterned oscillation in which one side of the electrode oscillated with a frequency twice as high as the one at the other side of the electrode (Fig. 59a), just as was observed during IO_4^- reduction when the RE was placed close to one side of the WE (cf. Fig. 57). Note, however, that edge effects due to an insulator/conductor transition in the plane of the working electrode are present in the calculations, but are minimized in the experiment. Thus, the effect has to be reproduced with the geometry of the experiment before final conclusions can be drawn.

The last set of calculations by Birzu et al. to be discussed here was done with disk electrodes [28]. Above, we discussed that, in the one-variable model, stationary

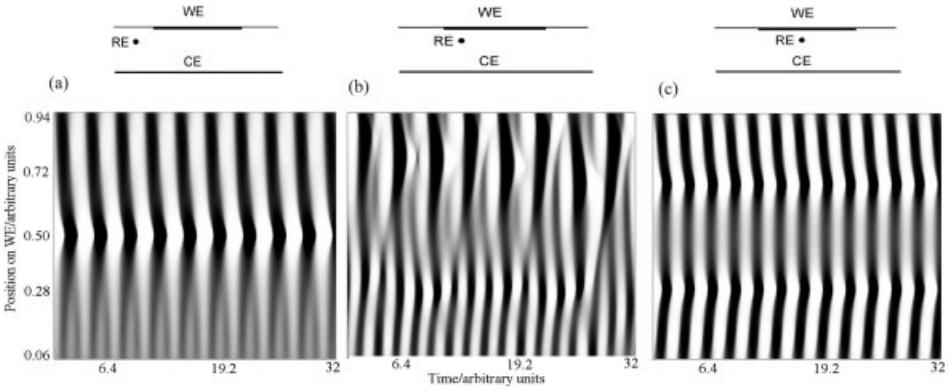

Fig. 59. Calculated plot of the double layer potential of a ribbon WE as a function of position and time. The model geometry was two-dimensional with the relative positions of the electrodes as indicated above the spatiotemporal plots. (Reproduced from A. Birzu, B. J. Green, R. D. Otterstedt, N. I. Jaeger, J. L. Hudson, Phys. Chem. Chem. Phys. 2 (2000) 2715 by permission of The Royal Society of Chemistry on behalf of the PCCP Owner Societies.)

asymmetric patterns as shown in Fig. 50 arise when positioning the RE on the axis of, and close to the disk. In the two-variable system, the crescent-moon-like domains can rotate around the center of the disk. This is the two-dimensional counterpart of the pulses that travel around ring electrodes, and in fact, when plotting the angular position versus time for a given distance to the center of the ring, a pulse pattern is obtained. This is reminiscent of the active regions rotating around the center of a Co disk electrode observed by Otterstedt et al. (cf. Fig. 51). A crucial, as yet not understood, difference is, however, that in the calculated pattern the interfacial region between the predominantly active and predominantly passive parts of the electrode seems to be minimized, whereas in the experiment this is clearly not the case. In Fig. 60 we see how the counterpart of the standing waves on ring electrodes manifests itself on disk electrodes. The spatiotemporal behavior along the azimuthal direction at a given point on the radial coordinate is indistinguishable from solutions obtained with ring electrodes (Fig. 60a). Along the radial direction, however, the symmetry is also broken: an active region of varying size and shape is traveling back and forth. The resulting motion can be seen in the snapshots reproduced in Fig. 60b.

Another type of pattern that appeared in the presence of negative global coupling is an oscillating cluster. A cluster pattern consists of two or three spatial regions in which the behavior is uniform with sharp boundaries between these regions. Often, also the local oscillations are characterized by sharp transitions between two phases of an oscillation. A typical cluster pattern observed during oscillations in the active/passive transition region of a Fe ring electrode is reproduced in Fig. 61 [186]. For similar conditions, a further symmetry breaking of this state that divided the electrode in four parts had been reported earlier by the same group [187]. During successive oscillations, two opposing quadrants of the ring electrode were activated at a time. Hudson et al. [178] observed also for Fe disk electrodes the separation of the electrode into two parts, whereby one half of the disk electrode was activated every other oscillation.

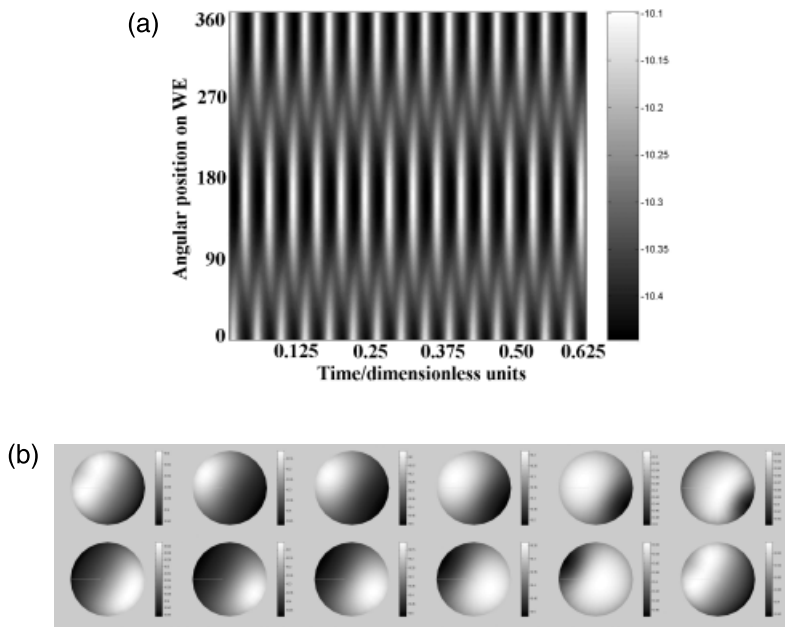

Fig. 60. Spatiotemporal dynamics on a disk electrode with close and centric RE. (a) Potential drop across the double layer as a function of angular position on the disk (for a given intermediate radius) and time. (b) Potential on the disk working electrode at different times during one period of the oscillation. (Reprinted from A. Birzu, B. J. Green, R. D. Otterstedt, J. L. Hudson, N. I. Jaeger, Z. Phys. Chem. 216, 459 (2002) with permission from Oldenbourg Wissenschaftsverlag.)

At this point, also another type of spatiotemporal dynamics during the anodic oxidation of iron should be mentioned. It apparently requires a negative global coupling, but it is not clear yet whether the dynamics are related to cluster formation. The anodic oxidation of iron exhibits a second oscillatory region on the diffusion-limited plateau of the current-voltage curve. Compared with the oscillations in the active/passive transition region, the amplitudes of these oscillations are much smaller, and their frequencies range between some 10 and 1000 Hz; they are thus several orders of magnitude higher. To obtain a spatiotemporal picture, Hudson and coworkers used arrays of electrodes whereby they could measure the current flowing through each electrode independently. Anti-phase oscillations measured with a ring array of iron electrodes can be seen in Fig. 62. The partition of the electrode into two parts is obvious. However, the two oscillating regions are not as sharply separated from each other as for the cluster states in Fig. 61, or the ones that are discussed next.

A large parameter range in which cluster patterns dominated the spatiotemporal dynamics was also observed for the oscillatory oxidation of H_2 in the presence of electrosorbing cations and anions [175]. Characteristically, the cluster-type patterns were found at lower concentrations of Cu^{2+} ions compared with the pulse-type motions shown in Fig. 56. Examples of two-phase and three-phase clusters are depicted in Fig. 63. In these figures the homogeneously oscillating mode has been subtracted.

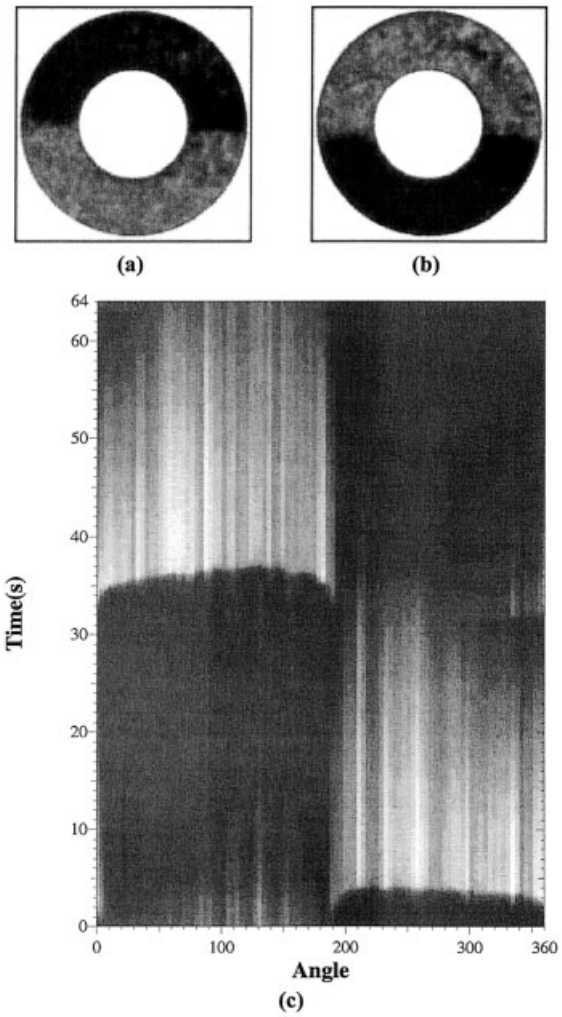

Fig. 61. Cluster pattern observed during the electrodissolution of a Fe ring electrode in the active/passive transition region under potentiostatic conditions. The RE was located in the plane of the WE. (a) and (b) Snapshots taken during two successive oscillations of the total current. (c) Spatiotemporal plot of the azimuthal intensity. (Reproduced with permission from B. J. Green and J. L. Hudson, Phys. Rev. E 63 (2001) 026214, © (2001) by the American Physical Society).

In Fig. 63a the two-phases acquire the respective other state with the period of the global oscillation, such that only after two oscillations of the current the system is again in an identical state. Besides theses period-2 two-phase clusters also period-1 two-phase clusters, in which the two phases exchange positions within one oscillation were observed [175]. So far, the cluster behavior has not yet been reproduced in electrochemical models. It was found, however, in experiments and simulations of two other chemical systems: the light-sensitive BZ reaction where the global feedback resulted from the illumination [188, 189], and the heterogeneously catalyzed CO oxidation on Pt(110), with a delayed regulation of the CO pressure depending on an average quantity [20, 190–192]. The bifurcations leading to cluster states are not yet fully understood.

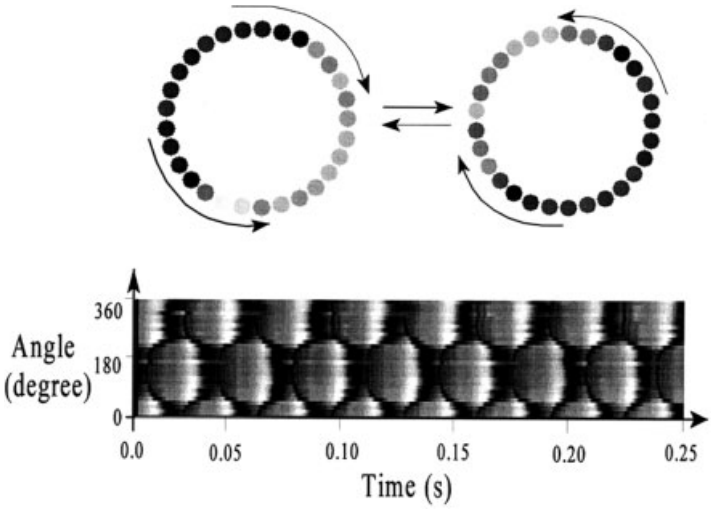

Fig. 62. Snapshots and space-time current densities measured with ring-arrays of Fe electrodes in the oscillatory region on the transport-limited plateau of the current-potential curve. (Reproduced with permission from Z. Fei, J. Green and J. L. Hudson, J. Phys. Chem. B103 (1999) 2178, © (1999) American Chemical Society.)

4.1.3 Positive Global Coupling: Galvanostatic Control

As explained in Section 2.3, the typical experimental condition in which a positive global coupling is involved is the galvanostatic control. Also, any ohmic resistor in the external circuit gives rise to a positive global coupling. In many, though not all,

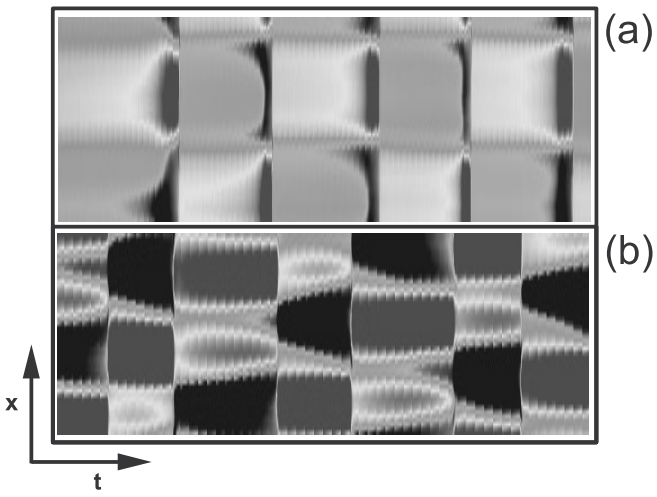

Fig. 63. Cluster-type patterns observed during the electrooxidation of H_2 on Pt ring electrodes. (Electrolyte: 1 mM H_2SO_4, 10^{-6} mM $CuSO_4$, 10^{-5} mM HCl.) (a) Period 2 two-phase clusters; and (b) three-phase clusters. (Shown is only the spatially varying part of the data.)

respects, a positive global coupling has an opposite effect on pattern formation compared with the negative global coupling. Consider, for example, the calculated transition in the bistable region shown in Fig. 35e. As in all the other transitions shown in this figure, initially a small portion of the spatial domain was set into the globally stable state, the remaining part of the electrode in the metastable state, with a narrow interface connecting both regions. In contrast to all the transitions shown under potential control, in the case of current control, no sharp interface develops. Rather, the initially sharp potential profile broadens quickly, resulting in a nearly homogeneous transient. As demonstrated by Mazouz et al. [32], for weak global coupling, the interaction between the positive global coupling and the reaction part will lead to accelerated front motion in a similar manner as the nonlocal migration coupling does.

This front behavior can also be easily rationalized mathematically. Recall that under galvanostatic control, the evolution equation of ϕ_{DL} can be written as

$$C\frac{\partial \phi_{\mathrm{DL}}}{\partial t} = g(\phi_{\mathrm{DL}}) + \frac{\sigma}{w}(\langle \phi_{\mathrm{DL}} \rangle - \phi_{\mathrm{DL}}) - \sigma\left(\left.\frac{\partial \phi(\mathbf{r},t)}{\partial z}\right|_{z=\mathrm{WE}} - \frac{i_0}{\sigma}\right), \tag{60}$$

where i_0 is the preset current density and the other symbols have their usual meanings. Thus, the structure of this equation is identical to the one with a negative global coupling under potential control, the only qualitative difference being the sign in front of the global coupling term. When performing a linear stability analysis, as done for the negative global coupling, and plotting the growth rate of a perturbation with the wave number n versus n, the curve will monotonically decrease for $n > 0$, and exhibit a discontinuity at $n = 0$, but with the jump towards positive values (cf. Fig. 47). Consequently, if in the one variable system a homogeneous steady state undergoes any instability, the first mode to become unstable is always the homogeneous mode. Thus, in N-NDR systems stationary domains do not exist under galvanostatic control.

This argumentation can be easily extended to two-variable (H)N-NDR systems. Performing a linear stability analysis of a homogeneous stationary state, it is straightforward to show that a homogeneous stationary state can never become unstable in a nontrivial Hopf bifurcation with $n = 1$. Thus, whenever a Hopf bifurcation occurs, a homogeneous limit cycle is born. Standing waves and pulses are therefore not to be expected under current control.

However, it would be too simple to conclude that in N-NDR systems patterns do not exist under current control in general. In fact, among the first electrochemical patterns that were investigated utilizing the theory of dynamical systems are potential waves that were obtained under galvanostatic control [193, 194]. In these experiments, the dissolution of 10 to 20 cm long Ni wires was investigated and the local current distribution was recorded with 16 equally spaced reference microelectrodes. The CE, a Ni wire as well, was arranged parallel to the WE in a distance of 6–12 mm. During galvanostatic oscillations, the current in one part of the electrode was always shifted by 180° relative to the other part of the electrode. This behavior was maintained down to the smallest electrodes tested, which had a length of 1 cm. An

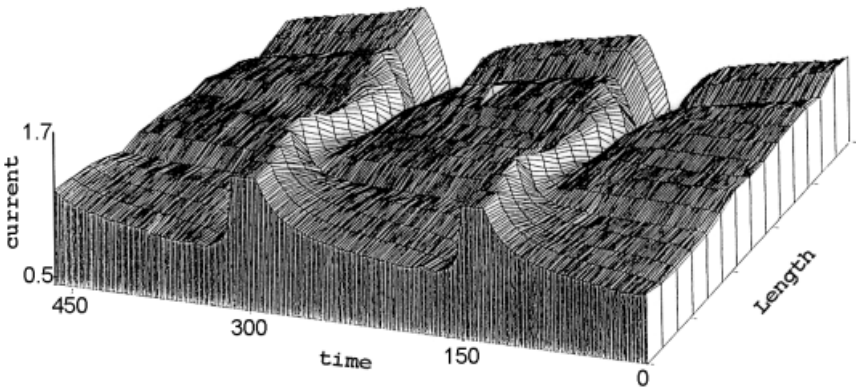

Fig. 64. Local current distribution of antiphase oscillations during the dissolution of Ni under galvanostatic control. (Reproduced with permission from O. Lev, M. Sheintuch, L. M. Pismen, and C. Yarnitzky, Nature 336, 488, 1988, © (1988) Macmillan Magazines Limited.)

example of these antiphase oscillations, also referred to as standing waves, is shown in Fig. 64.

Another example of an electrochemical wave measured under galvanostatic conditions is reproduced in Fig. 65. It stems again from the oxidation of hydrogen on a Pt ring-electrode in the presence of Cu^{2+} and Cl^{-} ions [64]. For the sake of clarity, the homogeneous oscillation was subtracted from the spatiotemporal data. It is clear from Fig. 65b that the oscillations have a strong relaxation-like character. The inhomogeneous structure forms mainly at the two flanks of the oscillation. Similar to the previous example, the overall dynamics can be viewed as a superposition of a homogenous oscillation and a standing wave. For identical conductivity and cell geometry, this type of wave motion existed under galvanostatic and under potentiostatic control.

Hence, we can so far conclude that in the oscillatory region a positive global coupling does not prevent pattern formation at the electrode|electrolyte interface. Moreover, since global coupling and migration coupling have both a synchronizing effect, it is intuitive that if migration coupling can destabilize homogeneous oscillations, so can a positive global coupling. It can be also expected that in certain situations the migration coupling alone is not sufficient to destabilize a homogeneous oscillation, but under galvanostatic conditions wave patterns exist.

The impact of a positive global coupling on arrays of individual oscillators is an active field of research. In the electrochemical context, Hudson and coworkers greatly contributed to this problem by systematic experimental studies [195–200]. They designed an experimental set-up in which the strength of the positive global coupling could be systematically varied without affecting the homogeneous dynamics of the system. It consisted of an array of electrodes connected to the potentiostat through individual resistors and one collective resistor (Fig. 66). By varying the ratio between the collective resistance, R_{coll}, and the individual resistance, R_{ind}, the global coupling could be continuously varied between 0 and a maximum value. The

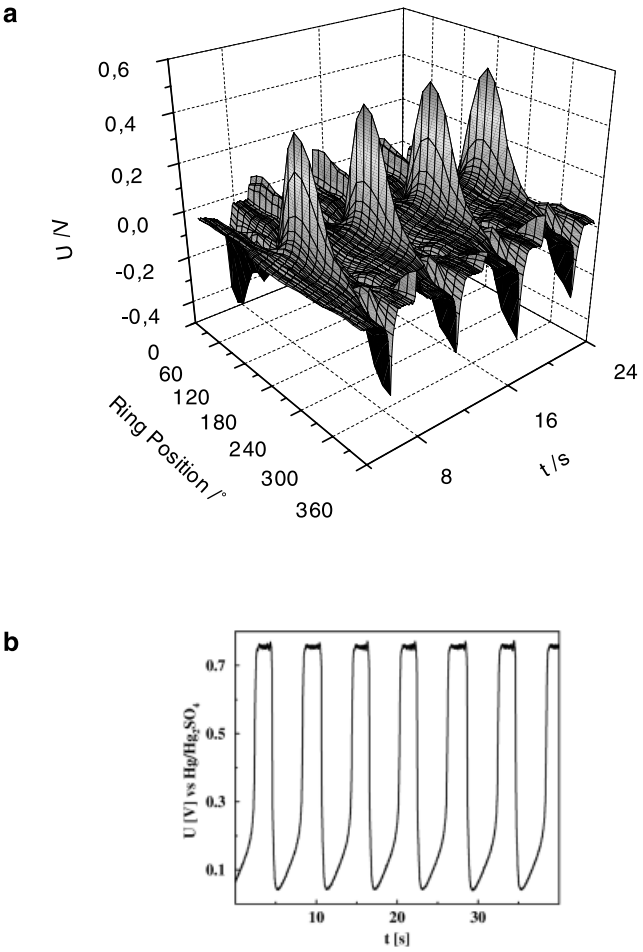

Fig. 65. Spatiotemporal evolution of the potential at a Pt electrode during the galvanostatic oxidation of H_2 in the presence of Cu^{2+} and Cl^- ions after subtraction of the homogeneous oscillating part [64]. (b) Temporal evolution of the total current. The first four oscillations correspond to the time interval shown in (a).

collective resistance fraction, $\varepsilon = (R_{\text{coll}}/R_{\text{tot}})$, is a suitable measure to characterize the strength of the global coupling. Here R_{tot} is the total resistance, given by $R_{\text{tot}} = R_{\text{coll}} + (R_{\text{ind}}/n)$, where n is the number of electrodes. If $\varepsilon = 0$, then the external resistors furnish no global coupling; for $\varepsilon = 1$, it is maximum.

The experiments were carried out on arrays consisting of from 1 to 64 nickel electrodes. The anodic dissolution of Ni in sulfuric acid is a HN-NDR oscillator that exhibits also chaotic oscillations. Its dynamics has been thoroughly studied by Sheintuch and coworkers [201–203] (see also the discussion in Ref. [9]). The synchronization experiments were carried out with periodically and chaotically oscillating individual electrodes.

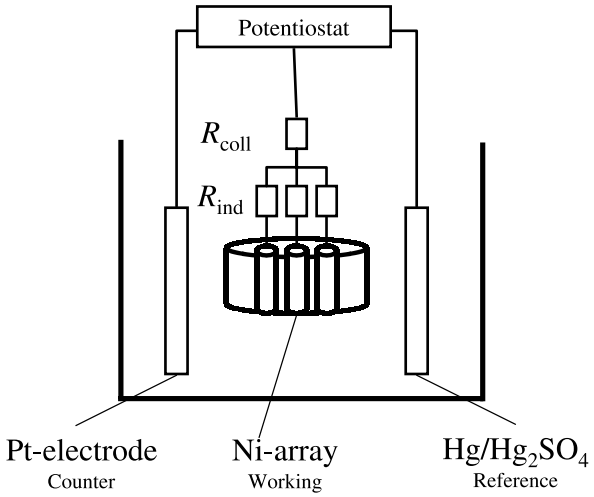

Fig. 66. Experimental set-up that allows varying the strength of the global coupling without affecting the homogeneous dynamics. (Courtesy of J.L. Hudson.)

In the case of periodic oscillators, without global coupling there was a small variation in frequency between the individual oscillators [195]. Thus, intrinsic, small variations of the electrodes were not equalized by the migration coupling, which is probably weakened due to the individual resistors. Kiss et al. considered harmonic and relaxation oscillations that occur in two regions of parameter space. As global coupling is added to the arrays of harmonic oscillators, the distribution of frequencies becomes narrower until synchronization is attained; further increase brings the phases together.

Coupling of the relaxation oscillators led to more complicated behavior (Fig. 67) [195]. As the global coupling strength is increased from zero, there is first a tendency for the system to synchronize (Fig. 67, top right), but this synchronized state then breaks up with increasing coupling. Irregular behavior with transient clusters occurs that are stabilized at stronger coupling (Fig. 67, bottom left). The individual currents can be either irregular or periodic. At still higher coupling strengths, anti-phase oscillations occur where the clusters are made up of equal or approximately equal number of oscillators (Fig. 67, bottom right). Maximum coupling synchronizes the oscillators again. The anti-phase clusters at intermediate to high coupling strength are reminiscent of the two-phase clusters found for negative global coupling (cf. Fig. 61 and 63). Also in the mentioned studies of heterogeneous CO oxidation on Pt(110) with global feedback the formation of clusters occurred for positive and negative feedback [192]. This suggests that the mechanism that induces cluster formation, and the bifurcations involved, are independent of the polarity of the global coupling. Further studies are needed to corroborate this conjecture.

When globally coupling arrays of chaotic oscillators, strong coupling again transforms a system of independent elements to a state of complete synchronization [197]. The variations in behavior with a change of the coupling strength are still more diverse than for periodic oscillators, involving a maximum in complexity of the individual currents at intermediate coupling strength as well as the formation of stable

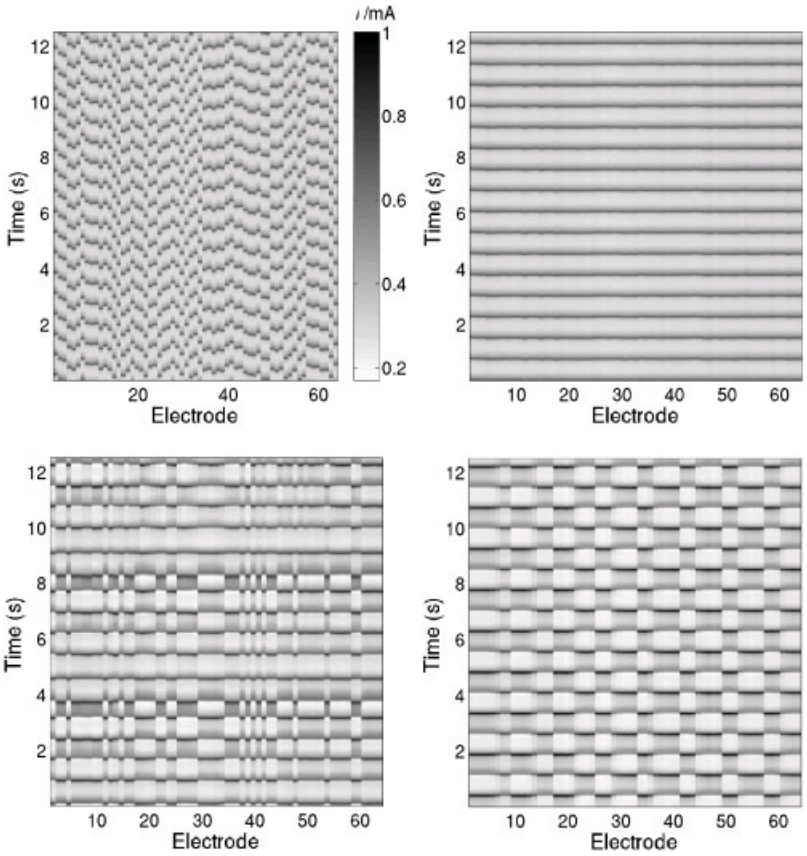

Fig. 67. Current as a function of space and time for an array consisting of 64 Ni electrodes exhibiting relaxation oscillations and different strength of the global coupling. Dark corresponds to high current. Top left: $\varepsilon = 0$; top right: $\varepsilon = 0.28$; bottom left: $\varepsilon = 0.67$; and bottom right: $\varepsilon = 0.95$. (Reproduced with permission from I. Z. Kiss, W. Wang, J. L. Hudson, J. Phys. Chem. B 103 (1999) 11433–11444, © 1999, American Chemical Society.)

clusters, whereby all the elements in one cluster follow the same chaotic trajectory, but each cluster has its own dynamics, up to a fully synchronized periodic behavior [196, 197].

The synchronization of large assemblies of oscillators, and of different parts of a spatially extended medium, especially if the behavior is turbulent, is of great importance. Imposing a direct global coupling as described above is one way to achieve synchrony. Two different and more versatile ways to impose a global coupling are through the external variation of a global parameter or through a delayed feedback proportional to the average of a spatially varying quantity. Such studies have just been taken up [189, 191]. As demonstrated by Hudson's group, electrochemical systems can serve here as suitable model systems. First results of how these two different coupling methods can be exploited to direct the spatiotemporal behavior into a desired regime can be found in [199, 200].

4.2 S-NDR Systems: The Electrode Potential as Negative Feedback Variable

4.2.1 Nonlocal Migration Coupling

In many respects, a synchronizing spatial coupling acting on the inhibitor variable has an opposite effect to that acting on the activator variable. The most impressive manifestation of this is the existence of stationary Turing structures, i.e. stationary patterns with a characteristic wavelength that is independent of the system length [17, 204, 205]. Turing patterns were originally predicted to exist in reaction-diffusion systems of the activator-inhibitor type, if the inhibitor diffused faster than the activator. Only recently it was concluded from theoretical studies that Turing patterns should emerge in electrochemical S-NDR systems under potentiostatic control in wide and experimentally well-accessible parameter ranges [33].

At first, this result was obtained for the prototype S-NDR model, whose homogeneous dynamics is given by Eqs. (43–45). The cell geometry considered was a 2-d simplified cylindrical geometry of the electrolyte with a ring WE (cf. Fig. 3d) and with the RE far away from the WE such that any additional global coupling could be neglected. In the dimensionless formulation the model equations for the spatially extended system read [33]

$$\frac{\partial \tilde{c}}{\partial \tilde{t}} = f(\tilde{c}, \tilde{\phi}_{\mathrm{DL}}) + \frac{\partial^2 \tilde{c}}{\partial \tilde{x}^2} \tag{61a}$$

$$\frac{\partial \tilde{\phi}_{\mathrm{DL}}}{\partial \tilde{t}} = g(\tilde{c}, \tilde{\phi}_{\mathrm{DL}}) - \frac{d}{\beta}\left(\left.\frac{\partial \tilde{\phi}}{\partial \tilde{z}}\right|_{\tilde{z}=-1} + (\tilde{U} - \tilde{\phi}_{\mathrm{DL}})\right), \tag{61b}$$

where the tilde indicates again that the corresponding quantities are dimensionless variables or parameters. The autocatalytic chemical species, c, is assumed to diffuse within the reaction plane or on the electrode surface, whereby the diffusion coefficient is normalized to 1. This results in the following scaling of the dimensionless conductivity d:

$$d = \frac{L\sigma}{2\pi D C_0}. \tag{62}$$

Here, L is the length of the electrode, σ the conductivity, D the diffusion coefficient of species c and C_0 the specific capacity of the electrode. d is a measure of the ratio of the characteristic rates of the diffusion of species c and migration. $d > 1$ means that the characteristic time of migration is shorter than that of diffusion, or, in other words, that the transport process associated with the inhibitor is faster than the one associated with the activator.

The original condition for the development of a Turing pattern, namely that the inhibitor diffuses faster than the activator, can be generalized allowing also for transport processes different from diffusion, in which case this necessary condition becomes: A stationary pattern with a characteristic wavelength may develop if the

transport process associated with the inhibitor is faster than the one associated with the activator. Hence, in our case we would have a situation that fulfills a necessary requirement for the existence of Turing-type patterns if $d > 1$. Inserting typical values for L, σ, C_0 and D into Eq. (62) namely, 1 cm, $2 * 10^{-5}$ Ω cm^{-1}, 20 μF cm^{-2} and 10^{-5} cm^2 s^{-1}, respectively, d is of the order of 1000. Thus, it is much larger than 1, and this is true not only for the considered, but for any cell geometry.

Furthermore, when performing a linear stability of the homogeneous steady state with respect to small perturbations of the form $(\delta c \cos(nx), \delta\phi_{\mathrm{DL}} \cos(nx))$, the plot of the growth rate λ_n of the perturbation vs. the wave number n, the so-called dispersion relation, characteristically possesses a maximum at some finite value n in a certain region of U (Fig. 68). When the I/U plot is single-valued, owing to the ohmic drop within the electrolyte (cf. Fig. 26), the growth rate close to the maximum of the curve becomes positive for values of U around the inflection point of the I/U curve, i.e. for conditions under which the homogeneous state corresponds to the unstable branch of the S-shaped I/ϕ_{DL} curve. Perturbations lying within the wavelength range n, for which $\lambda(n) > 0$ will grow, and the final state is a stationary structure with a defined

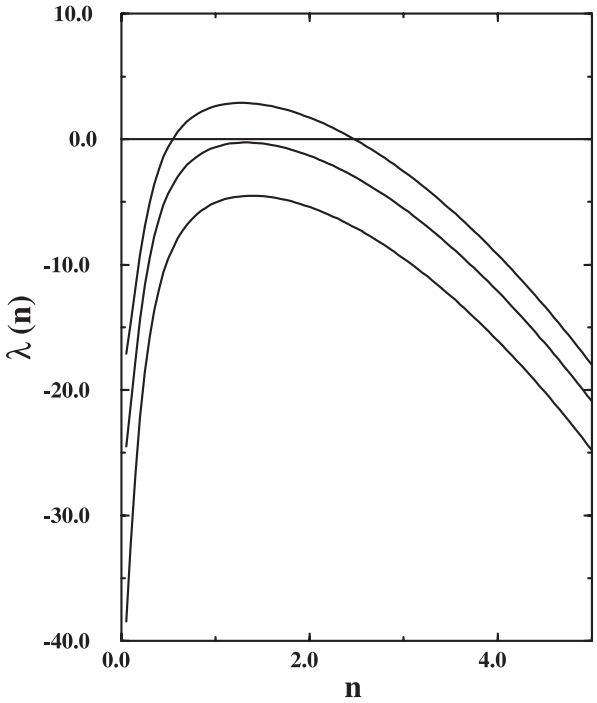

Fig. 68. Typical dispersion relations, displaying the growth rate of perturbations, $\lambda(n)$, vs. their wave number, n, of an S-NDR system for three different homogeneous steady states [33]. The lowest curve depicts the case of a stable homogeneous state, the middle one is close to a Turing-type bifurcation in which a stationary structure with the integer wave number closest to the maximum of the curve is born. The uppermost curve shows a situation for which the homogeneous state is unstable with respect to perturbations lying within the wavelength range n, for which $\lambda(n) > 0$.

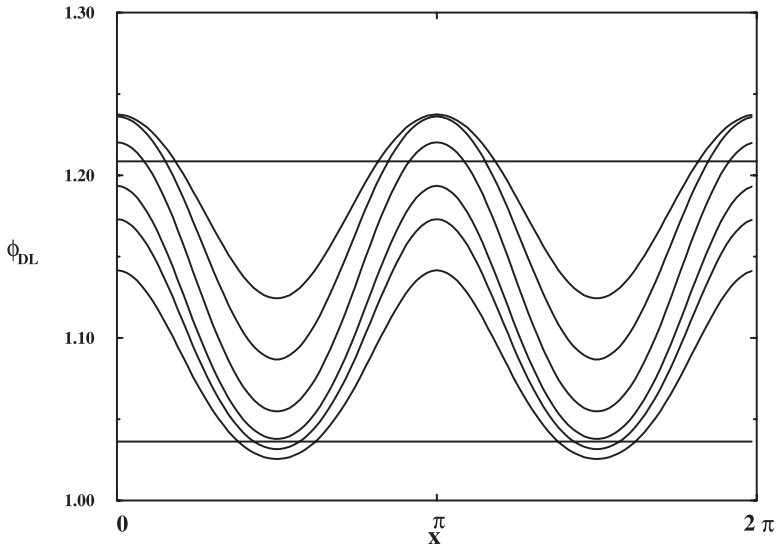

Fig. 69. Stationary solutions of Eqs. (61a,b) for different values of the external voltage U [33]. From top to bottom, U is increased. For the highest and lowest value of U, the homogeneous state is stable, whereas for intermediate values the only stable solutions are stationary potential patterns with a defined wavelength.

wavelength. Fig. 69 reproduces the final stationary states obtained in simulations for different values of U. For the lowest and highest value chosen, the respective homogeneous state is stable. However, in a range in-between these two values of U the only stable solutions are stationary structures with a defined wavelength. A change in the system size L with a constant value of β leads to a shift of the dispersion relation along the abscissa, such that the characteristic wavelength of the pattern remains constant [33]. Hence, in contrast to the bifurcations involving a global coupling, the wavelength is solely determined by the system's parameters, such as rate constants and conductivity, but not by the length of the electrode.

The region in the U/d^{-1} parameter plane in which the electrode takes on a patterned state is mapped out in Fig. 70B, together with the region in which the homogeneous system exhibits bistability. The Turing-unstable region (indicated by horizontal stripes) loops around the bistable region. Its location is similar to the location of the Hopf bifurcation set (giving rise to an oscillatory instability of the homogeneous state if the kinetic of species c is particularly fast (cf. Fig. 26)).

The theoretical predictions prompted an experimental search for "electrochemical Turing structures" that was successful shortly after. The first experimentally observed Turing structures are reproduced in Fig. 71. They stem from the periodate reduction on Au in the presence of camphor whose homogeneous dynamics was introduced in Section 3.2.2. The patterns could be made visible with surface plasmon microscopy (cf. Fig. 54). When changing the composition of the electrolyte, the wavelength of the patterns changed, in accordance with the theoretical result that the wavelength depends on the system's parameters, but not on the dimension of the

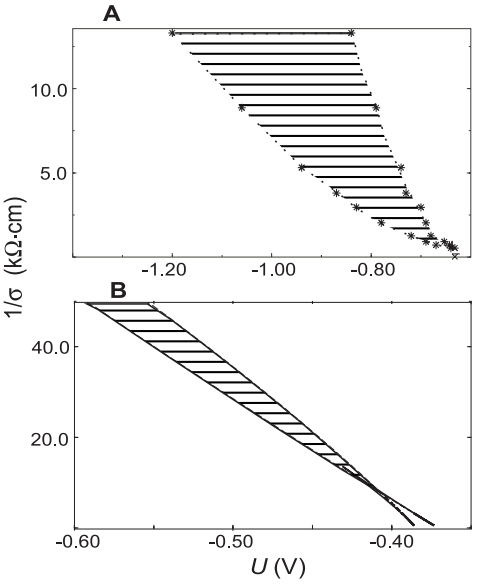

Fig. 70. Existence region of patterns in the electrolyte resistance versus external voltage plane [160]. (A) Experimental diagram obtained with the Camphor,IO_4^-|Au system; (B) Calculated diagram using the prototype S-NDR model (See Eqs. (61a,b).)

electrode. The patterns emerged in a certain voltage interval as soon as the electrolyte resistance was overcritical such that the I/U curve became single-valued. In the specific resistance vs. external voltage parameter plane, the stationary patterns existed in a V-shaped region that opens toward large overvoltage and resistance, and compares favorably with the simulations (Fig. 70A).

Although the periodate, camphor/Au system is thus far the only system in which Turing patterns were reported, the mechanism that leads to their emergence strongly suggest that they exist in all S-NDR systems in wide parameter ranges. This is quite in contrast to chemical reaction-diffusion systems in which only in exceptional cases the diffusion coefficients of the inhibitor is sufficiently larger than the one of the activator species.

4.2.2 Positive and Negative Global Coupling

Also a global coupling strongly favors the occurrence of inhomogeneous solutions in S-NDR systems, and this is not only the case for the negative global coupling as in N-NDR systems but also for positive global coupling, i.e. under galvanostatic control [206]. In the presence of a global coupling, Eq. (61b) becomes (cf. Section 2.3)

$$\frac{\partial \tilde{\phi}_{\mathrm{DL}}}{\partial \tilde{t}} = g(\tilde{c}, \tilde{\phi}_{\mathrm{DL}}) + \frac{d}{\beta}\frac{\gamma'}{(1+\gamma')}(\langle \tilde{\phi}_{\mathrm{DL}} \rangle - \tilde{\phi}_{\mathrm{DL}}) - \frac{d}{\beta}\left(\left.\frac{\partial \tilde{\phi}}{\partial \tilde{z}}\right|_{\tilde{z}=-1} + (\tilde{U} - \tilde{\phi}_{\mathrm{DL}}) \right) \quad (63)$$

where $\gamma = R_G/R_{\mathrm{cell}} = R_G * \beta/d$ depends again on external, uncompensated and cell resistances (cf. Eq. (32)). Comparing systems with identical steady states, one of

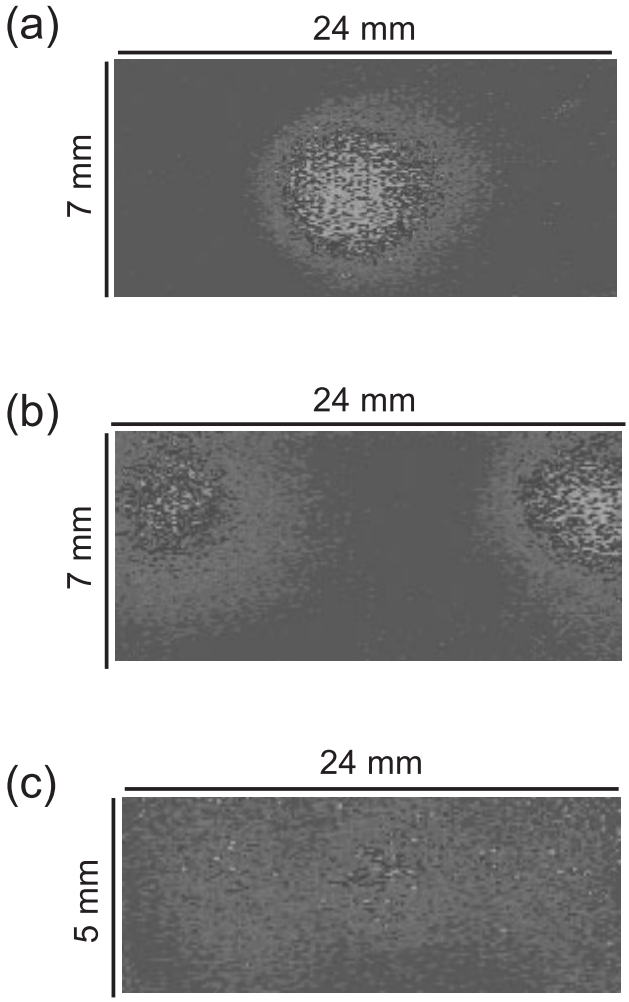

Fig. 71. Stationary patterns of different wavelength emerging in the camphor, periodate|Au system for different compositions of the electrolyte [160]. The images were obtained with a surface plasmon microscope.

which is subject to a global coupling, the other one not, it is straightforward to deduce the impact of the global coupling on the stability of the homogeneous steady state [206]: If the homogeneous steady state is a saddle point, a positive global coupling can stabilize it, but not a negative global coupling. In contrast, only a negative global coupling may stabilize an unstable focus (Fig. 72).

Let us first investigate which states the system will take on if the homogeneous component of a saddle point is stabilized by a positive global coupling. In the absence of the global coupling, homogeneous states lying on the sandwiched NDR-branch of the S-shaped I/U-curve are saddle points. Imposing a constant current

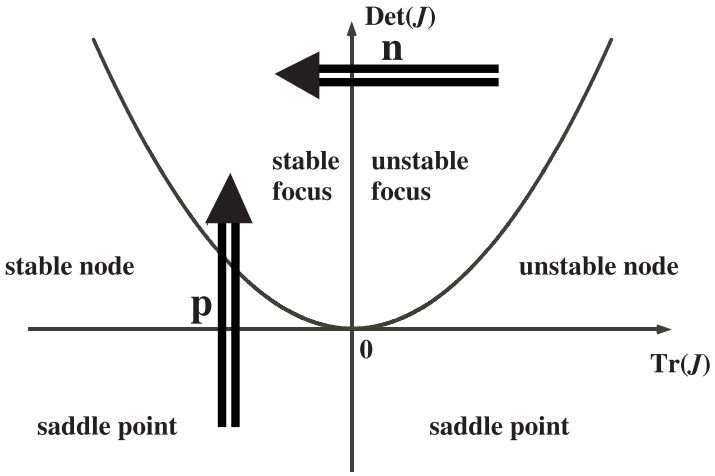

Fig. 72. Stability diagram showing how Tr(**J**) and Det(**J**), where **J** is the Jacobian matrix of Eqs. (61a, 63) linearized about a homogeneous fixed point, are changed by the presence of a global coupling [206]. The arrow marked **n** indicates that the homogenous mode of an unstable focus can be stabilized by a negative global coupling; the arrow marked **p** indicates that the homogeneous component of a saddle point with $\mathrm{Tr}(\mathbf{J}) < 0$ can be stabilized by a positive global coupling.

and thus a positive global coupling, the homogeneous mode can be stabilized. However, this does not mean that we can access this state experimentally. If the size of the electrode exceeds a critical value, the homogeneous fixed point is still unstable with respect to spatial perturbations, and the system will take on a stationary patterned state. For sufficiently high conductivity of the electrolyte, the most unstable mode is the mode with the wave number $n = 1$, and stationary domains develop which are similar to the ones existing in N-NDR systems with negative global coupling. The domains consist of regions of high and low current density corresponding to the upper and lower branches of the S with an interfacial region in between (Fig. 73a). The double layer potential, on the other hand, is nearly uniform over the entire electrode. Upon changing the applied current density the relative sizes of the two phases change whereas the average potential is hardly affected (Fig. 73b).

Plenge et al. [22] derived analytical expressions for the existence range of stationary domains and homogeneous oscillations as a function of the most important parameters, such as system size and relative time scales of activator and inhibitor variable for systems with high conductivity. They further demonstrated that, for fast changes of the chemical species, the stationary domains might become unstable themselves in an oscillatory instability, giving rise to breathing domains. Moreover, these oscillating structures can undergo a period doubling cascade to spatiotemporal chaotic motions (Fig. 73c). This is an impressive example of how complex spatiotemporal behavior can arise in comparatively simple systems subject to global constraints. For lower conductivity, the global coupling can also stabilize Turing-type structures with a defined wavelength [206]. This feature is unique to S-NDR systems, as is the occurrence of Turing structures under potential control.

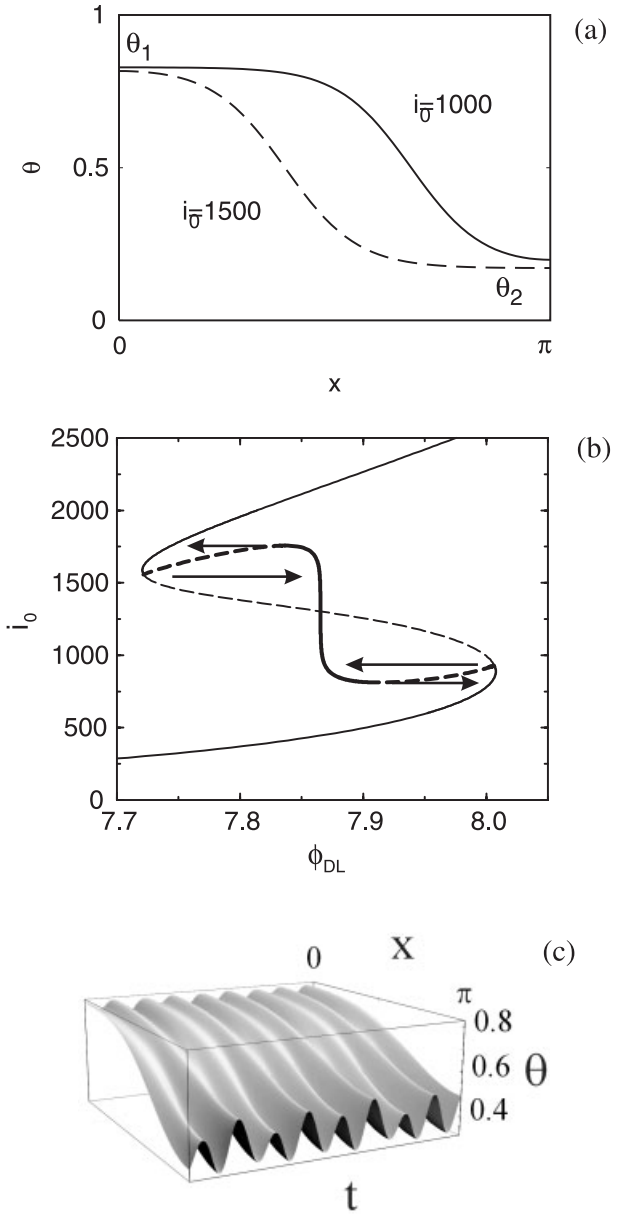

Fig. 73. Dynamic behavior in S-NDR systems with high conductivity under galvanostatic conditions [22]. (a) Stable stationary domains for two values of the imposed current density. (b) I/ϕ_{DL} plot showing stable and unstable states. The thin lines denote the homogeneous solutions, the thick ones domain solutions. Solid line: stable state; dashed line: unstable state. The arrows indicate the transitions between homogeneous and domain states that would be observed in a galvanodynamic experiment. (c) Chaotically breathing domains that exist in small parameter regions if the characteristic time of the autocatalytic chemical variable is much faster than that of the double layer potential.

Finally, let us discuss which behavior emerges if the negative global coupling stabilizes the homogeneous mode of a focus. We encountered such a situation already for N-NDR systems, in which case the dominant structures were pulses or standing waves with wave number 1. For S-NDR systems we can expect in principle analogous behavior if the conductivity is high; however, it will occur less often, since S-NDR systems oscillate only if ϕ_{DL} is the slow variable, which is true only in exceptional cases. For low conductivity and slow variations of ϕ_{DL}, the instability giving rise to standing waves or pulses might interact with the Turing bifurcation [206]. This results in an abundance of patterns. Such interactions are currently being studied in the framework of theoretical studies of reaction-diffusion systems [207]. Its experimental realization in electrochemical systems is a demanding and rewarding task.

5 Summary and Perspectives

Concepts developed in nonlinear dynamics facilitated the classification of nonlinear phenomena in electrochemical systems and revealed the origins of the diversity of temporal and spatial patterns in electrochemical systems. The diversity results on the one hand from the fact that the electrode potential might act as a positive or as a negative feedback variable. On the other hand, it is a consequence of the different kinds of spatial coupling present in an electrochemical cell and of the unique property that the extent of the spatial couplings is influenced by parameters that can be easily manipulated in an experiment.

The basic spatial coupling present in any electrochemical system is migration coupling, which is mediated through the electric field in the electrolyte. It is intrinsically nonlocal, that is, a change of state at a particular location induces noticeably and instantly changed migration currents at the electrode in an expanded, surrounding area. In contrast, diffusive coupling is a nearest-neighbor coupling, and in this sense it is local. In migration coupling, the conductivity of the electrolyte takes the role of the diffusion coefficient in diffusive coupling. Obviously, in most cases the diffusion coefficient can only be affected from the outside through a temperature variation (that affects also all other rate constants), whereas the conductivity can be changed easily in an experiment.

Furthermore, the migration coupling depends on the potential distribution in the electrolyte, and thus on the geometry of the cell. The most important parameter in this respect is the distance between the WE and the CE, or, more precisely the aspect ratio of the distance between the WE and the CE and the extension of the WE in one pattern forming direction. For an aspect ratio larger than 1, the maximum range is attained. For increasingly smaller aspect ratios the coupling range decreases continuously. In the extreme case of an infinitely small distance, nonlocal coupling turns into diffusive coupling. Thus, electrochemical systems possess the peculiarity that the range of the spatial coupling can be varied as can the characteristic time of the spatial coupling.

Further effects that are superimposed on the mentioned general characteristics of migration coupling arise for certain geometries. Two basic types of geometries have to be distinguished. In the fist type (type I), the WE extends from one end of the cell to the other one; in the other (type II), it is embedded into an insulator. In type II geometries, a homogeneous potential distribution at the electrode can never coexist with a homogeneous current density, which manifests itself in the evolution equation for the electrode potential in parameters that vary in space. This excludes the existence of homogeneous solutions a priori. Also the migration coupling is qualitatively different in this case: every location of the electrode is coupled to locations close to the edge of the electrode as strongly as to immediately neighboring ones. This leads to a pronounced edge effect in the dynamics. Another aspect concerns the location of the RE. If it is placed asymmetrically with respect to the WE, then the asymmetry might show up again in the interfacial patterns.

Two kinds of global coupling can occur aside from the migration coupling, depending on the experimental conditions. If the distance between the working electrode and the reference electrode is small, then the feedback through the potentiostat results in a negative global coupling. This negative global coupling induces an antiphase behavior and highly favors pattern formation. In contrast, a positive global coupling exists for galvanostatic conditions, which acts in a synchronizing manner.

All three types of coupling, migration coupling as well as negative and positive global coupling, depend solely on the electrical properties of the system. Therefore, they are independent of the electrode reaction. Thus, everything we summarized up to now applies to all electrochemical systems considered in this article. The type of pattern that develops in a given system depends on the interaction of the spatial coupling and the dynamics of the homogeneous system. Here, the electrode reactions come into play. With a few exceptions, under conditions for which instabilities are observed electrode reactions can be divided into just two classes despite large chemical variations: systems with an N-shaped I/ϕ_{DL} characteristic, and systems with an S-shaped I/ϕ_{DL} characteristic. Both classes are activator-inhibitor systems as are chemical reactions that oscillate in homogeneous phase. The electrode potential is the activator for N-NDR systems, and the inhibitor for S-NDR systems. Thus, the three types of spatial couplings discussed above act either on the activator variable or on the inhibitor variable.

The variety of combinations results in a broad spectrum of spatial instabilities and patterns. These are summarized in Table 1: If the electrode potential represents the activator, then the migration coupling leads to potential fronts, which often propagate in an accelerated manner because the coupling is nonlocal. Furthermore, it can destabilize homogeneous oscillations, leading to modulated waves that were found in some instances to be irregular in time and space and resemble turbulent states. An additional positive global coupling enhances the accelerated expansion, on the one hand, and, on the other hand, it can result in the formation of clusters in the oscillatory range. If a negative coupling superposes the migration coupling, the homogeneous stationary state might become unstable with respect to spatial perturbations, resulting in standing domains, standing waves with wave number 1 or pulses, depending on the parameters. In addition, also domain formation is observed in the oscillatory region, which can manifest itself in different manners.

Table 1. Summary of typical spatiotemporal behaviors in (H)N-NDR and S-NDR systems under different experimental conditions corresponding to different types of spatial coupling. (n is the wave number of the resulting pattern.)

	Nonlocal migration coupling through the electrolyte (always present)	Negative global coupling: potentiostatic control with Haber–Luggin capillary	Positive global coupling: galvanostatic control
(H)N-NDR systems ϕ_{DL}: activator	accelerated waves, inhomogeneous (BF unstable) oscillations	stationary domains, standing waves, anti-phase oscillations with $n = 1$; pulses, target patterns, clusters	enhanced acceleration of potential fronts, mainly homogenizing effect; cluster formation in the oscillatory region
S-NDR systems ϕ_{DL}: inhibitor	Turing-like structures ($n \geq 1$)	standing waves, anti-phase oscillations with $n = 1$ or mixed-mode structures with $n \geq 1$; pulses	stationary domains ($n = 1$ or $n \geq 1$)

If the electrode potential is the inhibitor, the migration currents can destabilize a homogeneous potential distribution in a Turing-like instability. Stationary patterns with a characteristic wavelength result. Since migration currents and positive global coupling act similarly in S-NDR systems, positive global coupling leads to the formation of stationary domains as well. The wavelength of the domains, however, is then the same as the length of the system. Negative global coupling, on the other hand, changes pattern formation only qualitatively if the system oscillates. In that case, negative global coupling can result in the formation of standing waves with wave number 1 just like for N-NDR systems. For parameter values for which migration coupling leads to the formation of Turing-like structures, the interaction of both instabilities can yield a complex wave pattern characterized by two wave numbers, $n = 1$ and $n > 1$. However, oscillations do normally not occur in S-NDR systems. Therefore, the latter patterns are expected to be observable only in exceptional cases.

It may appear that Table 1 contains an essentially complete summary of patterns that may form in electrochemical systems. This impression is misleading, since Table 1 only roughly summarizes results observed so far or predicted with models. These are investigations concentrating on phenomena that can be described with two essential variables (two-component systems). This survey is certainly not yet completed. Furthermore, numerous examples of current or potential oscillations involve complex time series. Only in a few cases does the complex time series result from the spatial patterns. In most cases, the additional degree of freedom will be from a third dependent variable, such as from a concentration that adds an additional feedback loop into the system, as discussed in Section 3.1.3. Spatial pattern formation in three-variable systems is an area that currently develops strongly in nonlinear dynamics. In the electrochemical context, the problem of pattern formation in three-variable systems has not yet been approached.

One should also have in mind that, though seldom and thus far not well studied, there are a few electrochemical systems in which the electrode potential is not an essential variable, or at least in which an activator-inhibitor subset exists, in which both activator and inhibitor are chemical variables. The only system in which the reaction kinetics has been understood in detail is discussed in Ref. [15]. Another system that has been speculated for some time to belong to this class is the oxidation of Fe in HNO_3 [9]. In this system unusual pattern formation was detected recently [208].

Concerning future directions of studies on nonlinear phenomena, there seem to be two main streams. Firstly, their input to fundamental questions of nonlinear dynamics will still grow. The reasons are a combination of three incidents. Electrochemical systems cover a wide spectrum of both, different behaviors of the homogeneous dynamics as well as different types of spatial coupling. This fact is closely linked to the commonness of instabilities in electrochemical systems. Furthermore, they allow for accurate measurements with relatively cheap instrumentation, and, even more importantly, for an easy control. In this respect, we have just learned how the control can also be extended over parameters that determine the spatial coupling, a property that is peculiar to electrochemical systems. The systematic use of this knowledge will provide us with further, so far unknown, manifestations of nonlinear behaviors. One example along this line are the modulated, intermittently accelerating and decelerating activation waves observed during the anodic dissolution of Co by Otterstedt et al. [170, 176]. Besides, electrochemical systems will continue to serve as experimental model systems to test newly developed theories in the field of nonlinear dynamics.

In this context, also the potential impact of studies of electrochemical wave propagation on a better understanding of activation waves in nerve axons or coupled neurons should be mentioned. This statement actually brings us back to the beginning of studies on nonlinear electrochemical behavior, which were mainly motivated by the similarity between the propagation of active areas in electrochemical systems and nerve-impulse propagation [76, 79, 83, 209, 210]. Undoubtedly, in both cases we are dealing with the excitation and propagation of electrical disturbances. Typical propagation velocities in these two types of system are much faster than, for example, in chemical systems in which concentration waves occur. As we described above, a peculiarity in electrochemical systems is the nonlocality of the spatial coupling, which is linked to the electric field inside the bulk electrolyte. Concerning nerve-impulse propagation, its principle features could be successfully described by the Hodgkin–Huxley theory [211], which incorporates a reaction-diffusion system, and thus local coupling. However, after what we have learned about nonlocal coupling in electrochemical systems, it appears to be worthwhile to investigate to what extent a corresponding Ansatz yields quantitatively better results.

Secondly, besides fundamental questions, the large challenge for the coming years is to utilize our knowledge about instabilities to achieve a better performance of industrial processes. In this regard, one important and promising issue concerns a possible increase in yield under non-stationary or non-homogeneous operation conditions. Consider, for instance, the oxidation of small organic molecules that are potential fuels. Under reaction conditions favorable from an energetic point of view,

the electrode is readily poisoned by reaction intermediates or side products, but can be driven easily into an oscillatory regime. During spontaneous oscillations, the electrode surface periodically enters a ''de-poisoned'' state of increased activity. This might result in an overall reaction rate that exceeds the one under stationary conditions. The first experimental hints that non-stationary operation conditions can indeed be superior to stationary ones were obtained by Schell et al. [212]. These authors conducted galvanostatic experiments with a periodically varying parameter. They observed a considerable decrease in the average surface potential, which is attributed to a sustained decrease in the coverage of poisoning species. This finding indicates that the exploitation of nonlinear effects might become a standard tool in applied electrochemistry.

Another promising idea proposed recently [184] involves the operation of a reaction in a state where the spatial symmetry is broken. This can be achieved most easily by making use of the desynchronizing effect of a negative global coupling. The latter implies that partial poisoning of the electrode in some region enhances the catalytic activity in a distant region. In this way, the homogeneous potential distribution becomes unstable and the above-mentioned sustained stationary, traveling, or oscillating patterns form. In the patterned state the complete poisoning of the electrode is inhibited, which makes it likely that the overall catalytic activity is increased. Above, we discussed that a negative global coupling is introduced into a system if the RE is positioned close to the WE. However, industrial processes are generally carried out in a two-electrode arrangement. Here a negative global coupling can be realized by introducing in series to the cell an electronic device which acts like a negative resistor, as discussed above in connection with Li et al.'s experiments [41]. Besides achieving an increase in yield, there is also the prospect to utilize unstable kinetics in sensors. The switching between bistable states or the onset of oscillations seems to be a suitable process to indicate if a threshold concentration is exceeded.

Another intriguing idea is to make use of spatial instabilities to produce regularly structured surfaces. Out of the spatial instabilities described above, a favorable candidate seems to be the Turing instability present in all S-NDR systems. However, with respect to this mechanism, it is too early to predict any applications. More experimental examples and fundamental studies are needed, especially concerning the parameters that control the wavelength. Spatial structures obtained so far had wavelengths in the mm to cm region, which is certainly not in the focus of interest when one is thinking of regularly spaced clusters or arrays on an electrode. But nanometer-scale pattern formation has been observed in electrochemical systems. During electropolishing of aluminum, a variety of surface structures, including amazingly regular stripes or hexagons with amplitudes of 10 nm and wavelengths of 50–150 nm were found to develop [23, 24]. The formation of the patterns is attributed to preferential adsorption of organic molecules on the convex portion of the electrode that is associated with an enhanced electric field. The structure formation was successfully described by nonlinear partial differential equations, although they were not of the pure reaction-migration type, like those discussed in this article. These observations point to the potential self-assembly processes can have in the fabrication of nanostructures.

In conclusion, the interdisciplinary aspect of any study of self-organization phenomena, and potential technological applications of nonlinear electrochemical behaviors, together ensure that the study of self-organization phenomena in electrochemistry will remain a vital field of research.

6 References

1. H. Haken, Synergetics, Springer, Berlin (1977).
2. A. S. Mikhailov, Foundations of Synergetics I, Springer, Berlin (1994).
3. S. H. Strogatz, Nonlinear Dynamics and Chaos, Addison Wesley, Reading (1994).
4. G. Nicolis, Introduction to Nonlinear Science, Cambridge University Press, Cambridge (1995).
5. M. G. T. Fechner, Schweigger J. für Chemie Physik 53, 129 (1828).
6. J. Wojtowicz, in: Modern Aspects of Electrochemistry, J. O. M. Bockris and B. E. Conway (eds.), Butterworths, London (1973).
7. J. L. Hudson, T. T. Tsotsis, Chem. Eng. Sci. 49, 1493 (1994).
8. M. T. M. Koper, Electrochim. Acta 37, 1771 (1992).
9. M. T. M. Koper, in: Advances in Chemical Physics, Vol. 92, I. Prigogine and S. A. Rice (eds.), Wiley, New York (1996).
10. K. Krischer, in: Modern Aspects of Electrochemistry, Vol. 32, B. E. Conway, J. O. M. Bockris and R. White (eds.), Kluwer Academic/Plenum, New York (1999).
11. M. T. M. Koper, J. Electroanal. Chem. 409, 175 (1996).
12. P. Strasser, M. Eiswirth, M. T. M. Koper, J. Electroanal. Chem. 478, 50 (1999).
13. I. R. Epstein, J. A. Pojman, An Introduction to Nonlinear Chemical Dynamics, Oxford Press, New York (1998).
14. J. D. Murray, Mathematical Biology, Springer, Berlin (1990).
15. G. Bourceanu, V. Melnig, J. Vatamanu, R. Vasiliu, Electrochim. Acta 43, 1031 (1998).
16. M. Eiswirth, A. Freund, J. Ross, in: Advances in Chemical Physics, Vol. 80, I. Prigogine and S. A. Rice (eds.), Wiley, New York (1991).
17. R. Kapral, K. Showalter (eds.), Chemical Waves and Patterns, Kluwer Academic Publishers, Dordrecht, 1995.
18. D. Luss, Physica A 188, 68 (1992).
19. E. Schöll, Nonlinear Spatiotemporal Dynamics and Chaos in Semiconductors, Cambridge University Press, Cambridge (2001).
20. M. Falcke, H. Engel, M. Neufeld, Phys. Rev. E 52, 763 (1995).
21. D. Battogtokh, A. Preusser, A. S. Mikhailov, Physica D 106, 327 (1997).
22. F. Plenge, P. Rodin, E. Schöll, K. Krischer, Phys. Rev. E 64, 056229 (2001).
23. S. Bandyopadhyay, A. E. Miller, H.-C. Chang, G. Banerjee, V. Yuzhakov, D. F. Yue, R. E. Ricker, J. Jones, J. A. Eastman, E. Baugher, M. Chandrasekhar, Nanotechnology 7, 360 (1996).
24. V. V. Yuzhakov, P. V. Takhistov, A. E. Miller, H.-C. Chang, Chaos 9, 62 (1999).
25. J. Newman, Electrochemical Systems, Prentice Hall, Englewood Cliffs (1991).
26. G. Flätgen, K. Krischer, J. Chem. Phys. 103, 5428 (1995).
27. A. Birzu, B. J. Green, R. D. Otterstedt, N. I. Jaeger, J. L. Hudson, Phys. Chem. Chem. Phys. 2, 2715 (2000).
28. A. Birzu, B. J. Green, R. D. Otterstedt, J. L. Hudson, N. I. Jaeger, Z. Phys. Chem. 216, 459 (2002).

29. A. Birzu, B. J. Green, N. I. Jaeger, J. L. Hudson, J. Electroanal. Chem 504, 126 (2001).
30. G. Flätgen, K. Krischer, G. Ertl, Z. Naturforsch. 50a, 1097 (1995).
31. N. Mazouz, G. Flätgen, K. Krischer, Phys. Rev. E 55, 2260 (1997).
32. N. Mazouz, G. Flätgen, K. Krischer, I. G. Kevrekidis, J. Electrochem. Soc. 145, 2404 (1998).
33. N. Mazouz, K. Krischer, J. Phys. Chem. B 104, 6081 (2000).
34. N. Mazouz, K. Krischer, G. Flätgen, G. Ertl, J. Phys. Chem. B 101, 2403 (1997).
35. J. Christoph, R. D. Otterstedt, M. Eiswirth, N. I. Jaeger, J. L. Hudson, J. Chem. Phys. 110, 8614 (1999).
36. J. Christoph, P. Strasser, M. Eiswirth, G. Ertl, Science 284, 291 (1999).
37. J. Christoph, Ph.D. Thesis, FU Berlin, Berlin, Germany (1999).
38. D. Haim, O. Lev, L. M. Pismen, M. Sheintuch, Chem. Eng. Sci. 47, 3907 (1992).
39. A. Karantonis, S. Nakabayashi, Electrochim. Acta 46, 745 (2000).
40. J. Newman, J. Electrochem. Soc. 113, 501 (1966).
41. Y.-J. Li, F. Plenge, K. Krischer, in preparation, (2002).
42. P. Grauel, J. Christoph, G. Flätgen, K. Krischer, J. Phys. Chem. B 102, 10264 (1998).
43. H. Kaesche, Die Korrosion der Metalle, Springer, Berlin (1990).
44. T. Matsuda, H. Hommura, Y. Mukouyama, S. Yae, Y. Nakato, J. Electrochem. Soc. 144, 1988 (1997).
45. Y. Mukouyama, S. Nakanishi, Y. Nakato, Bull. Chem. Soc. Jpn. 72, 2573 (1999).
46. Y. Nakato, Denki Kagaku 66, 234 (1998).
47. H. Jehring, U. Kürschner, J. Electroanal. Chem. 75, 799 (1977).
48. H. Jehring, N. V. Huyen, T. X. Gian, E. Horn, C. Hirche, J. Electroanal. Chem. 135, 37 (1979).
49. H. Dörfler, E. Müller, J. Electroanal. Chem. 135, 37 (1982).
50. M. T. M. Koper, P. Gaspard, J. Chem. Phys. 96, 7797 (1992).
51. M. T. M. Koper, P. Gaspard, J. H. Sluyters, J. Chem. Phys. 97, 8250 (1992).
52. R. Jurczakowski, M. Orlik, J. Electroanal. Chem. 478, 118 (1999).
53. G. Flätgen, S. Wasle, M. Lübke, C. Eickes, G. Radhakrishnan, K. Doblhofer, G. Ertl, Electrochim. Acta 44, 4499 (1999).
54. C. Eickes, K. G. Weil, K. Doblhofer, Phys. Chem. Chem. Phys. 2, 5691 (2000).
55. Y. Mukouyama, S. Nakanishi, H. Konishi, Y. Nakato, J. Electroanal. Chem. 473, 156 (1999).
56. S. Nakanishi, Y. Mukouyama, Y. Nakato, J. Phys. Chem. B. 105, 5751 (2001).
57. Y. Mukouyama, S. Nakanishi, T. Chiba, K. Murakoshi, Y. Nakato, J. Phys. Chem. B. 105, 7246 (2001).
58. A. N. Frumkin, Z. Elektrochem. 59, 807 (1955).
59. L. E. Gierst, in: Transactions of the Symposium on Electrode Processes, E. Yeager (ed.), Wiley, New York (1961).
60. A. Frumkin, O. Petrii, N. Nicolaeva-Fedorovich, Dok. Akad. Nauk. SSSR 136, 1158 (1961).
61. A. Gokhstein, A. Frumkin, Dokl. Akad. Nauk. SSSR 132, 388 (1960).
62. W. Wolf, J. Ye, M. Purgand, M. Eiswirth, K. Doblhofer, Ber. Bunsenges. Phys. Chem. 96, 1797 (1992).
63. K. Krischer, J. Electroanal. Chem. 501, 1 (2001).
64. K. Krischer, N. Mazouz, P. Grauel, Angew. Chem. Int. Ed. 40, 851 (2001).
65. M. T. M. Koper, J. H. Sluyters, J. Electroanal. Chem. 308, 151 (1991).
66. H. Nyquist, Bell. Syst. Tech. J. 11, 126 (1932).
67. I. Z. Kiss, V. Gaspar, L. Nyikos, J. Phys. Chem. A 102, 909 (1998).
68. M. T. M. Koper, J. H. Sluyters, J. Electroanal. Chem. 352, 51 (1993).
69. S. Nakanishi, Y. Mukouyama, K. Karasumi, A. Imanishi, N. Furuya, Y. Nakato, J. Phys. Chem. B 104, 4181 (2000).

70. Y. Mukouyama, K. Konishi, S. Nakanishi, Y. Nakato, Chem. Lett. (10), 1009 (1998).
71. Y. Mukouyama, H. Hommura, S. Nakanishi, T. Nishimura, H. Konishi, Y. Nakato, Bull. Chem. Soc. Jpn. 72, 1247 (1999).
72. Y. Mukouyama, S. Nakanishi, H. Konishi, K. Karazumi, Y. Nakato, Phys. Chem. Chem. Phys. 3, 3284 (2001).
73. T. Nishimura, Y. Mukouyama, S. Nakanishi, H. Konishi, Y. Nakato, Kag. Kog. Ronbunshu 25, 510 (1999).
74. M. T. M. Koper, Ber. Bunsenges. Phys. Chem. 100, 497 (1996).
75. M. T. M. Koper, P. Gaspard, J. H. Sluyters, J. Phys. Chem. 96, 5674 (1992).
76. H. L. Heathcote, Z. Phys. Chem. 37, 368 (1901).
77. W. Ostwald, Z. Phys. Chem. 35, 204 (1900).
78. W. Ostwald, Z. Phys. Chemie 35, 33 (1900).
79. K. F. Bonhoeffer, W. Renneberg, Z. Phys. 118, 389 (1941).
80. K. F. Bonhoeffer, Z. Elektrochem. 47, 147 (1941).
81. K. F. Bonhoeffer, G. Vollheim, Z. Naturforsch. 8b, 406 (1953).
82. U. F. Franck, Z. Naturforsch. 4a, 378 (1949).
83. U. F. Franck, Z. Elektrochem. 55, 154 (1951).
84. U. F. Franck, L. Meunier, Z. Natuforsch. 8b, 396 (1953).
85. U. F. Franck, Z. Elektrochem. 62, 649 (1958).
86. U. F. Franck, R. FitzHugh, Z. Elektrochem. 65, 156 (1961).
87. M. T. M. Koper, J. H. Sluyters, J. Electroanal. Chem. 347, 31 (1993).
88. P. Russell, J. Newman, J. Electrochem. Soc. 130, 547 (1983).
89. R. Otterstedt, Ph.D. Thesis, Universität Bremen, Bremen, Germany (1997).
90. M. Pagitsas, D. Sazou, J. Electroanal. Chem. 334, 81 (1992).
91. M. C. H. McKubre, D. D. Macdonald, J. Electrochem. Soc 128, 524 (1985).
92. M. T. M. Koper, J. H. Sluyters, J. Electroanal. Chem. 371, 149 (1994).
93. P. Strasser, M. Lübke, C. Eickes, M. Eiswirth, J. Electroanal. Chem. 462, 19 (1999).
94. Z. L. Li, J. L. Cai, S. M. Zhou, J. Electroanal. Chem. 432, 111 (1997).
95. Z. L. Li, Q. H. Yuan, B. Ren, X. M. Xiao, Y. Zeng, T. ZQ., Electrochem. Commun. 3, 654 (2001).
96. Y. Mukouyama, S. Nakanishi, H. Konishi, Y. Ikeshima, Y. Nakato, J. Phys. Chem. B. 105, 10905 (2001).
97. K. Krischer, M. Lübke, W. Wolf, M. Eiswirth, G. Ertl, Electrochim. Acta 40, 69 (1995).
98. W. Wolf, K. Krischer, M. Lübke, M. Eiswirth, G. Ertl, J. Electroanal. Chem. 385, 85 (1995).
99. G. Horányi, C. Visy, J. Electroanal. Chem. 103, 353 (1979).
100. T. Yamazaki, T. Kodera, Electrochim. Acta 34, 969 (1989).
101. T. Kodera, T. Yamazaki, N. Kubota, Electrochim. Acta 31, 1477 (1986).
102. T. Kodera, T. Yamazaki, M. Masuda, R. Ohnishi, Electrochim. Acta 33, 537 (1988).
103. K. Krischer, M. Lübke, W. Wolf, M. Eiswirth, G. Ertl, Ber. Bunsenges. Phys. Chem. 95, 820 (1991).
104. M. Eiswirth, M. Lübke, K. Krischer, W. Wolf, J. L. Hudson, G. Ertl, Chem. Phys. Lett. 192, 254 (1992).
105. K. Krischer, M. Lübke, M. Eiswirth, W. Wolf, J. L. Hudson, G. Ertl, Physica D 62, 123 (1993).
106. W. Wolf, M. Lübke, M. T. M. Koper, K. Krischer, M. Eiswirth, G. Ertl, J. Electroanal. Chem. 399, 185 (1995).
107. M. C. Deibert, D. L. Williams, J. Electrochem. Soc. 116, 1290 (1969).
108. T. Yamazaki, T. Kodera, Electrochim. Acta 36, 639 (1991).
109. N. M. Markovic, C. A. Lucas, B. N. Grgur, P. N. Ross, J. Phys. Chem. B. 103, 9616 (1999).

110. S. Nakanishi, H. Hommura, Y. Mukouyama, T. Matsuda, Y. Nakato, Chem. Lett., 977 (1998).
111. Y. Mukouyama, T. Nishimura, S. Nakanishi, Y. Nakato, J. Phys. Chem. B 104, 11186 (2000).
112. M. Breiter, Electrochemical Processes in Fuel Cells, Springer-Verlag, Berlin (1969).
113. A. Capon, R. Parsons, J. Electroanal. Chem. 44, 239 (1973).
114. R. Parsons, T. Vandernoot, J. Electroanal.Chem. 257, 9 (1988).
115. T. Iwasita, S. H. Xia, J. Electroanal.Chem. 411, 95 (1996).
116. T. Iwasita, X. H. Xia, H. D. Liess, W. Vielstich, J. Phys. Chem. B. 101, 7542 (1997).
117. J. Wojtowicz, N. Marincic, B. E. Conway, J. Chem. Phys. 48, 4333 (1968).
118. M. Schell, F. N. Albahadily, J. Safar, Y. H. Xu, J. Phys. Chem. 93, 4806 (1989).
119. F. Raspel, R. J. Nichols, D. M. Kolb, J. Electroanal. Chem. 286, 279 (1990).
120. F. Raspel, M. Eiswirth, J. Phys. Chem. 98, 7613 (1994).
121. F. N. Albahadily, M. Schell, J. Electroanal. Chem. 308, 151 (1991).
122. X. Cai, M. Schell, Electrochim. Acta 37, 673 (1990).
123. Y. Xu, M. Schell, J. Phys. Chem. 94, 7137 (1990).
124. N. M. Markovic, P. N. Ross, J. Phys. Chem. 97, 9771 (1993).
125. H. Okamoto, N. Tanaka, M. Naito, Chem. Phys. Lett. 248, 289 (1996).
126. P. Strasser, M. Eiswirth, G. Ertl, J. Chem. Phys. 107, 991 (1997).
127. A. Tripkovic, K. Popovic, R. R. Adzic, J. Chim. Phys. 88, 1635 (1991).
128. P. Strasser, M. Eiswirth, G. Ertl, J. Chem. Phys. 107, 991 (1997).
129. M. Naito, N. Tanaka, H. Okamoto, J. Chem. Phys. 111, 9908 (1999).
130. M. Naito, H. Okamoto, N. Tanaka, Phys. Chem. Chem. Phys. 2, 1193 (2000).
131. T. J. Schmidt, B. N. Grgur, N. M. Markovic, P. N. Ross, J. Electroanal. Chem. 500, 36 (2001).
132. S. L. Chen, T. Noles, M. Schell, Electrochem. Commun. 2, 171 (2000).
133. S. L. Chen, D. Lee, M. Schell, Electrochem. Commun. 3, 81 (2001).
134. S. L. Chen, M. Schell, J. Electroanal. Chem. 504, 78 (2001).
135. S. L. Chen, D. Lee, M. Schell, Electrochim. Acta 46, 3481 (2001).
136. G. Inzelt, V. Kertesz, Electrochim. Acta 40, 221 (1995).
137. J. Lee, J. Christoph, P. Strasser, M. Eiswirth, G. Ertl, J. Chem. Phys. 115, 1485 (2001).
138. M. Hachkar, M. M. deChoy, A. Rakotondrainibe, B. Beden, C. Lamy, Phys. Rev. A 43, 2480 (1991).
139. H. Okamoto, N. Tanaka, Electrochim. Acta 38, 503 (1993).
140. H. Okamoto, N. Tanaka, M. Naito, Electrochim. Acta 39, 2471 (1994).
141. H. Okamoto, N. Tanaka, M. Naito, J. Phys. Chem. A 101, 8480 (1997).
142. H. Okamoto, N. Tanaka, M. Naito, J. Phys. Chem. A 102, 7343 (1998).
143. H. Okamoto, N. Tanaka, M. Naito, J. Phys. Chem. A 102, 7353 (1998).
144. H. Okamoto, N. Tanaka, M. Naito, J. Electrochem. Soc. 147, 2629 (2000).
145. Y. H. Xu, H. H. Wu, H. P. Dai, S. M. Zhou, Prog. Nat. Sci. 4, 248 (1994).
146. B. W. Mao, B. Ren, X. W. Cai, L. H. Xiong, J. Electroanal. Chem. 394, 155 (1995).
147. M. T. M. Koper, M. Hachkar, B. Beden, J. Chem. Soc.-Faraday Trans. 92, 3975 (1996).
148. T. O. Pavela, Suomen Kemistilehti 30, 138 (1957).
149. R. P. Buck, L. R. Griffith, J. Electrochem. Soc. 109, 1005 (1962).
150. M. Novak, G. Visg, Acta Chim. Acad. Hung. 105, 47 (1980).
151. A. A. Inocencio, M. A. Inocencio, Port. Electrochim. Acta 9, 355 (1991).
152. M. Krausa, W. Vielstich, J. Electroanal. Chem. 399, 7 (1995).
153. T. Page, R. Johnson, J. Hormes, S. Noding, B. Rambabu, J. Electroanal. Chem. 486, 34 (2000).
154. M. Hachkar, B. Beden, C. Lamy, J. Electroanal. Chem. 287, 81 (1990).
155. J. Lee, C. Eickes, M. Eiswirth, G. Ertl, Electrochim. Acta 47, 2297 (2002).

156. K. Krischer, H. Varela, in: Handbook of Fuel Cells, W. Vielstich, H. Gasteiger and A. Lamm (eds.), (2003).
157. M. M. E. Lejay, R. Wiart, C. R. Acad. Sc. Paris 277C, 833 (1973).
158. I. Epelboin, M. Ksouri, E. Lejay, R. Wiart, Electrochim. Acta 20, 603 (1975).
159. M. T. M. Koper, T. J. Schmidt, N. M. Markovik, P. N. Ross, J. Phys. Chem. B. 105, 8381 (2001).
160. Y. J. Li, J. Oslonovitch, N. Mazouz, F. Plenge, K. Krischer, G. Ertl, Science 291, 2395 (2001).
161. H. Striegler, Ph.D. Thesis, Universität Ulm, Ulm, Germany (1998); H. Striegler, D. Krznavic, D. M. Kolb, J. Electroanal. Chem. 532, 227 (2002).
162. A. N. Frumkin, B. B. Damaskin, in: Modern Aspects of Electrochemistry, J. O. Bockris and B. E. Conway (eds.), Butterworths, London (1964).
163. H. A. Gasteiger, N. M. Markovic, P. N. Ross, J. Phys. Chem. B. 99, 16757 (1995).
164. N. M. Markovic, T. J. Schmidt, B. N. Grgur, H. A. Gasteiger, R. J. Behm, P. N. Ross, J. Phys. Chem. B 103, 8568 (1999).
165. D. C. Azevedo, A. L. N. Pinheiro, E. R. Gonzales, Electrochem. Solid State Lett. 5, A51 (2002).
166. G. Flätgen, K. Krischer, Phys. Rev. E 51, 3997 (1995).
167. R. D. Otterstedt, P. J. Plath, N. I. Jaeger, J. C. Sayer, J. L. Hudson, Chem. Eng. Sci. 51, 1747 (1996).
168. R. Baba, Y. Shiomi, S. Nakabayashi, Chem. Eng. Sci. 55, 217 (2000).
169. S. Nakabayashi, R. Baba, Y. Shiomi, Chem. Phys. Lett. 287, 632 (1998).
170. R. D. Otterstedt, P. J. Plath, N. I. Jaeger, J. L. Hudson, Phys. Rev. E 54, 3744 (1996).
171. T. Benjamin, J. Feir, J. Fluid Mech. 27, 417 (1967).
172. N. Mazouz, Ph.D. Thesis, FU Berlin, Berlin, Germany (1999).
173. P. Grauel, H. Varela, K. Krischer, Faraday Discussions 120, 165 (2001).
174. H. Varela, K. Krischer, Catal. Today 70, 411 (2001).
175. H. Varela, K. Krischer, unpublished results.
176. R. D. Otterstedt, N. I. Jaeger, P. J. Plath, J. L. Hudson, Phys. Rev. E 58, 6810 (1998).
177. A. Pigeau, H. B. Kirkpatrick, Corrosion 25, 209 (1969).
178. J. L. Hudson, J. Tabora, K. Krischer, I. G. Kevrekidis, Phys. Lett. A 179, 355 (1993).
179. R. D. Otterstedt, N. I. Jaeger, P. J. Plath, Int. J. Bifurcation and Chaos 4, 1265 (1994).
180. Z. Fei, R. G. Kelly, J. L. Hudson, J. Phys. Chem. 100, 18986 (1996).
181. K. Agladze, S. Thouvenel-Romans, O. Steinbock, Phys. Chem. Chem. Phys. 3, 1326 (2001).
182. P. Grauel, K. Krischer, Phys. Chem. Chem. Phys. 3, 2497 (2001).
183. R. D. Otterstedt, P. J. Plath, N. I. Jaeger, J. L. Hudson, J. Chem. Soc.-Faraday Trans. 92, 2933 (1996).
184. P. Strasser, J. Christoph, W. F. Lin, M. Eiswirth, J. L. Hudson, J. Phys. Chem. A 104, 1854 (2000).
185. G. Flätgen, K. Krischer, B. Pettinger, K. Doblhofer, H. Junkes, G. Ertl, Science 269, 668 (1995).
186. B. J. Green, J. L. Hudson, Phys. Rev. E 6302, 6214 (2001).
187. J. C. Sayer, J. L. Hudson, Ind. Eng. Chem. Res. 34, 3246 (1995).
188. V. K. Vanag, A. M. Zhabotinsky, I. R. Epstein, J. Phys. Chem. A 104, 11566 (2000).
189. V. K. Vanag, L. Yang, M. Dolnik, A. M. Zhabotinskz, I. R. Epstein, Nature 406, 389 (2000).
190. M. Falcke, H. Engel, J. Chem. Phys. 101, 6255 (1994).
191. M. Kim, M. Bertram, M. Pollmann, A. v. Oertzen, A. S. Mikhailov, H. H. Rotermund, G. Ertl, Science 292, 1357 (2001).
192. M. Bertram, A. S. Mikhailov, Phys. Rev. E 63, 66102 (2001).
193. O. Lev, M. Sheintuch, L. M. Pismen, C. Yarnitzky, Nature 336, 488 (1988).

194. O. Lev, M. Sheintuch, H. Yarnitsky, L. M. Pismen, Chem. Eng. Sci. 45, 839 (1990).
195. I. Z. Kiss, W. Wang, J. L. Hudson, J. Phys. Chem. B 103, 11433 (1999).
196. I. Z. Kiss, W. Wang, J. L. Hudson, Phys. Chem. Chem. Phys. 2, 3847 (2000).
197. W. Wang, I. Z. Kiss, J. L. Hudson, Chaos 10, 248 (2000).
198. I. Z. Kiss, J. L. Hudson, Phys. Rev. E 64, 046215 (2001).
199. W. Wang, I. Z. Kiss, J. L. Hudson, Phys. Rev. Lett. 86, 4954 (2001).
200. W. Wang, I. Z. Kiss, J. L. Hudson, Ind. Eng. Chem. Res. 43, 330 (2002).
201. D. Haim, O. Lev, L. M. Pismen, M. Sheintuch, J. Phys. Chem. 96, 2676 (1992).
202. O. Lev, A. Wolffberg, A. Sheintuch, L. M. Pismen, Chem. Eng. Sci. 43, 1339 (1988).
203. O. Lev, A. Sheintuch, L. M. Pismen, A. Wolffberg, J. Phys. Chem. 93, 1661 (1989).
204. A. M. Turing, Philos. Trans. R. Soc. London 237, 37 (1952).
205. A. deWit, in: Advances in Chemical Physics, Vol. 109, I. Prigogine and S. A. Rice (eds.), Wiley, New York (1999).
206. K. Krischer, N. Mazouz, G. Flätgen, J. Phys. Chem. B 104, 7545 (2000).
207. E. Nicola, M. Or-Guil, W. Wolf, M. Bär, Phys. Rev. E, 055101 (2002).
208. K. Agladze, O. Steinbock, J. Phys. Chem. A 104, 9816 (2000).
209. R. S. Lillie, Science 48, 51 (1918).
210. R. Suzuki, Adv. Biophys. 9, 115 (1976).
211. A. L. Hodgkin, A. F. Huxley, J. Physiol. 117, 500 (1952).
212. M. Schell, F. N. Albahadily, J. Safar, J. Electroanal. Chem. 353, 303 (1993).

Advances in Electrochemical Science and Engineering, Volume 8. Edited by Richard C. Alkire

ISBNs: 3-527-30211-5 (Hardback); 3-527-60078-7 (Electronic)

The Electrochemistry of Diamond

Yuri V. Pleskov

A.N. Frumkin Institute of Electrochemistry, Russian Academy of Sciences, Leninsky Prospekt 31, 119071 Moscow, Russia

Contents

Summary

Owing to its extraordinary chemical stability, diamond is a prospective electrode material for use in theoretical and applied electrochemistry. In this work studies performed during the last decade on boron-doped diamond electrochemistry are reviewed. Depending on the doping level, diamond exhibits properties either of a superwide-gap semiconductor or a semimetal. In the first case, electrochemical, photoelectrochemical and impedance-spectroscopy studies make the determination of properties of the semiconductor diamond possible. Among them are: the resistivity, the acceptor concentration, the minority carrier diffusion length, the flat-band potential, electron phototransition energies, etc. In the second case, the "metal-like" diamond appears to be a corrosion-stable electrode that is efficient in the electrosyntheses (e.g., in the electroreduction of hard to reduce compounds) and electroanalysis. Kinetic characteristics of many outer-sphere

and inner-sphere redox reactions, along with the impedance characteristics of diamond electrodes, are collected. Comparative studies of single crystal and polycrystalline diamond electrodes, as well as amorphous diamond-like carbon electrodes, revealed the role of crystal structure in the electrochemical behavior of diamond. In particular, the intercrystallite boundaries were shown to contribute but insignificantly to the polycrystalline diamond electrode properties. Possible applications of diamond electrodes are discussed.

1 Introduction

Diamond is a material possessing unique properties. It has extraordinarily high atomic density, hardness, insulating ability, thermal conductivity, and chemical inertness (see Table 1). The history of its intensive electrophysical, physico-chemical, and optical studies covers many decades [1, 2]. Its applications in materials science [3], microelectronics [4], and so on, are ever widening.

Owing to its extraordinary chemical stability, semiconductor diamond undoubtedly offers serious competition to other electrode materials. However, unlike other carbonaceous materials (e.g. graphite, glassy carbon, etc.), which gained a wide application in electrochemistry, diamond became an object of electrochemical investigation only as late as the decade of the 1990s. Until then, there was a serious handicap to such an investigation. First, diamond was an extremely rare, hard-to-access material. Second, diamond as such is a dielectric; hence, it cannot be used as electrode.

The situation reversed owing to progress in the technology of deposition of diamond thin films from gas phase at a subatmospheric pressure. Highly efficient tech-

Table 1. The principal physical properties of diamond [1].

Properties	Cubic natural diamond	HTHP- diamond	Epitaxial diamond films
Lattice parameter at 300K nm^{-1}	0.356683 0.35672	–	0.35664
Thermal coefficient of expansion at 300K	$0.8 \cdot 10^{-6}$	–	–
Refractive index at $\lambda = 590$ nm	2.417	2.419	2.38
Permittivity ε	5.7	–	–
Bandgap E_g at 300K/eV	5.48	–	–
Electron drift mobility μ_e/cm^2 V^{-1} s^{-1}	2500	–	–
Hole drift mobility μ_h/cm^2 V^{-1} s^{-1}	2100	–	–
Density/g cm^{-3}	3.51	–	–
Heat capacity at 300K/J mol^{-1} K^{-1}	6.12	–	–

niques were developed that made it possible to deposit polycrystalline diamond films on diamond and non-diamond substrates. In large-scale production, these films are expected to be not expensive. By doping the films with boron, a well-conducting material would be obtained, which is semiconductor in its nature [5]; moreover, heavily doped diamond is a quasi-metal. With the first studies of diamond electrodes, a new field emerged in the electrochemistry of semiconductor materials [6], namely, the electrochemistry of diamond. Formally, the first paper in the electrochemistry of diamond was that of Iwaki et al. [7]. These authors attempted the fabrication of an electrode, starting with a dielectric diamond crystal. To impart conductance if only to a thin outer layer of the crystal and thus to be able to pass electric current, they implanted the crystal with Ar^+, N^+, O^+, and Zn^+ ions. Yet argon is not a dopant in diamond, since it does not affect the diamond conductance; neither do the admixtures of nitrogen or oxygen at room temperature. The ion implantation resulted in an amorphization of the crystal outer layer [8, 9]. Indeed, the authors of [7] suggested: "The phenomenon may be also explained by the increasing thickness of the amorphous layer." The deterioration of crystal lattice and emergence of a great amount of carbon atoms with the sp^2-hybridization of C–C orbitals would result in a significant increase in the conductance [10]. The effect of Zn has been not revealed at the moment ("The conductivity enhancement for Zn^+ implantation may be caused not only by an amorphous phase but also by the implanted metallic elements themselves" [7]).

Thus, in the strict sense the paper [7] falls in the electrochemistry of non-diamond (amorphous) carbon, rather than in the diamond electrochemistry.

Actually, the electrochemistry of diamond dates back to the paper [11]. A current-voltage curve of crystalline diamond electrode was first taken there, as well as the differential capacitance measured at the diamond/electrolyte solution interface. The diamond electrodes turned out to be photosensitive, and their photoelectrochemical behavior was compared with their semiconductor nature.

After a few years scientists from Japan, Israel, France, USA, and other countries followed these studies. Whereas in the first papers the diamond electrodes, although of very good crystallinity, were not intentionally doped (their conductance was attributed to some unidentified impurities or point defects imparted by special thermal treatment), turning to boron-doped diamond samples [12] gave impetus to further progress in diamond electrochemistry. The number of laboratories involved in the studies of diamond electrodes is ever increasing in the last few years.

Below we give an overview of electrochemical behavior of synthetic diamond films and discuss some applications of electrochemical methods to their characterization. We attempt to predict prospects for this new area of electrochemistry. When touching fundamentals of the electrochemistry of semiconductors, we refer to the monograph [6] for details.

2 Fabrication of the Diamond Thin-Film Electrodes

Starting with the paper [11] and until recent years, the studies in diamond electrochemistry were concerned entirely with diamond films grown by the chemical vapor

deposition (CVD) techniques. An important stage in developing the CVD processes is associated with the studies performed by Derjaguin et al. [13] in the 1970s and 1980s. The method, in essence, is [3, 14]: the deposition would be performed from an activated gas phase, comprising a volatile carbon-containing compound and hydrogen, under subatmospheric pressure. In the temperature and pressure ranges under discussion, diamond is metastable; it is another carbon allotrope – graphite – that is stable there. The objective to be pursued by the activation of gas phase is two-fold: (1) to generate a sufficiently high concentration of active carbon-containing species that, when striking a heated substrate, decompose, thus producing carbon atoms; the latter form the diamond crystal lattice; and (2) to generate an agent that efficiently suppresses the deposition of non-diamond carbon, that is, graphite and amorphous carbon. (Notice that it is the simultaneous formation and growth of the non-diamond carbon, which blocks the substrate surface, rather than the metastability of diamond per se at the low pressure, that inhibits the deposition of diamond.) This agent is atomic hydrogen, which acts to "burn down" graphite, whereas diamond remains unharmed.

The principal methods of gas activation are thermal and electrical; much less common are chemical and photochemical activation. In the most commonly used thermal activation technique – the hot filament technique – a W or Ta wire is arranged in the immediate vicinity of the substrate to be coated by diamond (Fig. 1). The wire is heated until it reaches the temperature when H_2 molecules dissociate readily. The gas phase is a mixture of a carbon-containing gas (e.g. methane, acetone or methanol vapor), at a concentration of a few per cent, and hydrogen. Upon the contact of the gas with the activator surface, excited carbon-containing molecules and radicals are produced, in addition to the hydrogen atoms. They are transferred to the substrate surface, where deposition occurs. Table 2 gives an indication of the hot-filament deposition process parameters.

Various types of electric discharge (arc, glow discharge) underlie the electric activation; both dc and ac regimes (high-frequency, microwave, and pulse current) are used. Every activation method has its advantages and disadvantages. E.g., the arc discharge makes it possible to achieve very high deposition rates: tens and hundreds of microns per hour; in the plasma-assisted deposition, very homogeneous growth conditions are set over large substrate surface area, etc.

The substrate materials are: metals (W, Mo, Ti), silicon (e.g. mirror-polished wafers used in the production of semiconductor devices), glassy carbon, graphite [15], etc., depending on manufacturer or user preferences. Diamond nanocrystals are used as seed-crystals on the substrate surface to enhance the nucleation and make the film growth more uniform. The silicon substrate can be then etched off, and a free-standing diamond film is thus produced.

When a single crystal diamond (synthetic or natural) is the substrate, epitaxial growth occurs: the growing diamond replicates the substrate crystal lattice and turns to single crystal film. The film thickness usually comes to a few microns; however, films of 1 mm in thickness were reported. The diamond-coated area would achieve 10 cm in diameter by order; for industrial applications, much larger areas (e.g. 40 by 60 cm) are covered. Samples destined for the electrochemical measurements used to have dimensions ca. 1 by 1 cm.

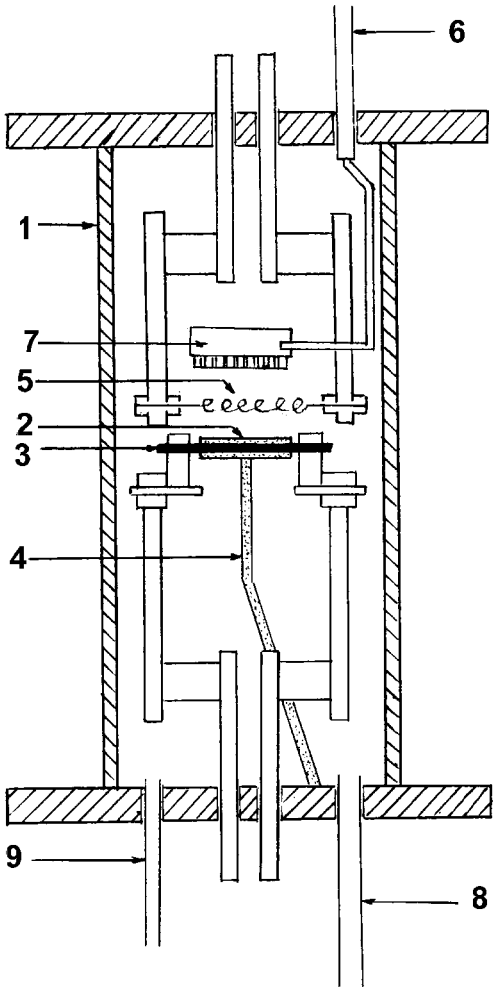

Fig. 1. Schematic diagram of hot-filament-assisted CVD-diamond growth system: (1) reactor chamber, (2) substrate, (3) substrate heater, (4) thermocouple, (5) tungsten filament, (6) source gas inlet, (7) gas diffuser, (8) to vacuum pump, (9) to pressure gage.

Table 2. Growth conditions of CVD-diamond (after Ref. [3]).

Main parameters	Typical conditions	Best films
Substrate temperature/°C	700–1000	950–1050
Total pressure/kPa	0.013–12	5.3–12
CH_4 content in gas phase/%	0.1–5.0	0.1–1.0
Gas flow/cm^3 min^{-1}	20–200	50–100
Filament temperature/°C	1800–2500	2000–2500

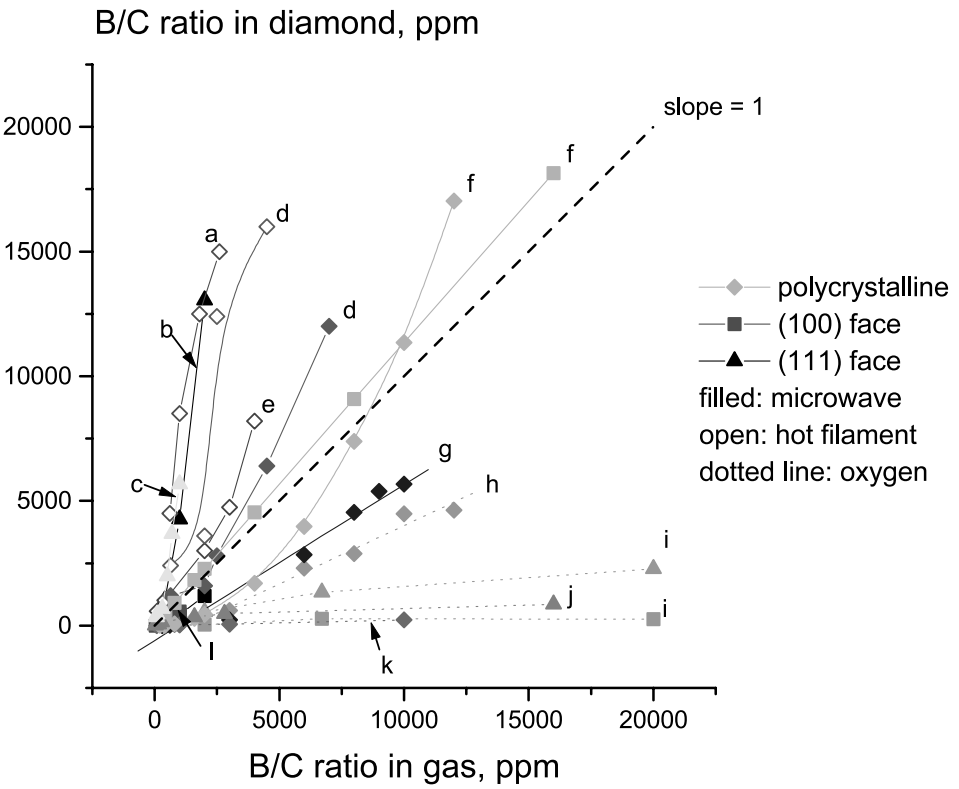

Fig. 2. Atomic ratio, B/C, in diamond vs. atomic ratio in gas phase from different sources: (a) H. Spicka et al., Diamond and Related Mater., 5, 383 (1996); (b) K. Ushizava et al., Ibid., 7, 1719 (1998); (c) B.-J. Lee et al., Ibid., 8, 251 (1999); (d) M. C. Polo et al., Thin Solid Films, 253, 136 (1994); (e) A. Argoitia, private communication; (f) E. Gheeraert et al., Carbon, 73, 107 (1999); (g) P. Gonon et al., J. Appl. Phys., 78, 7404 (1995); (h) A. Fujishima, private communication; (i) R. Samlenski et al., Diamond and Related Mater., 5, 947 (1996); (j) R. Locher et al., Ibid., 4, 678 (1995); (k) H. Kawarada et al., Phys. Rev. B, 47, 3633 (1993); (l) N. Fujimori et al., J. Appl. Phys., 29 (pt. 1), 824 (1990). Equal incorporation rates of B and C occur along the dashed line (slope = 1) [16].

As mentioned, to make diamond film conducting, it is doped with boron (usually in the course of growth). To this purpose, a volatile boron compound is added to the reactive gas mixture, e.g., trimethyl borate at a concentration of 10 to 10,000 ppm. Sometimes, a solid boron source is arranged near the activator; then, boron is transferred to the gas phase under the action of the activation. Data on the B/C ratio in the gas phase and in the films, taken from numerous literature sources, are compiled in Fig. 2 [16]. Despite the scatter in the results of different groups, some general conclusions can be drawn. First, for the particular growth method and fixed conditions, the boron concentration in diamond is proportional to that in the source gas. The proportionality coefficient varies within wide limits (a dashed line in Fig. 2 corresponds to the unit B/C ratio). In particular, the incorporation of boron is greater on {111} surfaces than on {100}. In hot-filament reactors, the boron incorporation is greater than in microwave reactors. Finally, the B incorporation appears much less

when oxygen is present in the source gas. Note that the dopant atoms can form clusters and even microdomains. Not only do the boron atoms therein appear to be electrically inactive and not to affect the film's conductance, but the microdomains, when exposed to the film surface, also can interfere with the electrochemical processes studied.

The diamond films' specific resistance (ρ) depends on the boron content and varies, e.g., from some 10^4 Ω cm at a boron concentration of 10^{18} cm^{-3} to a value of tenths and even thousandths of Ω cm for boron concentration as high as 10^{21} cm^{-3}. Correspondingly, diamond changes its nature, starting as a dielectric, then sequentially converting to a semiconductor, degenerate semiconductor, and finally a quasi-metal.

The boron ionization energy is 0.37 eV; it decreases with increasing B concentration [17] due to the atomic interaction and formation of a narrow band in the diamond bandgap. Because the cited value is much higher than the thermal energy kT (= 0.025 eV at 25 °C), the boron atoms are weakly ionized at room temperature; thus, the majority carrier (hole) concentration is 2 to 3 orders of magnitude lower than the dopant (boron) concentration. We note that, in addition to the intentionally added acceptor-dopant (boron), the CVD-diamond films contain an inevitable impurity of nitrogen; and nitrogen is a donor in the diamond crystal. The nitrogen ionization energy is as high as 1.7 eV; thus, nitrogen exerts no effect on the diamond conductivity at room temperature, as was mentioned. However, because of mutual compensation of the boron (acceptor) and nitrogen (donor) impurities, the free hole concentration in the compensated diamond is determined by the uncompensated acceptor concentration N_A–N_D, rather than the boron concentration.

Of particular interest are diamond films of highly dispersed surface; their study began recently. Two types of fabrication process were used in the preparation of such films [18]: (1) the oxygen plasma etching of CVD polycrystalline diamond films, using an anodic alumina mask (obtained by anodizing a perforated Al sheet) or a SiO_2 mask; and (2) synthesis of diamond cylindrical structures on top of "ordinary" diamond films using highly ordered porous alumina as a template (which is subsequently etched off). These techniques allow for producing nanohoneycomb diamond membranes for optoelectronic or electrochemical applications.

We conclude this section by noting that chemical (as well as physical) vapor deposition techniques are widely used for the growth of amorphous carbon (a-C) films [10]. In this material, no long-range order in the arrangement of C–C bonds occurs, hence, no actual crystal structure exists; however, short-range order exists. Depending on the deposition method, the amorphous carbon films are hydrogenated (a-C:H, approx. 30 at. % of H) or hydrogen-free. By convention the great variety of a-C:H types can be grouped to graphite-like and diamond-like carbon films. In the former, the sp^2-hybridization of carbon orbitals prevails, whereas in the latter, the sp^3-hybridization prevails. In line with this microstructure, the graphite-like carbon has a relatively narrow bandgap (<1 eV) and reasonable conductance. The bandgap of diamond-like carbon (DLC) is as wide as 2 to 4 eV; correspondingly, this material is much less conductive. In some properties, the DLC approaches the crystalline diamond (hence, its name) whereas in many others, it still is inferior to diamond. An electrochemical method of amorphous carbon growth was reported recently [19].

In addition to thin-film electrodes, compact diamond single crystals grown at high temperature and high pressure have become the object of electrochemical study in recent years. These so-called HTHP crystals can be obtained by crystallization from a carbon solution in a metal melt (e.g., based on the Ni–Fe–Mn system) at *p,T*-ranges that correspond to the conditions of thermodynamic stability of diamond. These crystals can be also doped with boron in the course of growth.

3 Crystal Structure and Principal Electrophysical Characteristics of CVD Diamond films

3.1 Crystal Structure

Polycrystalline films consist of diamond crystallites whose dimensions are ever increasing during film growth, in proportion to the film thickness, until they achieve a few microns in size. On such film surfaces, the crystallites' microfaces form a characteristic faceted morphology (Fig. 3). Of the three low-index faces – (100), (110), and (111) – the last is the most abundant. Looking at Fig. 3, one is inclined to think that the diamond surface has a great deal of inhomogeneity. In addition to the faceted morphology, other types of surface morphology also occur.

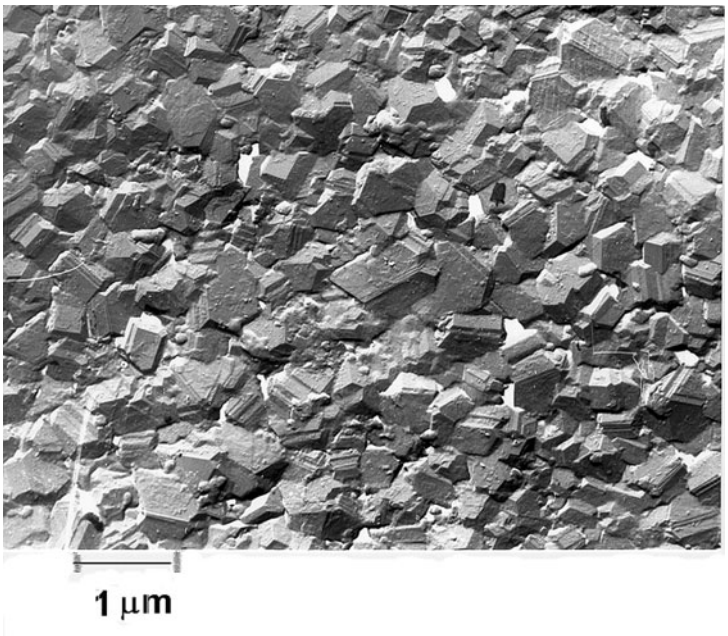

Fig. 3. A SEM image of polycrystalline diamond film surface with faceted morphology.

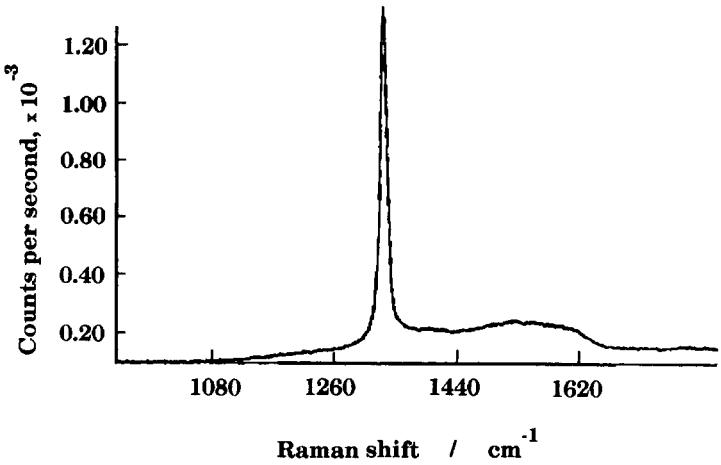

Fig. 4. A Raman spectrum for a polycrystalline diamond film.

To evaluate the crystallinity of the films, Raman spectroscopy is used. A typical Raman spectrum is presented in Fig. 4. Of the crystalline diamond, a narrow peak at a frequency of 1332 cm^{-1} is characteristic, which is caused by the first-order phonon scattering by the crystal lattice. The non-diamond carbon is represented in the spectrum by two diffuse bands at ca. 1350 and 1550 cm^{-1}. When comparing the peaks' height, one should keep in mind that the Raman signal is 50 times more sensitive to the non-diamond carbon than to the crystalline diamond [20]. In the high-quality diamond films used as electrodes, the non-diamond carbon component rarely exceeds 1%. Raman spectroscopy data have been corroborated by the independent impedance spectroscopy measurements (see below). According to [21], the inner layer of a diamond film is enriched with the admixture of non-diamond carbon as compared to its outer layer.

It turned out that the admixture of sp^2-carbon exerts a decisive effect on the "electrode quality" of diamond films. And yet, modern physical and optical experimental techniques, like Raman and Auger spectroscopy, AFM, etc., failed in the elucidation of subtle effects exerted by the admixture of non-diamond carbon on the behavior of polycrystalline diamond films; it is the electrochemical measurements that give plausible information [22] (see Section 6.3).

The non-diamond carbon phase in polycrystalline diamond films (often referred to as graphite, although this conclusion is far from accurate [23]) is first and foremost the disordered carbon in the intercrystallite boundaries. Their exposure to the film surface can be visualized by using a high-resolution SEM techniques [24]; the intercrystallite boundaries' thickness comes to a few nanometers. In addition to the intercrystallite boundaries, various defects in the diamond crystal lattice contribute to the non-diamond carbon phase, not to mention a thin (a few nanometers in thickness) amorphous carbon layer on top of diamond. This layer would form during the latest, poorly controlled stage of the diamond deposition process, when the gas phase activation has ceased. The non-diamond layer affects the diamond surface conduc-

tance markedly, increasing the surface conductance of dielectric films, whereas that of the doped (conducting) films often decreases. To remove the amorphous carbon surface layer, diamond samples would be heated in air at 520 °C for some 20 min or exposed to boiled concentrated $HClO_4$, $CrO_3 + H_2SO_4$ mixture, or other strong oxidants [8]; the non-diamond carbon is then oxidized to CO_2.

3.2 Film Conductance

Diamond film resistivities are determined by both free charge carrier concentration and mobility. Polycrystalline films have a moderate hole mobility (as low as 1 cm^2 V^{-1} s^{-1} [25–27]) that is much lower than that given in Table 1 for single crystal diamond. However, in high-quality films the mobility comes to dozens and hundreds of cm^2 V^{-1} s^{-1} [28, 29]. We notice that, due to lattice perturbation, doping with boron can adversely affect hole mobility. In single crystal films, the mobility is 1 to 2 orders higher than in the polycrystalline films grown under comparable conditions [24]. On the contrary, in amorphous DLC films the mobility is several orders lower than in crystalline diamond [25].

To elucidate the conductance nature of a nonhomogeneous medium, polycrystalline diamond film being an example, an impedance spectroscopy method was used [30]. A dot of silver-based paste was put on the film surface, thus making an ohmic contact to diamond; the W-substrate served the second ohmic contact. (A thin tungsten carbide interlayer, formed on the tungsten substrate surface at an initial stage of the CVD process, in all probability affords both a good adhesion of diamond film to the substrate and the nonrectifying nature of the W/diamond junction.) The real and imaginary components of impedance of the solid-state structure were measured over a wide frequency range. The complex-plane plot of the impedance spectrum is a nearly perfect semicircle (Fig. 5). Such a plot can be explained with use of the equivalent circuit shown in the figure. The physical nature of its elements was elucidated by using a simple model of the nonhomogeneous medium, presented on Fig. 6 (bottom). The film is composed of reasonably conducting crystallites, separated by poorly conducting intercrystallite boundaries. The boundaries form a continuous matrix; the crystallites, uniform in size, form a regular structure; the total volume of the boundary-phase matrix is a small portion of the film volume. The model undoubtedly is an oversimplification because in a real film the crystallites are distributed in size; moreover, some columnar crystallites penetrate throughout the film. Nevertheless, the model can be applied to moderately doped diamond films whose crystallites are much better conducting than the intercrystallite boundaries consisting of amorphous carbon, which have a capacitive nature. By using the effective-medium theory developed [31, 32] for the quantitative description of the model, the resistance R_1 was related to the resistivity of the diamond crystallite bulk, whereas the resistance R_0 and capacitance C_0, to the properties of the amorphous-carbon intercrystallite boundaries. The summary, thickness of the intercrystallite boundaries can be estimated from the C_0 value; hence, the volume portion of the boundary phase (the amorphous carbon) was estimated to be a few per cent [30], in reasonable agreement with Raman spectroscopy data. In the frequency dependence

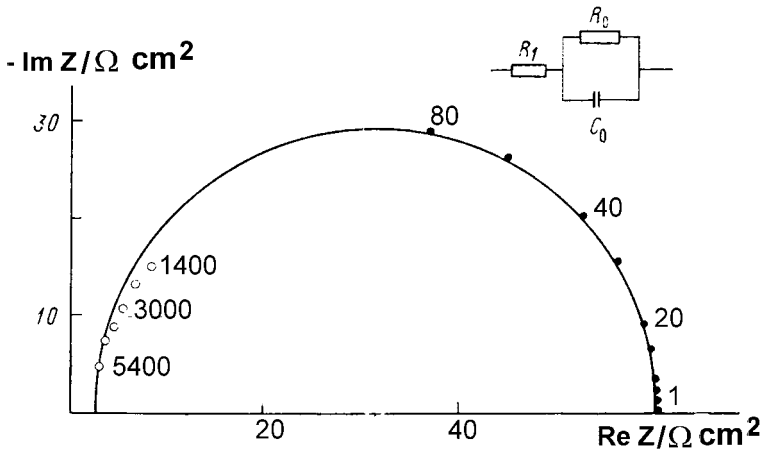

Fig. 5. Complex-plane plot of impedance spectrum for a polycrystalline diamond film between two ohmic contacts. Frequency/kHz shown on the figure. Solid circles: data obtained with ac bridge. Open circles: data obtained with phase-sensitive analyzer. Top: equivalent circuit [30].

of the film active resistance (Fig. 6, top), the high-frequency limit is equal to R_1, whereas the low-frequency limit, to the sum $R_1 + R_0$. From these quantities, the conductivities of the crystallite bulk and intercrystallite boundaries were estimated as 10^{-4} and 10^{-7} Ω^{-1} cm^{-1}, respectively [30].

Similar conclusions on the character of conductance in the polycrystalline diamond films were derived in [33]. The resistive intercrystallite boundaries can involve nonlinear resistance in polycrystalline diamond films moderately doped with boron [34]. Later, more sophisticated analysis [35–37] of the frequency dependence of impedance of polycrystalline diamond films resulted in a conclusion that at higher temperatures, in addition to the aforementioned electric conductance caused by the motion of free holes in the valence band, a second component of conductance manifests itself. The second component is due to the hopping of charge carriers between local traps possibly associated with the intercrystallite boundaries.

4 Synthetic Diamond Thin-Film Electrodes: Their Preliminary Characterization

4.1 Background Current vs. Potential Characteristics

Of primary importance in evaluating new electrode materials to be used in electrolysis, electroanalysis, electrochemical sensors, etc., are their corrosion stability, reproducibility of characteristics, value of background current, and the potential window in which the background current remains low and thus does not interfere with the electrode characteristics. Diamond meets all these criteria perfectly.

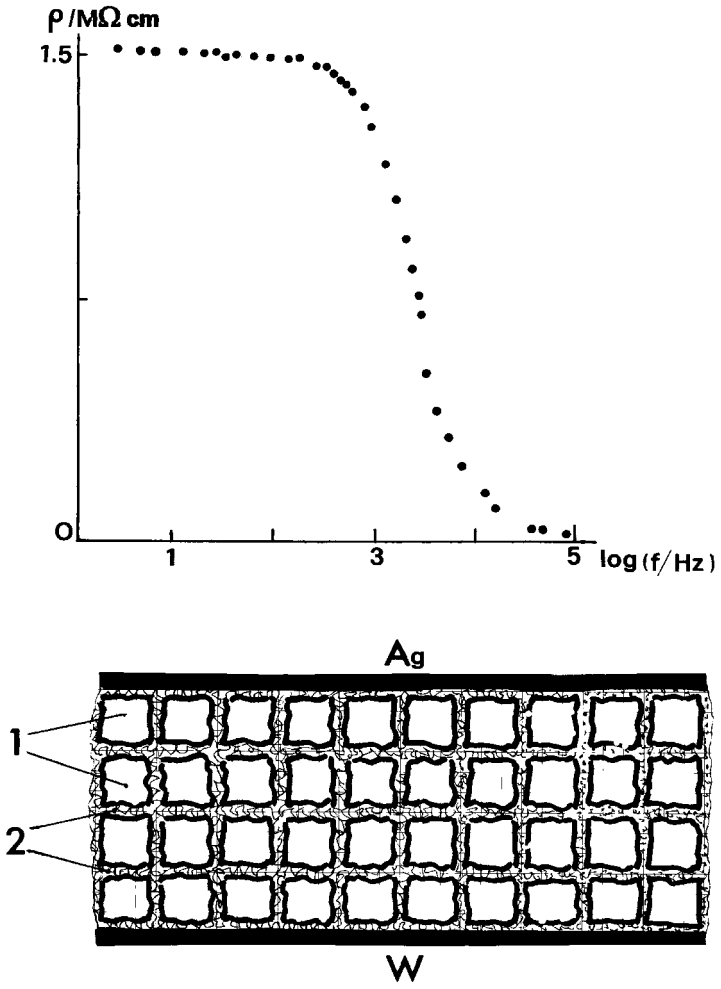

Fig. 6. Top: frequency dependence of the polycrystalline film active resistivity. Bottom: model of the non-homogeneous film between two ohmic contacts; (1) diamond crystallites; (2) intercrystallite boundaries [30].

It goes without saying that it is required of the films destined as electrodes that they have reasonable conductance, as low an sp^2-carbon content as possible, and no pinholes. To meet the last condition, the film must be at least few μm in thickness.

We first discuss current-potential curves in supporting electrolyte solutions [38, 39] as a base characteristic of diamond electrodes. It is these curves that are the background against which the kinetic, impedance, photoelectrochemical, electro-analytical properties of diamond electrodes manifest themselves.

In Fig. 7 we present typical background current curves taken in a supporting electrolyte (0.5 M H_2SO_4) solution on polycrystalline diamond thin-film electrodes, as well as on traditional – Pt and highly oriented pyrographite (HOPG) – electrodes.

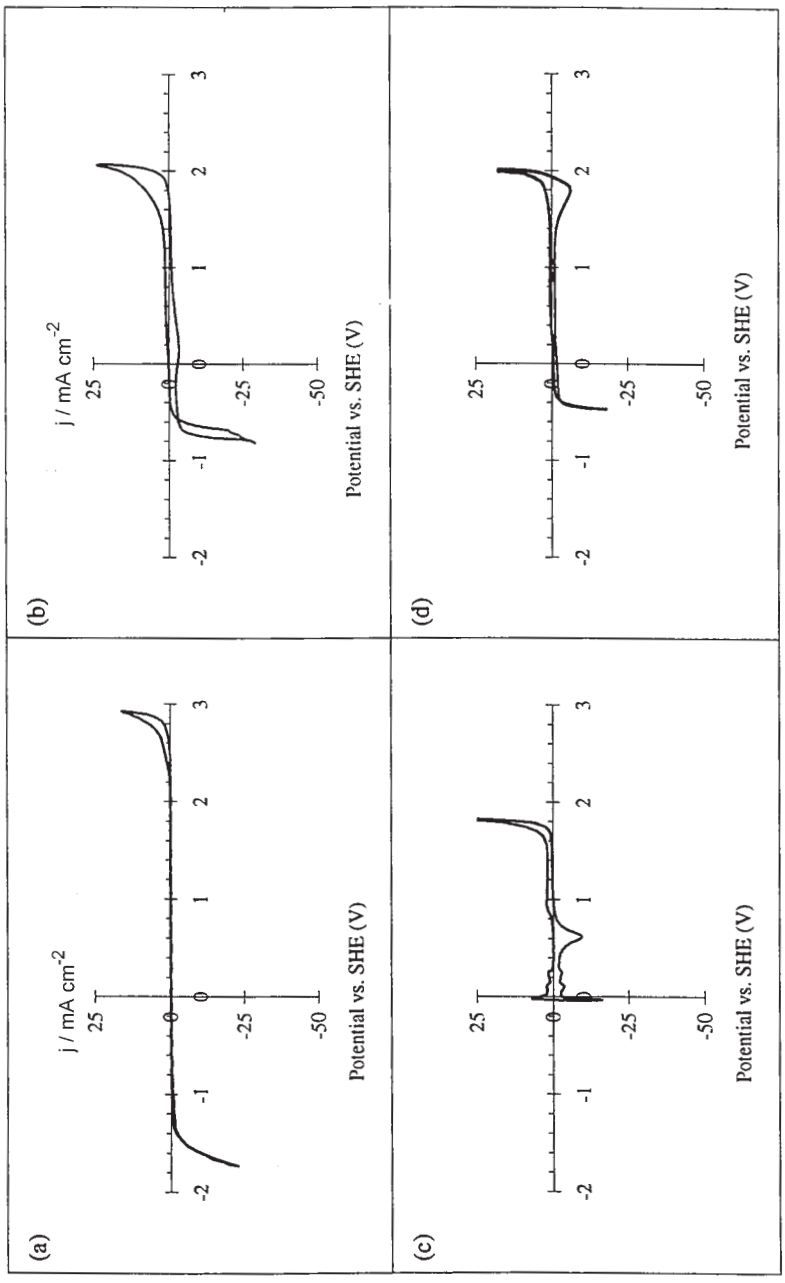

Fig. 7. Cyclic voltammograms of background current for (a) and (b) polycrystalline diamond, (c) platinum, and (d) highly oriented pyrolytic graphite (basal plane) in 0.5 M H_2SO_4: (a) high-quality film; (b) low-quality film [38]. Reproduced by permission of The Electrochemical Society, Inc.

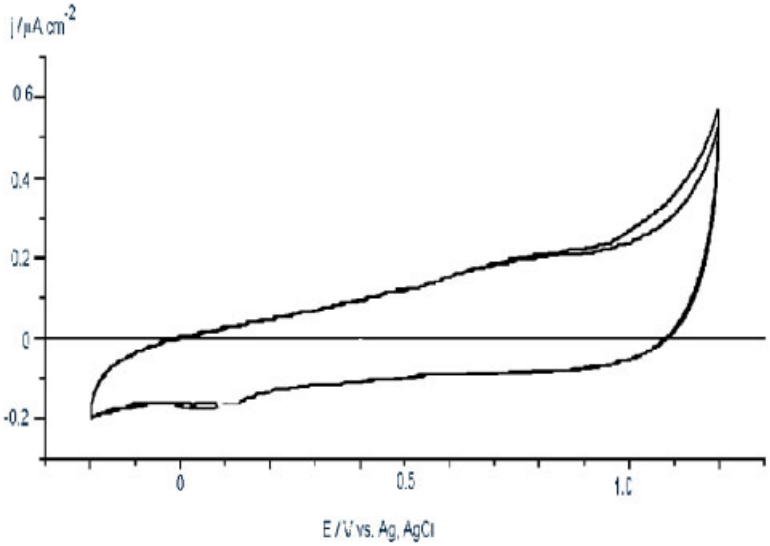

Fig. 8. Cyclic voltammogram of background current on a single-crystal diamond film in 0.1 M H_2SO_4 [40].

The potentiodynamic curves were taken in a cyclic regime. According to Angus et al. [38], diamond films used as electrodes can be classified as high-quality films and low-quality films, depending on the broadness of so-called ideal polarizability range, or potential window, corresponding to a small background current. For a high-quality electrode, a broad potential range (approximately from −1.25 to +2.3 V vs. SHE; see Fig. 7a) was observed. Thus the potential window exceeds 3 V in the mA cm^{-2} range, whereas it is at least 1.5 V in the μA cm^{-2} range (Fig. 8), at a low (few mV s^{-1}) potential scan rate [40]. For low-quality electrodes (Fig. 7b), the potential window was significantly smaller (from −0.6 to +1.7 V vs. SHE), resembling that for a HOPG electrode (Fig. 7d); in addition, a significant hysteresis was observed, which obviously lowers the potentialities of these films as electrodes. The physical meaning of the ''high-quality film'' concept has not been unambiguously specified [38]. In general such films were deposited at a lower content of the carbon-containing gas (less than 1% of methane) in the source gas, whereas the low-quality films were deposited from a 4%-methane-containing gas mixture.

The advantage of diamond electrodes – a broad potential window and low background current – is best demonstrated in comparison with other materials commonly used as electrodes, e.g. platinum, glassy carbon, graphite, etc. In addition to Fig. 7, such a comparison is shown in Fig. 9 for diamond and glassy carbon; we see that the background current for diamond is an order lower [41].

The coin has its reverse, however. The broadening of the potential window that is often bordered by the solvent electrochemical decomposition potentials (e.g. cathodic hydrogen evolution and anodic oxygen evolution from water) is due to an increase in reactions overvoltage. This may be caused by a diamond's lower electrochemical activity, as compared with the glassy carbon and like electrode materials. On the whole, this conclusion is corroborated by the kinetics studies on diamond electrodes

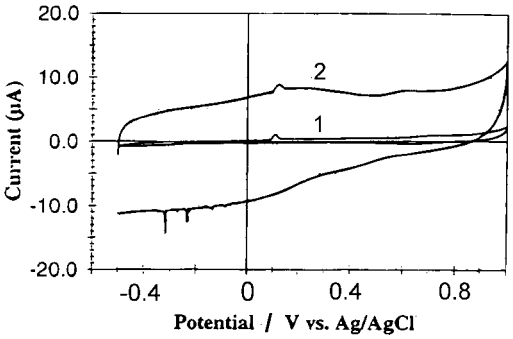

Fig. 9. Cyclic voltammograms of background current for (1) polycrystalline diamond and (2) glassy carbon in 0.1 M KCl. Reprinted with permission from [41]. Copyright (1996) American Chemical Society.

(see Section 6.1, below). Thus, in evaluating the actual electrode quality of diamond for a particular application, one has to compromise on various requirements to the electrode material, which often are mutually contradictory. Nevertheless, sometimes diamond is still superior to traditional electrode materials: in particular, the rate of redox reactions in the $Fe(CN)_6^{4-/3-}$ and $IrCl_6^{2-/3-}$ systems appeared practically equal for diamond and glassy carbon electrodes [38], whereas the background currents differ significantly (see Fig. 9).

The as-grown diamond film surfaces are hydrogen-terminated (owing to the procedure of deposition from activated hydrogen atmosphere, described in Section 2), like the films subjected to the hydrogen plasma treatment [42]. For this reason, films are hydrophobic. Because the dangling bonds on the surface are terminated by hydrogen atoms, the latter inhibit adsorption sites; thus, the surface behaves as if passivated. On the contrary, an oxidized surface is coated with oxygen-containing groups [43] and, hence, is hydrophilic (note that the HTHP crystal surface is always oxidized because strong oxidants would be used in etching off the solidified metal after completion of the crystallization process; see Section 2). These two types of diamond surfaces can be realized electrochemically, namely, by the cathodic or anodic polarization in aqueous electrolyte solutions [44]. The particular properties of oxidized diamond surfaces will be discussed at greater length in Sections 5.1 and 6.2.

4.2 Corrosion Resistance and Electrochemical Etching

Diamond demonstrates extraordinary stability against corrosion in aggressive media and at extreme potentials. Swain [45, 46] showed that a long-term potential cycling in an aggressive 1 M HNO_3 + 0.1 M HF solution, ranging between the potentials of cathodic hydrogen evolution and anodic oxygen evolution, has no effect on diamond surface morphology (according to SEM studies) and the ratio of diamond and non-diamond carbon phases on the electrode surface (as shown by Raman spectra). By comparison, glassy carbon and pyrographite electrodes are prone to severe corrosion under the same conditions. Similar tests were conducted in 1 M HNO_3 + 2 M NaCl solution at the potential of anodic chlorine evolution [47]. Here again, neither the diamond surface morphology, nor the surface impurity content, was subject to change, as the XPS data show (see also Ref. 48).

And yet, a long-term potential cycling in 15% KOH solution resulted in a corrosion damage of diamond surface. Generally, the extent to which diamond is affected depends on its growth conditions; however, the nature of this dependence has not been elucidated. The non-diamond carbon of the intercrystallite boundaries appeared less stable against damage [49]; therefore, corrosion leads to formation of a microporous diamond layer.

The long-term electrode polarization may, on occasion, result in emergence of pinholes in diamond film. Then, the electrolyte penetrates to a substrate [50–53]. In all probability, the pinholes were due to some defects formed during films growth. Occasionally, diamond film electrodes have inactive spots caused by non-uniform doping, or by local peeling-off from the conducting substrate [54]. However, high-quality films stand the corrosion perfectly; moreover, diamond coatings reliably protect the substrate metal (Mo) [55, 56].

It is well known that preparation of semiconductor surfaces involves chemical or electrochemical etching [6]. In particular, the removal of a damaged layer (formed during mechanical processing) and surface impurities and defects requires etching. Unfortunately, with diamond, unlike many other semiconductor materials, methods of etching are very scarce. And yet, some electrochemical techniques were developed for renewal of diamond surface [57]. To this purpose, diamond was first exposed to ion bombardment that resulted in an amorphization of a thin surface layer (see Introduction). Subsequently, the sample was arranged in an electrochemical cell as a bipolar electrode (in a non-contact mode) and a 50 V-bias was applied between anode and cathode of the cell, until the amorphized zone had been etched off, thus exposing the underlying material. Other versions of the ''bipolar surface treatment'' are described in Refs. 58, 59.

To conclude with the primary electrode characteristics, we describe briefly the DLC electrodes. The data are scarce and partly contradictory, probably due to the differences in film preparation methods. According to Howe [60], even films as thin as 50 nm are quite stable against corrosion. However, in later works [61, 62] such thin films turned permeable for electrolytes. The penetration of the electrolyte to a substrate metal resulted in its corrosion and, ultimately, in film peeling. Thicker films (0.1 to 1 μm) were less subjected to damage. The current-potential curves in supporting electrolytes resemble those for crystalline diamond electrodes (see Figs. 7, 8); the potential window is narrower, however [63]. Fluorination of a-C:H enhances corrosion resistance of the films significantly [64].

5 Impedance Spectroscopy and the Semiconductor Properties of Diamond Electrodes

5.1 Linear Impedance. The Equivalent Circuit

Measurements of the frequency characteristics of electrochemical systems provide insight into the charge distribution at interfaces, as well as the kinetics of the charge

transfer processes thereon. In linear impedance measurements, a harmonic electric signal of frequency f would be imposed on electrochemical cell. By analyzing the system's response spectrum, a real component ReZ and imaginary component ImZ of electrode impedance Z can be obtained.

Two features manifest themselves in the impedance behavior of diamond electrodes, namely, the effects of semiconductor nature of diamond (with moderately doped films) and a specific type of frequency dependence of impedance, which is characteristic of a great majority of films.

Generally, the impedance of a thin-film electrode can be modeled by an equivalent circuit shown in Fig. 10a. It consists of two RC couples, one of which relates to the film proper, and the other to the diamond/electrolyte solution interface. (In the general case, one more RC couple must be added to the equivalent circuits of Fig. 10, which relates to the Helmholtz layer at the interface; however, for semiconductor electrodes the Helmholtz capacitance is typically orders of magnitude higher than the other capacitances and can be neglected [6]). In the equivalent circuit, R_s is the ohmic resistance of the diamond film (for simplicity, assume the film to be homogeneous, otherwise the circuit shown in Fig. 5 (top) should be substituted for R_s); C_g is the film geometrical capacitance that can be calculated by substituting the film thickness d and the permittivity of diamond $\varepsilon = 5.7$ into the formula of a plane-plate capacitor; C_{sc} is the differential capacitance of the space charge region at the diamond/electrolyte solution interface; and R_F is the differential resistance associated with charge transfer at the interface (often called the faradaic resistance).

The geometrical capacitance C_g is of the order of 10^{-10} F cm^{-2} for the majority of films studied, whose thickness is 1 μm by order; the corresponding impedance would be an order higher than the film resistance R_s (with exception of very low-doped films) and can be neglected. We then obtain a simpler three-element circuit (Fig. 10b) often called the Randles' circuit [65]. An essential assumption is that all elements of the circuits in Figs. 10a and b are frequency-independent.

Occasionally, the impedance spectra of diamond electrodes are well described by the Randles' equivalent circuit with a frequency-independent capacitance (in the 1 to 10^5 Hz range) [66]. Shown in Fig. 11 is the potential dependence of the reciprocal of capacitance squared, a well-known Mott–Schottky plot. Physically, the plot reflects the potential dependence of the space charge region thickness in a semiconductor [6]. The intercept on the potential axis is the flat-band potential E_{fb}; whereas the slope of the line gives the uncompensated acceptor concentration $N_A - N_D$; in what follows, we shall for brevity denote it as N_A:

$$N_A = \frac{-2}{e\varepsilon_0\varepsilon}\left[d(C^{-2})/dE\right]^{-1} \tag{1}$$

where ε and ε_0 are the permittivity of diamond and of free space, respectively, and e is the electron charge. In deriving the formula, it was assumed that (a) during the electrode polarization, the entire interfacial potential drop is located in the space charge region (and not e.g. in the Helmholtz layer); (b) no deep acceptor ionization occurs; (c) the capacitance C is the space charge region capacitance proper and does

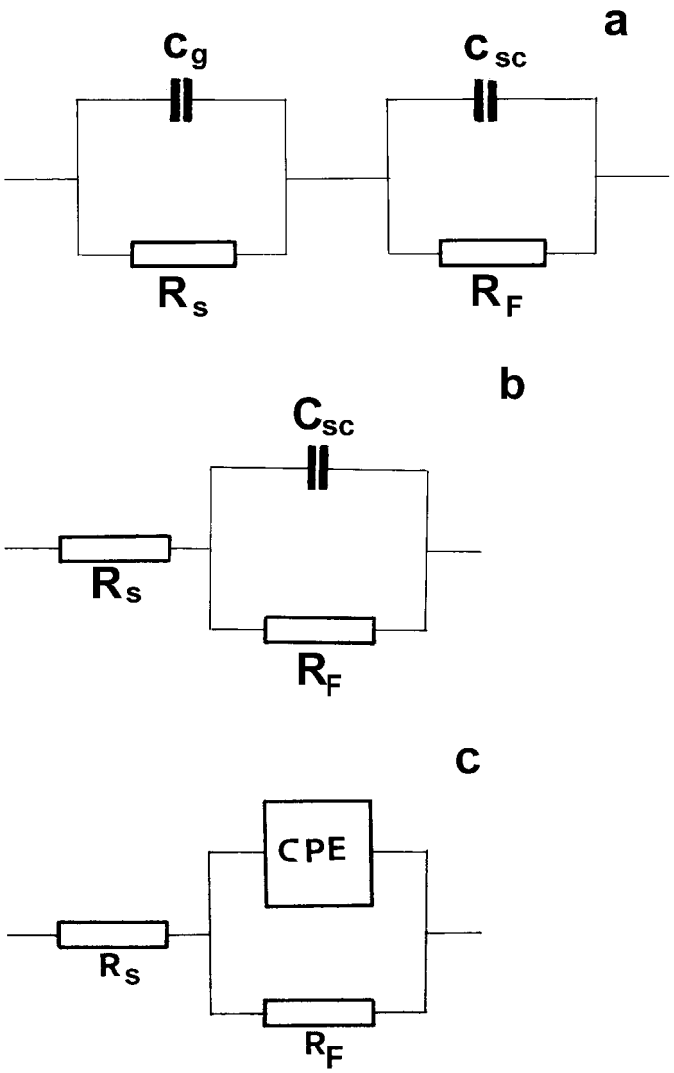

Fig. 10. Equivalent circuits of electrode: (a) general circuit of a thin-film electrode; (b) the Randles' circuit; and (c) circuit with a constant phase element.

not include e.g. the surface-states' capacitance, adsorption capacitance, etc. For the film under discussion (Fig. 11), $N_A = 3.1\ 10^{18}$ cm^{-3} [66].

In the above analysis, we used the concept of space charge layer, to be more precise, a depletion layer that would form in a doped, wide-gap semiconductor contacting another phase (a metal, an electrolyte solution, or vacuum). The polycrystalline diamond/metal junctions (where metal is Au, Pt, Pd, etc.) often show rectifying properties [67, 68]; and their capacitance characteristics resemble those of a diamond/electrolyte solution junction.

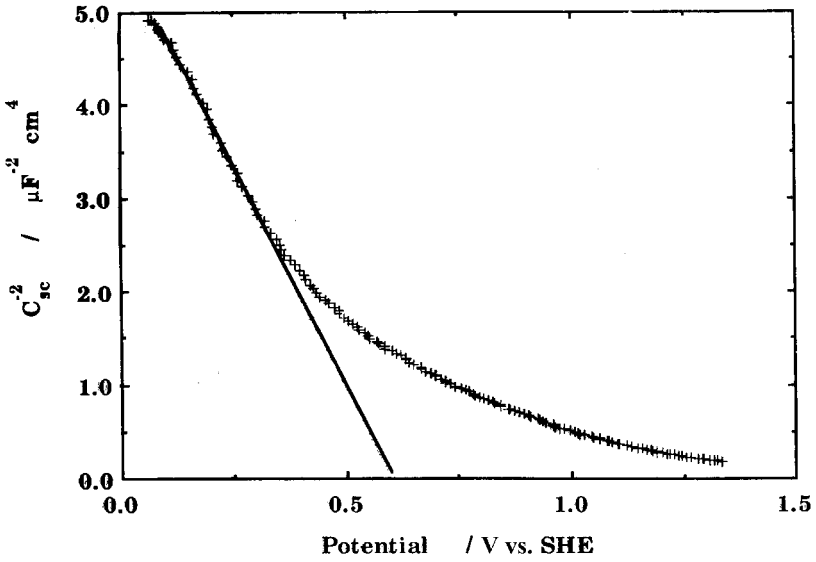

Fig. 11. Mott–Schottky plot for a polycrystalline diamond electrode with frequency-independent capacitance in 0.5 M H_2SO_4. Solid line shows a linear fitting [66]. Reproduced by permission of The Electrochemical Society, Inc.

The above-described situation is but an exception rather than the rule. Generally, the diamond electrode capacitance is frequency-dependent. In Fig. 12 we show a typical complex-plane plot of impedance for a single-crystal diamond electrode [69]. At lower frequencies, the plot turns curved (Fig. 12a), due to a finite faradaic resistance R_F in the electrode's equivalent circuit (Fig. 10). And at an anodic or cathodic polarization, where R_F falls down, the curvature is still enhanced. At higher frequencies (1 to 100 kHz), the plot is a non-vertical line not crossing the origin (Fig. 12b). Complex-plane plots of this shape were often obtained with diamond electrodes [70–73].

The characteristic frequency dependence shown in Fig. 12b implies the presence of a so-called constant phase element (CPE) in the electrode's equivalent circuit. The CPE impedance equals to [65]

$$Z_{\mathrm{CPE}} = \sigma^1 (i\omega)^{-\mathbf{a}}, \tag{2}$$

where $i = (-1)^{1/2}$, $\omega = 2\pi f$ is the ac angular frequency, the power **a** determines the character of frequency dependence, and the quantity σ is expressed in $F^{\mathbf{a}}\ \Omega^{\mathbf{a}-1}\ cm^{-2}$ units. To analyze the impedance spectra, the equivalent circuit presented in Fig. 10c was used; it is derived from the Fig. 10b circuit by substituting a CPE for the frequency-independent capacitance C_{sc}. The equivalent circuit elements would be calculated by minimization of the root-mean-square deviation of the measured impedance modulus from that calculated for the equivalent circuit, e.g. by using software described in [74].

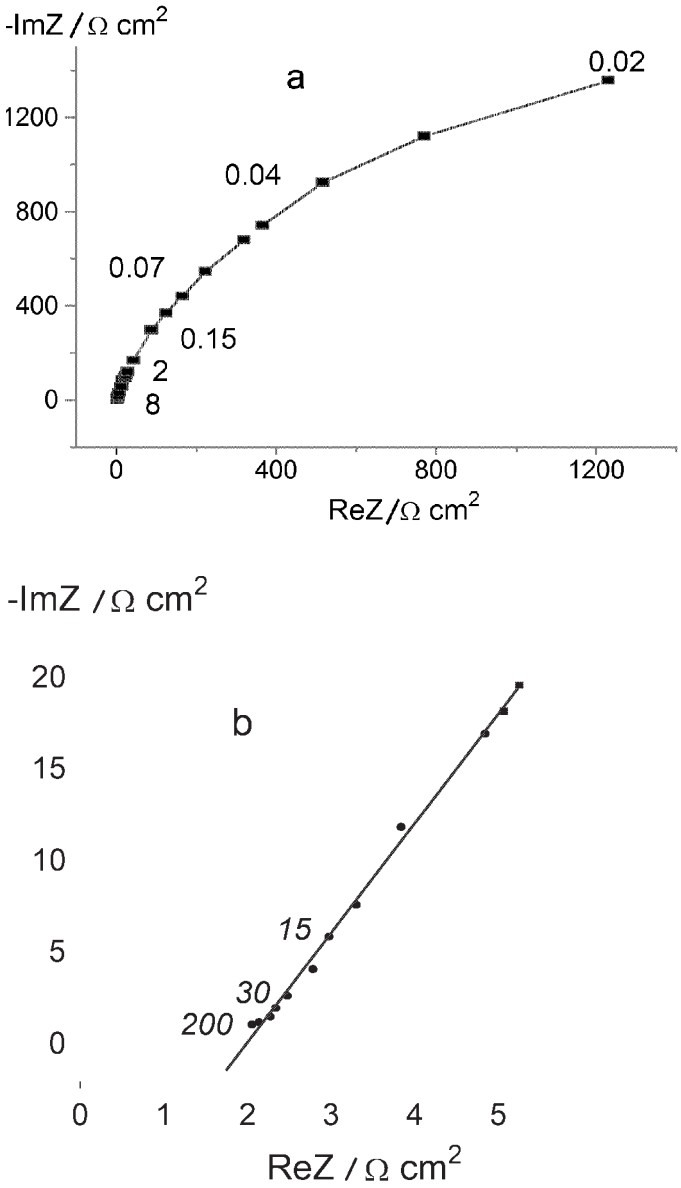

Fig. 12. (a) Complex-plane plot of impedance spectrum for a single-crystal diamond thin-film electrode, taken in 0.5 M H_2SO_4 at open-circuit potential; (b) its high-frequency portion. Frequency/kHz shown on the figure [69].

Typical values of σ and **a**, as well as the faradaic resistance R_F, series resistance R_s (and the film resistivity ρ calculated thereby, assuming that the electrolyte resistance can be neglected) are presented in Table 3 for polycrystalline and single-crystal diamond electrodes and a DLC electrode [69–77]. By comparing the impedance

Table 3. Comparative impedance characteristics of diamond electrodes (determined from impedance spectra taken at open-circuit potential in 0.5 M H_2SO_4 solution) [69, 75–77].

Substrate; film thickness / μm	**a**	$R_s/\Omega\ cm^2$	σ [a]	ρ/Ω cm	$R_F/\Omega\ cm^2$
Polycrystalline films					
W / 2.4	0.92	1.5	1.5	$0.7 \cdot 10^4$	$3 \cdot 10^5$
Si / 3	0.95	0.6	1–2	$0.2 \cdot 10^4$	$3 \cdot 10^4$
Single-crystal film					
Synthetic single crystal/≅10	0.96	32	2.7	0.1[b]	10^7
HTHP single crystals					
–	0.92	2.8	2.5	30	10^6
–	0.93	56	0.5	560	$5 \cdot 10^6$
Amorphous, diamond-like carbon film					
Glassy carbon / 0.07	0.9	–	0.05	$0.8 \cdot 10^5$	10^6

[a] σ expressed in the $\mu F^a\ \Omega^{a-1}\ cm^{-2}$ units.
[b] Resistivity measured by four-point probe technique.

parameters for single-crystal and polycrystalline diamond thin-film electrodes, we conclude that these are practically indistinguishable both qualitatively (having the same equivalent circuit that contains a CPE) and quantitatively (by the typical values of parameters **a**, σ, and R_F). Indeed, they all have **a** equal to 0.9 to 1, $\sigma \sim 1\ \mu\ F^{\mathbf{a}}\ \Omega^{\mathbf{a}-1}\ cm^{-2}$, and $R_F \sim 10^4$ to $10^5\ \Omega\ cm^2$, as measured at a steady-state potential in the supporting electrolyte. (Still higher R_F values $\sim 10^8\ \Omega\ cm^2$ were reported in Refs. [52, 53].) Should one assume that the measured integral impedance parameters characterize the electrical double layer structure at diamond electrodes, one has to conclude that this structure is almost identical for polycrystalline and single-crystal samples. (The small distinctions observed do not go beyond the limits of a scatter, which is probably caused by the difference in the level of boron doping or different surface conditions.) Moreover, the double-layer structure on electrodes of crystalline diamond and wide-bandgap diamond-like carbon is similar, on the whole.

The rather high values of the faradaic resistance R_F are due to the above-mentioned low background currents and negligible corrosion rate of diamond in aqueous solutions. Relatively high σ values, as compared with other semiconductor electrodes [6], reflect the higher doping level of diamond films: the acceptor concentration N_A would be no less than $10^{18}\ cm^{-3}$.

It goes without saying that the frequency dependence of capacitance, which follows from the complex-plane plots of the type shown in Fig. 12, manifests itself in a frequency-dependent slope of Mott–Schottky plots (Fig. 13) [78]. The complications in calculating N_A thus involved will be discussed at length in Section 5.3 below.

Here it is worth noting that the flat-band potential (E_{fb}) values reported by dif-

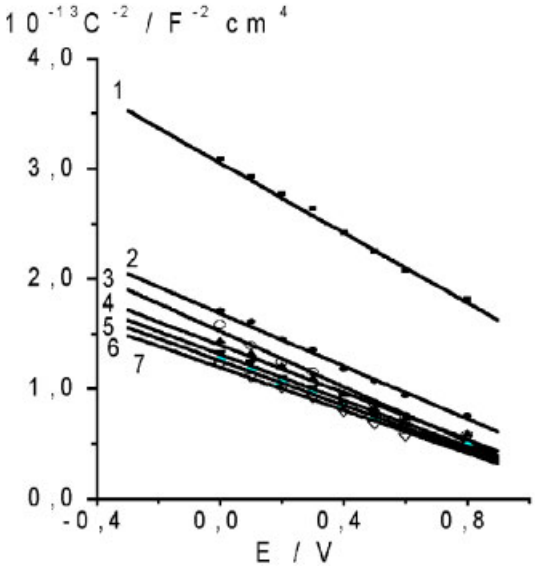

Fig. 13. Mott–Schottky plot for a single-crystal thin-film electrode in 0.5 M H_2SO_4. Experimental curves, frequency/Hz: (1) 21,544, (2) 10,000, (4) 4642, (5) 2154, (6) 1000, (7) 215; (3) calculated curve for C_{calc} (discussed in section 5.3, below). Potential vs. Ag/AgCl electrode [78].

ferent authors fall within the range of 0.5 V vs. SCE [66] to 1.2 V vs. SCE [69]. The scatter of data might be explained, at least in part, by a different state of oxidation of diamond surface, resulting from the electrodes' pretreatment. It has been known [6] that anodic oxidation of a variety of semiconductor materials results in a positive shift of their flat-band potential; cathodic reduction, in a negative shift. This shift is to a large extent due to changes in the dipole potential drop across the monolayer of adsorbed oxygen on the electrodes' surfaces.

We now continue to refine the equivalent circuit for diamond electrodes. One might expect this circuit to be synthesized from the two circuits shown in Figs. 10b and c. In particular, as suggested e.g. in [79] for InP semiconductor electrode, it could contain both the frequency-independent capacitance C_{sc} of the space charge region and the CPE that specifies the frequency dependence of the electrode response to a perturbing signal (whatever might be the cause of this dependence, see Section 5.3). To separate C_{sc} and CPE, one has to extrapolate the measured summary capacitance C to an infinite frequency. Indeed, at $f = \infty$ the capacitive component of CPE vanishes [see Eq. (2)], thus the extrapolation leaves behind the capacitance C_{sc}. The extrapolation is shown in Fig. 14 [80]; to linearize the plot for $\mathbf{a} = 0.7$, the coordinates C vs. $f^{-0.3}$ were used [compare Eq. (2)]. The extrapolated lines turned to cross the origin; hence, $C_{sc} = 0$. Thus, the electrode equivalent circuit does not contain any frequency-independent capacitance that would describe the properties of space charge region in diamond. This means that the CPE proper, with its characteristic potential dependence, relates to the space charge region. We shall return to this point in Section 5.3 below.

Of special interest is impedance of nanoporous honeycomb diamond electrodes [81] whose fabrication was briefly described in Section 2. By oxygen-plasma etching, an ordered structure of vertical pores (60 to 80 nm in diameter, 500 nm deep) was

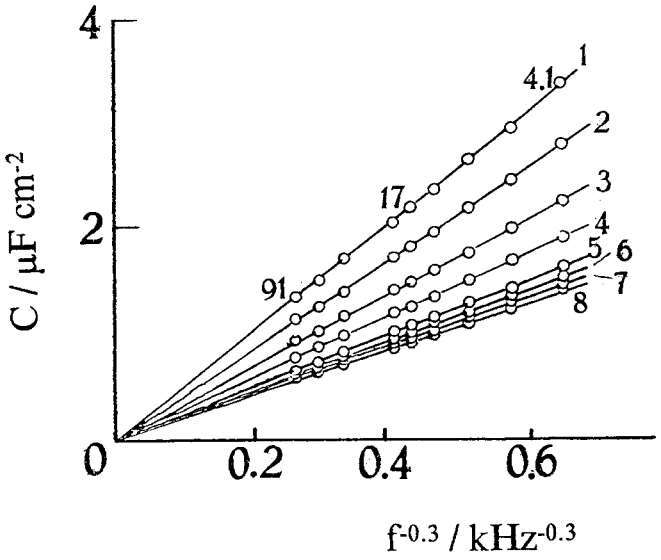

Fig. 14. Dependence of measured capacitance of a polycrystalline film on frequency to the power of −3. Potential/V: (1) 0.40, (2) 0.35, (3) 0.30, (4) 0.25, (5) 0.20, (6) 0.15, (7) 0.10, (8) 0.05. Frequency/kHz shown on the figure. Reprinted from [80]. Copyright (1996), with permission from Elsevier Science.

produced in polycrystalline films (Fig. 15). Such electrodes show wide potential window (~2.5 V), like films with as grown surface; however the background current is 20-fold higher. Their capacitance is as large as 2000 μF cm^{-2} (geometric area), due to the very high roughness factor. The frequency spectrum can be described by an equivalent circuit containing a transmission line reflecting the surface capacitance and the distributed electrolyte-in-pores resistance. At low frequencies, **a** = 0.5, which

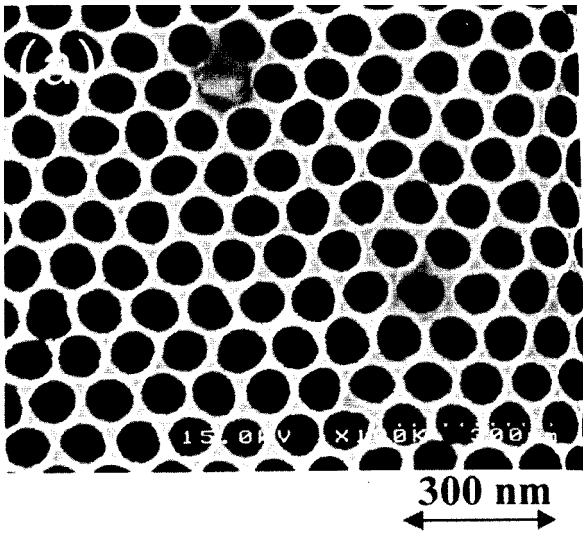

Fig. 15. SEM image of a nano-honeycomb diamond electrode [81]. Reproduced by permission of The Electrochemical Society, Inc.

is characteristic of porous electrodes [82]. Owing to their very high specific capacitance, these structures are promising candidates for supercapacitors.

To conclude, we notice that diamond crystals grown at a high temperature and high pressure (the HTHP technology) also were recently used as electrodes [76, 77]. Their impedance characteristics are similar to those of the CVD thin-film electrodes discussed above (see Table 3).

5.2 Nonlinear Impedance

In studying a system by a nonlinear impedance method, use is made of the system's nonlinear characteristics. A variant of the nonlinear impedance method called the amplitude demodulation method was first applied in the electrochemistry of semiconductors, in particular to diamond electrodes, in [83] (see the quoted paper for the theory of the method and the experimental set-up). A perturbing current signal of a high frequency ω, modulated in amplitude at a low frequency Ω, is applied to electrochemical cell; the demodulated low-frequency voltage signal is to be measured at the frequency Ω. In accordance with the theory of the method [83], under the condition of formation of a depletion layer in a semiconductor electrode, the in-phase component of the cell response $\mathrm{Re}\, E_\Omega$ is inversely proportional to $d(C^{-2})/dE$. Hence, for the acceptor concentration in the semiconductor we have [compare Eq. (1)]:

$$N_A = -J_0{}^2/(2\varepsilon_0 \varepsilon e \omega^2 \,\mathrm{Re}\, E_\Omega), \tag{3}$$

where J_0 is the perturbing current signal amplitude. As in Eq. (1), Eq. (3) was derived using the Schottky depletion-layer theory. Therefore, the above conditions (a) to (c) (Section 5.1) must be also fulfilled. The advantage of the amplitude demodulation method is that it enables one to bring the upper frequency limit to as high a level as 1 MHz. This is demonstrated in Fig. 16, where the frequency dependence of the slope of Mott–Schottky plot $d(C^{-2})/dE$ is given. For the above-discussed electrode with a frequency-independent capacitance (see Fig. 11), N_A was found to equal (3.0–3.4) 10^{18} cm^{-3}, in a reasonable agreement with linear impedance data.

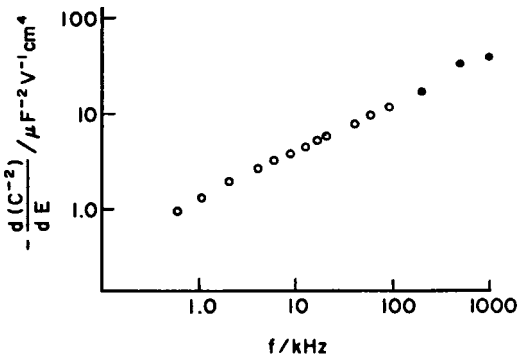

Fig. 16. Dependence of $d(C^{-2})/dE$ on the logarithm of frequency, obtained by linear (open circles) and nonlinear (solid circles) impedance techniques. Polycrystalline electrode [83]. Reproduced by permission from Elsevier Science.

5.3 On the Frequency Dependence of Differential Capacitance of Diamond Electrodes

The problem of the frequency dependence of the differential capacitance of diamond electrodes, which manifests itself in the frequency dependence of the slope of Mott–Schottky plots, can be subdivided into two aspects: (1) by the process(es) causing the frequency dependence; and (2) the most convenient format for the presentation of this dependence.

The nature of the frequency dependence of Mott–Schottky plots for semiconductor electrodes has been discussed in the electrochemical literature for more than three decades (see e.g. reviews [6, 84]). It has been speculated that it can be caused by the following factors: (1) frequency dependence of dielectric relaxation of the space charge region [85], (2) roughness of the electrode surface [84], (3) slow ionization of deep donors (acceptors) in the space charge region in the semiconductor [86], and (4) effect of surface states.

We shall briefly discuss these hypotheses as applied to diamond electrodes [78, 87]. The first hypothesis seems to be improbable for the range of frequencies commonly used in electrochemical impedance spectroscopy (that is, 1 to 10^5 Hz). The second hypothesis undoubtedly is worthy of consideration. Indeed, when a highly conducting (e.g. metal) electrode with a rough surface is placed into a poorly conducting electrolyte, its equivalent circuit contains a distributed series resistance that is caused by the fact that the current path is longer (hence, effective solution resistance is greater) to the bottom of the hollows on electrode surface than to the top of the protrusions. [The resistivity ρ of diamond films studied (10^3 to 10^4 Ω cm) is much higher than that of a strong electrolyte solution, no matter how dilute (e.g. 0.005 M). Hence, it is the diamond, rather than the solution, that plays the role of a poorly conducting phase at the diamond/solution junction. In other words, here the two phases kind of exchange their places; however, this does not change the physical nature of the effect under discussion.] Neglecting this effect can lead to a frequency-dependent error in the determination of the differential capacitance. Indeed, a numerical simulation of a semiconductor electrode with rough surface enabled Oskam et al. [84] to obtain a distinctive frequency dependence of the slope of the Mott–Schottky plots.

Nevertheless, despite the fact that the theory [84] looks convincing, we think it doubtful that the electrode surface roughness alone, without any additional conditions imposed, should not only cause the frequency dispersion of the capacitance, but also provide for its characteristic potential dependence, described by the Schottky theory. Moreover, a well-substantiated conclusion was drawn recently that the roughness of electrode surface does not necessarily cause the emergence of a CPE in the electrode's impedance [88].

The capacitance of surface states is undoubtedly frequency-dependent. However, in order to ensure the linear C^{-2} vs. E dependence observed experimentally, one has to make very strict assumptions concerning the energy distribution function of the surface states, and this appears very unnatural. Therefore, a slow ionization, in the space charge region of a diamond crystal, of atoms with a relatively deep-lying

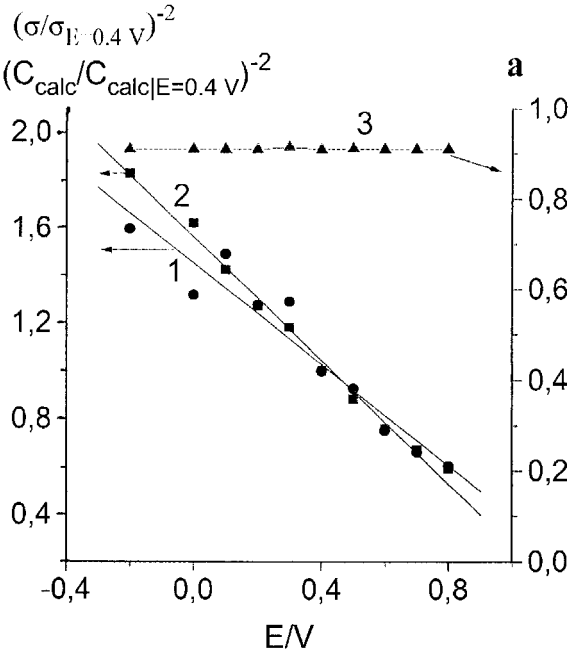

Fig. 17. Plots of (1) $[\sigma/\sigma|_{E=0.4\ V}]^{-2} - E$; (2) $[C_{calc}/C_{calc}|_{E=0.4\ V}]^{-2} - E$; and (3) **a** $- E$ for a single crystal electrode, calculated from the data of Fig. 13 [78].

energy level was assumed [73] as a tentative explanation for the frequency dependence of the Mott–Schottky plots for diamond electrodes. This hypothesis is supported by the fact that the σ value reasonably fairly follows the changes in the thickness of the space charge region (that is, in accordance with the Schottky theory); see Fig. 17, curve 1, whereas **a** is practically potential-independent (Fig. 17, curve 3). Nor does **a** depend on the dilution of solution. Note that the two factors affect the state of the electrode surface. Hence, it was concluded that the frequency dependence of the capacitance observed is due to a process proceeding in the space charge layer in diamond, rather than on its surface (that is, involving the surface states). The exception arises from a few polycrystalline samples; for example, the above-discussed film (Fig. 11), whose differential capacitance did not depend on the frequency. Their behavior has been left unexplained.

Finally, we shall discuss different formats of presentation of the Mott–Schottky plots for the case when they are frequency-dependent (as applied to diamond electrodes). As mentioned above, this is precisely the case that is typical for the electrochemistry of a great variety of semiconductor electrodes [6]. Figures 13 and 17 exemplify three different presentations of such data. The first is a sheaf of straight lines relating to a number of measuring frequencies, plotted by using the capacitance values directly measured at preset frequencies and potentials (Fig. 13). The second is a $C_{calc}{}^{-2}$ vs. E curve shown in Fig. 13 as curve 3 and in Fig. 17 as curve 2. When calculating C_{calc}, the real equivalent circuit presented in Fig. 10c is arbitrarily replaced by a simpler circuit (Fig. 10b), where a frequency-independent capacitance is substituted for the CPE. Because the whole body of data obtained over the entire frequency range is used in plotting this graph, the $C_{calc}{}^{-2}$ vs. E curve formally is

frequency-independent. The third format (applicable to cases where CPE is present in the equivalent circuit) involves plotting a σ^{-2} vs. E graph (Fig. 17, curve 1). We notice that $\sigma \rightarrow C_{calc}$ when $\mathbf{a} \rightarrow 1$. The CPE-containing circuit was shown [80] to describe the results of measurements more adequately than a simpler equivalent circuit containing a frequency-independent capacitance.

Yet, apart from the purely quantitative criterion, one should also take into consideration general reasoning. When comparing the discussed methods, we note that the σ^{-2} vs. E plot is frequency-independent; indeed, this is because σ is frequency-independent by definition [see Eq. (2)]. This plot is believed to be the most universal for comparing results of different experiments because the contribution, coming from the frequency-dependent factor proper, is separated in this case. Unfortunately, the dimensionality of σ precludes a correct comparison of the results thus computed with the directly measured capacitance values published in the literature.

No dimensionality problem exists with the ${C_{calc}}^{-2}$ vs. E plot. Its disadvantage, inherent also in method (1) discussed above, is a somewhat formal character of the C_{calc} quantity.

The sheaf of the C^{-2} vs. E straight lines generally evidences some slow process proceeding either on the semiconductor surface (e.g. adsorption, charging of surface states) or in the space charge region (e.g. the deep donor or acceptor ionization mentioned above).

Thus, we have to conclude that, without knowing the physical nature of the frequency dependence of the differential capacitance of a semiconductor electrode, the donor (or acceptor) concentration in the electrode cannot be reliably determined on the basis of the Schottky theory, irrespective of the Mott–Schottky plot presentation format. Therefore, the reported in literature acceptor concentrations in diamond, determined by the Schottky theory disregarding the frequency effect under discussion, must be taken as an approximation only. However, we believe that the σ^{-2} vs. E plot (the more so, when the exponent **a** approaches 1), or the ${C_{calc}}^{-2}$ vs. E plot, are more convenient for a qualitative comparison of electrodes made of the same semiconductor material.

6 Kinetics of Electrode Reactions

6.1 Outer-Sphere Reactions on "Metal-Like" Diamond Electrodes

It is conventional to classify electrochemical reactions as outer-sphere and inner-sphere. The former involve the outer coordination sphere of a reacting ion. Thus, little if any change inside the ion solvate shell occurs; they proceed without breaking-up intramolecular bonds. But in the latter, involving the inner coordination sphere, electron transfer is accompanied by breaking up or formation of such bonds. Often the inner-sphere reactions are complicated by adsorption of reactants and/or reaction products on the electrode surface. The electron transfer in the ${Fe(CN)_6}^{3-/4-}$ system is example of an outer-sphere reaction (with due reservation for some complications

caused by O-containing groups on the carbon electrode surface [89]). The oxidation or reduction of water molecules with O_2 or H_2 evolution, respectively, exemplifies inner-sphere reactions.

A variety of outer-sphere reactions were studied on diamond electrodes by Swain, Miller, Ramesham, and others, using potentiodynamic curves taken under the linear potential scan. This method is appropriate for both qualitative and quantitative characterization of the electrode kinetics (for details, see monographs [90, 91]).

Figure 18 gives typical cyclic voltammograms taken in four redox systems at relatively heavily doped diamond electrodes [92]. Outer-sphere reactions proceed in

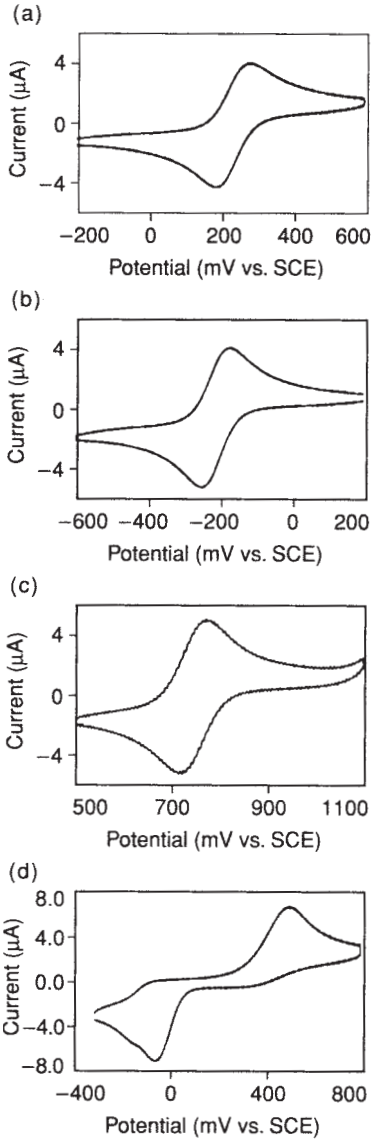

Fig. 18. Cyclic voltammograms for a polycrystalline diamond electrode exposed to 10^{-4} M solutions of (a) $Fe(CN)_6^{3-/4-}$; (b) $Ru(NH_3)_6^{2+/3+}$; and (c) $IrCl_6^{2-/3-}$ on the background of 0.1 M KCl. (d) Quinone/hydroquinone on the background of 0.1 M $HClO_4$. Reprinted with permission from [92]. Copyright (1997) American Chemical Society.

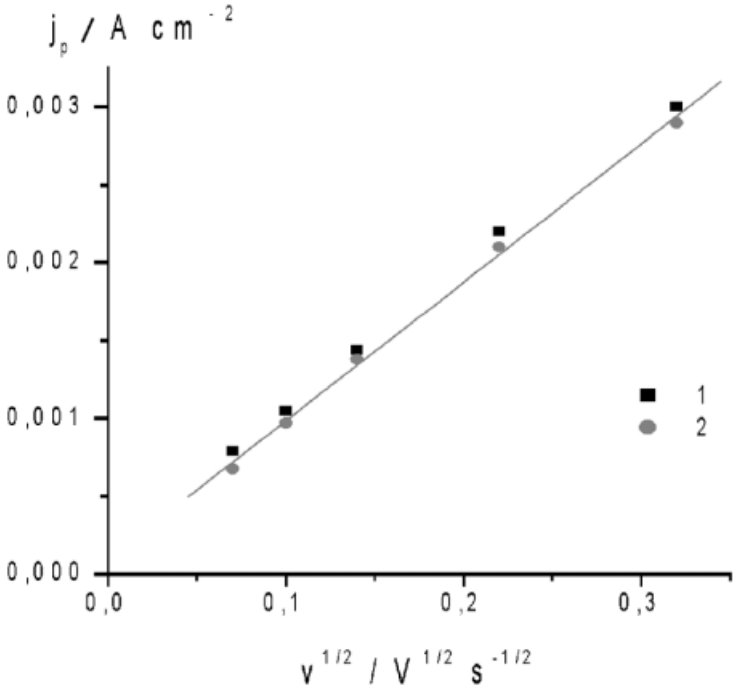

Fig. 19. Dependence of (1) hydroquinone oxidation and (2) quinone reduction peak current on the square root of potential scan rate. Solution of 0.01 M hydroquinone (or quinone) +0.5 M H_2SO_4. Polycrystalline electrode (data of Yu. V. Pleskov and Yu. E. Evstefeeva).

the first three systems; an inner-sphere reaction, in the fourth. The characteristic shape of the curves, with the anodic or cathodic current peaks, testifies that the stage of charge transfer at the interface is relatively fast; therefore, the reaction experiences difficulties that are due to slow mass transfer in solution to the electrode surface. This conclusion is corroborated by the linear dependence of the peak current on the square root from the potential scan rate, observed at diamond electrodes in the ferro-ferricyanide [93], quinone/hydroquinone [94], and Ce^{3+} ions [95] (see Fig. 19). From the slope of the lines, the reactant diffusion coefficient D can be determined. For example, for Ce^{3+} ions it was found that [95]:

Supporting electrolyte (0.1 M)	H_2SO_4	HNO_3	$HClO_4$
10^5 D, cm^2 s^{-1}	1.05	0.55	0.53

Analysis of potentiodynamic curves makes it possible to determine, in addition to the diffusion coefficient, the reaction kinetic characteristics: the apparent transfer coefficients of the cathodic reaction (α) and anodic reaction (β) and the rate constant k^0. Quantitative determination will be discussed in the next section; qualitatively, the more the potential difference ΔE_p for the anodic and cathodic current peaks (at a

given potential scan rate and in the absence of *IR* potential drop), the less reversible the electrode reaction. According to the theory of cyclic potentiodynamic curves [90, 91], $\Delta E_p = 56$ mV at room temperature for a reversible reaction, irrespective of the reactant concentration and potential scan rate. For the first three systems in Fig. 18, ΔE_p equals 88, 72, and 65 mV, respectively. Thus, the reactions proceed as quasi-reversible at the heavily doped diamond. On the contrary, in the quinone/hydroquinone system, the reaction is significantly irreversible: $\Delta E_p = 560$ mV. These qualitative estimates correlate with the rate constant values determined for the listed redox systems [96]:

	$Fe(CN)_6^{3-/4-}$	$Ru(NH_3)_6^{2+/3+}$	$IrCl_6^{2-/3-}$	quinone/hydroquinone
k^0, cm s^{-1}	$9\ 10^{-4}$	$3\ 10^{-3}$	$4\ 10^{-3}$	$<10^{-6}$

The rate constant values depend markedly on both the boron doping level (see Section 6.2 below for more detail) and electrode surface pretreatment; the figures are given here for the purpose of illustration only. On the whole, from the studies of a variety of systems, the following conclusions were derived [97]: (1) outer-sphere reactions are more reversible than the inner-sphere ones; (2) systems with more positive equilibrium potential are more reversible than those with negative equilibrium potential (the $Ce^{3+/4+}$ system being an exception [69]); and (3) on heavily doped (metal-like) diamond electrodes, the reactions proceed in a more reversible manner than on moderately doped electrodes demonstrating semiconductor behavior. Items (2) and (3) are illustrated by Fig. 20, where peak-to-peak potential separation of cyclic voltammograms for four redox couples on diamond are shown. Heavily doped, semimetallic electrodes are on the left; lightly doped, semiconducting electrodes are on the right. These qualitative conclusions have been corroborated in many works [98–

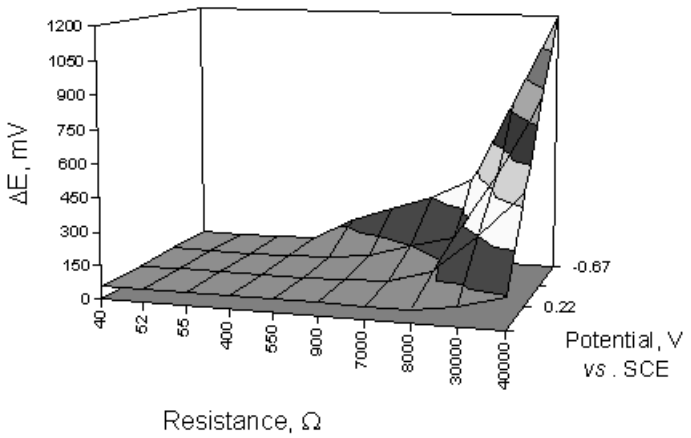

Fig. 20. Peak-to-peak potential separation of cyclic voltammograms for four redox couples: Fe(o-phenantroline)Cl_3 (reversible redox potential 0.86 V vs. SCE), ferrocene(1,1′)dimetanol (0.2 V), $Ru(NH_3)_6Cl_3$ (−0.23 V), and methyl viologen (−0.67 V). Polycrystalline electrodes; data corrected for IR drop [16].

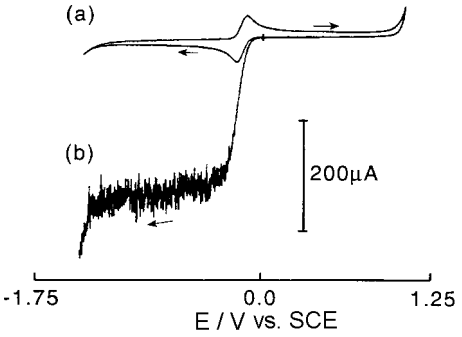

Fig. 21. (a) Cyclic voltammogram obtained for the reduction of 1 mM $Ru(NH_3)_6^{3+}$ in 0.1 M KCl at a polished polycrystalline diamond electrode with potential scan rate of 100 mV s^{-1}; (b) Sonovoltammogram obtained under the same conditions with 90 W cm^{-2} ultrasound intensity. Reprinted from [109]. Copyright (1999), with permission from Elsevier Science.

103]. We turn back to this point in the next section; now we call attention to the fact that even on metal-like diamond electrodes the reaction rate is lower than on metal electrodes known for their electrocatalytic activity, e.g. platinum. This poses the problem of improving the electrocatalytic properties of diamond electrodes intended for industrial applications. Getting ahead in the story of metal electrodeposition (see Section 6.4.3 below), we note that preliminary studies showed [104, 105] that electroplating of Pt nanoparticles onto diamond surface lowers the cathode reactions' overvoltage. To attach Pt to the diamond surface more strongly, a fresh portion of diamond was deposited over the Pt clusters (partly covering them); then the catalyst is tightly bound to the surface [106]. We touch on an attempt to solve this problem with DLC electrodes in Section 6.5 below.

To conclude the discussion on quasi-reversible reactions, we now direct our attention to sonoelectrochemical reactions on diamond electrodes [107–109]. In sonoelectrochemistry, power ultrasound is applied to electrochemical cell, causing forced convection in the electrode-electrolyte system. As a result of the enhanced mass transfer, non-steady-state potentiodynamic curves with current peak turn to steady-state curves with a limiting current plateau (Fig. 21). Notice a significant increase in the current. It must be emphasized that in sonoelectrochemistry electrode materials are exposed to extreme conditions with mechanical strains induced by pressure waves and cavitation-induced liquid jets strong enough to cause severe erosion. Diamond withstands the sonoelectrochemical conditions perfectly. This opens up fresh possibilities for efficient electrolyses and electroanalyses with diamond electrodes.

6.2 Semiconductor Properties of Diamond and the Electrode Kinetics

In this section, unlike the previous one, we deal with less heavily doped, semiconductor diamond. Quantitative studies of reaction kinetics have been performed in $Fe(CN)_6^{3-/4-}$, quinone/hydroquinone (recall that this is an inner-sphere reaction), and $Ce^{3+/4+}$ systems [94, 104, 110]. Potentiodynamic curves recorded in solutions containing only one (either reduced or oxidized) component of a redox system are shown on Figs. 22a and b; the dependences of anodic and cathodic current peak po-

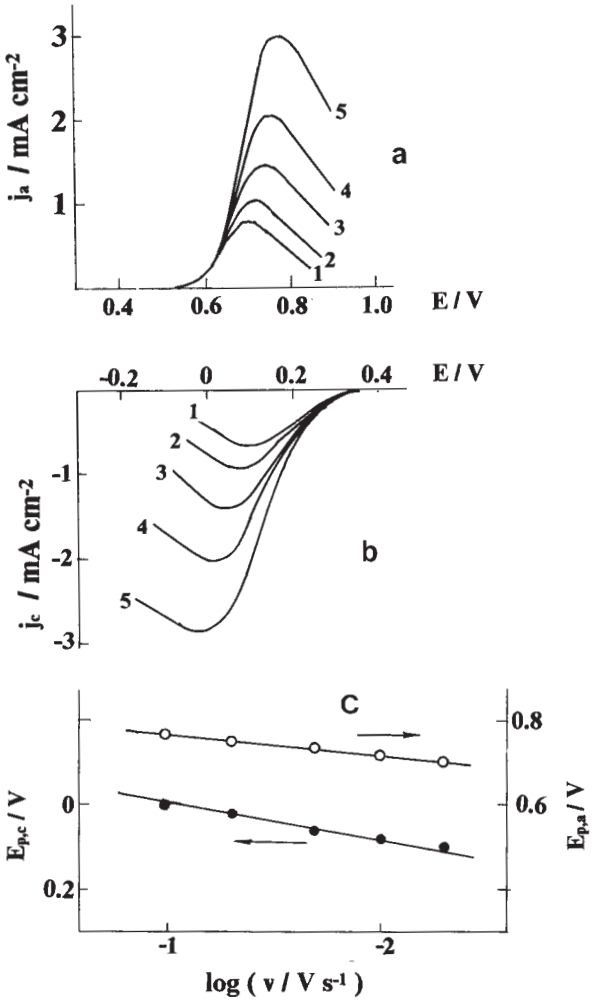

Fig. 22. Current-potential curves taken at a linear potential scan for (a) hydroquinone (0.01 M) oxidation and (b) quinone (0.01 M) reduction in 0.5 M H_2SO_4 solution on a polycrystalline diamond electrode. The potential scan rate v/ V s^{-1}: (1) 0.005, (2) 0.01, (3) 0.02, (4) 0.05, and (5) 0.1. (c) Dependence of the cathodic ($E_{p,c}$) and anodic ($E_{p,a}$) current peak potential on logarithm of the potential scan rate. Potentials given vs. Ag/AgCl electrode [94].

tentials E_p on the logarithm of the potential scan rate v are plotted on Fig. 22c. Quite unexpectedly, cathodic and anodic curves are almost symmetric, like the curves taken for metal (or metal-like diamond) electrodes; no rectification effect is observed. We turn back to this point at the end of this section.

From the slope of the lines in Fig. 22c, and by using the above-mentioned theory of potentiodynamic curves [90], the apparent transfer coefficients of cathodic reaction α (or anodic reaction β) can be calculated by the following formulas:

$$E_p = \text{const} - (RT/2\alpha nF)\ln v; \tag{4}$$

$$E_p - E_{p/2} = -1.857(RT/\alpha nF), \tag{5}$$

where $E_{p/2}$ is the half-wave potential of the reaction, n is the number of electrons participating in the reaction, F is the Faraday number. Another method of the determination of α (β) is as follows: the dependence of the exchange current j_0 on the concentration of the oxidized form c_{ox} is measured while the concentration of reduced form c_{red} has been kept constant (or vice versa), then α is calculated by formula:

$$j_0 = nFk^0 {c_{ox}}^{1-\alpha} {c_{red}}^{\alpha}, \tag{6}$$

where k^0 is the rate constant. The j_0 value is calculated from the faradaic resistance R_F (see Section 5.1 above) measured in the redox solution at the equilibrium potential:

$$R_F = RT/(nFj_0). \tag{7}$$

Recall that the faradaic resistance can be determined as a low-frequency cut-off at the complex-plane plot of impedance spectrum (compare the equivalent circuit in Fig. 10b). Such plots measured in the $Fe(CN)_6^{3-/4-}$ solutions of different concentrations are given in Fig. 23a [104] (similar results were obtained in [111]). The plots are (somewhat depressed) semicircles, whose radii decreased with increasing redox couple concentration. Figure 23b shows the line plotted by using the data in Fig. 23a, in accord with Eq. (6). We notice that all three methods yielded similar results.

Typical values of transfer coefficients α and β thus obtained are listed in Table 4 for single crystal and polycrystalline thin-film electrodes [69] and for a HTHP diamond single crystal [77]. We see for $Ce^{3+/4+}$ system (as well as for $Fe(CN)_6^{3-/4-}$ and quinone/hydroquinone systems [104]), that, on the whole, the transfer coefficients are small and their sum is less than 1. We recall that an ideal semiconductor electrode must demonstrate a rectification effect; in particular, a reaction proceeding via the valence band has transfer coefficients $\alpha = 0$, $\beta = 1$; $\alpha + \beta = 1$ [6]. Actually, the ideal behavior is rarely the case even with single crystal semiconductor materials fabricated by advanced technologies. Departure from the "ideal" semiconductor behavior is likely because the interfacial potential drop is located in part in the Helmholtz layer (due e.g. to a high density of surface states), or because the surface states participate in the reaction. As a result, the transfer coefficients α and β take values intermediate between those characteristic of a semiconductor (0 or 1) and a metal (~ 0.5).

In this context we discuss an energy diagram of the boron-doped semiconductor diamond/redox electrolyte interface (Fig. 24) [110]. The plotting of such diagrams is discussed at length, e.g. in [6]; here we recall that the position of Fermi level of a diamond electrode in the electrode potential scale is unambiguously determined by the value of flat-band potential E_{fb}. First, attention is drawn to the fact that the conduction band is arranged very high, close to the vacuum level (zero point on

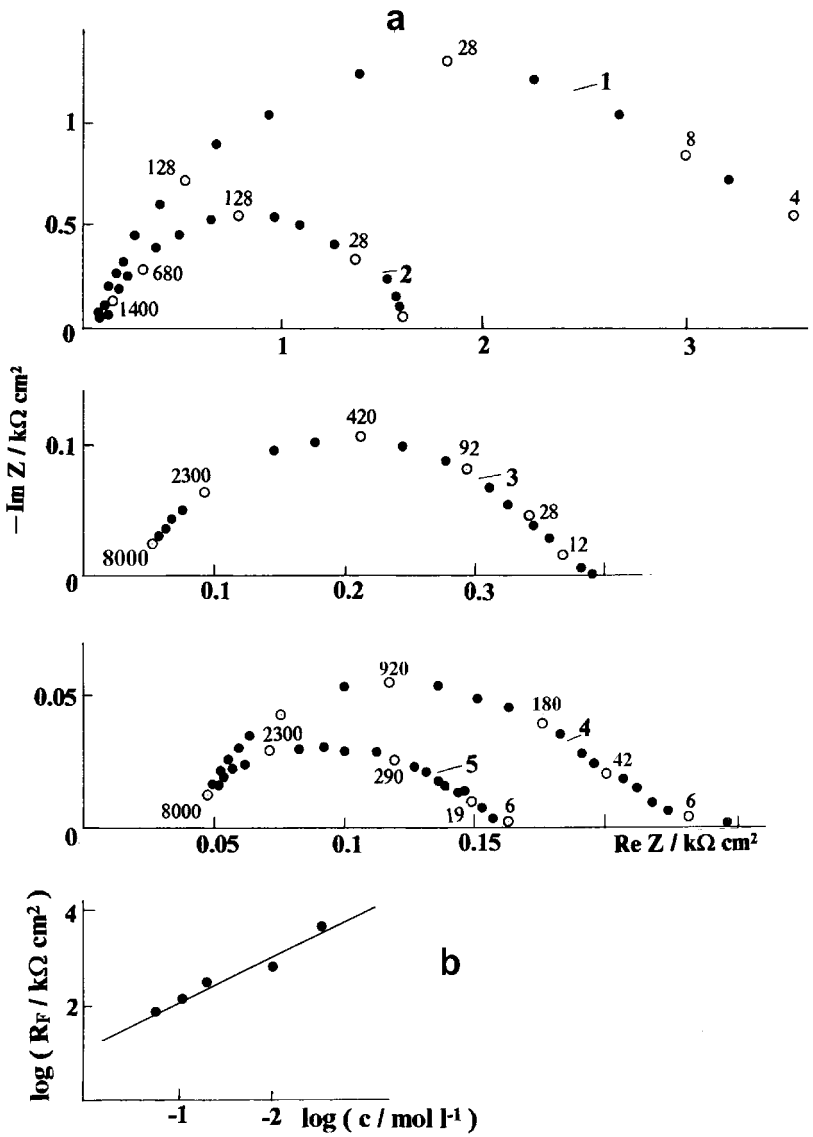

Fig. 23. (a) Complex plane plots of impedance spectra measured for a polycrystalline electrode at the equilibrium potential in 1 M KCl + x M $K_3Fe(CN)_6$ + x M $K_4Fe(CN)_6$ solution at a value of x: (1) 3.3 10^{-3}; (2) 10^{-2}; (3) 5 10^{-2}; (4) 10^{-1}; (5) 2 10^{-1}. Frequency f/Hz shown on the figure. (b) Dependence of faradaic resistance on logarithm of the redox electrolyte concentration [104].

the energy E scale), and sometimes exceeds this level (at the solid/vacuum interface this would correspond to a negative electron affinity of diamond). Hence, electrons in the conduction band (photoelectrons in particular, see Section 7 below) are basically very strong reducing agent capable of the reduction of hard to reduce compounds.

Table 4. Comparative kinetic characteristics of diamond electrodes [determined in 0.01 M Ce^{3+} (or Ce^{4+}) + 0.5 M H_2SO_4 solution] [69, 75].

α	β	k^0/cm s^{-1}
Polycrystalline film		
0.16	0.46	$6 \cdot 10^{-9}$
Single-crystal film		
0.2	0.43	$6.5 \cdot 10^{-7}$
HTHP single crystal		
0.33	0.27	$4.4 \cdot 10^{-6}$

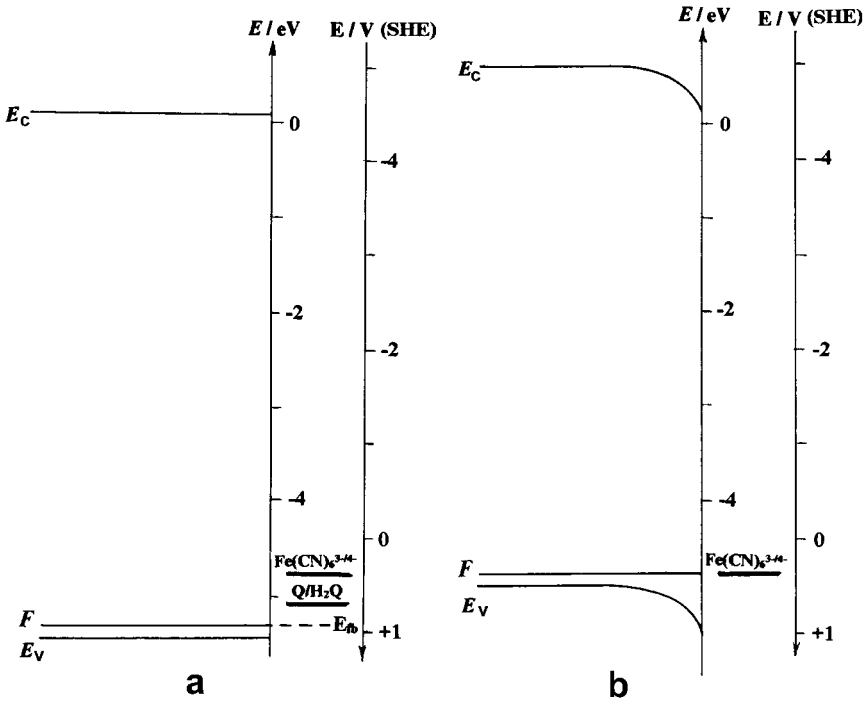

Fig. 24. Energy diagram of the boron-doped diamond/aqueous redox electrolyte solution interface: (a) at the flat-band potential; (b) at the equilibrium potential of $Fe(CN)_6^{3-/4-}$ system. E_c is the energy of conduction band bottom, E_v is the energy of valence band top, F is the Fermi level, E_{fb} is the flat-band potential. Shown are the electrochemical potential levels of the $Fe(CN)_6^{3-/4-}$ and quinone/hydroquinone (Q/H_2Q) systems in solution. The electrode potential axis E is related to the standard hydrogen electrode (SHE). Reprinted from [110]. Copyright (1997), with permission from Elsevier Science.

Second, because (in accord with the Franck–Condon principle) the electron transitions at interfaces involve levels of equal energy [6], an overlap of the available energy states in redox electrolyte and in an allowed band in semiconductor electrode is required for an efficient charge transfer at the interface. Therefore, electrode reactions whose electrochemical potential levels are located close to the top of valence band E_v exchange charges with diamond most efficiently. This reasoning explains the above-mentioned observations [97] concerning the dependence of reaction rate on the redox potential of a solute. In particular, we see from Fig. 24 that the electrochemical potential level of $Fe(CN)_6^{3-/4-}$ system is arranged close to the valence band; it is well off from the conduction band. Hence, the electrode reactions of $Fe(CN)_6^{3-}$ and $Fe(CN)_6^{4-}$ ions proceed via the valence band, rather than the conduction band. A more sophisticated analysis of the complex-plane plots of impedance, taken in redox solutions, resulted in the conclusion that these reactions involve surface states at the interface [111]. This is possibly why no rectification is observed for the diamond/redox electrolyte solution interface. As mentioned above, the high-frequency cut-off on the ReZ axis (Fig. 23a) gives the diamond film resistance R_s, from which the diamond resistivity ρ can be calculated. The low-frequency cut-off gives the faradaic resistance R_F. In Fig. 25 we show dependences of R_F on electrode resistivity ρ for two redox systems. Taking into account Eq. (7) we conclude that, first, the exchange current j_0 in $Fe(CN)_6^{3-/4-}$ system must be three orders higher than that in quinone/hydroquinone system, in full agreement with the (Section 6.1) rate constant values listed above. Second, the exchange current is

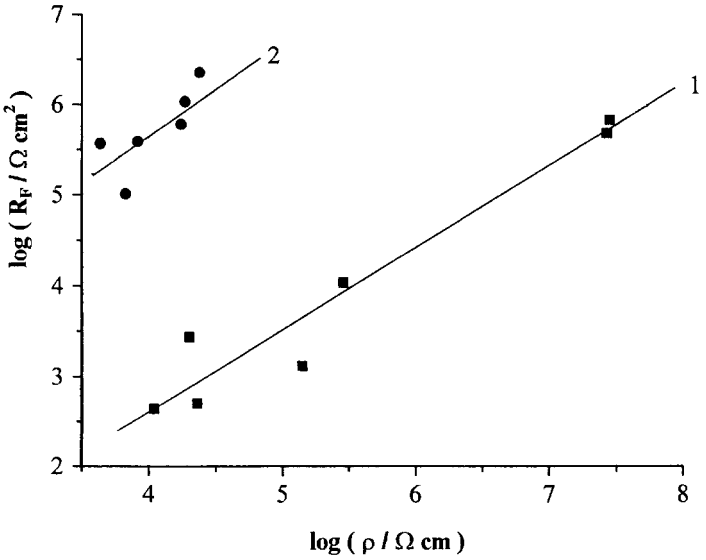

Fig. 25. Dependence of faradaic resistance measured at the equilibrium redox potential on the polycrystalline film resistivity for (1) $Fe(CN)_6^{3-/4-}$ and (2) quinone/hydroquinone systems. Reprinted from [110]. Copyright (1997), with permission from Elsevier Science.

inversely proportional to resistivity over a wide range of ρ (which is in a qualitative agreement with the above-indicated dependence [97] of reaction rate on the doping level).

Such an interrelationship is a manifestation of the effect of potential distribution at the semiconductor/electrolyte interface on the electrochemical kinetics on semiconductor electrodes. At an "ideal" semiconductor electrode the potential drop in the Helmholtz layer is small in comparison with the potential drop in the space charge layer [6]. Energy band edges E_c and E_v (Fig. 24) are as if "pinned" at the interface, irrespective of the doping level; hence, the bulk free carrier concentration (which is inversely proportional to the diamond resistivity, assuming the hole mobility to be independent of the boron content). So, the surface free carrier concentration in a semiconductor electrode does not depend on the doping either. Electrochemical reaction rate on the semiconductor electrode, which is proportional to the surface concentration of the charge carriers participating in the reaction, must therefore be doping-independent (provided the bandgap value remains constant) [6, 112]. This is not the case with diamond electrodes (Fig. 25). From the experimental R_F vs. ρ dependence we thus draw the conclusion that the potential distribution at the diamond/electrolyte solution interface in the redox solutions depends on the diamond doping level, the more so for more heavily doped samples. This is why the semiconductor diamond behavior is far from "ideal" and why, in particular, no current rectification is observed on diamond electrodes.

Moderately doped diamond demonstrates almost ideal semiconductor behavior in inert background electrolytes (linear Mott–Schottky plots, photoelectrochemical properties (see below), etc.), which provides evidence for band edge "pinning" at the semiconductor surface. By comparison in redox electrolytes, a metal-like behavior is observed with the band edges "unpinned" at the surface. This phenomenon, although not yet fully understood, has been observed with numerous semiconductor electrodes (e.g. silicon, gallium arsenide, and others) [113]. It must be associated with chemical interaction between semiconductor material and redox system, which results in a large and variable Helmholtz potential drop.

An example of such interaction, the effect of diamond surface oxidation on the "band-edge movement" was investigated recently [114, 115]. We recall that the as-grown surface of chemical-vapor-deposited diamond is hydrogen-terminated, and that its flat-band potential (determined by extrapolating Mott–Schottky plot) is close to 0 V (SCE). Upon treatment in oxygen plasma (or anodic polarization), the flat-band potential shifted to 1.0–1.1 V. Thus, energy bands at diamond/electrolyte interface move downward in the energy diagram due to the change of the Helmholtz potential drop. On oxidized diamond, the flat-band potential appeared to be pH-dependent (as is typical of oxidized semiconductor electrodes [6]). Of interest is that oxidation strongly affects the kinetics of reactions in the $Fe(CN)_6^{3-/4-}$ couple: a nearly reversible reaction at a hydrogen-terminated surface becomes highly irreversible at an oxidized one, as the peak-to-peak potential difference shows (Fig. 26). However no effect of surface oxidation was observed with the $Ru(NH)_3^{2+/3+}$ couple. Obviously, the former system is sensitive to O-containing groups on the diamond surface.

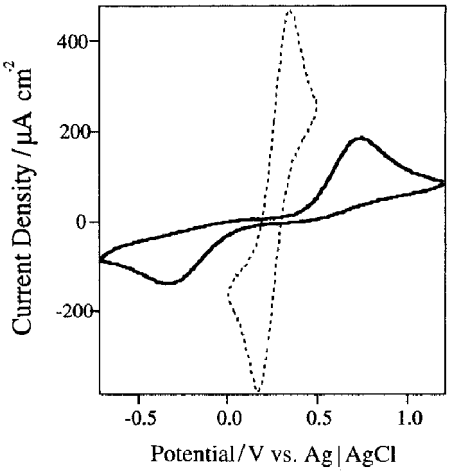

Fig. 26. Cyclic voltammograms for a polycrystalline diamond electrode before (broken line) and after (solid line) oxygen plasma treatment for 1 min, taken in 0.1 M Na_2SO_4 + 1mM $Fe(CN)_6^{3-/4-}$ solution. Scan rate 100 mV s^{-1}. Reprinted from [115]. Copyright (1999), with permission from Elsevier Science.

6.3 Crystal Structure and Electrode Kinetics: Comparison of Single Crystal and Polycrystalline Diamond and Amorphous Carbon Electrodes

As shown in Section 3.2, polycrystalline diamond film is a heterogeneous system comprising diamond crystallites and intercrystallite boundaries, presumably consisting of amorphous carbon. This brings up the question: To what extent do intercrystallite boundaries affect the electrochemical behavior of polycrystalline diamond electrodes? To answer this question, the electrochemical properties of polycrystalline and single crystal diamond and amorphous carbon should be compared. In such a comparison, a model material of the intercrystallite boundaries should be chosen.

In Section 2 we showed that the properties of amorphous carbon vary over a wide range. Graphite-like thin films are similar to thoroughly studied carbonaceous materials (glassy carbon and alike) in their electrode behavior. Redox reactions proceed in a quasi-reversible mode on these films [75]. On the contrary, no oxidation or reduction current peaks were observed on diamondlike carbon electrodes in $Ce^{3+/4+}$, $Fe(CN)_6^{3-/4-}$, and quinone/hydroquinone redox systems: the measured current did not exceed the background current (see below, Section 6.5). We conventionally took the rather wide-gap DLC as a model material of the intercrystallite boundaries in the polycrystalline diamond. Note that the intercrystallite boundaries cannot consist of the conducting graphite-like carbon because undoped polycrystalline diamond films possess excellent dielectric characteristics.

By comparing measured values of α, β, and k^0 (Table 4), it was concluded that single crystal and polycrystalline diamond electrodes are similar in their kinetic behavior. Because DLC films turned out to be fully inactive, we concluded that the intercrystallite boundaries do not contribute to the electrode behavior of polycrystalline diamond films. The conclusion that the diamond crystallites determine behavior is corroborated by the comparative study of impedance (Table 3) characteristics of

polycrystalline and single crystal diamond electrodes, and holds at least over a moderate electrode polarization range [69].

And yet, at high anodic potentials (+1.7 V vs. SHE, just prior to the onset of the O_2 evolution) a minor current peak is observed at potentiodynamic curves taken with polycrystalline electrodes [38, 116]. As scans were repeated, the peak current increased until it reached a steady-state value (Fig. 27). The peak is found to be more pronounced for electrodes with higher sp^2-carbon content. And, vice versa, it was not observed on single crystal electrodes. The peak current still is as low as 1 μA cm^{-2}; therefore, it would be overlooked with Fig. 7 and similar graphs. The surface redox couple that manifests itself in this manner was ascribed to the oxidation of sp^2-carbon of intercrystallite boundaries. The total charge transferred, if related to oxygen bound to surface carbon sites, indicated only 0.05% of the sites participated in

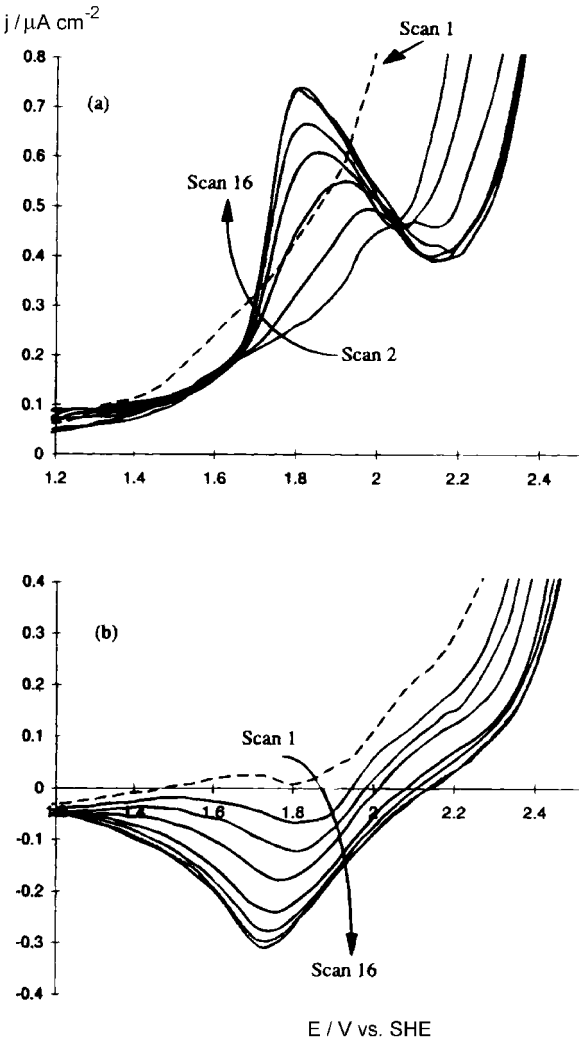

Fig. 27. Repeatedly taken (a) anodic and (b) cathodic potentiodynamic curves for a polycrystalline diamond electrode exposed to 0.5 M H_2SO_4 solution. Potential scan rate was 200 mV s^{-1}. Scan numbers shown on Figure [38]. Reproduced by permission of The Electrochemical Society, Inc.

the reversible oxidation and reduction of the surface. No other features have been observed that could be assigned to the possible effects of intercrystallite boundaries, more generally, sp^2-carbon on the electrochemical behavior of polycrystalline diamond [89].

6.4 Kinetics of Inner-Sphere Reactions

6.4.1 Reaction Involving Gas Evolution or Consumption

Among the inner-sphere reactions are cathodic hydrogen evolution and anodic oxygen evolution, which frame the potential window in aqueous electrolyte solutions (see Figs. 7 and 8). As indicated earlier (Section 4.1), the higher the electrode quality, the higher the overvoltage of these reactions. For H_2 evolution, the exchange current was estimated at 10^{-10} A cm^{-2}, the transfer coefficient $\alpha = 0.30$; for O_2 evolution, $5 \cdot 10^{-11}$ A cm^{-2} and $\beta = 0.25$, respectively [38].

The reverse reaction, dissolved O_2 reduction in alkaline and acid solutions, was also studied [117, 118]. The reduction was found to be highly inhibited, probably due to the lack of adsorption sites for oxygen and/or reduced intermediates. The reaction is hypothesized to proceed mainly at sp^3-sites; the non-diamond sp^2 carbon was deactivated by anodic prepolarization. The kinetic parameters were found as $\alpha = 0.24$, $k^0 = 7 \cdot 10^{-5}$ cm s^{-1} in alkaline medium. It is significant that, owing to its high overvoltage, the dissolved O_2 reduction does not interfere with other reactions, which thus can be studied on diamond electrodes without air removal from the cell; this could be advantageous in certain types of analytical applications.

In addition to the O_2 anodic evolution, ozone formation takes place on boron-doped diamond anodes. The higher the boron concentration, the less the reaction overvoltage, in full agreement with observations discussed in Sections 6.1 and 6.2. Compared with traditional PbO_2 anodes, the overvoltage still is much higher (by 0.7 V for the 5000-ppm boron-containing diamond), as seen in Fig. 28. The faradaic efficiency of O_3 production comes to a few per cent. No significant change in surface morphology was observed; nor did the sp^2-carbon form on the surface, as Raman tests indicated. The consumption rate of diamond was about 0.4 mg A^{-1} h^{-1}, which is an order of magnitude lower than that of Pt under the same conditions. Diamond electrodes are fairly stable: the electrode life is as long as 900 h at a current density of 2 A cm^{-2}. (Then the diamond layer is undercut and peels off [119, 120].) At a lower temperature (-2 °C), the faradaic efficiency is as high as 12 to 15 % [121]. Thus, diamond electrodes have good potentialities for purging chemical and biological contaminants in wastewaters [122].

The potential window can be limited by the decomposition potential of a solute, not just a solvent. In particular, reactions of anodic oxidation of halides (Cl^-, Br^-, and I^-) on diamond are highly irreversible and have much higher overvoltage (for Cl^-, by 1 V) than on platinum or graphite electrodes [97, 123, 124]. In all probability this is due to poor adsorption of intermediates, that is, Cl, Br, and I atoms, on the diamond electrode surface. We recall that the outer-sphere reactions discussed in Section 6.1 generally do not involve adsorption of intermediates and thus are not

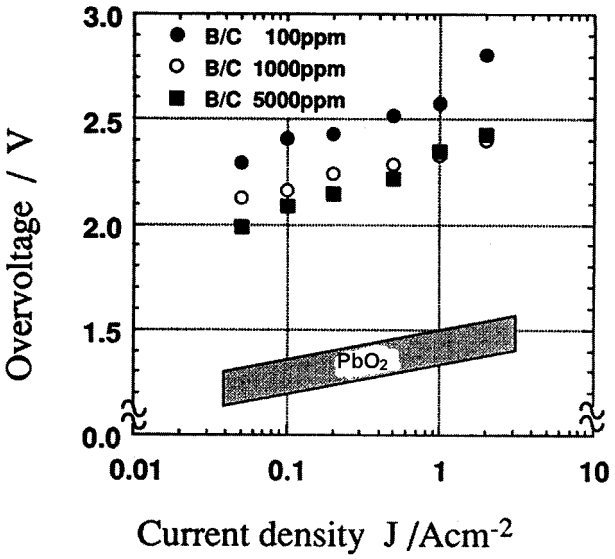

Fig. 28. Anodic O_3 evolution plots for polycrystalline diamond thin-film electrodes (top) and PbO_2 electrodes exposed to 10 vol. % H_2SO_4 solution. The boron/carbon ratio in the source gas during the films growth shown on the figure [119]. Reproduced by permission of The Electrochemical Society, Inc.

affected by poor adsorbability of the diamond surface. The traces of sp^2-carbon on diamond surface were supposed to reduce the overvoltage for I^- oxidation [125]. Preliminary observations on the CO_2 reduction in NaCl–KCl molten salt electrolyte at 750 °C were reported in Ref. [126].

6.4.2 Reactions of Organic and Inorganic Compounds. The Diamond Electrodes in the Preparative Electrolysis

In addition to quinone reduction and hydroquinone oxidation, electrode reactions of many organic compounds are also inner-sphere. In these charge transfer is accompanied by profound transformation of the organic molecules. Some reactions are complicated by reactant and/or product adsorption. Anodic oxidation of chlorpromazine [54], ascorbic acid [127], anthraquinone-2,6-disulfonate [128], amines [129], phenol, and isopropanol [130] have been investigated. The latter reaction can be used for purification of wastewater. The cyclic voltammogram for cathodic reduction of fullerene C_{60} in acetonitrile solution exhibits 5 current peaks corresponding to different redox steps [131].

An efficient possible application of diamond electrodes is their use in the reduction of hard-to-reduce compounds. Fujishima, Tenne, Levy-Clement et al. studied the electroreduction of nitrate and nitrite ions to ammonia [132–134]. The reaction

$$NO_3^- + 7\,H_2O + 8\,e^- \rightarrow NH_4OH + 9\,OH^-$$

proceeds in an alkaline KNO_3 solution on a heavily doped ($N_A \sim 10^{21}$ cm^{-3}) diamond cathode at a high current density: 300 mA cm^{-2} at $E = -5$ V (SCE). No distinct corrosion of the cathode was observed even upon extensive electrolysis.

The most striking feature of these reactions is that their faradaic efficiency exceeds the theoretical value of 100 %. This fact was first attributed to a simultaneous (conjugated) reaction involving the silicon substrate, provided pinholes existed in the diamond film. However, on a free-standing, diamond-film electrode (see Section 2) the efficiency has a still abnormal, albeit somewhat lower, value. This effect was left unexplained.

One more inorganic electrosynthesis, peroxodisulphate production, has been studied [135]. Despite an inevitable side-reaction (oxygen evolution), the current efficiency obtained was as high as 75 %.

6.4.3 Electrodeposition of Metals onto Diamond

Information concerning metal electrodeposition on diamond is scarce and in part contradictory. The nucleation kinetics during Hg electrodeposition on heavily doped diamond electrodes were studied in Ref. 136. Judging by the time dependence of deposition current, and based on the kinetic theory of electrodeposition, the authors distinguished between two mechanisms that would be realized upon different conditions. Namely: (1) the primary instantaneous formation of a high density of nuclei and their successive growth; or (2) the deposition under the progressive nucleation. Figure 29 shows an example of this analysis for the electrodeposition of silver (for

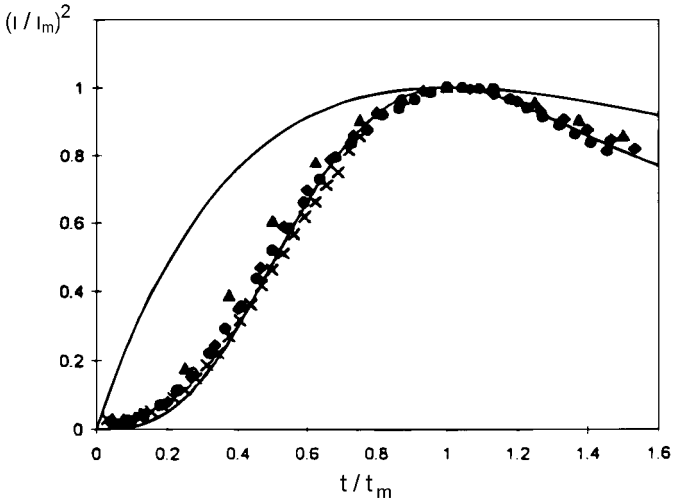

Fig. 29. Electrodeposition of Ag from 0.017 M AgCN + 0.92 M KCN + 0.11 M K_2CO_3 solution: dimensionless analysis of experimental potentiostatic current transients (I_m and t_m are the current and time corresponding to the maximum on the current transient curve, respectively). Upper curve calculated for the instantaneous nucleation mechanism; lower curve, for the progressive nucleation mechanism. Different symbols/experimental points relating to different potentials [136]. Reproduced by permission of The Electrochemical Society, Inc.

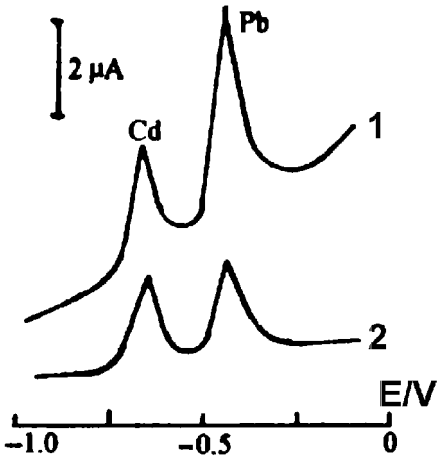

Fig. 30. Anodic stripping voltammograms of 100 μg/l Pb and Cd at (1) boron-doped diamond and (2) glassy carbon electrodes.

which the case of progressive nucleation is observed). Desorption of H and O from diamond surface, resulting from its electron irradiation, facilitates the Ag electrodeposition [137].

Lead and mercury are deposited as micron-sized clusters, predominantly at intercrystallite boundaries [105]; so does lithium from the polyethylene oxide solid electrolyte. What is more, Li intercalates into the sp^2-carbon [22, 138]. Thus, observations on the Li intercalation and deintercalation enable one to detect non-diamond carbon on the diamond film surface. Copper is difficult to plate on diamond [139]. There is indirect evidence that Cu electrodeposition, whose early stages proceed as underpotential deposition, also involves the intercrystallite boundaries [140]. We note that diamond electrodes seem to be an appropriate tool for use in the well-known electroanalytical method of detection of traces of metal ions in solutions by their cathodic accumulation followed by anodic stripping. The same holds for anodic deposition, e.g. of, Pb as PbO_2 with subsequent cathodic reduction [141, 142]. Figure 30 shows the voltammograms of anodic dissolution of Cd and Pb cathodically predeposited from their salt mixtures on diamond and glassy carbon electrodes. We see that the dissolution peaks are clearly resolved. The detection limit for Zn, Cd, and Pb is as low as a few ppb [143].

A procedure for $Ni(OH)_2$ deposition on diamond was developed [144], with the intent of exploiting the structure in a battery. The $Ni(OH)_2$ film adhered well to the diamond substrate and retained its capacity even after 4000 charging/discharging cycles.

Preliminary results were recently reported [145] on the use of CdTe electrodeposition on diamond in the fabrication of a solid-state solar cell based on the boron-doped p-type diamond/n-type CdTe junction. In this cell, the wide-bandgap diamond is an optical window that generates photovoltage, whereas the narrow-bandgap CdTe generates photocurrent. We note that no appropriate p-type material for the fabrication of optical windows has existed so far; therefore, one would use an n-type CdS window coupled with narrow-bandgap p-type CdTe. However, the pro-

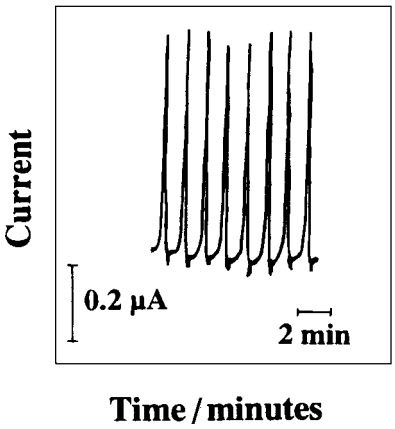

Fig. 31. The determination of ethylamine by flow-injection analysis with electrochemical detection. Chronoamperogram with repeated 20 μl injections of 0.25 mM ethylamine in 0.1 M carbonate buffer, pH 10, to a flowing (0.5 mL min^{-1}) carbonate buffer solution. Reprinted with permission from [146]. Copyright (1997) American Chemical Society.

duction technology of n-type CdTe is better developed than that of the p-type CdTe; moreover, diamond is superior to CdS because of its higher conductance.

6.4.4 Electroanalytical Applications

Potentialities of boron-doped diamond as a tool for electroanalysis are determined by its high corrosion resistance, good stability, and, in many cases, selectivity. Diamond detecting electrodes can be used in combination with different analytical methods: liquid chromatography, electrodialysis, etc. Numerous examples of electroanalytical applications of diamond electrodes are available [128, 142, 146, 147]. A thin-layer flow-through cell with a rather heavily doped diamond electrode ($N_A = 10^{19}$ cm^{-3}) was used in the detection of ethylamine, ethylene diamine, and azide ions N_3^- in a flow-injection analysis (FIA) with electrochemical detection technique. The detection was performed in a dynamic regime, by injecting a microprobe of a test solution into flowing indifferent electrolyte and tracing the electrode current response (Fig. 31). The cell function turned to be linear over the $3 \cdot 10^{-3}$ to 10^{-7} M range; the detection limit is (nM):

N_3^-	Chlorpromazine	Ascorbic acid	Dopamine	4-methylcatechol
8	4	12	2.5	2

An example of the selectivity of diamond electrodes is the detection of dopamine in the presence of 1000-fold excess of ascorbic acid (typical of the composition of neural extracellular fluid). On an H-terminated diamond, potentials of the dopamine (DA) and ascorbic acid (AA) oxidation peaks on potentiodynamic curves are very close each other; the peaks cannot be resolved (Fig. 32). To impart selectivity to diamond electrode, it was subjected to anodic pre-treatment (discussed in Section 6.2). The treated electrode exhibited a substantial shift in the positive direction for the peak potential for AA oxidation, thus making it possible to discriminate between the DA

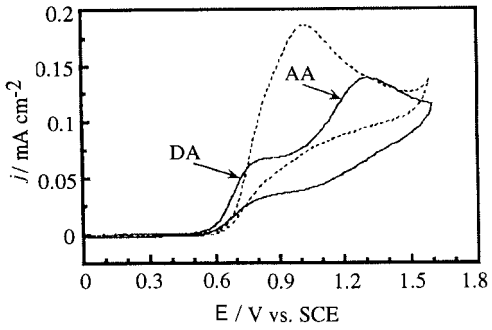

Fig. 32. Cyclic voltammograms for a 0.1 M $HClO_4$ solution containing 0.1 mM dopamine (DA) + 1 mM ascorbic acid (AA) at untreated (dashed line) and oxidized (solid line) diamond electrodes. Potential scan rate: 100 mV s^{-1} [148]. Reproduced by permission of The Electrochemical Society, Inc.

and AA responses. Electrode function is linear both in higher concentration range (1 to 70 μM DA, 1 mM AA) and in lower concentration range (0.1 to 1 μM DA, 0.1 mM AA); detection is possible by using voltammetry and cronoamperometry, respectively [148, 149]. Similarly, uric acid can easily be determined in a background of excess of ascorbic acid, as current peaks of uric acid and ascorbic acid are well resolved on the anodic cyclic voltammograms.

Compared to conventional (macroscopic) electrodes discussed hitherto, microelectrodes are known to possess several unique properties, including reduced *IR* drop, high mass transport rates and the ability to achieve steady-state conditions. Diamond microelectrodes were first described recently: diamond was deposited on a tip of electrochemically etched tungsten wire. The wire is further sealed into glass capillary. The microelectrode has a radius of few μm [150]. Because of a nearly spherical diffusion mode, voltammograms for the microelectrodes in $Ru(NH_3)_6^{3-}$ and $Fe(CN)_6^{4-}$ solutions are S-shaped, with a limiting current plateau (Fig. 33a), unlike those for macroscopic plane-plate electrodes that exhibit linear diffusion (see e.g. Fig. 18). The electrode function is linear over the micro- and submicromolar concentration ranges (Fig. 33b) [151].

These results, even if obtained on a laboratory scale, demonstrate the great potentialities of diamond electrodes in electroanalysis.

6.5 Diamond-Like Carbon Electrodes

In Section 2 we showed that the properties of amorphous carbon vary over a wide range. Graphite-like thin films are similar to other carbonaceous materials (glassy carbon, and the like) in their electrode behavior. Redox reactions proceed in a quasi-irreversible regime on these films. In particular, the cathodic reduction of nitrate previously studied on crystalline diamond electrodes (see Section 6.4.2) was performed with amorphous carbon films prepared by UHV laser deposition and comprising both sp^2- and sp^3-carbon [152]. Reduction current density as high as 2 mA cm^{-2} was reached in neutral or alkaline solutions. The use of such electrodes in microgravimetry is discussed [153].

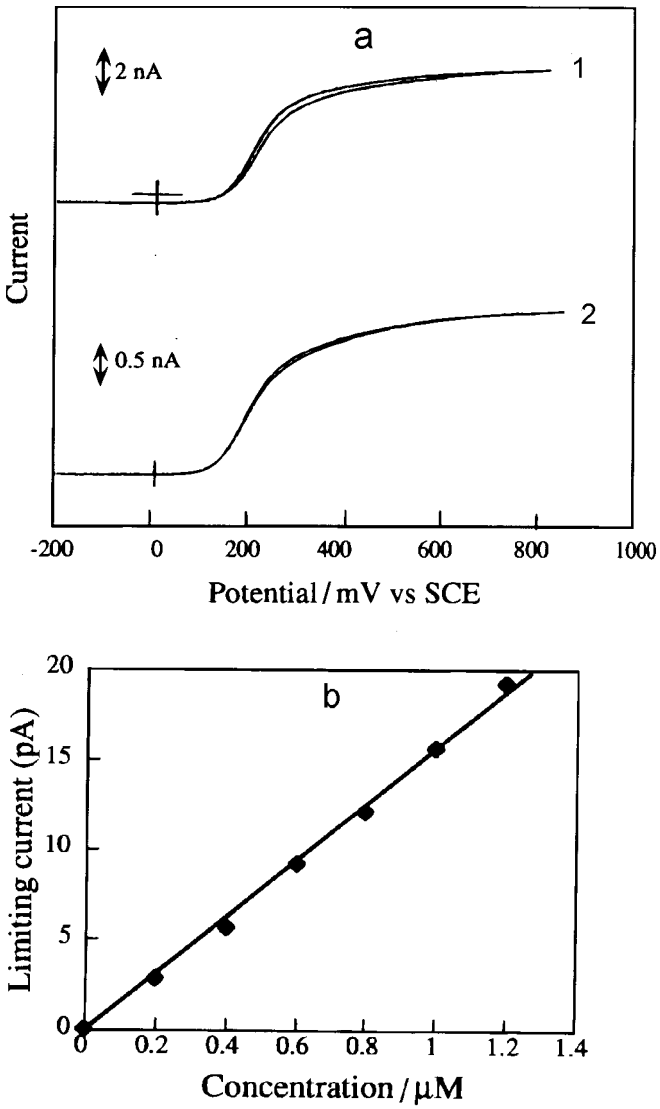

Fig. 33. (a) Cyclic voltammograms for 1 mM $K_4Fe(CN)_6$ oxidation at diamond microelectrodes in 0.1 M KCl solution. Potential scan rate: 10 mV s^{-1}; electrode radii: (1) 20 μm, (2) 6 μm. (b) Calibration curve for the 20-μm-radius microelectrode [151]. Reproduced by permission of The Electrochemical Society, Inc.

On the contrary, no oxidation or reduction current peaks were observed on the sp^3-carbon-comprising wide-gap DLC ($E_g \sim 1.7$ eV) electrodes in $Ce^{3+/4+}$, $Fe(CN)_6^{3-/4-}$, and quinone/hydroquinone redox systems, as already mentioned in Section 6.3. Thus, we conclude that DLC is electrochemically inactive in itself. It gains electrochemical activity upon introducing a significant (ca. 10 %) admixture of platinum to the film bulk. Figure 34 shows the dependence of the $Fe(CN)_6^{3-}$ reduc-

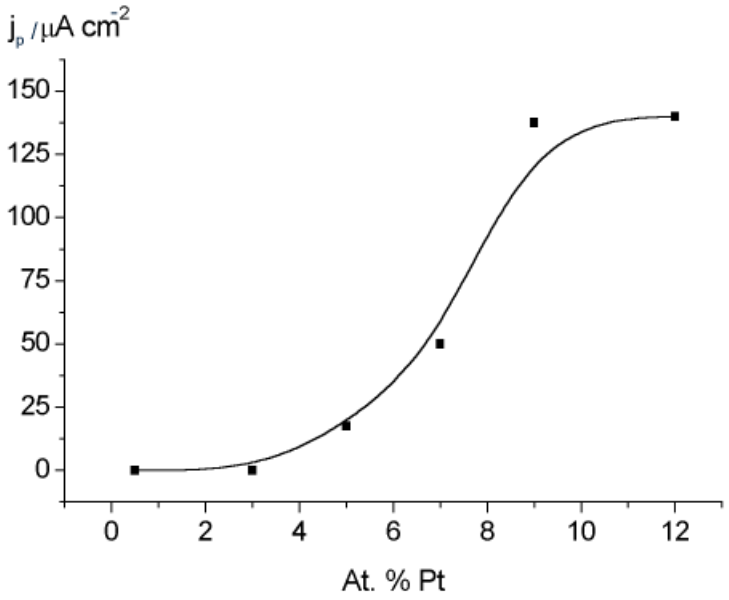

Fig. 34. Dependence of the $Fe(CN)_6^{3-}$ reduction peak current on the Pt content in DLC (a-C:H) thin-film electrodes. Solution of 0.01 M $K_3Fe(CN)_6 + 0.5$ M H_2SO_4. Data of Yu. V. Pleskov, Yu. E. Evstefeeva and A. M. Baranov.

tion peak current on the Pt content. The platinum-rich DLC:Pt electrodes qualitatively resemble the above-discussed crystalline boron-doped diamond electrodes in their electrochemical characteristics. The oxidation and reduction reactions proceed as irreversible reactions under mixed diffusion-kinetic control and have moderate overvoltage [63].

By the method of introducing Pt into the DLC, the platinum metal is assumed to be distributed over the carbonaceous material bulk as discrete atoms or clusters [154]. Essentially, Pt is not a dopant in the DLC, in the sense that the term is used in semiconductor physics. Nor is the percolation threshold surpassed, since the admixture of Pt (not exceeding 15 at. %) did not affect the a-C:H resistivity, as was shown by impedance spectroscopy tests: $\rho \sim 10^5$ Ω cm, like that of the undoped DLC (see Table 3). It was thus proposed that the Pt effect is purely catalytic one: Pt atoms on the DLC surface are the active sites on which adsorption and/or charge transfer is enhanced [75]. (And the contact of the carbon matrix to the Pt clusters is entirely ohmic.) This conclusion was corroborated by the studies of Co tetramethylphenylporphyrin reaction kinetics at the DLC:Pt electrodes [155]: redox reactions involving the Co central ion proceed partly under the adsorption of the porphyrin ring on the electrode.

These data offer basic possibilities of developing efficient electrodes made of corrosion-resistant carbonaceous material (DLC) by introducing a small admixture of an electrocatalyst metal, like Pt, into its bulk. A simultaneous magnetron sputtering of carbon and Pt targets is best suited for the purpose. When using CVD techniques, a volatile Pt compound should be added to the reaction gas mixture.

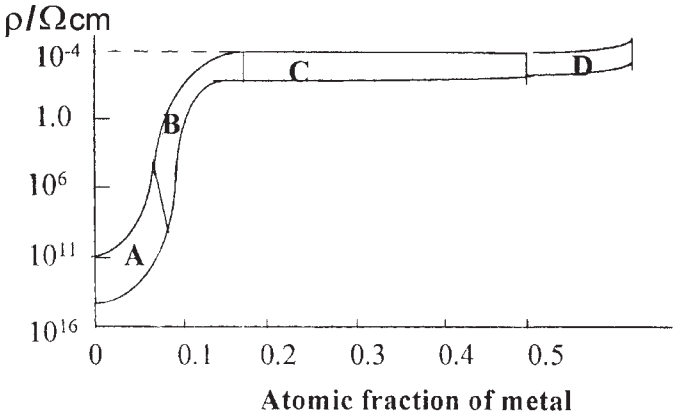

Fig. 35. The relationships between the atomic fraction of metal admixture in DLC and resistivity [157]. Reproduced by permission of The Electrochemical Society, Inc.

At still higher amounts of metal added to the carbon matrix, another type of the DLC-metal composite electrodes was obtained. The relationships between the atomic fraction of metal admixture and the resistivity are schematically shown on Fig. 35. According to [156], in films with resistivities equal to or exceeding 10^5 Ω cm (like the above-discussed DLC:Pt electrodes), the metal atoms are believed to intercalate into the DLC network structure (area A on Fig. 35). For films with 10^5–10^{-2} Ω cm resistivities, metal forms an amorphous network throughout the diamond-like carbon network, the metal concentration exceeding the percolation threshold (area B). For films with resistivities in the range from 10^{-2} to 10^{-4} Ω cm (area C), the metal fills in the nanopores in the DLC [157, 158]. They were fabricated by microwave plasma-assisted deposition. W, Cr, and Hf metals were introduced to DLC to the extent of 12 to 25 at. %. At such a metal concentration, the film resistivity dropped to $\sim 10^{-3}$ Ω cm. With increase in the W or Cr content, the hydrogen evolution overvoltage decreases steeply. At still higher metal concentration (>50 at. %, area D), the DLC network breaks down.

Nitrogenation is another method to impart electrical conductance to amorphous diamondlike carbon. Such a-C:N:H films were deposited from $N_2 + CH_4$ plasma source [159, 160]. The conductance in a-C:N:H films is probably due to the hopping of electrons between localized trapping centers (point defects), rather than to free carrier transport in the allowed energy bands. The increase in N_2/CH_4 ratio in the gas mixture leads to a decrease in electrical resistivity ρ and optical bandgap of the films from $3 \cdot 10^{10}$ to $5 \cdot 10^6$ Ω cm and from 1.3 to 0.6 eV, respectively. Simultaneously, the concentration of electrically active point defects increased significantly and charge transfer at the a-C:N:H film/redox electrolyte interface was facilitated. This is shown in Fig. 36 as the log ρ dependence of peak-to-peak potential difference ΔE_p for cyclic voltammograms taken in the $Fe(CN)_6^{3-/4-}$ system: the higher the N content (the lower ρ), the less irreversible is the electrode reaction.

One more variety of amorphous carbon is the so-called tetrahedral amorphous carbon (ta-C). Unlike the above-discussed a-C:H films, ta-C contains practically

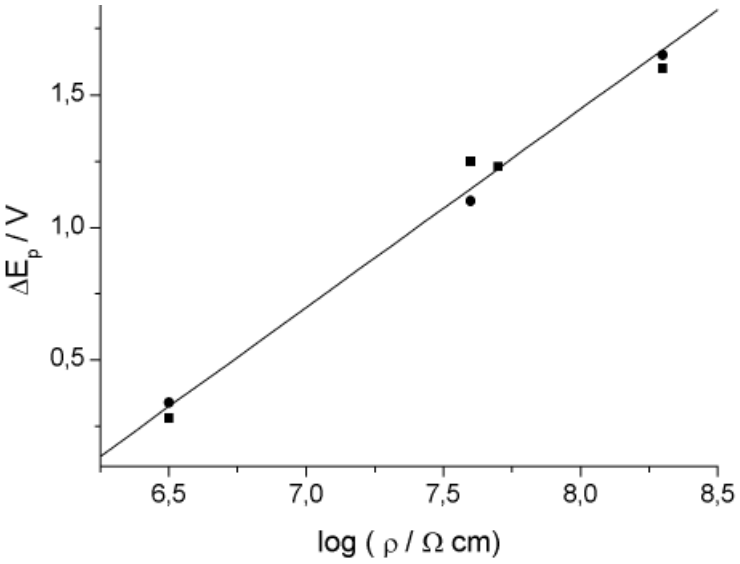

Fig. 36. Dependence of the current peak potentials difference ΔE_p on the logarithm of a-C:N:H films resistivity for the cyclic voltammograms taken in 1 N H_2SO_4 + 0.005 N $Fe(CN)_6^{3-}$ + 0.005 N $Fe(CN)_6^{4-}$ solution. The potential scan rate is 5 mV s^{-1} [160].

no hydrogen; the sp^3 carbon fraction in ta-C can be as high as 85% [161]. Nitrogen-incorporated ta-C, deposited from C and N ion source, turned out to be excellent anode material for chlorine evolution [162]. At the atomic fraction of nitrogen ~10%, the film resistivity approached 10 Ω cm. This material demonstrated more active charge transfer properties in a number of redox systems than H-terminated boron-doped diamond electrodes. In particular, a 100% current efficiency for anodic Cl_2 evolution from HCl solution was reached at $[Cl^-]$ as small as 50 mM (as compared with 2 M for boron-doped diamond electrodes). The films are extremely stable: more than 10^4 times the coulombs necessary for C complete oxidation to CO_2 can be passed during the Cl_2 evolution, without noticeable change in voltammetric properties.

This concise overview demonstrates the great promise of inexpensive and easy-to-prepare amorphous diamond-like carbon electrodes for electrosynthetic and electroanalytical applications.

7 Photoelectrochemistry of Diamond

The semiconductor nature of diamond manifests itself in a photoelectrochemical response caused by the photogeneration of free charge carriers. With the dielectric diamond, photoconductance (that is, an increase in the conductance due to an increase in majority carrier concentration) can be observed. With the conducting

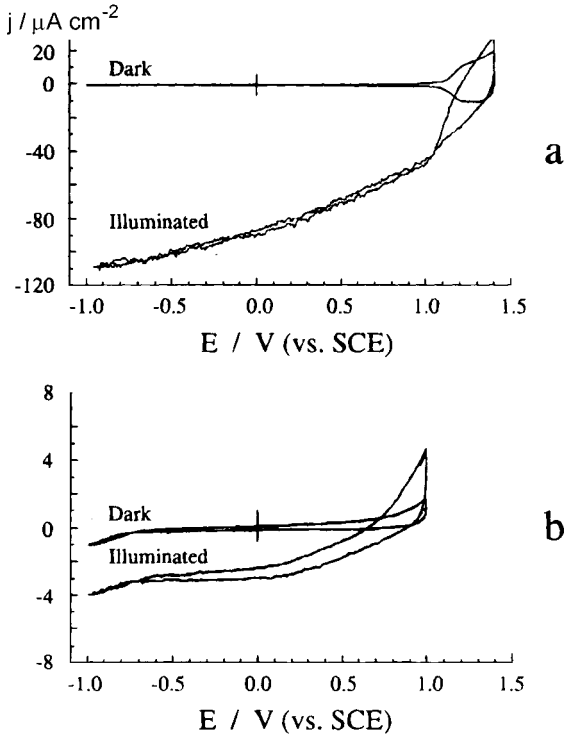

Fig. 37. Potential dependences of current in dark and under illumination for polycrystalline diamond electrode in 0.1 M KH_2PO_4 solution. Light quantum energy: (a) 6.4 eV; (b) 5 eV. Incident power density: 80 mW cm^{-2} [163]. Reproduced by permission of The Electrochemical Society, Inc.

(boron-doped) material, the interfacial phenomena arise owing to minority-carrier photogeneration effects that influence interface charging and/or electrode processes. Photocurrent would be recorded in the potentiostatic regime; photopotential, in the galvanostatic or coulostatic regime.

In early stages of the photoelectrochemistry of diamond, the electrodes were studied under sub-bandgap illumination [11]. Since the diamond bandgap E_g is as wide as 5.5 eV (Table 1), visible and long-wavelength ultraviolet light obviously should not be able to excite valence band electrons to the conduction band. The free carrier generation was due to some light-sensitive impurity or defect states in the diamond forbidden band (the so-called extrinsic, or impurity, photosensitivity). Only recently, by using an excimer laser as a source of light with high-energy quanta (wavelength of 193 nm, which corresponds to $h\nu = 6.4$ eV), photocurrent vs. potential curves were recorded for diamond electrodes under the band-to-band excitation (the intrinsic photosensitivity) [163]. Figure 37 clearly shows the large difference in the (cathodic) photocurrent under the supra-bandgap (Fig. 37a) and sub-bandgap (Fig. 37b) excitation. With sub-bandgap illumination, the quantum yield used to be $\cong 0.01$ % [164]. Whereas under the supra-bandgap illumination, the quantum yield is as high as 34 % (although it decreases with increasing incident power density, probably due to enhanced recombination). Open-circuit illumination of diamond electrodes yields a positive potential shift, as would be expected for p-type semiconductors

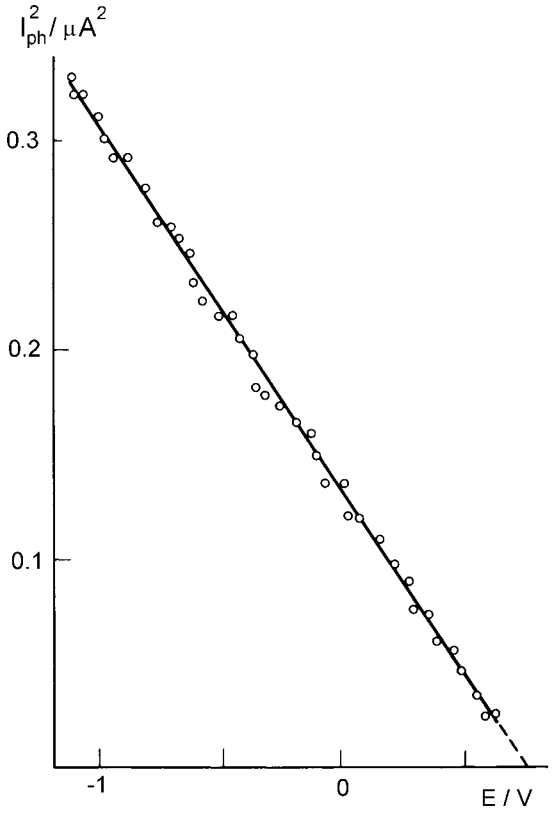

Fig. 38. Potential dependence of photocurrent squared for polycrystalline diamond electrode in 1 M KCl solution. Potentials given vs. SCE. Reprinted from [11]. Copyright (1987), with permission from Elsevier Science.

[6]. And yet in addition to the cathodic photocurrent, characteristic of the p-type semiconductor, occasionally anodic photocurrent was observed [12, 66, 165]. The anodic photocurrent is still not clearly understood.

Figure 37 shows that the photocurrent density increases in absolute value with cathodic polarization. To gain greater insight into this effect, we plotted the photocurrent squared as a function of potential (Fig. 38) [11]. This plot is the photoelectrochemical equivalent of the better known Mott–Schottky plot (compare Fig. 11). Both plots reflect the potential dependence of the space charge region thickness in semiconductor diamond. Upon illumination, the photogenerated charge carriers of different sign are separated in the electric field existing in the space charge region. The minority carriers (electrons in the boron-doped diamond) migrate to the interface to be consumed in the electrochemical reaction or, in coulostatic regime, to charge the interface. The majority carriers (holes) migrate to the diamond bulk, propagate to the ohmic contact and eventually to the external circuit of the electrochemical cell. Hence, the thicker the space charge region over which the minority carriers are collected, the higher the photocurrent. By extrapolating the line in Fig. 38 to $I_{ph} \rightarrow 0$, one obtains the flat-band potential just as one does with the Mott–Schottky line (Fig. 11). Both methods would yield similar results.

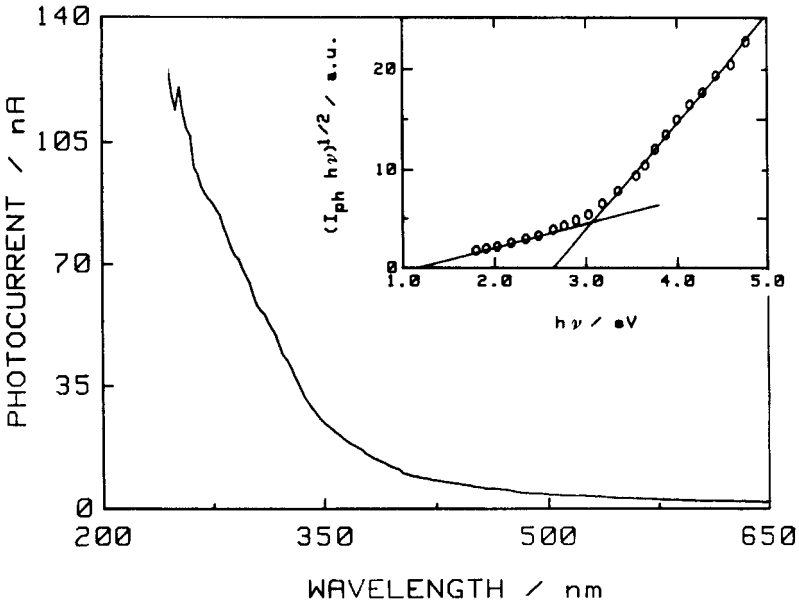

Fig. 39. Cathodic photocurrent spectrum for a polycrystalline diamond electrode exposed to 0.5 M H_2SO_4 solution at a potential of 0.05 V vs. NHE. Inset: determination of the threshold energy assuming indirect electron transitions [66]. Reproduced by permission of The Electrochemical Society, Inc.

Figure 39 gives a typical cathodic photocurrent I_{ph} spectrum taken under sub-bandgap illumination ($h\nu \leq E_g$) of a polycrystalline diamond electrode. The inset in the figure shows the treatment of the spectrum in $(I_{ph} \cdot h\nu)^{1/2}$ vs. $h\nu$ coordinates, which is common practice for determination of threshold energies of the indirect electron transitions being the basis of free carrier photogeneration (see [6] for more details). Occasionally, the plots comprise two linear sections giving two threshold energies (see Fig. 39). The problem of identification of the physical nature of the energy levels in the diamond bandgap, involved in the photocurrent generation, is far from a solution. Some transitions with the threshold energy close to 4 eV were identified with the phototransition of valence band electrons to the nitrogen N^+ levels located 1.7 eV below the conduction band bottom E_c [165].

Illumination of diamond electrode may induce some fine effects. In particular, the morphology of Cu electrodeposit, plated in dark and at an illuminated diamond surface, is different. Moreover, a "photographic memory effect" was observed with polycrystalline diamond electrodes: the Cu "dark" electrodeposition on a pre-illuminated electrode yields morphology that is characteristic of a deposit produced at illuminated electrodes. This effect is hypothesized to be caused by "subsurface" hydrogen in diamond [166].

The above-discussed photocurrent measurements were performed under the steady-state illumination of electrodes. In the pulse illumination mode, the photo-

potential magnitude and the dynamics of its decay on the switching-off light would be measured [164, 167, 168]. The photogenerated minority-carrier flux results in electrode capacitance charging; hence, in a shift of open-circuit potential. By using a somewhat modified equivalent circuit of Fig. 10b, to allow for the charging of surface states, the photopotential response was analyzed and adequately modeled. This approach yielded the equivalent circuit elements (resistances and capacitances) that agree with those directly measured using the impedance spectroscopy method, thus proving the self-consistency of the approach.

The photocurrent decay, under pulsed illumination, is strongly accelerated upon anodic or O-plasma oxidation of diamond surface. This effect is believed to be due to removal of the above-mentioned subsurface hydrogen [169].

Photocurrent-potential curves and photocurrent spectra have been reported for DLC electrodes [61, 62, 170]. Under illumination, the DLC demonstrates properties of an intrinsic wide-gap semiconductor or insulator. By treating the spectra in the above-described way, the mobility gap in this disordered carbon material was estimated.

8 Electrochemical and Photoelectrochemical Characterization of Diamond

We briefly list the methods of electrochemical characterization, discussed at length in previous sections:

- bulk resistivity ρ determination from the "series" resistance measured by the impedance-spectroscopy techniques (Section 5.1);
- uncompensated acceptor concentration N_A determination either from Mott–Schottky plots (Section 5.1) or by the nonlinear impedance method (Section 5.2);
- flat-band potential E_{fb} determination from Mott–Schottky plots (Section 5.1).

Photoelectrochemical measurements also provide an approach to the determination of electrophysical characteristics of diamond. In addition to the threshold energies of electron phototransitions, determined by the analysis of the photocurrent action spectra (Section 7), the diffusion length of minority carriers in polycrystalline diamond films was estimated (at 2 to 4 μm) by comparing light absorption spectra and open-circuit potential spectra [171].

Below, we discuss one more (photoelectrochemical) method for determination of the flat-band potential [40, 172]. The flat-band potential can be determined (i) as the photocurrent onset potential E_{onset}; (ii) from the dependence of electrode open-circuit photopotential $E_{oc}{}^{ph}$ on light intensity J, as the limiting value of E_{oc} at a sufficiently high J; and (iii) by extrapolating, to zero photocurrent, the potential dependence of the photocurrent j_{ph} squared (see Section 7). These methods are based on the concept

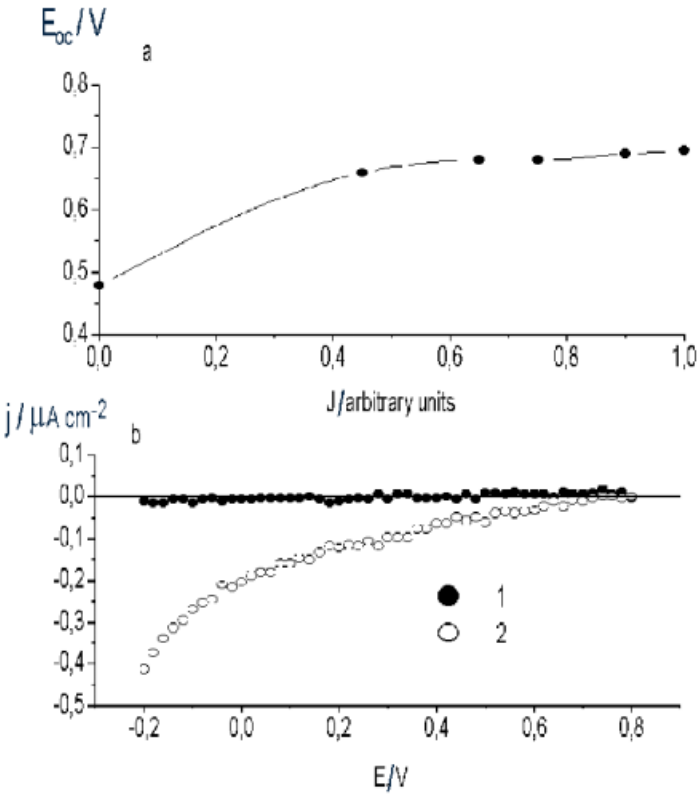

Fig. 40. (a) Dependence of the open-circuit potential E_{oc} on the illumination intensity J, and (b) dependence of the (1) dark current and (2) photocurrent density j_{ph} on the electrode potential E. Potentials given vs. Ag,AgCl electrode [172]. Reproduced by permission of The Electrochemical Society, Inc.

of photogenerated charge carrier separation in the electric field of the space charge region near the semiconductor/electrolyte interface [6]. Additionally, method (ii) is based on the assumption that the charge carrier photogeneration results in unbending of energy bands, which causes a shift of electrode potential. At sufficiently high illumination intensity, the bands become fully unbent; the limiting value of the open-circuit electrode potential is thus the flat-band potential E_{fb}.

To compare these methods, in Fig. 40 we show (a) E_{oc} vs. J and (b) j_{ph} vs. E plots for a CVD single crystal thin-film electrode. We see that with increase in illumination intensity J, the open-circuit potential E_{oc} approaches a limit of 0.7 V, which is close to the photocurrent onset potential (0.75 V). [The photocurrent density squared vs. potential dependence for this electrode, although far from linear (unlike that of Fig. 38), by the extrapolation to $j_{ph} \rightarrow 0$ gives the potential value of approx. 0.65 V.] It is concluded that, on the whole, methods (i) and (ii) are in a good agreement and can be used in the determination of the flat-band potential. Similar results were obtained with HTHP single crystals.

9 Conclusions

As evidenced by the foregoing account, the recent decade of intensive studies in the electrochemistry of diamond resulted in the formation of a self-consistent, if incomplete, view of electrochemical behavior of this new electrode material. At the same time, scatter of data and discrepancies that still exist between the data of different research groups call for better film quality and their reliable evaluation.

Recent studies revealed great potentialities of the boron-doped diamond electrodes for electroanalytical and environmental-oriented applications.

The very fact of emergence of a new field in electrochemistry is embodied in regularly held international conferences and symposia concerning the electrochemistry of diamond [173–178]. A few concise journal articles on the diamond electrochemistry were published recently [38, 179].

One may expect that future work on the electrochemistry of diamond should take two paths, namely, an extensive investigation (search for new processes and applications of the carbon allotropes in the electrochemical science and engineering) and intensive one (elucidation of the reaction mechanisms, revealing the effects of crystal structure and semiconductor properties on the electrochemical behavior of diamond and related materials). It is expected that better insight into these effects will result in the development of standard procedures for thin-film-electrodes growth, their characterization, and surface preparation.

It is also felt that some applications, even if to a limited extent, just are around the corner. Among them probably are corrosion–stable electrodes, like DSA, for the preparative electrolysis, microelectrodes for sensors and the electroanalytical purposes and electrode arrays for discharging toxic contaminants, among others.

Acknowledgements

The author gratefully acknowledges the contribution of his colleagues, M. D. Krotova, Yu E. Evstefeeva, I. G. Teremetskaya, and V. P. Varnin to the studies partly described in this review.

This work was supported in part by the Russian Foundation for Basic Research, project No. 01-03-32045, and NEDO International Joint Research Grant Program (project 011MB9).

10 References

1. V. S. Vavilov, A. A. Gippius, E. A. Konorova, Electronic and Optical Processes in Diamond (in Russian), Nauka, Moscow, 1985.
2. The Properties of Natural and Synthetic Diamond, J. Field (ed.), Academic Press, London and New York, 1992.
3. K. E. Spear, J. Am. Ceram. Soc., 72, 171 (1989).

4. V. S. Vavilov, Usp. Fiz. Nauk, 167, 17 (1997).
5. V. S. Vavilov, Usp. Fiz. Nauk, 164, 287 (1994).
6. Yu. V. Pleskov, Yu. Ya. Gurevich, Semiconductor Photoelectrochemistry, Consultants Bureau, New York, 1986.
7. M. Iwaki, S. Sato, K. Takahashi, H. Sakairi, Nucl. Instrum. and Methods, 209/210, Pt II, 1129 (1983).
8. S. L. Lee, S. J. Liu, J. Hwang, J. Electrochem. Soc., 141, 291 (1994).
9. B. Miller, R. Kalish, L. C. Feldman, A. Katz, N. Moriya, K. Short, A. E. White, J. Electrochem. Soc., 141, L41 (1994).
10. J. Robertson, Advances in Physics, 35, 317 (1986).
11. Yu. V. Pleskov, A. Ya. Sakharova, M. D. Krotova, L. L. Bouilov, B. V. Spitsyn, J. Electroanal. Chem., 228, 19, (1987).
12. K. Patel, K. Hashimoto, A. Fujishima, J. Photochem. and Photobiol. A: Chem., 65, 419 (1992).
13. B. V. Spitsyn, L. L. Bouilov, B. V. Derjaguin, J. Cryst. Growth, 52, 219 (1981).
14. D. V. Fedoseev, V. P. Varnin, B. V. Derjaguin, Usp. Khimii, 53, 753 (1984).
15. R. Ramesham, Thin Solid Films, 339, 82 (1999).
16. J. C. Angus, H. B. Martin, U. Landau, Y. E. Evstefeeva, B. Miller, N. Vinokur, New Diamond and Frontier Carbon Technol., 9, 175 (1999).
17. M. Werner, R. Job, A. Zaitsev, W. R. Fahrner, W. Seibert, C. Johnston, P. R. Chalker, Phys. Stat. Sol. (a), 154, 385 (1996).
18. H. Masuda, M. Watanabe, K. Yasui, D. A. Tryk, A. Fujishima, Adv. Mater., 12, 444 (2000).
19. V. P. Novikov, V. P. Dimont, Dokl. Akad. Nauk Belarusi, 40, 60 (1996).
20. P. Bou, L. Vandenbulcke, J. Electrochem. Soc., 138, 2991 (1991).
21. K. Hashimoto, Y. Muraki, R. Baba, A. Fujishima, J. Electroanal. Chem., 397, 339 (1995).
22. L.-F. Li, D. A. Totir, N. Vinokur, B. Miller, G. Chottiner, E. A. Evans, J. C. Angus, D. A. Scherson, J. Electrochem. Soc., 145, L85 (1998).
23. J. E. Butler (private communication).
24. P. J. Fallon, L. M. Brown, Diamond and Related Mater., 2, 1004 (1993).
25. Yu. Pleskov, A. Tameev, V. Varnin, I. Teremetskaya, A. Baranov, Fiz. Tech. Poluprovodn., 31, 1142 (1997).
26. Yu. V. Pleskov, A. R. Tameev, V. P. Varnin, I. G. Teremetskaya, J. Solid State Chem., 3, 25 (1998).
27. D. M. Malta, J. A. von Windheim, H. A. Wynands, B. A. Fox, J. Appl. Phys., 77, 1536 (1995).
28. M. Deguchi, M. Kitabatake, T. Hirao, Thin Solid Films, 281–282, 267 (1996).
29. L. S. Pan, S. Han, D. R. Kania, M. A. Plano, M. I. Landstrass, Diamond and Related Mater., 2, 820 (1993).
30. A. Ya. Sakharova, A. E. Sevastyanov, Yu. V. Pleskov, G. L. Teplitskaya, V. V. Surikov, A. A. Voloshin, Elektrokhimiya, 27, 263 (1991).
31. A. E. Ukshe, E. A. Ukshe, Elektrokhimiya, 17, 776 (1981).
32. N. G. Bukun, A. E. Ukshe, E. I. Moskvina, E. A. Ukshe, Elektrokhimiya, 21, 269 (1985).
33. G. A. Sokolina, A. A. Botev, L. L. Bouilov, S. V. Bantsekov, O. I. Lazareva, A. F. Belyanin, Fiz. Tech. Poluprovodn., 24, 175 (1990).
34. N. Vinokur, B. Miller, Y. Avygal, R. Kalish, Electrochem. and Solid-State Lett., 1, 265 (1998).
35. S. Nath, J. I. B. Wilson, Diamond and Related Mater., 5, 65 (1996).
36. Y. Muto, T. Sugino, K. Kobashi, J. Shirafuji, Japan J. Appl. Phys., Pt. 2, 31, L4 (1992).

37. M. M. Bataineh, D. K. Reinhard, Diamond and Related Mater., 6, 1689 (1997).
38. H. B. Martin, A. Argoitia, U. Landau, A. B. Anderson, J. C. Angus, J. Electrochem. Soc., 143, L133 (1996).
39. G. M. Swain, A. B. Anderson, J. C. Angus, MRS Bulletin, 23, 56 (1998).
40. V. M. Mazin, Yu. E. Evstefeeva, Yu. V. Pleskov, V. P. Varnin, I. G. Teremetskaya, V. A. Laptev, Elektrokhimiya, 36, 655 (2000).
41. J. W. Strojek, M. C. Granger, G. M. Swain, T. Dallas, M. W. Holtz, Anal. Chem., 68, 2031 (1996).
42. R. Ramesham, M. F. Rose, Thin Solid Films, 315, 222 (1998).
43. E. P. Smirnov, O. G. Taushkanova, V. B. Aleskovskii, Dokl. Akad. Nauk SSSR, 290, 901 (1986).
44. P. E. Pehrsson, M. Marchywka, J. P. Long, J. E. Butler in: Applications of Diamond Films and Related Materials: Proc. of 3rd Int. Conf., August 21–24, 1995, A. Feldman, Y. Tseng, W. A. Yarbrough, M. Yoshikawa, M. Murakawa (eds.), Gaitherburg, MD, USA, 1995, p. 267.
45. G. M. Swain, J. Electrochem. Soc., 141, 3382 (1994).
46. G. M. Swain, Adv. Mater., 6, 388 (1994).
47. Q. Chen, M. Granger, T. E. Lister, G. M. Swain, J. Electrochem. Soc., 144, 3806 (1997).
48. Z. Peilin, Z. Jianzhong, Y. Shenzhong, Z. Xikang, Z. Guoxiong, Fresenius J. Anal. Chem., 353, 171 (1995).
49. R. DeClements, G. M. Swain, J. Electrochem. Soc., 144, 856 (1997).
50. P. U. Natishan, A. Morrish, Mater. Res., 8, 269 (1989).
51. I. Garsia, A. Conde, J. J. de Danborenea, A. J. Vazquez, Thin Solid Films, 310, 217 (1997).
52. R. Ramesham, M. F. Rose, Corrosion Sci., 39, 2019 (1997).
53. R. Ramesham, M. F. Rose, Diamond Films and Technol., 7, 1 (1997).
54. C. H. Goeting, F. Jones, J. S. Foord, J. C. Eklund, F. Marken, R. G. Compton, P. R. Chalker, C. Johnston, J. Electroanal. Chem., 442, 207 (1997).
55. R. Ramesham, M. F. Rose, Diamond and Related Mater., 6, 17 (1997).
56. R. Ramesham, M. F. Rose, Thin Solid Films, 300, 144 (1997).
57. M. J. Marchywka, P. E. Pehrsson, S. C. Binary, D. Moses, J. Electrochem. Soc., 140, L19 (1993).
58. M. J. Marchywka, P. E. Pehrsson, D. J. Vestyck, D. Moses, Appl. Phys. Lett., 63, 3521 (1993).
59. P. E. Pehrsson, J. P. Long, M. J. Marchywka, J. E. Butler, Appl. Phys. Lett., 67, 3414 (1995).
60. A. T. Howe, J. Electrochem. Soc., 134, 2470 (1987).
61. A. Ya. Sakharova, Yu. V. Pleskov, F. Di Quarto, S. Piazza, C. Sunseri, S. S. Gerasimovich, V. V. Sleptsov, J. Electroanal. Chem., 398, 13 (1995).
62. A. Ya. Sakharova, Yu. V. Pleskov, F. Di Quarto, S. Piazza, C. Sunseri, S. S. Gerasimovich, V. V. Sleptsov, Elektrokhimiya, 32, 1298 (1996).
63. M. D. Krotova, Yu. E. Evstefeeva, Yu. V. Pleskov, V. V. Elkin, A. M. Baranov, Elektrokhimiya, 34, 1039 (1998).
64. C. Srividia, M. Sunkara, S. V. Babu in: Proc. 5th Int. Symp. on Diamond Materials, J. L. Davidson, W. D. Brown, A. Gicquel, B. V. Spitsyn, J. C. Angus, (eds.), The Electrochemical Society, Pennington, NJ, USA (1998), p. 324.
65. J. R. Macdonald, W. B. Johnson in: Impedance Spectroscopy, J. R. Macdonald (ed.), J. Wiley, New York, 1987, p.1.
66. A. Ya. Sakharova, Yu. V. Pleskov, F. Di Quarto, S. Piazza, C. Sunseri, I. G. Teremetskaya, V. P. Varnin, J. Electrochem. Soc., 142, 2704 (1995).
67. W. P. Kang, Y. Gurbuz, J. L. Davidson, D. V. Kerns, J. Electrochem. Soc., 141, 2231 (1994).

68. J. A. von Windheim, V. Venkatesan, D. M. Malta, K. Das, Diamond and Related Mater., 2, 841 (1993).
69. Yu. E. Evstefeeva, M. D. Krotova, Yu. V. Pleskov, V. V. Elkin, V. P. Varnin, I. G. Teremetskaya, Elektrokhimiya, 34, 1171 (1998).
70. A. Sakharova, L. Nyikos, Yu. Pleskov, Electrochim. Acta, 37, 973 (1992).
71. Yu. V. Pleskov, V. Ya. Mishuk, M. A. Abaturov, V. V. Elkin, M. D. Krotova, V. P. Varnin, I. G. Teremetskaya, J. Electroanal. Chem., 396, 227 (1995).
72. R. Ramesham, Thin Solid Films, 322, 158 (1998).
73. Yu. V. Pleskov, V. Ya. Mishuk, M. A. Abaturov, V. V. Elkin, M. D. Krotova, V. P. Varnin, I. G. Teremetskaya, Elektrokhimiya, 33, 67 (1997).
74. B. A. Boukamp, Solid State Ionics, 20, 31 (1986).
75. Yu. V. Pleskov, Yu. E. Evstefeeva, M. D. Krotova, V. V. Elkin, A. M. Baranov, A. P. Dement'ev, Diamond and Related Mater., 8, 64 (1999).
76. Yu. E. Evstefeeva, M. D. Krotova, Yu. V. Pleskov, V. A. Laptev, Elektrokhimiya, 35, 138 (1999).
77. Yu. V. Pleskov, Yu. E. Evstefeeva, M. D. Krotova, V. A. Laptev, Electrochim. Acta, 44, 3361 (1999).
78. Yu. E. Evstefeeva, M. D. Krotova, Yu. V. Pleskov, V. M. Mazin, V. V. Elkin, V. Ya. Mishuk, V. P. Varnin, I. G. Teremetskaya, Elektrokhimiya, 34, 1493 (1998).
79. Z. Hens, W. P. Gomes, Phys. Chem. and Chem. Phys., 1, 3607 (1999).
80. Yu. V. Pleskov, V. V. Elkin, M. A. Abaturov, M. D. Krotova, V. Ya. Mishuk, V. P. Varnin, I. G. Teremetskaya, J. Electroanal. Chem., 413, 105 (1996).
81. K. Honda, T. N. Rao, D. A. Tryk, A. Fujishima, M. Watanabe, K. Yasui, H. Masuda, J. Electrochem. Soc., 147, 659 (2000).
82. R. De Levie, in: Advances in Electrochemistry and Electrochemical Engineering, Vol. 6, P. Delahay (ed.), J. Wiley, New York, 1967, p. 329.
83. M. A. Abaturov, V. V. Elkin, M. D. Krotova, V. Ya. Mishuk, Yu. V. Pleskov, A. Ya. Sakharova, Elektrokhimiya, 31, 1214 (1995).
84. G. Oskam, D. Vanmaekelbergh, J. J. Kelly, J. Electroanal. Chem., 315, 65 (1991).
85. E. C. Dutoit, R. L. Van Meirhaeghe, F. Cardon, W. P. Gomes, Ber. Bunsenges. phys. Chem., 79, 1206 (1975).
86. J. F. McCann, S. P. S. Badwal, J. Electrochem. Soc., 129, 551 (1982).
87. Yu. V. Pleskov, Yu. E. Evstefeeva, M. D. Krotova, V. V. Elkin, V. M. Mazin, V. Ya. Mishuk, V. P. Varnin, I. G. Teremetskaya, J. Electroanal. Chem., 455, 139 (1998).
88. Z. Kerner, T. Pajkossy, J. Electroanal Chem., 448, 139 (1998).
89. M. C. Granger, G. M. Swain, J. Electrochem. Soc., 146, 4551 (1999).
90. P. Delahay, New Instrumental Methods in Electrochemistry, Interscience Publishers, New York, 1954.
91. Z. Galus, Teoretyczne podstavy elektroanalizy chemicznej, Panstwowe Wydawnictwo Naukowe, Warsaw, Poland, 1971.
92. J. Xu, M. C. Granger, Q. Chen, J. W. Strojek, T. E. Lister, G. M. Swain, Anal. Chem., 69, 591A (1997).
93. G. M. Swain, R. Ramesham, Anal. Chem., 65, 345 (1993).
94. Yu. E. Evstefeeva, Yu. V. Pleskov, V. P. Varnin, I. G. Teremetskaya, Elektrokhimiya, 34, 234 (1998).
95. Y. Maeda, K. Sato, R. Ramaraj, A. Fujishima, Electrochim. Acta, 44, 3441 (1999).
96. S. Alehashem, F. Chambers, J. W. Strojek, G. M. Swain, R. Ramesham, Anal. Chem., 67, 2812 (1995).
97. N. Vinokur, B. Miller, Y. Avyigal, R. Kalish, J. Electrochem. Soc., 143, L238 (1996).
98. R. Ramesham, M. F. Rose, J. Mater. Sci. Lett., 16, 1693 (1997).
99. R. Ramesham, Sensors and Actuators B, 50, 131 (1998).

100. S. Yang, J. Zhu, Y. Yao, X. Lu, X. Zhang, Proc. Soc. Photo-Opt. Instrum. Eng., 2364, 562 (1994).
101. V. Fisher, D. Gandini, S. Laufer, E. Blank, C. Comninellis, Electrochim. Acta, 44, 521 (1998).
102. A. Neudeck, F. Marken, R. G. Compton, Electroanalysis, 11, (1999).
103. B. Fausett, M. C. Granger, M. L. Hupert, J. Wang, G. M. Swain, D. M. Gruen, Electroanalysis, 12, 7 (2000).
104. A. D. Modestov, Yu. V. Pleskov, V. P. Varnin, I. G. Teremetskaya, Elektrokhimiya, 33, 60 (1997).
105. M. Awada, J. W. Strojek, G. M. Swain, J. Electrochem. Soc., 142, L42 (1995).
106. J. Wang, G. M. Swain, T. Tachibana, K. Kobashi, J. New Electrode Mater. for Electrochem. Systems, 3, 75 (2000).
107. C. H. Goeting, F. Marken, A. Gutierrez-Sosa, R. G. Compton, J. S. Foord, New Diamond and Frontier Carbon Technol., 9, 207 (1999).
108. R. G. Compton, F. Marken, C. H. Goeting, R. A. J. McKeown, J. S. Foord, G. Scarsbrook, R. S. Sussman, A. J. Whitehead, Chem. Commun., 1961 (1998).
109. C. H. Goeting, J. S. Foord, F. Marken, R. G. Compton, Diamond and Related Mater., 8, 824 (1999).
110. A. D. Modestov, Yu. E. Evstefeeva, Yu. V. Pleskov, V. M. Mazin, V. P. Varnin, I. G. Teremetskaya, J. Electroanal. Chem., 431, 211 (1997).
111. J. van de Lagemaat, D. Vanmaekelbergh, J. J. Kelly, J. Electroanal. Chem., 475, 139 (1999).
112. A. M. Kuznetsov, Electrochim. Acta, 13, 1293 (1968).
113. Yu. V. Pleskov, Yu. Ya. Gurevich, in: Modern Aspects of Electrochemistry, Vol. 16, B. E. Conway, R. E. White, J. O'M. Bockris (eds.), Plenum Press, New York, 1985, p. 189.
114. T. N. Rao, D. A. Tryk, K. Hashimoto, A. Fujishima, J. Electrochem. Soc., 146, 680 (1999).
115. I. Yagi, H. Notsu, T. Kondo, D. A. Tryk, A. Fujishima, J. Electroanal Chem., 473, 173 (1999).
116. H. B. Martin, A. Argoitia, J. C. Angus, U. Landau, J. Electrochem. Soc., 146, 2959 (1999).
117. T. Yano, D. A. Tryk, K. Hashimoto, A. Fujishima, J. Electrochem. Soc., 145, 1870 (1998).
118. T. Yano, E. Popa, D. A. Tryk, K. Hashimoto, A. Fujishima, J. Electrochem. Soc., 146, 1081 (1999).
119. N. Katsuki, E. Takahashi, M. Toyoda, T. Kurosu, M. Iida, S. Wakita, Y. Nishiki, T. Shimamune, J. Electrochem. Soc., 145, 2358 (1998).
120. N. Katsuki, S. Wakita, Y. Nishiki, T. Shimamune, Y. Akiba, M. Iida, Jpn. J. Appl. Phys., 36 (Part 2), L260 (1997).
121. A. Perret, W. Haenni, P. Niedermann, N. Skinner, C. Comninellis, D. Gandini in: Proc. 5th Int. Symp. on Diamond Materials, J. L. Davidson, W. D. Brown, A. Gicquel, B. V. Spitsyn, J. C. Angus, (eds.), The Electrochemical Society, Pennington, NJ, USA (1998), p. 275.
122. J. J. Carey, C. S. Christ, S. N. Lowery, US Patent 5399247 (1995).
123. F. Beck, H. Krohn, W. Kaiser, M. Fryda, C. P. Klages, L. Schaefer, Electrochim. Acta, 44, 525 (1998).
124. J. W. Glesener, P. M. Natishan, W. E. O'Grady, J. Aiken, A. A. Morrish, Mater. Lett. 37, 138 (1998).
125. N. Vinokur, B. Miller, Y. Avyigal, R. Kalish in: Proc. 5th Int. Symp. on Diamond Materials, J. L. Davidson, W. D. Brown, A. Gicquel, B. V. Spitsyn, J. C. Angus (eds.), The Electrochemical Society, Pennington, NJ, USA (1998), p. 267.

126. V. I. Shapoval, I. A. Novosyolova, V. V. Malyshev, H. B. Kushkhov, Electrochim. Acta, 40, 1031 (1995).
127. R. DeClements, G. M. Swain, T. Dallas, M. W. Holtz, R. D. Herrik II, J. L. Stickney, Langmuir, 12, 6578 (1996).
128. J. Xu, Q. Chen, G. M. Swain, Anal. Chem., 70, 3146 (1998).
129. M. D. Koppang, M. Witek, J. Blau, G. M. Swain, Anal. Chem., 71, 1188 (1999).
130. A. Perret, W. Haenni, N. Skinner, X.-M. Tang, D. Gandini, C. Comninellis, B. Correa, G. Foti, Diamond and Related Mater., 8, 820 (1999).
131. Z. Wu, T. Yano, D. A. Tryk, K. Hashimoto, A. Fujishima, Chem. Lett., 43 (1998).
132. R. Tenne, K. Patel, K. Hashimoto, A. Fujishima, J. Electroanal. Chem., 347, 409 (1993).
133. C. Reuben, E. Galun, H. Cohen, R. Tenne, R. Kalish, Y. Muraki, K. Hashimoto, A. Fujishima, J. E. Butler, C. Levy-Clement, J. Electroanal. Chem., 396, 233 (1995).
134. F. Bouamrane, A. Tadjeddine, J. E. Butler, R. Tenne, C. Levy-Clement, J. Electroanal. Chem., 405, 95 (1996).
135. P.-A. Michaud, E. Mahe, W. Haenni, A. Perret, C. Comninellis, Electrochem. and Solid-State Lett., 3, 77 (2000).
136. N. Vinokur, B. Miller, Y. Avyigal, R. Kalish, J. Electrochem. Soc., 146, 125 (1999).
137. C. H. Goeting, F. Marken, C. Salter, R. G. Compton, J. S. Foord, Chem. Commun., 1697 (1999).
138. L. F. Li, D. A. Totir, B. Miller, G. Chottiner, A. Argoitia, J. C. Angus, D. A. Scherson, J. Am. Chem. Soc., 119, 7875 (1997).
139. S. Nakabayashi, D. A. Tryk, A. Fujishima, N. Ohta, Chem. Phys. Lett., 300, 409 (1999).
140. F. Bouamrane, A. Tadjeddine, R. Tenne, J. E. Butler, R. Kalish, C. Levy- Clement, J. Phys. Chem. B, 102, 134 (1998).
141. J. Zhu, D. Lu, G. Zhang, J. Shanghai Univ., 2, 311 (1998).
142. A. J. Saterlay, C. Agra-Gutierrez, M. P. Taylor, F. Marken, R. G. Compton, Electroanalysis, 11, 1083 (1999).
143. M. C. Granger, J. Xu, J. W. Strojek, G. M. Swain, Anal. Chim. Acta, 397, 145 (1999).
144. T. E. Lister, J. W. Strojek, G. M. Swain in: Proc. 5th Int. Symp. on Diamond Materials, J. L. Davidson, W. D. Brown, A. Gicquel, B. V. Spitsyn, J. C. Angus, (eds.), The Electrochemical Society, Pennington, NJ, USA (1998), p. 377.
145. P. von Huth, R. Tenne, Abstracts, The Second International Mini-Symposium on Diamond Electrochemistry and Related Topics, June 8–9, 1998, Tokyo, Japan, p. S4.
146. S. Jolley, M. Koppang, T. Jackson, G. M. Swain, Anal. Chem., 69, 4099 (1997).
147. J. Xu, G. M. Swain, Anal. Chem., 70, 1502 (1998).
148. E. Popa, H. Notsu, T. Miwa, D. A. Tryk, A. Fujishima, Electrochem. and Solid-State Lett., 2, 49 (1999).
149. A. Fujishima, T. N. Rao, E. Popa, B. V. Sarada, I. Yagi, D. A. Tryk, J. Electroanal. Chem., 473, 179 (1999).
150. J. B. Cooper, S. Pang, S. Albin, J. Zheng, R. M. Johnston, Anal. Chem., 70, 464 (1998).
151. B. V. Sarada, T. N. Rao, D. A. Tryk, K. Hashimoto, A. Fujishima, J. Electrochem. Soc., 146, 1469 (1999).
152. F. Bouamrane, W. Kautek, M. Sahre, A. Tadjeddine, E. Rzepka, C. Levy-Clement in: Proc. 5th Int. Symp. on Diamond Materials, J. L. Davidson, W. D. Brown, A. Gicquel, B. V. Spitsyn, J. C. Angus, (eds.), The Electrochemical Society, Pennington, NJ, USA (1998), p. 309.
153. J.-M. Moon, S. Park, Y.-K. Lee, G. S. Bang, Y.-K. Hong, C. Park, I. C. Jeon, J. Electroanal. Chem., 464, 230 (1999).
154. K. I. Schiffmann, Mikrochim. Acta, 125, 107 (1997).
155. Yu. E. Evstefeeva, L. A. Khanova, Yu. V. Pleskov, A. M. Baranov, Elektrokhimiya, 35, 1277 (1999).
156. V. F. Dorfman, Thin Solid Films, 212, 267 (1992).

157. M. Sunkara, M. Wadsborn, E. Yeap, V. Ralchenko, B. N. Pypkin, M. L. Shubekin, S. V. Babu in: Proc. 5th Int. Symp. on Diamond Materials, J. L. Davidson, W. D. Brown, A. Gicquel, B. V. Spitsyn, J. C. Angus, (eds.), The Electrochemical Society, Pennington, NJ, USA (1998), p. 297.
158. M. K. Sunkara, H. Chandrasekaran, P. Koduri, New Diamond and Frontier Carbon Technol., 9, 407 (1999).
159. Yu. V. Pleskov, M. D. Krotova, V. I. Polyakov, A. V. Khomich, A. I. Rukovishnikov, B. L. Druz, I. Zaritskiy, Proc. Int. Conf. of the Mater. Res. Soc., Nov. 1999, Boston, Mass.
160. Yu. V. Pleskov, M. D. Krotova, V. I. Polyakov, A. V. Khomich, A. I. Rukovishnikov, B. L. Druz, I. Zaritskiy, Elektrokhimiya, 36, no. 9 (2000).
161. A. Gill, Diamond and Related Mater., 8, 428 (1999).
162. K. Yoo, B. Miller, R. Kalish, S. Xu, Electrochem. and Solid-State Lett., 2, 233 (1999).
163. L. Boonma, T. Yano, D. A. Tryk, K. Hashimoto, A. Fujishima, J. Electrochem. Soc., 144, L142 (1997).
164. Yu. V. Pleskov, V. P. Varnin, I. G. Teremetskaya, A. V. Churikov, J. Electrochem. Soc., 144, 175 (1997).
165. A. Ya. Sakharova, Yu. V. Pleskov, F. Di Quarto, S. Piazza, C. Sunseri, I. G. Teremetskaya, V. P. Varnin, Elektrokhimiya, 31, 188 (1995).
166. S. Yoshihara, K. Shinozaki, T. Shirakashi, K. Hashimoto, D. A. Tryk, A. Fujishima, Electrochim. Acta, 44, 2711 (1999).
167. Yu. V. Pleskov, J. Chem. Vapor Depos., 5, 126 (1996).
168. Yu. V. Pleskov, A. Ya. Sakharova, A. V. Churikov, V. P. Varnin, I. G. Teremetskaya, Elektrokhimiya, 32, 1164 (1996).
169. I. Yagi, K. Tsunosaki, D. A. Tryk, A. Fujishima, Electrochem. and Solid-State Lett., 2, 457 (1999).
170. A. Pinkowski, U. Stimming, J. Winter, J. Electrochem. Soc., 136, 1849 (1989).
171. Yu. V. Pleskov, A. Ya. Sakharova, E. V. Kasatkin, V. A. Shepelin, J. Electroanal. Chem., 344, 401 (1993).
172. Yu. V. Pleskov, V. M. Mazin, Yu. E. Evstefeeva, V. P. Varnin, I. G. Teremetskaya, V. A. Laptev, Electrochem. and Solid-State Lett., 3, 141 (2000).
173. Abstracts, The International Mini-Symposium on Diamond Electrochemistry and Related Topics, March 17–18, 1997, Tokyo, Japan.
174. Abstracts, The Second International Mini-Symposium on Diamond Electrochemistry and Related Topics, June 8–9, 1998, Tokyo, Japan.
175. Abstracts, The Third International Mini-Symposium on Diamond Electrochemistry and Related Topics, June 7–8, 1999, Tokyo, Japan.
176. Abstracts, 4th International Mini-Symposium on Diamond Electrochemistry and Related Topics, May 31–June 1, 2000, Tokyo, Japan.
177. Abstracts, The International Conference ''The Electrochemistry of Carbon Allotropes: Graphite, Fullerenes and Diamond'', October 20–27, 1997, Cleveland, OH, USA.
178. 3rd Workshop ''Diamond Electrodes'', May 11–12, 2000, Neuchâtel, Switzerland.
179. R. Tenne, C. Levy-Clement, Israel J. Chem., 38, 57 (1998).

Advances in Electrochemical Science and Engineering, Volume 8. Edited by Richard C. Alkire

ISBNs: 3-527-30211-5 (Hardback); 3-527-60078-7 (Electronic)

Passivity of Metals

Hans-Henning Strehblow

Institut für Physikalische Chemie und Elektrochemie, Heinrich-Heine-Universität Düsseldorf, Universitätsstr. 1, D-40225 Düsseldorf, Germany

List of Contents

List of Abbreviations

A_j	amplitude of coordination shell j
AES	Auger Electron Spectroscopy
ARXPS	angular resolved XPS
C	capacity
C_H	capacity of Helmholtz layer
$C_{\mathrm{Me,ox}}$	capacity of metal/oxide interface
C_{ox}	capacity of oxide layer
CB	conduction band
d	thickness
d_{SC}	thickness of space charge layer
e	elementary charge
E	electrode potential
E_B	binding energy
E_B	Potential within bulk of semiconductor
E_C	energy of conduction band edge
E_F	Fermi energy
E_{Fb}	flatband potential
E_{Fl}	Flade potential
E_g	band gap energy
$E_{I,i}$	ionization energy of level i
E_I	inhibition potential
E_{kin}	kinetic energy
E_P	passivation potential
E_{Pit}	pitting potential
E_S	potential at surface of semiconductor
E_V	energy of valence band edge
Ef	efficiency of metal dissolution
ΔE	energy of tunnel barrier
EXAFS	Extended X-ray Absorption Fine Structure
F	Faraday constant
f_j	reflection amplitude of coordination shell j
FEFF	program for calculation of EXAFS
FT	Fourier Transform
G	Gibbs free energy
$\Delta G_0^{\ddagger}$	free activation energy (enthalpy)
$\Delta G^{\ddagger}$	free activation energy including potential drop
h	Planck's constant
hv	photon energy
k	Boltzmann constant or wave vector
i	current density
i_c	corrosion current density
$i_{c,s}$	stationary corrosion current density
$i_{c,s}(0)$	stationary corrosion current density for pH 0
i^0	exchange current density
i_l	current density of layer formation
i_D	disc current density
i_{Ph}	photocurrent density
i_R	ring current

ISS	Ion Scattering Spectroscopy
m, M	mass, molar mass
m^*	effective mass of electron
N	concentration of ions or charge carriers
N_A	concentration of acceptors
N_D	concentration of donors
N_j	coordination number of shell j
$n(E)$	complex refraction index
PICS	photo ionization cross-section
Q	electric charge
R	gas constant
R_j	radius of coordination shell j
$R(E)$	reflectivity
$R_0(E)$	reflectivity without oscillatory part
RBS	Rutherford Backscattering Spectroscopy
ReflEXAFS	EXAFS in reflection mode
RRD	rotating ring disc electrode
HMRRD	hydrodynamically modulated rotating ring disc electrode
SFM	Scanning Force Microscopy
SHE	Standard Hydrogen Electrode ($E = 0$ V)
SIMS	Secondary Ion Mass Spectroscopy
STM	Scanning Tunneling Microscopy
T	temperature
Tr	Transmission function of energy analyzer
V_M	molar volume
VB	valence band
w_t	tunnel probability
X	intensity of X-ray source
X_i	cationic or anionic fraction of species i
XANES	X-ray Absorption Near Edge Structure
XAS	X-ray Absorption Spectroscopy
XPS	X-ray Photoelectron Spectroscopy
XRD	X-ray Diffraction
Z	charge of ions

List of Symbols

α	absorption or charge transfer coefficient
β	Debye length
$\beta(E)$	imaginary part of refraction index
$\beta_0(E)$	non-oscillatory part of $\beta(E)$
$\Delta\beta(E)$	oscillatory part of $\beta(E)$
δ	jump distance
$\delta(E)$	real part of diffraction index
δ_0	non-oscillatory part of $\delta(E)$
$\Delta\delta(E)$	oscillatory part of $\delta(E)$
$\varepsilon, \varepsilon_0$	dielectric constant, index 0 in vacuum
$\eta_{2,3}$	overvoltage at oxide/electrolyte interface
η	photocurrent efficiency
$\Delta\varphi$	potential drop, index: 1,2 metal/oxide, 2,3 oxide/electrolyte, ox oxide, H Helmholtz layer, SC space charge layer
Φ_0	photon flux
$e\Phi_{\mathrm{Th}}$	theshold energy
$e\Phi_w$	work function

1 Introduction

Corrosion is the degradation of materials because of their interaction with the environment. Any materials may be affected, among them semiconductors and even polymers. The aggressive environment may be the gas phase or an aqueous or non-aqueous electrolyte. The losses due to corrosion are enormous. Almost 3.5 % of the gross national product is lost by corrosion, a third of which can be avoided by the application of the present knowledge of corrosion research. For any field of industry and the everyday life, corrosion may cause serious damage, as e.g. large constructions in various plants, road constructions, houseware and even metallic films on integrated electronic circuits. Most metals are reactive in an oxidizing environment and thus are not chemically stable and their surface has to be protected. A very effective protection is the formation of passivating surface layers. They cover many metal surfaces as poreless continuous films, which block effectively the dissolution of the metallic substrate. Usually these layers are thin invisible oxide films of up to a few nm in thickness. The formation of these oxide films causes a characteristic polarization curve of metals, as depicted in Fig. 1. Metal dissolution starts when the Nernst equilibrium potential is exceeded. The related current density passes through a maximum, which may reach several 100 mA cm^{-2} depending on the metal and the electrolyte composition (pH). For further potential increase, it drops by many orders of magnitude at the passivation potential (E_P). Within the adjacent passive potential range the stationary corrosion current density is only a few μA cm^{-2} or even less. In the transpassive potential range the current density increases again due to the formation of higher valent metal ion species, which dissolve faster. A well-known example is the formation of soluble chromates and dichromates on passive chromium and of Ni^{3+} at positive potentials. Furthermore, the current density increases due to the evolution of oxygen or the oxidation of other redox species within the electrolyte

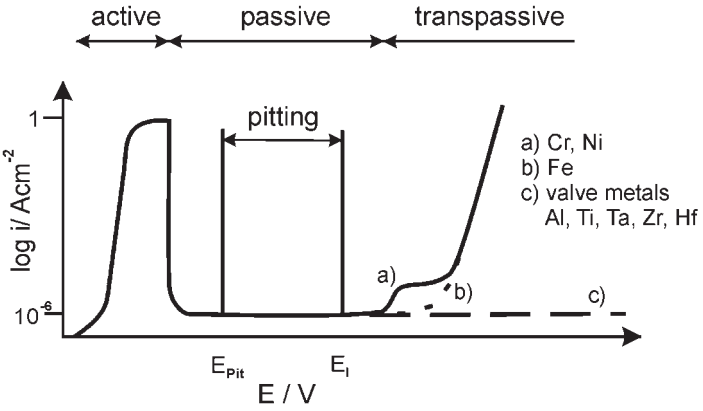

Fig. 1. Polarization curve of metals with active, passive and (a) transpassive potential range including oxygen evolution; (b) passive potential range going directly to oxygen evolution; (c) continuing passivity for valve metals to very positive potentials. Pitting between critical pitting E_{Pit} and inhibition potential E_I in the presence of aggressive anions and inhibitors.

related to the semiconducting properties of the passive layer. If the passive layer is a semiconductor with a large band gap or an insulator the passive range may extend to more than 100 volts as for the so-called valve metals like Al, Nb, Ta, Ti, Zr, Hf and others. Their passive layers may grow with the potential to more than 100 nm in thickness.

It should be mentioned that passive layers are not protective in all environments. In the presence of so-called aggressive anions, passive layers may break down locally, which leads to the formation of corrosion pits. They grow with a high local dissolution current density into the metal substrate with a serious damage of the metal within very short time. In this sense halides and some pseudo halides like SCN^- are effective. Chloride is of particular interest due to its presence in many environments. Pitting corrosion starts usually above a critical potential, the so-called pitting potential E_{Pit}. In the presence of inhibitors an upper limit, the inhibition potential E_I is observed for some metals. Both critical potentials define the potential range in which passivity may break down due to localized corrosion as indicated in Fig. 1.

Passivity of metals is a phenomenon that has been known for many years. H. Uhlig describes in his review on the history of passivity [1] that M. Lomonosov was the first who observed, in 1738, the lack of dissolution of Fe in concentrated nitric acid [2]. W. Ostwald mentioned in his history of electrochemistry [3] that J. Keir authored in 1790 the passivity of iron in nitric acid [4], and C. Wenzel made a similar observation in 1782 according to Gmelin [5]. In 1807 W. Hiesinger and J. Berzelius found that passivity could be achieved by anodic polarization [5]. This result was confirmed in 1836 by C. Schönbein for iron anodized in diluted nitric, sulphuric and phosphoric acid [6]. M. Faraday's correspondence with Schönbein confirmed the galvanic nature of passivity and he speculated already on the presence of a protecting film at the metal surface, assumed to be an electronic conductor as a result of his experiments [7]. Since these early investigations, passivity has been examined extensively by many groups, this because of its technical importance. Eight international conferences have been dedicated to passivity. Decisive progress has been made up to now due to the application of various methods that have been developed with time. In the 1950s and 1960s, electrochemical methods were applied predominantly, including electrode kinetics. Optical methods like ellipsometry and reflection spectroscopy were applied in the late 1960s and *ex situ* surface analytical methods like X-ray Photoelectron Spectroscopy (XPS) Auger Electron Spectroscopy (AES) and Ion Scattering Spectroscopies (ISS and RBS) were applied from the 1970s to 1980s up to the present time to learn about the chemistry of these films. For about 15 years, structure-sensitive *in situ* methods, like Scanning Tunneling (STM) and Scanning Force Microscopy (SFM), and the application of synchrotron radiation for X-ray Absorption Spectroscopy (XAS) and X-ray Diffraction (XRD), provided *in situ* information on the structure of these films. These methods brought progress to the understanding of the structure and properties of these films and opened further possibilities to investigate mechanistic details on their formation and degradation down to a mesoscopic, or even an atomic, level. Their continuing application promises to provide further insight and to give answers to still many open questions.

The present paper intends to review the main experimental results and theoretical concepts of passivation and passivity of metals, rather than giving a full compilation

of all details of the various systems. The main topics discussed include the growth and composition of passive layers, their structure and electronic properties, and their breakdown with a restricted number of examples. The specific properties of binary alloys are added in separate chapters. It is intended to show that the application of electrochemical and spectroscopic methods in close combination gives a reliable insight into the passive behavior of the metals leaving as little as possible reason for speculation. A short description of the most important analytical methods with special attention to their application to the study of passivated metal surfaces is given.

2 Thermodynamics of Passivation

H.H. Uhlig defines passivity in his historical review [1, 8] by two closely linked definitions:

1. A metal is passive if it substantially resists corrosion in a given environment resulting from marked anodic polarization.
2. A metal is passive if it substantially resists corrosion in a given environment despite a marked thermodynamic tendency to react.

These definitions imply both factors for chemical or electrochemical reactions, i.e. the thermodynamical or equilibrium conditions and the kinetic conditions. Apparently passivity blocks corrosion, despite the large thermodynamic driving force for the oxidation of most metals which is a consequence of a negative Gibbs free energy ΔG or a sufficiently high electrode potential E, both of which are closely related ($\Delta G = -zFE$). The weak solubility of anodic oxides, especially in neutral and alkaline electrolytes, causes the formation of protective layers that are in dissolution equilibrium with the contacting electrolyte. On the other hand, slow kinetics of the dissolution of anodic oxides lead similarly to a stable metal surface with an almost negligible corrosion rate. Thus, both factors, thermodynamics and kinetics, have to be taken into account in order to get the right interpretation of the observed behavior. Thermodynamic data have been compiled for almost all elements in the form of potential-pH diagrams, so called Pourbaix diagrams [9]. Figs. 2 and 3 give two examples that demonstrate their usefulness, but also the danger of misinterpretation if kinetic factors are neglected.

Copper follows the predictions of its diagram. For this seminoble metal, the potential has to be sufficiently positive to get anodic oxidation. In acidic electrolytes this causes anodic dissolution, and the oxide layers dissolve sufficiently fast so that they are non-protective. For pH > 5.0 these oxides are insoluble, i.e. they are in dissolution equilibrium with the electrolyte. Passivity is achieved when oxide formation occurs at sufficiently positive potentials according to the reactions of Eqs. (1) and (2).

$$\mathrm{Me} + n\,\mathrm{H_2O} \rightarrow \mathrm{MeO}_n + 2n\,\mathrm{H^+} + 2n\,\mathrm{e^-} \tag{1}$$

$$\mathrm{MeO}_n + x\,\mathrm{H_2O} \rightarrow \mathrm{MeO}_{n+x} + 2x\,\mathrm{H^+} + 2x\,\mathrm{e^-} \tag{2}$$

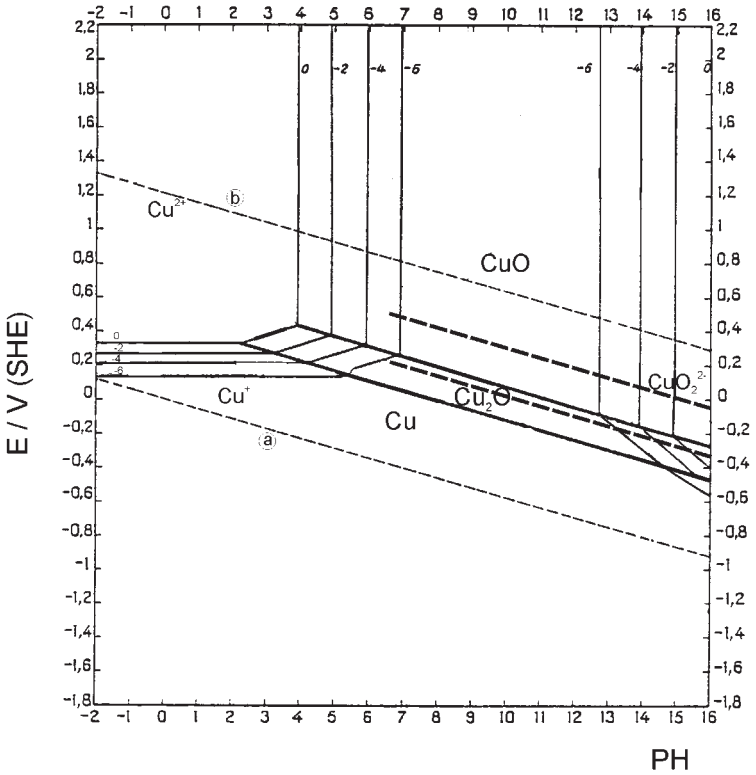

Fig. 2. Potential pH diagram after M. Poubaix for Cu with stability range for Cu_2O and CuO. Experimental oxide formation potential for Cu_2O and CuO dark dashed line, a) H_2/H^+, b) H_2O/O_2 electrode [9].

Fig. 2 distinguishes the domains of immunity, corrosion and passivity. At low pH corrosion is postulated due to an increased solubility of Cu oxides, whereas at high pH protective oxides should form due to their insolubility. These predictions are confirmed by the electrochemical investigations. The potentials of oxide formation as taken from potentiodynamic polarization curves [10] fit well to the predictions of the thermodynamic data if one takes the average value of the corresponding anodic and cathodic peaks, which show a certain hysteresis or irreversibility due to kinetic effects. There are also other metals that obey the predictions of potential-pH diagrams like e.g. Ag, Al, Zn.

There is a second group of metals like Fe, Cr, Ni and their alloys, which do not follow all predictions of their potential-pH diagrams. As an example, the Pourbaix Diagram for iron of Fig. 3 predicts corrosion for all potentials in strongly acidic electrolytes. However, experiments show that it is passive for potentials above a potential of $E_P = 0.58 - 0.059$ pH. For these conditions the passive layer is far from any dissolution equilibrium and its protecting properties have to be related to its slow dissolution kinetics. The same arguments hold for the passivation of Cr, Ni and their alloys.

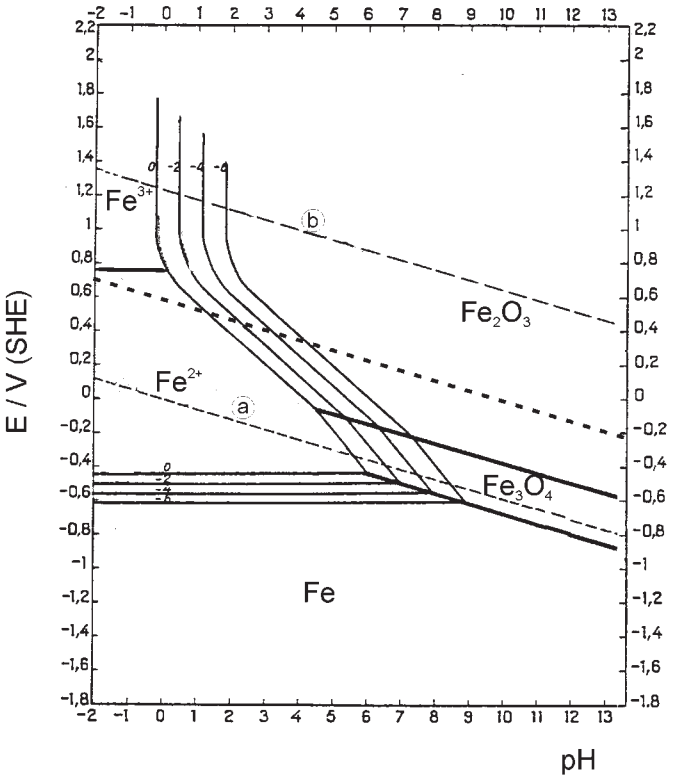

Fig. 3. Potential pH diagram after M. Pourbaix for Fe with stability range of its oxides, experimental passivation potential in acidic electrolytes dark dashed line, (a) H_2/H^+; (b) H_2O/O_2 electrode [9].

The passivation potential E_P of iron in acidic electrolytes is much too positive to be related to the formation of an oxide on a metal according to Eq. (1). The thermodynamical values yield for all three iron oxides FeO, Fe_3O_4 and Fe_2O_3 a very similar value of ca. $E_P = -0.05 - 0.059$ pH/V ($E_P(0)$ for FeO: -0.06 V, Fe_3O_4: -0.040 V, Fe_2O_3: -0.015 V) [10]. These values are found experimentally in alkaline solutions where these oxides are in dissolution equilibrium with the electrolyte, a requirement of the potential-pH diagrams. The positive values in strongly acidic electrolytes are interpreted by the oxidation of Fe_3O_4 to γ-Fe_2O_3 according to Eq. (2), i.e. passivity is related to the formation of an outer layer of slowly dissolving γ-Fe_2O_3. The thermodynamic data for Eq. (2) yield the experimental value of $E_P(0) = 0.58$ V for pH 0. Furthermore Fe_3O_4 is the only oxide in equilibrium with iron metal. It is dissolving with a high rate in acidic electrolytes so that it is not protective by itself and may even not be detected by electrochemical charging curves in 0.5 M H_2SO_4 [10]. Only the intermediate adsorption of OH^- or O^{2-} could be detected [11]. XPS investigations confirmed this interpretation on the basis of thermodynamic arguments [12]. According to these measurements the passive layer consists of an inner Fe_3O_4 and an outer Fe_2O_3 layer. For both oxides an inverse spinel

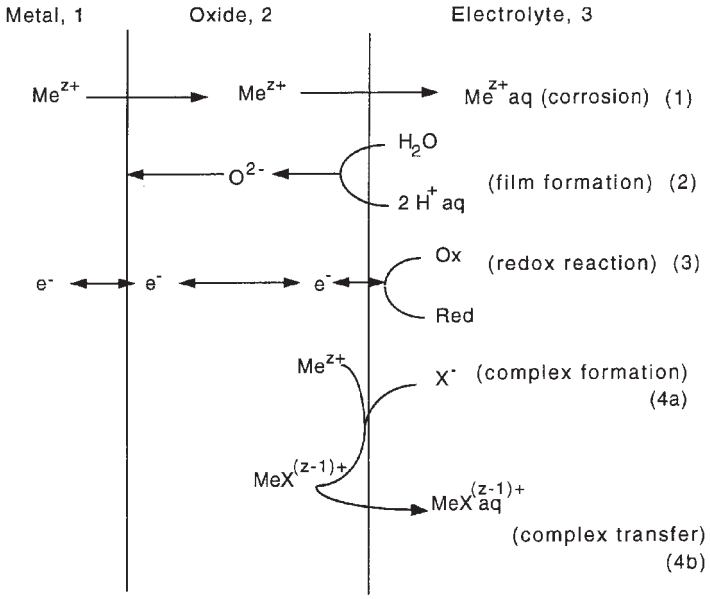

Fig. 4. Schematic diagram of passive metals with electrode reactions: (1) Metal corrosion; (2) film formation; (3) redox reactions with electron transfer to or from metal substrate; (4a,b) complex formation and enhanced dissolution in the passive state.

structure has been proposed. They are miscible and thus change continuously from one composition to the other. A duplex or multilayer structure is found for passive layers of many other pure metals and alloys, as will be discussed in section 5 page 303.

Fig. 4 shows a simple phase diagram for a metal (1) covered with a passivating oxide layer (2) contacting the electrolyte (3) with the reactions at the interfaces and the transfer processes across the film. This model is oversimplified. Most passive layers have a multilayer structure, but usually at least one of these partial layers has barrier character for the transfer of cations and anions. Three main reactions have to be distinguished. The corrosion in the passive state involves the transfer of cations from the metal to the oxide, across the oxide and to the electrolyte (reaction 1). It is a matter of a detailed kinetic investigation as to which part of this sequence of reactions is the rate-determining step. The transfer of O^{2-} or OH^- from the electrolyte to the film corresponds to film growth or film dissolution if it occurs in the opposite direction (reaction 2). These anions will combine with cations to new oxide at the metal/oxide and the oxide/electrolyte interface. Finally, one has to discuss electron transfer across the layer which is involved especially when cathodic redox processes have to occur to compensate the anodic metal dissolution and film formation (reaction 3). In addition, one has to discuss the formation of complexes of cations at the surface of the passive layer, which may increase their transfer into the electrolyte and thus the corrosion current density (reaction 4). The scheme of Fig. 4 explains the interaction of the partial electrode processes that are linked to each other by the elec-

troneutrality condition. The processes at the oxide/electrolyte interface are submitted to the same potential drop $\Delta\varphi_{2,3}$, which in turn is determined by their equilibria and/or kinetics. The passivation potential for most metals follows a -0.059 pH dependence. This is expected from the thermodynamic data of oxide formation as deduced also from Pourbaix diagrams. On the other hand, passivity is observed frequently for metals far from any dissolution equilibrium as for Fe, Cr, Ni in strongly acidic electrolytes. The slow dissolution of cations according to reaction 1 of Fig. 3 is apparently a consequence of the high activation energy for this reaction. In the case of stationary conditions the formation of cations at the metal/oxide interface and their transfer across the film is balanced by their dissolution. This situation leads consequently to equilibrium for reaction 2. The oxide thickness will remain unchanged and thus oxide and O^{2-} formation does not occur. This equilibrium causes a pH dependence of the potential drop of $\Delta\varphi_{2,3}$ according to Eq. (3), which enters the electrode potential, i.e. the potential difference between the passivated metal and the standard hydrogen electrode. $\Delta\varphi_{2,3}(0)$ is the potential drop for an electrolyte of pH 0.

$$H_2O \longleftrightarrow O^{2-} + 2\,H^+ + 2\,e^-$$

$$\Delta\varphi_{2,3} = \Delta\varphi_{2,3}(0) - (RT/2F)\ln(a^2{}_{H^+}) = \Delta\varphi_{2,3}(0) - 0.059\,\mathrm{pH} \tag{3}$$

For instationary conditions of the passive layer, i.e. if layer formation occurs and O^{2-} will be formed, $\Delta\varphi_{2,3}$ will deviate from its equilibrium value by an overpotential $\eta_{2,3}$. These kinetic parameters of a complicated system as the passivated metal surface will be discussed in the next section.

3 Kinetics of Processes at the Passivated Electrode Surface

The potential drop at the phase boundaries and its influence on the reaction rates of Fig. 4 has been subject to various investigations. Iron in acidic electrolytes is an interesting system because its stationary passive current density $i_{c,s}$ is potential-independent (Fig. 5) although it changes with the electrolyte composition, i.e. the pH and the kind of anions. This is not the case for Ni, whose $i_{c,s}$ changes continuously in the passive potential range and increases with a peak in the transpassive potential range. This variation has been ascribed to the change of the composition of the surface of the passive layer [13]. Small changes of the oxidation state of the oxide may lead to a variation of the potential drop $\Delta\varphi_{2,3}$ and thus to a change of the transfer rate of cations. The postulated presence of Ni^{3+} ions and their transfer into the electrolyte has still not been confirmed in acidic electrolytes. These ions decompose within the electrolyte apparently too fast to be detected by a rotating Pt-ring Ni-disc electrode. On the other, hand they are found by XPS within the passive layer in alkaline solution [14]. This is expected, since NiOOH is known to be the oxidized form of a layer on the Ni electrode of accumulators in alkaline solution. Similarly the

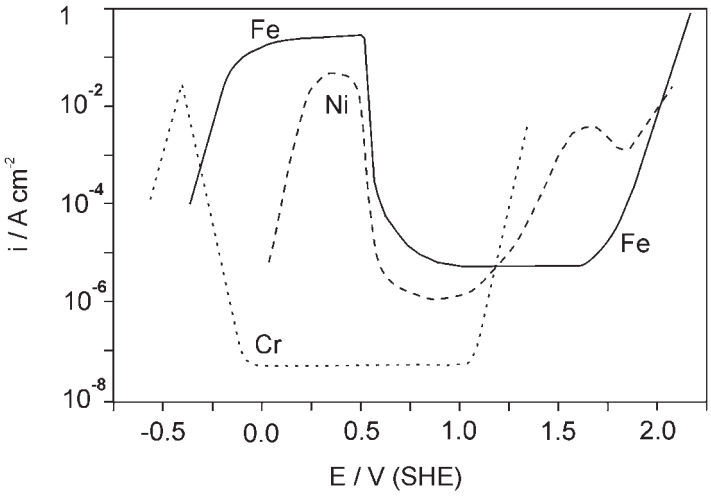

Fig. 5. Polarization curves of 3 passivating metals, Fe, Ni, Cr in 0.5 M H_2SO_4.

oxidation of Cr^{3+} ions of the passive layer on chromium to Cr(VI), i.e. to soluble CrO_4^{2-} in alkaline solution or $Cr_2O_7^{2-}$ in acidic environment (Fig. 5), causes the increase to the transpassive dissolution before oxygen evolution. Because of the not too complicated situation of passive iron, its properties have been studied in detail in the past. Relating the pH dependence of its experimentally determined stationary passive current density to the potential drop $\Delta\varphi_{2,3}$ and thus to the pH of the electrolyte according to Eq. (3) one obtains the Butler–Volmer equation (4) for the cation transfer. ${i^0}_{c,s}$ is the exchange current density of the dissolution process 3 of Fig. 4 and $i_{c,s}(0)$ the stationary current density at pH 0. With $z = +3$ for the Fe^{3+} ions dissolving in the passive state and the experimental value for the pH dependence of the stationary corrosion current density one obtains a charge transfer coefficient $\alpha = 0.28$ according to Eq. (5).

$$i_{c,s} = {i^0}_{c,s} \exp[(\alpha z F \Delta\varphi_{2,3,s})/(RT)] \tag{4}$$

$$i_{c,s} = i_{c,s}(0) \exp[-\alpha z \,\mathrm{pH}]/2.303] \tag{4a}$$

$$i_{c,s}(0) = {i^0}_{c,s} \exp[(\alpha z F \Delta\varphi_{2,3,s}(0))/(RT)] \tag{4b}$$

$$d \log i_{c,s}/d\,\mathrm{pH} = -3\alpha = -0.84 \tag{5}$$

For unstationary conditions Eq. (4) is rewritten with the current density i_c and a potential drop at the oxide/electrolyte interface that contains the overvoltage $\eta_{2,3}$ as usual for electrode processes, $\Delta\varphi_{2,3} = \Delta\varphi_{2,3,s} + \eta_{2,3}$. As a consequence a factor $\exp(\alpha * * zF\eta_{2,3}/RT)$ enters Eqs. (4a) and (4b), which yields Eq. (6) for the overvoltage as a function of the corrosion current density.

$$\eta_{2,3} = (0.02/\alpha) \log i_c - (0.02/\alpha) \log i_{c,s} \tag{6}$$

The rate of layer formation is subject to the same overvoltage at the surface of the passive film. As a consequence, the log of the current density of layer formation i_l is proportional to the overvoltage $\eta_{2,3}$, as well as to log $i_{c,s}$. These details have been studied in detail by Vetter and Gorn [16]. The dissolution rate has been investigated by analysis of the solution with colorimetry of the red complex of Fe^{3+} with SCN^- [17] or with the rotating ring disc technique (RRD) [18].

Potentiostatic transients lead to an increase of both partial current densities $i_{c,s}$ and i_l. The necessary transfer of cations and anions across the passive layer has to occur by migration within the high electric field strength of the passive film. For stationary conditions the cation transfer equals the dissolution rate at the oxide/electrolyte interface. For unstationary conditions a higher cation transfer has to compensate for the increased corrosion reaction, but also for the layer formation. This in turn becomes possible due to higher electrical field strength within the film (Fig. 6). For potentiostatic conditions the growth of new layer causes a decrease of the field strength with time until it assumes the same value again for the new steady state. $\Delta\varphi_{2,3}$ assumes then the stationary value again as given by the equilibrium of Eq. (3) and the total potential increase is located within the passive film. This in turn causes a linear growth of the stationary oxide thickness with potential.

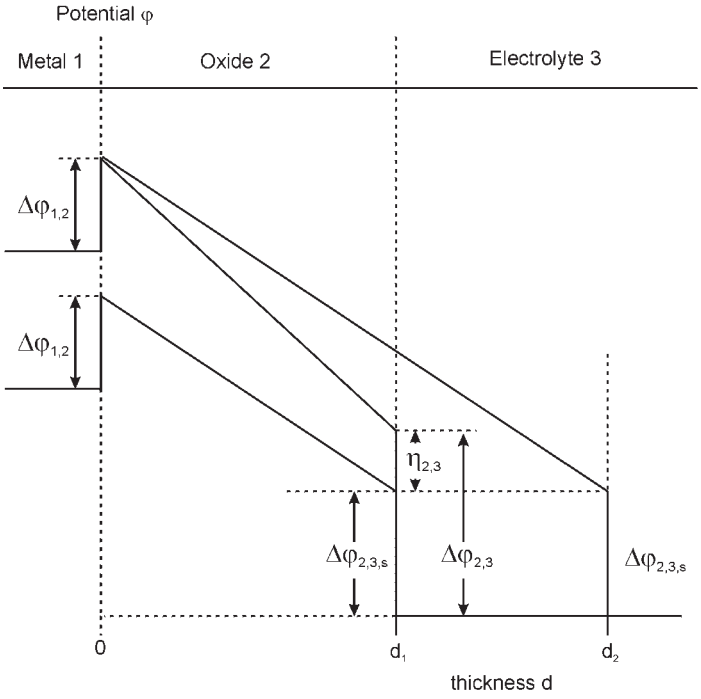

Fig. 6. Potential diagram for passivated metals for steady and unsteady conditions with an overvoltage $\eta_{2,3}$ at the oxide/electrolyte interface leading to increased dissolution and oxide growth of d_1 to d_2 where a new stationary state is reached.

3.1 Film Growth Laws and the High Field Mechanism

According to the discussion of Fig. 4 the total current density consists of a corrosion part i_c and a layer formation part i_l. If one may determine i_c separately, e.g. with a rotating ring disc electrode, i permits the determination of $i_l = i - i_c$. In several cases i_c is very small so that i equals approximately i_l. Within the passive layer, cations and anions may all migrate. There has been some activity especially for valve metal with thick anodic oxide layers to determine the transference numbers for the ions within the film. Some surface analytical methods permit determination of where new oxide is grown in addition to a pre-existing film, at the metal surface or at the oxide/electrolyte interface. For this purpose new oxide may be grown in aqueous solutions enriched with the isotope O^{18} with a subsequent secondary ion mass spectroscopic (SIMS) depth profile. Xenon implantation into a pre-existing oxide layer and further anodic oxide growth has been used to determine the position of the noble gas tracer within the film using Rutherford Backscattering (RBS) techniques, thus demonstrating where the new oxide has formed. In most cases the new anodic oxide was grown at both interfaces with a transference number close to 0.5 for both cations and anions [19–21]. Crystalline oxides on zirconium and hafnium suppress almost completely the migration of cations, which has been ascribed to an effective migration of O^{2-} along grain boundaries [20].

The formation of new oxide requires ionic transfer at the metal/oxide and oxide/electrolyte interface and across the layer. The kinetics of film growth may be ruled by any of these processes and their activation energy determines the rate-determining step. The transfer rates have to compensate each other to conserve electroneutrality. For all three processes the flux density of ions dN/dx and the related current density i_l yields a Butler–Volmer type kinetic equation. Because of the presence of an electrical field strength of several 10^6 V cm^{-1} within the passive layer, but also at the interfaces, the high field mechanism should dominate the ion transfer across the film and at these interfaces (Fig. 6). Thus, cations will migrate towards the electrolyte and anions like O^{2-} in the opposite direction. The high field strength will suppress any inward migration of cations or outward migration of anions. The following discussion for the ion transport across the film will be similar to that at the interfaces and thus will lead to the same final equation. The ionic flux density of ions per unit surface area dN/dt is given by Eq. (7) [22]. The frequency factor ν is in the order of oscillations of ions within a crystal lattice of ca. 10^{13} s^{-1}. N is the concentration of the ions in an energetically favored position as interstitials or sites close to vacancies, which favors their transfer to another position in its direct vicinity with the jump distance δ. These parameters should depend strongly on the atomic structure of the anodic films. As they are usually highly defective or even amorphous their values should be seen as an average. An evaluation of the electrochemical data of oxide growth yields reasonable values. The ion migration within the passive layer requires the Free Activation Energy $\Delta G^{\neq}$, which is modified by the electrical work $\alpha z F \Delta\varphi_2 \delta/d$. α is a symmetry factor corresponding to the charge transfer coefficient for charge transfer processes at electrode surfaces. It describes that part of the potential drop along the jump distance δ which is kinetically effective, i.e. which may reduce the Free Activation Energy $\Delta G^{\neq}{}_0$ (Fig. 7). Its value is usually close to 0.5.

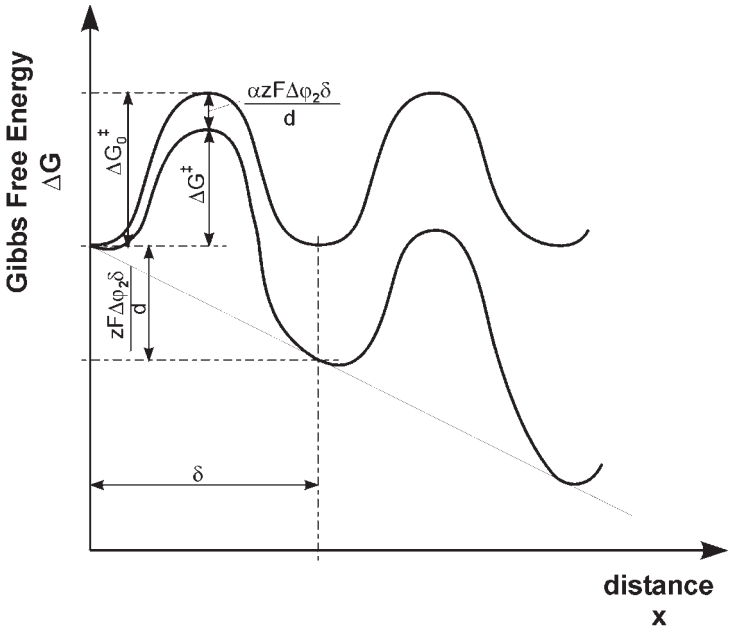

Fig. 7. Diagram of Gibbs free energy ΔG for the ion transfer through a passive layer with a Free Activation energy ΔG between two favoured sites for anions (interstitials or vacancies) under the influence of a high electrical field strength and without field (horizontal curve) explaining the high field mechanism for oxide growth.

$\Delta\varphi_2$ is the potential drop within the layer, d the layer thickness and thus $\Delta\varphi_2/d$ the electrical field strength within the layer. Applying Faraday's law, one obtains the current density of layer formation i_l of Eq. (8) which sums up several parameters in the exchange current density $i_l{}^0$ (Eq. (8c)). The experimental investigation of layer formation yields thus in many cases an exponential relation (8a). $E - E_P$ is the deviation from the critical potential of passivation E_P, the major part of which is located within the layer. For unstationary conditions part of it will appear as an overpotential at the interfaces.

$$dN/dt = N\delta v \exp(-\Delta G^{\neq}/RT) \tag{7}$$

$$\Delta G^{\neq} = \Delta G^{\neq}{}_0 - (\alpha zF\Delta\varphi_2\delta/d) \tag{7a}$$

$$i_l = zF\, dN/dt = i_l{}^0 \exp(\alpha zF\Delta\varphi_2\delta/RTd) \tag{8}$$

$$i_l = i_l{}^0 \exp[\beta(E - E_p)/d] \tag{8a}$$

$$\beta = \alpha zF\delta/RT \tag{8b}$$

$$i_l{}^0 = zFN\delta v \exp(-\Delta G^{\neq}{}_0/RT) \tag{8c}$$

Applying Faraday's law to Eq. (8) yields the increase of the layer thickness d with time t (Eq. (9)). Its integration yields the growth of d as a function of t. Unfor-

tunately Eq. (9) does not permit an exact analytical solution. An approximation is the direct logarithmic and the inverse logarithmic law of Eqs. (10) and (11) [10]. Experimental data often fit equally well to both time laws.

$$dd/dt = (V_M/zF)i_l{}^0 \exp(\beta\Delta\varphi_2/d) \tag{9}$$

$$d = A + B\log(t + t_0) \tag{10}$$

$$1/d = A - B\log(t + t_0) \tag{11}$$

$$B = 1/\beta(E - E_P) \tag{11a}$$

Experimental studies of oxide growth require a direct evaluation of the layer thickness as a function of time. This may be achieved by various *in situ* and *ex situ* surface analytical methods, i.e. the Quartz Micro Balance (QMB), Ellipsometry, and methods working in the UHV, which will be discussed in the following section (4.2). Another possibility is the combination of electrochemical methods. This involves simply the measurement of currents and charges of potentiostatic or galvanostatic experiments and the independent analysis of the electrolyte, which permits the calculation of the charge or current of metal dissolution. The dissolution rate may be obtained applying colorimetry to colored complexes of dissolved cations or atomic absorption spectroscopy. The rotating Ring Disc (RRD) technique permits the determination of dissolution rates with a time resolution of less than a second. Subtraction of the corrosion current density i_C from the total current density i_t yields the current density of layer formation i_l ($i_l = i_t - i_C$).

Applying Eq. (8a) to experimental data permits the determination of the exchange current density $i_l{}^0$ and the jump distance δ of ions. Both are correlated to each other. A $\log i_l/(E - E_F)$ plot yields both $i_l{}^0$ and β. Small variations of β require large changes of $i_l{}^0$, so that an exact determination of these kinetic parameters is difficult. This is in part a consequence of the fact that the current density can be followed only for a restricted range of the electrical field strength within the passive layer. According to Eq. (8b) experimental data for β lead to reasonable δ – values in the range of 0.1 to 1 nm. The exchange current density of Eqn (8c) contains the concentration N of mobile ions, i.e. of the charge carriers, and the frequency v. Usually $v = 10^{11}$ to 10^{13} s^{-1} and $N = 10^{14}$ to 10^{21} cm^{-3} are in agreement with the kinetic data of oxide growth. For potentiostatic conditions a stationary state is reached for the passive layer with a small anodic current density, which corresponds to the dissolution of metal ions in the passive state. For these conditions the current density provides as many cations as are lost by dissolution to the electrolyte, which gives a constant layer thickness d. With $dd/dt = 0$ Eq. (9) yields an oxide thickness increasing linearly with the electrode potential E according to Eq. (12), which corresponds to a constant electrical field strength $(E - E_P)/d$. This situation has been verified especially for iron, which shows a potential-independent stationary current density within the passive potential range in acidic electrolytes, and thus a potential independent voltage drop $\Delta\varphi_{2,3}$ at the oxide/electrolyte interface.

$$d = \alpha zF\delta(E - E_p)/RT \tag{12}$$

4 Analytical Methods and their Application to Passivity and Corrosion

Electrochemical investigations of surface layers have their limits. Even the evaluation of the thickness and the growth of a surface film requires the knowledge of its chemical composition and structure. Thermodynamic arguments have been used to deduce this information from such electrochemical results as e.g. the potential at which layer formation and reduction is detected by anodic or cathodic current peaks. Since the thermodynamic data do not permit any conclusion about kinetics, and detailed chemical information cannot be obtained simply from polarization curves, the application of appropriate surface analytical techniques is a necessity to obtain a reliable insight into chemical and structural data. Therefore, spectroscopic methods are of increasing importance for corrosion research and electrochemical surface science. For a better understanding, these methods are briefly introduced with special attention to the study of the electrode/electrolyte interface and anodic oxide films. There have to be distinguished between *in situ* and *ex situ* methods. Although *in situ* methods do not interrupt the contact of the electrode to the electrolyte, and thus may ensure potential control during the measurement, *ex situ* methods provide such rich chemical information that their application to passivity and corrosion is urgently needed. Appropriate precautions and broad experience with many passivating metals ensures a reliable analysis without artifacts.

4.1 Electrochemical Methods

Electrochemical methods are usually *in situ* techniques. Potentiostatic potentiodynamic and galvanostatic methods have been applied for many decades and are well known by electrochemists and corrosion engineers. Even transient techniques had been already developed by the 1950s, although the electronic equipment has made great progress in the last 30 years. Especially important has been the development of cheap and fast computers in the last 20 years; these facilitate the acquisition, manipulation and evaluation of data. Impedance measurements provide data for the capacity of electrodes and kinetic parameters for the processes at their surface. The already-mentioned Rotating Ring Disc technique permits the evaluation of the rate of dissolution with a time resolution of less than a second. Because these methods are of wide spread use in the community, they are not discussed here specifically.

However, the application of the Split Ring Disc electrode especially with hydrodynamic modulation of its rotation speed (HMRRD) will be mentioned briefly. The construction of appropriate ring disc electrodes including a modified commercial disc rotator and the necessary electronic tripotentiostat have been already described in detail elsewhere [25]. The investigations of K.G. Heusler on passive iron in 0.5 M sulphuric acid have been already mentioned [18]. Another example is shown for Cu in alkaline solution [26]. Two half rings permit determination of the formation of two Cu species simultaneously. The transfer efficiency from the disc to the ring has been

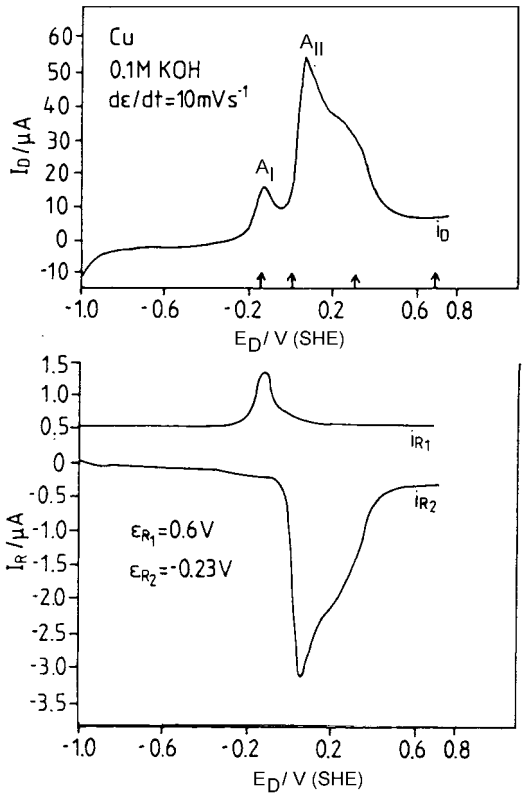

Fig. 8. Potentiodynamic polarization curve for a rotating Cu disc in 0.1 M NaOH with two analytical Pt half rings detecting soluble Cu^{+} (i_{R1}) and Cu^{2+} ion formation (i_{R2}) [62].

calculated and determined experimentally to 13 % for the actual dimensions of the Pt half-ring Cu-disc assembly in close agreement. Fig. 8 shows the polarization curve of a Cu disc in 0.1 M KOH with the two peaks of Cu oxide formation and the beginning passive range at $E > 0.4$ V. The ring current i_{R1} indicates the formation of Cu(I) ions at the first anodic peak AI and a larger dissolution of Cu(II) ions at the anodic peak AII which supports the formation of Cu_2O and CuO respectively. Passivation transients at the indicated potentials of Fig. 6 yield a relatively large efficiency for metal dissolution $Ef = i_c/(i_c + i_l)$, which increases with the electrode potential. For times less than a second, Ef is very small due to preferential layer formation. It increases within a few seconds to a stationary value. Even during the first 10 seconds, a major part of the total disc current is used for metal corrosion and only a small fraction for oxide formation. Up to 90 % are achieved within a few seconds. In agreement with the relatively large currents in the range of peak AII the oxide layer grows to a visible thickness, which supports a dissolution and precipitation mechanism for these conditions. When entering the passive range at $E > 0.4$ V the passive layer grows to some few nm at most, which confirms the formation of a dense and protecting film. For these conditions, Ef will reach finally 100 %, however, at a very low level of the total current density $i = i_l + i_c$ of less than 0.1 mA cm^{-2}.

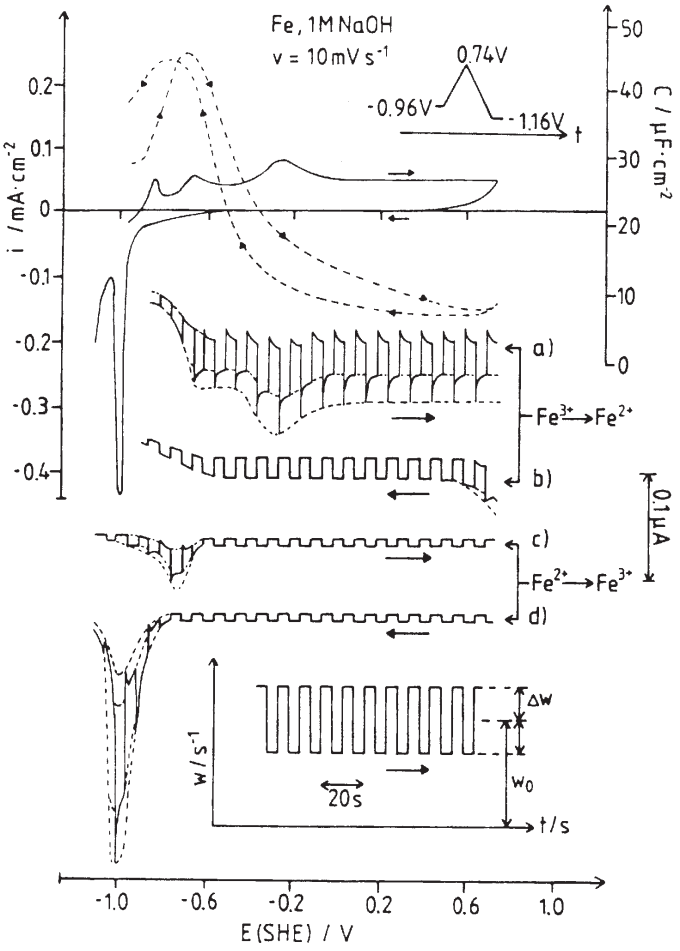

Fig. 9. Polarization curve of an Fe-disc Pt-split-ring electrode with hydrodynamic square wave modulation. In 1 M NaOH with anodic and cathodic scan including capacity of the Fe disc (dashed curve), modulation frequency of rotation $\omega = 0.05$ Hz (insert), simultaneous detection of Fe(II) and Fe(III) ions at Pt half rings [12].

Another example for the HMRRD electrode is given in Fig. 9 for Fe in alkaline solutions [12, 27]. The square wave modulation of the rotation frequency ω causes the simultaneous oscillation of the analytical ring currents. They are caused by species of the bulk solution. Additional spikes refer to corrosion products dissolved at the Fe disc. This is a consequence of the change of the Nernst diffusion layer due to the changes of ω. This pumping effect leads to transient analytical ring currents. Besides qualitative information, also quantitative information on soluble corrosion products may be obtained. The size of the spikes is proportional to the dissolution rate at the disc, as has been shown by a close relation of experimental results and calculations [28–30]. As seen in Fig. 7, soluble Fe(II) species are formed in the po-

tential range before the second anodic peak, whereas Fe(III) production starts at the second anodic peak at $E = -0.7$ V up to $E > 0.7$ V. In the reverse scan, Fe(II) production starts again during the reduction of the anodic oxide at the cathodic peak at $E = -1.0$ V where Fe(III) oxide is reduced to Fe(II) and Fe. These findings support the XPS results on the chemical changes during oxide formation and reduction, which are discussed in the following section. The decreasing capacity (dashed curve) to less than 10 μF cm^{-2} indicates the formation of the passive layer.

4.2 *Ex Situ* Surface Analytical Methods

In situ methods permit the examination of the surface in its electrolytic environment with application of the electrode potential of choice. Usually they are favored for the study of surface layers. Spectroscopic methods working in the ultra high vacuum (UHV) are a valuable alternative. Their detailed information about the chemical composition of surface films makes them an almost inevitable tool for electrochemical research and corrosion studies. Methods like X-ray Photoelectron Spectroscopy (XPS), UV Photoelectron Spectroscopy (UPS), Auger Electron Spectroscopy (AES) and the Ion Spectroscopies as Ion Scattering Spectroscopy (ISS) and Rutherford Backscattering (RBS) have been applied to metal surfaces to study corrosion and passivity.

Table 1 summarizes the most important surface analytical methods working in the UHV, with their characteristics and advantages, which have been applied successfully to the study of passivity and corrosion research as well as the solution of

Table 1. Characteristics of some UHV-surface analytical methods

Method	In-depth resolution	Lateral resolution	Information
XPS (X-ray photoelectron spectroscopy)	2 nm	100 nm	composition of surface and surface films, binding and oxidation state
UPS (UV photoelectron spectroscopy)	1 nm	>1 mm	work function, threshold energies, band structure, binding orbitals
AES, SAES [(scanning) Auger electron spectroscopy]	2 nm	20 nm	composition of surface and surface films, high lateral information
ISS (ion scattering spectroscopy)	0.3 nm	20 nm	composition of surface and surface films, modest lateral information
RBS (Rutherford back-scattering)	5 nm	0.1 mm	quantitative quasi-non-destructive depth profile
SEM (scanning electron microscopy)	2 nm	1 nm	surface topography with high lateral resolution
EM (electron microprobe)	2 μm	2 μm	composition of surfaces and surface layers

corrosion problems in industry. XPS is a very powerful tool to get qualitative and quantitative chemical information with a soft treatment of the surface. UPS has been applied to learn about the electronic properties of passive films via the measurement of work functions and threshold energies. AES permits detailed examination of localized effects due to its high lateral resolution when Auger electrons are excited with a focused electron beam. The small escape depth of Auger electrons and photoelectrons causes a surface sensitivity of a few nm for these electron spectroscopies, which is the thickness of passive layers on many metals. In this regard, the scanning electron microscope and the electron microprobe should be mentioned as very valuable routine methods in corrosion research to study the topography of a surface with a lateral resolution of some 10 nm, and the elemental composition with a lateral and in depth information of several μm resolution. These methods have been applied to the study of breakdown phenomena of passive layers. Modern scanning methods like STM and SFM with a lateral resolution down to atomic dimensions should be mentioned, although they may be applied as *in situ* techniques. They are currently used very successfully together with synchrotron methods like X-ray Absorption Spectroscopy (XAS) and X-ray Diffraction (XRD) for the study of the structure of passive layers which will be discussed in detail in Section 7.

4.2.1 Electrochemical Specimen Preparation and Transfer into the UHV

The surface analytical investigation of electrochemically prepared specimens with methods working in the UHV involve the problem of their transfer with the loss of contact to the electrolyte and of the externally applied potential and a change of the composition of surface films by contamination and a possible oxidation by the laboratory atmosphere. Some groups apply a specimen preparation within a glove box and a specimen transfer via a transfer vessel, which may be flanged to it and to the UHV system. Others attach a special electrochemical preparation chamber to the UHV system with an appropriate specimen transfer between its various chambers [31–34]. To minimize or to avoid changes during sample transfer, a closed system has been constructed by the author, which allows a very effective sample transfer via a purified argon atmosphere to the UHV. This equipment has been described in detail previously [35, 36]. A short summary is given in the following section (Fig. 10). It permits even the study of the electrode/electrolyte interface of emerged electrodes [35]. These studies require hydrophobic conditions of the emerged electrode surface to study exclusively the double layer without dried-on bulk electrolyte [35, 37a–c, 38]. In the case of oxide layers one may rinse usually the electrode surface with water without any loss of the film.

The special construction of the spectrometer permits not only a safe specimen transfer without chemical changes, but also a well-defined specimen pre-treatment by sputtering previous to the electrochemical preparation. This is very important in the case of alloys because active dissolution or etching and transpassive corrosion or electropolishing may change the surface by preferential dissolution of one component. The altered surface composition may have an effect on the kinetics of passivation and on the composition of the passive layer, formed subsequently as has been

found for Fe/Cr alloys [39]. Furthermore, an air-formed oxide film prevents the start of passivation studies with an oxide-free metal surface with known composition. Argon ion sputtering previous to passivation is a reliable method to get rid of any contaminants and to avoid an uncontrolled starting condition for passivation studies. XPS analysis of the surface is an excellent control of its chemical situation. For many binary systems like Fe/Cr or Fe/Ni alloys, the masses of the components are very close to each other and lead to no change of the composition during Ar-ion bombardment. If the electrode is introduced into the electrolyte at sufficiently negative potentials, one may start a passivation transient with a potential of choice with well-known composition of the electrode surface. The described procedures permit the examination of passive films formed at very negative potentials, or in a short time. Thus, one may get information for a large potential range and also for the kinetics of passive layer formation starting in the millisecond range without any oxide at the metal surface.

Surface analysis was performed with a commercial three chamber vacuum system (ECALAB 5 and ESCA 200X, both VG Instruments), with an analyzer and a preparation chamber and a fast entry air lock (Fig. 10). All vessels were separated by valves. Diffusion pumps and a Ti sublimation pump at the analyzer chamber provided a vacuum in the range of $<10^{-9}$ mbar. A fourth chamber was flanged to the air lock for the electrochemical preparation containing a small electrolyte vessel of ca. 2 cm^3 content. The electrolyte and the water for cleaning were purged with purified Ar (Oxisorb, Messer Griesheim) in a 1 L glass container. Small amounts of ca. 100 cm^3

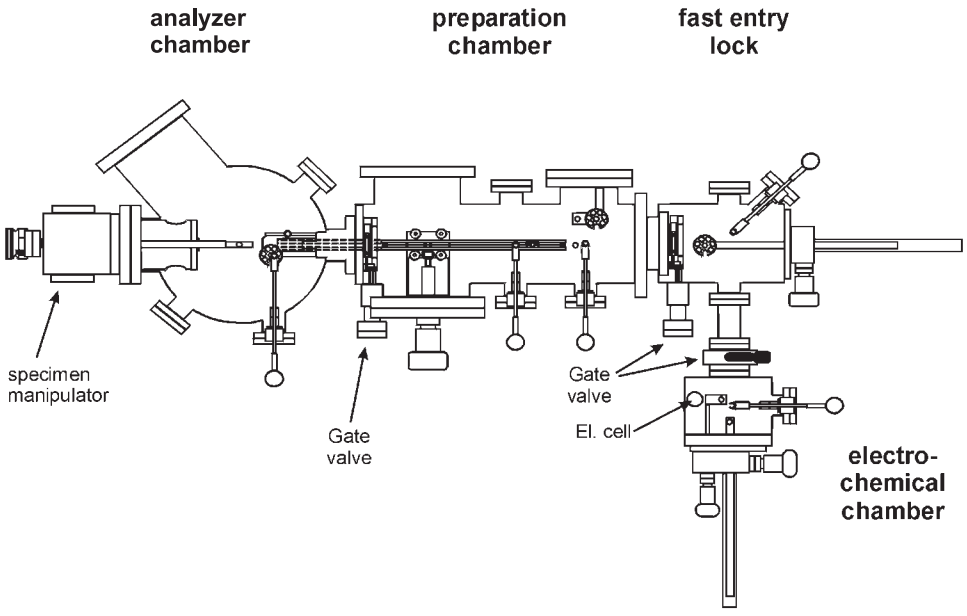

Fig. 10. XPS spectrometer with three vacuum chambers and a forth chamber for electrochemical specimen preparation, providing specimen transfer without contact to the laboratory atmosphere [36].

were purged again in a smaller vessel to remove any traces of oxygen and from there filled into the electrolyte vessel via appropriate connections. A rack and pinion drive system permits a very effective and flexible transfer of specimens between the different parts of the equipment.

The specimens were mounted on stubs and attached to a rotary drive within the electrochemical vessel and turned upside down to contact the electrolyte surface with their circular front plane. The electrolyte level was arranged such that the specimens were not wetted around the edge (hanging meniscus). Short passivation times of less than 1 second were finished by disconnection of the counter electrode with a relay, thus opening the potentiostatic circuit. Alternatively, the potential was pulsed to a value where no further reaction occurs.

A typical specimen preparation involved mechanical polishing down to 1 μm grain size of alumina or diamond spray, Ar-ion sputtering (Specs IQP 10/63, 4,5 mA, 4 keV, 10 min) transfer to the electrochemical vessel, immersion in the range of slight hydrogen evolution and a pulse to the potential in the passive range of choice for the desired time. Then the specimens were washed with Ar-purged water, which replaced the electrolyte in the vessel and finally transferred via the entry lock and the preparation to the analyzer chamber. The vacuum environment of the specimens was thus improved in a cascade to ca. 10^{-9} mbar within 3 to 5 min.

All solutions were prepared from analytically pure substances and deionized water (Millipore, Milli Q water purification system). Hg/HgO/1 M NaOH ($E = 0.14$ V) and Hg/Hg_2SO_4/0.5 M H_2SO_4 ($E = 0.68$ V) served as reference electrodes and were attached outside of the electrochemical chamber. All electrode potentials are given in reference to the standard hydrogen electrode (SHE) and are corrected for liquid junction potentials if necessary.

4.2.2 Ion Spectroscopies

Mass spectrometric methods have been applied to passivity and corrosion research. Adsorbed molecules and components of surface layers may be desorbed by a soft sputtering with a subsequent mass analysis with quadrupole or time-of-flight mass spectrometers. The large variation of the sensitivity of Secondary Ion Mass Spectrometry (SIMS) by orders of magnitude with the properties of the matrix of surfaces may be a serious problem for its quantitative application in surface analysis. However, the post-ionization of sputtered species with an electron beam, or the application of a glow discharge to the specimen surface, help to stabilize the ion yield. With this modification SIMS became a reliable quantitative method for depth profiles of surface films. These mass spectrometric methods are very sensitive to small amounts of layer components. They also open the possibility of mechanistic studies with isotope tracers. A possible application is the location of O^{18} tracers within a passive layer during further oxide growth. Apart from cations and anions of surface films, large molecules may be examined by their fragments, and also as entire molecules. For this purpose often time-of-flight mass spectrometers are used.

Backscattering of noble gas ions at solid surfaces is a useful tool to obtain elemental depth profiles. The two main ion spectroscopies work with different primary

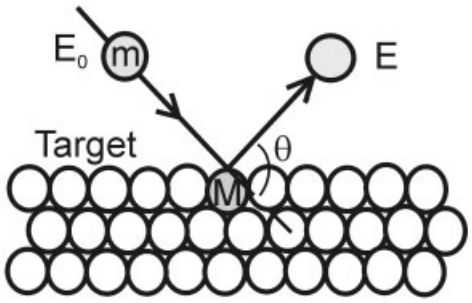

Fig. 11. Binary collision process between noble gas ions of mass m and target atoms of mass M explaining ISS. E_0 = primary energy; E = energy after collision.

energies of the ion beam. Ion Scattering Spectroscopy (ISS) uses a few keV, and Rutherford Back Scattering (RBS) a Helium beam of 2 MeV. If ions with a few keV hit the specimen's surface, then their backscattering is a classical elastic binary collision process (Fig. 11). The ratio of the energies before E_0 and after the collision E for backscattering of ions of mass m at surface atoms of a larger mass M follows Eq. (13). Eq. (14) refers to a scattering angle $\Theta = 90°$. Consequently, the energy spectrum of the backscattered ions contains a peak for each sort of target atoms related to their mass M.

$$E/E_0 = m^2/(m+M)^2(\cos\Theta + [(M/m)^2 - \sin^2\Theta]^{1/2})^2 \tag{13}$$

$$E/E_0 = (M-m)/(M+m) \qquad (\text{for } \Theta = 90°) \tag{14}$$

The ISS analysis was performed with He ions, especially if oxygen and other lighter elements should be analyzed. If the separation of the signals of heavier elements with similar masses was a problem, e.g. for Fe/Cr or Fe/Ni, Ne was used as a probe gas with a primary energy of 3 keV instead of 1 keV [40–42]. For these conditions the mass separation was sufficient for analysis. A 3×3 mm scan with an ion current of 30 nA (EX05, VG Instruments) was used for analysis and 300 nA with a wider scan (6×6 mm) was applied for sputtering with otherwise unchanged conditions. The different scan areas prevented the influence of the crater effect to these measurements. The low ion currents caused a slow depth profiling which was intended for the analysis of these thin passive layers in the range of a few nm thickness.

The intensities of the integrated signals may be evaluated on the basis of well-characterized standards. Consequently ISS provides qualitative and quantitative information on the composition of the surface. Noble gas ions that penetrate the first layers of the surface are backscattered as neutrals, and thus may not pass the energy analyzer. As a consequence, only ions backscattered at the first atomic layer are detected and the method is sampling the outmost atomic layer. A soft sputter process by noble gas ions yields an ISS depth profile with atomic depth resolution. Therefore ISS has been applied to the study of very thin oxide films, as e.g. of passivated Fe/Cr alloys. This method may be applied in addition to XPS due to its high depth resolution.

Rutherford Backscattering is a valuable tool to get quasi-non-destructive depth profiles of thin films on surfaces. According to their high primary energy, He^{2+} ions

penetrate into solid surfaces up to ca. 1 μm and emerge back to the vacuum after a binary collision process with a target atom. This collision process follows Eq. (13) similar to ISS, which yields for $\Theta = 180°$ (backscattering):

$$E/E_0 = (M - m)^2/(M + m)^2 \tag{15}$$

The energy spectrum of the backscattered He ions yields a peak for each atomic species. Its size is proportional to its concentration. As the He ions are submitted to further ineslastic energy losses during their way in and out, broad signals appear that depict the depth profile of the element. Usually the depth resolution is poor and corresponds to the energy resolution of the detector (ca. 5 nm). This method is therefore well suited for thick films. An example on the anodic oxidation of Cu/Al will be presented in a following chapter.

4.2.3 Electron Spectroscopies

If electromagnetic radiation with a sufficiently short wavelength hits a specimen, then electrons may be excited and leave its surface. By the use of X-rays, also electrons of core levels may be emitted. X-ray Photoelectron Spectroscopy (XPS) examines the kinetic energy of these photo-emitted electrons in an electrostatic energy analyzer. A simple energy balance permits the evaluation of the binding energy E_B of the level from which the electron is emitted.

$$h\nu = E_B + E_{\mathrm{kin},A} + (e\Phi_A) \tag{16}$$

Eq. (16) contains the work function of the energy analyzer $(e\Phi_A)$, which is a consequence of the reference of all binding energies E_B to the Fermi level E_F of solid specimens and the relation of the Fermi levels of the specimen and the analyzer to each other in the spectrometer (Fig. 12). $(e\Phi_A)$ is constant for a given spectrometer

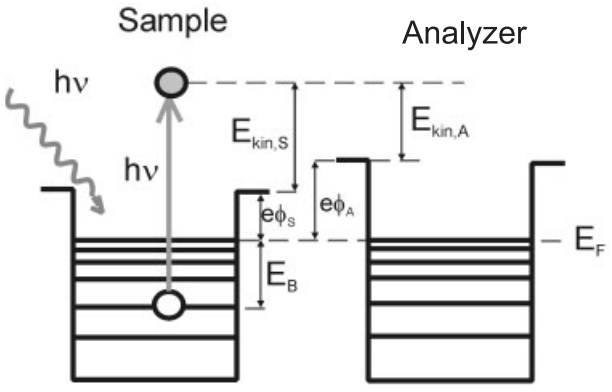

Fig. 12. Potential diagram for XPS with sample and analyzer and their related work functions $e\Phi_S$ and $e\Phi_A$, the binding energy E_B and the kinetic energy relative to the sample $E_{\mathrm{kin},S}$ and the analyzer $E_{\mathrm{kin},A}$.

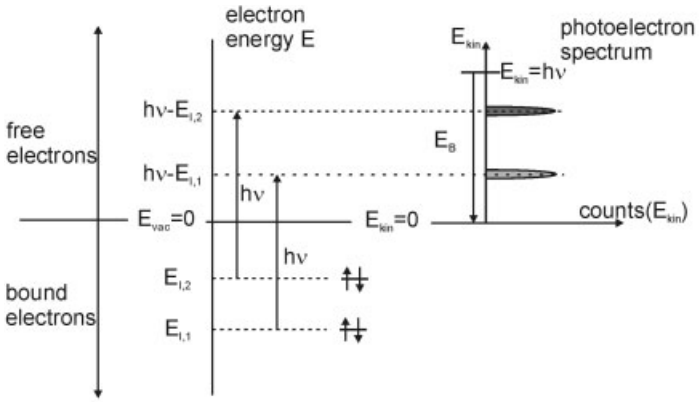

Fig. 13. Excitation of photoelectrons with X-rays of energy $h\nu$ from 2 core levels and their energetic balance and relation to the signals with binding energies E_B and kinetic energies E_{kin}, simplified, work function and retardation voltage omitted.

and is internally compensated which permits one to omit this term at the right side of Eq. (16). With the known energy $h\nu$ of the X-rays, Eq. (16) allows one to calculate E_B when E_{kin} is measured. Fig. 13 illustrates E_B and E_{Kin} of XPS signals and the relation to their core levels. For simplicity the work function $e\Phi_A$ has been omitted equivalent to its internal compensation in the spectrometer. E_{I1} and E_{I2} are the ionization energies of the core levels.

The free level of the emitted photoelectron is filled with electrons at energetically higher levels. The energy of this process may be used for the emission of an Auger electron or X-ray fluorescence as a competing process. Therefore an XPS spectrum contains always the X-ray-induced Auger lines. They are used if the chemical shift of the XPS signals is too small to distinguish different oxidation states of components of a surface layer due to their often-larger chemical shift. Auger lines have been used to distinguish Cu metal and Cu(I) ions to calculate the amount of anodic Cu(I)oxide [43].

For the XPS measurements presented here, an X-ray source with an Al/Mg twin anode was used at 300 W power (15 kV, 20 mA). The appropriate radiation was applied to avoid the interference of XPS and Auger lines. The XPS spectra were run with fixed analyzer transmission (FAT) with a pass energy of 20 eV. The energy scale of the spectrometer was calibrated with the following lines: Ni Fermi edge $E_B = 0$ eV, Au $4f_{7/2}$ $E_B = 84{,}0$ eV, Cu L_3MM $E_B = 568{,}0$ eV and Cu $2p_{3/2}$ $E_B = 932{,}7$ eV. In modern spectrometers the photoelectrons are focused by electrostatic lenses to the entrance slit of a spherical sector analyzer, which permits a large working distance for the specimen (Fig. 14). A constant voltage at the spheres of the analyzer provides constant pass energy of the electrons. To obtain the energy spectrum of the photoelectrons, a continuously changing retardation voltage between the sample and the entrance slit of the analyzer reduces their kinetic energy, thus providing a chance for all electrons to reach the detector via the analyzer when a spectrum is taken. Sensitive spectrometers work with an array of several channeltrons or channel plates to

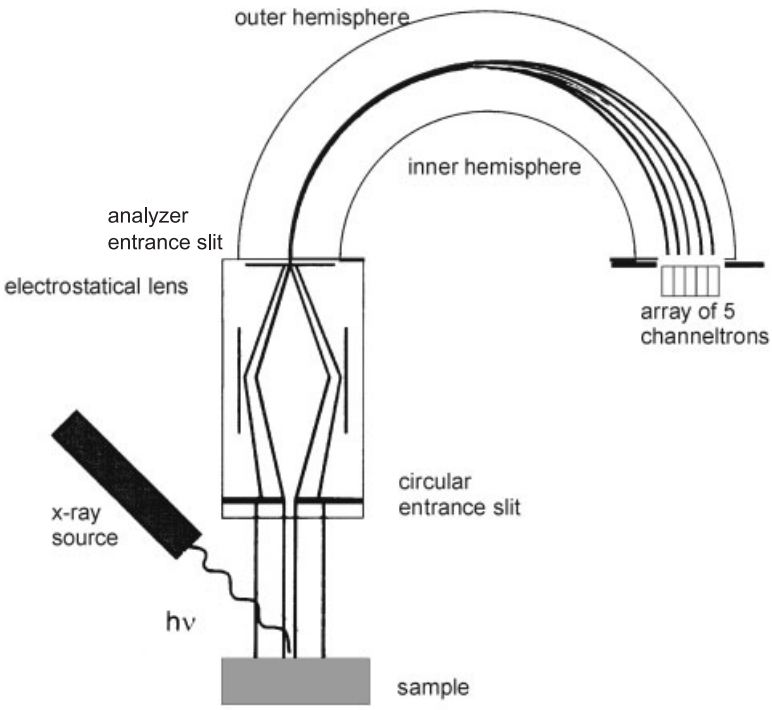

Fig. 14. Schematic diagram for XPS measurements with a spherical sector analyzer and electrostatic lenses.

get high count rates with a computer-assisted shift of the individual data of each channeltron for their proper superposition to obtain an XP-spectrum. The reduction of the surface area from where photoelectrons are accepted leads to a lateral resolution of XPS of ca. 100 μm. This small area XPS is achieved by a small entrance slit of the electrostatic lenses. The polarity of the voltage supply of the hemispheres of the analyzer may be changed so that also the spectrum of positive ions may be taken in the case of ISS.

Each core level of a component of a specimen appears as a characteristic peak in the energy spectrum (Fig. 15). These core level peaks provide a qualitative measure of the composition of the surface. The size of the signal is proportional to the surface concentration of the element under study. For a quantitative evaluation, the relative sensitivities of the elements that depend in first order on their photo-ionization cross-section (PICS) have to be taken into account. The PICS are listed in appropriate tables [44]. The exact energy position of a XPS signal depends on the charge or valency of the atom. Therefore the chemical shift of an element depends on its binding situation. This chemical shift provides valuable qualitative and quantitative chemical information in addition to the elemental composition of a surface. Because of the interaction of the photoelectrons with atoms during their transfer to the UHV the XPS signals have a large background, which requires a background correction. In most cases the signals then have to be deconvoluted to contributions of atoms in

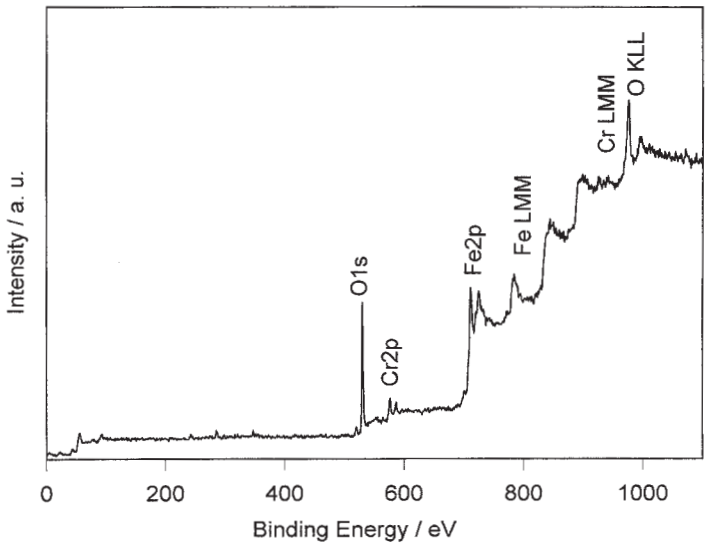

Fig. 15. XPS spectrum of a passivated Fe/Cr alloy with the predominant signals O1s, Fe2p, Cr2p and the Auger signals of the metals.

different chemical conditions (oxidation state, binding state). This is usually done on the basis of well-characterized standards. Fig. 16 gives an example for the $Fe2p_{3/2}$ signal of a passivating layer on Fe alloys with contributions of Fe(0) metal Fe(II) and Fe(III).

XPS is surface sensitive due to the mean free path λ of the photoelectrons within a specimen in the range of some few nm. Their inelastic losses lead to an exponential attenuation of the signal with depth. Thus, only those electrons may contribute to the signal that originate at a depth not larger than 3λ. λ changes in a first approximation with the square root of the kinetic energy of the electrons. The matrix effect is included by a constant empirical value B for metals, inorganic and organic compounds

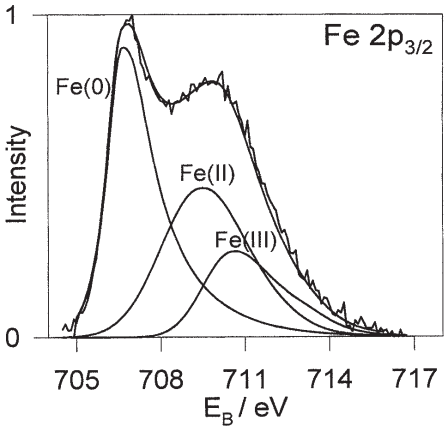

Fig. 16. Deconvolution of the Fe 2p3/2 signal of a Fe/20Cr sample passivated in 0.5 M H_2SO_4 at $E =$ 1.1 V in contributions of the metal substrate Fe(0) and of the oxide components Fe(II) and Fe(III).

according to Eq.(17) [45,46]. The intensity I_i of a component i with a particle concentration N_i of a thin layer follows Eq. (18) with an exponential self-attenuating factor (bracket) which approaches 1 for a large thicknesses d_1.

$$\lambda = B\sqrt{E_{\text{kin}}}, \text{with } B = 0{,}054 \text{ Å/eV for elements [45, 46]} \tag{17}$$

and $B = 0{,}096$ Å/eV for inorganic compounds

$$I_i = X_S \,\text{Tr}\, \sigma_i \lambda_i N_i [1 - \exp\{-d_1/\lambda_i \cos\Theta\}] \tag{18}$$

X_S considers the special design of the spectrometer and its settings, and Tr is the transmission function of the energy analyzer. Both are characteristic for the individual spectrometer. The formation of intensity ratios of species cancels most of the specific factors and thus yields general results independent of the specific spectrometer. The coverage by an additional layer of thickness d_2 adds a further attenuating factor $\exp\{-d_2/\lambda \cos\Theta\}$ to Eq. (18), which yields specific intensity ratios as shown for the bilayer structure of the passive layer on Fe (Eqs. (19)–(21)). The variation of the take-off angle Θ of the photoelectrons (measured relative to the surface normal of the specimen) permits the determination of the depth of a species within a surface layer, and thus the determination of non-destructive depth profiles. The intensity ratio of XPS signals of two species changes characteristically with Θ, enhancing the contribution of those being located directly at the surface relative to those in deeper parts of a film. This angular resolved XPS (ARXPS) is applied to detect, and to prove, a multilayer structure of a thin surface film of some few nm thickness in corrosion research. A good example is the development of a passive layer on iron in alkaline solution with time (Fig. 17) [12, 36]. After the deconvolution of the contributions of Fe(II) and Fe(III) of the $Fe2p_{3/2}$ signal one obtains the integrated signals I of both components and their ratio with a compensation of the special spectrometer characteristics and their photo ionization cross sections.

$$\frac{\text{I}_{\text{FeIII}}}{\text{I}_{\text{FeII}}} = \frac{\text{N}_{\text{FeIII}}\left[\exp\left(\dfrac{d_2}{\lambda_{\text{ox}} \cos\Theta}\right) - 1\right]}{\text{N}_{\text{FeII}}\left[1 - \exp\left(\dfrac{-d_1}{\lambda_{\text{ox}} \cos\Theta}\right)\right]} \tag{19}$$

This ratio cancels most of the pre-exponential factors except the density of atoms N. The intensity ratio is small for a 100 ms oxidation of Fe and gets larger for longer oxidation times t_P due to a first formation of Fe(II)hydroxide and its later oxidation to Fe(III)oxide for sufficiently positive potentials. The upward bending of the ratio for longer times is typical for a bilayer structure, as depicted in Fig. 17. Apparently the bilayer structure develops with time when a sufficient amount of Fe(III) is formed by metal oxidation and by oxidation of the initially formed Fe(II). The details of the passive layer on Fe are discussed in Section 5.1.1.

The quantitative evaluation of the XPS signals requires a background correction according to Shirley [47], and a further calculation on the basis of the spectra of standards. For this purpose the standard spectra were described with a set of Gauss–

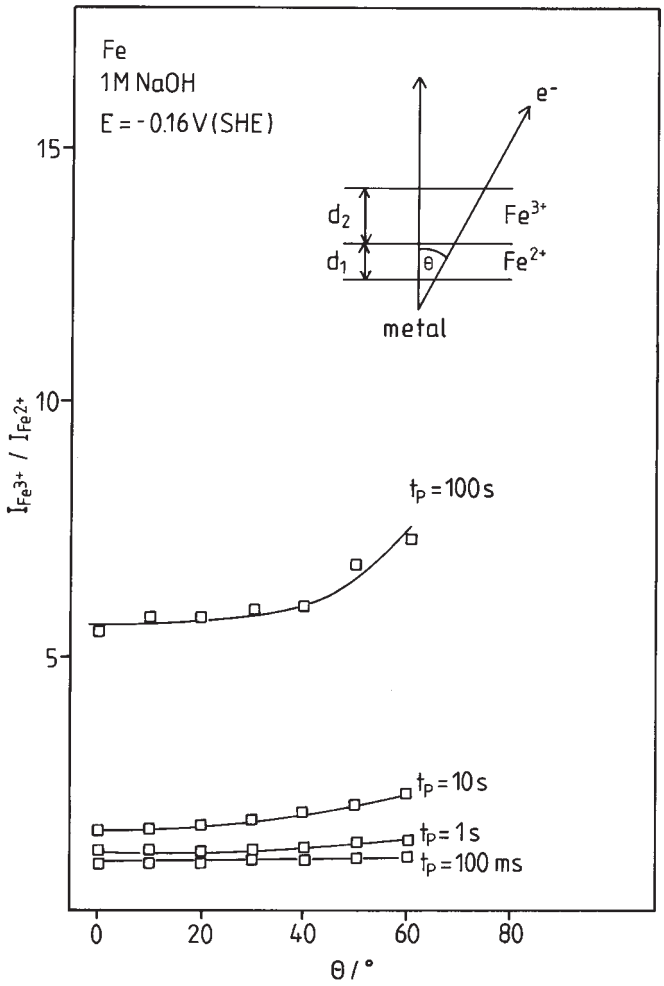

Fig. 17. Angular dependence of the XPS intensity ratio of Fe(III) to Fe(II) components of an Fe specimen passivated in 1 M NaOH at $E = -0.16$ V for times in the range of 100 ms to 100 s [12].

Lorentz curves with a tail function for the asymmetry of the XPS signals for these transition elements. These sets were kept constant in position, shape and size relative to each other. The XPS spectrum of an actual specimen was described with a least-square fit by variation of the size of the appropriate standard sets [36]. Various standards were prepared and measured for a subsequent data analysis of actual specimens. Only some few examples are mentioned here. Pure metal standards are Ar-sputter cleaned specimens. Fe(III) oxide corresponds to a thick passive layer formed at the positive end of the passive range. For Fe(II), a passive layer formed on Fe5Cr is reduced in 1 M NaOH at ca. $E = -1.0$ V (SHE) [12]. For NiO, oxide grown at 1000 °C on pure Ni in air was used as a standard. For Ni(III)oxyhydroxide, NiOOH was deposited by oxidation of Ni^{2+} from weakly alkaline solution or formed

by anodic oxidation of Ni in 1 M NaOH in the transpassive range. For Ni(II)hydroxide, $Ni(OH)_2$ was formed by reduction of a NiOOH layer in 1 M NaOH [14]. Standards of other metals were prepared in a similar way. Often powder specimens of the compounds of interest are a simple alternative. As the cation ratio of these signals may be influenced by a matrix effect, appropriate standards for alloys were obtained often by their chemical and electrochemical oxidation. Especially the Ni2p peak of NiO raises these problems for Fe/Ni alloys [15,48]. Further information on the standards are given when the passive layers on specific metals are discussed.

4.2.4 XPS Data Evaluation

The analysis of the XPS measurements of the passive layers and their interpretation require a model for their structure. This will be discussed for the formation of passive layers on Fe in 1 M NaOH. Similar procedures have been applied for several other systems, as will be discussed in detail in the following sections of this paper. Passive layers are generally not homogeneous and at least a duplex structure has to be accepted. Angular-dependent XPS measurements suggest this situation, as has been shown already for the case of Fe in alkaline solution (Fig. 17). Quantitative XPS allows the determination of the intensity ratio of the Fe species of different valency. The intensity ratios according to Eqs. (20) and (21) provide a possibility to calculate the thickness of the inner d_1 and outer d_2 part. Eq. (19) permits the conclusion about which species is located at the inner and which at the outer side.

$$\frac{I_{Fe(II)}}{I_{Fe(0)}} = \frac{N_{Fe(II)}\lambda_{ox}}{N_{Fe(0)}\lambda_M}\left[\exp\left(\frac{d_1}{\lambda_{ox}\cos(\Theta)}\right) - 1\right] \tag{20}$$

$$\frac{I_{Fe(III)}}{I_{Fe(0)}} = \frac{N_{Fe(III)}\lambda_{ox}}{N_{Fe(0)}\lambda_M}\left[\exp\left(\frac{d_2}{\lambda_{ox}\cos\Theta}\right) - 1\right]\exp\left(\frac{d_1}{\lambda_{ox}\cos\Theta}\right) \tag{21}$$

Alloys with two or more components lead to a more complicated situation. Even for a simple, single-layer structure of the passivating film, and a binary alloy of the components A and B, various reactions have to be taken into account, as depicted in Fig. 18. The rate of transfer of metal components at the metal/oxide interface, and the corresponding rate of transfer at the oxide/electrolyte interface, has to be considered for both cations. In many cases cations of more than one valence state may be transferred into the passive layer and to the electrolyte, which increases the number of variables. Usual electrochemical investigations provide currents and charges by their integration. Knowing the kind and amount of dissolved species, e.g. by rotating-ring-disc studies, one gets the rate of cation dissolution and the related partial corrosion current densities $i_{c,A}$ and $i_{c,B}$. Together with this information, the total current density yields the part for layer formation $i_l = i_{l,A} + i_{l,B}$ and its related charge, which may serve to calculate the layer thickness if the composition, structure and density of the passive layer, are known. Besides layer formation and dissolution a possible preferential oxidation of one metal component at the metal/oxide interface has to be considered which leads to an accumulation of the other component at the

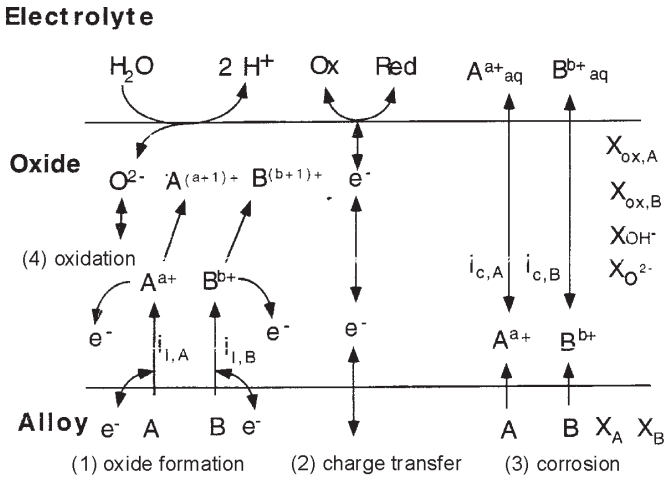

Fig. 18. Schematic diagram for a binary alloy with a passivating oxide film in contact to electrolyte with the reactions of (1) oxide formation, (2) electron transfer, and (3) corrosion, including (4) oxidation of lower-valent cations and the indication of ionic and atomic fractions X as variables for the composition of the layer and the metals surface.

metal surface underneath the film. The still-simplified situation of Fig. 18 requires more than a mere electrochemical investigation to learn about the kinetics and thermodynamics of the corrosion process, i.e. two partial current densities of layer formation $i_{l,A}$ and $i_{l,B}$ and corrosion $i_{c,A}$ and $i_{c,B}$ respectively, and the layer thickness d. Film analysis by XPS and ISS provides various additional data: the layer thickness d and the composition of the film, i.e. the cationic fractions $X_{\mathrm{ox},A}$ and $X_{\mathrm{ox},B}$, including a possible depth profile and the composition of the metal surface $X_{m,A}$ and $X_{m,B}$.

The still-simple case of a binary alloys with a single layer structure of the passive film with a homogeneous cation composition involves the evaluation of at least 7 unknown values, the thickness, 4 cation and anion fractions for the oxide or hydroxide and 2 for the metal surface underneath, which requires 7 independent equations including the trivial sum of the atomic fractions for the metal and oxide phase [15, 48]. XPS supplies the necessary information. The data for such systems were analyzed by the Newton Raphson algorithm to find simultaneously the roots of 5 equations. A bilayer or multilayer structure, or a continuously varying film composition, increases still more the number of variables. This procedure has been applied to several systems by the group of the author [49] to obtain the chemical structure of passive layers on binary alloys. Examples are given in the following part. K. Asami and K. Hashimoto followed this approach [50].

4.2.5 UPS Measurements

With the light of a UV source (HeI: 21.2 eV, HeII: 42.1 eV), electrons may be emitted from the valence band of a solid specimen. Besides the features related to the

density of electronic states in the valence band, one can determine the work function of a metal, i.e. the energetic position of the Fermi level relative to the vacuum or the position of the upper valence band edge for a semiconductor. The leading edge of the UV photoelectron spectrum corresponds to the Fermi level or the valence band edge with the highest possible kinetic energy of the photoelectrons. The cut-off edge refers to photoelectrons that have lost most of their energy. They have a vanishingly small kinetic energy and thus can just leave the solid surface. As a consequence of a simple energetic balance, the width of the UP spectrum ΔE yields the work function $e\Phi_w$ or threshold energy $e\Phi_{\text{th}}$ for a metal or semiconductor respectively Eq. (22).

$$e_0\Phi = h\nu - \Delta E \tag{22}$$

4.2.6 XPS-, ISS- and RBS Depth Profiling

Sputter depth profiles are a valuable tool to determine the distribution of the elements within the layer. In many cases, the masses of the components of the alloys are close to each other so that preferential sputtering does not alter the composition of the thin oxide film or the metal surface underneath. However, oxygen is sputtered generally by a higher rate, which leads to reduction of the oxide film. In consequence, the distribution of the cations may be measured, whereas their valency becomes unreliable. The depth resolution of XPS profiles is determined by the mean free path of the photoelectrons, which is in the range of some nm, i.e. of the passive layer thickness itself. To improve this situation, ISS is a valuable alternative, with a monolayer resolution due to its unique surface sensitivity. Thick films of a few nm up to several hundred nm may be examined with Rutherford Backscattering of He ions. This method yields quantitative depth profiles especially for heavy cations in a light matrix, however with a resolution of ca. 5 nm only, which corresponds to the resolution of the energy dispersive analyzer. An example will be given for the passivation of Al with small amounts of Cu.

5 Chemical Composition of Passive Layers

The analysis of several pure metals and binary alloys yields generally at least a duplex and in some cases a multilayer structure of the passive film, as depicted schematically in Fig. 19. These systems have been examined with surface analytical methods, mainly XPS, but also ISS in some cases. The systematic variation of the electrochemical preparation parameters gives insight to the related changes of layer composition and layer development, and support a reliable interpretation of the results. Usually the lower valent species are found in the inner part and the higher valent species in the outer part of the passive layer. It is a consequence of the applied potential which of the species is dominating. Higher valent species are formed at sufficiently positive potentials only and may suppress the contribution of the lower

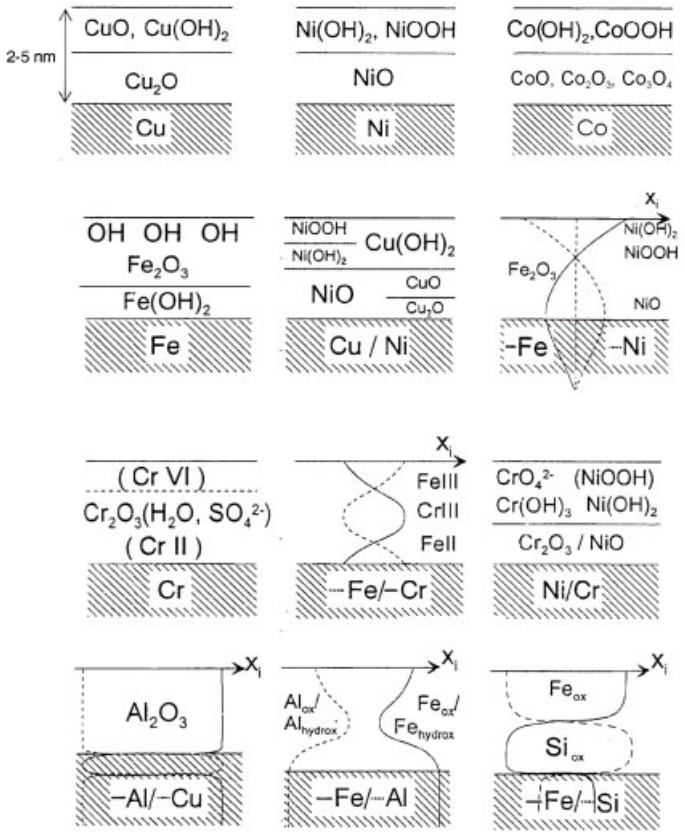

Fig. 19. Schematic diagram of the composition of passive layers on pure metals and binary alloys according to detailed investigation with XPS and ISS.

valent species underneath in the spectra. This situation is in agreement with thermodynamic requirements. The metal should be in equilibrium with the contacting oxide, which contains usually the lower valent cations. Hydroxides are generally located in the outer parts of the film. Apparently, the oxides lose their water during formation in the high-strength electrical field applied by the external circuit, or by the presence of a redox system. Hydrogen ions migrate voluntarily to the electrolyte leaving oxygen ions, which form new oxide with the transfer of new cations at the metal/oxide interface. In some cases, the water content is closely related to the kind of cations. Fe(II) ions form $Fe(OH)_2$ in alkaline solutions at sufficiently negative electrode potentials whereas Fe(III) oxide is formed at more positive potentials. The outer position of hydroxides, as for passive layers on Ni, has been confirmed by ARXPS by several groups [51–54]. This result justifies the assumption that specimen transfer into the UHV does not alter the chemical composition of the surface film. Dehydration in a vacuum should start at the surface and proceed to the inner parts of the film, thus reversing the sequence of the partial layers in comparison to the actual result.

5.1 Pure Metals

5.1.1 Iron

Fig. 20 presents the data of a quantitative XPS evaluation for the passive layer formed in 1 M NaOH at different potentials on pure Fe [12,36]. In alkaline solutions, all Fe oxides are insoluble, and thus may be examined without dissolution during emersion of the electrode. Fig. 20 contains the polarization curve in 1 M NaOH with the identical potential scale for comparison. Fe shows at high pH passivity already at very negative potentials without pronounced dissolution of Fe(II) ions. $Fe(OH)_2$ is the dominating layer component starting at $E = -1.00$ V. Fe(III) starts at $E =$

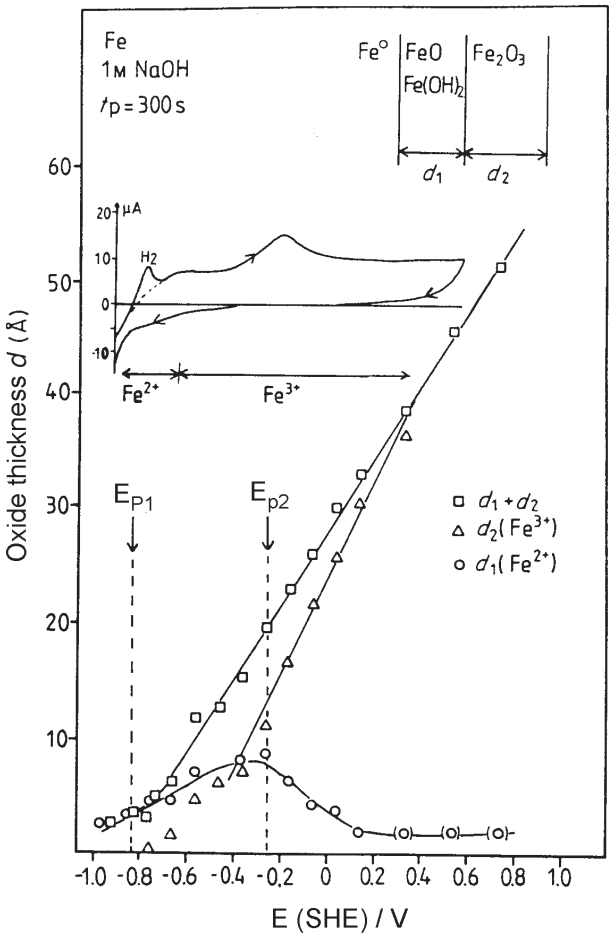

Fig. 20. Composition (Fe(II) and Fe(III)) of the passive layer formed for 300 s on Fe in 1 M NaOH calculated from XPS measurements on the basis of a bilayer model including the potentiodynamic polarization curve with indication of formation of soluble Fe^{2+} and Fe^{3+} species. E_{P1} and E_{P2} are the passivation potentials in alkaline solution and acidic electrolytes (Flade potential) extrapolated to pH 12.9 [12].

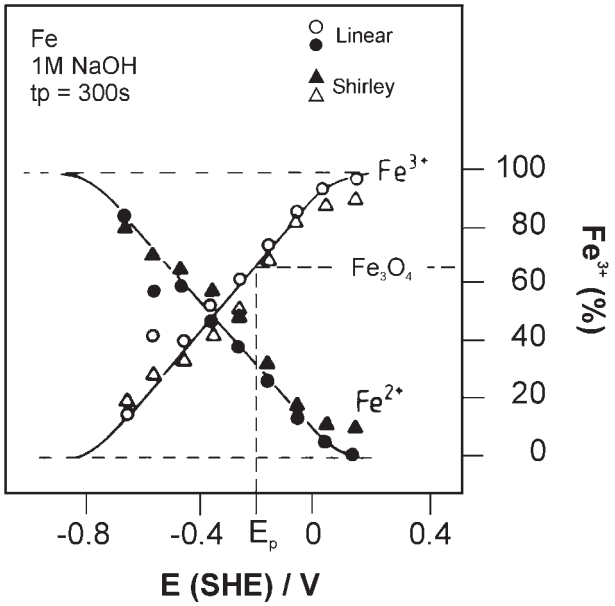

Fig. 21. Composition of the passive layer on Fe formed in 1 M NaOH for 300 s as a function of the electrode potential from XPS results on the basis of a homogeneous layer model, two methods for background correction for data analysis: at the extrapolated passivation potential $E_{P2} = -0.18$ V (Flade potential), the layer composition corresponds to Fe_3O_4.

-0.70 V, which is close to the thermodynamic potential (E_{F1}) for the formation of all Fe(III) containing Fe oxides. At the Flade Potential $E_{F2} = 0.58 - 0.058$ pH, i.e. the passivation potential of Fe in acidic electrolytes, Fe(II) is oxidized to Fe(III) with the related decrease of the Fe(II) part and a steep increase of Fe(III) according to the evaluation of the XPS results of Fig. 20. This process is closely related to the anodic peak at $E = -0.2$ V of the polarization curve. Angular resolved measurements prove the outer position of Fe(III) relative to the inner location of Fe(II) (Fig. 17). Instead of the calculation of the partial layer thickness, one may deduce the average composition i.e. the average cationic fraction X(Fe(III)) = I(FeIII) / [I(Fe(III)) + I(Fe(II))]. At the Flade potential, its value corresponds to the oxide composition Fe_3O_4 (Fig. 21). This result is in close agreement with the interpretation of the Flade potential as the thermodynamic value for the oxidation of Fe_3O_4 to Fe_2O_3 [55] (see Section 2). The chemistry of layer formation may be followed also with time resolution in the range of ms to several 100 s. Similar to the dependence in the potential domain $Fe(OH)_2$ is formed first in the ms region which then is oxidized to Fe(III) oxide [12, 36]. The oxidation occurs earlier with increasing electrode potentials. Parallel to this oxidation a change from hydroxide to oxide is observed. A reverse sequence may also be followed during reduction of passive layers stepping the potential from very positive to negative values [12, 36]. Fe(III) oxide is reduced to Fe(II) hydroxide and finally to Fe metal. The reduction of passive layers on Fe/Cr alloys, i.e. in the presence of Cr, stops at Fe(II) and only negligible portions are reduced to the metallic

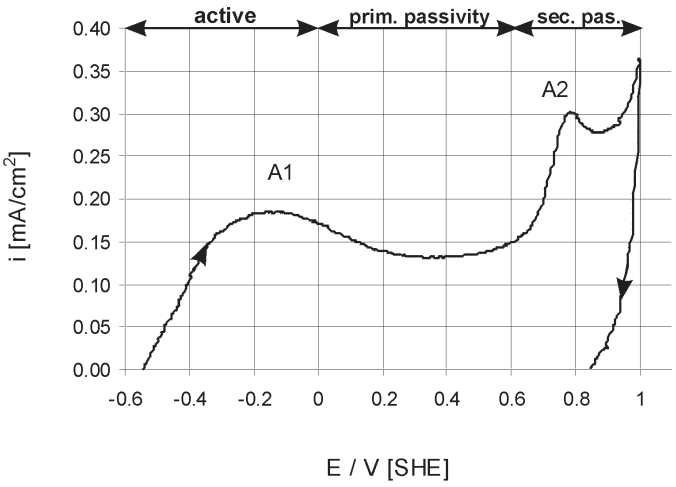

Fig. 22. Potentiodynamic polarization curve of Co in borate buffer pH 9.3 with potential ranges of active behavior, primary and secondary passivity and their relation to the oxidation peaks A1 and A2 [57].

state. Cr(III) is not reduced and remains within the passive layer. This example shows that one may follow with XPS not only the formation of the film, but also the change of its chemical composition with potential and time.

5.1.2 Cobalt

With respect to the polarization curve of Co, one may distinguish the potential range of primary and secondary passivity as shown for 0.1 M NaOH in Fig. 22. In strongly acidic electrolytes the dissolution current densities are relatively high, in the range of some mA/cm^2 and only a small plateau of secondary passivity appears immediately before the onset of oxygen evolution at 1.4 V (pH 2.2) [56, 57]. The separation of the potential range of primary and secondary passivity improves with increasing pH. The potential of the first anodic peak A1 and the onset of oxygen evolution shift by $E = -0.059$ V / pH, whereas A2 at the transition of the two passive ranges changes less.

The composition and thickness of the passive layer changes with potential in agreement with the polarization curve. In borate buffer pH 9.3, the thickness increases linearly with the potential in the primary passive range ($E = 0.0$ to 0.70 V) within ca. 1 nm and takes a step to 4 nm at $E = 0.75$ V [57]. In 0.1 M NaOH, pH 13, the thickness grows up to ca. 15 nm in the primary passive range ($E = -0.4$ to 0.40 V) and drops to ca. 5 nm in the secondary passive range ($E = 0.3$ to 0.70 V) with a further linear increase with the potential [58]. In the active potential range, negligible amounts of Co(II) hydroxide are found in both solutions. In 0.1 M NaOH, $Co(OH)_2$ covers the metal surface in the primary passive range which changes to Co(III) oxide in the range of $E = 0.2$ to 0.4 V and to pure Co(III) for $E > 0.4$ V (Fig. 23a). This formation of the Co(III) film coincides with the change of primary to sec-

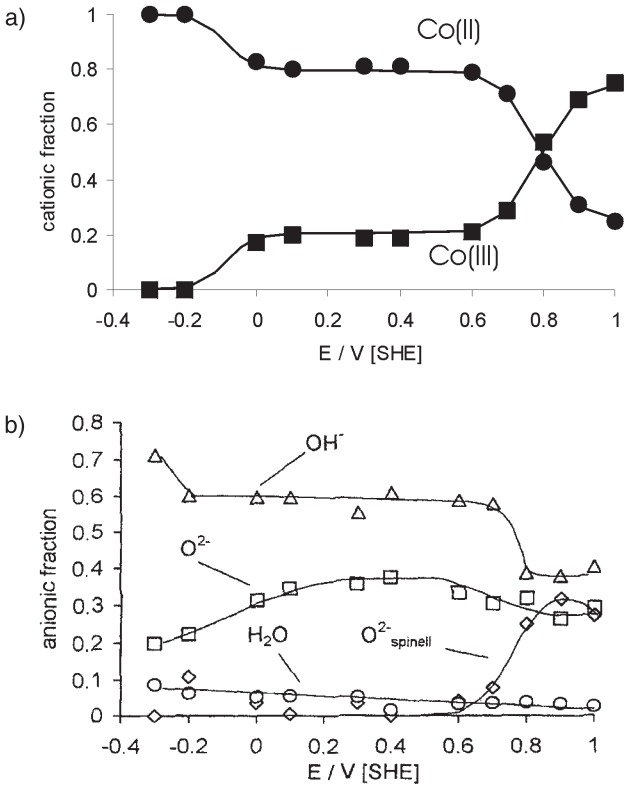

Fig. 23. Cationic (a) and anionic (b) fractions of the composition of passive layers formed on Co in borate buffer pH 9.3 as a function of the electrode potential [57].

ondary passivity with a characteristic sharp anodic peak in the polarization curve at 0.3 V [58]. Its charge of 750 μC cm^{-2} corresponds to the oxidation of ca. 4.7 monolayers of $Co(OH)_2$ to CoOOH. Freshly formed $Co(OH)_2$ has the layered structure of CdI_2 with a sequence of OH–Co–OH layers and a larger gap between the sequence of two of these sandwiches [59]. Within this water-containing gap, the necessary exchange of H^+ ions occurs sufficiently fast during the oxidation of $Co(OH)_2$ to CoOOH to form a sharp peak in the polarization curve. This peak disappears if the hydroxide is aged with the loss of this gap, and thus a much slower oxidation reaction. During the transition of primary to secondary passivity, a special peak at 530.3 eV contributes to the O1s signal of the XP spectrum, which is interpreted by the formation of a spinel oxide at the metal surface. The O1s signal proves the simultaneous presence of hydroxide, oxide, and spinel with the same concentration (Fig. 23b).

The passive layer formed at 0.6 V in 0.1 M NaOH within the range of secondary passivity keeps its composition during stepping the potential to more negative values till 0.25 V and changes from Co(III) oxide to Co(II) hydroxide at $E \leq 0.2$ V, as may be followed by the Co2p and O 1s signals. Simultaneously with the change of an

oxide to a hydroxide, the spinel signal is disappearing. $Co(OH)_2$ is not reduced to metal at potentials as low as −0.8 V within 5 min in 0.1 M NaOH.

The formation of the passive layer on Co has been followed also in the time domain [58]. During the first seconds, Co(II) forms predominantly, even in the range of secondary passivity, but disappears gradually within several minutes, whereas Co(III) increases at the same extent. Simultaneously, hydroxide is replaced by oxide, although finally it is still present up to 30 %. Again, the formation of Co(III) is accompanied by the appearance of the spinel signal.

The application of XPS to the investigation of passivity of Co shows a complicated sequence of anodic oxides, which are formed and may be reduced according to the electrode potential. Angular resolved XPS suggest an outer position of hydroxide and an inner position of oxide.

5.1.3 Copper

Pure copper forms protecting oxide films in weakly acidic and alkaline solutions only, whereas for $pH < 5$ a continuous dissolution with increasing potential is observed. Fig. 24 presents an example for polycrystalline Cu in 0.1 M KOH with the indication of the composition of the anodic films, including the species dissolving into the electrolyte as determined with a rotating ring-disc electrode [60]. The chemical composition of the anodic oxides grown at different potentials in the passive range has been examined with XPS [60–62] and X-ray-induced AES [61]. AES permits one to distinguish between Cu metal and Cu(I) oxide, which is not possible for XPS due to the almost negligible chemical shift of the XPS signals of both species. The polarization curve shows two anodic and cathodic peaks (Fig. 24) [60]. Peak AI refers to the formation of Cu_2O, and AII to the formation of CuO, with contributions of $Cu(OH)_2$. Peaks CI and CII refer to the reverse reactions. From $E = -0.25$ V to $E = 0.05$ V, a simple Cu_2O film is observed. In the potential range of $E = 0.4$ to 0.9 V depth profiles by ISS show a duplex structure of the passive film with an inner Cu_2O and an outer CuO part [60, 62]. XPS studies show a strong OH contribution for the duplex layer, thus its outer part should be seen as a CuO, $Cu(OH)_2$ film. The sharp reduction peaks C1 and C2 have been used to determine the oxide thickness with the reactions as indicated in Fig. 24. Up to 1.2 nm of Cu_2O have been found for the Cu_2O and the Cu_2O / CuO,$Cu(OH)_2$ duplex film. The outer Cu(II) film grows linearly with the potential up to 2 nm CuO or 4 nm $Cu(OH)_2$ respectively [60]. The reduction of the passive layer occurs via the formation of Cu islands, according to reoxidation studies after partial film reduction [63]. Short-time anodic transients followed by an immediate reduction of the oxide suggest the formation of precursors in the ms range, which suggests a composition similar to Cu(I) oxide. This precursor forms during aging Cu_2O or a duplex film within 10 to 100 s only [64]. This observation is important for structural studies by STM, which will be discussed in a following section. In the potential range of peak AII the oxide thickness grows with time in alkaline solutions (0.1 m NaOH) to visible films (slow scans or rest at AII). They get thicker with increasing pH of the solution. These films show for slow scans (1 mV s^{-1}) one main sharp reduction peak at very negative potentials

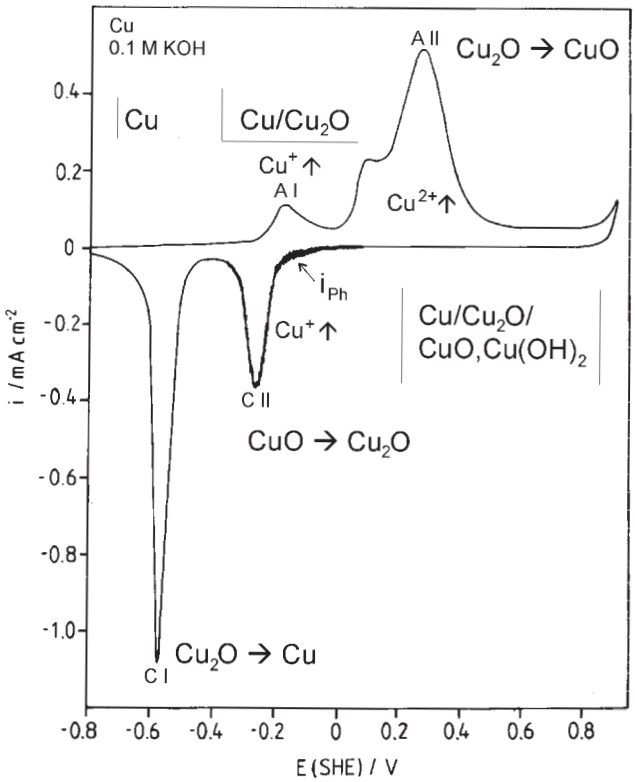

Fig. 24. Potentiodynamic polarization curve of Cu in 0.1 M KOH with anodic and cathodic current peaks and the related reactions of oxide formation or reduction; dissolution of cations and the indication of the stability ranges of the Cu_2O and duplex oxide layer. i_{Ph} at CII indicates oscillating photocurrent due to a chopped light beam [86].

($E = -0.65$ V). The mechanism of formation of these thick layers and their reduction is still not fully understood. They presumably grow with a dissolution/precipitation mechanism.

5.1.4 Chromium

Chromium passivates very effectively down to very negative potentials even in strongly acidic electrolytes (Fig. 5). The cathodic current density of hydrogen evolution is followed by a small potential range of $E = -0.4$ to O V of anodic metal dissolution where Cr dissolves as Cr^{2+}. At $E > 0$ V Cr passivates with a drop of the current density to less than 0.1 μA cm^{-2}. In this potential range Cr^{3+} is the corrosion product. RRD studies have been applied to determine quantitatively the formation of Cr^{3+} ions. In principle the dissolution of Cr^{3+} at a Cr disc may be studied with two concentric analytical rings with their reduction to Cr^{2+} at the inner ring and its

reoxidation to Cr^{3+} at the outer concentric ring [65]. This method has been tested analytically with glassy carbon (GC) rings with an inner ring sensitized by Ag/Hg deposits to get an effective Cr^{3+} reduction and not too much hydrogen evolution [65]. Because of this simultaneous hydrogen evolution, the inner ring current cannot be applied directly for the determination of Cr^{3+} dissolution at the disc. However, its reoxidation at an outer GC ring can be followed without disturbing additional reactions. Although the analytical performance of this special RRD electrode has been still improved by hydrodynamic modulation no Cr^{3+} could be detected [66]. Its dissolution rate is below the detection limit of the method which corresponds to a bulk concentration ca. 5×10^{-6} M and a Cr^{3+} dissolution current density at the disc of 5 μA cm^{-2}. Even for potentiostatic passivation transients no soluble Cr^{3+} could be detected. The total current density of the Cr disc drops from some 100 μA cm^{-2} to a few μA cm^{-2} within the first 10 seconds. From these results, it was concluded that much less than 10% of the total current is used for Cr^{3+} dissolution and the major part for layer formation [66].

At $E > 1.0$ V transpassive dissolution as $Cr_2O_7^{2-}$ is obtained in 0.5 M H_2SO_4, with a strong increase of the current density (Fig. 5). At $E > 1.7$ V oxygen evolution contributes to the large anodic current. These characteristic electrochemical properties indicate the importance of Cr as an alloying additive to obtain corrosion-resistant alloys, especially at negative potentials and in acidic solutions.

In close relation to the polarization curve, and agreement with electrochemical and XPS investigations, the formation of the passivating anodic film on Cr in 0.5 M H_2SO_4 starts already at $E = -0.2$ V. Fig. 25 sums up the thickness d deduced from XPS evaluation, the charge of anodic oxidation Q and the inverse capacity 1/C as a function of the electrode potential [66]. d increases linearly with E as expected for a high field mechanism. The thickness does not get much below 1 nm due to oxide formation by water decomposition, which cannot be avoided during emersion and the transfer of the wet specimen to the UHV of the spectrometer even in absence of traces of oxygen. The extrapolation of the linear d/E relation leads to $E = -0.2$ V for the start of oxide formation in close agreement with the electrochemical results. 1/C increases linearly with E to a maximum at $E = 0.7$ V with a following decrease. As the thickness is increasing, this should be related to a change of the electronic properties of the layer. Similarly Q increases with a different slope for $E > 0.7$ V. It has been suggested that higher-valent Cr species are incorporated into the anodic layer when approaching the potential range of transpassivity, which would explain the larger charge for the same increase of the layer thickness and the change of the electronic properties of the anodic film. According to the O1S and S1S signals, the passive film consists of an oxide with contributions of hydroxide and sulphate inclusions. Even the Cr2p3/2 signal contains contributions that may be attributed to hydroxide.

5.1.5 Nickel

The polarization curve of Ni in 0.5 M H_2SO_4 shows a similar behavior to Cr with a clear separation of the anodic peaks of active dissolution, the passive range of 0.5

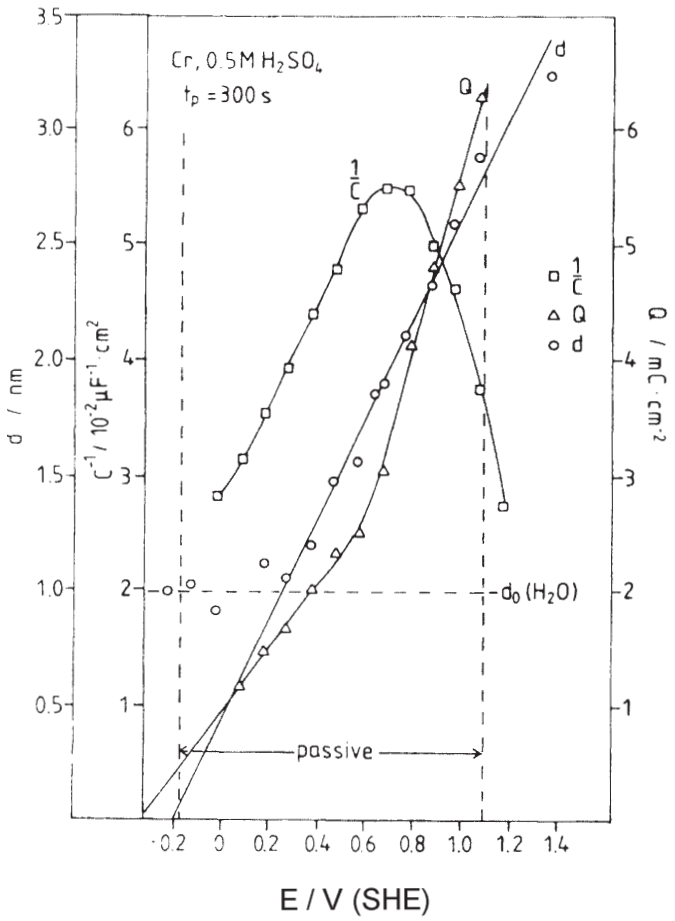

Fig. 25. Oxide thickness d, anodic charge of layer formation Q and inverse capacity 1/C of Cr passivated in 0.5 M H_2SO_4 for 300 s, d_0 is the minimum layer thickness due to exposure of sputtered Cr to water [66].

to 1.5 V and the transpassive range up to 1.8 V with a final current increase at $E > 1.8$ V due to oxygen evolution (Fig. 5) [67, 68]. In 1 M NaOH similar features are observed in the polarization curve however at a much lower current level due to the insolubility of corrosion products at high pH. The anodic peaks are appropriately shifted by ca. 0.9 V to negative values. In acidic solution the main passivating film is NiO with a small contribution of 0.5 nm hydroxide on top. Layer formation starts at $E = 0.6$ V with a thickness of 2 nm which grows with the potential to only 2.5 nm. At 1.6 V the layer disappears completely due to transpassive dissolution. One usually assumes the formation of higher valent Ni ions as Ni^{3+} in the transpassive range, which do not form a protecting film in strongly acidic solutions. They are not stable and thus have not been found by appropriate methods like the RRD technique. However, the results for alkaline solutions strongly suggest their presence. In 1 M NaOH, the evaluation of the XPS data yields an increasing oxide thickness starting

at $E = -0.45$ V and reaching 3.5 nm at 0.95 V [68]. With an almost constant hydroxide film of 1.5 nm one observes a maximum layer thickness of 5 nm at ca. $E =$ 1.0 V. Angular resolved XPS measurements prove the outer position of $Ni(OH)_2$ and the inner location of NiO. Very interesting changes are found in the potential range of 0.5 to 0.6 V. All binding energies related to the anodic layer, i.e. the Ni 2p3/2, the O1s, and the C1S signal of the traces of carbon contamination are shifted by 0.8 eV to lower binding energies. UPS measurements show a shift of the cut-off edge of the photoelectrons in the same potential interval, which leads to an increase of the work function by again 0.8 eV. These observations are interpreted by a shift of the Fermi level of the anodic oxide by 0.8 eV, which causes an increase of all binding energies given by convention relative to the Fermi level (of the anodic oxide) and a decrease of the work function by the same amount. At $E > 0.64$ V changes of the Ni 2p3/2 XPS signal suggest the appearance of a new species. A mere shift of the Ni signals gives no satisfactory fit and a further species has to be accepted. Larger amounts of this species may be obtained at potentials of vigorous oxygen evolution, i.e. at $E = 1.64$ V. For these conditions equal contributions of OH^- and O^{2-} are found for the anodic layer. Apparently the outer $Ni(OH)_2$ film is changed to NiOOH, which may explain both effects, the changes of the electronic properties of the layer due to oxidation of Ni(II) to Ni(III)ions and the release of a hydrogen ion to change $Ni(OH)_2$ to NiOOH. This oxidation of the hydroxide part of the passive layer is expected in close relation to reactions of $Ni(OH)_2$ films in batteries.

In the passive range the oxide thickness grows linearly with log t in the time scale of 1 ms to 1000 s. For $E > 0.7$ V the change of $Ni(OH)_2$ to NiOOH at $t > 0.1$ s causes less regular film growth. For this system again at first NiO and $Ni(OH)_2$ grow which then change to the higher valent species.

5.2 Binary Alloys

For alloys the corrosion properties, as well as the composition of the passive layers, depend strongly on the chemical properties of the alloy components. For an alloy of chemically very different components, the noble metal tends to stay within the metal matrix, whereas the non-noble partner enters preferentially the oxide matrix or is dissolved more readily. The more-noble component enters the passive layer or is dissolved only if the potential is sufficiently positive. The more-noble component will be oxidized also later on a time scale if the potential is sufficiently positive. Besides thermodynamics also the kinetic properties of the system under study have a decisive influence on the various reactions. This involves the rate of transfer reactions at the metal/oxide and oxide/electrolyte interface, as well as the transfer of the cations and anions across the oxide matrix.

5.2.1 Fe/Cr Alloys

Fe/Cr alloys have been studied by many groups with electrochemically and surface analytical methods, this owing to their importance for their industrial applications. Cr is the important component that renders the resistance of stainless steel to the

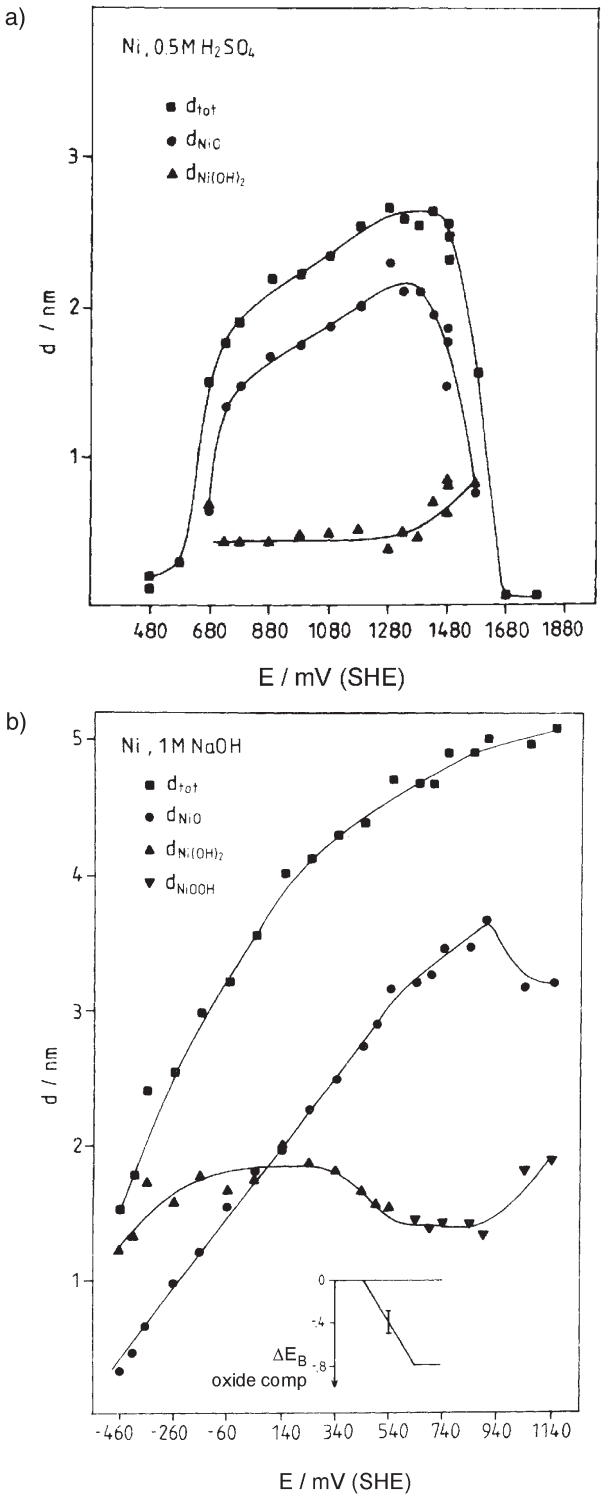

Fig. 26. Total thickness and partial thicknesses of NiO and $Ni(OH)_2$ of passive layers on Ni formed for 300 s in (a) 0.5 M H_2SO_4 and (b) in 1 M NaOH as a function of potential E, NiOOH formation in NaOH at $E = 0.55$ V and dissolution of passive layer at $E = 1.5$ V in H_2SO_4 [68].

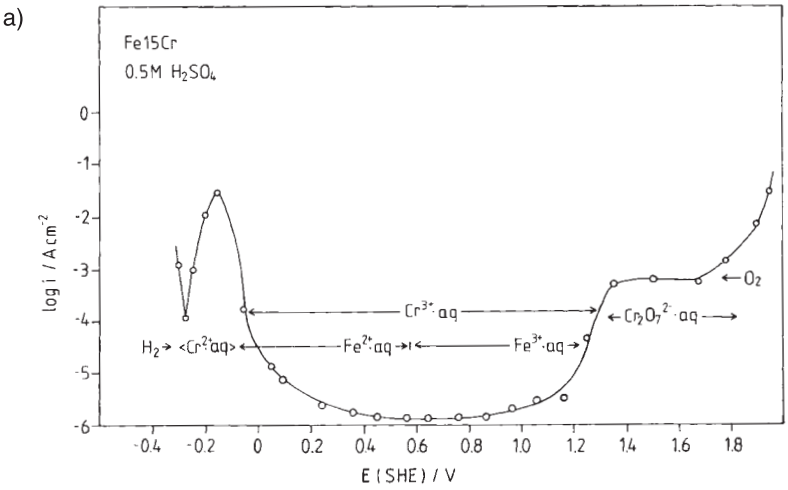

Fig. 27a. Potentiodynamic polarization Curve of Fe5Cr in 0.5 M H_2SO_4 with potential ranges of hydrogen evolution, active dissolution (Cr^{2+}), passivity (Cr^{3+}), transpassivity ($Cr_2O_7^{2-}$), and oxygen evolution [69].

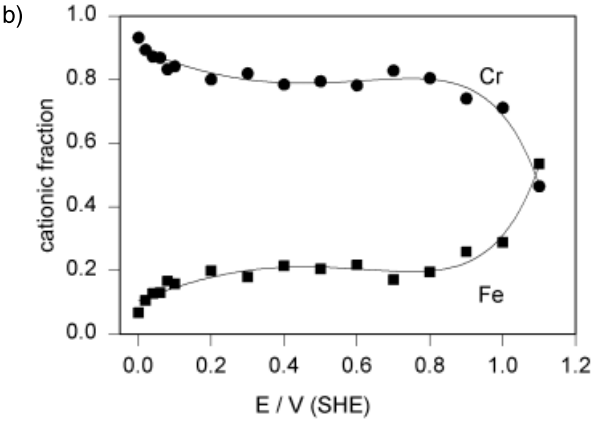

Fig. 27b. Cationic fraction calculated from XPS measurements of passive layer on Fe20Cr formed in 0.5 M H_2SO_4 for 300 s as a function of potential [72].

attack of electrolytic and gaseous environments. For Fe/Cr alloys, both metals are very reactive and enter the oxide matrix or are dissolved. The corrosion current density of passive Cr at the oxide/electrolyte interface, i.e. reaction 1 of Fig. 4, is extremely small even in strongly acidic electrolytes as 0.5 M H_2SO_4. Fig. 27a presents a polarization curve of Fe–15Cr in 0.5 M H_2SO_4 with the potential range of active dissolution, passivity, transpassivity and oxygen evolution, as well as the formation of soluble species. The shape and the characteristic potentials are closely related to those of pure Cr, as was shown in Fig. 5. The smaller corrosion current density in the

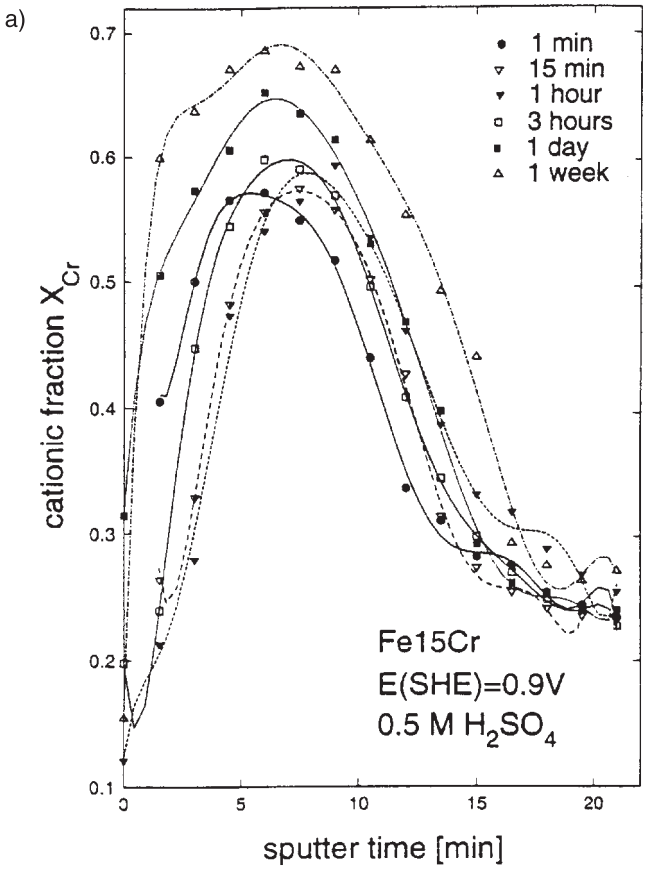

Fig. 28. Composition of passive layers on Fe15Cr from ISS sputter depth profiles formed: (a) in 0.5 M H_2SO_4 at 0.90 V as a function of time.

transpassive range of several 100 μA cm^{-2} is caused by the presence of the passive layer of Fe, which reduces the dissolution rate of Cr as $Cr_2O_7^{2-}$.

Both reactive metal components are oxidized at the metal/oxide interface. However, in the passive range Fe(III) ions are dissolved preferentially with a slow, but still larger, rate by at least one order of magnitude. This situation leads to an accumulation of Cr(III) within the passive layer. XPS studies yield a Cr content of >70 at. % [69–72]. In the active/passive transition range, Cr is accumulated to 90% and it reaches a plateau of 80% in the passive range. Finally, it decreases for $E \geq 1.0$ V in the transpassive range (Fig. 27b).

A detailed insight into the layer composition is obtained with ISS (Fig. 28 a) [69, 70]. The excellent depth resolution of the method yields a sharp distribution with a maximum in the centre of the film. Up to 70 at. % Cr(III) are obtained at the maximum for Fe15Cr alloy. A layer of only some few 0.1 nm directly at the surface is still Fe-rich, however, the Fe ions are lost with passivation time [69]. There is still ob-

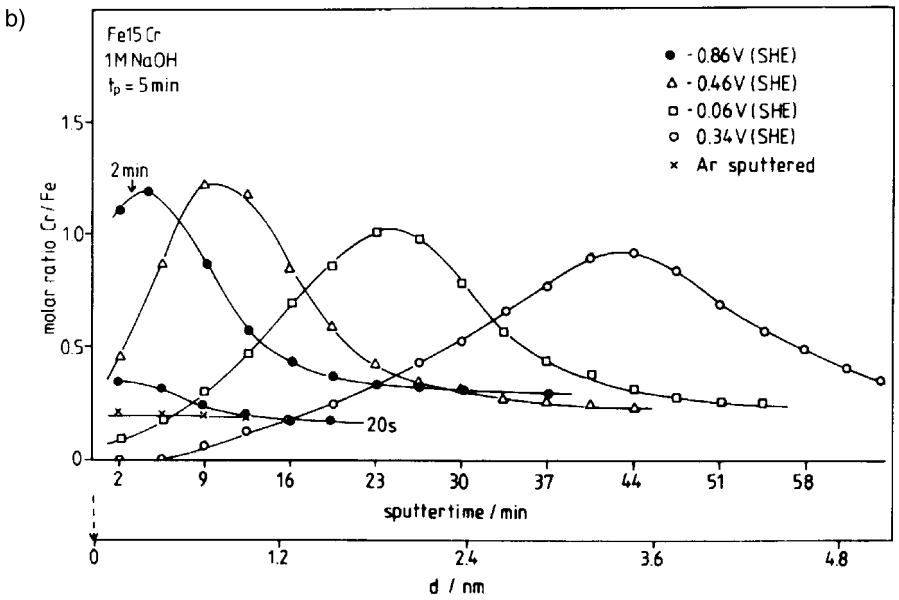

Fig. 28. (b) formed in 1 M NaOH as a function of potential for 300 s and 20 s and 2 min including a sputter-cleaned sample [69, 70].

served change within one week with the loss of the Fe-rich outer layer and still some increase of the maximum of the Cr distribution. Alkaline solutions like 1 M NaOH cause the presence of a large outer Fe-oxide layer of several nm, which is increasing with the potential (Fig. 28 b) [69–71]. This is a consequence of its insolubility at high pH. The preparation conditions of the metal surface have also a decisive influence on the cation composition of the anodic oxide film. The usual procedure for XPS investigations in our group involves a sputter cleaning with argon ions, the control of the surface composition by XPS and the subsequent anodic passivation of an oxide-free surface within the closed system without air contact. If an Fe/Cr alloy is activated, i.e. if it is previously dissolved in the active potential range to remove any residual oxide, Cr is accumulated at the metal surface which is a consequence of preferential Fe dissolution. Therefore, these specimens show a higher Cr content within the subsequently formed passive layer [69]. The influence of the surface composition of an alloy before passivation is often neglected in surface analytical studies but should be taken seriously into account. To our knowledge, a well defined pretreatment of the alloy surface and the information of its composition before passivation seems to be a necessary condition to obtain reliable results. Furthermore, the change of the composition with time is an additional detail that should be investigated with care. For Fe/Cr the composition changes most during the first minutes, but this process continues for days (Fig. 28a). The passivation of alloys should be seen as a process with changes on a large scale in the time domain, i.e. from milliseconds to days. This detail will be discussed in the following part for several other alloys.

The chemical composition of the passive layer of Fe/Cr alloys shows further in-

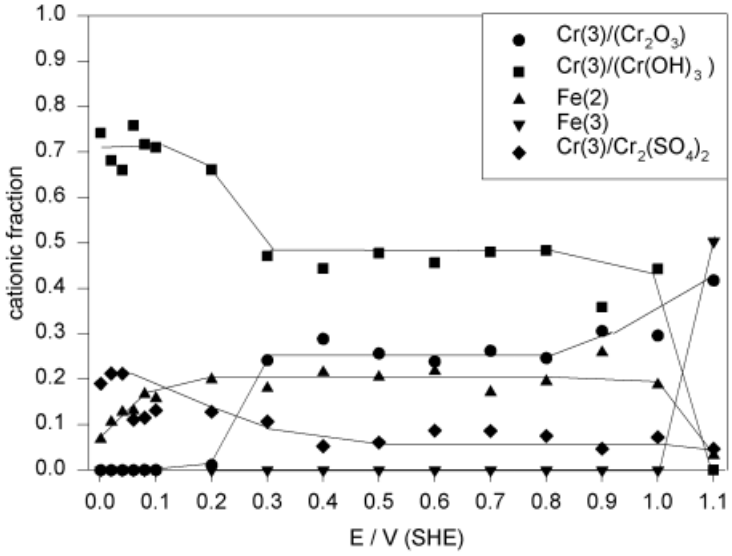

Fig. 29. Cationic fraction of the various cations within the passive layer on FeCr formed in 0.5 M H_2SO_4 as a function of the electrode potential.

teresting changes with the electrode potential in close relation of the polarization curve. For these XPS studies with a more detailed separation of the species within the passive layer, a specimen preparation with exclusion of the laboratory atmosphere is absolutely necessary to have a chance to distinguish Fe(II) and Fe(III) species without Fe(II) oxidation due to air exposure during sample transfer. Reliable $Fe(OH)_2$ standards are obtained by reduction of passive layers in 1 M NaOH as has been described already previously [12]. Fig. 29 shows in 0.5 M H_2SO_4 for the active to passive transition range i.e. for $E = 0.0$ to 0.3 V a large contribution of $Cr(OH)_3$ of 70 at. %, which drops to a plateau of about 50% for $E \geq 0.3$ V when Cr_2O_3 steps to 25%. In addition, 10% $Cr_2(SO_4)_3$ is found, which decreases to less than 10% when the potential enters the passive range. Sulphate should be interpreted as adsorbed species. It is removed completely by light Ar-ion sputtering when most of the passive layer is still present which proves its outer position, i. e. it is not incorporated into the inner parts of the layer. When entering the transpassive range at $E > 1.0$ V, $Cr(OH)_3$ disappears and Cr_2O_3 still increases. Rather astonishing is the presence of Fe(II) within the whole passive range, although Fe(III) is expected at least above the Flade potential of pure iron at $E = 0.58$ V [72]. This result has been carefully investigated with XPS by deconvolution of the Fe2p3/2 signal on the basis of Fe(II) standards. It may be obtained only if one avoids any oxygen access and if one starts passivation with an oxide free metal surface by previous Ar-ion sputtering. Although Fe(II) hydroxide is dissolving rapidly in strongly acidic electrolytes, Fe(II) apparently is stabilized by the Cr(III)oxide matrix. The quantitative evaluation suggests the presence of Chromite ($FeCr_2O_4$), which apparently dissolves slowly enough to form a protective layer. The passive range of pure Cr in 0.5 M H_2SO_4 extends to 1.0 V (Fig. 5). In the transpassive range Cr_2O_3 dissolves as $Cr_2O_7^{2-}$. The passive range of Fe

extends from 0.58V to 1.6 V (Fig. 5). Therefore the Fe component of Fe/Cr alloys forms a stable film for $E > 1.0$ V which, however, is not ideally protective due to Cr dissolution with current densities in the range of 1 mA/cm^2. At $E > 1.0$ V Fe(II) disappears and only Fe(III) is found within the film (Fig. 29). The transpassive dissolution of Cr requires Fe(III)oxide as a slowly dissolving species to provide at least some protection against high corrosion rates. Apparently Fe(II) is oxidized to Fe(III) when Cr(III) is dissolved leaving an increasing concentration of Fe(III) within the film. Within the passive range the layer thickness is small, ca. 0.7 nm, and almost constant. It increases for $E > 1.0$ V to some nm, a value also observed for pure Fe.

In alkaline solution the polarization curves show the characteristic peak structure of pure Fe, however to a decreasing extent with increasing Cr content of the alloy [73]. For repetitive scans, a characteristic pair of oxidation and reduction peaks at $E = 0.50$ and 0.80 V, respectively, pile up, referring to the accumulation of Fe at the surface, which is oxidized and reduced between the Fe(II) and Fe(III) state similar to the observations for pure Fe [12]. Apparently Fe oxide is not lost during the cathodic scan. This has been also found by XPS after cathodic reduction of the passive layer on Fe/Cr [73]. In contrast to pure Fe, the reduction stops at $Fe(OH)_2$ and does not proceed to the metallic state. The change from an oxide to a hydroxide during reduction has also been confirmed by investigation of the XPS–O1s signal. The Cr_2O_3 content of the oxide layer cannot be reduced and remains at the surface. Its presence may explain the difference of the properties of the Fe-oxide component on Fe/Cr alloys in comparison with pure Fe. The total oxide thickness increases linearly with the potential for alloys with 5, 10, 15, and 20 at. % Cr. As in the case of pure Fe, Fe(II) is formed first and oxidized later within ca. 10 s if the potential is sufficiently positive, i.e. positive to the Flade potential of Fe according to the relation $E_P = 0.58 - 0.059$ pH. XPS yields a virtually decreasing Cr content of the film with increasing potential. However, this result is misleading because the film composition has a detailed profile that may be seen by sputter profiling. Fig. 28b shows ISS depth profiles with a large amount of Cr-free Fe oxide in the outer part of the film and a pronounced Cr enrichment in the inner part [40]. Fe^{3+} ions are not soluble in alkaline solutions, and thus have to accumulate at the surface; however, they are lost by dissolution in the case of acidic electrolytes. This difference is obvious by comparison of the ISS depth profiles of Figs. 28a and b.

5.2.2 Fe/Ni Alloys

Ni is a frequent component for alloys as e.g. for stainless steels. Polarization curves of Fe53Ni and Fe10Ni still show features known for pure Ni (Fig. 5). The current increase and the peaks in the transpassive range are suppressed to a large extent in acidic and alkaline solutions due to the influence of Fe [15, 48]. Angular resolved XPS measurements indicate a bilayer structure of the passive film with an outer hydroxide and an inner oxide part. Circa 1 nm hydroxide is found with no change with the electrode potential. The oxide part increases linearly with the potential up to 5 nm and levels off to a constant value for the transpassive potential range at 0.70 V in 1 M NaOH and at 1.40 V for pH 2.9 [15, 48]. At 0.70 V in 1 M NaOH one observes

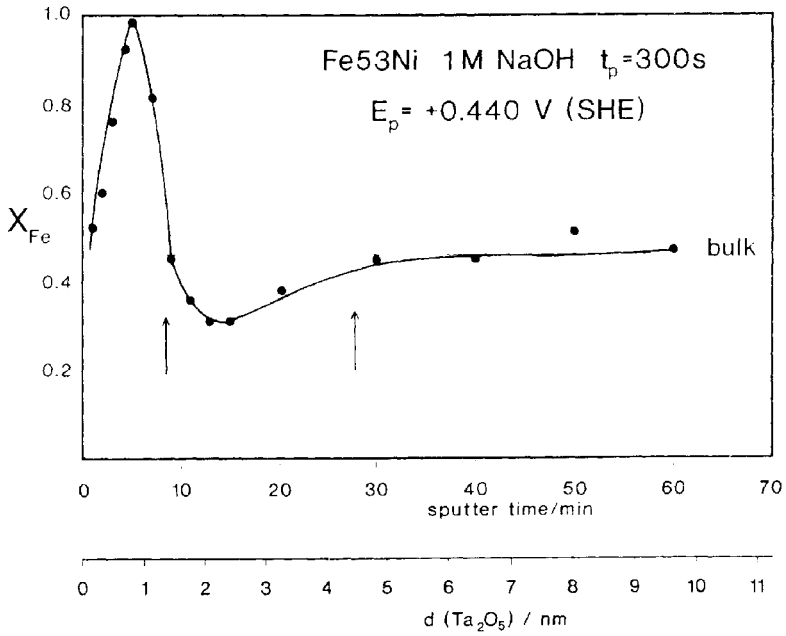

Fig. 30. Composition of a passive layer formed on Fe53Ni for 300 s at $E = 0.440$ V in 1 M NaOH, calculated from an ISS depth profile [74].

a shift of the binding energies and an increase of the work function by ca. 0.6 eV, similar to the results for pure Ni. At the same potential, the evaluation of the Ni 2p3/2 signal requires the inclusion of a contribution of a Ni(III) species, which indicates the formation of NiOOH in the outer layer. Apparently, the electronic properties of the passive layer are strongly influenced by the Ni component. Detailed ISS depth profiling of passive layers formed in 1 M NaOH on Fe53Ni yields a thin outer film that is enriched in Fe with a maximum of 90 to 100 at. % and an inner part depleted in Fe to only 30 at. % at the minimum (Fig. 30) [74]. These profiles with high depth resolution cannot be obtained with XPS. Because of the relatively high information depth of some nm, this method averages the influence of the accumulation and depletion zones. ISS profiles confirm qualitatively and quantitatively many results of XPS investigations. The thickness of the outer hydroxide increases only slightly with potential, whereas the inner oxide grows linearly with the potential up to ca. 6 nm [74]. The thickness increases with a step within the first 0.1 s and then grows linearly with log t. The composition of the layer is reached within 0.01 s with no further change, except for a still slight increase of Ni at the metal surface [15, 74].

5.2.3 Ni/Cr Alloys

Ni base alloys with additions of Cr and Mo are widely used as long-term corrosion-resistant metals as e.g. for containers of nuclear waste. For this reason Ni20Cr and

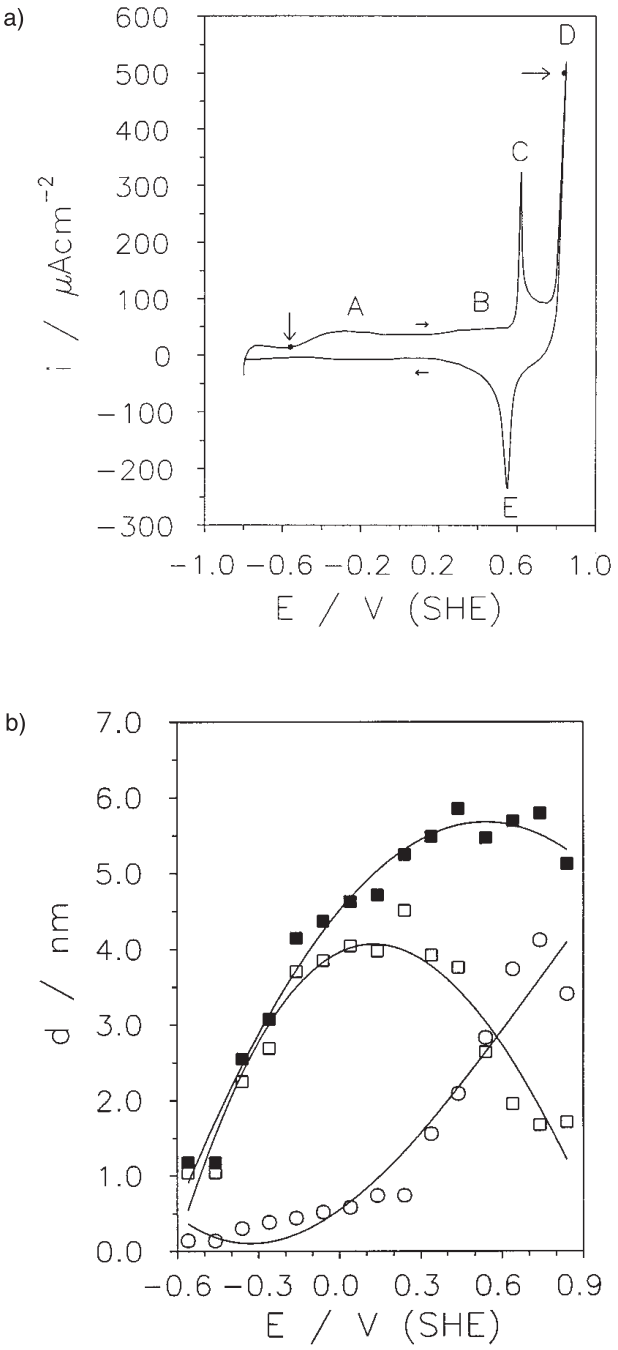

Fig. 31. (a) Potentiodynamic polarization curve of sputter cleaned Ni20Cr in 1 M NaOH with 10 mV s^{-1}, the start and reverse potential are indicated by arrows; (b) thickness of Oxide(○), (□) hydroxide, ■ and total layer; cationic fractions of (c) outer hydroxide and (d) inner oxide layer, □Ni(II), ■ Ni(II) plus Ni(III), ○ Cr(III) and • Cr(VI) [75].

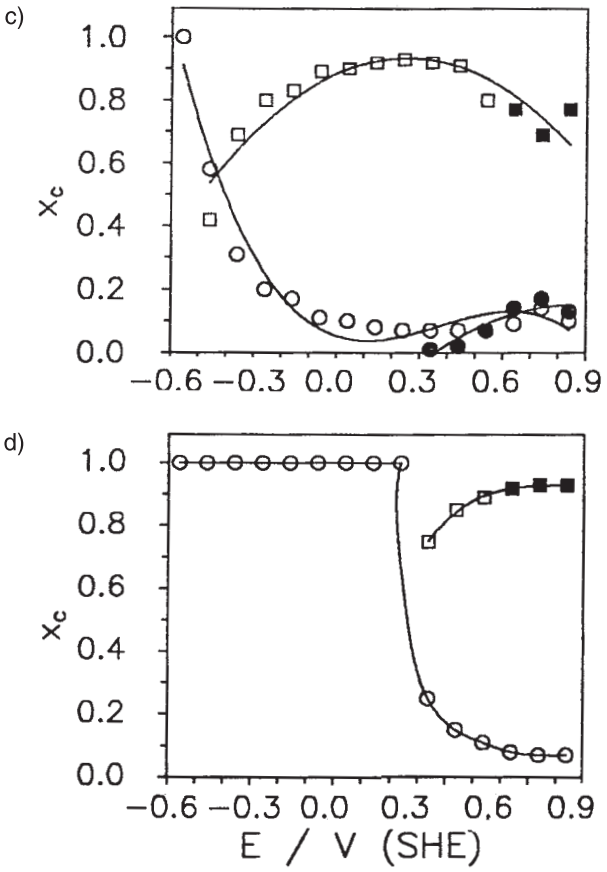

Fig. 31 (continued)

Ni34Cr have been studied in 1 M NaOH and 0.5 M H_2SO_4. Potentiodynamic polarization curves show the characteristic behavior of the metal components with an active, passive and transpassive potential range. Even in 0.5 M H_2SO_4 the active dissolution peak reaches only 25 μA cm^{-2}, which indicates the influence of passivating Cr. In 1 M NaOH, a well-pronounced anodic peak at 0.6 V of Ni(III) formation and the related reduction peak at 0.58 V are found (Fig. 31a). The intense current increase at $E > 0.7$ V and 1.3 V for 1 M NaOH and 0.5 M H_2SO_4 respectively, corresponds to the formation of soluble CrO_4^{2-} and $Cr_2O_7^{2-}$ and Ni^{3+}. An additional shoulder at 0.3 V and 0.8 V for both solutions has a close relation to characteristic features of the XPS results. The evaluation of XPS spectra yields an explanation of the features of the polarization curves [75]. No Ni(II) and only small amounts of Cr(III) are found at potentials negative to the small peak of anodic oxide formation, which is a consequence by a mere exposure of the specimens to water at open circuit during their emersion. In the passive potential range a bilayer structure is found by

angular resolved XPS with an inner oxide and an outer hydroxide part. The total layer thickness increases with the potential up to a maximal value of 3.5 nm in 0.5 M H_2SO_4 and 6 nm in 1 M NaOH (Fig. 31b) at the transition to the transpassive behavior. At negative potentials ($E < 0.0$ V pH 12.9 and $E < 0.6$ V 0.5 M H_2SO_4) the film consists mainly of hydroxide and contains negligible amounts of oxide, which, however, are growing with potential. In 1 M NaOH the oxide layer on Ni20Cr attains a thickness similar to that of the hydroxide at 0.6 V, whereas in 0.5 M H_2SO_4 the oxide thickness is still smaller at the beginning of transpassive behavior at 1.2 V. In 1 M NaOH the hydroxide film contains more than 80 at. % $Ni(OH)_2$, whereas the oxide is almost a pure Cr_2O_3. This situation changes for the oxide to the opposite at $E \geq 0.3$ V when Cr(VI) appears within the film (Fig. 31c). Ni(III) is detected at $E \geq 0.6$ V. The large amount of $Ni(OH)_2$ should be seen as a consequence of its insolubility in strongly alkaline solutions. In 0.5 M H_2SO_4 both partial layers consist of pure Cr_2O_3 or $Cr(OH)_3$, respectively, with only negligible contributions of Ni. Only traces of less than 10 at. % Cr(VI) are found in the outer hydroxide part. At the metal surface Ni is slightly enriched with respect to the bulk metal composition. In 1 M NaOH the appearance of Ni(III) and the sharp anodic peak at 0.6 V go along with an decrease of the binding energies of all oxide species by ca. 1 eV. UPS investigations of emerged electrodes suggest the increase of the threshold energies by the same value. These findings closely relate to the situation of passive layers on Ni and Fe/Ni alloys, which has been explained by an appropriate shift of the Fermi level within the anodic layer to lower energies [14, 15]. The film growth occurs linearly with log t for both layers.

5.2.4 Fe/Al Alloys

Al and Si are very reactive elements that may improve the corrosion resistance of Fe as alloying additives. An increase of the Al content reduces the corrosion current density in acidic electrolytes (pH 5.0, 3.8), especially the active dissolution negative to the passivation potential (Fig. 32 a) [76, 77]. Already 4 at. % Al reduce the current maximum of active dissolution of Fe by a factor of 10. At pH 3.8, 12 or 22 at. % Al are required to suppress this active current peak. XPS and ISS analysis of passivated specimens show a pronounced Al enrichment within the passive layer. ARXPS suggests a uniform distribution of Al. This is however an artifact due to the restricted depth resolution of the method. XPS and ISS depth profiles show a sharp and pronounced Al enrichment in the centre of the layer. Especially the high depth resolution of ISS provides a sharp peak of the Al profile with up to 90 at. % for 22 at. % bulk composition (Fig. 32b). ARXPS analysis yields an unusual outer position of Fe(II) on top of Fe(III) for positive potentials [77]. This situation is apparently a consequence of the low electronic conductivity of the Al-rich part of the inner oxide. During anodic oxidation Fe(II)ions are formed first and are oxidized in a later stage as has been found previously for passive layers on pure Fe [12]. This oxidation process requires transport of electrons across the oxide to the metal substrate, as shown in the diagrams Figs. 4 and 18. Al_2O_3 is an insulator. The Al(III)-rich central part of

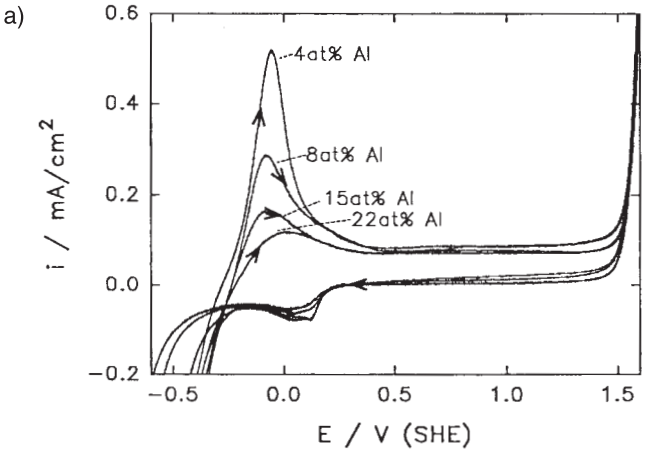

Fig. 32a. Potentiodynamic polarization curve of rotating disc electrodes of Fe/Al alloys in phthalate buffer pH 5.0 with $dE/dt = 20$ mV s^{-1} [76].

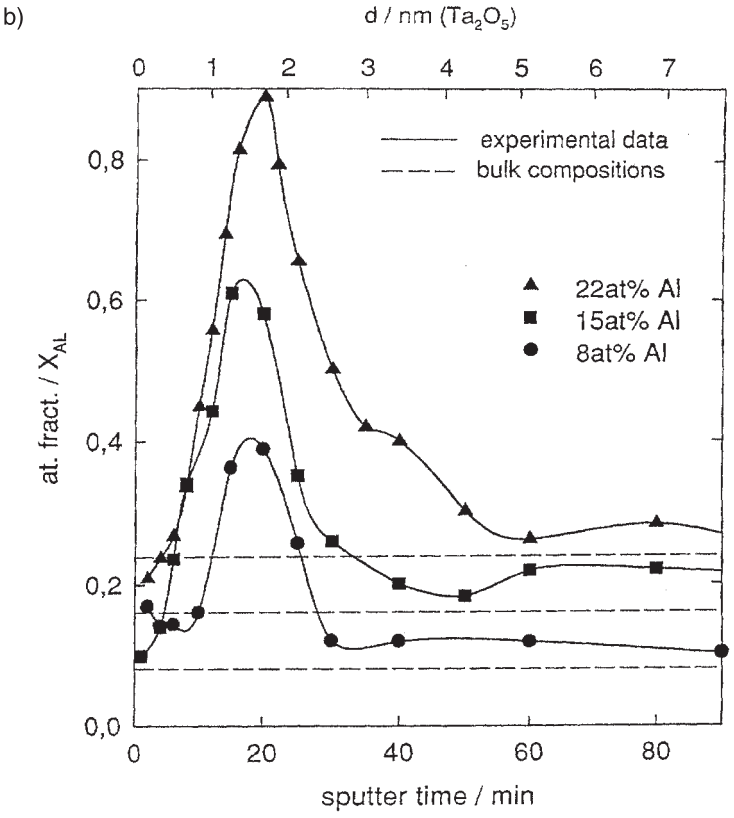

Fig. 32b. Composition of passive layers on Fe/Al alloys from ISS sputter depth profiles formed in phthalate buffer pH 5.0 at $E = 1.0$ V for 300 s [76].

the passive layer apparently may prevent the oxidation of Fe(II) ions in the outer part of the layer where they remain trapped.

5.2.5 Fe/Si Alloys

Fe/Si (single phase) alloys change their passivating properties in a characteristic way with the Si content. Polarization curves in acetate buffer pH 5.0 yield an increase of the passivation current density and the passivation potential with the Si content up to 7.6 at. % (Fig. 33a) [78]. In more acidic solutions as 0.01 M H_2SO_4 alloys with ≤ 7.6 at. % Si even cannot be passivated. If however the Si content gets to ≥ 21 at. % the alloys may be passivated again (Fig. 33b). For 25 at. % Si the passive behavior has remarkably improved with respect to pure Fe. Apparently a sufficient amount of Fe or Si is required to form a protecting continuous Fe_2O_3 or SiO_2 layer. ISS depth profiles show a large accumulation of Si within the anodic oxide layer (Fig. 34) [78]. In the outer part of the film a pure Fe oxide is found for borate buffer pH 9.0, whereas only 50 at. % Fe is obtained for pH 5.0. The inner part consists of almost

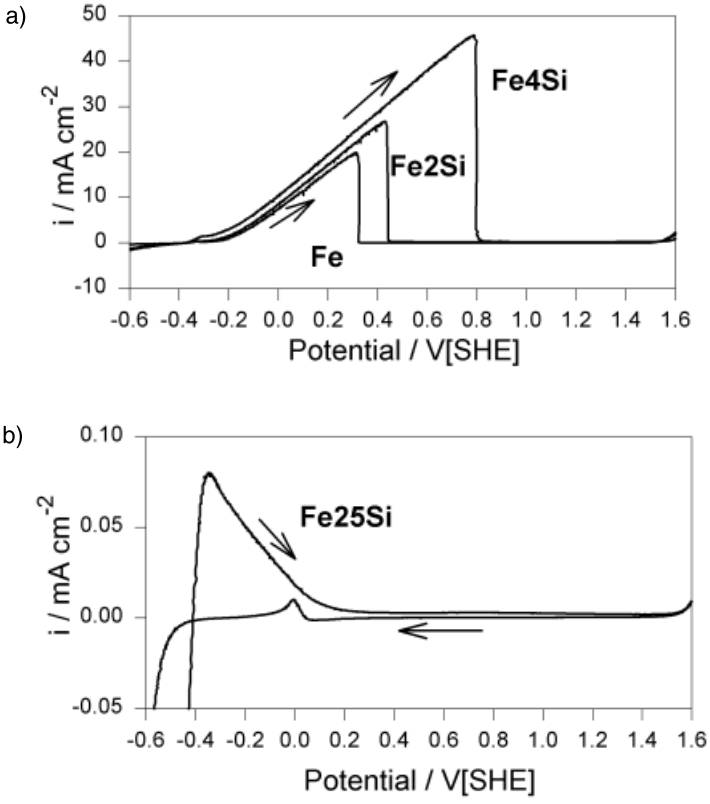

Fig. 33. Potentiodyamic polarization curves of Fe and FeSi alloys with 1 mV s^{-1} in acetate buffer pH 5.0: (a) Fe with 0, 2, and 4 atom % Si; (b) Fe25Si [78].

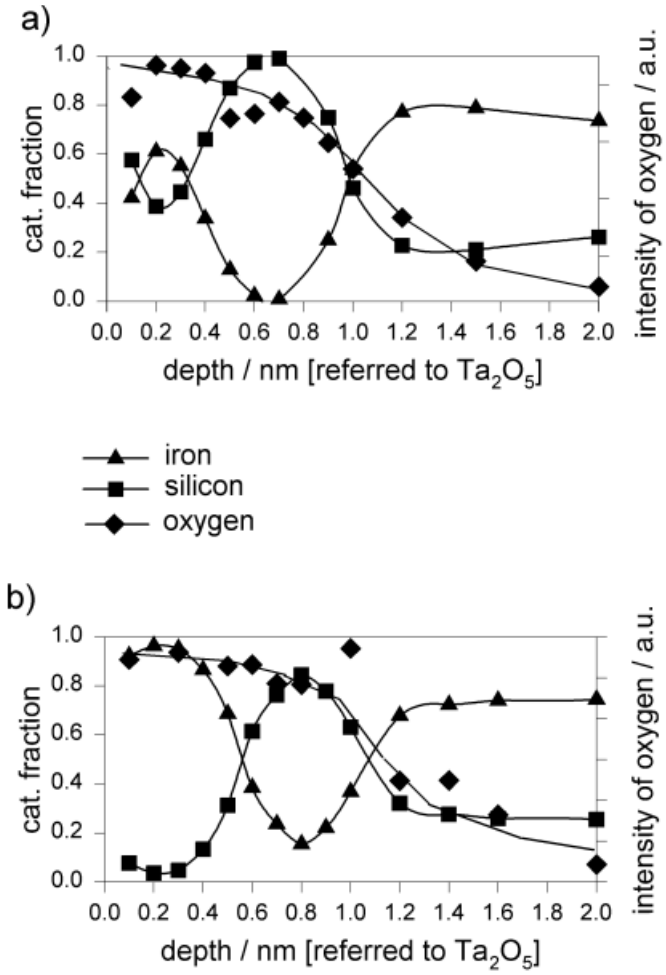

Fig. 34. Composition of passive layers on Fe25Si from ISS depth profiles including the intensity of the oxygen signal formed for 5 min in: (a) acetate buffer pH 5.0 at 1.0 V; and (b) in borate buffer pH 9,0 at $E = 0.90$ V [78].

pure SiO_2 for pH 5.0 and only 80 at. % for pH 9.0. This behavior mirrors the dissolution characteristics of both alloying elements. Fe is dissolved in solutions of low pH, whereas SiO_2 is almost insoluble in both electrolytes. Similar depth profiles are obtained with XPS, however with less depth resolution [78, 79]. In strongly acidic electrolytes, almost pure protecting SiO_2 is formed in the case of high Si content whereas Fe is dissolved. The growth of the passive layer and the change of its chemical composition and structure has been investigated with time resolved measurements [79]. During the first ms, Si is oxidized as the less-noble component. Fe(II) enters the film, but is oxidized to Fe(III) within the first seconds. Finally, Fe(III) is lost slowly by dissolution in acidic electrolytes (pH 5.0) with a remaining SiO_2 film. For high Si-containing alloys this film remains permanently protective. However,

low Si-containing alloys start to dissolve again when Fe(III) is lost. The whole protective film is lost within ca. 1000 s for Fe 2 at. % Si in acetate buffer pH 5.0. The change of a current decay and increase may be followed simultaneously with XPS, which explains the chemical processes during film growth and dissolution. A high Si content of the alloy may even prevent pitting in the presence of chloride. A SiO_2 film is stable with respect to the complexing properties of the so-called aggressive anions, i.e. the halides, and thus a protecting SiO_2 layer is left without attack [80].

According to ARXPS, Fe(II) is located in the outer parts of the anodic oxide and remains trapped up to very positive potentials, especially in alkaline, but also weakly acidic electrolytes. Similar to the situation of Fe/Al alloys, its oxidation is prevented due to the poor conductivity of a large SiO_2 content at the metal surface, i.e. in the inner parts of the film [79]. Fe(II) oxidation requires electronic conductivity from the outer parts of the passive layer to the metal surface.

5.2.6 Cu/Ni Alloys

A special situation arises for an alloy with a reactive and a semi-noble metal. In this case the thermodynamic properties favor the oxidation of the non-noble component, whereas the noble partner accumulates at the metal surface. Cu/Ni is a typical example, which has been studied with various alloy compositions and pH values of the electrolyte [81, 82]. Both pure metals show already a detailed chemistry of oxide formation with two valence states, as discussed above. Similar to the elements, Cu/Ni forms an inner oxide and an outer hydroxide (Fig. 35) [81]. The main constituent for low potentials is $Ni(OH)_2$ with small amounts of oxide. The oxide part is increasing with potential. Within the transpassive potential range, i.e. for $E > 0.5$ V, $Ni(OH)_2$ is oxidized to NiOOH. The hydroxide layer is almost pure $Ni(OH)_2$ and NiOOH in the transpassive range. The main constituent of the oxide is Cu_2O in the inner part and CuO in the outer part of the layer with NiO additives increasing with the electrode potential. The metal surface is enriched in Cu due to preferential oxidation of Ni. This chemical structure of the passive layer is also found with ISS. Fig. 36 depicts a quantitatively almost identical depth profile for XPS and ISS, which clearly shows the outer Ni-rich hydroxide and the inner Cu-rich oxide. A further subdivision of these partial layers with regard to the oxidation states by ISS is not possible because this method distinguishes only the masses of the layer components. NiOOH may be reduced to $Ni(OH)_2$ when the potential is stepped back to 0.5 V. The oxide is reduced at 0 V and leaves pure $Ni(OH)_2$ at the metal surface. Ni20Cu shows principally the same layer structure with some Cu entering the oxide film. The layer structure shows similar changes in the time domain with a first formation of $Ni(OH)_2$ followed by a CuO and NiO containing inner oxide and finally the oxidation of the outer hydroxide to NiOOH.

5.2.7 Al/Cu Alloys

For Cu-containing Al, the thermodynamic data of the metal components differ still more. Al forms a pure oxide with no Cu content. Cu accumulates at the metal sur-

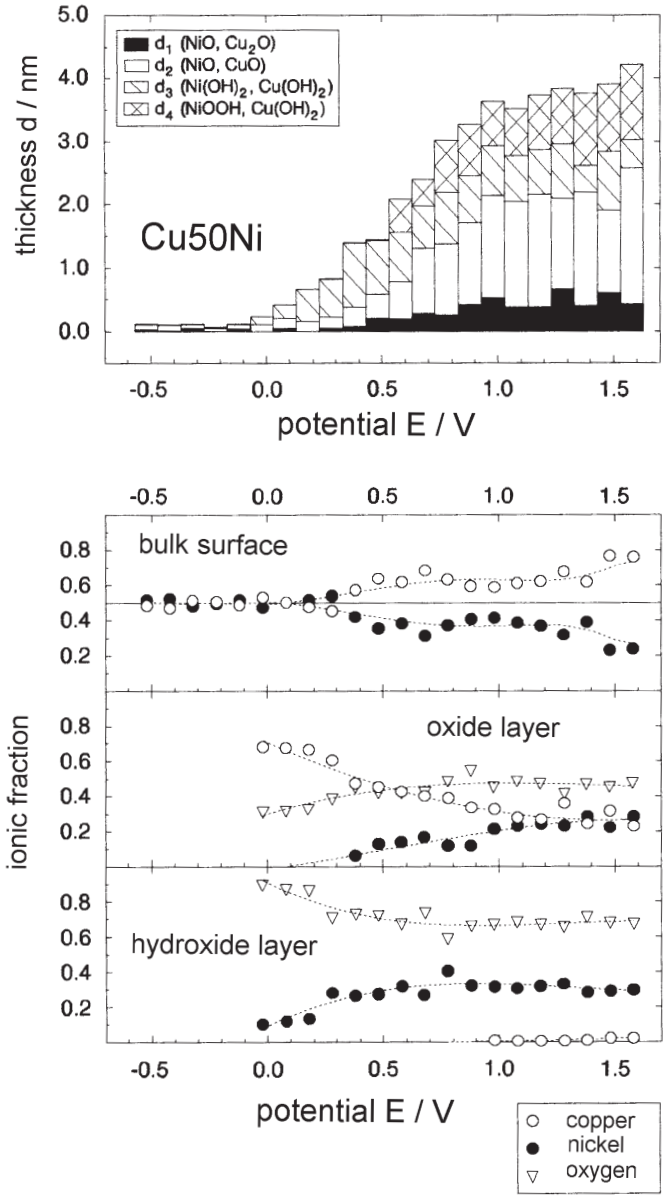

Fig. 35. Thickness and composition of the Cu substrate surface, the inner oxide and the outer hydroxide of passive layers on Cu50Ni formed in phthalate buffer pH 5.0 for 300 s as a function of the electrode potential with distinction of the hydroxide and oxide species with different valences [82].

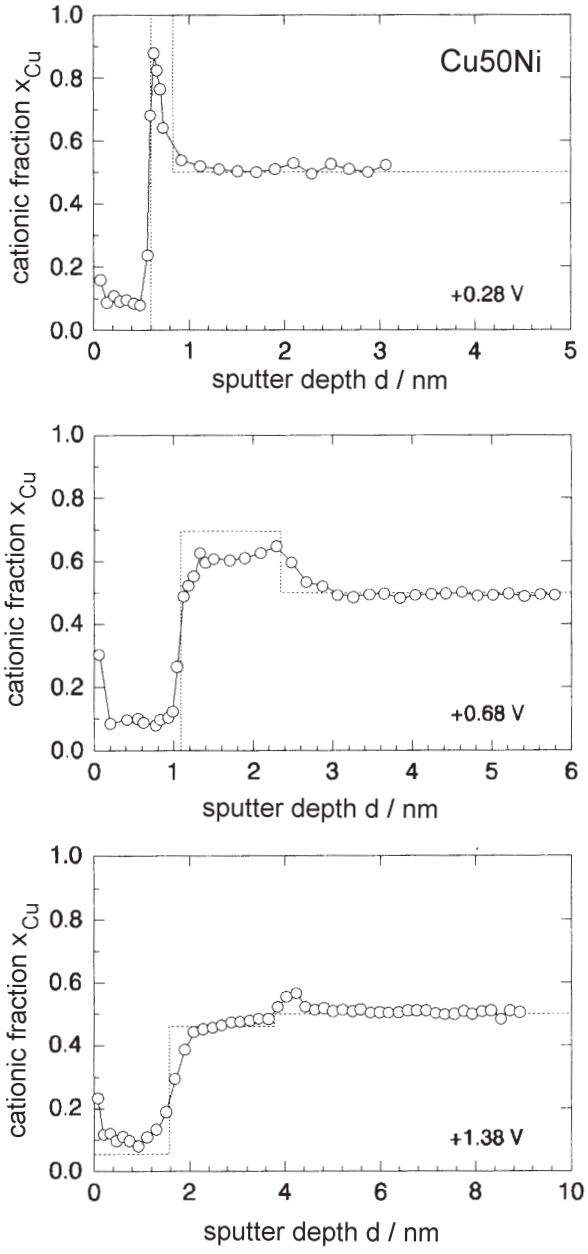

Fig. 36. Composition of passive layers on Cu50Ni from ISS depth profiles and XPS analysis (dashed line) for comparison formed in phthalate buffer pH 5.0 for 300 s at three characteristic potentials as indicated [82].

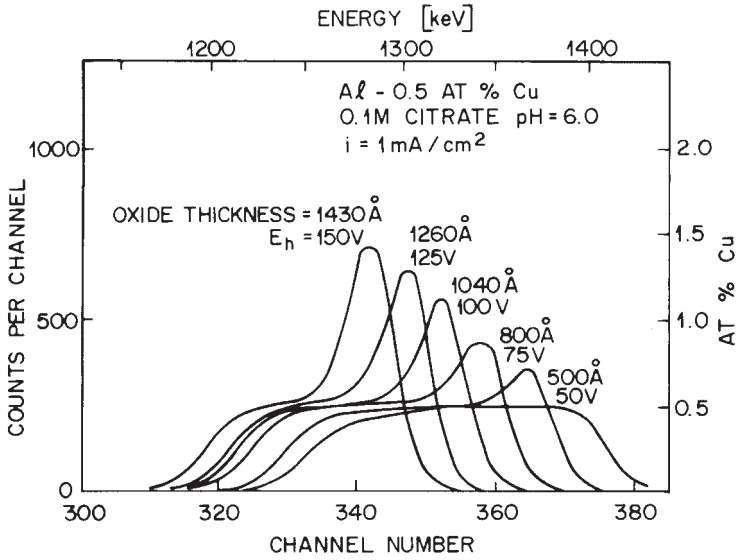

Fig. 37. Copper RBS signal of Al 0.5 atom % Cu vapor-deposited films on quartz passivated galvanostatically with 1 mA cm^{-2} in 0.1 M citrate buffer pH 6.0 to increasing potentials including a film as deposited. Thickness calculated from complete RBS spectrum and applied charge [84].

face and blocks the formation of Al_2O_3 locally due to its presence. Layer formation under galvanostatic conditions leads finally to local breakdown of the passive layer and a perforation of the vapor-deposited alloy films [83]. In this case, the oxide layers are several 10 nm thick and are studied best with Rutherford Backscattering. This method provides a non-destructive depth profile, which clearly shows the Cu accumulation at the interface (Fig. 37) [84]. Cross-sections of anodized Al specimens have confirmed a thin layer of Cu enrichment [85]. In a later stage of film growth, these Cu enrichments get locally larger and less uniform, which may be seen as a roughening of the Cu accumulation zone or a penetration of Cu oxide into the anodic Al_2O_3 layer. The Cu-accumulation peak of Fig. 37 is broadening correspondingly. At the sites of a large Cu concentration, the growth of anodic Al_2O_3 is blocked, which leads finally to the observed breakdown of the passive layer and the locally enhanced dissolution [83].

6 Electronic Properties of Passive Layers

Passive layers of various metals have semiconducting properties; others have insolating properties. As usual, this is a consequence of the band gap. The anodic oxides of metals like Fe, Cr, Ni, Co and Cu show semiconducting properties, whereas the valve metals like Al, Ta, Zr, Hf and Ti form electronically insolating

oxides. The latter do not permit oxygen evolution even at very positive potentials of more than 100 V, which is a consequence of their missing electronic conductivity. Anodic oxide films usually do not consist of perfect crystals. They have small crystalline areas and may be even amorphous. In most cases they have at least a lot of defects, which has consequences for their electronic conductivity, which will influence redox reactions at the surface of passive metals in the dark as well as under illumination. In this chapter an introduction to the application of various methods is given; these provide information on the electronic properties of passive metals. A short overview on the electronic properties of passive layers on various metals is given and the possible mechanisms of redox reactions are presented. As an example, passive copper is discussed more in detail to elucidate some methods that provide information on the electronic properties of passivating films.

The oxide layer of a metal such as copper may be seen as a semiconductor with a band gap, which may be measured by absorption spectroscopy or photocurrent spectroscopy and photopotential measurements. Valuable additional data are obtained by Schottky–Mott plots, i.e. the $C^{-2} - E$ evaluation of the potential dependence of the differential capacity C. For thin anodic oxide layers usually electronic equilibrium is assumed with the same position of the Fermi level within the metal and the oxide layer. The energetic position of the Fermi level relative to the valence band (VB) or conduction band (CB) depends on the p- or n-type doping. Anodic Cu_2O is a p-type semiconductor with cathodic photocurrents, whereas most passive layers have n-character.

An important property of many passive layers is the high doping level with a large concentration of localized states within the band gap. In the case of Cu_2O one has to assume for crystalline material a large concentration of localized states in a larger distance of VB and CB, which may be seen even as a sub-band within the band gap [86–88]. This sub-band causes electronic conduction and electrochemical reactions with redox systems of the contacting electrolyte even in the dark. As the Fermi level of Cu is not close to the VB or CB they essentially do not participate in this electron transfer. A similar situation arises for STM investigations of this anodic oxide. In this case electron transfer has to occur from the tip via the oxide to the metal involving the subband of the oxide layer [89, 90]. To understand these processes qualitatively and quantitatively, information on the semiconducting properties of the anodic oxide layers is required which may be obtained with *in situ* spectroscopic techniques as well as UHV techniques.

6.1 Electronic Properties of Various Passive Oxides

As seen in Fig. 38a the potential distribution across a passivated metal surface with a simple barrier type of oxide layer involves two interfaces and one thin film. Many passivating oxides have semiconducting properties as will be discussed in detail for Cu_2O. Depending on their doping level, semiconductors contain a much smaller concentration of charge carriers as metals. Consequently, the double layer is no longer restricted to the electrolyte and a space charge layer extends into the semiconducting film (Fig. 38b). Usually one assumes that at the metal/oxide interface the

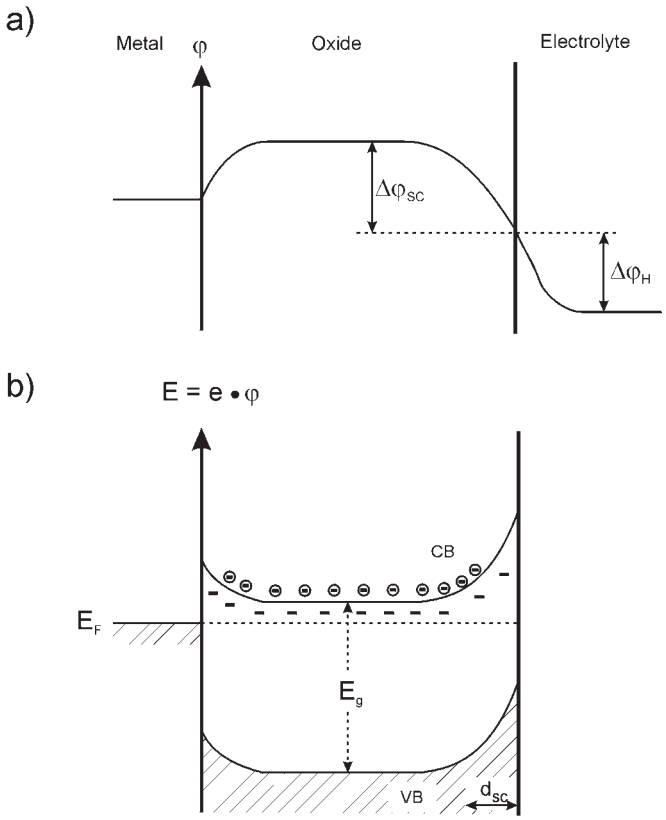

Fig. 38. (a) Potential diagram (φ) with potential drop at the interfaces including the space charge layer $\Delta\varphi_{SC}$ and Helmholtz layer $\Delta\varphi_H$; and (b) semiconductor model of a metal with a n-type passive layer, with the band gap E_g, space charge layer d_{SC}, conduction band CB, and valence band VB.

space charge layer is small, owing in large part to a fast transfer of metal cations from the metal into the oxide layer [91]. Therefore, this interface does not seem to have an influence on the capacity and charge transfer reaction of passivated metal surfaces. The oxide/electrolyte interface takes over most of the potential drop. It may be divided in $\Delta\varphi_H$ of the Helmholtz layer in front of the electrode within the electrolyte, and $\Delta\varphi_{SC}$ of the space charge layer within the semiconducting oxide. As discussed already, the potential drop within the Helmholtz layer is determined by O^{2-} formation from the water at this interface, or the adsorption of species from the electrolyte at the anodic film like OH^- or H^+ ions or other anions from the electrolyte. This adsorption process is in equilibrium as long as it is not disturbed by the application of an overpotential, which may cause the formation of new oxide or its dissolution (positive of negative overpotential). As will be shown in the case of passive copper, the potential increase is located within the semiconducting oxide and a space charge layer is formed within the oxide at the oxide/electrolyte interface. It depends on the applied potential and the charge carrier concentration how far it will

extend into the oxide. The characteristic measure is the Debye length β (Eq. (22a)), which decreases with the concentration of the donor N_D or acceptor levels N_A. The potential will drop within the distance d_{SC} of the space charge layer to a constant level within the bulk of the semiconductor. The thickness of the space charge layer d_{SC} is given by Eq. (22b) and increases with the square root of the potential drop within the semiconducting oxide, which equals to the deviation of the electrode potential E from the flat band potential E_{Fb}. The space charge layers extends deeper into the oxide with increasing potential E and donor or acceptor concentration N.

$$\beta = \sqrt{\frac{\varepsilon\varepsilon_0 kT}{N_D e^2}} \tag{22a}$$

$$d_{SC} = \beta\sqrt{\frac{2e(E - E_{Fb})}{kT}} \tag{22b}$$

The passive layers of several metals like Fe, Ni, Cr and their alloys are only up to a few nm thick, and thus the Debye length is larger than the oxide thickness. In these cases the potential drop extends linearly across the whole anodic layer. The insolating oxides of the so called valve metals such as Al, Zr, Hf, and also on Ti, may be grown anodically to large thicknesses by applying electrode potentials of several 10 to 100 V without any redox reactions (e.g. oxygen evolution). For these thick oxide films, the potential may drop within the space charge layer to a constant value within the bulk oxide. Some anodic oxides (IrO_2, PbO_2) are metallic so that the potential drop is located within the Helmholtz layer as in the case of metals.

The band gap of the anodic oxides varies from the large values of insulators to those of semiconductors and metallic oxides. These values may be obtained from photocurrent spectra as discussed in the case of Cu oxides [97,98] or absorption spectra [99]. Photo Acoustic Spectroscopy has been used as an alternative [100]. It is also based on the absorption of chopped light and uses only the detection of sound to record the spectra. Fig. 39 presents a schematic drawing of the most common oxides taken from literature [101]. The doping of these anodic oxides is usually relatively high in the range of up to some 10^{21} cm^{-3}. Consequently, the Fermi level E_F is close to the energy of the conduction (E_C) or valence band (E_V) in the case of a n- or p-type semiconductor respectively. As the doping level is frequently not known and depends strongly on the preparation conditions, an energy difference $E_C - E_F = 0.25$ eV and $E_F - E_V = 0.25$ eV is assumed in Fig. 39. The positions of the bands are given relative to the energy scale related to the vacuum level or the standard hydrogen electrode. Both scales are related to each other by a difference of 4.6 eV [92–96]. Fig. 39 also contains some redox systems, which are commonly used for electrochemical charge transfer studies. The energy position of the bands is related to these scales by a simple discussion involving the band bending between the semiconductor surface and its bulk $\Delta\varphi_{SC} = E_S - E_B$ and the potential drop in the Helmholtz layer $\Delta\varphi_H = E_{Sol} - E_S$ [91].

$$E_{F,ox} = e[-4.6 + E_{Fb} - (E_s - E_{sol})] \tag{23}$$

$$\Delta\varphi_H = E_S - E_0 = \Delta\varphi_H(0) - 0.059\,\mathrm{pH} \tag{23a}$$

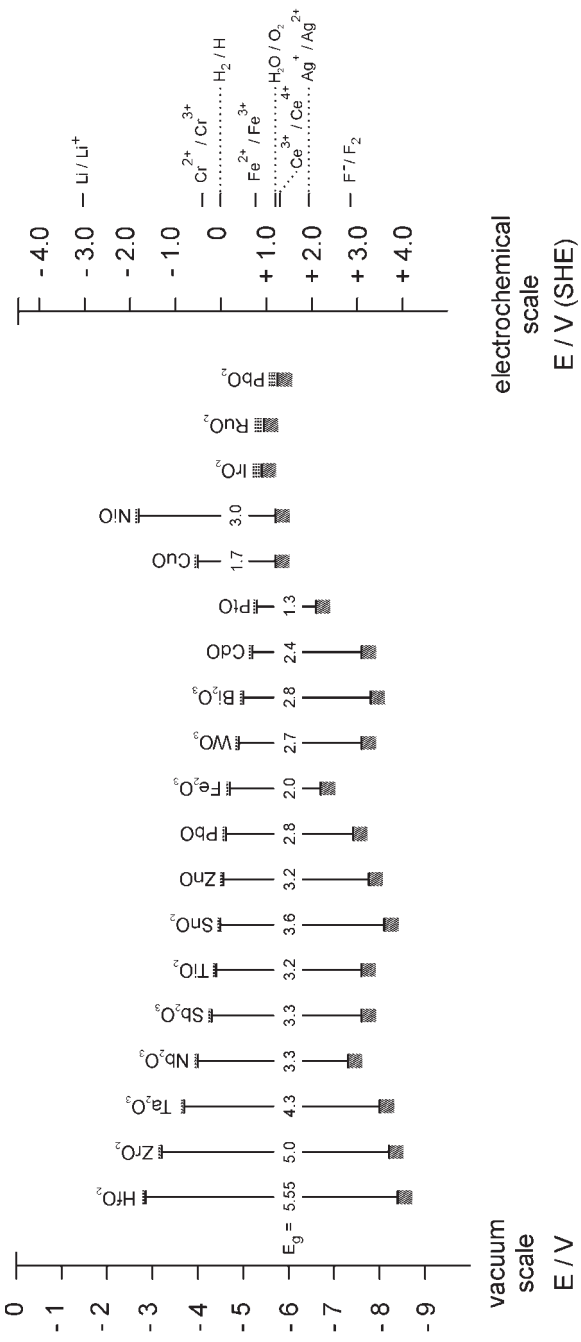

Fig. 39. Band gap and position of bands within the energy scale for various oxides including several electrochemical redox systems, both energy scales, relative to the vacuum level and relative to the standard hydrogen scale (SHE) are given [91].

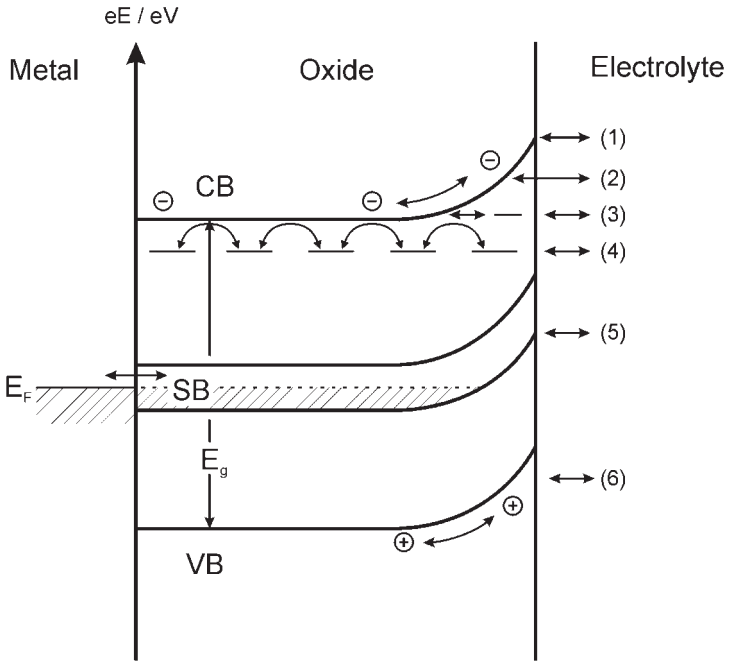

Fig. 40. Electron transfer from redox systems within the electrolyte across a semiconducting passive layer (n-type): (1) direct tunnelling to CB; (2) tunnelling through space charge layer; (3) transfer via surface states; (4) hopping mechanism via interband states; (5) transfer via sub-band; and (6) transfer via valence band.

For the flat band potential situation, i.e. at $E = E_{\mathrm{Fb}}$ and for $e\Delta\varphi_{\mathrm{SC}} = e(E_S - E_B) = 0$, one obtains an appropriate relation for the Fermi level of the oxide $E_{F,\mathrm{ox}}$ in dependence of E_{Fb} and the potential drop in the Helmholtz layer $E_S - E_{\mathrm{sol}}$ (Eq. (23)). The potential drop $\Delta\varphi_H$ changes with pH according to Eq. (23a), which corresponds to the discussion of Section 2, Eq. (3). It is obtained from the adsorption equilibrium at the oxide surface, i.e. from its isoelectric point. The flat band potential E_{Fb} may be determined by extrapolation of the potential dependence of the photocurrent as will be shown in Fig. 40 of Section 6.2 for passivating Cu_2O on Cu. With these data the positions of the energy bands of Fig. 39 have been determined, however with the assumption of an energy difference of the Fermi level from the conduction or the valence band of 0.25 eV, respectively. For the anodic oxides of Cu, the position of the bands has been determined independently by UPS measurements (Section 6.2).

The Fermi level and the doping concentration have been determined for various passive layers by capacity measurements. The capacity of a metal covered by an oxide layer may be split in three contributions $C_{\mathrm{Me/ox}}$ of the metal/oxide interface, C_{ox} of the oxide layer and C_H of the Helmholtz layer at the metal/oxide interface. As these capacities are in series one has to add their inverse values to obtain the measured reciprocal capacity C according to Eq. (24). $1/C$ equals approximately $1/C_{\mathrm{ox}}$ due to the larger values of C_H and $C_{\mathrm{Me/ox}}$. For insulating oxides, C follows the sim-

ple condenser equation and $1/C$ increases linearly with the thickness d (Eq. (25)). For these cases the capacity may be used to measure the oxide thickness, which may be obtained independently from the integrated charge of oxide formation by applying simply Faraday's law to the reaction of layer formation. As d often increases linearly with the electrode potential, one obtains a linear $1/C - E$ dependence. The band bending of the space charge layer of a semiconductor is related to the capacity C by the equation of Schottky–Mott (Eq. (26)). An appropriate $1/C^2 - E$ plot yields by extrapolation for $1/C^2 = 0$ the flat band potential E_{Fb}. From its slope, the density of charge carriers N is obtained; n-type semiconductors yield a positive, and p-type a negative, slope.

$$\frac{1}{C} = \frac{1}{C_{\mathrm{Me,Ox}}} + \frac{1}{C_{\mathrm{Ox}}} + \frac{1}{C_{\mathrm{H}}} \tag{24}$$

$$\frac{1}{C} = \frac{d}{\varepsilon\varepsilon_0} \tag{25}$$

$$\frac{1}{C^2} = \frac{2}{e\varepsilon\varepsilon_0 N}\left(E - E_{\mathrm{Fb}} - \frac{kT}{e}\right) \tag{26}$$

The energetic relations of the bands of semiconducting passive layers and the existence of possible states within the band gap within the layer or at its surface are of decisive importance for electrochemical reactions at passivated metal surfaces. Charge-transfer reactions require an isoenergetic transfer of electrons from the metal surface to the redox system. According to the Born–Oppenheimer approximation and the Franck–Condon principle, the fast electron transfer (10^{-15} s) does not allow simultaneous changes to the solvation shell of the redox species, which occurs within the time of oscillations only (10^{-13} s). Direct tunnelling of electrons between the metal and the redox system within the electrolyte may occur if very thin oxide layers cover the metal surface (<1 nm), as in the case of some noble metals like Pt and Au and reactive metals like Cr and Ni. If the thickness of the anodic oxide exceeds 1 nm, then electron transfer has to occur via states within the oxide. Thus, a charge transfer has to occur via the valence or the conduction band, or via states within the band gap, as shown schematically in Fig. 40. Usually the anodic oxides are seriously doped and one has a high density of states below the conduction band, or above the valence band. This situation leads to a high concentration of charge carriers within the bands. Their presence may mediate a horizontal isoenergetic electron transfer within the band gap. These immobilized states permit electron transfer by a hopping mechanism. A large concentration of these states may extend the energy range of electron transfer, and thus the anodic or cathodic current density. These states reduce the minimum excitation energy during light absorption, and thus cause a tailing of the photocurrent spectra, as found for Cu_2O in Fig. 40b. For these cases a mobility gap rather than a band gap is discussed. A high density of states within the band gap leads to an overlap of their orbitals and thus may form a subband which will also mediate electron transfer across the anodic layer as has been suggested for anodic and crystalline Cu_2O (Fig. 40). Thus, the knowledge on the electronic properties are of decisive importance for the understanding of redox processes on metal electrodes

covered by semiconducting oxide films. This is not only important for corrosion phenomena on passivated metals, but also generally for redox processes at electrode surfaces.

6.2 Electronic Properties of Cu_2O and of the Cu_2O/CuO, $Cu(OH)_2$ Duplex Layer

The Cu_2O passive layer on Cu has semiconducting properties. Its band gap has been determined by absorption spectroscopy [99] and photoacoustic spectroscopy [100]. The latter method detects the acoustic signal with a microphone or piezo-detector, which forms due to the absorption of a chopped light beam. By both methods the band gap has been measured with sufficient agreement with the results obtained by photocurrent measurements [97, 98]. Applying light to oxide-covered Cu electrodes electrons are excited from VB to CB and travel to the oxide/electrolyte interface due to the downward bending of the bands within the range of the depletion layer. The positive holes move in the opposite direction and enter the metal phase. The high electrical field strength ensures a very effective separation of the electron hole pairs and avoids their recombination. At the oxide surface electrons are transferred to the empty states of the oxidized form of the redox system, which causes a cathodic photocurrent i_{ph}. Any species that may be reduced within the solution may serve as an electron acceptor including constituents of the anodic film itself. In the case of passive Cu, photocurrent measurements have been performed with AsO_4^{3-}, H_2O_2, the $[Co(NH_3)_5Cl]^{2+}$ complex, CuO_2^{2-}, and even the CuO, $Cu(OH)_2$ part of the duplex layer formed at positive potentials [97].

For the interpretation of the photocurrent measurements of a passivated metal like Cu one may apply the semiconductor model of W. Gärtner [102]. In this model the photocurrent i_{ph} is proportional to the flux of photons Φ_0 arriving at the electrode surface and depends exponentially on the absorption coefficient α of the incoming light, the layer thickness d, and the band bending which is the deviation of the electrode potential E from the flat band potential E_{Fb} (Eq. (27)). This relation holds for a thickness d smaller than the width of the band bending so that the space charge layer coincides with d and no contribution to the photocurrent arises by diffusion of charge carriers from a deeper part of the passive film with no electric field. For a large optical penetration depth $1/\alpha \gg d$, the exponential term may be developed in a Mac Laurin series, which yields Eq. (28). α is given for energies hv in the vicinity of the band gap energy by Eq. (29). Its introduction in Eq. (28) yields finally Eq. (30). $n = 1$ or $n = 4$ takes account of a direct or indirect band gap. $\eta = i_{ph}/e\Phi_0$ is the photocurrent efficiency of the light.

$$i_{ph} = e\Phi_0[1 - \exp(-\alpha d\sqrt{E - E_{Fb}})] \tag{27}$$

$$\left[\frac{i_{ph}}{\alpha d e \Phi_0}\right]^2 = E - E_{Fb} \tag{28}$$

$$\alpha = \text{const}\frac{(hv - E_g)^{n/2}}{hv} \tag{29}$$

$$\frac{hvi_{ph}}{e\Phi_0} = \eta hv = \text{const}\sqrt{(E - E_{Fb})}d(hv - E_g)^{n/2} \tag{30}$$

$$\eta = i_{ph}/e\Phi_0$$

$$n = 1 \text{ direct transition } (\eta hv)^2 \propto hv - E_g$$

$$n = 4, \text{ indirect transition } \sqrt{\eta hv} \propto hv - E_g$$

Anodic Cu oxide layers show all p-type semiconducting properties with cathodic photocurrents, which decrease with increasing electrode potential. Reports of other authors of n-type oxides refer often to a formation in solutions with additives as e.g. halides, which affect the composition of the anodic layer (CuCl) and thus change its semiconducting character. Several redox systems have been added to the electrolyte as H_2O_2, AsO_4^{3-}, $[Co(NH_3)_5Cl]^{2+}$, CuO_2^{2-}, or $[Cu(C_4H_3O_6)_2]^{4-}$ (Fehling's solution) to serve as redox partners [97]. Even the Cu(II) ions of the duplex film may serve as a redox partner for photocurrent measurements. Appropriate plots of the efficiency of the photocurrent η as a function of the light energy hv according to Eq. (30), i.e. $(\eta hv)^2/hv$ for the direct and $(\eta hv)^{1/2}/hv$ for the indirect transition yield the related band gap energies. Anodic Cu_2O has an indirect band gap of 2.5 eV (Fig. 41a) and a direct band gap of 2.9 eV (Fig. 41b). These band gaps decrease with the oxide thickness to 2.0 and 2.4 eV respectively for thicker Cu_2O films electrodeposited by reduction from alkaline CuO_2^{2-} solutions [98, 86]. For this purpose reduction of a 2×10^{-3} M solution of $[CuO_2]^{2-}$ in 5 M KOH at $E = -0.235$ V was performed on a Cu surface covered with Cu_2O obtained by the partial reduction of the duplex film. The amount of deposited oxide grows linearly with the reduction time. It has been grown by this method to more than 30 nm. An interesting feature is the tail in the plot of Fig. 41a. It suggests a large concentration of states in the band gap with a smaller energy of excitation. Their high concentration leads to the formation of a small sub-band that permits electron transfer within the band gap. This electron transfer across the oxide is required for redox processes in the dark, as well as the possible imaging of Cu oxides by STM, which will be discussed in Section 7.2.2.

Photocurrent spectra of the Cu_2O / $CuO,Cu(OH)_2$ duplex film suggest a smaller band gap of the CuO layer with respect to the value of Cu_2O [97]. However, the investigation of a simple anodic Cu(II) oxide layer was not possible. All trials to prepare this layer without a Cu_2O contribution were not successful.

The i_{ph}^2/E plot yields a flat band potential of anodic Cu_2O of $E_{Fb} = -0.25$ V (Fig. 42a). The electronic properties of the duplex film are somewhat more difficult and reflect the influence of both compounds Cu_2O and CuO, $Cu(OH)_2$. Fig. 42b shows an i_{ph}^2/E plot for a duplex film at two wavelengths. For $\lambda = 300$ nm, two straight lines show the influence of the two partial layers. At more negative potentials mainly Cu_2O is dominating the photocurrent with a flat band potential of $E_{Fb} = -0.23$ V, whereas at more positive potentials the extrapolation of the second line leads to $E_{Fb} = -0.00$ V, which apparently reflects the influence of the Cu(II) layer on top of the duplex film. For $\lambda = 450$ nm one observes the influence of the $CuO,Cu(OH)_2$ layer only with a single line whose extrapolation yields $E_{Fb} = -0.05$ V. Apparently, the energy of the radiation at this wavelength is not sufficient to ex-

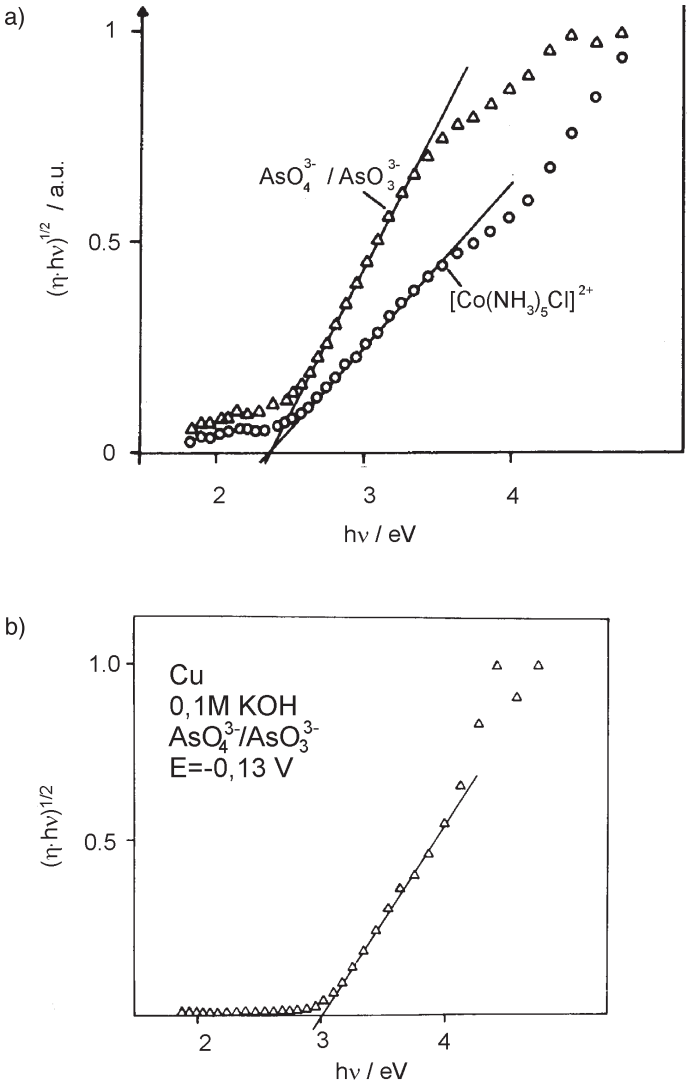

Fig. 41. $(\eta h\nu)^n/h\nu$ plots of the efficiency of the photocurrent of a Cu/Cu_2O electrode in solutions with redox systems for the determination of the band gap for: (a) an indirect and (b) a direct transition [86, 97].

cite photoelectrons within Cu_2O, however, for CuO with its smaller band gap a photocurrent is observed. Fig. 43 depicts the band model of the duplex layer which explains the results of the i_{ph}/E plots of Fig. 39b with a flat band situation for the $CuO,Cu(OH)_2$/electrolyte interface at $E = 0.00$ V and for the Cu_2O/CuO, $Cu(OH)_2$ interface at $E = -0.23$ V.

The position of the bands within the energy scale has been determined by the measurements of the threshold energy $e\Phi_{Th}$ with UPS according to Eq. (22) (Section

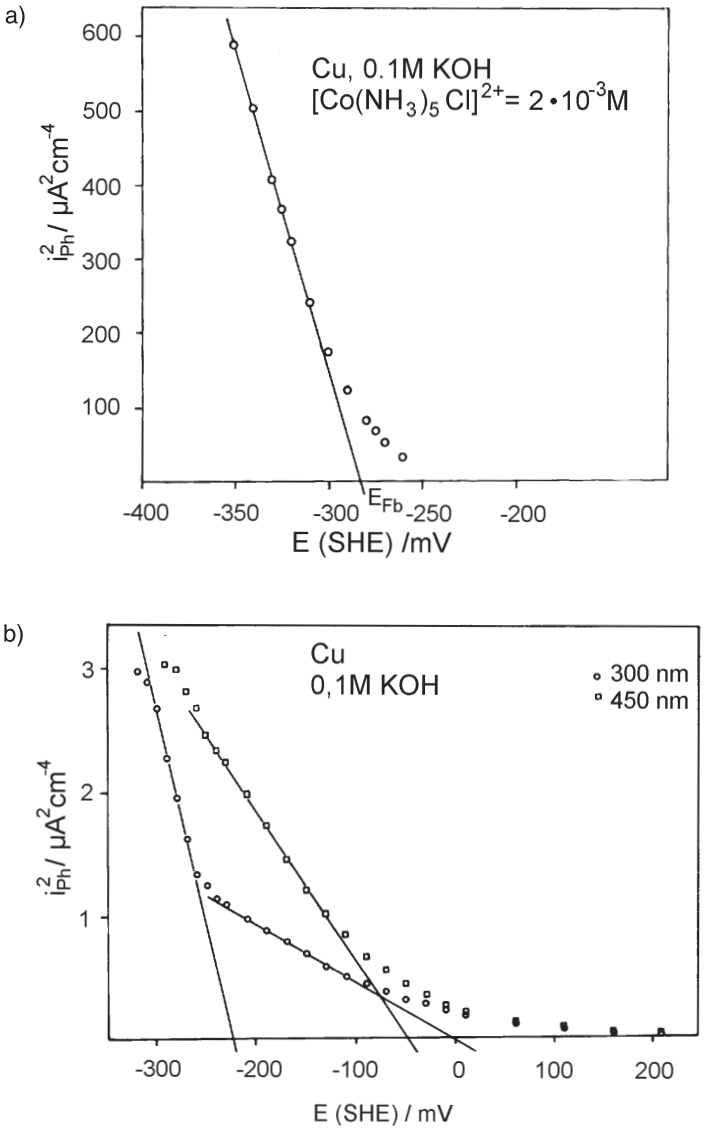

Fig. 42. i^2_{Ph}/E plot of the photocurrent of passivated Cu in 0.1 M NaOH with the Co complex as redox system, a) Cu/Cu_2O, b) $Cu/Cu_2O/CuO$, $Cu(OH)_2$ (duplex layer) with light of two wavelengths, $\lambda =$ 300 nm and $\lambda = 450$ nm [86, 97].

4.2.5). The photoelectrons were excited with the He(I) line ($hv = 21.2$ eV). An emerged oxide-free Cu electrode has a work function of 4.3 eV; the anodic oxides, a threshold energy of 5.15 eV for Cu_2O, and 4.55 eV for CuO.

$$\Delta E = hv - e\Phi_{Th} \tag{22}$$

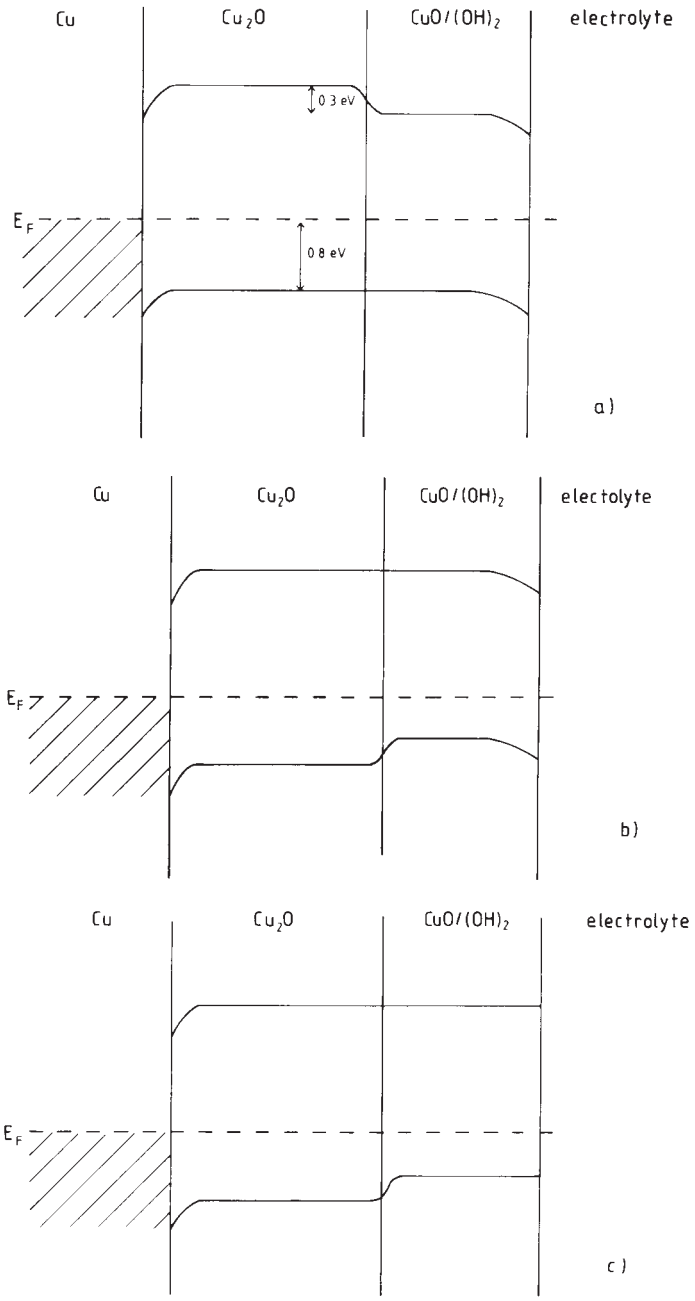

Fig. 43. (a) Band model for the $Cu/Cu_2O/CuO$, $Cu(OH)_2$ duplex film on Cu with different flat band conditions; (b) for the Cu_2O/CuO interface; and (c) for the CuO/electrolyte interface [98].

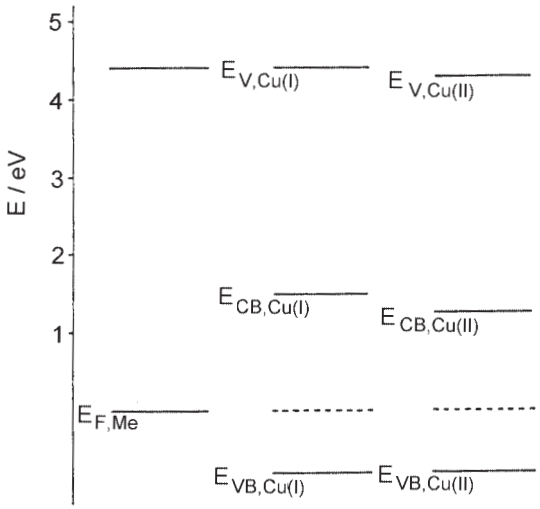

Fig. 44. Energy diagram for the band structure of Cu and its passivating oxides with the levels E_{CB}, E_{VB}, and E_V of the conduction and valence band and the vacuum, respectively [86].

The photoelectrochemical and UPS results yield the energy diagram of Fig. 44 for a Cu electrode covered with the anodic oxides. For these diagrams an electronic equilibrium is assumed that leads to the same energy position of the Fermi level for Cu and its two anodic oxide layers. This situation defines an energetic difference of the upper valence band edge of Cu_2O and the Fermi level of 0.8 eV.

On the basis of this band model of Cu, with its passive layers, one may interpret conclusively its polarization curve in alkaline solutions with its current peaks and the potential domains of its anodic oxides. Starting at the flat band potential of $E = -0.25$ V, the increasing electrode potential leads to an upward bending of the energy bands with a final crossing of the valence band with the Fermi level at $E = 0.55$ V (Fig. 45). At this potential, a large accumulation of positive holes causes the formation of the higher valent Cu oxide and thus the formation of the duplex film with a redistribution of the potential drop within the two partial layers. The further increase of the electrode potential causes the crossing of the valence band edge of the Cu(II) film with the Fermi level at $E = 0.95$ V which causes a location of the further increase of the potential at the oxide/electrolyte interface, i.e. within the Helmholtz layer. This increasing potential drop accelerates the kinetics of the electrochemical reactions at this interface i.e. the dissolution of Cu^{2+} from the oxide surface and oxygen evolution.

At the Cu/Cu_2O surface redox reactions may be measured also in the dark. Fig. 46 depicts the related energy diagram including the presence of the $[Co(NH_3)_6]^{2+/3+}$ redox system within the electrolyte. The diagram includes both energy scales i.e. that related to the vacuum level and that to the standard hydrogen electrode (SHE). The dark current which has been observed for this system [86] cannot be understood on the basis of this band model due to a missing overlap of the states of the semiconducting oxide and the redox system within the electrolyte. It requires the subband within the band gap as deduced already from conductivity measurements [87, 88] and the tailing of the photocurrent spectrum of Cu_2O (Fig. 41a). The cathodic photo-

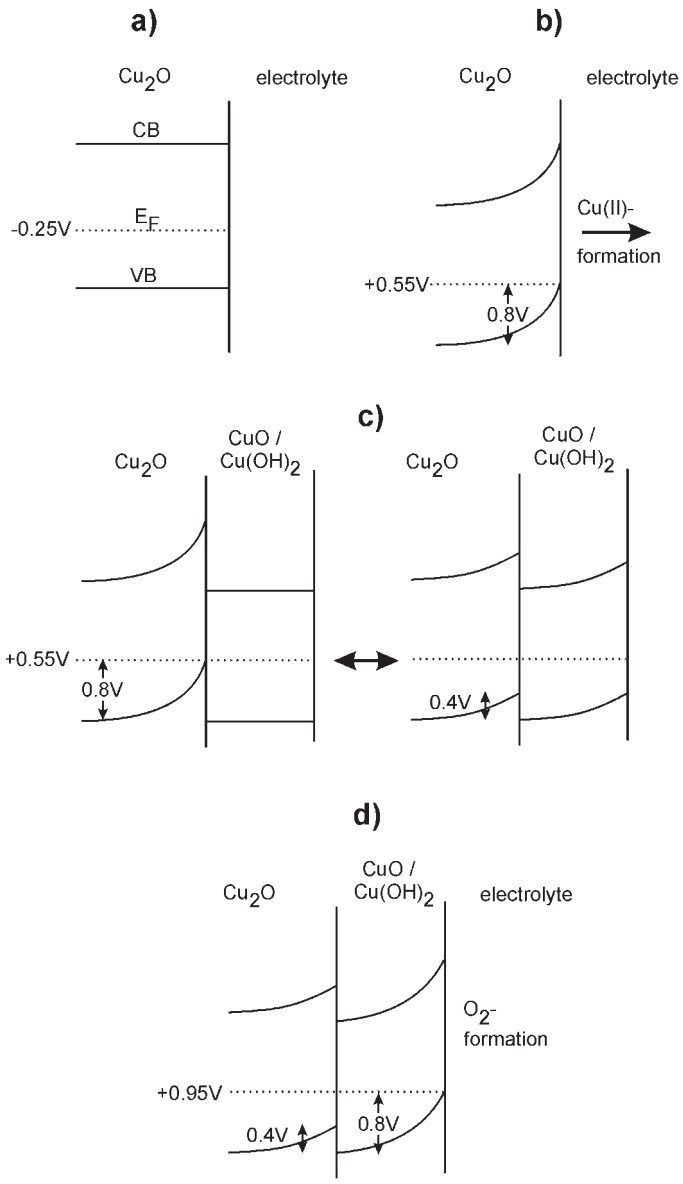

Fig. 45. Band structure model for passive layers on Cu for increasing potential explaining quantitatively the formation of the duplex film and the transpassive behavior [86].

current occurs via the conduction band and surface states as also indicated in Fig. 46. The photo-generated electron-hole pairs are separated in the electrical field of the space charge layer. The holes travel within the valence band to the metal substrate, the electrons move in the conduction band towards the electrode surface and are trapped in surface states form where they are transferred to the redox system.

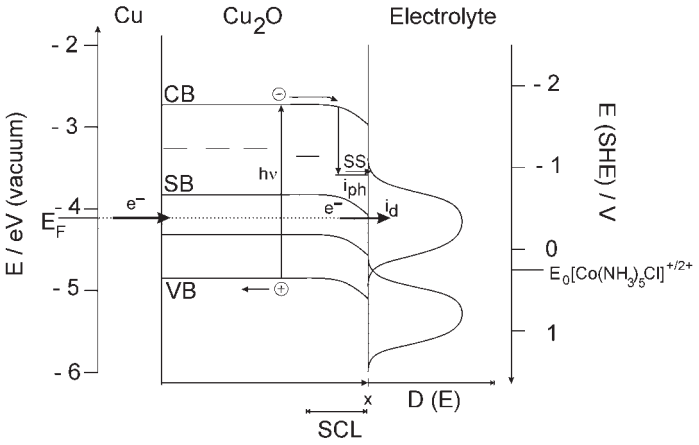

Fig. 46. Band structure model of Cu/Cu_2O/electrolyte with the space charge layer SCL, the valence band VB, the conduction band CB, and the sub-band SB formed by interband states, mediating electron transfer between the metal to the redox states of the Co(III) complex within the electrolyte. The formation of electron hole pairs by photoexcitation and the transfer of electrons to the empty states of the redox system via surface states SS is also indicated.

The existence of these surface states has been concluded also from photo-transient measurements in our laboratory. Applying light pulses, e.g. with a chopped light source to the passivated Cu surface, one obtains an overshoot of the photo-current, which relaxes with a half-life period of 0.05 s to a stationary value. This extra current and charge is used to fill the interband states. The rate of formation of charge carriers due to irradiation contains a generation term via the photoelectrons in the conduction band and a term for their consumption for the reduction of a redox system within the electrolyte at the electrode/electrolyte interface. The kinetic evaluation of the photo-transients on the basis of this simple reaction mechanism yields a trap concentration of $N_T = 10^{18}$ cm^{-3} that is independent of the layer thickness and the redox system within the electrolyte. This result suggests a homogenous distribution of these interband states across the total layer, which supports the idea of a sub-band.

7 The Structure of Passive Layers

The electrochemical properties of passive layers lead to the question of their structure on a mesoscopic scale and at atomic resolution. Their barrier character with respect to metal corrosion postulates a dense, poreless film; their electronic properties, in some cases, crystalline structures. The change of their properties with film aging, as in e.g. film-breakdown phenomena, support the existence of many defects that may heal with time. In many cases an amorphous structure is assumed. Some *ex situ*

methods have been applied to get an answer to this question, for instance electron diffraction for thin, or X-ray diffraction (XRD) for thick, anodic films. Many of these methods require vacuum conditions. XRD in its conventional form needs film thicknesses of several 10 nm at least and a crystalline structure. Several authors suggest that only *in situ* methods are reliable for the determination of the structure of passive layers due to changes during emersion of the sample. The loss of contact to the electrolyte and of the potential control, the exposure to the UHV and to an electron beam might change the structure. Although the structure of passive layers has been in discussion for many years, thin films of some nm thickness have been investigated systematically *in situ* with structure-sensitive methods only within the last 10 years. Two main lines have been followed, methods applying synchrotron radiation as XRD and X-ray Absorption Spectroscopy (XAS), and the scanning methods like Scanning Tunneling Microscopy (STM) and Scanning Force Microscopy (SFM).

In a first part of this section, the synchrotron methods are described as they might still not be so common to many scientists in the field of corrosion research. The scanning methods are discussed only briefly, as they have been introduced by numerous papers on *in situ* studies of the structure of electrode surfaces. Several good reviews are found in literature, and are recommended to the interested reader; they describe the application of STM to adsorption and Under Potential Deposition (UPD) metal dissolution and deposition and nano-structuring by deposition of small metal clusters [103–105]. In a following part, results are presented for a number of systems that have been studied in detail with special attention to Cu.

7.1 Synchrotron Methods in Corrosion Research

Thin anodic films are a challenging system for *in situ* structural analysis. They often are only a few nm thick and are mostly on the surface of their own metal. One therefore has to apply special methods to enhance the information originating from the layer and to suppress the contribution of the substrate. Grazing incidence of X-rays may help to overcome these difficulties. This however requires an extremely strong X-ray source that is available at the beam lines of synchrotron sources. Undulator or wiggler beam lines increase the intensity still by more than 1 order of magnitude, which helps to get a sufficient sensitivity to study even monolayers or less than a monolayer during adsorption and oxidation studies. Furthermore, the absorption of the radiation of X-rays in water is a serious problem, especially for XAS. If the energy of the absorption edge of an element for X-rays is sufficiently high, then the absorption problems within the electrolyte may be overcome even for a grazing incidence geometry. The related path of the X-rays gets automatically long to permit the required interaction with the electrode surface. XAS in reflection mode (ReflexAS) has been applied to the study of Cu with an absorption edge of 8 980 eV or elements with absorption at higher energies, like Ag at 25 510 eV. The contribution of the substrate may be suppressed in principle if the angle of incidence is below its critical value of total reflection, i.e. of 0.35^0 for Cu and 0.13^0 for Ag. This situation is a consequence of the higher optical density for X-rays for the vacuum in comparison to metals.

Two special electrochemical cells are used for XRD and XAS measurements. In one case a polymer membrane is pressed on the specimen surface after its electrochemical treatment to reduce the water layer on top, but still permitting potential control during the measurements. In an other case the beam penetrates an electrolyte layer in front of the electrode, which corresponds to the specimen's dimensions, but which is thick enough to reduce the danger of ohmic drops and crevices. Beam lines often provide the exact orientation of the samples with the cell by a goniometer. For XAS measurements a special low cost refraction stage has been constructed which permits the orientation of the sample within 0.01 degrees and which has been used for the study of several systems [108].

7.1.1 XAS and RefleXAS

The fine structure of XAS in the range up to some 100 eV from the absorption edge, i.e. the Extended X-ray Absorption Fine Structure (EXAFS), contains information on the near range order of the surface layers under study. The absorbed X-rays cause the ionization of electrons from the core level of the related absorption edge. These outgoing electrons are reflected from the electrons of the coordination shells of the central absorber (Fig. 47). As a consequence, the outgoing electron wave interferes with the reflected electron wave and the background-corrected relative-absorption coefficient $(\mu - \mu_0)/\mu_0$ consists of oscillations. Thus these EXAFS oscillations are an interference phenomenon due to electron reflection at the coordination shells of the absorbing atoms under study. The distance of the coordination shells R_j determines together with the phase shift δ_j whether this interference is constructive or destructive according to the EXAFS function $\chi(k)$ of Eq. (31). This equation sums the contribution of several coordination shells. Its amplitudes A_j are a function of the coordi-

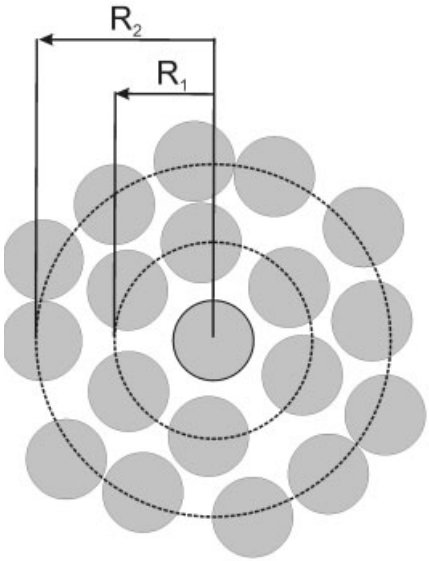

Fig. 47. Coordination shells of radius R of an X-ray-absorbing central atom leading to EXAFS by reflection of the emitted electrons. Second shell disordered.

nation number N_j, the reflection amplitude f_j, depending on the kind of the reflecting atoms, the exponential Debye–Waller factor, containing the mean-square displacement due to thermal and structural disorder ${\sigma_j}^2$, and the exponential attenuation of the electrons due to inelastic interactions with the material with their mean free path $\lambda(k)$ (Eq. (32)). Some of these variables depend on the wave vector k, and thus on the kinetic energy of the ejected electrons (Eq. (33)).

$$\chi(k) = \frac{\mu - \mu_0}{\mu_0} = \sum A_j(k) \sin[2kR_j + \Phi_j(k)]_j \tag{31}$$

$$A_j(k) = N_j f_j(k) \exp(-2\sigma_j^2 k^2) \frac{\exp\left(-\dfrac{2R_j}{\lambda(k)}\right)}{kR_j^2} \tag{32}$$

$$k = \sqrt{\left(\frac{2m}{\hbar^2}\right)(E_{\text{kin}})} \tag{33}$$

With a Fourier transformation of $\chi(k)$ in the distance space, one obtains a separation of the contribution of the various coordination shells. This Fourier transform yields the structural parameters R_j, N_j and σ_j, and thus the near range order of the specimen with respect to the absorbing atoms. The EXAFS analysis for the different absorber atoms within the material yields their specific near range order. Thus, one may get the structure seen form several kinds of absorbing atoms. EXAFS does not require highly crystalline materials. It is a suitable method to study disordered, or even amorphous, structures. The σ–values provide quantitative information about the thermal and structural disorder.

The reflectivity spectra R(E) and the reflectivity-EXAFS $\chi_R(E) = [R(E) - R_0(E)]/R_0(E)$ are similar, but not identical, to the absorption spectra and $\chi(E)$ obtained in transmission mode. $R(E)$ is related to the complex refraction index $n(E) = 1 - \delta(E) - i\beta(E)$ and $\beta(E)$ to the absorption coefficient $\mu(E)$ by $\beta = \mu\lambda/4\pi$. β and δ are related to each other by a Kramers–Kronig transformation. β and δ may be also separated in an oscillatory $(\Delta\beta, \Delta\delta)$ and non-oscillatory part (β_0, δ_0) and may be used to calculate χ_R. This is, briefly, how the reflectivity EXAFS may be calculated from $\mu(E)$, which itself can be obtained by experimental transmission EXAFS of standards, or by calculation with the help of commercial programs such as FEFF [109] with the parameters R_j, N_j and σ_j, which characterize the near range order. The fit of the simulated to measured reflectivity yields then a set of appropriate structure parameters. This method of data evaluation has been developed and has been applied to a few oxide covered metal electrodes [110, 111]. Fig. 48 depicts a condensed scheme of the necessary procedures for data evaluation.

Several papers investigate passive metals with EXAFS on a qualitative basis [112], or examine the structure of the leading edge of absorption, the so called X-ray Absorption Near Edge Structure (XANES) [113], to get *in situ* information on the kind of oxide that has been formed. It should be mentioned, however, that the changes at the absorption edge, which are related to the chemical properties of the surface layer, are small and the superposition of the absorption of the substrate

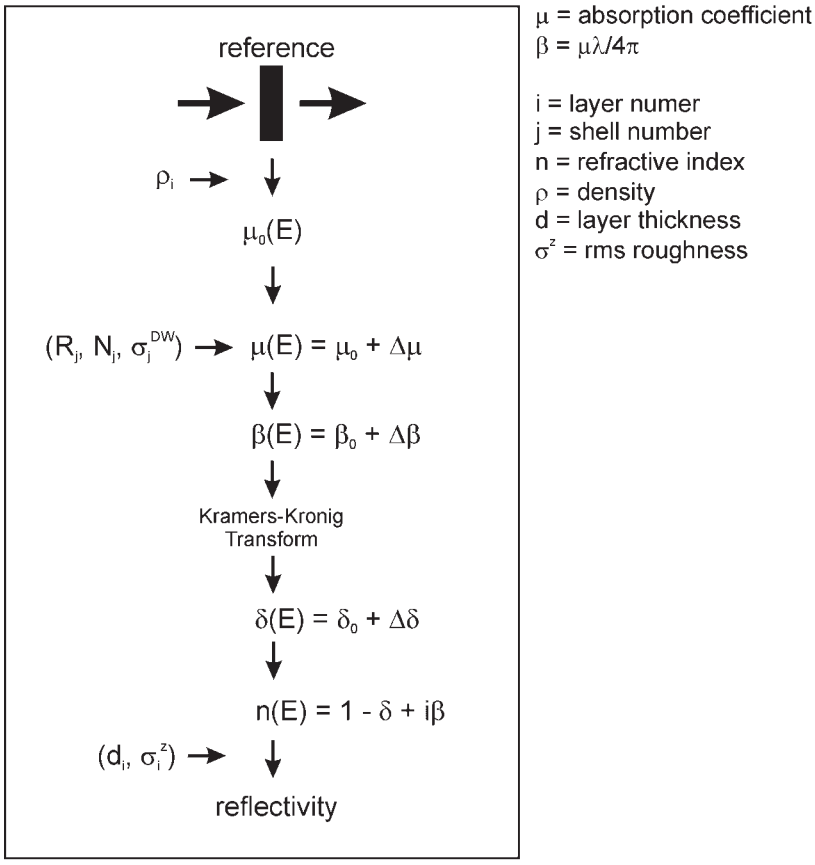

Fig. 48. Scheme for the calculation of the X-ray reflectivity from experimental transmission EXAFS of standards or calculation with a first set of structure parameters (R_j, N_j, σ_j) and the fit procedure with the experimental reflectivity using the program FEFF.

and a possible multilayer structure lead to mixed information, which is hard to be separated. Nevertheless, *in situ* XANES studies of passivated iron suggest by comparison of absorption edges of standards the presence of a spinel-like structure, i.e. Fe_3O_4 or γ-Fe_2O_3 [113]. An additional option of XANES is the close relation of the change of the height of the absorption edge to the amount of the thin film material, which may be lost partially by dissolution during anodic polarization [114]. However, these results may be obtained also by XPS of emerged electrodes, which has been described already above. The *ex situ* conditions are not a serious problem for most systems if one takes care for a special specimen handling (closed system), their advantages are obvious. Experiments at a beam line require a large effort and experience besides the always-restricted beam time. The main advantage for the application of synchrotron methods should be seen in the excellent possibility for the *in situ*

determination of the structure of thin layers on electrodes, which is possible only for very few other analytical tools, e.g. the scanning methods STM and SFM, which provide additional information.

There exists still a problem for the evaluation of reflectivity EXAFS data. Although the experimental data were obtained with a grazing incidence angle of 0.0 to 0.2 degrees, passive layers are too thin to avoid a contribution of the substrate. These studies require of course extremely flat and smooth specimens, realized with vapor-deposited films on such appropriate substrates as float glass or silicon wafers. However, even below the critical angle of total reflection the electromagnetic wave penetrates ca. 2 nm into the electrode surface with an exponential decrease of its intensity [115]. Furthermore, passive layers have a multilayer structure, which has been found for many systems by XPS and ISS analysis. As a consequence, the calculation of the reflectivity of actual specimens has to occur on the basis of a multilayer model including the substrate contribution to meet the experimental situation. The experimental effort of grazing incidence studies may be overcome with the investigation of extremely thin vapor-deposited films in the range of only up to 5 nm, which may be consumed completely by anodic layer formation with practically no remaining metal. With a thin membrane as a substrate, studies may be performed from the rear side of a specimen with the front being in contact with the electrolyte. In this case the measurement of X-ray fluorescense is the appropriate method to take the X-ray spectra. This concept raises the question whether the anodic films keep their structure when they are no longer in contact to their substrate. Furthermore, the formation of a continuous metal film cannot be guaranteed for ≤ 5 nm thickness only. Thicker films will contain remaining metal underneath, which will contribute to the spectra as in the case of a solid bulk electrode.

Fig. 50 depicts the measured and simulated reflectivity spectra of the passive film on Cu45Ni. In these calculations enter the structural parameters of an outer $Ni(OH)_2$ and an inner CuO layer, which meets the somewhat simplified results obtained from XPS measurements. Fig. 50 presents the results of a specimen after electrochemical reduction at $E = -0.90$ V with only an air-formed oxide film and after its passivation at $E = 0.50$ V. The reflectivity-XAS for both elements Cu and Ni is shown simultaneously. The best fit from the passivated specimen is obtained with an inner 1.5 $Ni(OH)_2$ and an outer 1.0 nm CuO layer on the Cu45Ni substrate. Differing thicknesses and a reverse sequence of the partial layers yields less agreement of the measured and calculated results. The Fourier transform of the Cu and Ni part of the reflectivity is in agreement with the simulated data and yields a near range order of the proposed crystalline materials of the assumed bilayer structure (Fig. 49) [108]. The most remarkable change is the appearance of the metal-oxygen distance at 0.15 nm of the passivated specimen especially for the Ni signal and to a much smaller extend for the Cu signal. This is in agreement with the dominating contribution of Ni to the anodic layer as found by XPS and ISS studies (see Section 5.2.6).

As another example, oxide films on a vapor-deposited Ag substrate are presented [116]. Detailed XPS investigations show the development of Ag_2O already 0.15 V below its equilibrium potential of $E = 0.35$ V [115]. Fig.50a presents the k-weighted Fourier Transform of the reflectivity-EXAFS, $FT(\Delta Rk)$, of a 2.5 nm thick oxide film formed in 1 M NaOH at $E = 0.40$ V at an angle $\Theta = 0.09^0$ relative to the surface.

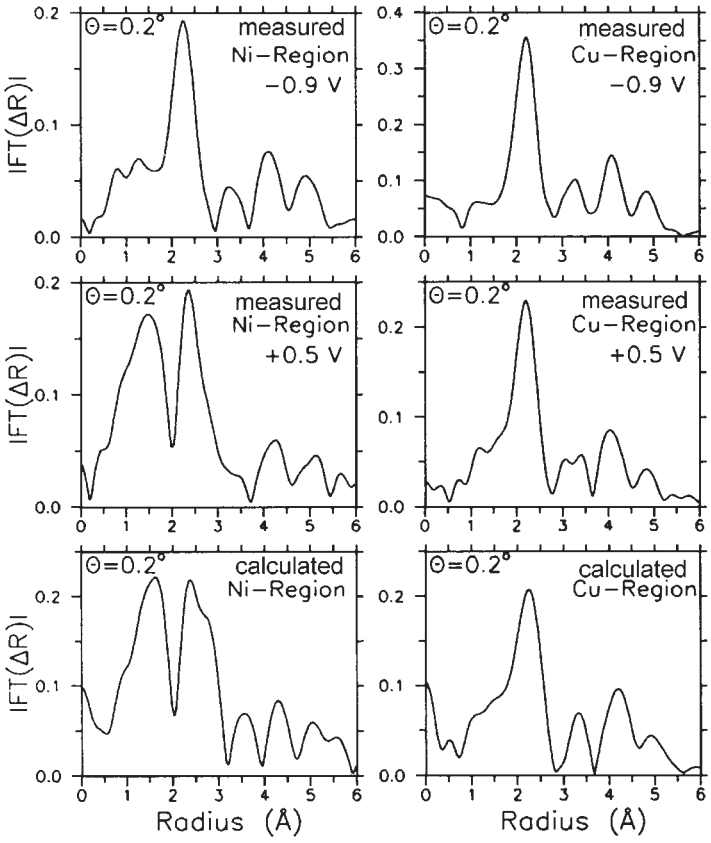

Fig. 49. Comparison of the Fourier Transform of the ReflEXAFS of the Cu and Ni region of a reduced ($E = -0.9$ V) and passivated ($E = 0.5$ V) Cu45Ni electrode and the calculated results with 1.5 nm $Ni(OH)_2$/1.0 nm CuO/Cu45Ni [108].

The critical angle of total reflection is at the energies of the Ag absorption edge very small, i.e. 0.13^0 for Ag and 0.11^0 for Ag_2O. Even for angles below 0.1^0 the penetration depth of the X-rays is ca. 2.4 nm with an information depth of ca. 7 nm for the exponential decrease of their intensity. Therefore, Fig.50a contains also the contributions of the substrate and the experimental results have to be compared to simulations presented in Fig. 50b as described above. A best fit was obtained for a 2.7 nm thick crystalline Ag_2O film on Ag metal. The peaks at 0.14 nm refer to the Ag–O distance and are absent for an oxide-free metal film. The pronounced peak at 0.27 nm belongs to the Ag–Ag distance of the substrate. The peak at $R = 0.38$ nm of the simulation belongs to the second Ag–Ag coordination of Ag_2O. However, it is missing in the experimental results. This indicates a rather defective structure of this thin anodic oxide that has been formed just above the equilibrium potential. Further coordination shells of Ag_2O cannot be seen because they interfere with the shells of the metal substrate. The peaks at $R = 0.43$, 0.48 and 0.52 nm refer to the 2^{nd}, 3^{rd}

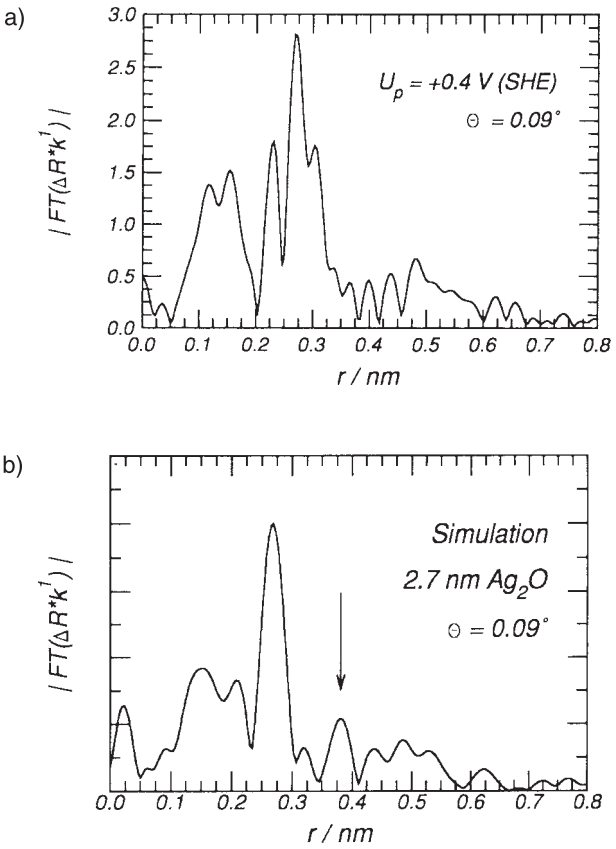

Fig. 50. Fourier Transform of: (a) ReflEXAFS of Ag passivated at $E = 0.45$ V (missing peak at 0.38 nm) in 1 M NaOH and its comparison to (b) the calculation with 2.7 nm Ag_2O on Ag [116].

and 4th coordination shells of the metal substrate. If the film has been formed at $E = 0.41$ V the small peak at 0.38 nm appears also in the experimental data (Fig. 51). A decrease of the angle to $\Theta = 0.9^0$ enhances the oxide signals relative to those of the metal substrate. Ag_2O films exceeding the information depth permit a study of the anodic films without contributions of the substrate. Fig. 52 presents the Fourier Transform of a thick layer formed in 1 M NaOH at $E = 0.70$ V and its excellent agreement with the simulated data for a 70 nm Ag_2O film on Ag. More than 5 coordination shells may be seen which strongly supports the presence of a crystalline film which is also supported by the coincidence of the structural parameters like R, N, and σ of the reflectivity- and the transmission-EXAFS of the anodic film and a Ag_2O powder specimen respectively.

Film formation in 1 M NaOH at potentials $E > 0.72$ V or the oxidation of anodic Ag_2O at these potentials yields a thick AgO film. These films have been investigated qualitatively and quantitatively in detail with XPS. The width of the Ag 3d5/2 XPS signal suggests the presence of two Ag ions, Ag^+ and Ag^{3+}, which has

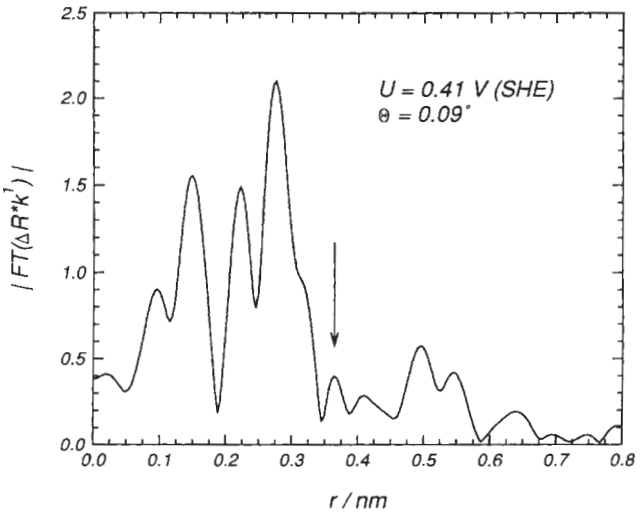

Fig. 51. Fourier Transform of ReflEXAFS of a Ag specimen passivated in 1 M NaOH at 0.41 V with appearing peak at 0.37 nm [116].

been already proposed from the XRD analysis of the bulk material [117]. This result is additionally supported by reflectivity-EXAFS [119]. Fig. 53 shows the Fourier transform of a AgO film with more than 7 coordination shells demonstrating its crystalline structure. The first two shells refer to the Ag^{3+}–O distance with planar quadratic coordination and the Ag^{+}–O shell in linear coordination. The 3 smaller

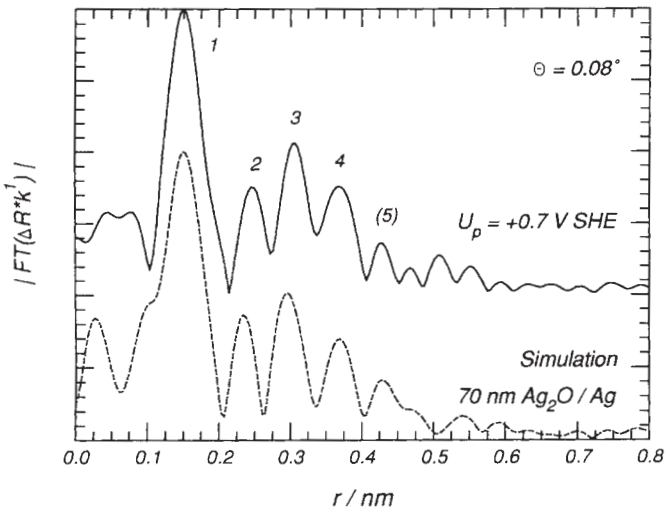

Fig. 52. Comparison of the Fourier Transform of ReflEXAFS of Ag passivated in 1 M NaOH at $E = 0.70$ V with calculated data with 70 nm Ag_2O on Ag [116].

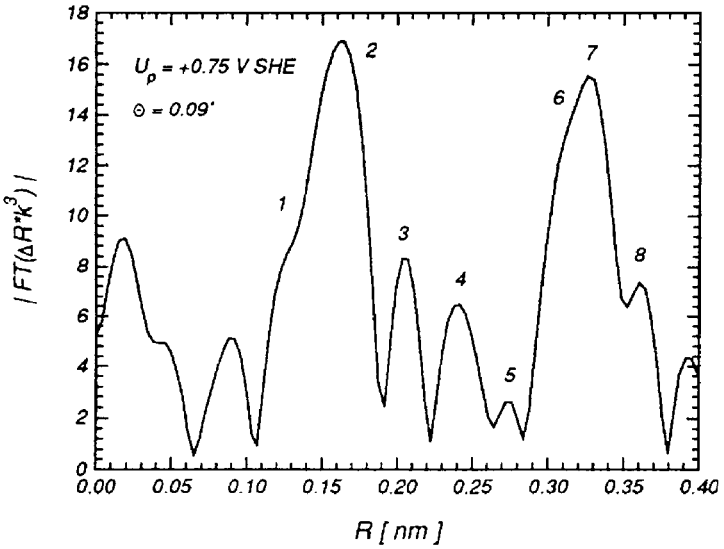

Fig. 53. Fourier transform of ReflEXAFS of Ag passivated at $E = 0.75$ V showing 8 coordination shells, ca. 90 nm AgO on Ag [119].

peaks of Fig. 53 refer to a Ag–O coordination with $R = 0.265$ nm, 0.277 nm and 0.289 nm. The peaks 6 and 7 belong to the Ag^{3+}–Ag^{+} coordination at $R =$ 0.325 nm, 0.336 nm, 0.340 nm, and 0.348 nm. These results of reflectivity-EXAFS agree well with those of transmission EXAFS studies of crystalline bulk AgO specimens. The back transform of the truncated first two shells into the k-space yields after the fit of the phase and amplitude [109] the structural parameters that are presented as a function of the potential of formation in Fig. 54. Although the structural parameters of transmission-EXAFS of crystalline bulk specimen fit closely to crystallographic data of crystalline AgO deviations are found for the anodic films. Starting with the data of anodic Ag_2O the first Ag–O shell of Ag_2O splits in two shells with the distances R_1 and R_2 when the oxidation to AgO occurs at potentials $E \geq 0.725$ V (Fig. 54a). The Ag–O distance of 0.195 nm for Ag_2O decreases to 0.192 nm for the Ag^{3+}–O distance of the first AgO coordination shell. The Ag^{+}–O distance of 0.214 nm for the second coordination shell is considerably larger. Both values are smaller than the XRD data. Recent *ex situ* EXAFS studies in transmission of polycrystalline AgO, and AgO obtained by chemical oxidation of Ag in NaOH, yield similar results [118].

The most remarkable changes are found for the coordination numbers N (Fig. 54b) [119]. They stay constant at $N = 2$ for the Ag^{+}–O shell, but change continuously with the electrode potential from 2 to 3.6 without reaching the expected value $N = 4$. Apparently this anodic AgO layer is a highly oxygen-deficient. It has been proposed to describe the composition of this anodic oxide as Ag_4O_3 [118]. This result is supported by quantitative XPS studies of anodic layers on emerged Ag electrodes. According to these data, the O/Ag ratio changes after oxidation from 0.5 for Ag_2O to ca. 0.8 in the potential range of $E = 0.725$ to $E = 1.1$ V (Fig. 54c).

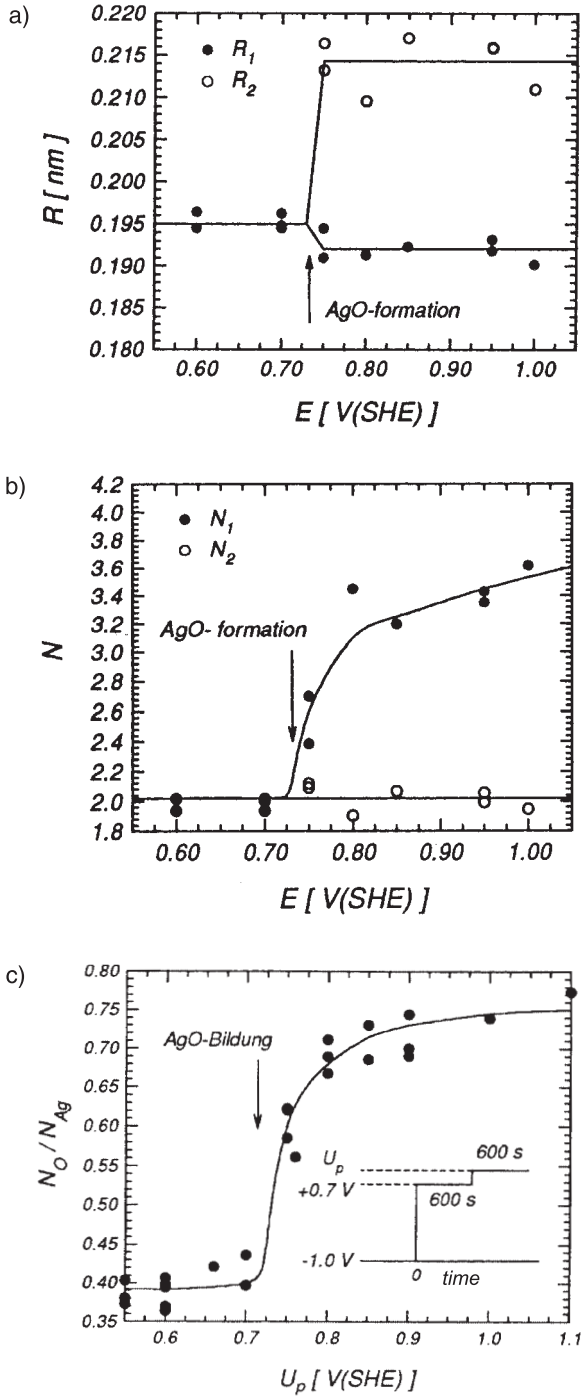

Fig. 54. (a) Radius R and (b) coordination number N from ReflEXAFS data of the first two coordination shells of anodic AgO layer; and (c) N_O/N_{Ag} atomic ratio from XPS analysis of Ag with anodic AgO layer formed for 600 s in 1 M NaOH at $E > 0.725$ V as a function of the potential [119].

Some further passivated metals have been studied with reflection-EXAFS. For Cu passivated at $E = 0.80$ V in 0.1 M NaOH and partially reduced at $E = -0.30$ V, the Fourier Transform of ΔR shows a very good agreement with the simulated data with 3 nm cuprite on Cu for three incident angles $\Theta = 0.15^0$, 0.25^0 and 0.40^0 [108]. The measured reflectivity EXAFS of passivated Cu requires an evaluation by comparison with simulated data. Here again, the thin oxide film cannot avoid a contribution of the metal substrate. The increasing angle causes the expected decrease of the signal of the Cu–O distance relative to that of the Cu–Cu distance of the metal substrate. Apparently, the anodic oxide film has a cuprite structure. This result is supported by *in situ* transmission EXAFS studies of a Cu_2O layer formed on a glassy carbon substrate by cathodic reduction of alkaline CuO^{2-} solutions [120]. Similar results are obtained for an *in situ* Reflection EXAFS study of a Cu film with an Cu_2O layer formed, as mentioned above, by anodic oxidation in 0.1 M NaOH at 0.80 V followed by a partial reduction at $E = -0.30$ V. For these measurements, a 3.6 mm broad Cu–film on float glass has been examined in the specially designed electrochemical cell instead of a specimen with an optimum length of 1.5 mm, which is too difficult to handle within the cell. The comparison of the experimental results with the simulations suggest the presence of ca. 3 nm crystalline Cu_2O on a Cu metal film (Fig. 55).

A further possibility to overcome the influence of the substrate entails the use of a very thin film or a metal monolayer on a foreign substrate. For this purpose, UPD layers of Cu on Pt have been investigated [121]. When Pt clusters were used on a carbon substrate *in situ*, EXAFS investigations in transmission became possible due to the very large specific surface, and thus a sufficiently large amount of electrodeposited Cu. After reduction of the substrate and UPD deposition of Cu from 10^{-3} M $CuSO_4$ in 1 M H_2SO_4 at appropriate potentials, the Cu monolayer could be oxidized and reduced in 1 M NaOH without its loss by dissolution into the electrolyte. A similar dissolution-resistant behavior is observed for UPD layers of Cu on Pt single crystal surfaces, however, with its stability depending on the orientation of the surface of the substrate. For these specimens, the near range order structure and its change during oxidation could be followed *in situ* by EXAFS. It should be mentioned however that the structure of a monolayer of Cu oxide on a Pt substrate is definitely different from a thin anodic oxide film on a Cu surface. The structural data include also Cu-Pt distances besides the coordination shells of Cu and O in the two dimensional lattice [121]. Furthermore, there are indications of a mixing of the Cu oxide with Pt oxide at the electrode surface, which, however, seems to be reversible when reduced.

7.1.2 X-Ray Diffraction

XRD requires a periodic two- or three-dimensional structure at the surface of a specimen. The measurements are performed in a similar electrochemical cell as described for XAS. The removal of the electrolyte due to the pressing of the polymer window on the specimen surface reduces the disturbing X-ray scattering from water. The grazing incidence geometry weakens the contribution of the diffraction of the

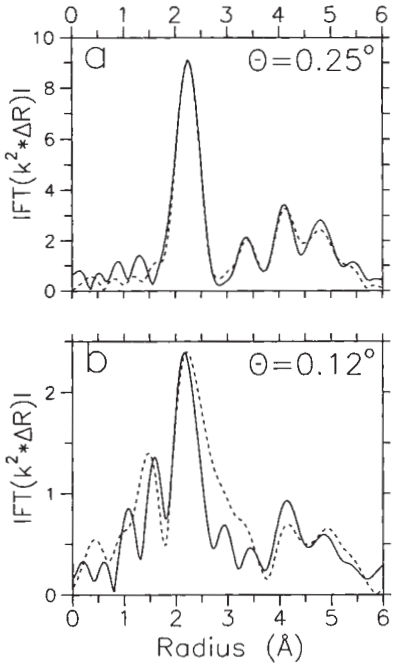

Fig. 55. Fourier transform of *in situ* ReflEXAFS of Cu in 0.1 M NaOH (a) reduced at $E = -0.60$ V; (b) with Cu_2O layer formed at $E = 0.80$ V and reduction of the CuO part at $E = -0.30$ V at **grazing** angles Θ below the critical angle, dashed lines: calculated data of a pure Cu surface and Cu covered with 3 nm Cu_2O [108].

X-ray beam of the metal substrate. XRD has been applied for the investigation of the structure of various adsorbate layers. Only very little work has been performed for the study of passive layers, partially because these layers on several metals are amorphous or their structure is seriously disturbed. However, interesting results are obtained for passive layers on Ni and Fe. For the determination of the structure of passive layers on iron, *in situ* and *ex situ* XRD results have been compared [122]. The evaluation of the various diffraction peaks suggests the presence of a spinel-type γ-Fe_2O_3 or Fe_3O_4 with similar lattice parameters in plane and perpendicular to the substrate of 0.839 nm and 0.83 nm, respectively. These distances are mainly determined by the close packing of the oxygen ions. No other oxide or hydroxide is in agreement with these parameters. The oxides are epitaxially oriented, oxide (001) parallel to Fe(001) and oxide (111) parallel to Fe(110). The T (10) direction is parallel to Fe(100) due to the similarity of the oxide (220) and the Fe metal (100) plane with spacings of 0.296 nm and 0.289 nm. A more detailed evaluation of the diffraction data suggests a highly defective spinel structure with a large number of cations in interstitial positions. The average lateral size of the oxide crystallites is determined to 6.0 and 4.5 nm for the Fe(001) and the Fe(110) surface. The diffraction intensities grow with time reaching asymptotically a constant value after ca. 2 days. This observation is explained by a growth of the crystals or a thickening of the film with time. These results agree well with those obtained by STM investigations [123]. XRD does not provide information on possible contributions of amorphous constituents of the film, or even an outer amorphous hydroxide and an inner crystalline oxide part. However, this cannot be expected from the application of a method that measures

ordered structures. Therefore, a combination of XRD with XAS and the scanning methods like STM and SFM provides a better insight into these complicated structures. XRD results on passive layers on Ni are mentioned in combination to studies by STM in the following section.

7.2 Scanning methods, STM and SFM

STM and SFM investigate the local structure of specimen surfaces with a high lateral resolution, including atomic resolution. Both methods sample the surface only and thus cannot provide information of the in-depth structure of a surface layer. They also give a direct image and thus a very clear insight into the surface structures. These methods are therefore a valuable addition to XRD, which samples the average of the structure of a surface film. They are widely used for investigations of solid surfaces including *in situ* studies of electrode surfaces. Many reviews have been published so that no detailed explanation of these methods is intended. Successful measurements require a careful surface preparation of the single crystal surfaces with respect to both the chemical cleanliness and the formation of large, flat, and atomically smooth terraces. Tips of tungsten and platinum-rhodium are usually prepared by electrochemical etching. They have to be isolated by wax or a resin to avoid as much as possible electrochemical reactions of the tip materials, including disturbing currents of redox reactions. Usually an electrochemical leakage current of less than 1 nA is tolerated. Although various recipes are applied by the different groups, a very common and reliable procedure is the electrochemical etching of a tungsten wire in non-stirred 3 M NaOH till the lower part of the wire falls off and the subsequent coverage of the freshly formed tip with Apiezon wax. The images were taken with a constant tunnel current during the scan of the tip across the specimen's surface with the adjustment of the distance to keep the current constant. One thus samples the topography and the electronic properties of the sample surface. A bipotentiostat permits setting the electrode potential and the tip bias independently of each other. Unfortunately the built-in commercial potentiostats of electrochemical STMs are very slow, meaning fast-pulse methods for an *in situ* specimen preparation require the intermediate connection to a fast potentiostat and the subsequent reconnection to the electronic circuit of the STM. This may be done using fast relays. A specimen preparation by fast potentiostatic transients permits the investigation of fast-developing surface structures, the growth of which may be stopped by an appropriate potential step. As an example, the investigation of initial stages of localized corrosion may be mentioned [124]. These corrosion structures of a few nm size grow within less than 1 ms on passive metal surfaces in the presence of aggressive anions, e.g. chloride at sufficiently positive potentials and stop growing after a potential step to negative values where they may be examined with the relatively slow STM method within ca. 1 min. It should be mentioned that fast STMs have been developed and applied for an imaging of processes at solid surfaces in the UHV and in electrolytes with atomic resolution and high time resolution. Low temperatures or low electrode potentials with a blocking of the surface by strongly adsorbed species slows the kinetics so that the movements and reaction of species may be followed. In this way, surface diffu-

sion and reaction of molecules at catalysing surfaces [125] and the dissolution of Cu at the steps of Cu(100) terraces inhibited by adsorbed chloride have been studied successfully [126].

SFM applies a commercial tip of Si or SiN, which follows the topography while scanned across the specimen's surface. Usually the beam of a laser is reflected at the rear side of the cantilever and transfers the changes of the deflection to a photo detector. Its signal composes the image of the surface topography. Although more difficult, one may achieve atomic resolution of surface structures with a sufficiently sharp tip. The tip feels the repulsive forces of the sample surface. Besides the contact mode, the tapping mode may be applied; this reduces the interaction of the tip with the sample surface. This soft treatment preserves soft surfaces like those of polymers and biological material, which otherwise may be seriously damaged. Besides the topography, also the mechanical properties like the hardness may be measured. One major advantage of the method with respect to STM is that it does not require electronic conductivity of the specimen. One thus may study even surface layers of insulating materials. Therefore SFM is successfully applied in industry with moderate lateral resolution, whereas STM is used mostly for fundamental research in electrochemistry and corrosion research. The requirement of conductivity for STM may be seen as an appropriate possibility to get further information with respect to the electronic properties of surface layers. The ideal situation is of course the application of both methods to get better insight into the properties of surfaces and surface layers.

The investigation of anodic oxide on various metals shows that at first usually amorphous structures are formed with a dense coverage of the terraces with grains, which change to nano-crystallites with time. The extent and the rate of this change depend on the system under study. This crystallization occurs for Cr within hours [127], whereas Cu keeps the amorphous grain structure for a very few minutes only and develops a well-ordered, faceted, crystalline layer covering the whole electrode surface [128, 129]. In the next section, the details of the structure of layers formed on Cu are discussed, followed by a summary of some other more reactive metals like Ni and Cr.

7.2.1 The Passive Layer on Cu

Cu is a suitable subject for *in situ* STM studies of anodic oxide formation. Usually the investigation of Cu single-crystal surfaces involves mechanical polishing with diamond spray to a final 0.5 μm grading, and thereafter cleaning with alcohol and water, electropolishing in 20% orthophosphoric acid. Annealing in hydrogen gas at 600 °C overnight helps to enlarge the size of the terraces. Pre-existing, air-formed, thin oxide layers after this pre-treatment may be easily reduced at negative potentials within the electrochemical cell of the STM, which yields a flat and undisturbed structure of the terraces. Apparently, the surface mobility of Cu atoms formed by reduction of a thin, air-formed film is sufficient to be deposited at the step edges of terraces, thus avoiding any roughening of the metal surface. Very detailed investigations have been performed on Cu(111) in alkaline solutions. The polarization curve of Cu in 0.1 M NaOH has been already presented in Fig. 24. Besides the peaks

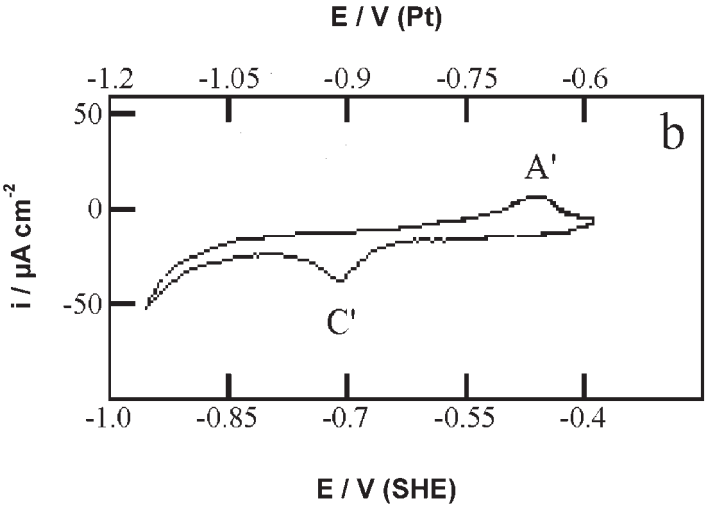

Fig. 56. Polarization curve of Cu(111) in 0.1 M NaOH in STM cell with peaks of OH-adsorption A' and OH-desorption C' [130].

of oxide formation AI and AII and their reduction at CII and CI one observes a small anodic A' and cathodic peak C' at $E = -0.46$ and -0.71 V respectively (Fig. 56). These peaks have been ascribed to the formation of an adsorption layer of OH^- on the Cu(111) terrace according to Eq. (34) [130], which is in agreement with studies with Surface Enhanced Raman Spectroscopy of Cu(111) in NaOH [131] and polycrystalline Cu [132] in perchlorate solutions. *In situ* SFM studies on Cu(111) and Cu(110) in acidic perchlorate solution yield also ordered superstructures due to OH adsorption [133, 134].

$$Cu + OH^- \rightarrow Cu{-}OH_{ads} + e^- \tag{34}$$

The charge of the anodic and cathodic peak amounts to 55 µC cm^{-2} which corresponds to a surface concentration for OH adsorbates of 0.34 10^{15} cm^{-2}. The density of Cu atoms on the Cu(111) terraces is 1.75 10^{15} cm^{-2}. These numbers yield a surface coverage of 0.19 of a monolayer if a 1 to 1 relation of OH to Cu is assumed [130].

The *in situ* STM images at $E = -0.60$ V show a dark structure which starts to grow preferentially at the step edges and extends slowly within ca. 180 s across the whole terrace [130]. These changes occur faster with increasing potential. The image gets much clearer than before at more negative potentials, where frizzy steps at the terraces are observed due to a high surface mobility of the Cu atoms (Fig. 57a–c). Parallel to this process, the terraces get larger and bright spots appear at its end. At larger magnification, one observes a well-ordered hexagonal structure with a characteristic lateral parameter of 0.6 nm, which is quite different from the expected 0.256 nm of the Cu substrate surface (Fig. 57d,e). Two orientations with 10^0 and 20^0 rotation relative to the substrate lattice are found. According to Wood's notation, they

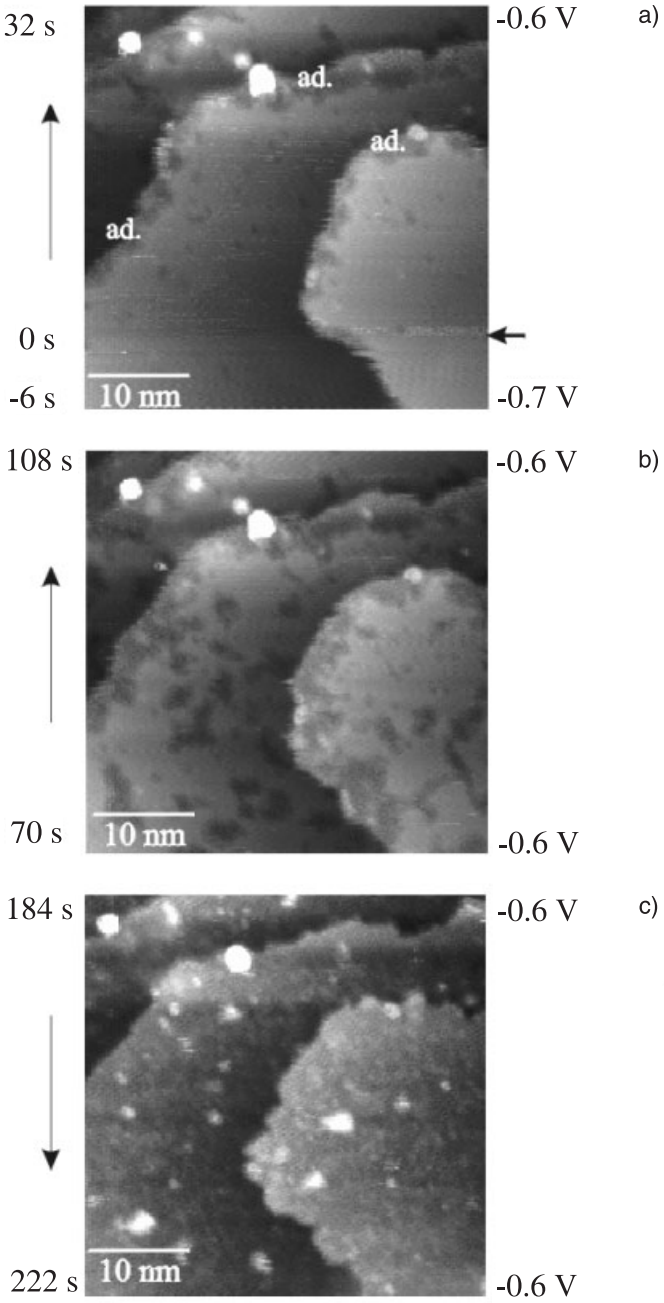

Fig. 57. Sequence of STM images of Cu(111) after stepping the potential from negative values to $E = -0.60$ V (horizontal arrow) in 0.1 M NaOH showing the adsorption and reconstruction with time after: (a) 0, (b) 70, and (c) 180 s.

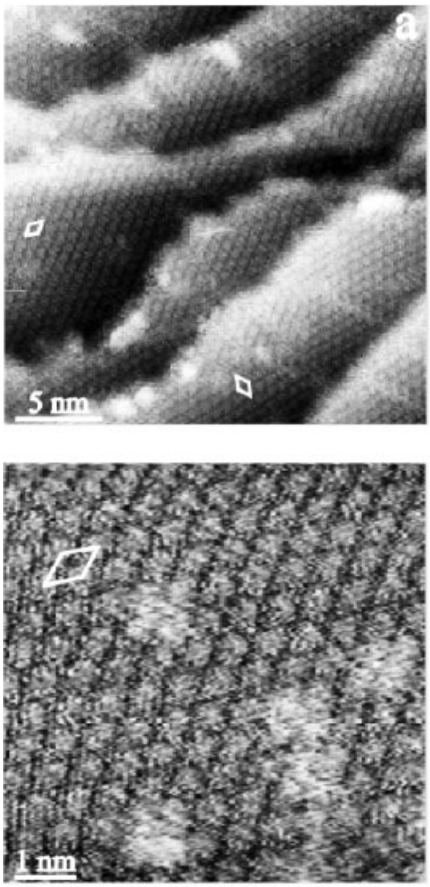

Fig. 57. (d), (e) detailed image of the reconstructed Cu (111) surface [130].

have a $(\surd 21 \times \surd 21)R.10^0$ and a $(\surd 49 \times \surd 49)R.20^0$ structure (Fig. 58). The coincidence cells contain 4 or 9 cells of the adsorption layer, and 21 or 49 of the substrate. Assuming 1 OH ion for each mesh, one gets again an atomic ratio OH to Cu of 0.19 or 0.18 in close agreement with 0.19 for the electrochemical results. The small bright spots of Fig. 57e refer to oxygen vacancies. Their apparent height corresponds to 0.05 nm as for the difference between the surface with and without OH adsorbate. The dark spots of Figs. 57a to c suggest a 0.05 nm lower position, which, however, is an artifact. It is well known from studies in the UHV that the adsorption of oxygen reduces the tunnel current which requires a closer approach of the tip to the surface to keep it at the preset value [135]. Thus, this observation is an electronic rather than a topographic effect. The observed structures are caused by adsorption of OH^- from the alkaline electrolyte, which goes along with a reconstruction of the Cu(111) surface. This reconstruction causes a decrease of the Cu concentration at the surface and a diffusion of ejected atoms to the step edges, with a related growth of the terraces.

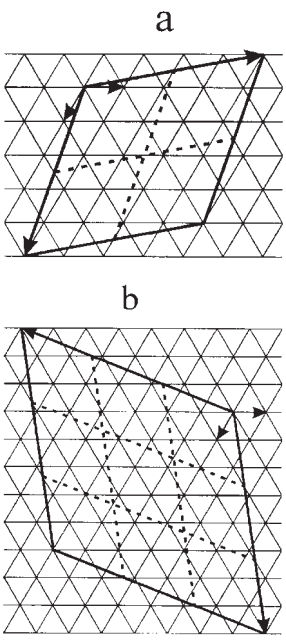

Fig. 58. Coincidence cells of ad layer lattice dark and dashed lines and the Cu(111) substrate surface thin lines showing (a) $(\sqrt{21}x\sqrt{21})R.10^0$ and (b) the $(\sqrt{49}x\sqrt{49})R.20^0$ coincidence cells [130].

Because of the advancing adsorption structure and its formation at the inner parts of the terrace, some still-unreconstructed surface areas remain. At these sites, the Cu atoms form islands with an apparent height of ca. 0.2 nm, which are the bright spots within the otherwise fully reconstructed Cu surface at the end of the process (Fig. 57c). When the surface is progressively covered by the OH adsorption layer, the excess Cu atoms are trapped and can no longer diffuse at the Cu surface to the step positions. A diffusion across the adsorbate layer does not occur. A slight decrease of the electrode potential to $E = -0.70$ V reverses the adsorption and surface reconstruction and the smooth terrace, with its original size, is restored. The reaction rate at the surface increases with the electrode potential due to a larger driving force. At $E = -0.65$ V the whole process is completed within 380 s, whereas only 70 s are required at $E = -0.55$ V.

The Cu surface concentration is apparently reduced after its reconstruction. A very interesting feature is the close match of the structure of the OH adsorbate layer and that of the oxygen atoms in the (111) plane of crystalline Cu_2O (cuprite). In the [111] direction cuprite consists of Cu planes embedded between two O planes. The hexagonal packing of the O planes have a 2×2 structure with respect to the Cu plane with atomic distances of 0.604 nm and 0.302 nm respectively. 0.6 nm is also the length of the unit cell of the adsorbate structure as determined by STM. OH adsorption on an unreconstructed Cu(111) surface would have 5 Cu atoms per unit cell with only 20% of an OH monolayer with respect to the densely packed Cu(111) plane. This result suggests a reconstruction of the Cu surface to match the structure of cuprite and the transfer of 20 % of the Cu atoms to the edge positions of the terrace during OH adsorption. This leads to the growth of the terraces during the

adsorption process as observed with STM. Thus, the O/Cu ratio increases to $\frac{1}{4}$, which refers to the cuprite structure.

According to the polarization cure of Fig. 24, anodic oxide formation is expected at $E = -0.20$ V in 0.1 M NaOH. STM images show the formation of small oxide grains starting preferentially at the step edges, but also within the Cu(111) terraces. They take over the whole terrace with time (Fig. 59a). The rate of formation of these oxide grains depends apparently on the electrode potential and time of passivation and the pH of the solution. One observes a very slow oxide formation first at $E = -0.22$ V, which gets faster with increasing potential (-0.17 V, -0.12 V). At $E = -0.12$ V a fast formation of many grains is observed covering the whole surface. In borate buffer pH 9.3, oxide grains appear at $E = 0.0$ V in agreement with the predictions of the Pourbaix diagram with a -059 V/pH shift of the potential of oxide formation. In the potential range of $E = -0.01$ to 0.0 V, the STM images show in borate buffer pH 9.3, a roughening due to a slow step-flow on the Cu(111) surface caused by metal dissolution at the steps of the terraces. The formation of oxide grains at the steps blocks the dissolution at these sites. At 0.01 to 0.03 V, the faster nucleation and growth of grains leads to a complete coverage of the surface by oxide nuclei and the formation of a three-dimensional oxide film [89]. This process is completed within ca. 100 s at $E = 0.03$ V and is much faster at more positive potentials due to a larger driving force. Although the oxide grains nucleate preferentially at the step positions, they are also formed on the terraces. At $E > 0.05$ V the image is lost in borate buffer pH = 9.3 due to the growing film thickness and its low electronic conductivity. The small oxide nuclei in both solutions have a diameter of 1.5 to 3 nm and a height of 0.25 to 0.3 nm, which is slightly higher than the monoatomic step of the terrace. The oxide grains show no indication of a crystalline structure. They have an approximately disc-like form and do not show any epitaxial relationship with the Cu(111) substrate. No atomic structure could be resolved on these grains at pH 9.3 even after 1 hour of anodic oxidation. Therefore, one may conclude that these granular anodic films are non-crystalline. From the charge of potentiodynamic reduction of a layer formed at 0.03 V for 300 s, one may calculate a layer thickness of 0.8 nm, which corresponds to two (100)-oriented elementary cells of cuprite on top of each other. At 0.06 V the STM images become unstable in borate buffer with the growth of the film and are finally lost.

A completely different result is obtained in 0.1 M NaOH for prolonged anodic polarization [90, 129]. Ca. 2 min after the oxide grains appeared, triangular structures with sharp edges are formed and take over the whole surface, indicating a crystalline structure of the oxide layer. These oxide crystals have a high density of steps, as shown in Fig. 59b. The width of these regular facets is 1.5 nm. It is very likely that the epitaxial relationship of the Cu_2O crystals to the Cu(111) substrate causes stress and the faceting leads to its release. At higher magnification one observes an atomic lattice on these narrow terraces with a hexagonal structure and ca. 0.3 nm atomic distance [129]. Apparently, STM images the periodicity of the Cu planes of the abovementioned cuprite structure in the (111) orientation. It is still not fully understood why the (111) plane of the Cu_2O (111) crystals is not terminated by the oxygen structure. For the STM image of the oxygen plane of cuprite, one expects a 0.6 nm distance. A possible explanation could be an adsorption layer of OH with a

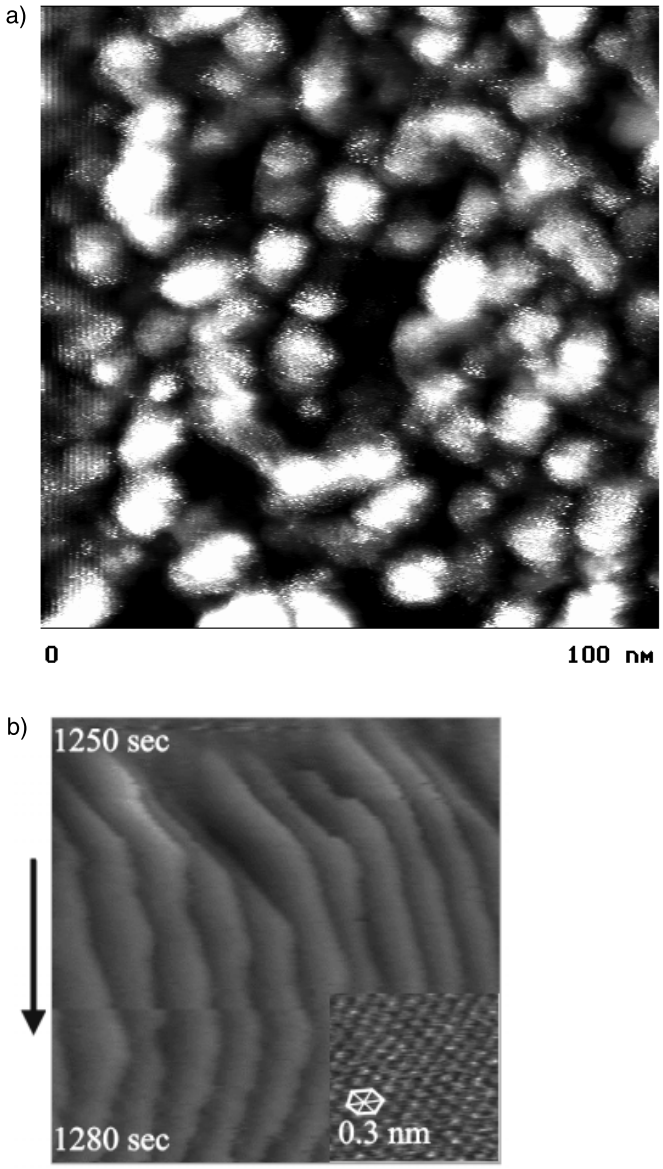

Fig. 59. (a) Cu_2O oxide grains; and (b) later-appearing, faceted Cu_2O oxide crystals formed on Cu(111) in 0.1 M NaOH at $E = 0.2$ V. Insert: atomic resolution of hexagonal structure showing the of Cu–Cu distances of (111)-oriented cuprite [128, 129].

one-by-one relation to the Cu ions. Angular resolved XPS measurements of passivating anodic Cu_2O layers on Cu(111) show indeed an OH layer on top of the oxide [136]. For energetic reasons the passive film should not be terminated with a Cu^+ plane. An outermost OH or O plane is required to render electroneutrality to the

surface film due to the formation of complete O–Cu–O sandwiches in the [111] direction.

The Cu(100) surface shows in 0.1 M NaOH a similar anodic and cathodic peak both at $E = -0.8$ V [137]; however, no reconstruction of the surface could be found. This is presumably not necessary because the Cu(100) surface is less densely packed in comparison with Cu(111) and matches already the cuprite structure. Similarly, the close match of the anodic and cathodic peaks without a hysteresis is an additional indication for a faster adsorption process, whereas the surface reconstruction of Cu(111) with the diffusion of the Cu atoms to the step edges slows the adsorption process. The anodic film forms at first also a granular structure and a final crystalline film. First STM studies suggest an orientation of Cu(100) parallel to $Cu_2O(100)$ with a distance parameter of 0.3 nm which corresponds again to the Cu–Cu distance within the cuprite structure.

SFM yields corresponding results to those found by STM investigations [138]. In these studies the periodicity of the O^{2-} ions has been imaged with a distance of 0.60 nm and 0.43 nm for the anodic Cu_2O film on Cu(111) and Cu(100) respectively. The Cu_2O lattice is found with the oxide plane (111) parallel to Cu(111) and the oxide plane (100) parallel to the Cu(100) substrate.

Reduction of thin Cu_2O layers reproduces smooth terraces of the Cu surface, however, with multi-atomic steps in between. This result is further proof for the high surface mobility of Cu atoms on pure Cu(111) terraces. Reduction of the thicker duplex film yields a rougher metal surface. During the rearrangement of several atomic layers smooth large terraces cannot be achieved.

The Cu_2O / CuO, $Cu(OH)_2$ duplex layer which grows at potentials positive to peak AII consists in 0.1 M NaOH of large crystals with sharp edges. Large terraces of up to 20 nm and with steps of 0.3 nm are achieved. This layer is apparently crystalline and an ordered structure could be resolved at larger magnification.

7.2.2 Mechanism of STM Imaging of Anodic Oxides on Cu

The imaging of anodic oxides raises the question about the necessary electron transfer. A thin film of less than 1 nm permits direct tunnelling from the tip to the substrate metal. However, if the film thickness exceeds ca. 1 nm, then tunnelling should not be possible according to relation 35 for the tunnel probability, which contains the energy ΔE and the width x for the barrier of the tunnel process and the effective mass of the electron m^*. If the oxide layer is thicker than 1 nm, then the electrons have to tunnel

$$w_t = \exp\left(-\frac{2\sqrt{m^*}}{\hbar} x\sqrt{\Delta E}\right) \tag{35}$$

from energy states close to the Fermi level of the tip to states within the oxide layer, from where they have to move to the metal substrate. The energetic position of the bands have been discussed in detail in Section 6.2 (Figs. 44, 46) With these results one obtains the energetic relation of the electronic levels within the tip and the oxide-covered specimens depicted in Fig. 60. For a stable STM image, one requires occu-

pied states within the tip and empty states within the passive layer at the same energy level. With the applied electrode potential and the tip bias the occupied levels of the tip are at a level within the band gap of the oxide layer so that an electron transfer should not be possible. However, as described in detail, Cu_2O has a high density of localized states within the band gap, which even form a small sub-band and may mediate the electron transfer from the tip to the Cu substrate. These states have been postulated to explain the electronic conductivity of crystalline Cu_2O and the electron transfer for redox reactions of oxide-covered Cu electrodes in the dark. If this sub-band is located at the Fermi level, then it easily may explain the necessary electron transfer through the oxide film. Consequently there is no problem for a stable STM imaging of anodic oxide layers on Cu as has been found experimentally in strongly alkaline solutions as e.g. for 0.1 M NaOH (pH = 12.9). Figs. 60a and b depict the situation for the flat band potential and a more positive potential.

A similar situation arises for the Cu_2O / CuO, $Cu(OH)_2$ duplex film at more positive potentials. In this case the sub-band extends through both parts of the passive layer. At sufficiently positive potentials, even an electron transfer to the empty states of the conduction band becomes possible (Figs. 60c and d).

There is some difficulty for the passive layer formed in borate buffer pH 9.3. In this case only the very thin Cu_2O film could be imaged. When this film gets thicker at $E > 0.05$ V, the image is lost. This observation has been repeated by numerous experiments and it should be seen as a principal effect. It also agrees with the experience that it is very difficult or impossible to obtain STM images of thicker anodic oxide layers on many other metals. A parallel observation is that in this electrolyte the Cu_2O film remains amorphous, i.e. the surface remains covered by small round oxide grains that do not yield a crystalline structure at larger resolution. This thin amorphous film, which consumes one monolayer of Cu at maximum, permits a direct tunnelling from the tip to the substrate and thus allows an imaging of the surface. Apparently, a crystalline structure is required for thicker films to get a sufficiently high density of electronic states within the band gap to permit an electron transfer via the oxide layer. The thick Cu_2O films formed in borate buffer pH 9.3 are apparently amorphous and thus cannot be imaged. They presumably have a non-ordered accumulation of interband states that cannot mediate an electron transfer via a hopping mechanism. When the duplex film is formed one gets again a stable image, even in borate buffer. However, when the outer part of this duplex film is reduced to Cu_2O, the image is lost again.

7.2.3 Passive Layers on Ni and Cr

The structure of the passive layer on Ni has been studied very carefully with STM [139] by the group of P. Marcus and with XRD by the group of R.J. Behm [140]. Ni surfaces usually have at room temperature a thin layer of an air-formed film that consists of 0.6 nm thick inner oxide, and 0.3 nm thick outer hydroxide, parts, according to XPS investigations of several authors; this was discussed in detail in Section 5.1.5. Potentiodynamic cathodic polarization in 0.1 M Na_2SO_4 solution of pH 3 yields a small reduction peak at $E = -0.1$ V with a charge of ca. 1000 μC cm^{-2}

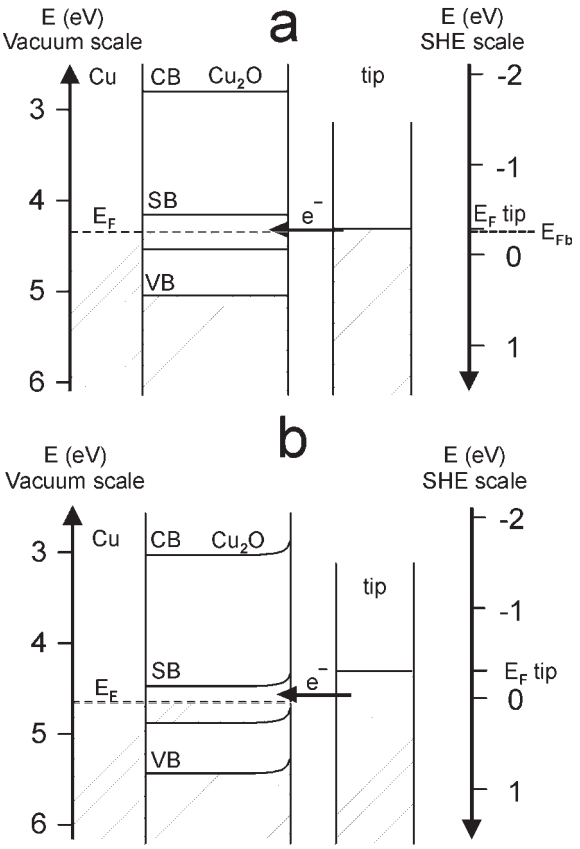

Fig. 60. Tunneling mechanism via states within the band gap (sub-band SB) of a Cu_2O layer explaining stable STM imaging of oxide layers at: (a) flat band potential $E_{Fb} = -0.25$ V and (b) $E = 0.1$ V

corresponding to 0.6 nm NiO. This air-formed film shows a grain structure. According to *in situ* STM studies, these grains cover the terraces completely, but with a clear appearance of the step edges, suggesting the formation of a thin, homogeneous layer [139]. This oxide/hydroxide film may be reduced producing extended, atomically flat, pure Ni-surfaces showing the expected hexagonal arrangement of the Ni atoms of the Ni(111) substrate surface without reconstruction which supports previous findings with XPS.

In situ STM studies confirm previous XPS results of a $Ni(OH)_2/NiO$ bilayer structure of the passive film on Ni. Images of Ni passivated in 0.1 M Na_2SO_4 of pH 3 with a small tunnel current density depict the outer parts of the layer, showing the grainy structure of the outer hydroxide layer [139]. The grains of 2 to 5 nm width grow with time of passivation to ca. 2 to 8 nm within 3 hours. They are rounded with no features showing any orientation relative to the Ni(111) substrate. At larger magnification, no ordered atomic structure could be detected, which gives further

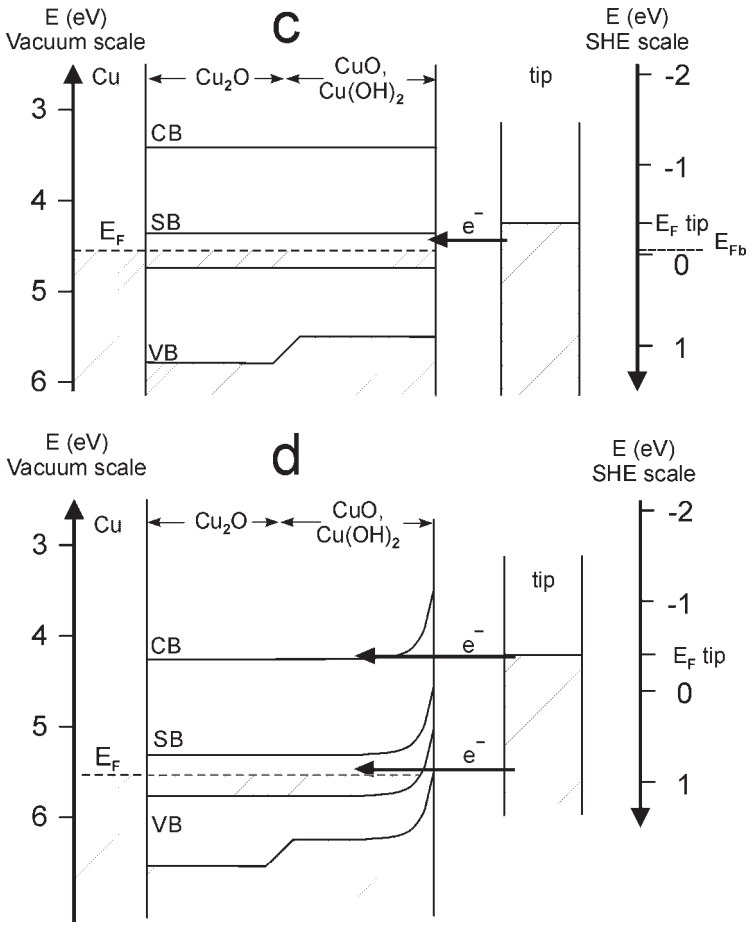

Fig. 60. (c) imaging of duplex layer at flat band potential $E = 0$ V and (d) $E = 1.0$ V [89, 128].

proof that this part of the layer is amorphous. A larger tip current density leads to a closer approach of the tip to the surface, thus imaging the crystalline inner oxide layer. Here triangular oxide terraces are detected that present a hexagonal, well-ordered atomic structure at larger magnification with a lattice vector of 0.3 nm, which corresponds to the distance of NiO(111) (0.295 nm) and of $Ni(OH)_2(1000)$ (0.317 nm). Apparently, the inner NiO layer is (111) oriented to the (111) Ni substrate. The orientation of the hexagonal surface structure of the oxide is parallel or antiparallel to that of the Ni substrate supported by the already mentioned XRD studies of passivated Ni, which yield an antiparallel orientation for the NiO part of the passive layer [140]. According to the length of the terraces and the height of the steps of the crystalline oxide, a tilt of 1^0 to 10^0 relative to the substrate is concluded with an average of 3^0 [139], similar to the findings of an average of 3.3^0 obtained by XRD studies [140]. This tilt has been explained as a possibility for the system to

overcome the stress at the metal/oxide interface due to a lattice mismatch between the Ni substrate and its anodic oxide of 18 %. Similar results have been found for anodic films with well-ordered facets of the crystalline Cu_2O layer, as described in Section 6.1.2 (Fig. 59b) [80, 129]. The polar structure of the (111)-oriented NiO crystallites yields a termination of the oxide film with a Ni^{2+} or an O^{2-} plane, which is stabilized by an outer adsorption layer of OH. The measured step height of multiples of 0.12 nm at the oxide terraces suggests that STM samples the Ni^{2+}–O^{2-} distance within the oxide. The reason for this result is not yet fully understood. A termination by an O^{2-} or a Ni^{2+} layer is not favored because of energetic reasons. Oxidation studies in the vacuum yield a 2×2 reconstruction of the surface during the loss of hydroxide [141] and the surface readily adsorbs OH in the presence of a small water pressure returning to the unreconstructed (111) (1×1) orientation.

In the case of passive layers the outer hydroxide film is always present. It is hydrated to a large extent, and thus does not correspond to crystalline $Ni(OH)_2$. The incorporation of water leads to an amorphous structure of the outer part of the passive layer with the observed characteristic dense package of small grains. All these detailed investigations lead to the structure of the passive layer on Ni with a an inner crystalline oxide with a antiparallel orientation of its (111) planes relative to the (111)-oriented Ni surface with a tilt of 3^0 and an outer amorphous hydroxide part.

The passive layer on Cr(110) shows a similar structure of hydroxide grains at low potentials and short passivation times. Crystalline oxide is found after prolonged anodization at sufficiently positive potentials [127]. At $E = 0.35$ V, only oxide grains of 3 to 7 nm diameter and 0.1 to 0.4 nm height have been observed with a rounded shape and no orientation relative to the substrate. At larger magnification no atomic structure could be found. At $E = 0.75$ V, facets of oxide appear with a hexagonal structure with the close packed rows parallel to and at 30^0 of the [001] orientation of the metal substrate. The formation of the crystalline structure may be followed as a function of time at lower potential. At $E = 0.55$ V, it takes ca. 4 hours to change the grain structure of the hydroxide to that of the oxide which occurs much faster at $E = 0.75$ V. Apparently, first a granular amorphous hydroxide layer is formed that is transformed into a crystalline oxide with time. This transition gets faster with increasing electrode potential, as in the case of passivating Cu_2O on Cu. In agreement with XPS results, this transition has been ascribed to the dehydration of $Cr(OH)_3$ by further oxidation of Cr according to Eq. (36).

$$Cr(OH)_3 + Cr \rightarrow Cr_2O_3 + 3\,H^+ + 3\,e^- \tag{36}$$

Different from the situation of the passive layer on Ni, passive Cr does not show a two-layered structure. Variation of the tunnel current does not cause the change from an amorphous to a crystalline structure [127]. Depending on the potential one observes the amorphous granular structure of the hydroxide, or the crystalline oxide. The lattice parameter measured by STM is 0.28 nm, which corresponds to the distance in the O plane of 0001-oriented α-Cr_2O_3. Apparently, STM samples the distance of the O ions. The distance of Cr^{3+} ions should be 0.485 nm due to a lower density of the cations. Crystalline bulk CrO(OH) and $Cr(OH)_3$ have a similar structure. The parameters of the hydroxide or oxyhydroxide are somewhat larger, i.e.

0.307 and 0.531 respectively. The passive layer consists of a sequence of O^{2-} and Cr^{3+} layers. Because of energetic reasons, the passive film is again terminated by an OH^- layer. In case of an oxyhydroxide, the O plane consists of a mixture of an O^{2-} and OH^- ions. The predominant step heights on the crystalline layer of 0.11 nm are related to emerging stacking faults within the Cr^{3+} layers, which for energetic reasons is easier to explain by their lower density with respect to the O^{2-} planes. The distance of a Cr^{3+}–O^{2-} layer sequence amounts to 0.22 nm, which is rarely found in the STM images.

8 Breakdown of Passivity

Although the passive layer provides an optimum of corrosion protection to most of the otherwise very reactive metals, the protective layers can suffer local breakdown, owing to various environmental conditions. As a consequence, the metal dissolves locally with very high current densities, which correspond to the applied positive electrode potentials resulting in the growth of corrosion pits. At least for very short times in the ms range, local current densities of up to more than 100 A cm^{-2} have been measured for nickel and several 10's of A cm^{-2} for iron before the precipitation of accumulated corrosion products lowers the current density to still high values of some 100 mA cm^{-2} [142, 143]. This breakdown of passivity occurs in the presence of so-called aggressive anions, such as the halides and other anions like SCN^-, and ClO_4^- at very positive potentials. In the presence of fluoride in strongly acidic electrolytes, iron and nickel undergo a general breakdown of passivity, whereas usually pitting is observed [142, 143]. Only in solutions with a high chloride content (≥ 1 M) general breakdown of passivity is obtained. The large protected surface with conductive passive layers may serve as a large cathode for the reduction of appropriate redox systems within the electrolyte to compensate for the intense anodic metal dissolution at the surface of the corrosion pits. Thus, in the presence of aggressive anions, especially chloride, many metals are seriously attacked. For most metals, a characteristic potential has to be reached above which a stable pit growth becomes possible, which causes a characteristic current increase in the passive range above the critical pitting potential. In the presence of inhibitors, a positive limit within the passive range of localized corrosion has been found with a related inhibition potential [143].

Many investigations have sought to explain the mechanisms of pit nucleation and pit growth and the topic continues to be controversial. It is not intended in this review to include a detailed description of pitting corrosion. Good reviews and book chapters are recommended to the interested reader, which provide an insight into the details of this interesting corrosion phenomenon that is important from a technological and scientific point of view [142, 143, 145, 146]. Although the mechanisms are discussed rather controversially, some basic factors should be mentioned briefly that are closely related to passivity, and that refer to the opinion of the author of this review and may be read in detail at Ref. [143].

The essential condition for pitting of a passive metal surface is the presence of a sufficient concentration of the aggressive halides. A concentration of $\geq 10^{-3}$ M is required to provide a growing pit with the necessary amount of Cl^-. These halides increase the rate of dissolution of the passive layer by forming a complex with the cations at the oxide/electrolyte interface as described schematically by reaction 4 in Fig. 4, Section 2. This complex is transferred at a higher rate into the electrolyte than an uncomplexed cation of the oxide matrix. If the accumulation of the complexing aggressive anions is sufficiently large, then the whole passive layer will be removed, thus exposing a bare metal surface to the electrolyte. At these unprotected sites, the local dissolution current density attains the extremely high values of the applied electrode potential. The necessary accumulation of corrosion products within the pits causes locally a high halide concentration, and thus a self-stabilization of their continuous growth. The well-known, very strong, complexing properties of fluoride for cations like Fe^{3+} and Ni^{2+} cause a complete breakdown of passivity of Fe and Ni, thus leading to a less complicated situation compared with a local breakdown. In this sense, fluoride is well suited as a model system for pitting studies. The related thinning of a passive layer by these anions has been confirmed with surface analytical methods like XPS of emerged electrodes. The different stages of breakdown have been also followed with the rotating ring-disc technique, which supports the concept of cation complexing as an essential step for breakdown of passivity, pit nucleation, stable pit growth and the prevention of repassivation of a corrosion pit. Further stabilizing factors for pit growth are the acidification of the pit electrolyte due to hydrolysis of corrosion products and ohmic drops with increasing size of the pits. The breaking of the film due to mechanical stress and electrostriction may be an additional mechanism for pit nucleation.

9 Concluding Remarks

Passive layers are essential for the protection of reactive metals and are a necessary requirement for their use under environmental conditions. The self-healing property of the poreless, protecting oxide films on many metals and alloys, with their extremely slow dissolution rates, are unique. Since the days of the detection of passivity of metals ca. 200 years ago, a detailed understanding has been achieved due to the application of electrode kinetics and various surface analytical methods in the past when they became available. UHV methods like the electron spectroscopies XPS, AES and the ion spectroscopies ISS and RBS provide information about the chemical composition of the anodic layers, whereas methods applying synchrotron radiation, e.g. XRD and XAS, and scanning methods, e.g. STM and SFM, give insight into the structure of these films on a mesoscopic and nanoscopic scale down to atomic dimensions. These more recent analytical tools give also *in situ* access to the details of growth and breakdown of passive layers. As in all other fields of electrode kinetics, one has an excellent opportunity to follow *in situ* electrode kinetics on an atomistic scale. In this sense, fundamental research provides a better understanding

of corrosion mechanisms, which may help in engineering to predict the corrosion behavior of even complicated alloys in a complex environment. The continuing application of these modern tools to the various systems will lead to a better understanding for corrosion phenomena and reduce the various observations to a restricted number of leading mechanisms. In this sense, the application of surface science to corrosion phenomena like passivity is promising for future research, and a deeper understanding to the benefit of science and technology.

10 References

1. H. H. Uhlig, in Passivity of Metals, R. P. Frankenthal, J. Kruger editors, Corrosion Monograph Series, 1–28, The Electrochemical Society, Princeton New Jersey (1978).
2. N. Tomashov, Theory of Corrosion and Protection of Metals, 7, 325, Macmillan Co. New York (1966).
3. W. Ostwald, Elektrochemie, 696–697, Leipzig (1896).
4. J. Keir, Phil. Trans. 80, 359 (1790).
5. Gmelin Handbuch der Anorganischen Chemie, Teil 59A, 313, Berlin (1929–1932).
6. M. Schönbein, letter to M. Faraday in M. Faraday, Experimental Researches in Electricity, Vol. 2, 238, Dover Pub, New York (1965).
7. M. Faraday, as 6, 234–250.
8. H. H. Uhlig, Corrosion Handbook, 21, Wiley, New York (1948).
9. M Pourbaix, Atlas d'Equilibres Electrochimiques, Paris, Guthiers Villars & Cie, (1963), Atlas of Electrochemical Equilibria in Aqueous Solutions, Pergamon, Oxford, (1966).
10. K. J. Vetter, Electrochemical Kinetics, Academic Press, New York (1967) 783.
11. K. Heusler, K. G. Weil, K. F. Bonhoeffer, Z. Physik. Chem. N. F. 15, 149 (1958).
12. S. Haupt, H.-H. Strehblow, Langmuir 3, 873 (1987).
13. as 10. page 717.
14. H. W. Hoppe, H.-H. Strehblolw, Surf. Interf. Anal. 14, 121 (1989).
15. H. W. Hoppe, H.-H. Strehblow, Corr. Sci. 31, 167 (1990).
16. K. J. Vetter F. Gorn, Electrochimica Acta, 18, 321 (1973).
17. K. J. Vetter, F. Gorn, Werkstoffe Korrosion 21, 703 (1970).
18. K. E. Heusler, Ber. Bunsen Ges. Phys. Chem. 72, 1197 (1968).
19. J. P. S. Pringle, Electrochim. Acta 25, 1403 (1979).
20. J. P. S. Pringle, Electrochim. Acta 25, 1423 (1979).
21. J. A. Davies, B. Domeij, J. P. S. Pringle, F. Brown, J. Electrochem. Soc. 112, 675 (1965).
22. F. P. Fehlner, N. F. Mott, Oxid. Met. 2, 59 (1970).
23. as 10, 767.
24. N. Cabrera, N. F. Mott, Rep. Prog. Phys. 12, 163 (1948–49).
25. B. P. Löchel, H.-H. Strehblow, Werkstoffe Korrosion 31, 353 (1980).
26. H.-H. Strehblow, H. D. Speckmann, Werkstoffe Korrosion 35, 512 (1984).
27. S. Haupt, H.-H. Strehblow, Corr. Sci. 29, 163 (1989).
28. G. Engelhardt, T. Jabs, D Schaepers, H.-H. Strehblow, Acta Chimica Hungaria 129, 551 (1992).
29. G. Engelhardt, D, Schaepers, H.-H. Strehblow, J. Electrochem. Soc. 139, 2170 (1992).
30. G. Engelhardt, T. Jabs, H.-H. Strehblow, J. Electrochem. Soc. 139, 2176 (1992).
31. E. Yeager, W. E. O'Grady, M. Y. C. Woo, P. Aagans, J. Electrochem. Soc. 125, 348 (1978).

32. A. T. Hubbard, R. M. Ishikama, J. Katekaru, J. Electroanal. Chem. 86, 274 (1978).
33. F. T. Wagner, P. N. Ross, J. Electrochem. Soc. 130, 1789 (1983).
34. I. Olefjord, B. O. Elfstrom, Corrosion 38, 46 (1982).
35. S. Haupt, U. Collisi, H.-D. Speckmann, H.-H. Strehblow, J. Electroanal. Chem. 194, 179 (1985).
36. S. Haupt, C. Calinski, H. W. Hoppe, H.-D. Speckmann, H.-H. Strehblow, Surf. Interf. Anal. 9, 357 (1986).
37a. D. M. Kolb, D. L. Rath, R. Wille, W. N. Hansen, Ber. Bunsen Ges. Phys. Chem. 87, 1108 (1983).
37b. W. N. Hansen, D. M. Kolb, J. Electroanal. Chem. 100, 493 (1979).
37c. D. M. Kolb, Z. Phys. Chem. N.F. 154, 179 (1987).
38. D. Lützenkirchen-Hecht, H.-H. Strehblow, Electrochimica Acta 43, 2957 (1998).
39. S. Haupt, H.-H. Strehblow, Corr. Sci. 37, 43 (1995).
40. C. Calinski, H.-H. Strehblow, J. Electrochem. Soc. 136, 1328 (1989).
41. A. Rossi, C. Calinski, H.-W. Hoppe, H.-H. Strehblow, Surf. Interf. Anal. 18, 269 (1992).
42. H.-H. Strehblow, C. Calinski, S. Simson, P. Druska, H.-W. Hoppe, A. Rossi, in Modification of Passive Films , P. Marcus, B. Baroux, M. Keddam editors, European Federation of Corrosion, Publication No. 12, The Institute of Materials 1994.
43. H. D. Speckmann, S. Haupt, H.-H. Strehblow, Surf. Inerf. Anal. 11, 148 (1988).
44. H. Scofield, J. Electron Spectrosc. 8, 129 (1976).
45. M. P. Seah, W. A. Dench, Surf. Interf. Anal. 1, 2 (1979).
46. D. Briggs, M. P. Seah, Practical Surface Analysis, J. Wiley & Sons (1983), p187.
47. D. A. Shirley, Phys. Rev. 135, 4709 (1972).
48. H. W. Hoppe, H.-H. Strehblow, Surf. Interf. Anal. 16, 271 (1990).
49. H.-H. Strehblow, Proceedings of 3rd K. Schwabe Corrosion Symposium, Zakopane, Poland (2000).
50. K. Asami, K. Hashimoto, S. Shimodaira, Corr. Sci. 17, 713 (1977).
51. P. Marcus, J. Oudar, I Olefjord, J. Microsc. Spectrosc. Electron 4, 63 (1979).
52. B. P. Löchel, H.-H. Strehblow, J. Electrochem. Soc., 131, 713 (1984).
53. F. T. Wagner, T. E. Moylan, J. Electrochem. Soc. 136, 2498 (1989).
54. D. F. Mitchell, G. I. Sproule, M-J. Graham, Appl. Surf. Sci. 21, 199 (185).
55. K. J. Vetter, Electrochemical Kinetics, Academic Press, New York 1967, p. 780.
56. K. E. Heusler, in Passivity of Metals, R. P. Frankenthal, J. Kruger editors, Electrochem. Soc. Princeton NJ, 790 (1978).
57. A. Foelske, H.-H. Strehblow, Surf. Interf. Anal. 29, 548 (2000).
58. H.-H. Strehlow, A. Foelske, Proceedings of the Corrosion Symposium, Electrochem. Soc./ISE Meeting, San Francisco, USA, September 2001.
59. W. Feitknecht, W, Lotmar, Helv. Chim. Acta, 18, 1369 (1935).
60. H.-H. Strehblow, B. Titze Electrochim. Acta 25, 839 (1980).
61. H. D. Speckmann, S. Haupt, H.-H. Strehblow, Surf. Interf. Anal. 11, 148 (1988).
62. H.-H. Strehblow, H. D. Speckmann, Werkstoffe Korr. 35, 512 (1984).
63. H. D. Speckmann, M. M. Lohrengel, J. W. Schultze, H.-H. Strehblow, Ber. Bunsen Ges. Phys. Chem. 89, 392 (1985).
64. M. M. Lohrengel, J. W. Schultze, H. D., Speckmann, H.-H. Strehblow, Electrochim. Acta, 32, 733 (1987).
65. S. Haupt, H.-H. Strehblow, J. Electroanal. Chem, 216, 229 (1987).
66. S. Haupt, H.-H. Strehblow, J. Electroanal. Chem. 228, 365 (1987).
67. K. J. Vetter Electrochemical Kinetics, Academic Press, New York, 757 (1967).
68. H. W. Hoppe, H.-H. Strehblow, Surf. Interf. Anal. 14, 121 (1989).
69. S. Haupt. H.-H. Strehblow, Corr. Sci. 37, 43 (1995).
70. C. Calinski, H.-H. Strehblow, J. Electrochem. Soc. 136, 1328 (1989).

71. H.-H. Strehblow, C. Calinski, S. Simson, P. Druska, H.-W. Hoppe, A. Rossi, European Symposium on Modification of Passive Films, Paris (1933). European Federation of Corrosion Publication 12, 46 (1994), Editors P. Marcus, B. Baroux, M. Keddam.
72. V. P. Keller, H.-H. Strehblow; submitted.
73. H.-W. Hoppe, S. Haupt, H.-H. Strehblow, Surf. Interf. Anal. 21, 514 (1994).
74. A. Rossi, C. Calinski, H.-W. Hoppe, H.-H. Strehblow, Surf. Interf. Anal. 18, 269 (1992).
75. Jabs, P. Borthen, H.-H. Strehblow, J. Electrochem. Soc. 144, 1231 (1997).
76. D. Schaepers, H.-H. Strehblow, J. Electrochem. Soc. 142, 2210 (1995).
77. D. Schaepers, H,-H. Strehblow, Corr Sci. 39, 2193 (1997).
78. C. Schmidt, H.-H.Strehblow, J. Electrochem. Soc. 145, 834 (1998).
79. C. Schmidt, H.-H. Strehblow, Surf. Interf. Anal. 27, 984 (1999).
80. U. Wolff, dissertation, Universität Dresden (1999).
81. P. Druska, H.-H. Strehblow, S. Golledge, Corr. Sci. 38, 835 (1996).
82. P. Druska, H.-H. Strehblow, Corr. Sci. 38, 1369 (1996).
83. H.-H. Strehblow, C. J. Doherty, J. Electrochem. Soc. 125, 30 (1978).
84. H.-H. Strehblow, C. M. Melliar Smith, W. M. Augustyniak, J. Electrochem. Soc. 125, 916 (1978).
85. H. Habazaki, M. A. Paez, K. Shimizu, P. Skeldon, G. E. Thompson, G. C. Wood and X. Zhou, Corrosion Science 38, 1033–1042 (1996), X Zhou, G. E. Thompson, H. Habazaki, K. Shimizu, P. Skeldon and G. C. Wood, Thin Solid Films 293, 327–332 (1997).
86. H.-H. Strehblow, U. Collisi, P. Druska, Int. Symp. on Control of Copper and Copper Alloys Oxidation. Rouen 1992, Édition de la Revue de Metallurgie, Paris, 33 (1993).
87. C. Noguet, M. Tapiero, J. P. Zielinger, Phys. Stat Sol. (a) 24, 565 (1974).
88. J. P. Zielinger, M.Tapiero, C. Noguet, Phys. Stat. Sol. (a) 33, 155 (1985).
89. V. Maurice, H.-H. Strehlow, P. Marcus, J. Electrochem. Soc. 146, 524 (1999).
90. H.-H. Strehblow, V. Maurice, P. Marcus, Electrochim. Acta 46, 3755 (2001).
91. W. Schmickler, J. W. Schultze, in Modern Aspects of Electrochemistry, 17, J. O'M. Bockris, B. E. Conway, R. E. White editors, Plenum Publishing Corporation, p. 357, (1986).
92. E. R. Kötz, H. Neff and K. Müller, J. Electroanal. Chem., 215, 331 (1986).
93. S. Trasatti, J. Electroanal. Chem., 52, 313 (1974).
94. D. M. Kolb., Z. Phys. Chem. NF, 154, 179 (1987).
95. R. Gomer and S. Tryson, J. Chem. Phys, 66, 4413 (1977).
96. D. Lützenkirchen-Hecht and H.-H. Strehblow, Electrochim. Acta, 43, 2957 (1998).
97. U. Collisi, H.-H. Strehblow, J. Electroanal. Chem., 210, 213 (1986).
98. U. Collisi, H.-H. Strehblow, J. Electroanal. Chem., 284, 385 (1990).
99. S. Brahms, S. Nikitine, Solid State Comm. 3209 (1965).
100. Sander, H.-H. Strehblow, J. K. Dohrmann, J. Phys. Chem. 85, 447 (1981).
101. J. W. Schultze, Electrochim. Acta 45 3193 (2000).
102. W. Gärtner, Phys. Rev. 116, 84 (1959).
103. D. M. Kolb, Electrochim. Acta, 45, 2837 (2000).
104. E. Budevski, G. Staikov, W. J. Lorenz, Electrochemical Phase Formation and Growth, Verlag Chemie, Weinheim, Germany, (1996).
105. J. Lipkowski, P. N. Ross, Imaging of Surfaces and Interfaces, Wiley-VCH, New York, (1999).
106. L. Bosio, R. Cortes, A. Defrain, M. Froment, J. Electroanal. Chem. 180, 265 (1984).
107. H.-H. Strehblow, P. Borthen, D. Lützenkirchen-Hecht, Synchrotron Radiation News 11, 12 (1998).
108. P. Borthen, doctoral dissertation, Heinrich–Heine–Universität, Düsseldorf, Germany (1996).

109. J. J. Rehr, R. C. Albers, S. L. Zabinsky, Phys. Rev. Lett. 69, 3397 (1992).
110. P. Borthen, H.-H. Strehblow, Physica B, 208, 8209, 421 (1995).
111. P. Borthen, H.-H. Strehblow, Phys. Rev. B52, 3017 (1995).
112. G. G. Long, J. Kruger, D. R. Black, M. Kurayama, J. Electroanal. Chem. 150, 603 (1983).
113. A. J. Davenport, M. Sansone, J. Electrochem. Soc. 142, 725 (1995).
114a. P. Schmuki, S. Virtanen, A. Davenport, C. Vitus, J. Electrochem. Soc. 143, 574 (1996).
144b. S. Virtanen, P. Schmuki, M. Büchler, H. S. Isaacs, J. Electrochem. Soc. 146, 4087 (1999).
115. Borthen, H.-H. Strehblow, J. Phys. IV France, 7, C–187 (1997).
116. D. Hecht, P. Borthen, H.-H. Strehblow, Surf. Sci. 365, 263 (1996).
117. V. Scattarin, P. L. Bellon, A. Salkind, J. Electrochem. Soc. 108, 819 (1961).
118. A. N. Mansur, J. Phys. Chem. 94, 1006 (1990).
119. D. Hecht, doctoral dissertation, Universität Düsseldorf (1997).
120. P. Druska, H.-H. Strehblow, J. Electroanal. Chem. 335, 55 (1992).
121. P. Borthen, B. J. Hwang, D. M. Kolb, J. Phys. Chem. B, 104, 5078 (2000).
122. M. F. Toney, A. J. Davenport, L. J. Oblonsky, M. P. Ryan, C. M. Vitus, Phys. Rev. Lett. 79, 4282 (1997).
123. M. P. Ryan, R. C. Newman, G. E. Thomson, J. Electrochem. Soc. 142, L177 (1995).
124. H.-H. Strehblow, Mechanisms of Pitting Corrosion, in Corrosion Mechanisms in Theory and Practice, P. Marcus editor, Marcel Dekker, Inc. (2002).
125. J. Wintterlin, Adv. Catal. 45, 131 (2000).
126. L. Zitzler, B. Gleich, O. M. Magnussen, R. J. Behm, Proc. Electrochem. Soc. 99–28, 29 (2000).
127. D. Zuili, V. Maurice, P. Marcus, J. Phys. Chem. B 103, 7896 (1999).
128. H.-H. Strehblow, V. Maurice, P. Marcus, Electrochim. Acta 46, 3755 (2001).
129. J. Kunze, V. Maurice, L. H. Klein, H.-H. Strehblow, P. Marcus, J. Phys. Chem. B, 105, 4263 (2001).
130. V. Maurice, H.-H. Strehblow, P. Marcus, Surf. Sci. 458, 185 (2000).
131. S. Härtinger, B. Pettinger, K. Doblhofer, J. Electroanal. Chem. 397, 335 (1995).
132. H. Y. H. Chan, C. G. Takoudis. M. J. Weaver, J. Phys. Che,. B 103, 357 (1999).
133. B. J. Cruikshank, D. D. Sneddon, A. A. Gewirth, Surf. Sci. 281, L308 (1993).
134. J. R. LaGraff, A. A. Gewirth, Surf. Sci. 326, L461 (1995).
135. F. Besenbacher, J. K. Norskov, Prog. Surf. Sci. 44, 5 (1993).
136. A. Drexler, Diploma thesis, Heinrich–Heine–Universität, Düsseldorf, (2000).
137. J. Kunze, H.-H. Strehblow, unpublished results.
138. N. Ikemiya, T. Kubo, S. Hara, Surf. Sci. 373, 81 (1995).
139. D. Zuili, V. Maurice, P. Marcus, J. Electrochem. Soc. 147, 1393 (2000).
140. O. M Magnussen, J. Scherer, B. M. Ocko, R. J. Behm, J. Phys. Chem. B, 104, 1222 (2000).
141. F. Rohr, K. Wirth, J. Libuda, D. Cappus, M. Bäumer, H.-J. Freund, Surf. Sci. 315, L977 (1994).
142. H.-H. Strehblow, Werkstoffe Korrosion, 35, 437 (1984).
143. H.-H. Strehblow in Corrosion Mechanisms in Theory and Praxis, P. Marcus, J. Oudar editors, Marcel Dekker inc., New York page 201 (1995), 2nd edition page 243, (2002).
144. H.-H. Strehblow, B. Titze, Corr. Sci. 17, 461 (1977).
145. S. Szlarska-Smialowska, Pitting Corrosion of Metals, NACE, Houston Texas, (1986).
146. H. Böhni, in Corrosion Mechanisms, F. Mansfeld editor, Marcel Dekker inc., New York, 285 (1987).